Pramana – journal of physics

Editor

R Nityananda

Raman Research Institute, Bangalore

Associate Editor

H R Krishnamurthy

Indian Institute of Science, Bangalore

Editorial Board

G S Agarwal, *University of Hyderabad, Hyderabad*
V Balakrishnan, *Indian Institute of Technology, Madras*
M Barma, *Tata Institute of Fundamental Research, Bombay*
P Chaddah, *Centre for Advanced Technology, Indore*
B M Deb, *Panjab University, Chandigarh*
P K Kaw, *Institute for Plasma Research, Gandhinagar*
H S Mani, *Indian Institute of Technology, Kanpur*
N Mukunda, *Indian Institute of Science, Bangalore*
T Padmanabhan, *Inter-University Centre for Astronomy and Astrophysics, Pune*
J C Parikh, *Physical Research Laboratory, Ahmedabad*
G Rajasekaran, *Institute of Mathematical Sciences, Madras*
V S Ramamurthy, *Institute of Physics, Bhubaneswar*
R Ramaswamy, *Jawaharlal Nehru University, New Delhi*
K R Rao, *Bhabha Atomic Research Centre, Bombay*
Probir Roy, *Tata Institute of Fundamental Research, Bombay*
A K Sood, *Indian Institute of Science, Bangalore*

Editor of Publications of the Academy

G Srinivasan

Raman Research Institute, Bangalore

Subscription Rates
(Effective from 1989)

All countries except India	1 year	3 years	5 years
(Price includes AIR MAIL charges)	US$ 175	$ 470	$ 700
India	1 year Rs. 100	10 years (1989–1998 only) Rs. 500	

All correspondence regarding subscription should be addressed to the **Circulation Department** of the Academy

Editorial Office

Indian Academy of Sciences, C V Raman Avenue,
P.B. No. 8005, Bangalore 560080, India

Telephone: 334 2546
Telex: 845-2178 ACAD IN
Telefax: 91-80-334 6094

© 1994 by the Indian Academy of Sciences. All rights reserved.

"Information for contributions" is printed in the last issue of every volume.

Pramana – journal of physics

Volume 43
1994

Published by The Indian Academy of Sciences
Bangalore 560 080

Pramana – journal of physics

Editor

R Nityananda
Raman Research Institute, Bangalore

Associate Editor

H R Krishnamurthy
Indian Institute of Science, Bangalore

Editorial Board

G S Agarwal, *University of Hyderabad, Hyderabad*
V Balakrishnan, *Indian Institute of Technology, Madras*
M Barma, *Tata Institute of Fundamental Research, Bombay*
P Chaddah, *Centre for Advanced Technology, Indore*
B M Deb, *Panjab University, Chandigarh*
P K Kaw, *Institute for Plasma Research, Gandhinagar*
H S Mani, *Indian Institute of Technology, Kanpur*
N Mukunda, *Indian Institute of Science Bangalore*
T Padmanabhan, *Inter-University Centre for Astronomy and Astrophysics, Pune*
J C Parikh, *Physical Research Laboratory, Ahmedabad*
G Rajasekaran, *Institute of Mathematical Sciences, Madras*
V S Ramamurthy, *Institute of Physics, Bhubaneswar*
R Ramaswamy, *Jawaharlal Nehru University, New Delhi*
K R Rao, *Bhabha Atomic Research Centre, Bombay*
Probir Roy, *Tata Institute of Fundamental Research, Bombay*
A K Sood, *Indian Institute of Science, Bangalore*

Editor of Publications of the Academy

G Srinivasan
Raman Research Institute, Bangalore

Subscription Rates
(Effective from 1989)

All countries except India	1 year	3 years	5 years
(Price includes AIR MAIL charges)	US$ 175	$ 470	$ 700
India	1 year Rs. 100	10 years (1989–1998 only) Rs. 500	

All correspondence regarding subscription should be addressed to the **Circulation Department** of the Academy

Editorial Office

Indian Academy of Sciences, C V Raman Avenue,
P.B. No. 8005, Bangalore 560080, India

Telephone: 3342546
Telex: 845-2178 ACAD IN
Telefax: 91-80-3346094

© 1994 by the Indian Academy of Sciences. All rights reserved.

"Information for contributors" is printed in the last issue of every volume.

Pramana – journal of physics

CONTENTS – VOLUME 43

(July–December 1994)

Number 1

Search for a precursor crystal-to-crystal phase transition to amorphization in α-GeO_2 and α-$AlPO_4$ under pressure ..... *M S Somayazulu, Nandini Garg, Surinder M Sharma and S K Sikka* 1

Effect of Fe substitution on the thermal expansion of the high T_c superconductor $Y_1Ba_2Cu_3O_y$ ..... *Ashok Rao, Om Prakash, S N Das and P N Dheer* 11

Magnetism, exchange and crystal field parameters in the orbitally unquenched Ising antiferromagnet $FePS_3$ ..... *Nirmala Chandrasekharan and Sukumaran Vasudevan* 21

X-ray diffraction studies of RbBr–RbI mixed crystals ..... *T Kumara Swamy, K G Subhadra and D B Sirdeshmukh* 33

Interplay of superconductivity and antiferromagnetism in $SmRh_4B_4$ ..... *T C Loya and S L Kakani* 41

Photoconductivity and dark conductivity studies of solution-gas interface grown Ag_2S films ..... *P S Nikam and C B Shinde* 55

Enhanced bistability with the line-narrowed modes in a nonlinear modulated index Fabry–Perot cavity ..... *S Dutta Gupta* 67

New band system of MnSe molecule ..... *K N Uttam, R Gopal and M M Joshi* 73

Thermal diffusion factors of hydrogenic trace mixtures with helium by column calibration factor ..... *G Dasgupta, A K Dutta and S Acharyya* 81

Construction of broadband homonuclear TOCSY sequences via numerical optimization ..... *N Sambasiva Rao and Narsimha Reddy* 91

Design and fabrication of a high temperature X-ray powder diffraction camera ..... *Mohd. Ateequddin, K A Hussain, K G Subhadra and D B Sirdeshmukh* 101

Number 2

Stationary anharmonic oscillators in the particle-in-a-box basis: Near-exact results ..... *A K Chandra and K Bhattacharyya* 117

First-order transition in a 2D classical XY-model using microcanonical Monte Carlo simulations ..... *Smita Ota and S B Ota* 129

Perturbative and nonperturbative quark masses in structure functions ..... *D K Choudhury and Ranjita Deka* 139

Electromagnetic mass differences of t-flavored hadrons in modified bag model .... *Bishwaranjan Dash, Sripati Kumar Nayak and Lambodar P Singh* 155

Single nucleon distribution based on shell-model and matrix ensemble theory ..... *Nazakat Ullah* 165

Electron impact double ionization of Ba and Ba^+ ..... *L K Jha, S N Chatterjee and B N Roy* 169

Use of a diabatic molecular expansion in studies on electron capture by He^{2+} ions in helium at keV energies ..... *C Chaudhuri, S Sanyal (nee Ganguly) and T K Rai Dastidar* 175

Number 3

Second order elastic anomalies in barium titanate from orthorhombic to rhombohedral phase transition ..... *B Subramanyam* 181

High pressure studies on $AgI-Ag_2O-MoO_3$ glasses ..... *B Vaidhyanathan, S Asokan and K J Rao* 189

Investigation of phonon anomalies in intermediate valence compounds SmS and $Sm_{0.75}Y_{0.25}S$ ..... *Prafulla Kumar Jha and Sankar P Sanyal* 193

Computation of collective modes and acoustic investigations at different temperatures of vitrous silica ..... *R V Gopala Rao and R Venkatesh* 201

Even harmonics of AC susceptibility in some sintered pellets of high temperature superconductors ..... *A Das, A Bajpai, A Banerjee and R Srinivasan* 211

Electric and dielectric properties of solution-gas interface grown amorphous AgCl films ..... *P S Nikam and K A Pathan* 219

Overtone spectroscopy of benzaldehyde ..... *P K Srivastava, G Ullas and S B Rai* 231

Fluorescence quenching in dyes under an optically thin approximation ..... *George C Chennattucherry, G Ajithkumar and N V Unnikrishnan* 237

Photoconductivity studies of $(PbCrO_4-HgO-ZnO)$ composites ..... *Sadhana Devi and S G Prakash* 245

Number 4

A basis-free approach to time-reversal for symmetry groups ..... *L C Biedenharn and E C G Sudarshan* 255

The Lorentz-Dirac equation in curved spaces ..... *Jose L López-Bonilla, Jesús Morales and Marco A Rosales* 273

Energy levels of the Schrödinger equation for some rational potentials in two-dimensional space using the inner product technique ..... *M R M Witwit and J P Killingbeck* 279

A new formalism for the statistical dynamics of vector spin systems ..... *Kamlesh Kumari and Deepak Kumar* 289

Collective mechanism for nuclear stopping and transverse flow in heavy-ion collisions ..... *Jitesh R Bhatt, Predhiman K Kaw and Jitendra C Parikh* 307

Effect of two body core on the charge form factor of ^{3}He including three body force and meson exchange current ..... *Kalyani Prasad Kanta and Tapan Kumar Das* 313

Distribution of fusion barriers ..... *A K Mohanty and S K Kataria* 319

Level structure in the odd-odd nucleus ^{180}Re ..... *Ashok Kumar Jain, Prakash C Sood and Raymond K Sheline* 339

Number 5

Sound velocity in binary liquid mixtures and the statistical mechanical theories ..... *J D Pandey, Shikha, A K Shukla and Anil K Singh* 353

Isothermal compressibility and sound velocity of binary liquid systems: Application of hard sphere models ..... *J D Pandey, P Jain and V Vyas* 361

Transport coefficients of quasicrystals ..... *K Rama Mohana Rao and P Hemagiri Rao* 373

Phonons and periodons in IV–VI semiconductor superlattices ..... *Nabonita D Chowdhury and Sankar P Sanyal* 379

Electronic contribution to electric field gradient in β-gallium ..... *B K Acharya and N C Mohapatra* 391

Application of laser beam deflection technique to study the diffusion process in electrolyte solutions ..... *Achamma Kurian, C V Bindhu, S S Harilal, Riju C Issac, V P N Nampoori and C P G Vallabhan* 401

Addendum

Electric field gradient in transition metal: Scandium ..... *B B Panigrahi and N C Mohapatra* 407

Corrigendum 409

Number 6

A new perturbative approach to the classical anharmonic oscillator ..... *S S Vasan and M Seetharaman* 411

Scaling relations in the Lyapunov exponents of one dimensional maps ..... *P R Krishnan Nair, V M Nandakumaran and G Ambika* 421

Controlling chaos: Stabilization of fixed points and creation of new stable attractors in 1-D maps ..... *Sangeeta D Gadre and V S Varma* 431

Mass spectrum of elementary particles in a temperature-dependent model..... *G P Malik, Santokh Singh and V S Varma* 443

New answer to the solar neutrino problem ..... *Marc Dixmier* 453

Dynamic color screening in a classical quark plasma..... *Jitesh R Bhatt, Predhiman K Kaw and Jitendra C Parikh* 467

Systematic trends in the line strengths of E1 transitions in the oxygen isoelectronic sequence ..... *Anju Agrawal and K L Baluja* 477

Einstein A-coefficients for rotational transitions in the HN_2O^+ ..... *S Chandra and A K Sharma* 487

Vibrationally elastic $e^- - H_2O$ scattering at intermediate energies ..... *K N Joshipura, Minaxi Vinodkumar and P M Patel* 495

String theory in five dimensional cosmological models..... *Subenoy Chakraborty and Gopal Chandra Nandy* 503

Subject Index 509

Author Index 513

Information for Contributors

PRAMANA
— journal of
physics

© Printed in India

Vol. 43, No. 1,
July 1994
pp. 1–9

Search for a precursor crystal-to-crystal phase transition to amorphization in α-GeO_2 and α-$AlPO_4$ under pressure

M S SOMAYAZULU, NANDINI GARG, SURINDER M SHARMA and S K SIKKA
High Pressure Physics Division, Bhabha Atomic Research Centre, Bombay 400085, India

MS received 25 April 1994

Abstract. Recent X-ray diffraction studies on α-quartz (SiO_2) by Kingma *et al* [1], have shown the occurrence of a reversible, crystalline-to-crystalline, phase transition just prior to amorphization at ≈ 21 GPa. This precursor transition has also been confirmed by our recent molecular dynamics simulation study [2]. In order to investigate the possibility of a similar behaviour in other isostructural compounds, which also undergo pressure induced amorphization, α-GeO_2 and α-$AlPO_4$ (berlinite form) were studied using energy dispersive X-ray diffraction. In either of these materials, no such phase transition is detected prior to amorphization. The onset of amorphization and its reversal is found to be time dependent in GeO_2.

Keywords. Precursor phase transition; pressure-induced amorphization; α-GeO_2; α-$AlPO_4$; high pressure energy dispersive X-ray diffraction.

PACS Nos 61·42; 61·50; 62·50

1. Introduction

Over the last few years there have been a number of theoretical and experimental studies on the pressure-induced amorphization in α-quartz. Some of the striking features of the amorphization have been the direct observation of the change in Si coordination from 4 to ≈ 6 by IR spectroscopy [3], anisotropy of elastic constants in the amorphous phase [4], and the occurrence of a reversible, crystalline-to- crystalline phase transition just prior to amorphization [5]. Various molecular dynamics simulation studies have also supported these experimental observations [5–8, 2, 9]. The observation of the reversible phase transition at ≈ 21 GPa in α-quartz phase of SiO_2 has added a new dimension to this problem [1]. These authors have attributed the Brillouin scattering results regarding the anisotropy of amorphous phase as due to the presence of traces of the precursor crystalline phase in the amorphous phase [1]. We have shown through our MD results that the precursor phase in SiO_2 is a distorted superstructure of α-quartz phase. The super-structure is consistent with a recent proposal that $(\frac{1}{3}, \frac{1}{3}, 0)$ phonon mode goes soft in α-quartz phase prior to amorphization [6]. The d values in the diffraction patterns generated from our MD results are in good agreement with those from the experiments of Kingma *et al.*

α-GeO_2 is an excellent high pressure model for α-quartz (SiO_2), since the GeO_2 tetrahedra are more deformed in comparison to SiO_2 in the α-quartz phase [10, 11]. In fact the ambient structure of α-GeO_2 compares well with the structure of α-SiO_2 at 10 GPa. At this pressure the intertetrahedral Si–O–Si and Ge–O–Ge angles have

an average value of 130°. Although changes in Ge–O coordination from four to six is observed at 6 GPa [12, 11] complete amorphization is observed to occur above 20 GPa at which pressure the Raman spectrum is found to be similar to the GeO_2 glass. Interestingly selective area, HREM studies on decompressed samples of polycrystalline GeO_2 (decompressed from 20 GPa) shows new, non-quartz like diffraction spots [13]. Recent shock experiments on α-GeO_2, show the existence of new diffraction peak at $d = 4{\cdot}04$ Å and $3{\cdot}11$ Å, in the sample recovered from $6{\cdot}8$ GPa [14]. However, the sample shocked to 10 GPa does not show these additional lines.

The berlinite phase of $AlPO_4$ is isostructural to α-quartz, with the Al and P atoms replacing Si atoms in alternating polyhedra. The room pressure structure of berlinite $AlPO_4$ is closer to α-SiO_2 (as compared to α-GeO_2) in that the Al–O–P angle is 142° [15], (Si–O–Si angle in α-SiO_2 is 144°). $AlPO_4$ has been shown to become 'X-ray amorphous' at 12 GPa [16] at which pressure the Raman spectrum also disappears [17]. Single crystal studies [18] indicate the amorphization to be complete around 18 GPa. In contrast to α-GeO_2 and α-SiO_2, $AlPO_4$ reverts back to the crystalline phase on pressure release at ~ 7 GPa. In fact, the reversibility has been shown to have memory, since the single crystal reverts back to an identical crystallographic configuration when decompressed from the amorphous phase [18]. Recent Brillouin scattering studies on $AlPO_4$ [19] have confirmed the existence of elastic anisotropy in the pressure-amorphized phase (above 15 GPa) and the subsequent reversal to the starting crystalline phase on decompression. However, lack of complete reversibility has been noted in recent non-hydrostatic experiments [20].

Both of these compounds exist not only in the isostructural forms of α-quartz but also in other polymorphic forms of SiO_2. This underlying similarity of the three materials α-SiO_2, α-GeO_2 and α-$AlPO_4$ is also expected to show up in the similar nature of pressure-induced amorphization brought about by distortion of the inter-tetrahedral angles and change in coordination from four to six [21]. This prompted us to carefully investigate the existence of any new precursor transformation in these materials.

2. Experimental

High pressure energy dispersive X-ray diffraction (EDXRD) studies on polycrystalline samples of α-GeO_2 and $AlPO_4$ were done using the system described elsewhere [22]. Samples were loaded into stainless steel gaskets with a hole size of ≈ 150–$200\,\mu$. α-GeO_2 was prepared by S C Sabharwal of Technical Physics and Prototype Engineering Division of BARC by keeping crystalline GeO_2 in the high temperature stability field of α-phase and then quenching it. For GeO_2, in one experiment, methanol-ethanol and in two experiments Si oil (trade name DC704) was used, as the pressure medium. The latter was used, as in some experiments at high pressures, GeO_2 samples were reported to react with methanol-ethanol mixture [23]. However, in our study we find that, visually, GeO_2 particles in the methanol-ethanol medium do not undergo any substantial change in the range of pressure of our interest (≈ 11 GPa). Also in the case of retrieval, we get back the initial diffraction pattern of α-GeO_2. Sample pressure was determined using the ruby pressure scale [24, 25]. In an effort to investigate the possibility of phase transformations occurring during decompression, X-ray data on pressure release were also collected from various terminal pressures.

3. Results

The diffraction data from our experiments on α-GeO_2 are presented in figures 1–4. The data have been scaled with respect to the MoK_β fluorescence peak. As is evident from figure 1, the α-GeO_2 becomes 'X-ray amorphous' at ≈ 10 GPa. We also find that in GeO_2, both the onset of amorphization as well as its reversal/irreversal has considerable time dependence. Figure 2, shows the evolution of diffraction pattern at 9·4 GPa in experiment # 5, which uses DC704 oil as a pressure medium. The data of first three hours show clear diffraction pattern. Subsequently the diffraction pattern deteriorates progressively. For example, after about 44 hours diffraction patterns is

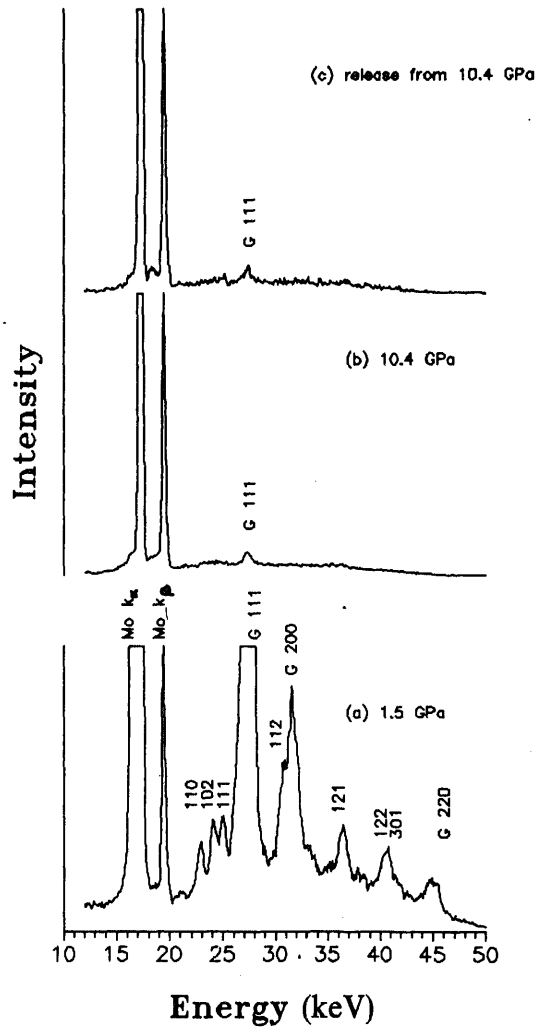

Figure 1. Diffraction pattern of α-GeO_2 at (a) 1·5 GPa, (b) 10·4 GPa and (c) after the release of pressure from 10·4 GPa. Gasket peaks are marked as G hkl. At higher pressures, the intensity of these peaks decreases due to widening of the gasket hole which was initially comparable to the collimated X-ray beam of $\sim 200\,\mu$. Pressure medium in this experiment was Si oil.

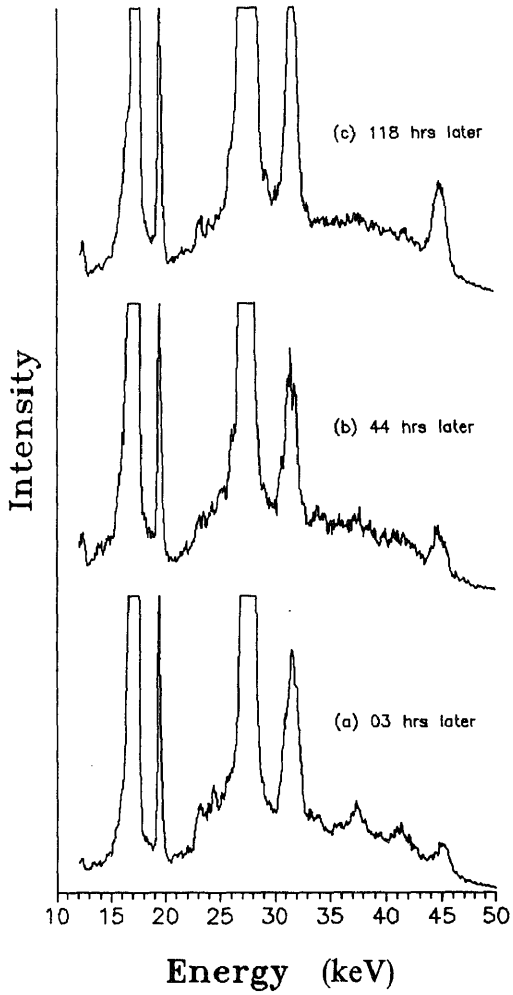

Figure 2. Time evolution of amorphous phase from α-GeO_2 at 9·4 GPa. (a) After 3 hrs of raising the pressure to 9·4 GPa, (b) after 44 hrs. and (c) after 118 hrs. Remnant peaks are Mok_α, MoK_β and gasket peaks as in figure 1. Higher intensity of gasket diffraction peaks here is due to the smaller gasket hole ($\sim 150\,\mu$) compared to that of figure 1 and figure 3. Si oil was used as a pressure medium in this run.

barely visible and even this is completely lost after about 116 hr. And on release of pressure, even after 17 hours there is no reappearance of diffraction pattern. The ruby spectrum at 9·4 GPa shows that the pressure was non-hydrostatic as the R_1-R_2 separation was ≈ 7 Å in constant to ≈ 14 Å in truly hydrostatic medium ([26]). The time dependence of emergence of crystalline phase on decompression depends on both the peak pressure as well as the deviation from the hydrostatic environment. We find that the samples pressurized beyond 11 GPa do not show re-emergence of the crystalline phase to within a few hours, but the ones loaded to smaller peak pressures do show reversibility. For example in run #3, in which methanol-ethanol is used as a pressure medium, we find that amorphous phase reverts back to crystalline phase after some time. Figure 3a shows complete loss of diffraction pattern at high

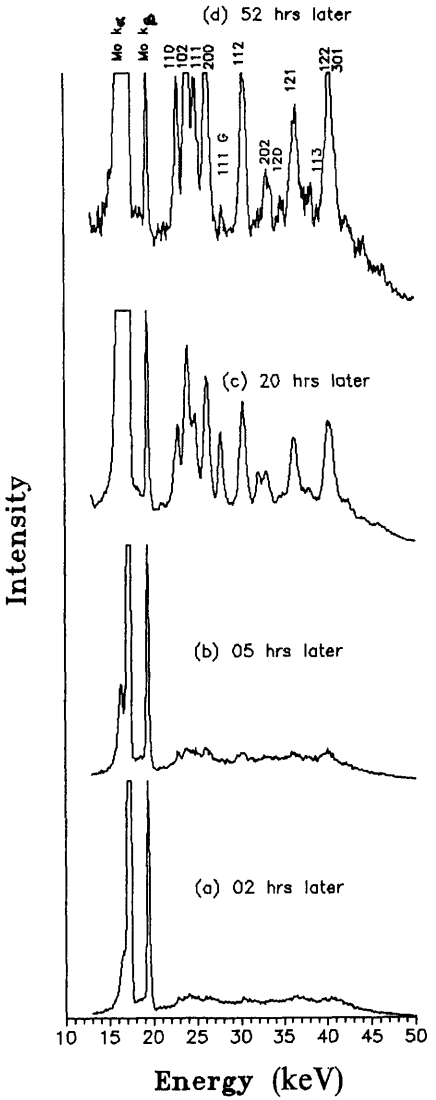

Figure 3. Evolution of crystalline α-GeO_2 from the amorphous phase after the release of pressure. (a) 2 hrs after the pressure release, (b) 5 hrs after the pressure release, (c) 20 hrs after the pressure release and (d) 52 hrs after the release of pressure. Methanol-ethanol mixture was used as a pressure medium in this experiment.

pressures. On unloading this, up to two hours there is no diffraction pattern, and therefore stays amorphous. But after about five hours a weak diffraction pattern appears which becomes substantially strong after 20 hr. After about 48 hr the material seems to have returned completely to crystalline form. Figure 4 shows the diffraction patterns at 1·5 and 7 GPa on compression and on release from 7 GPa. The decompressed sample is then raised to a pressure of 8·4 GPa which is also shown here. The diffraction pattern at still higher pressure viz. 9·4 GPa of this run has been given above in figure 2. On raising the pressure to 7 GPa, the background rises substantially

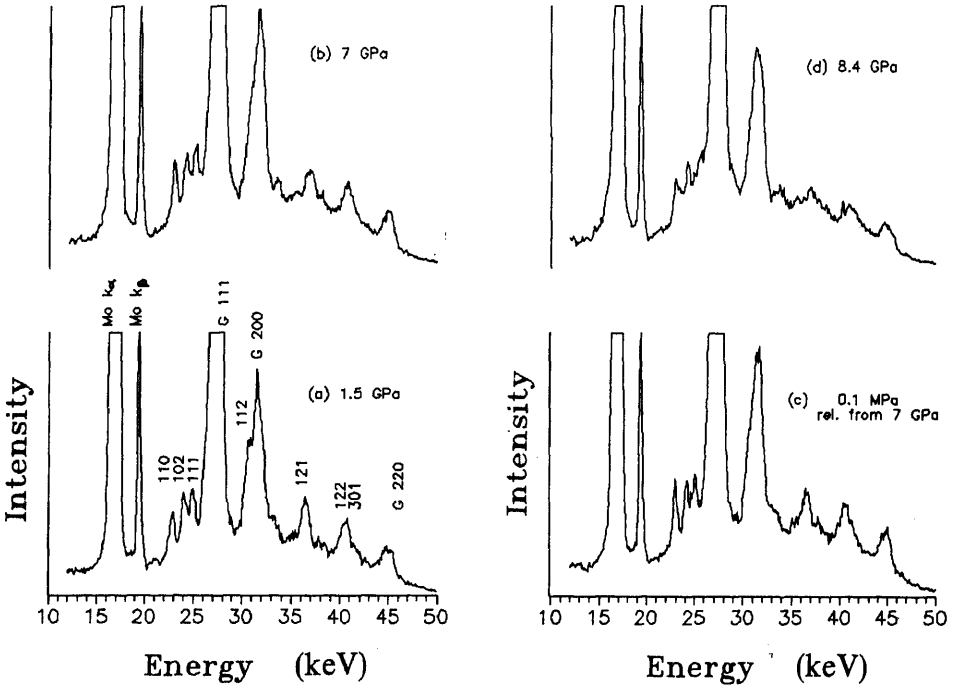

Figure 4. The diffraction pattern of α-GeO_2 at (a) 1·5 GPa, (b) 7 GPa, (c) after the release from 7 GPa and (d) the decompressed phase of (c) is raised to 8·4 GPa. Gasket peaks are marked as G hkl as in figure 2.

and irreversibly around 30 keV, but without much change in the FWHM of the overriding diffraction peaks. This should be contrasted with the observations of Suresh *et al* [14] who find irreversible broadening of all Bragg peaks on shock loading to 6·8 GPa. We also carefully checked the *d* values reported in the shock experiments and found no evidence of these additional diffraction lines in our experiments. In fact in all our experiments, no new diffraction lines are observed in α-GeO_2 prior to amorphization, or on decompression from various terminal pressures.

$AlPO_4$ is observed to become 'X-ray amorphous' between 13 and 15 GPa in complete agreement with the results of Sankaran *et al* [16]. As in the case of α-GeO_2, no new diffraction lines are observed prior to amorphization. On decompression, the crystalline X-ray pattern of the starting phase re-emerges with some hysteresis. Since the X-ray data for $AlPO_4$ is no different from our earlier data [16], we have chosen not to show the X-ray data from the current set of experiments. It may be noted that the $AlPO_4$ sample used for this run is from the same batch used by Sankaran *et al* [16].

4. Discussion

The present study on α-GeO_2 and $AlPO_4$ indicates that there exists no precursor phase prior to amorphization in either of the two materials. In contrast to the results of shock loading of GeO_2 [14], our studies show no new diffraction peaks on compression or decompression from pressures in the region 7–9 GPa. We also find that irreversibility of crystalline to amorphous phase transition may be dependent on the pressure as well as the amount of non-hydrostatic stresses present in an experiment.

It is particularly interesting to note that when the ruby spectrum shows the existence of non-hydrostatic stresses, GeO_2 transforms slowly but irreversibly to an amorphous phase at 9·4 GPa. A more hydrostatic medium like ethanol-methanol raises the pressure of irreversible amorphization to beyond 10 GPa. This signifies the importance of shear stresses in aiding the crystal to amorphous phase transition. Our experimental results suggest that the existence of non-hydrostatic stresses not only reduces the pressure of transformation, it also brings in irreversibility. Role of shear stresses in bringing about irreversibility in amorphization has also been noted earlier [27]. In fact a substantial amorphization of α-GeO_2 on shock loading this material to less than 7 GPa supports our suggestion. It should be noted that high resolution electron microscopy (HREM) studies of Wolf *et al* [13] indicate the disorder present even in the samples recovered from 7 GPa. Their Raman scattering results also indicate substantial irreversible change at 8·7 GPa. Present studies indicate that these results are likely to be both time dependent as well as significantly dependent on the presence of non-hydrostatic stresses. This study points out another result that whenever there is irreversible pressure induced amorphization, the limit of irreversibility may have kinetics dependence. Alternatively, the irreversibility within the time period of measurement may have either large shear stresses or a pressure considerably higher than the equilibrium value. Therefore, there is a limiting compression, from where the crystalline phase could re-emerge thereby indicating a reversible amorphization. A similar feature has also been noted in lithium triborate by Lin *et al* [28] though they have not stated this categorically.

Also in two of our experiments where we used Si oil, there may be a large amount of non-hydrostatic stresses present at about 10 GPa. Therefore it is reasonable to presume that α-GeO_2 does not transform to any new phases prior to amorphization even under non-hydrostatic conditions. The decompression also does not lead to any new phases.

Single crystal optical micrography studies on the behaviour of α-$AlPO_4$ under pressure, have been extensively carried out by Kruger and Jeanloz [18]. They report the occurrence of twin bands close to the amorphization pressure. Similar formation of twin walls has also been shown to precede the new crystalline to crystalline phase transformation in α-quartz (SiO_2) [1]. The absence of a similar transition in $AlPO_4$, therefore, suggests that the two phenomena are not necessarily correlated.

The presence of precursor phase in α-SiO_2 and its absence in α-GeO_2 and in $AlPO_4$ may be understood by the following arguments. It is well known that the pressure induced transformations involve small movements in positions of atoms and in that sense they are by and large displacive. In fact form the mechanism point of view, it is possible to classify these transformations in terms of a well defined symmetry classification [29, 30]. Many transformations proceed through multistage steps of symmetry ascent and descent. In this multistage process any arbitrary initial phase can descend to the lowest symmetry amorphous phase. We have shown that recently observed phase transformations in sulphur [31] demonstrate this point of view elegantly [32]. In this the ambient orthorhombic phase transforms to a monoclinic phase at 5 GPa which becomes amorphous at $\approx$ 25 GPa. At 78 GPa, the amorphous phase ascends to a low symmetry crystalline structure which becomes base centred orthorhombic at 83 GPa. At 162 GPa sulphur reaches the highest symmetry in rhombohedral β-Po type phase. In $LiKSO_4$, $LiCsSO_4$ and $LiRbSO_4$ also one notes the symmetry descent prior to amorphization [33-37]. Similar symmetry lowering transformations have also been noted in C_{60} as well as C_{70} ([38,39]). In this context,

the symmetry descent observed in α-quartz by Kingma *et al*, interpreted by us from $P3_121$ to a monoclinic phase, confirms this picture. So it could have been acceptable to see lower symmetry phase preceding the amorphous phase in GeO_2 and $AlPO_4$ also. Only way these opposing results could be understood is that in these systems the kinetics of the lower symmetry phases is such that these exist as a transient. It may be noted that in our MD results the monoclinic phase evolves systematically as a transient structure as stated above. It is probable that under some appropriate stresses, temperatures, defects or impurity conditions this transient structure gets stabilized. It is known that the HREM images of sample decompressed from 20 GPa show lattice plane spacings that could not be indexed to either the quartz or the rutile phases [13]. This and the observation of additional diffraction lines in the retrieved samples of shock loaded GeO_2 ([14]) may provide material for speculation as to whether these are related to the transient structures.

In conclusion, we report careful EDXRD studies on α-GeO_2 and α-$AlPO_4$, close to amorphization pressures. No new diffraction lines were observed in either of the two materials in spite of the close structural relationship with α-quartz, in which a precursor phase transition, prior to amorphization under pressure, was observed. In contrast with the HREM studies and shock results on decompressed samples of α-GeO_2, no new diffraction lines were observed when decompressed from pressures as high as ≈ 9 GPa. Changes in diffraction patterns of α-GeO_2 are reversible up to ≈ 9 GPa, although substantial broadening of diffraction peaks sets in above 7 GPa. Time dependence is noted in both the evolution of amorphous phase as well as the reverse transition on pressure release.

References

[1] K J Kingma, R J Hemley, H K Mao and D R Veblen, *Phys. Rev. Lett.* **70**, 3927 (1993)
K J Kingma, C Meade, R J Hemley, H K Mao and D R Veblen, *Science* **259**, 666 (1993)

[2] M S Somayazulu, Surinder M Sharma and S K Sikka, *Phys. Rev. Lett.* (1994) (accepted)

[3] Q Williams, R J Hemley, M B Kruger, R Jeanloz, *J. Geophys. Res.* Dec. 1993

[4] L E Mc Neil and M Grimsditch, *Phys. Rev. Lett.*, **68**, 83 (1992)

[5] S L Chaplot and S K Sikka, *Solid State Phys.* (DAE, India) **C33**, 328 (1990)

[6] S L Chaplot and S K Sikka, *Phys. Rev.* **B47**, 5710 (1993)
S L Chaplot and S K Sikka, *Phys. Rev. Lett.* **71**, 2674 (1993)

[7] J S Tse and Klug D D, *Phys. Rev. Lett.*, **67**, 3559 (1991)
J S Tse and D D Klug, *Phys. Rev. Lett.* **70**, 174 (1993)

[8] M S Somayazulu, Surinder M Sharma, Nandini Garg, S L Chaplot and S K Sikka, *J. Phys. Condensed Matter.* **5**, 6345 (1993)
M S Somayazulu, Surinder M Sharma, S K Sikka, Nandini Garg, and S L Chaplot *in the Proceedings of XIV AIRAPT/APS meeting* (Colorado Springs, 1993)

[9] Wei Jin, Rajiv K Kalia, P Vashishta, J P Rino, *Phys. Rev. Lett.* **71**, 3146, 1993

[10] L Levien, C T Prewitt and D J Weidner, *Am. Mineral.* **65**, 920 (1980)

[11] J P Itie, A Polian, G Calas, J Petiau, A Fontaine and H Tolentino, *Phys. Rev. Lett.* **63**, 398 (1989)
J P Itie, A Polian, G Calas, J Petiau, A Fontaine and H Tolentino, *High Pres. Res.* **5**, 717 (1990)

[12] B Houser, N Alberding, R Ingalls and E D Crozier, *Phys. Rev.* **B37**, 6513 (1988)

[13] George H Wolf, S Wang, C A Herbst, D J Durben, W F Oliver, Z C Kang and K Halvorson, *High Pres. Res: Application to earth and planetary sciences.* edited by Y Syono and M H Manghnani (TERRAPUB, Tokyo, 1992) p. 503

[14] N Suresh, G Jyoti, S C Gupta, S K Sikka, Sangeeta and S C Sabharwal, *J. Appl. Phys.* (1994) (Communicated)
[15] N Thong and Schwarzenbach, *Acta. Crystallogr.* **A35**, 658 (1979)
[16] H Sankaran, Surinder M Sharma, S K Sikka and R Chidambaram, *Pramana – J. Phys.* **35**, 177 (1990)
[17] A Jayaraman, D L Wood and R G Maines, *Phys. Rev.* **B30**, 8316 (1987)
[18] M Kruger and R Jeanloz, *Science* **249**, 647 (1990)
[19] A Polian, M Grimsditch and E Philipot, *Phy. Rev. Lett.* **71**, 3143 (1993)
[20] P Cordier, J C Doukhan and J Peyronneau, *Phys. Chem. Miner.* **20**, 176 (1993)
[21] S K Sikka and Surinder M Sharma, *Curr. Sci.* **63**, 317 (1992)
[22] S K Sikka, H Sankaran, Surinder M Sharma, V Vijayakumar, B K Godwal and R Chidambaram, *Indian J. Pure Appl. Phys.* **27**, 472 (1989)
[23] J F Mammone and S K Sharma, *Year Book Carnegie Inst.* Washington, 640 (1979)
[24] G J Piermarini, S Block, J D Barnett and R A Forman, *J. Appl. Phys.* **46**, 2774 (1975)
[25] H K Mao, P M Bell, J W Shaner and D J Steinberg, *J. Appl. Phys.* **49**, 3276 (1978)
[26] Surinder M Sharma and Y M Gupta, *Phys. Rev.* **B43**, 879 (1991)
[27] S R Elliot, *Physics of amorphous materials* (Longmans, London, 1983)
[28] Y Lin, G Xiong, G Lan, H Wang and L Xu, *J. Phys. Chem. Solids* **55**, 113 (1994)
[29] A G Christy, *Acta Crystallogr.* **B49** 987 (1993)
[30] S C Gupta and R Chidambaram, *High pressure research*, 1994 (in print)
[31] H Luo, R G Greene and A L Ruoff, *Phys. Rev. Lett.* **71**, 2943
[32] S K Sikka and Surinder M Sharma, *in International conference on advances in physical metallurgy* (ICPM-94), March 9–11, 1994, Bombay, India
[33] H Sankaran, S K Sikka, Surinder M Sharma and R Chidambaram, *Phys. Rev.* **B38**, 170 (1988)
[34] F E A Melo, V Lemos, F Cerdeira and J M Filho, *Phys. Rev.* **B35**, 3633 (1987)
[35] A K Arora and T Sakuntala, *Solid State Commun.* **75**, 855 (1990)
[36] M N Shashikala, N Chandrabhas, K Jayaram, A Jayaraman and A K Sood, *J. Raman Spectrosc.* **24**, 129 (1993)
[37] M N Shashikala, N Chandrabhas, K Jayaram, A Jayaraman and A K Sood, *J. Phys. Chem. Solids.* **55**, 107 (1994)
[38] S J Duclos, K Brister, R C Haddon, A R Kortan and F A Thiel, *Nature* (*London*) **351**, 380 (1991)
[39] C Christides, I M Thomas, T J S Dennis and K Prasides, *Europhys. Lett.* **22**, 611 (1993)

PRAMANA
— journal of
physics

© Printed in India

Vol. 43, No. 1,
July 1994
pp. 11–19

Effect of Fe substitution on the thermal expansion of the high T_c superconductor $Y_1Ba_2Cu_3O_y$

ASHOK RAO, OM PRAKASH, S N DAS and P N DHEER
Department of Physics and Astrophysics, University of Delhi, Delhi 110007, India

MS received 7 October 1993; revised 15 March 1994

Abstract. Thermal expansion measurements have been carried out on Fe substituted superconducting compounds $Y_1Ba_2(Cu_{1-x}Fe_x)_3O_y$ $(0 < x < 4\%)$ using a high resolution dilatometer employing the three terminal capacitance technique. The experimental set up is sensitive enough to detect changes in α of less than $10^{-8}K^{-1}$. Results show that the jump $\Delta\alpha$ in the coefficient of linear thermal expansion at the superconducting transition temperature, T_c, increases almost linearly with Fe concentration. The normal state thermal expansion coefficient α first decreases, attains a minimum value around $x = 1\%$ and then increases for higher Fe concentrations. The oxygen content per unit formula is almost constant up to $x = 1\%$ and then increases rapidly with x. It has also been observed that the anomalous behaviour of α around 260 K observed by Meingast *et al* [22] for Fe concentration $x = 5\%$ is due to inadequate annealing of the sample.

Keywords. Thermal expansion; high temperature superconductors; discontinuity in α; iodometric titrations.

PACS Nos 65·70; 74·60; 74·70

1. Introduction

It is well-known that addition of magnetic impurity to a superconductor results in a dramatic reduction in the superconducting transition temperature due to the breaking-up of Cooper pairs because of the magnetic interactions [1]. This phenomenon is more complicated in high T_c superconductors since the addition of the impurity ions may also cause changes in the structure and the oxygen content of the unit cell. There are several reports of the effect of substitution for Cu in $Y_1Ba_2(Cu_{1-x}M_x)_3O_7$(M = Ti, V, Cr, Mn, Fe, Co, Ni, Zn, Al and Ga) [2–18]. The effect of substitution on the structural changes have been studied using X-ray diffraction [2–4] and neutron diffraction [2, 4, 6] where it is found that the substitution of Al, Co, Fe and Ga causes a structural change from orthorhombic to tetragonal for about 2–3% of substituent [2, 4]. Site occupancies have been investigated by using various methods such as neutron diffraction [2, 4, 6–13], EXAFS [10, 14, 15] and Mössbauer spectroscopy [4, 16–18]. There have been disagreements about the site preference of a particular substituent, but now there is a general agreement that Co, Ga substitute for Cu(I) site whereas Ni [11, 12] goes into the Cu(II) site. In case of Fe, for low concentrations Fe goes almost entirely to Cu(I) positions; for higher concentrations Cu(II) sites are also occupied. Experiments [19, 20] also show that doping by Fe, increases the pressure dependence, dT_c/dP of T_c. Zhernov and Chuklin [21] have suggested that this increase in dT_c/dP is due to the increase in the density

of states at the Fermi level. As a result the discontinuity $\Delta\alpha$, in the coefficient of thermal expansion α at the superconducting transition, should increase with increasing Fe concentration. Furthermore, because of the structural changes, the coefficient of thermal expansion in the normal state of $Y_1Ba_2(Cu_{1-x}Fe_x)_3O_y$ should also exhibit a dependence on x, the Fe concentration.

The only measurements on the thermal expansion of $Y_1Ba_2(Cu_{1-x}Fe_x)_3O_y$ compounds in the normal and superconducting state seem to have been carried out by Meingast *et al* [22]. Meingast *et al* have indeed found that $\Delta\alpha$, increases nearly by a factor of 4 as x is increased to 5%. The normal state value of α seems to decrease first and then increase with a minimum around $x = 1\%$. These variations in α, although well beyond the limits of experimental error, are quite comparable to the sample to sample variations [23, 24] generally observed in the thermal expansion measurements. It was therefore decided to carry out an independent study of the thermal expansion of $Y_1Ba_2(Cu_{1-x}Fe_x)_3O_y$ compounds to ascertain if the results obtained by Meingast *et al* truly reflect dependence of α on x or are only indicative of random sample to sample variations.

2. Experimental details

The samples were prepared by the conventional solid state reaction technique [25]. Appropriate amounts of Y_2O_3, $BaCO_3$, CuO and Fe_2O_3 powders (all of purity 99·9%) were thoroughly mixed in an agate mortar and sintered in air at 930°C for 48 hr. This process was repeated three times in order to ensure homogeneous distribution of the substituted oxide. Finally the powder was reground and pressed into rectangular bars and annealed in flowing oxygen at 950°C for 48 hr. It was cooled slowly to 450°C and kept at this temperature in flowing oxygen for 72 hr, and then slowly cooled to room temperature. Typical XRD patterns shown in figure 1 indicate that the samples were single phased. The lattice parameters determined from the XRD patterns are given in table 1. It can be seen that the unit cell for all the samples is orthorhombic except for Fe = 4% which has a tetragonal structure. The transition temperature, T_c, and the transition width, ΔT_c, were determined by measuring the temperature dependence of resistance in the range 77–300 K using the standard four probe technique. The oxygen content of each sample was determined using an iodometric titration procedure suggested by Nazzal *et al* [26] with an accuracy of about $\pm 0{\cdot}03$. These parameters along with the density, ρ, for each specimen are also given in table 1.

Measurements of linear thermal expansion were carried out using the three terminal capacitance dilatometer developed by Om Prakash *et al* [27]. One of the plates of a parallel plate capacitor is mounted on the sample. Heating the specimen changes the capacitance of this capacitor from which the change, Δl, in the length of the sample can be determined as a function of the temperature, T. The dilatometer design is such that there are no significant contributions to Δl from the specimen mounting system. The dilatometer thus essentially yields absolute values of α. Each sample was cooled to 77 K and then heated in steps of about 0·3 K to higher temperatures. At each temperature the capacitance of the parallel plate condenser was measured using a GR-1620 capacitance bridge in the three terminal configuration. The experimental arrangement is sensitive enough to detect changes of about $10^{-8}(K)^{-1}$ in α.

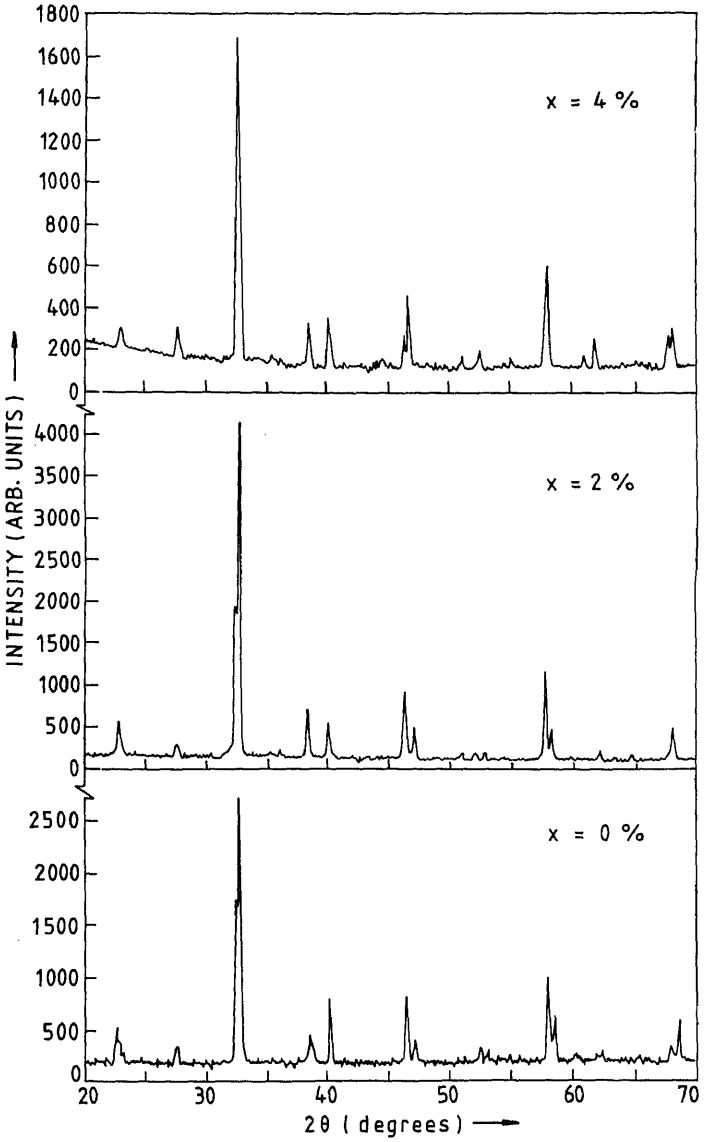

Figure 1. X-ray diffraction patterns for typical $Y_1Ba_2(Cu_{1-x}Fe_x)_3O_y$ compounds at room temperature.

3. Results and discussion

The temperature variation of the linear thermal expansion coefficient, α, in the temperature range 77 K $< T <$ 300 K for various samples is shown in figure 2. Figure 3 shows the behaviour of α in the transition region. Because of the large transition width, the results do not show a sharp discontinuity in α; instead α increases gradually as the specimen undergoes transition from normal to superconducting state. In order to estimate the discontinuity $\Delta\alpha$ for an ideal specimen, the following procedure, was adopted. Two polynomials in T one for $T < T_c$ and the other $T > T_c$ were fitted to

Table 1. Various parameters for the $Y_1Ba_2(Cu_{1-x}Fe_x)_3O_y$ compounds.

	Lattice parameters						
x (%)	a (Å) ($\pm$ 0·001)	b (Å) ($\pm$ 0·001)	c (Å) ($\pm$ 0·003)	T_c (K)	ΔT_c (K)	ρ (g/cm^3)	y ($\pm$ 0·003)
0	3·823	3·888	11·681	91·3	1·4	5·32	6·93
0·5	3·824	3·886	11·682	90·5	1·6	5·27	6·94
0·75	3·826	3·886	11·681	89·5	1·8	5·30	6·93
1·0	3·827	3·884	11·683	89·2	2·0	5·35	6·92
1.25	3·826	3·884	11·683	88·6	2·2	5·31	6·96
1·5	3·828	3·881	11·680	87·9	2·9	5·28	6·99
2·0	3·830	3·879	11·679	86·9	3·1	5·33	7·02
4·0	3·865	3·864	11·675	—	—	5·37	7·06

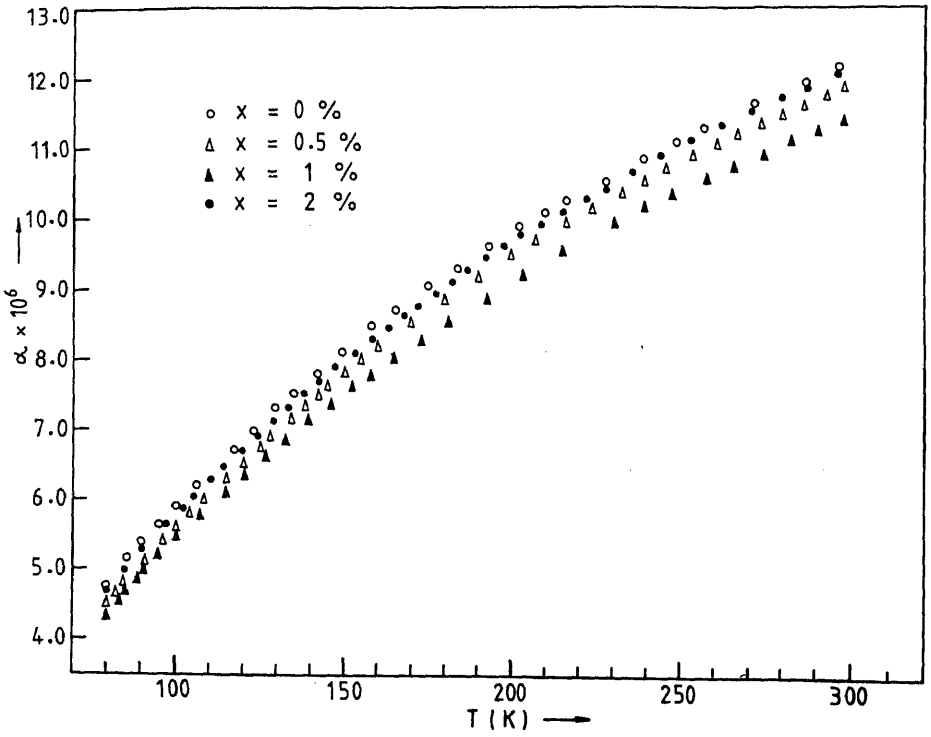

Figure 2. Temperature dependence of linear thermal expansion coefficient α for various specimens.

the experimental data of $\Delta l/l_0$ as a function of temperature T(l_0 = length of the sample at 77 K). Differentiation of the polynomials, thus obtained gives α as a function of temperature. The jump in α at T_c, given by $\Delta\alpha$, was determined by extrapolating the two branches of α vs T curves thus obtained (solid lines in figure 3) to T_c. The variation of $\Delta\alpha$ with Fe concentration obtained by using the extrapolation procedure is shown in figure 4(a) along with the results obtained by Meingast *et al* [22]. It can

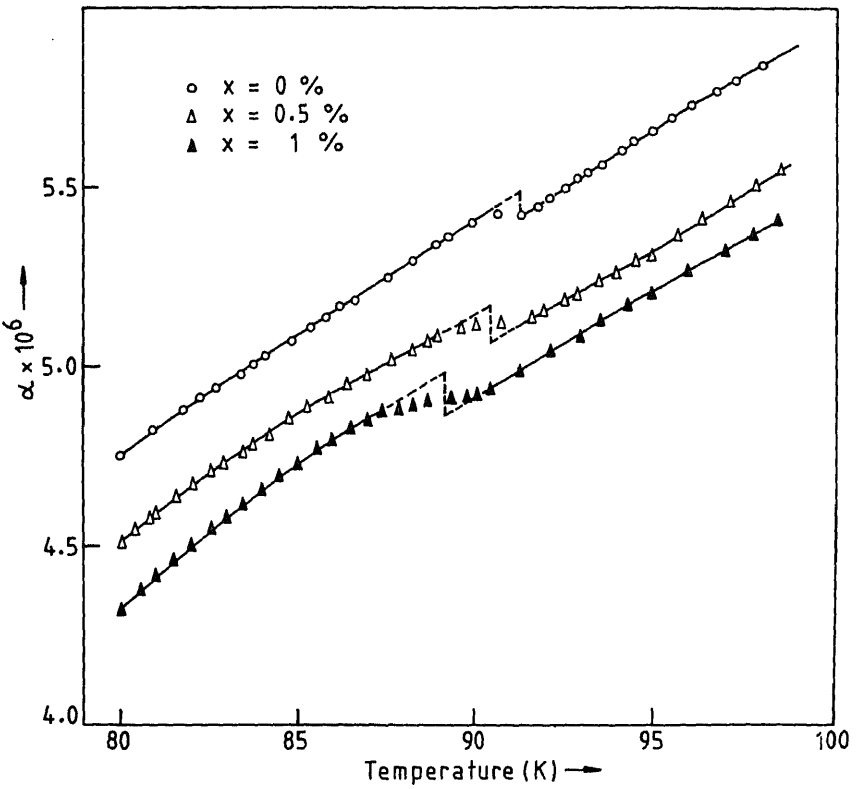

Figure 3. Behaviour of α in the vicinity of the transition temperature for some of the specimens.

be seen that the present results showing an almost linear dependence of $\Delta\alpha$ on x are in good agreement with those of Meingast *et al.* It might be mentioned that although T_c and oxygen content do not change appreciably (table 1) for Fe concentrations up to 1% there is almost a two-fold increase in $\Delta\alpha$.

Figure 4(b) shows the observed variation of the normal state α values (at $T = 95$ K) as a function of Fe concentration; the data of Meingast *et al* are also shown for comparison. Although there is significant difference in the absolute values of α, the dependence on Fe concentration observed by us is almost identical to that of Meingast *et al.* As x is increased, α at first decreases, attaining a minimum value around $x = 1\%$ and then increases for further increase of x. Figure 4(c) shows the variation of oxygen content y of the unit cell with Fe concentration. The oxygen content y is almost independent of Fe concentration up to about 1% and then increases rapidly with x. It thus appears that the minimum value of α occurs at that value of x at which there is a rapid increase in the oxygen content of the unit cell.

Meingast *et al* [22] have reported that in addition to the jump $\Delta\alpha$ at T_c, a specimen with high Fe concentration e.g. $x = 5\%$, showed additional anomalies e.g. a jump in α at $T = 250$ K, hysteresis in the temperature region $50 < T < 250$ K and non-reversible length changes at low temperatures ($T < 45$ K). They have also suggested that these anomalies are perhaps indicative of some structural transformation in the specimen and are characteristic features of a particular specimen. It is quite likely

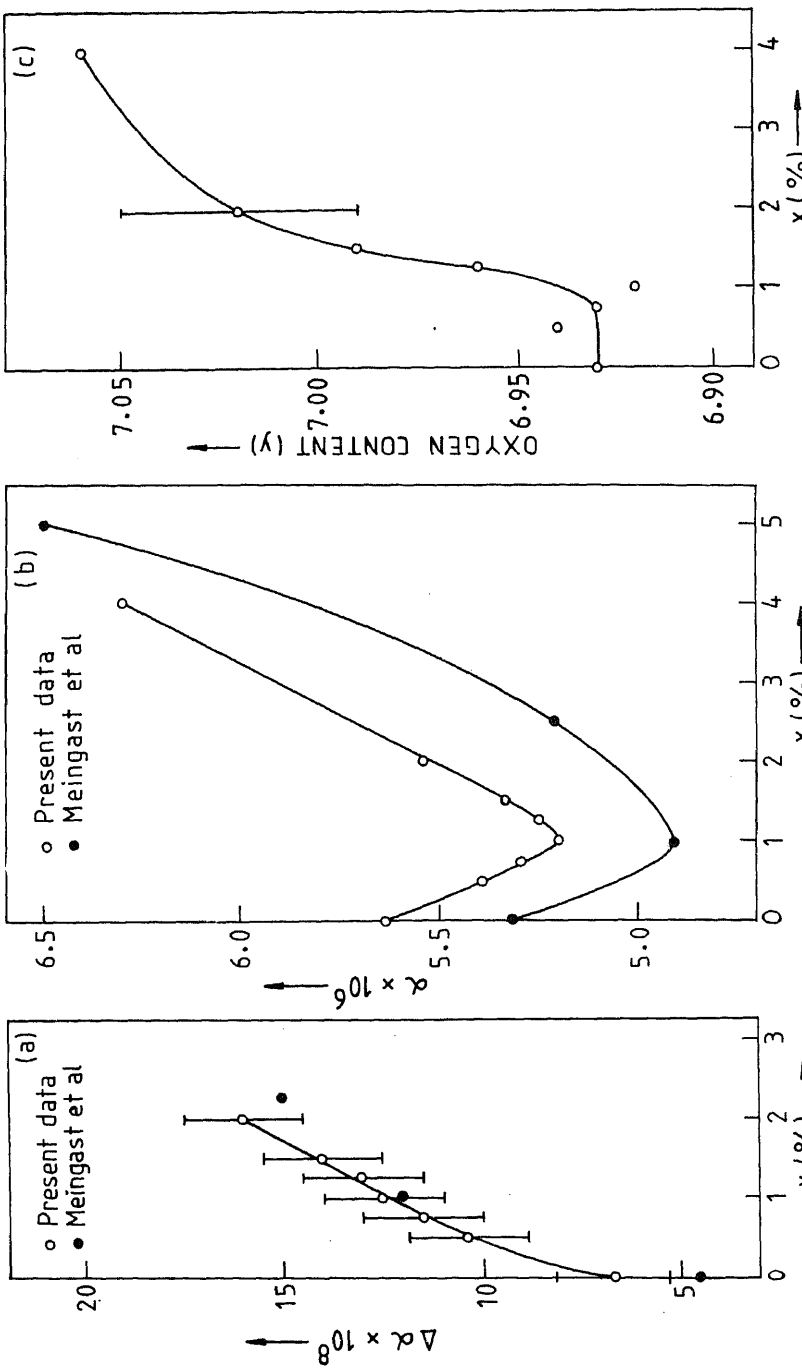

Figure 4. (a) The jump in the coefficient of thermal expansion as a function of Fe concentration, x. (b) Variation of the coefficient of linear thermal expansion in the normal state ($T = 95$ K) with Fe concentration. (c) Oxygen content variation with Fe concentration.

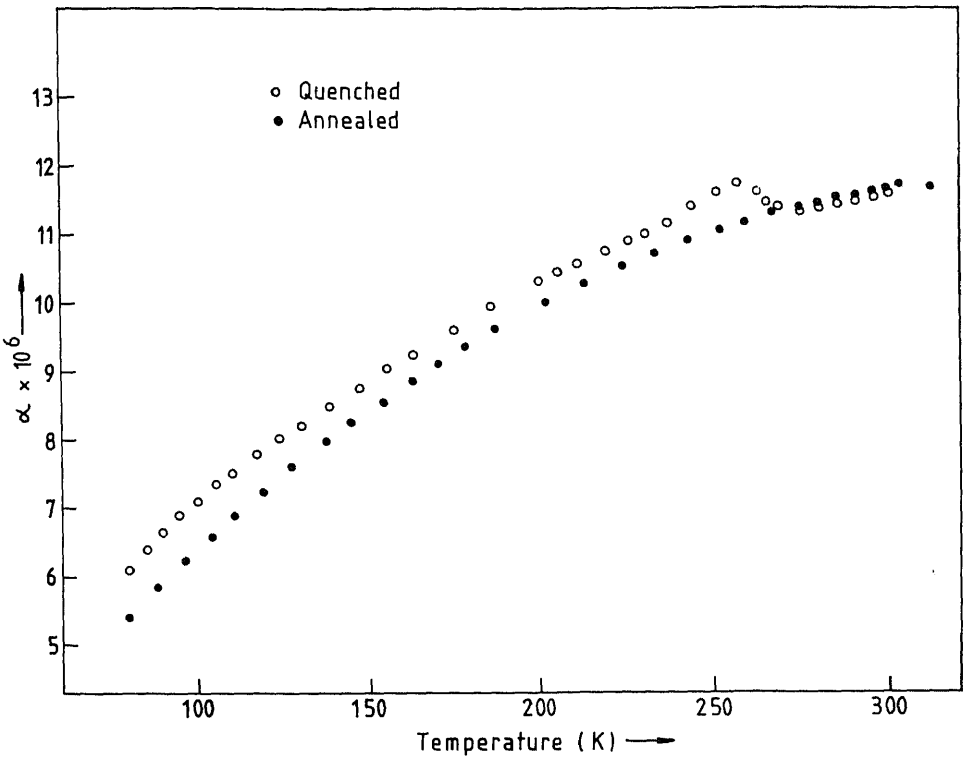

Figure 5. Thermal expansion coefficient vs temperature for the quenched and unquenched specimens with $x = 4\%$. The quenched specimen clearly shows an anomaly around 260 K.

that these anomalies arise because of internal strains or inhomogeneities in the specimen due to improper annealing. In order to understand the nature of the anomaly at $T = 250$ K the sample containing 4% Fe was deliberately quenched from 200°C to room temperature. The measurements of the thermal expansion were then repeated to this quenched sample. Figure 5 compares the observed temperature dependence of α for both the quenched and unquenched samples. It can be seen that the quenched sample shows an anomaly around 260 K similar to that observed by Meingast *et al*; the unquenched sample does not exhibit any such anomaly. In addition, in the temperature range $77 < T < 260$ K, the α values for the quenched sample are larger than those for the unquenched specimen. For $T > 260$ K the behaviour of both the samples is almost identical. These results do seem to suggest that presence of small strains in samples can markedly affect the temperature dependence of the linear thermal expansion coefficient and can also perhaps lead to the type of anomalies observed by Meingast *et al.* It may, however, be pointed out [28, 29] that there is strong evidence for phase instability of $Y_1Ba_2Cu_3O_{7-\delta}$ system at low temperature, particularly around $T = 200$°C, where [29] ageing for an extended length of time leads to a decomposition into oxygen ordered orthorhombic and vacancy ordered tetragonal phases. It is quite likely that such phase decomposition also takes place in the Fe doped samples and so leads to the observed anomaly at $T = 260$ K. The sample in the present study was kept at $T = 200$°C for only ~ 8 h. The phase

decomposition during this ageing period is likely to be rather small. However, further investigations are needed before the nature of the anomaly at 260 K can be unambiguously understood.

Acknowledgements

The authors are indebted to Prof. A Mansingh for providing the GR-1620 capacitance bridge and for useful discussion. Financial assistance received by (AR) from the University Grants Commission, India and (SND) from the Council for Scientific and Industrial Research, India, is gratefully acknowledged.

References

[1] A A Abrikosov and L P Gorkov, *Sov. Phys. – JETP* **12**, 1243 (1960)
[2] G Xiao, M Z Cieplak, D Musser, A Gavrin, F H Streitz, C L Chien, J J Rhyne and J A Gotaas, *Nature (London)* **332**, 238 (1988)
[3] Y Maeno, T Tomita, M Kyogoku, S Awaji, Y Aoki, K Hoshino, A Minami and T Fujita, *Nature (London)* **328**, 512 (1987)
[4] J M Tarascon, P Barboux, P F Miceli, L H Greene and G W Hull, *Phys. Rev.* **B37**, 7458 (1988)
[5] Y Xu, R L Sabatini, A R Moodenbaugh, Y Zhu, S G Shyu, M Suenaga, K W Dennis and R W McCallum, *Physica* **C169**, 205 (1990)
[6] P Bordet, J L Hodeau, P Strobel, M Marezio and A Santoro, *Solid State Commun.* **66**, 435 (1988)
[7] A M Balagurov, G M Mironova, A Pajaczkowska and H Szymczak, *Physica* **C158**, 265 (1989)
[8] G Roth, G Heger, B Renker, J Pannetier, V Caignaert, M Hervieu and B Raveau, *Z. Phys.* **B71**, 43 (1988)
[9] R Sonntag, D Hohlwein, A Hoser, W Prandl, W Schafer, R Kiemel, S Kemmler-Sack, S Losch, M Schlichenmaier and A W Hewat, *Physica* **C159**, 141 (1989)
[10] H Maeda, A Koizumi, N Bamba, E Takayama-Murocmachi, F Izumi, H Asano, K Shimizu, H Moriwaki, H Maruyama, Y Kuroda and H Yamazaki, *Physica* **C157**, 483 (1989)
[11] H Shaked, J Faber Jr, B W Veal, R L Hitterman and A P Paulikas, *Solid State Commun.* **75**, 445 (1990)
[12] T Kajitani, K Kusaba, M Kikuchi, Y Syono and M Hirabayashi, *Jpn. J. Appl. Phys.* **27**, L354 (1988)
[13] S Katano, T Matsumoto, A Matsushita, T Hatano and S Funahashi, *Phys. Rev.* **B41**, 2009 (1990)
[14] F Bridges, J B Boyce, T Claeson, T H Geballe and J M Tarascon, *Phys. Rev.* **B39**, 11603 (1989)
[15] M Qian, E A Stern, Y Ma and R Ingalls, *Phys. Rev.* **B39**, 9192 (1989)
[16] A Simopoulos and D Niarchos, *Phys. Rev.* **B38**, 8931 (1988)
[17] E R Bauminger, M Kowitt, I Felner and I Nowik, *Solid State Commun.* **65**, 123 (1988)
[18] D Heckel, I Nowik, E R Bauminger and I Felner, *Phys. Rev.* **B42**, 2166 (1990)
[19] M Kurisu, K Kumagai, Y Maeno and T Fujita, *Physica* **C152**, 339 (1988)
[20] J G Huber, W J Liverman, Y Xu and A R Moodenbaugh, *Phys. Rev.* **B41**, 8757 (1990)
[21] A P Zhernov and E P Chuklin, *Phys. Status. Solidi* **B173**, 691 (1992)
[22] C Meingast, R Ahrens, B Blank, H Burkle, B Rudolf and H Wuhl, *Physica* **C173**, 309 (1991)
[23] G K White, S J Collocott, R Driver, R B Roberts and A M Stewarts, *J. Phys.* **C21**, 631 (1988)
[24] Om Prakash, Ashok Rao, O Prakash and P N Dheer, *Pramana – J. Phys.* **41**, 421 (1993)
[25] S N Das, R Kapoor, S S Dubey and P N Dheer, *Physica* **B163** 245 (1990)

[26] A I Nazzal, V Y Lee, E M Engler, R D Jacowitz, Y Tokura and J B Torrance, *Physica* **C153–155**, 1367 (1988)
[27] Om Prakash, Ashok Rao and P N Dheer, *Pramana – J. Phys.* **39**, 665 (1992)
[28] A G Khachaturyan and J W Morris Jr, *Phys. Rev. Lett.* **64**, 76 (1990)
[29] T S Radhakrishnan, J Janaki, G V N Rao, S Kalavathi, V S Sastry, Y Hariharan, M P Janawadkar, K Govinda Rajan, P Parameswaran and O M Sreedharan, *Pramana – J. Phys.* **32**, L705 (1989)

PRAMANA
— journal of
physics

© Printed in India

Vol. 43, No. 1,
July 1994
pp. 21–31

Magnetism, exchange and crystal field parameters in the orbitally unquenched Ising antiferromagnet $FePS_3$

NIRMALA CHANDRASEKHARAN and SUKUMARAN VASUDEVAN
Department of Inorganic and Physical Chemistry, Indian Institute of Science, Bangalore 560012, India

MS received 7 January 1994

Abstract. $FePS_3$ is a layered antiferromagnet ($T_N = 123$ K) with a marked Ising anisotropy in magnetic properties. The anisotropy arises from the combined effect of the trigonal distortion from octahedral symmetry and spin-orbit coupling on the orbitally degenerate ${}^5T_{2g}$ ground state of the Fe^{2+} ion. The anisotropic paramagnetic susceptibilities are interpreted in terms of the zero field Hamiltonian, $\mathcal{H} = \Sigma_i[\Delta(L_{iz}^2 - 2) + |\lambda|\mathbf{L}_i \cdot \mathbf{S}_i] - \Sigma_{ij}\mathbf{J}_{ij}\mathbf{S}_i \cdot \mathbf{S}_j$. The crystal field trigonal distortion parameter Δ, the spin-orbit coupling λ and the isotropic Heisenberg exchange, J_{ij}, were evaluated from an analysis of the high temperature paramagnetic susceptibility data using the Correlated Effective Field (CEF) theory for many-body magnetism developed by Lines. Good agreement with experiment were obtained for $\Delta/k = 215{\cdot}5$ K; $\lambda/k = 166{\cdot}5$ K; $J_{nn}/k = 27{\cdot}7$ K; and $J_{nnn}/k = -2{\cdot}3$ K. Using these values of the crystal field and exchange parameters the CEF predicts a $T_N = 122$ K for $FePS_3$, which is remarkably close to the observed value of the T_N. The accuracy of the CEF approximation was also ascertained by comparing the calculated susceptibilities in the CEF with the experimental susceptibility for the isotropic Heisenberg layered antiferromagnet $MnPS_3$, for which the high temperature series expansion susceptibility is available.

Keywords. Layered antiferromagnet; crystal field; anisotropy; correlated effective field.

PACS Nos 75·10; 75·30; 75·70

1. Introduction

The layered transition metal thiophosphates MPS_3 ($M = Mn, Fe, Ni$) are a unique class of compounds; they represent one of the few known layered systems in which both magnetic and crystallographic lattices are two-dimensional [1, 2]. Unlike most other $2D$ magnetic systems e.g. those belonging to the K_2NiF_4 family [3] wherein magnetic layers are separated by diamagnetic layers, in the transition metal thiophosphates, the MPS_3 layers are separated by a van der Waals gap.

The transition metal thiophosphates are insulating antiferromagnets [4, 5]. The nature of metal-ligand interactions are ionic [6] and the d electron manifold of the transition metal ion is reasonably well described in the weak field limit of crystal field theory [7]. The anisotropic magnetic susceptibility of these compounds have been reported [5]. The most remarkable feature of magnetism in these compounds is that the anisotropy of the paramagnetic susceptibility is strongly dependent on the metal ion. While the susceptibility of $MnPS_3$ is isotropic and that of $NiPS_3$ shows only a weak anisotropy, $FePS_3$ exhibits a marked Ising like anisotropy. The anisotropy in these compounds has been shown to arise from crystal field effects—a combination

of spin-orbit coupling and trigonal distortion of the MS_6 octahedra, giving rise to a zero-field splitting of the ground state of the transition metal ion.

An interesting consequence of the layered structure of these compounds—the fact that the MPS_3 layers are separated by a van der Waals gap—is that it is possible to intercalate a wide variety of guest molecules and ions, similar to that observed in the transition metal dichalcogenides [8]. Subsequent to intercalation the major changes and in many cases the only change, are in the magnetic properties. For example, pyridine intercalation in the isotropic Heisenberg antiferromagnet, $MnPS_3$, leads to a weak ferromagnetic state [9] which has been shown to arise from a combination of Dzyaloshinsky – Moriya interactions and single ion anisotropy terms, neither of which were present in the parent compound [10]. Similarly, on pyridine intercalation in the Ising like antiferromagnet $FePS_3$, a spontaneously magnetized state is realized [11], while on amine intercalation the changes have been ascribed to random field Ising model behaviour [12].

An obvious prerequisite to a better understanding of the changes in magnetic properties on intercalation, is a quantitative evaluation of the exchange and crystal field parameters of the host. In this paper we have attempted to do so for $FePS_3$ from an analysis of the high temperature susceptibility data of Joy *et al* [5]. The model used for the analysis must in principle be able to account (i) for the complicated level structure of the transition metal ion arising from a combination of spin-orbit coupling, trigonal distortion and Zeeman splitting, which in the present case, completely lifts the 15-fold degeneracy of the ${}^5T_{2g}$ state of the Fe^{2+} ion and (ii) at the same time also be able to account for spin correlations which in these low-dimensional systems manifest at temperatures much higher than T_N [3]. It is for the latter reason that the mean field (MF) is a poor approximation, since by replacing all ions except one by their ensemble average, interion spin and orbital correlations are completely ignored. At the same time the complicated level structure of the M^{2+} ion makes it difficult to apply more refined theories, such as the renormalization group or even the *h*igh *t*emperature *s*eries *e*xpansion (HTSE). In this paper we have used the correlated effective field (CEF) approximation developed by Lines [13, 14]. This model is ideally suited for systems where excited orbital crystal field energies, exchange energies and thermal energies are all of the same order of magnitude. The formalism attempts to reduce the many-body problem to a single body non-interacting ensemble form, by the introduction of static temperature dependent spin correlation parameters which are evaluated by forcing consistency with the fluctuation-dissipation theorem. The model has been used with reasonable success in analyzing the high temperature susceptibility of $RbFeBr_3$ [15] and $RbFeCl_3$ [16].

In § 2 we provide a brief outline of the CEF formalism. In § 3 we discuss the CEF theory in the simpler context of a $2D$ isotropic Heisenberg system, by comparing the calculated susceptibilities in the CEF approximation with the experimental data for $MnPS_3$ and also the exact HTSE fit for the same. This was done to estimate the accuracy of the CEF approximation. The results are also compared with the analysis from other approximations such as the Oguchi [17, 18] and the MF treatment. In § 4 the crystal field levels of Fe^{2+} in the trigonally distorted environment of $FePS_3$ are described and the CEF calculations for $FePS_3$ performed. The exchange and crystal field parameters were evaluated by fitting the CEF susceptibilities to the experimental data. Finally in § 5 we summarize the results.

2. The correlated effective field approximation [13, 14]

The CEF approximation is applicable for systems where the total spin Hamiltonian may be written as

$$\mathscr{H} = \mathscr{H}_{\mathrm{CF}} + \sum_{ij} J_{ij}\mathbf{S}_i\mathbf{S}_j, \tag{1}$$

where $\mathscr{H}_{\mathrm{CF}}$ is the Hamiltonian in the absence of exchange.

In this model, the CEF for the ith spin S_i is obtained by replacing each S_j in (1) by the sum of two contributions, one its ensemble average $\langle S_j\rangle$, the other, a term proportional to the instantaneous deviation of S_i from its ensemble average value $\langle S_i\rangle$ i.e.

$$S_j^\lambda \rightarrow \langle S_j^\lambda\rangle + \alpha^\lambda(S_i^\lambda - \langle S_i^\lambda\rangle), \quad \lambda = x, y, z. \tag{2}$$

The α^λ's are temperature dependent static correlation parameters. Corresponding to this replacement, the effective Hamiltonian for the ith spin in the high temperature paramagnetic phase, where ensemble averages are zero, is

$$\mathscr{H}_i^0(\mathrm{eff}) = \mathscr{H}_{\mathrm{CF}} - \sum_{j\lambda} 2J_{ij}^\lambda \alpha^\lambda (S_i^\lambda)^2. \tag{3}$$

In the presence of a field $h = g\beta H^0$ applied in a direction γ, the effective Hamiltonian becomes

$$\mathscr{H}_i(\mathrm{eff}) = \mathscr{H}_i^0(\mathrm{eff}) - h\mu^\gamma + 2\sum_{j\gamma} J_{ij}^\gamma S_i^\gamma(\langle S_j^\gamma\rangle - \alpha^\gamma\langle S_i^\gamma\rangle), \tag{4}$$

where $\mu = 2S + L$. The ensemble averages in direction $\lambda \neq \gamma$ are zero.

It may be seen that $\mathscr{H}_i(\mathrm{eff})$ approximates the many-body Hamiltonian, by a single particle one and except for the sign of J, is identical for the ferromagnetic and antiferromagnetic case.

The field dependent ensemble averages are obtained by treating the last two terms of (4) as a perturbation on $\mathscr{H}_i^0(\mathrm{eff})$. $\mathscr{H}_i^0(\mathrm{eff})$ may be diagonalized and the eigenfunctions $|\psi_{n,\alpha}\rangle$ and eigenvalues $E_{n,\alpha}$ obtained as a function of the correlation parameters α. The field dependent ensemble averages are

$$kT\langle S(q)^\gamma\rangle_h = h(q)\langle\mu_i^\gamma : S_i^\gamma\rangle_0 + 2[J(q)^\gamma - \alpha^\gamma J^\gamma(0)]\langle S(q)^\gamma\rangle_h\langle S_i^\gamma : S_i^\gamma\rangle_0 \tag{5}$$

$$kT\langle L(q)^\gamma\rangle_h = h(q)\langle\mu_i^\gamma : L_i^\gamma\rangle_0 + 2[J(q)^\gamma - \alpha^\gamma J^\gamma(0)]\langle S(q)^\gamma\rangle_h\langle S_i^\gamma : S_i^\gamma\rangle_0 \tag{6}$$

where $S(q)$ and $L(q)$ are the fourier transform of the corresponding lattice quantity and $J(q) = \Sigma_{j-i} J_{ij}\exp(iqr_{ij})$ where r_{ij} is the vector connecting the ith atom to its jth neighbour and momentum q belongs to the first Brillouin zone. The colon product ensemble average is defined by

$$\langle A:B\rangle = \sum_n \rho_n\left(A_{nn}B_{nn} + 2kT\sum_{m,\alpha\neq n,\alpha}\frac{A_{nm}B_{mn}}{E_{m,\alpha} - E_{n,\alpha}}\right),$$

where $A_{nm} = \langle n, \alpha | A | m, \alpha \rangle$. ρ_n is the density matrix given by

$$\rho_n = \frac{\exp(-E_{n,\alpha}/kT)}{\sum_n \exp(-E_{n,\alpha}/kT)}.$$

The wave vector dependent susceptibility is then

$$\chi^\gamma(q) = \langle \mu^\gamma(q) \rangle / h(q) = \frac{\langle 2S^\gamma(q) + L'^\gamma(q) \rangle_h}{h(q)}. \tag{7}$$

Substituting for the ensemble averages from (5) and (6)

$$kT\chi_i(q) = \langle \mu_i^\gamma : \mu_i^\gamma \rangle_0 + K(q), \tag{8}$$

where

$$K(q) = \frac{2[J(q)^\gamma - \alpha^\gamma J^\gamma(0)] \langle \mu_i^\gamma : S_i^\gamma \rangle_0^2}{kT - 2[J(q)^\gamma - \alpha^\gamma J^\gamma(0)] \langle S_i^\gamma : S_i^\gamma \rangle_0}.$$

From the fluctuation theorem we have [13] $\Sigma_q K(q) = 0$ which allows for the complete determination of the correlation parameter α

$$\alpha^\lambda = \frac{\sum_q J(q)[kT - 2(J(q) - \alpha^\lambda J(0)) \langle S_i^\lambda : S_i^\lambda \rangle_0]^{-1}}{\sum_q J(0)[kT - 2(J(q) - \alpha^\lambda J(0)) \langle S_i^\lambda : S_i^\lambda \rangle_0]^{-1}}. \tag{9}$$

Once α^λ is obtained, the uniform static susceptibility directly follows

$$kT\chi_0^\gamma = \langle \mu_i^\gamma : \mu_i^\gamma \rangle_0 + \frac{\langle \mu_i^\gamma : S_i^\gamma \rangle_0^2 2 \sum_j J_{ij}(0)(1 - \alpha^\gamma)}{kT - \langle S_i^\gamma : S_i^\gamma \rangle_0 2z \sum_j J_{iJ}(0)(1 - \alpha^\gamma)}. \tag{10}$$

The above formalism is valid without restriction on the sign of J. For an antiferromagnet the Neel temperature—the temperature at which the staggered susceptibility, $\chi^\lambda(q = q^*)$ diverges (q^* is the antiferromagnetic ordering vector)—may be calculated in the CEF model as the temperature at which the denominator of (10) goes to zero (for $q = q^*$). Noting that for an antiferromagnet $J(q) = -J(0)$ it follows that the Neel temperature, T_N is

$$kT_N^\lambda = 2J(0)z(1 + \alpha^\lambda) \langle S_i^\lambda : S_i^\lambda \rangle_0. \tag{11}$$

It may be seen that the calculation of α's are crucial to the evaluation of susceptibilities as well as T_N. The calculation of α's involves the summation over the Brillouin zone. We have used the special k point scheme introduced by Chadi and Cohen [19] for obtaining the averages over the Brillouin zone. For $MnPS_3$ and $FePS_3$ for which the in-plane structure is the non-primitive honeycomb lattice, the special k points for the 2D hexagonal lattice reported by Cunningham were employed [20].

3. Comparison with a 2*D* isotropic Heisenberg antiferromagnet, $MnPS_3$

In order to gauge the strength and weakness as well as the accuracy of the CEF approximation, it is necessary to compare with the results of a more accurate or exact calculation. For this reason the calculated susceptibilities in the CEF approximation have been compared with the experimental data for the 2*D* isostructural $S = 5/2$ Heisenberg antiferromagnet, $MnPS_3$, for which the exact high temperature series expansion susceptibility is known. This exercise was also necessary to test the efficacy of the special k point scheme for providing the Brillouin zone average for a honeycomb lattice in the calculation of α, the static correlation parameter.

The results of the comparison are shown in figure 1. The experimental susceptibilities are from ref. [5]. The HTSE expression for the susceptibility of a 2*D* Heisenberg antiferromagnet as

$$\chi_m = \frac{Ng^2\beta^2 S(S+1)}{3kT} \cdot \frac{1}{1 + \sum_{i=1}^{6} (-1)^i b_i (|J|/kT)^i}. \tag{12}$$

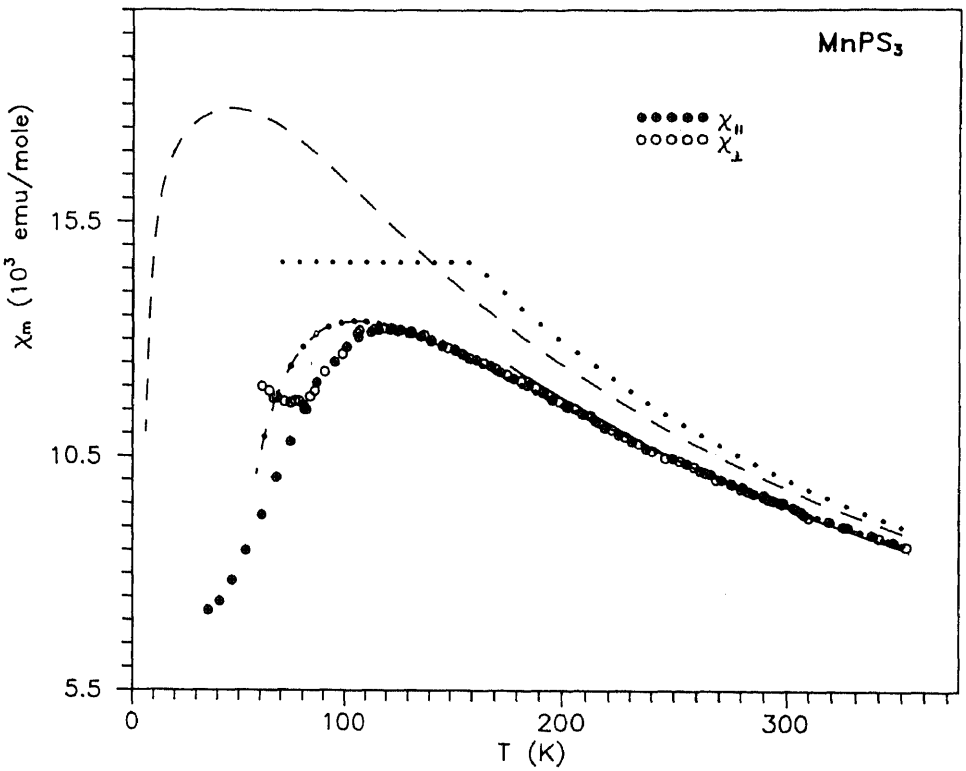

Figure 1. The isotropic magnetic susceptibilities, $\chi_\parallel$ and $\chi_\perp$ for $MnPS_3$ as a function of temperature. $\chi_\parallel$ and $\chi_\perp$ refer to the direction of the applied field with respect to the trigonal axis. (– · – · – · –) is the fit to the HTSE susceptibility expression in (12) for $J/k = -8{\cdot}1$ K and $g = 2{\cdot}01$. (———) is the fit of the calculated susceptibility in the CEF approximation for the same values of the parameters as in HTSE, while the (– – –) and (.....) lines are the calculated susceptibilities in the Oguchi and MFA for the same value of J/k and g.

The b_i's are the expansion coefficients, and depend on the type of magnetic lattice. The $(-1)^i$ term, accounts for the antiferromagnetic nature of exchange in the system. For a honeycomb lattice, to which $MnPS_3$ belongs, the constants have been calculated using the formula of Rushbrook and Wood [21]. The dashed-dotted line in figure 1 is the fit for the HTSE susceptibility. The best fit is obtained for $J = -8{\cdot}1$ K; $g = 2{\cdot}01$.

The solid line in figure 1 is the CEF susceptibility for $MnPS_3$ calculated using the same value of J and g which gave the best fit for the HTSE. The calculation of the CEF susceptibility for $MnPS_3$ is straightforward. $\mathscr{H}_{CF}$ is zero in (4) and α was evaluated from (9) using the special k point summation for the Brillouin zone averages [20].

It may be seen that the CEF susceptibility compares extremely well with the exact HTSE susceptibility. (The CEF susceptibility is not calculable above 177 K since the denominator in (10) goes to zero. This temperature however has no physical significance since in these 2D Heisenberg antiferromagnets the actual T_N is a consequence of weak 3D interlayer coupling).

It is also interesting to compare the results of the CEF approximation with other approximations such as the Oguchi molecular field [17, 18] which also introduce an element of spin correlation while retaining the simplicity of the mean field. In the Oguchi approximation [18] a small section of the crystal e.g. a pair of ions is treated exactly while interactions with the rest of the ions in the crystal are approximated by an effective field.

The susceptibility of $MnPS_3$ in the Oguchi approximation was derived from the exact expression for $\langle S^z \rangle_{\text{dimer}}$ for a pair of Mn^{2+} spins ($s_1 = s_2 = 5/2$). The susceptibility is

$$\chi_m = \frac{Ng^2\beta^2}{kT} \cdot \frac{F(J, T)}{G(J, T) - 2(z-1)jF(J, T)}; \quad j = J/kT. \tag{13}$$

$$F(J, T) = 1 + 5\exp(4j) + 14\exp(10j) + 30\exp(18j) + 55\exp(28j)$$

$$G(J, T) = 3 + \exp(-2j) + 5\exp(4j) + 7\exp(10j) + 9\exp(18j) + 11\exp(28j)$$

Figure 1 shows the Oguchi susceptibility, calculated using $J/k = -8{\cdot}1$ K and $g = 2{\cdot}01$. These values are the ones which gave the best fit to the HTSE susceptibility.

The Oguchi susceptibility although an improvement on the simple MFA still underestimates the antiferromagnetic correlation and is a poor second to the CEF, in comparison with the HTSE results.

The results of figure 1 clearly establish the effectiveness of the CEF approximation in evaluating the high temperature susceptibility of 2D systems. The results also establish the effectiveness of the special k point scheme in providing Brillouin zone averages in the calculation of the correlation parameter, α, the calculation of which is crucial in obtaining the correct values of the susceptibility in the CEF model.

4. CEF approximation applied to $FePS_3$

In $FePS_3$ the d^6 free ion ground term ^5D is split by the the octahedral crystal field into an upper orbtial doublet and a lower orbital triplet ($^5T_2$). In considering the effect of the trigonal distortion and spin-orbit coupling, the interaction of the $^5T_2$ state with the higher lying excited states are ignored. This is justifiable since it is known from optical absorption data that the closest lying excited state, ^5E, is

$8700\,cm^{-1}$ above the ground state. Within the lower triplet, use is made of the structural isomorphism of the T_2 and P symmetry groups to define a fictitious orbital angular momentum $L'=1$ [22]. For the $^5T_2$, the matrix elements of the orbital angular momentum L are -1 times the equivalent elements of L' within the P states; $L=\alpha L'(\alpha=-1)$. In terms of the fictitious orbital angular momenta the Hamiltonian representing the trigonal distortion from O_h symmetry as well as spin-orbit coupling has the form,

$$\mathscr{H}=\Delta(L_z'^2-2)-|\lambda|\mathbf{L}'\cdot\mathbf{S}. \tag{14}$$

The first term represents the trigonal component perturbation; z is the axis of this low symmetry perturbation. The Hamiltonian is evaulated within the 15 states, $|M_S, M_{L'}\rangle$ of a ^5P term. This breaks up into seven submatrices. These may be labelled by their M_J values which in the absence of a field is a good quantum number. There is essentially only one parameter Δ/λ which characterizes both the anisotropy as well as the g values for the magnetic ion [22]. The secular equations for the energies were solved numerically in terms of Δ'/λ. The energies as a function of the positive and negative values of Δ'/λ are shown in figure 2. ($\Delta'=3\Delta$).

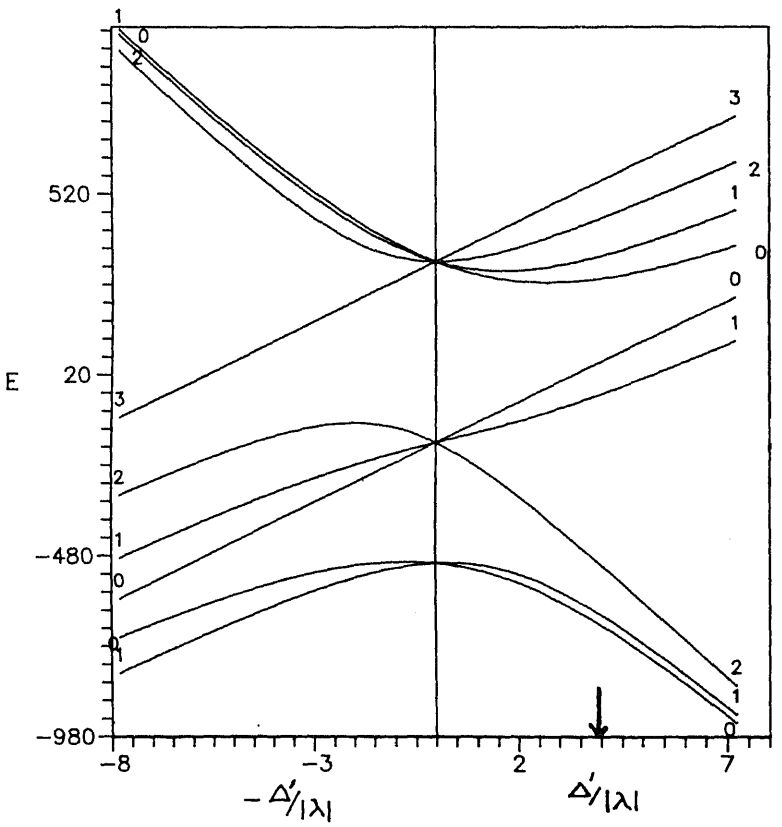

Figure 2. The splitting of the ground term of the high spin ferrous ion in a trigonal field. The energy in units of kelvin is given along the y-axis. The M_J values are marked against the corresponding energy state. The arrow indicates the value of $\Delta'/|\lambda|$ for $FePS_3$ as obtained from the analysis of the high temperature susceptibility.

The above Hamiltonian may be simplified under two extreme conditions i) $\lambda \gg \Delta$ or ii) $\Delta \gg \lambda$. In the first instance one need consider only the splitting of the ${}^5T_{2g}$ state by the spin-orbit coupling into the three levels ${}^5T_{21}, {}^5T_{22}, {}^5T_{23}$. For $FePS_3$ this is clearly not the situation since it would not account (see figure 4) for the experimentally observed large differences between $\chi_\parallel$ and $\chi_\perp$. In situations where $\Delta \gg \lambda$ one first considers the splitting of the ${}^5T_{2g}$ state by the low symmetry trigonal field into a doublet (${}^5E_g$) with $L_z = \pm 1$ and the singlet (${}^5A_{1g}$), $L_z = 0$. The effect of the spin-orbital coupling is considered only within the ground state manifold (either the ${}^5E_g$ or ${}^5A_{1g}$). In an earlier mean field analysis of the susceptibility of $FePS_3$ [5], the above assumption ($\Delta \gg \lambda$) had been made and only those states arising from the effect of spin-orbit coupling on the ${}^5E_g(L'_z)$ state were considered in the calculation of the susceptibility. In the light of the optical absorption data of $FePS_3$ [7] as well as the vibration spectra [10] the above assumption seems unjustified. Both experiments showed that in $FePS_3$ the iron atoms are in a highly ionic environment. Consequently the spin-orbit coupling constant is likely to be close to that of the free ion value of $-100\,\mathrm{cm}^{-1}$ [22]. If Δ was indeed much greater than λ the effect of the trigonal distortion field should have been observed in the optical spectra. This was not so and the simplification $\Delta \gg \lambda$ is unlikely to hold.

Since the Hamiltonian cannot be simplified for $FePS_3$ it implies that the entire 15 level structure of the ${}^5T_2$ state would have to be included in the evaluation of any ground state thermodynamic property.

Although the Fe^{2+} ions are orbitally degenerate, it is assumed that the exchange is isotropic and between real spins, so that ith ion spin Hamiltonian may be written as

$$\mathscr{H} = \Delta(L_z'^2 - 2) - |\lambda|\mathbf{L}'\cdot\mathbf{S} - \sum_j J_{ij}\mathbf{S}_i\cdot\mathbf{S}_j, \tag{15}$$

and the effective CEF Hamiltonian in the paramagnetic phase and in the absence of a magnetic field is

$$\mathscr{H}_i^0 \mathrm{eff} = \Delta(L_z'^2 - 2) - |\lambda|\mathbf{L}'\cdot\mathbf{S} - \sum_j J_{ij}(\alpha_\parallel - \alpha_\perp)S_{iz}^2. \tag{16}$$

Here $\parallel$ refers to the external field applied along the trigonal axis. The summation extends to the next nearest neighbour. This is necessary if the in-plane antiferromagnetic ordered structure for $FePS_3$ [23] is to be realized.

The correlation parameters were obtained from the solution of (9). The Brillouin zone average in the calculation of α was computed using the special k points for the $2D$ hexagonal lattice [20]. It may be seen that the equation for $\alpha_\parallel$ and $\alpha_\perp$ are not independent and were solved numerically. The variation of α's as a function of temperature is shown in figure 3. The static susceptibilities were calculated using (10). The exchange constants J_{nn}, J_{nnn} as well as Δ and λ were obtained by a least square fit of the CEF susceptibility to the experimental data. The best fit is shown as the solid line in figure 4 obtained for $J_{nn}/k = 27{\cdot}7\,\mathrm{K}$; $J_{nnn}/k = -2{\cdot}3\,\mathrm{K}$; $\Delta/k = 215{\cdot}5\,\mathrm{K}$; $|\lambda|/k = 166{\cdot}5\,\mathrm{K}$.

The fit is reasonably good and the λ value close to that of the free ion value for Fe^{2+}. This is in agreement with other experimental observations that in $FePS_3$ the Fe–S linkage is ionic. The results of the fit also justifies the retaining of the entire 15 level structure of the ${}^5T_{2g}$ state without any simplification in the calculation of the susceptibilities, since the value of Δ and $|\lambda|$ obtained are comparable ($\Delta/|\lambda| = 1{\cdot}3$).

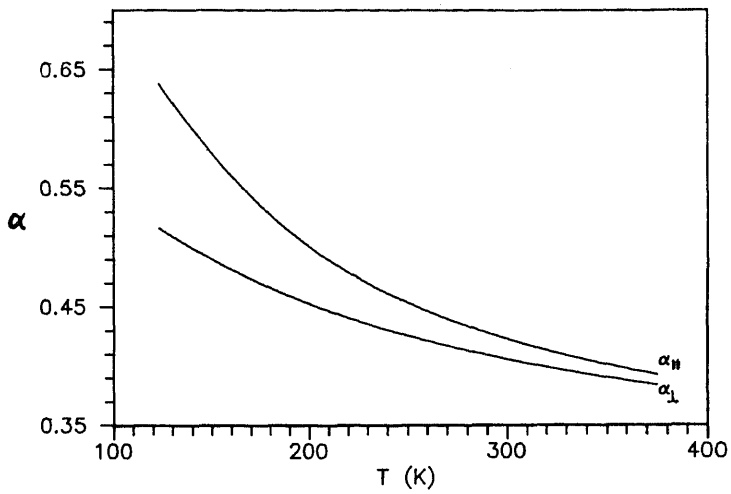

Figure 3. The temperature dependence of the correlation parameter $\alpha_{\parallel}$ and $\alpha_{\perp}$ calculated from the self-consistent Eq. (9) for $FePS_3$.

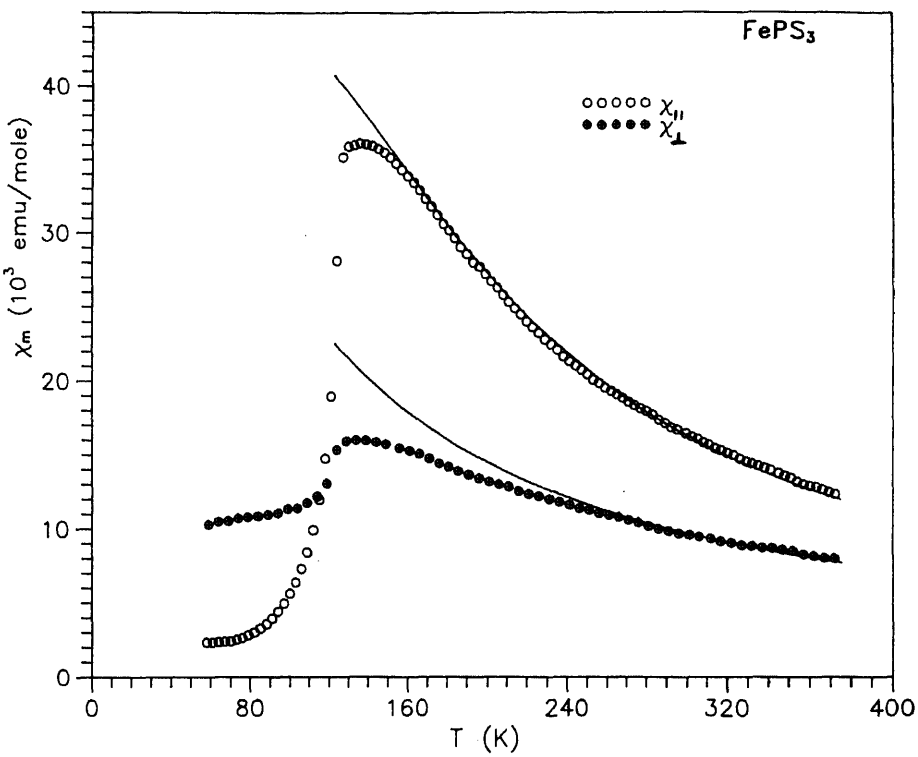

Figure 4. The anisotropic magnetic susceptibilities of $FePS_3$ parallel ($\chi_{\parallel}$) and perpendicular ($\chi_{\perp}$) to the trigonal axis, as a function of temperature. The solid lines are the best least squares CEF fit of the anisotropic susceptibility expression of eq. (10) to the experimental susceptibilities. The values of the microscopic parameters are $J_{nn}/k = 27{\cdot}7$ K; $J_{nnn}/K = -2{\cdot}3$ K; $|\lambda|/k = 166{\cdot}5$ K and $\Delta'/k = 215{\cdot}5$ K.

The results of the present CEF calculation are a considerable improvement on the earlier MFA analysis of Joy *et al* [5]. The earlier MFA analysis, apart from having assumed that $\Delta \gg \lambda$ could be fitted to the experimental data only by forcing an unphysical situation, in which the exchange constants J had opposite signs for $\chi_{\|}$ and $\chi_{\perp}$. Yet another merit of the CEF model, is its accurate prediction of the value of T_N. Substituting the values of J's and α from the fit in (11) gave a T_N value of 122 K. This is remarkably close to the experimental value of 123 K.

5. Conclusions

The anisotropic magnetic susceptibility of the 2*D* orbitally unquenched Ising antiferromagnet $FePS_3$ has been analyzed in the CEF approximation, developed by Lines. The formalism introduces spin correlations in the simplest possible manner while at the same time accounting for the excited states of the orbitally unquenched transition metal ion, the energies of which are comparable to exchange and thermal energies. In $FePS_3$ the degeneracy of the $^5\Gamma_2$ state is completely lifted by the combination of trigonal distortion of the FeS_6 octahedra, spin-orbit coupling and Zeeman splitting. In the calculation of the susceptibilities in the CEF approximation the entire 15 level structure of the $^5\Gamma_2$ state was retained. Good agreement with experiment were obtained for $\Delta/k = 215{\cdot}5$ K; $|\lambda|/k = 166{\cdot}5$ K; $J_{nn}/k = 27{\cdot}7$ K; and $J_{nnn}/k = -2{\cdot}3$ K. Using these values of the crystal field and exchange parameters the CEF predicts a $T_N = 122$ K for $FePS_3$ which is remarkably close to the observed value of T_N. The accuracy of the CEF approximation was also ascertained, by comparison of the calculated susceptibilities in CEF with the experimental susceptibility for the isotropic Heisenberg layered antiferromagnet $MnPS_3$ for which the high temperature series expansion susceptibility is available. The comparison also establishes the effectiveness of the special k point scheme in providing Brillouin zone averages in the computation of susceptibilities in the CEF approximation.

The results of the present analysis show that the CEF approximation provides a simple and elegant way to analyze the susceptibilities of exchange coupled systems in which the individual ion possesses a complicated level structure. In a subsequent paper, we shall show how the CEF approximation can be extended to more complicated multicomponent systems, like the solid solutions of the transition metal thiophosphates of the formula $M'_{1-x}M_xPS_3$(M', M = Mn, Fe, Ni) where M and M' have different energy level structures.

References

[1] W Klingen, R Otto and H Z Hahn, *Z. Anorg. Allg. Chem.* **396**, 271 (1973)
[2] R Brec, *Solid State Ionics* **22**, 3 (1986)
[3] L J De Jongh and A R Miedema, *Adv. Phys.* **23**, 1 (1974)
[4] G Le Flem, R Brec, G Ouvrard, A Louisy and P Segransen, *J. Phys. Chem. Solids* **43**, 455 (1982)
[5] P A Joy and S Vasudevan, *Phys. Rev.* **B46**, 5425 (1992)
[6] P A Joy and S Vasudevan, *J. Phys. Chem. Solids* **54**, 343 (1993)
[7] P A Joy and S Vasudevan, *Phys. Rev.* **B46**, 5134 (1992)
[8] S Whittingham and A Jacobson (ed.) *Intercalation chemistry* (Academic Press, New York, 1982)
[9] P A Joy and S Vasudevan, *J. Am. Chem. Soc.* **114**, 7792 (1992)
[10] P A Joy and S Vasudevan, *J. Chem. Phys.* **99**, 4411 (1993)

[11] R Clement, L Lomas and J P Audiere, *Chem. Mater.* **2**, 641 (1990)
[12] P A Joy and S Vasudevan, *Chem. Mater.* **5**, 1182 (1993)
[13] M E Lines, *Phys. Rev.* **B9**, 3927 (1974)
[14] M E Lines, *Phys. Rev.* **B9**, 3766 (1975)
[15] M E Lines and M Eibschütz, *Phys. Rev.* **B11**, 4853 (1975)
[16] M Eibschütz, M E Lines and L C Sherwood, *Phys. Rev.* **B11**, 4595 (1975)
[17] T Oguchi, *Prog. Theor. Phys.* (Kyoto) **13**, 148 (1955)
[18] J S Smart, *Effective field theories of magnetism* (W B Saunders Co., 1966)
[19] D J Chadi and M L Cohen, *Phys. Rev.* **B8**, 5947 (1973)
[20] S L Cunningham, *Phys. Rev.* **B10**, 4988 (1974) The wavevectors (in units of π/a) for the 2D Hexagonal lattice along with the weightage factors are (2/9, 2/9t), 1/9; (4/9, 4/9t), 1/9; (8/9, 8/9t), 1/9; (2/3, 2/9t), 2/9; (8/9, 4/9t), 2/9; (10/9, 2/9t), 2/9. $t = \sqrt{3}$
[21] G S Rushbrook and P J Wood, *Mol. Phys.* **1**, 257 (1958)
[22] J S Griffith, *The theory of transition-metal ions* (Cambridge University Press, Cambridge, 1961)
[23] K Kurosawa, S Saito and Y Yamaguchi, *J. Phys. Soc. Jpn.* **52**, 3919 (1983)

PRAMANA
— journal of
physics

© Printed in India

Vol. 43, No. 1,
July 1994
pp. 33–39

X-ray diffraction studies of RbBr–RbI mixed crystals

T KUMARA SWAMY, K G SUBHADRA and D B SIRDESHMUKH
Physics Department, Kakatiya University, Warangal 506 009, India

MS received 31 December 1993; revised 16 April 1994

Abstract. Mixed crystals of RbBr and RbI have been prepared from melt. Using an X-ray diffractometer powder patterns have been recorded. The lattice constants show slightly positive deviations from Vegard's law. From the integrated intensities, the mean Debye–Waller factor has been determined. The Debye–Waller factor shows a highly non-linear composition dependence with positive deviations from linearity, the values for intermediate compositions exceeding those for the end members. The Debye temperatures calculated from the Debye–Waller factors show a non-linear composition dependence with negative deviations from linearity.

Keywords. Alkali halides; mixed crystals; Debye–Waller factors; Debye temperature.

PACS Nos 61·10; 61·14; 63·20; 65·90

1. Introduction

The results of X-ray diffraction studies of KBr–RbBr, RbCl–RbBr and KCl–RbCl mixed crystals have been reported earlier by Srinivas and Sirdeshmukh ([1], hereinafter referred to as I), Srinivas *et al* [2] and Srinivas and Sirdeshmukh [3]. The results of similar studies on the RbBr–RbI mixed crystal system are reported here.

According to Tobolsky's [4] criterion for complete miscibility, RbBr and RbI should be miscible over the entire composition range at room temperature. On the other hand, Hovi [5], from calculations of heat of formation, suggested that these mixed crystals would be stable above 160°C; Ahtee and Koski [6] gave 73°C as the critical solution temperature. Nevertheless, Thomas and Wood [7], Ahtee and Koski [6] and Ahtee [8] were able to record X-ray powder patterns of single phase RbBr–RbI mixed crystals at room temperature in a dry atmosphere. Ahtee and Koski [6] and Ahtee [8] also determined the lattice constants, but there is considerable difference in the sets of values reported by them. Regarding the Debye–Waller factors and Debye temperatures, there is no reported work on this system.

2. Experimental

The starting materials RbBr and RbI used in the preparation of mixed crystals of the $RbBr_xI_{(1-x)}$ system were of 99·9% purity and were obtained from E Merck. RbBr and RbI were taken in the required molar proportion, mixed and ground into a fine powder. This mixture was placed in a ceramic crucible and heated in a furnace and melted. Heating was continued at this temperature for two hours and then the molten liquid was gradually cooled. Transparent single crystals with linear dimensions of

several mm were obtained. Mixed crystals were obtained over the whole composition range.

The crystals were ground into fine powder and used for further work. The composition of the crystals was determined by potentiometric titration. The composition thus determined was close to, but slightly different from, the starting composition. For X-ray work, the powders were packed in aluminium sample holders by slight pressing. The X-ray diffractograms were recorded with a JEOL JDX-8P diffractometer fitted with a NaI(Tl) scintillation counter. Filtered CuKα radiation was employed. The Bragg peaks were recorded in the $\theta - 2\theta$ mode with a scanning speed of 1/2°/min and a chart speed of 20 mm/min. Under these conditions, Bragg angles could be determined with an accuracy of $\pm 0{\cdot}01°$ in 2θ. The Bragg peaks were scanned over a range of 2 degrees in 2θ on either side of the peaks.

3. Analysis of data

The procedure for the accurate determination of lattice constant (a_0) is as discussed by Parrish and Wilson [9]. For the determination of the mean Debye–Waller factor (B_{obs}), the inputs are the observed integrated intensities (I_0) and the calculated intensities for a static lattice (I_c). The determination of I_0, the various corrections involved and the calculation of I_c using the atomic scattering factors is discussed in *I*. The procedure for removing the static contribution (B_{static}) from the observed Debye–Waller factor (B_{obs}) to yield the thermal Debye–Waller factor ($B_{thermal}$) is also given in *I*. $B_{thermal}$ in turn yields the Debye temperature using the well-known expression from the Debye–Waller theory. Recently, Horning and Staundenmann [10] pointed out that the Debye temperature thus obtained needs to be multiplied by $\sqrt{p}$ (where p is the number of vibrating units). This correction has been applied to yield the final Debye temperature (θ_M).

4. Results and discussion

4.1 *Stability*

As discussed in § 1, there is some controversy regarding the stability of this system. In the present study, all the crystals in the series showed complete mixing and the X-ray patterns corresponded to the single phase. Even after ageing over several months, the samples gave the same single phase X-ray patterns indicating that the RbBr–RbI system is quite stable at room temperature.

4.2 *Composition dependence of lattice constants*

The lattice constants (a_0) obtained in the present work are given in table 1 along with the values obtained by Ahtee and Koski [6] and Ahtee [8]. There is large difference between the values obtained by Ahtee and Ahtee and Koski. The present values also show differences from the data from these earlier reports, but between the two, our results are closer to those of Ahtee and Koski. The lattice constants of mixed crystals generally follow one of the following relations

$$a_0 = (x)a_1 + (1-x)a_2 \quad \text{(Vegard's law)} \tag{1}$$

$$a_0^3 = (x)a_1^3 + (1-x)a_2^3 \quad \text{(Retger's law)} \tag{2}$$

where a_1 and a_2 are the lattice constants of the two end members.

Table 1. Lattice constants (a_0) of $RbBr_xI_{(1-x)}$ mixed crystals.

	a_0(Å)		
x	Ahtee and Koski (1968)	Ahtee (1969)	Present work
0·00	7·3380	7·3291	7·3366 ± 0·0016
0·10	7·2960		
0·18			7·2551 ± 0·0029
0·20	7·2000	7·2414	
0·27			7·2139 ± 0·0030
0·30	7·2050	7·1975	
0·39			7·5193 ± 0·0008
0·40	7·1600	7·1560	
0·48			7·1182 ± 0·0018
0·50	7·1130	7·1090	
0·60	7·0700	7·0643	7·0662 ± 0·0010
0·68			7·0261 ± 0·0065
0·70	7·0180	7·0178	
0·79			6·9757 ± 0·0010
0·80	6·9730	6·9694	
1·00	6·8820	6·8768	6·8781 ± 0·0021

With regard to the composition dependence of the lattice constants of the RbBr–RbI system, Ahtee and Koski [6] stated that with their accuracy it was not possible to observe deviations from Vegard's law. On the other hand, Ahtee observed that his data show positive deviations with respect to Vegard's law and negative deviations with respect to Retger's law. However, Ahtee states that the composition of the crystals was estimated from the lattice constants assuming that they follow Vegard's law. When lattice constants are used to estimate the composition, they cannot, at the same time, be used to decide the law of composition dependence.

As far as the present results are concerned, the composition dependence of lattice constants is shown in figure 1. Because of the scale involved, this plot cannot reveal detailed information regarding composition dependence. For this purpose, following Slagle and McKinstry [11], we plot the difference between the observed lattice constant (a_0) and the value (a_c) calculated from laws of Vegard and Retger. These plots are shown in the inset of figure 1. It is seen that our values show positive deviations from Vegard's law and negative deviations from Retger's law. But the deviations from Vegard's law are much less than those from Retger's law.

4.3 *Debye–Waller factor*

The values of the mean Debye–Waller factor for the pure and mixed crystals are given in table 2. The present value of $2{\cdot}89 \pm 0{\cdot}18\,A^2$ for RbBr is larger than the experimental value of $2{\cdot}18 \pm 0{\cdot}08\,A^2$ obtained by Srinivas and Sirdeshmukh [1] but is closer to the mean value of $2{\cdot}44\,A^2$ obtained by Govindarajan [12] from lattice dynamics. In RbI the present value of $3{\cdot}36 \pm 0{\cdot}14\,A^2$ for the mean Debye–Waller factor is in good agreement with the value $3{\cdot}19 \pm 0{\cdot}11\,A^2$ obtained by Beg *et al* [13] from neutron diffraction. The composition dependence (figure 2) is highly non-linear

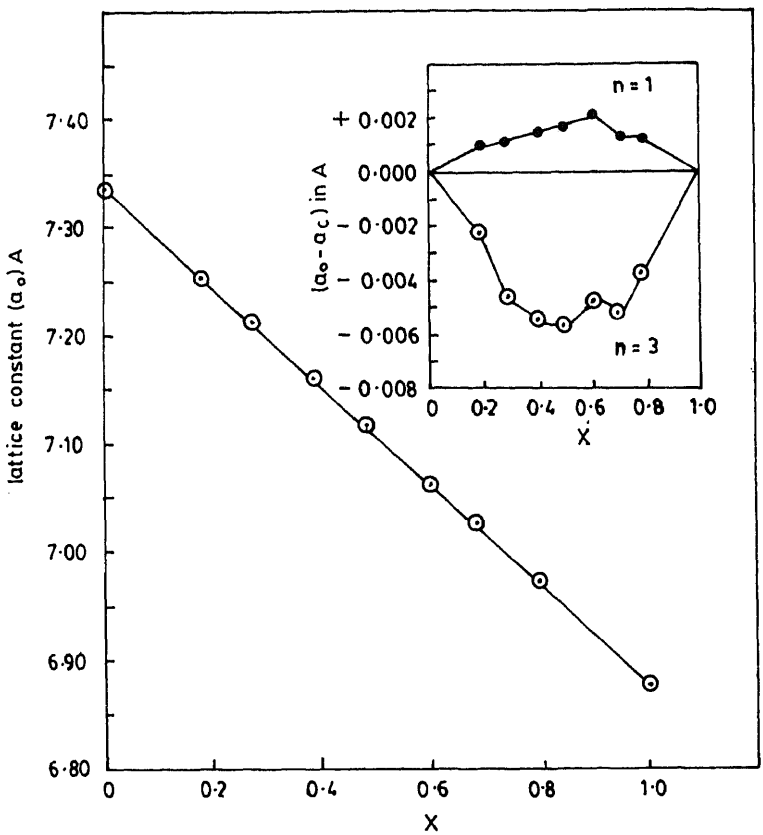

Figure 1. Plots of lattice constant (a_0) as a function of composition x; [inset, $(a_0 - a_c)$ vs x].

Table 2. Debye–Waller factors (B) and Debye temperatures (θ_M) for the $RbBr_xI_{(1-x)}$ system.

x	B (Observed) (A^2)	B (Static) (A^2)	B (Thermal) (A^2)	θ_M (K)
0·00	3·36 ± 0·14	0·00	3·36	139·2 ± 3
0·18	3·85 ± 0·20	0·22	3·63	136·6 ± 3
0·27	3·99 ± 0·22	0·30	3·69	137·0 ± 4
0·39	4·10 ± 0·25	0·36	3·74	138·3 ± 5
0·48	4·34 ± 0·29	0·38	3·96	135·8 ± 5
0·60	4·15 ± 0·26	0·37	3·78	140·9 ± 5
0·68	4·05 ± 0·27	0·33	3·72	143·8 ± 5
0·79	3·69 ± 0·17	0·25	3·44	151·5 ± 4
1·00	2·89 ± 0·18	0·00	2·89	170·6 ± 5

with positive deviations from linearity. The values for the intermediate compositions exceed the values for the pure end members. It is known that because of the difference in sizes of the Br^- and I^- ions, there will be a static component in the Debye–Waller factor. The values of this component calculated from the model of Dernier *et al* [14]

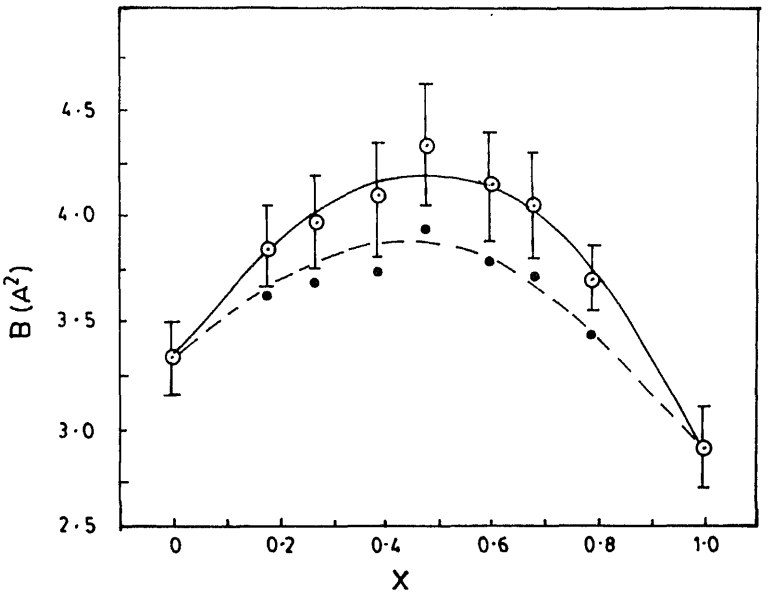

Figure 2. Plot of Debye–Waller factor vs x (⊙, B_{obs}; ●, $B_{Thermal}$).

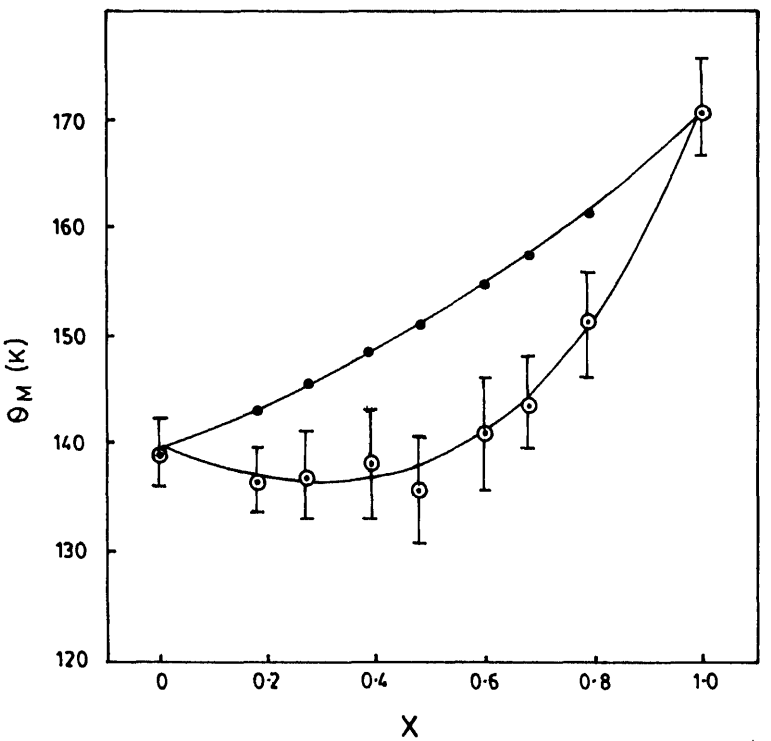

Figure 3. Plot of Debye temperature vs x(⊙, θ_M; ●, from Kopp-Neumann relation).

are given in the same table. The values of the Debye–Waller factor corrected for the static contributions ($B_{thermal}$) are also given in table 2 and shown in figure 2. It can be seen that even after this correction, the Debye–Waller factors of the mixed crystals are larger than the values expected from additivity. Ahtee *et al* [15] made similar observations in the case of KCl–KBr mixed crystals and attributed the enhancement of the Debye–Waller factor to an increase in the vibrational entropy. The same reason may be responsible for the enhancement of $B_{thermal}$ observed in the RbBr–RbI system.

4.4 *Debye temperature*

The values of Debye temperature for the pure and mixed crystals are included in table 2 and are shown in figure 3. The Debye temperature varies with composition in a non-linear manner showing negative deviations. Similar deviations were observed in our earlier studies of KBr–RbBr, RbCl–RbBr and KCl–RbCl mixed crystal systems. However, the maximum deviation from linearity (for the equimolar composition) is larger in this system than in the systems studied earlier.

Sirdeshmukh and Srinivas [16] analysed the data on the Debye temperatures of a large number of mixed crystals and concluded that, by and large, the composition dependence is well-described by the Kopp-Neumann relation (for a discussion, see Ghatak and Kothari [17]). The values calculated from this relation are shown in figure 3; the observed values are lower than these values. This excessive lowering of the Debye temperatures of the mixed crystals may also be related to the increase in the vibrational entropy.

5. Conclusions

Powder X-ray diffraction studies show that the mixed crystals in the RbBr–RbI system are essentially stable. The lattice constants are close to values expected from Vegard's law. The mean Debye–Waller factor shows a highly non-linear composition dependence, values for intermediate compositions being larger than those for the pure components. The Debye temperature shows a non-linear composition dependence with negative deviations from linearity.

Acknowledgements

This article is dedicated to Professor S Ramaseshan on his completing seventy years. Thanks are due to the Department of Science and Technology for funding a project on X-ray studies of crystals.

References

[1] K Srinivas and D B Sirdeshmukh, *Pramana – J. Phys.* **25**, 71 (1985)
[2] K Srinivas, M Ateequddin and D B Sirdeshmukh, *Pramana – J. Phys.* **28**, 81 (1987)
[3] K Srinivas and D B Sirdeshmukh, *Pramana – J. Phys.* **31**, 221 (1988)
[4] A V Tobolsky, *J. Chem. Phys.* **10**, 187 (1942)
[5] M Hovi, *Ann. Acad. Sci. Fenn.* **AVI**, 315 (1969)
[6] M Ahtee and H Koski, *Ann. Acad. Sci. Fenn.* **AVI**, 297 (1968)
[7] B Thomas and L J Wood, *J. Am. Chem. Soc.* **57**, 822 (1936)
[8] M Ahtee, *Ann. Acad. Sci. Fenn.* **AVI**, 313 (1969)

[9] W Parrish and A J C Wilson, In *International Tables for X-ray Crystallography* (Kynoch Press, Birmingham, 1959) Vol. II, 216
[10] R D Horning and J L Staudenmann, *Acta Crystallogr.* **A44** 136 (1988)
[11] O D Slagle and H A McKinstry, *Acta Crystallogr.* **21**, 1013 (1966)
[12] J Govindarajan, *Acta Crystallogr.* **A29**, 576 (1973)
[13] M M Beg, J Aslam, N Ahmad, Q H Khan and N M Butt, *Phys. Status Solidi* **B94** K45 (1979)
[14] P D Dernier, W Weber and L D Longinotti, *Phys. Rev.* **B14** 3635 (1976)
[15] M Ahtee, A Pesonen, P Salmo and O Inkinen, *Z. Naturforsch.* **A25** 1761 (1970)
[16] D B Sirdeshmukh and K Srinivas, *J. Mater. Sci.* **21**, 4117 (1986)
[17] A K Ghatak and L S Kothari, *Lattice dynamics* (Addison Wesley, London, 1972)

PRAMANA
journal of
physics

© Printed in India

Vol. 43, No. 1,
July 1994
pp. 41–54

Interplay of superconductivity and antiferromagnetism in $SmRh_4B_4$

T C LOYA and S L KAKANI*
Department of Physics, Government (Autonomous) College, Kota 324001, India
*Department of Physics, MLV Government (Autonomous) College, Bhilwara 311001, India

MS received 2 February 1994

Abstract. A microscopic theory of interplay of superconductivity and antiferromagnetism in rare earth ternary systems is developed from first principles for less than half filled f atomic shells. Self consistent equations for the superconducting order parameter Δ and magnetic order parameter Γ, are derived using a Green's function technique and equation of motion method. The theory is applied to explain the experimental results in the antiferromagnetic superconductor $SmRh_4B_4$. The present model explains true coexistence of superconductivity and antiferromagnetism and the suppression of superconductivity by antiferromagnetism. The behaviour of superconducting order parameter (Δ), magnetic order parameter (Γ), the specific heat, the density of states, free energy and critical field (H_c) is also studied for the system $SmRh_4B_4$.

Keywords. Superconductivity; antiferromagnetism; phase transition; Green's functions; magnetism order parameter.

PACS Nos 74·10; 74·60; 74·70; 75·10; 75·40; 76·10; 10·15

1. Introduction

The coexistence of superconductivity and antiferromagnetism in the same system has been a long-standing problem in the condensed matter physics. Almost since the discovery of superconductivity, it has been known that there is an antipathy between superconductivity and magnetism. The apparently contradictory conditions necessary to realize these two collective phenomena have for more than two decades, challenged both theoreticians and experimentalists alike.

Within the past few years several series of isostructural ternary rare earth compounds have been found that exhibit true coexistence of superconductivity and antiferromagnetism [1–9]. In the ternary rare earth systems under consideration, the magnetic rare earth ions are distributed periodically throughout the crystal lattice, and each rare earth ion has a partially filled $4f$ electron shell and a corresponding magnetic moment. These compounds are metallic and has provided for the first time experimentally realizable systems for studying the interplay between superconductivity and antiferromagnetism. The rare earth chalcogenides and rare earth rhodium borides are the typical examples of antiferromagnetic superconductors. On cooling, these compounds first become superconducting below the superconducting transition temperature (T_c) and then on further cooling below the Neél temperature (T_N) the system is antiferromagnetically ordered which coexist with superconductivity. Typical examples are $RE_xMo_6S_8$ (for RE = Gd, Tb, Dy and Er) with $x = 1{\cdot}0$ or $1{\cdot}2$ and RE

Rh_4B_4 (for RE = Nd, Sm and Tm). The most important result about these systems is the anomalous behaviour of the upper critical field Hc_2 versus temperatures T in the vicinity of T_N. The compound $Tb_2Mo_3Si_4$ [10] is an exception in the sense that its $T_c(\approx 0{\cdot}8\,K)$ is much below $T_N(\approx 19\,K)$. One of the most interesting and best investigated typical antiferromagnetic superconductors is $SmRh_4B_4$. The important experimental observations about this system are as follows:

(i) The unit cell of the $SmRh_4B_4$ is a primitive tetragonal with approximate lattice parameters $a = 5{\cdot}312\,Å$, $C = 7{\cdot}430\,Å$ and contains two formula units [11].
(ii) Electronic energy band structure calculations for the full 18 atom unit cell reveal that the conduction band is mainly formed by d electrons of Rh ions and $4f$ Sm electrons are highly localized [12]. One obtains the values of Fermi energy, E_F and the total density of states N(O) as about $1{\cdot}75 \times 10^{-18}$ J and 2×10^{19} per Joule per atom respectively. Band structure calculation further reveals that the exchange interaction between conduction electrons (d-band) and localised $4f$ electrons is very small because of its unique lattice structure. This ensures the possibility of coexistence of superconductivity and antiferromagnetism in $SmRh_4B_4$. The estimated value of exchange interaction is an order of magnitude smaller than values known for binary alloy systems [6].
(iii) Study of electrical resistance versus temperature in various applied magnetic fields for $SmRh_4B_4$ reveals that in all fields measured below its zero-temperature upper critical field $Hc_2 \sim 1{\cdot}85$ KOe, the sample exhibits only a single normal to superconducting state transition. The normal state resistance however markedly decreases below 0·87 K, indicative of magnetic phase transition below the zero field superconducting transition temperature $T_c = 2{\cdot}75$ K.
(iv) The upper critical field (Hc_2) versus temperature (T) data show a sharp discontinuity in its slope at about 0·87 K [14]; Below this temperature Hc_2 is considerably larger than would be expected from the high temperature portion of the curve. Thus the most important result about this system is the anomalous behaviour of Hc_2.
(v) Magnetic phase transition at 0·87 K does not influence the thermal conductivity in a drastic way. Below T_N, the thermal conductivity continues to decrease with decreasing temperature. Thermal conductivity measurements by Ott *et al* [13] indicate the persistence of bulk superconductivity in magnetically ordered $SmRh_4B_4$.
(vi) Specific heat versus temperature data [14] reveal a small jump in the heat capacity at T_c followed by a pronounced lambda (λ) type anomaly at $T_\lambda = 0{\cdot}87$ K, almost identical with the temperature at which the discontinuity in the slope of the Hc_2 versus T data occur.
(vii) The inverse susceptibility (χ^{-1}) versus temperature (T) data reveal a cusp near T_λ indicating that there is an antiferromagnetic transition at this temperature.

Recent discovery of high temperature superconductivity in $La_{2-x}Sr_xCuO_4$ ($T_c \approx 40$ K) [15] and $YBa_2Cu_3O_7$ ($T_c \approx 90$ K) [16] have reopened the problem of coexistence of antiferromagnetism and superconductivity in these systems. There is no clear experimental evidence that these two phases coexist in a high-T_c system, though there is some evidence from muon spin rotation that it is so [17, 18]. A clear detection of such coexistence would demonstrate directly the importance of exchange interactions in a superconducting phase.

Several attempts have been made to explain the interplay of superconductivity and antiferromagnetism in the same system [19–31]. Baltensperger and Strassler [19] were the first who concluded that the two phenomena were not incompatible. Several

mechanisms by means of which superconductivity is modified by antiferromagnetic order have been considered such as [20–31]:

(i) The reduction in pair breaking due to decrease of the mean magnetization and, in turn, the conduction electron spin polarization below T_N;
(ii) The increase of pair breaking due to magnetic moment fluctuations in the vicinity of T_N;
(iii) The decrease of the attractive phonon mediated electron–electron pairing interaction by antiferromagnetic magnons;
(iv) The reduction of available phase space for virtual pair scattering due to the introduction of gaps in one electron excitation spectrum $E(K)$ by the change in lattice periodicity associated with antiferromagnetic order;
(v) The pairing of electrons with finite momentum.

However, these models are phenomenological in nature and a microscopic model is still lacking. No doubt, these studies have provided a basic understanding of the interplay of superconductivity and antiferromagnetism. In the present work an attempt is made to develop the microscopic theory of antiferromagnetic superconductors for less than half filled f shells.

2. The model Hamiltonian

We consider a model situation in which besides the pairing interaction among conduction electrons, there is an effective antiferromagnetic coupling between nearest neighbour localized electrons alongwith a new two-body interaction between conduction and localized electrons. The antiferromagnetic ordering appears in this when intersite hopping is taken into account alongwith intrasite Coulomb repulsion [32]. When the system has both localized and conduction electrons, the mixing between the two states can lead to interesting interactions [33–35]. The above mechanism is relevant for rare earth ternary systems having less than half filled f-atomic shells [36]. In the light of the above features, the model Hamiltonian can be written as [28].

$$H = \sum_{K,\sigma} (\varepsilon_K - \mu) C^\dagger_{K\sigma} C_{K\sigma} - g \sum_{K,K'} C^\dagger_{K'\uparrow} C^\dagger_{-K'\downarrow} C_{-K\downarrow} C_{K\uparrow} + \sum_{l,\sigma} E_l C^\dagger_{l\sigma} C_{l\sigma}$$
$$+ \sum_{\substack{l,m \\ \sigma,\sigma'}} J_{lm} C^\dagger_{l\sigma} C^\dagger_{m\sigma'} C_{l\sigma'} C_{m\sigma} + \left(\sum_{K,l,m} G^{lm}_K C^\dagger_{l\uparrow} C^\dagger_{m\downarrow} C_{-K\downarrow} C_{K\uparrow} + \text{h.c.} \right) \qquad (1)$$

Where the first two terms are the BCS reduced Hamiltonian [37], with ε_K representing the single particle energy and μ the chemical potential and g the usual pairing interaction. The third and fourth terms respectively denote the single particle energy of localized electrons at sites 1 with energy E_l and the exchange interaction between localized spins, J_{lm} being the effective exchange constant. The last term is the new interaction involving conduction electron pairs and two localized electrons, one at site (say) 1 and another at m, G^{lm}_K being the interaction constant.

Here $C^\dagger_{K\sigma}$ and $C_{K\sigma}$ are the fermion creation and annihilation operators for the Bloch state $|\mathbf{K}\sigma\rangle$ with $\mathbf{K}$ the conduction electron wave vector and σ the spin. $(C^\dagger_{l\sigma}, C_{l\sigma})$ and $(C^\dagger_{m\sigma}, C_{m\sigma})$ are the fermion (creation and annihilation) operators for localized electrons. The fermion operators satisfy the usual fermion anticommutation rules.

We study the Hamiltonian (1) with the help of a Green's function technique, using the equation of motion method.

3. Green's functions

We define the following Green's functions:

$$\ll C_{K\uparrow}; C^{\dagger}_{K\uparrow} \gg = -i\theta(t)\langle [C_{K\uparrow}(t); C^{\dagger}_{K\uparrow}(0)]\rangle \tag{2a}$$

$$\ll C^{\dagger}_{-K\downarrow}; C^{\dagger}_{K\uparrow} \gg = -i\theta(t)\langle [C^{\dagger}_{-K\downarrow}(t); C^{\dagger}_{K\uparrow}(0)]\rangle \tag{2b}$$

$$\ll C_{l\uparrow}; C^{\dagger}_{l\uparrow} \gg = -i\theta(t)\langle [C_{l\uparrow}(t); C^{\dagger}_{l\uparrow}(0)]\rangle \tag{2c}$$

$$\ll C^{\dagger}_{m\downarrow}; C^{\dagger}_{l\uparrow} \gg = -i\theta(t)\langle [C^{\dagger}_{m\downarrow}(t); C^{\dagger}_{l\uparrow}(0)]\rangle. \tag{2d}$$

Where the first two Green's functions are defined for conduction electrons and last two are for localized electrons. These Green's functions satisfy the following equations:

$$(i\omega_n - \xi_K)\ll C_{K\uparrow}, C^{\dagger}_{K\uparrow} \gg = 1 - (\Delta - \Gamma)\ll C^{\dagger}_{-K\downarrow}; C^{\dagger}_{K\uparrow} \gg \tag{3}$$

$$(i\omega_n + \xi_K)\ll C^{\dagger}_{-K\downarrow}, C^{\dagger}_{K\uparrow} \gg = 1 - (\Delta - \Gamma)\ll C_{K\uparrow}; C^{\dagger}_{K\uparrow} \gg \tag{4}$$

where we have used $\xi_K = \varepsilon_K - \mu$ and defined superconducting order parameter (Δ) and magnetic order parameter (Γ) as

$$\Delta = |g| \sum_{K'} \langle C_{-K'\downarrow} C_{K'\uparrow}\rangle = |g| \sum_{K'} \langle C^{\dagger}_{K'\uparrow} C^{\dagger}_{-K'\downarrow}\rangle \tag{5}$$

and

$$\Gamma = \sum_{lm} G^{lm}_K \langle C_{m\downarrow} C_{l\uparrow}\rangle = \sum_{lm} G^{lm}_K \langle C^{\dagger}_{l\uparrow} C^{\dagger}_{m\downarrow}\rangle \tag{6}$$

with

$$\omega_n = (2n+1)\pi/\beta \text{ and } \beta = (k_B T)^{-1}$$

Similarly, one obtains

$$\left(i\omega_n - E_l + \sum_{l'} 2J_{ll'}\langle n_{l'\uparrow}\rangle\right)\ll C_{l\uparrow}; C^{\dagger}_{l\uparrow} \gg = 1 + \sum_m \Gamma_{lm} \ll C^{\dagger}_{m\downarrow}; C^{\dagger}_{l\uparrow} \gg \tag{7}$$

and

$$\left(i\omega_n + E_m - \sum_{m'} 2J_{mm'}\langle n_{m'\downarrow}\rangle\right)\ll C^{\dagger}_{m\downarrow}; C^{\dagger}_{l\uparrow} \gg = \Gamma_{ml} \ll C_{l\uparrow}; C^{\dagger}_{l\uparrow} \gg \tag{8}$$

where

$$\langle n_{l\sigma}\rangle = \langle C^{\dagger}_{l\sigma} C_{l\sigma}\rangle$$

and

$$\Gamma_{ml} = \sum_K G^{ml}_K \langle C_{-K\downarrow} C_{K\uparrow}\rangle$$

considering only nearest neighbour (lm) correlations, one obtains

$$\ll C_{K\uparrow}, C^{\dagger}_{K\uparrow} \gg = \frac{(i\omega_n + \xi_K)}{[(i\omega_n)^2 - \xi_K^2 - (\Delta - \Gamma)^2]} \tag{9}$$

$$\ll C^{\dagger}_{-K\downarrow}; C^{\dagger}_{K\uparrow} \gg = \frac{-(\Delta - \Gamma)}{[(i\omega_n)^2 - \xi_K^2 - (\Delta - \Gamma)^2]} \tag{10}$$

$$\ll C_{j\sigma}; C_{j\sigma}^{\dagger} \gg = \frac{i\omega_n + \tilde{E}_{j\sigma}}{[(i\omega_n)^2 - \tilde{E}_{j\sigma}^2 - \Gamma_j^2]} \tag{11}$$

$$\ll C_{m\sigma}^{\dagger}; C_{l-\sigma} \gg = \frac{\Gamma_{ml}}{[(i\omega_n)^2 - \tilde{E}_{m\sigma}^2 - \Gamma_m^2]} \tag{12}$$

where

$$\tilde{E}_{l\sigma} = E_l - \sum_{l'} 2J_{ll'} \langle n_{l'\sigma} \rangle \tag{13}$$

and

$$\Gamma_j^2 = \sum_l \Gamma_{jl} \Gamma_{lj} \tag{14}$$

summed over all nearest neighbours sites to J.

4. Order parameters

(i) *Superconducting order parameter* (Δ):

It is given by [38]

$$\Delta = k_B T \sum_{K'n} |g| \ll C_{-K'\downarrow}^{\dagger} C_{K'\uparrow}^{\dagger} \gg.$$

Using (10) one obtains

$$\Delta = \frac{1}{\beta} \sum_n \int \frac{d^3 K'}{(2\pi)^3} |g| \left\{ \frac{-(\Delta - \Gamma)}{(i\omega_n)^2 - \xi_{K'}^2 - (\Delta - \Gamma)^2} \right\} \tag{15}$$

where $|g|$ is the electron–electron phonon mediated coupling constant having the dimensions of energy. On using Poisson summation formulas and contour integration (15) yields:

$$\frac{1}{N(0)|g|} = \int_0^{\hbar\omega_D} d\xi_{K'} \frac{\left(\frac{\Delta - \Gamma}{\Delta}\right) \tanh\left[\frac{\beta}{2}\sqrt{\xi_{K'}^2 + (\Delta - \Gamma)^2}\right]}{[\xi_{K'}^2 + (\Delta - \Gamma)^2]^{1/2}} \tag{16}$$

where $N(0)$ (also expressed as $N(E_F)$ is the density of states for one spin projection at the Fermi surface. On putting $\Gamma = 0$, equation (16) reduces to the standard form of BCS equation of superconductivity [38]

$$\frac{1}{N(0)|g|} = \int_0^{\hbar\omega_D} d\xi_{K'} \frac{\tanh\left(\frac{\beta}{2}(\xi_{K'}^2 + \Delta^2)^{1/2}\right)}{(\xi_{K'}^2 + \Delta^2)^{1/2}} \tag{17}$$

(i) *Magnetic order parameter* (Γ):

It is given by

$$\Gamma = \frac{1}{\beta} \sum_{n,l,m} G_K^{lm} \ll C_{m\downarrow}^{\dagger}, C_{l\uparrow}^{\dagger} \gg.$$

Using (12), one obtains

$$\Gamma = \sum_{m,l} G_K^{ml} \frac{\Gamma_{ml} \tanh\left(\frac{\beta}{2}(\tilde{E}_{m\downarrow}^2 + \Gamma_m^2)^{1/2}\right)}{2(\tilde{E}_{m\downarrow}^2 + \Gamma_m^2)^{1/2}}. \tag{18}$$

where

$$\Gamma_{ml} = \frac{1}{\beta} \sum_{n,k} G_K^{ml} \ll C_{-K\downarrow}^{\dagger}; C_{K\uparrow}^{\dagger} \gg. \tag{19}$$

We note that Γ is in turn related to Δ through (19). This shows that two phases can coexist in some temperature range.

5. Superconducting transition temperature (T_c)

Within the limit $\Delta \to 0$, (17) yields

$$\frac{1}{N(0)|g|} = \int_0^{\hbar\omega_D} d\xi \left[\frac{\beta}{2} \frac{\Gamma^2 \operatorname{sech}^2 \frac{\beta}{2}(\xi^2 + \Gamma^2)^{1/2}}{\xi^2 + \Gamma^2} + \frac{\tanh \frac{\beta}{2}(\xi^2 + \Gamma^2)^{1/2}}{(\xi^2 + \Gamma^2)^{1/2}} \right] \tag{20}$$

6. Density of states $N(\omega)$

An important function and the one most susceptible to experimental verification is the density of states as a function of the excitation energy ε_K. The density of states per atom per spin $N(\omega)$ is given by

$$N(\omega) = \lim_{\varepsilon \to 0} \frac{i}{2\pi N} \sum_K [G_{\uparrow\uparrow}(K, \omega + i\varepsilon) - G_{\uparrow\uparrow}(K, \omega - i\varepsilon)]. \tag{21}$$

The one particle Green's function (9) can be rewritten as

$$G_{\uparrow\uparrow}(K, \omega) = \frac{1}{2}\left[\frac{((\xi_k/\alpha) + 1)}{(i\omega_n - \alpha)} - \frac{((\xi_K/\alpha) - 1)}{(i\omega_n + \alpha)} \right]$$

where

$$\alpha^2 = \xi_k^2 + (\Delta - \Gamma)^2. \tag{22}$$

Using the following properties of δ-function

$$\delta(x) = \frac{1}{2\pi i}\left\{ \frac{1}{x - i\varepsilon} - \frac{1}{x + i\varepsilon} \right\} \tag{23}$$

and

$$\delta\{g(t_n)\} = \sum_n \frac{1}{|g'(t_n)|} \delta(t - t_n) \tag{24}$$

where

$$g(t_n) = 0 \text{ and } g'(t_n) \neq 0.$$

One obtains from (21) and (22)

$$\frac{N(\omega)}{N(0)} = \frac{1}{N} \frac{\omega}{[\omega^2 - (\Delta - \Gamma)^2]^{1/2}} \tag{25}$$

which in the limit $\Gamma \to 0$, reduces to

$$\frac{N(\omega)}{N(0)} = \frac{1}{N}\frac{\omega}{(\omega^2-\Delta^2)^{1/2}} \quad \text{for} \quad \omega > \Delta$$
$$= 0, \qquad \text{otherwise.}$$

This is the same as obtained from the BCS theory [39].

7. Electronic specific heat (C_{es})

The electronic specific heat per atom of a superconductor is determined from

$$C_{es} = \frac{\partial}{\partial T}\frac{1}{N}\sum_K 2\xi_K \langle C^\dagger_{K\uparrow}, C_{K\uparrow}\rangle. \tag{26}$$

Correlation function appearing in (26) can be obtained from

$$\langle C^\dagger_{K\uparrow}, C_{K\uparrow}\rangle = \lim_{\varepsilon\to 0+}\frac{i}{2\pi}\int_{-\infty}^{\infty}\frac{\langle\langle C_{K\uparrow}C^\dagger_{K\uparrow}\rangle\rangle_{\omega+i\varepsilon} - \langle\langle C_{K\uparrow}C^\dagger_{K\uparrow}\rangle\rangle_{\omega-i\varepsilon}}{e^{\beta\omega}-1}\mathrm{d}\omega \tag{27}$$

using (9), (27) gives

$$\langle C^\dagger_{K\uparrow}C_{K\uparrow}\rangle = \frac{1}{2}\left[\frac{(1+(\xi_K/\alpha))}{e^{\beta\alpha}-1} + \frac{(1-(\xi_K/\alpha))}{e^{-\beta\alpha}-1}\right] \tag{28}$$

from (26) and (28) one obtains

$$C_{es} = \frac{N(0)}{N}\frac{1}{k_B T^2}\int_0^{\hbar\omega_D}\mathrm{d}\xi_K \xi_K^2 \operatorname{sech}^2\left(\frac{\alpha}{2k_B T}\right) \tag{29}$$

8. Free energy difference (F_S–F_N)

The free energy difference between the superconducting and normal state can be calculated by means of the formula [38].

$$\frac{F_S - F_N}{V} = \int_0^\Delta \mathrm{d}\Delta\,\Delta^2\frac{\mathrm{d}}{\mathrm{d}\Delta}\left(\frac{1}{|g|}\right) \tag{30}$$

from (16) and (30), one obtains

$$\frac{F_S - F_N}{V} = \frac{\Delta^2}{|g|} - 2N(0)\int_0^{\hbar\omega_D}\mathrm{d}\xi\left[\int_0^\Delta \mathrm{d}\Delta\frac{(\Delta-\Gamma)\tanh(\beta E/2)}{E}\right] \tag{31}$$

where

$$E = [\xi^2 + (\Delta-\Gamma)^2]^{1/2}$$

on evaluating Δ integral, one obtains

$$\frac{F_S - F_N}{V} = \frac{\Delta^2}{|g|} - \frac{4N(0)}{\beta}\int_0^{\hbar\omega_D}\mathrm{d}\xi \ln\frac{\cosh\left(\frac{\beta}{2}[\xi^2+(\Delta-\Gamma)^2]^{1/2}\right)}{\cosh\left(\frac{\beta}{2}(\xi^2+\Gamma^2)^{1/2}\right)} \tag{32}$$

$$\frac{F_S - F_N}{V} = \frac{\Delta^2}{|g|} - \frac{4N(0)}{\beta}\int_0^{\hbar\omega_D} d\xi\left[\ln(1+e^{-\beta E}) + \frac{1}{2}\beta(E-E')\right] + \frac{4N(0)}{\beta}\int_0^{\hbar\omega_D} d\xi \ln(1+e^{-\beta E'}) \tag{33}$$

$$= \frac{\Delta^2}{|g|} - N(0)\left[\frac{1}{2}\Delta(\Delta-2\Gamma) + (\Delta-\Gamma)^2\ln\left(\frac{2\hbar\omega_D}{\Delta-\Gamma}\right) - \Gamma^2\ln\left(\frac{2\hbar\omega_D}{1}\right)\right] + \frac{1}{3}\pi^2 N(0)(k_B T)^2 - \frac{4N(0)}{\beta}\int_0^{\hbar\omega_D} d\xi \ln(1+e^{-\beta E})$$

where

$$E' = [\xi^2 + \Gamma^2]^{1/2}. \tag{34}$$

The last integral in (33) have been evaluated by extending it to infinity because $\hbar\omega_D \gg k_B T$.

9. Critical field (H_c)

The low temperature critical field H_c is given by [38]

$$H_c = [8\pi|F_S - F_N|]^{1/2} \tag{35}$$

(32) and (35) yield

$$H_c = (8\pi V)^{1/2}\left[\frac{\Delta^2}{|g|} - \frac{4N(0)}{\beta}\int_0^{\hbar\omega_D} d\xi \ln\left(\frac{\cosh(\beta E/2)}{\cosh(\beta E'/2)}\right)\right]^{1/2}. \tag{36}$$

Using (34), one can also put H_c as

$$H_c = (8\pi V)^{1/2}\left[\frac{\Delta^2}{|g|} - N(0)\left\{\frac{1}{2}\Delta(\Delta-2\Gamma) + (\Delta-\Gamma)^2\ln\left(\frac{2\hbar\omega_D}{\Delta-\Gamma}\right) - \Gamma^2\ln\left(\frac{2\hbar\omega_D}{\Gamma}\right)\right\} + \frac{1}{3}\pi^2 N(0)(k_B T)^2 - 4N(0)k_B T\int_0^{\hbar\omega_D} d\xi \ln(1+e^{-\beta E})\right]^{1/2}. \tag{37}$$

In the limit $\Gamma \to 0$, (36) and (37) reduce to

$$H_c(T) = [4\pi N(0)\Delta_0^2]^{1/2}\left[1 - \frac{e^{2\gamma}}{3}\left(\frac{T}{T_c}\right)^2\right] \simeq H_c(0)\left[1 - 1{\cdot}06\left(\frac{T}{T_c}\right)^2\right] \qquad T \to 0 \tag{38}$$

where

$$H_c(0) = [4\pi N(0)\Delta_0^2]^{1/2}$$

with Δ_0 the zero temperature gap.

10. Phase transition

$$F_S - F_N \neq 0$$

shows that the phase transition at T_N is of the first order.

11. Results and discussion

In the absence of the exact quantitative knowledge of the various parameters appearing in the expressions for the physical properties of antiferromagnetic superconductors derived in § 4 to § 9, we take the values of these parameters for the system $SmRh_4B_4$ from band structure calculations and curve fitting data, for an order of magnitude estimate of various properties as given in table 1.

Using the values of various parameters, one obtains for the system

$$T_c = 2{\cdot}75\,\mathrm{K}$$

and

$$T_N = 0{\cdot}87\,\mathrm{K}$$

These values are in good agreement with the experimental values [14].

The variation of superconducting order parameter (Δ) and magnetization Γ with temperature as obtained from (16) and (18) are shown in figures 1 and 2 respectively. Variation of Δ with T shows that magnetism suppresses superconductivity. At T_N, Δ fastly decreases and then again on further lowering the temperature Δ rises.

The variation of density of states function $N(\omega)/N(0)$ with ω for $\Delta = 0{\cdot}27 \times 10^{-22}$ J and $\Gamma = 0{\cdot}14 \times 10^{-22}$ J is shown in figure 3. The dashed curve is obtained from the

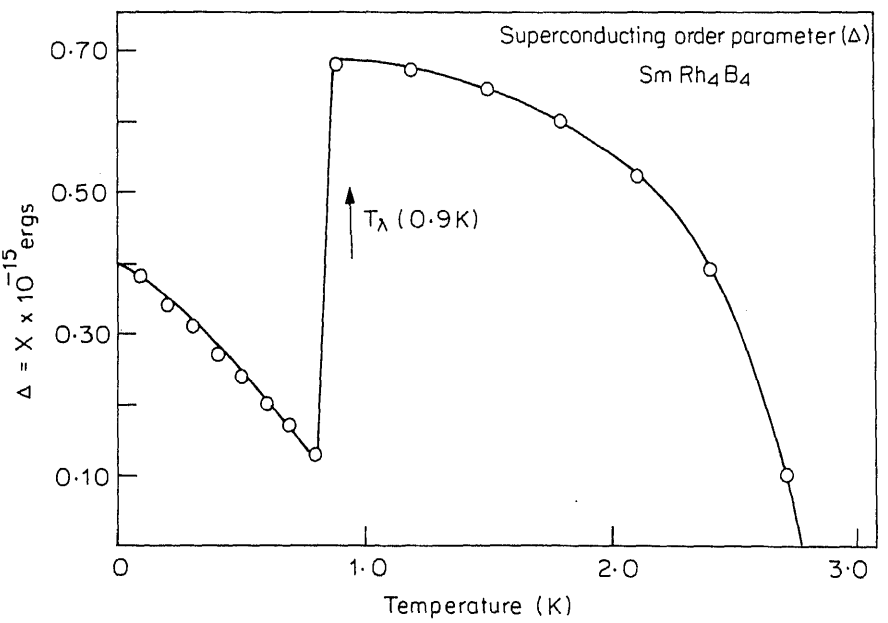

Figure 1. Variation of superconducting order parameter (Δ) with temperature (T).

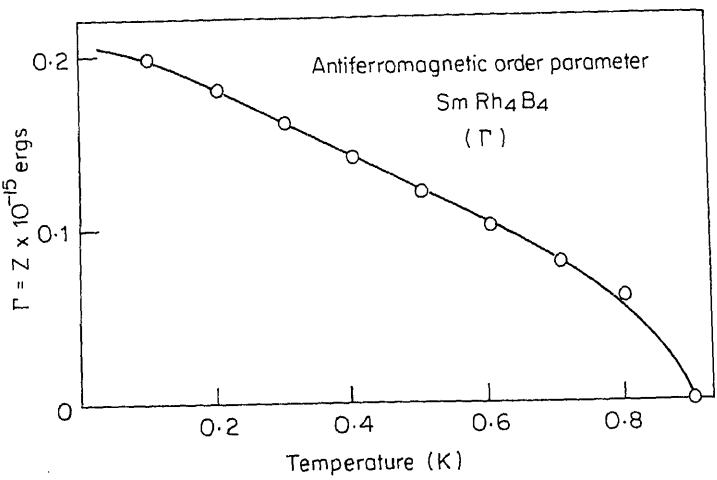

Figure 2. Variation of magnetization (Γ) with temperature (T).

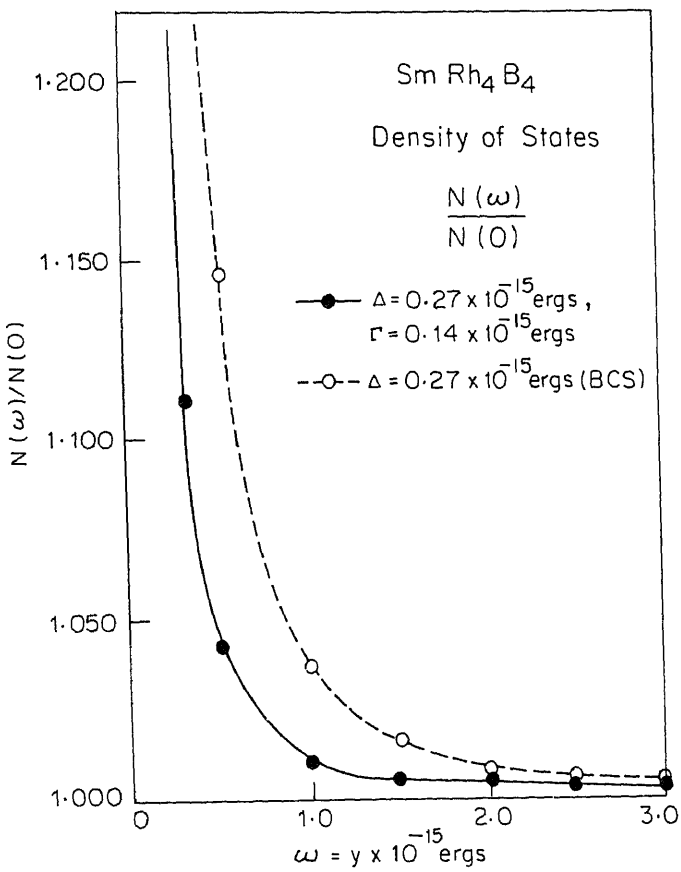

Figure 3. Variation of density of states function $N(\omega)/N(0)$ with ω. The dashed curve is that obtained from BCS theory. Both results are for $\Delta = 0{\cdot}27 \times 10^{-22}$ J.

BCS theory for the same value of Δ. The behaviour of $N(\omega)/N(0)$ is just similar to type I superconductors.

It is evident from figure 3 that the level moves below the band due to the development of antiferromagnetic correlations.

Table 1. Values of various parameters for the system $SmRh_4B_4$.

Density of states, $N(0)$	$0{\cdot}25 \times 10^{19}$ per Joule per atom	[12]
BCS attractive interaction strength $\|g\|$	$2{\cdot}41 \times 10^{-19}$ Joule	[1,2]
Phonon energy $\hbar\omega_D$	$1{\cdot}75 \times 10^{-22}$ Joule	[1,2]
Number of atoms per unit volume N	$\approx 10^{28}$ per m^3	[1,2]
Superconducting transition Temperature T_c	2·75 K	[14]
Neel temperature T_N	0·87 K	[14]
Structure type	$CeCo_4B_4$ primitive tetragonal	[11]
Space group	$P4_2/nmc$	[11]
Cell parameter	$a = 5{\cdot}312$ Å	
	$c = 7{\cdot}430$ Å	[11]
Effective magnetic moment μ_{eff}	$0{\cdot}632\,\mu_B$	[4]
Free ion value	$0{\cdot}84\,\mu_B$	[4]
Fermi wave vector K	$1{\cdot}568$ Å^{-1}	[1,2]

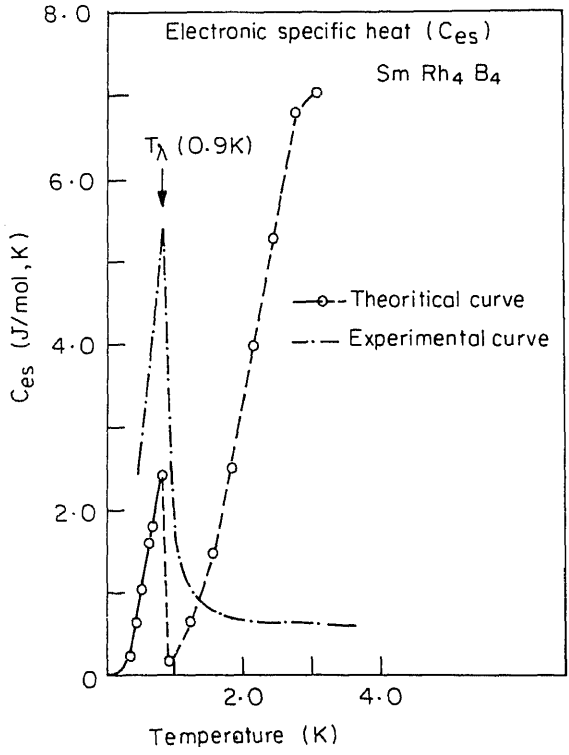

Figure 4. Variation of electronic specific heat with temperature.

Using various values of parameters from table 1, and $\Delta = x \times 10^{-22}$ J and $\Gamma = z \times 10^{-22}$ J, one can express (29) as

$$C_{es} = \frac{0{\cdot}9705}{T^2} \times 10^{-17} \int_0^1 dy\, y^2 \operatorname{sech}^2 \left[\frac{6{\cdot}34}{T} \{y^2 + 0{\cdot}3266(x-z)^2\}^{1/2} \right] \quad (39)$$

Solving (39) numerically, one obtains the variation of C_{es} with T as shown in figure 4.

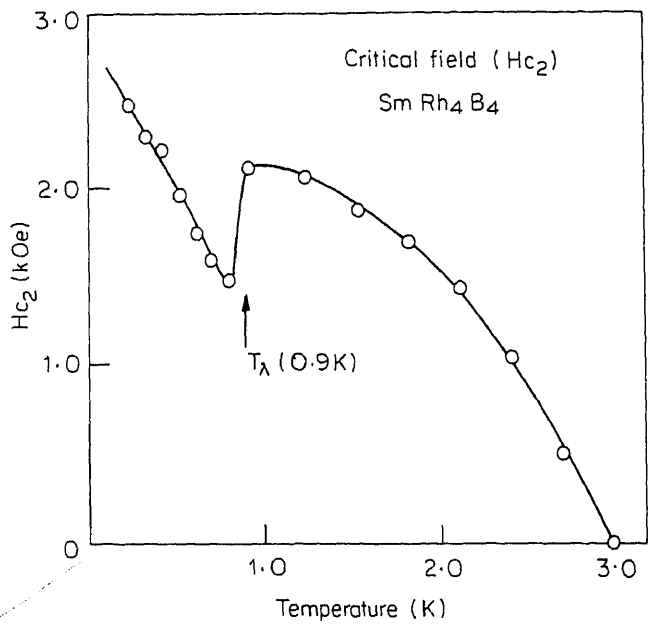

Figure 5. Variation of critical field with temperature.

Table 2. Free energy and critical field values.

Temperature T(K)	$F_S - F_N$ (J/mol)	H_c (kOe)
0·2	−0·243	2·471
0·3	−0·212	2·307
0·4	−0·197	2·224
0·5	−0·156	1·979
0·6	−0·123	1·757
0·7	−0·101	1·592
0·8	−0·090	1·503
0·9	−0·183	2·144
1·2	−0·173	2·084
1·5	−0·142	1·888
1·8	−0·114	1·692
2·1	−0·082	1·435
2·4	−0·046	1·074
2·7	−0·011	0·525
3·0	0·000	0·000

Specific heat behaviour clearly reveals a λ-type anomaly as observed experimentally at T_N.

Using table 1, free energy expression (32) can be expressed as

$$F_S - F_N = 0{\cdot}414x^2\ 10^{-18} - 0{\cdot}241\ 10^{-18}\ T \times \int_0^1 dy \ln\left[\frac{\cosh(6{\cdot}34/T)\{y^2 + 0{\cdot}3266(x-z)^2\}^{1/2}}{\cosh(6{\cdot}34/T)\{y^2 + 0{\cdot}3266z^2\}^{1/2}}\right] \quad (40)$$

Solving numerically, one obtains the values of $F_S - F_N$ at various temperatures as given in table 2. We note that at T_N, $F_S - F_N \neq 0$ and hence $\Delta^2 \neq 0$. This shows that phase transition at Neel temperature (T_N) is of first order.

Using table 1, one obtains from (36), the variation of critical field with temperature as given in table 2 and shown in figure 5. This shows a kink at T_N. This is in good agreement with the experimental observations.

Obviously, our model explains satisfactorily the behaviour of antiferromagnetic superconductor $SmRh_4B_4$.

Acknowledgements

We are highly thankful to Professors K P Sinha, U N Upadhyaya for helpful discussions and Dr P M Agrawal for helping in computer calculations. We also want to express our gratitude to Professors P S Bhargava, R N Mathur and G N Bhargava for providing facilities to complete this work.

References

[1] S L Kakani and U N Upadhyaya, *J. Low Temp. Phys.* **70**, 5 (1988)
[2] K P Sinha and S L Kakani, *Magnetic superconductors: Recent developments*, (Nova Science Publishers, New York, 1989) p. 21
[3] S L Kakani and C Hemrajani, *Recent advances in superconductivity* (Today and Tomorrow Publishers, New Delhi, 1990) p. 119
[4] M B Maple and ϕ Fischer (eds), *Superconductivity in ternary compounds* (Springer Verlag, New York, 1982) Vol. 34
[5] S V Vonsovsky, Yu N Izyumov and E Z Kurmaer, *Superconductivity of transition metals, their alloys and compounds*, (Springer Verlag, New York, 1982)
[6] K Machida, *Appl. Phys.* **A35**, 193 (1984)
[7] A I Buzdin and L H Bulaevskii, *Usp. Fiz. Nauk.* **149**, 45 (1986) [Sov. Phys. Usp. 29(5), 412 (1986)]
[8] M Tachiki, *Helv. Phys. Acta.* **56**, 189 (1983)
[9] C Rossel, *Il. Nuovo Cimento*, **2D**, 1834 (1983)
[10] F G Aliev, N B Brandt, V V Moshchalkov, Yu K Gorilenko and O P Petrenko, *Pisma Zh. Eksp. Teor. Fiz.* **43**, 143(1986) [*JETP Lett.* **43**, 182 (1986)]
[11] J M Vandenberg and B T Matthias, *Proc. Natl. Acad. Sci. USA* **74**, 1336 (1977)
[12] T Jarlborg, A J Freeman and T J Watson-Yang, *Phys. Rev. Lett.* **39**, 1032 (1977)
[13] H R Ott, W Odoni, H C Hamaker and M B Maple, *Phys. Lett.* **A75**, 243 (1980)
[14] H C Hamakar, L D Woolf, H B Mackay, Z Fisk and M B Maple, *Solid State Commun.* **31**, 139 (1979); **32**, 289 (1979)
[15] J G Bednorz and K A Muller, *Z. Phys.* **B64**, 189 (1986)
[16] P H Hor, L Gao, R L Meng, J L Huang, Y Q Wang, K Forster, J Vassilious, C W Chu, M K Wu, J R Ashburn and C J Torng, *Phys. Rev. Lett.* **58**, 911 (1987)
[17] A Weidinger, *Phys. Rev. Lett.* **62**, 102 (1989)

[18] J H Brewer, *Phys. Rev. Lett.* **60**, 1073 (1988)
[19] W Baltensperger and S Strassler, *Phys. Kondens Mater.* **1**, 20 (1963)
[20] P Pětalas and W Baltensperger, *Helv. Phys. Acta* **41**, 388 (1978)
[21] K Machida, *J Low Temp. Phys.* **37**, 583 (1979)
K Machida, *Jpn. J. Appl. Phys.* **19**, 385 (1980)
[22] K Machida, N Nokura and T Matsubara, *Phys. Rev. Lett.* **44**, 821 (1980)
[23] M J Nass, K Levin and G S Grest, *Phys. Rev.* **B23**, 1111 (1981)
[24] G Zwicknagl and P Fulde, *Z. Phys.* **B43**, 23 (1981)
[25] T V Ramakrishnan and C M Verma, *Phys. Rev.* **B24**, 137 (1981)
[26] O Sakai, M Tachiki, T Koyama, H Matsumoto and H Umezawa, *Phys. Rev.* **B22**, 2307 (1980)
[27] S D Mahanti, K P Sinha and M V Atre, *J. Low Temp. Phys.* **44**, 1 (1981)
[28] K P Sinha, *Solid State Commun.* **31**, 201 (1979)
[29] J Ashkenazi, C G Kuper and A Ron, *Phys. Rev.* **B28**, 418 (1983)
[30] K Levin, M J Nass and C Ro, in *Superconductivity in magnetic and exotic materials*, edited by T Masubara and A Kotani, (Springer–Verlag, New York, 1984), p. 106
[31] C Ro and K Levin, *Phys. Rev.* **B29**, 6155 (1984)
[32] P W Anderson, in *Magnetism* edited by G T Rado and H Suhl, (Academic Press, New York, 1963) Vol. 1
[33] P W Anderson, *Phys. Rev.* **126**, 41 (1961)
[34] J R Schrieffer and P A Wolff, *Phys. Rev.* **149**, 491 (1966)
[35] B Coqblin and J R Schrieffer, *Phys. Rev.* **185**, 847 (1969)
[36] J Hubbard, *Proc. R. Soc. (London)*, **A276**, 238 (1963)
[37] J Bardeen, L N Cooper and J R Schrieffer, *Phys. Rev.* **108**, 1675 (1957)
[38] A L Fetter and J D Walecka, *Quantum theory of many particle systems*, (McGraw Hill, New York, 1971) pp. 450
[39] D Sant James, E J Thomas and G Sarma, in *Type II superconductivity* (Pergamon Press, Oxford, 1969) p. 181

PRAMANA
— journal of
physics

© Printed in India

Vol. 43, No. 1,
July 1994
pp. 55–65

Photoconductivity and dark conductivity studies of solution-gas interface grown Ag_2S films

P S NIKAM and C B SHINDE*
PG Department of Physical Chemistry, MSG College, Malegaon Camp 423 105, India
*Department of Physics, Arts, Science and Commerce College, Satana 423 301, India

MS received 1 September 1993; 19 February 1994

Abstract. Ag_2S films of thicknesses ranging between 500–4000 Å were formed on glass substrate, employing solution-gas interface technique. Dark conductivity of Ag_2S films has been studied at different temperatures and Bi(III) concentrations. Photoconductivity of these films has been investigated at different temperatures, illumination levels, excitation energies and Bi(III) concentrations. Dark conductivity is explained on Slater and Neugebauer models, while photoconductivity is explained on Miccoci and Rose models.

Keywords. Dark conductivity; stationary photoconductivity; recombination process; Ag_2S films; solution-gas interface technique.

PACS No. 72·40

1. Introduction

Silver sulphide finds extensive applications in thermogenerators, bacterial studies, infrared millimeter devices such as modulators, variable attenuators, switchable polarisers and tunable filters. It has been shown as one of the promising materials in solar cells and selective coatings, photocells, optoelectronics and micro-electronics [1–5]. This material can be obtained in a thin film form by various methods [4–14]. For device fabrication applications, Ag_2S films should be stoichiometric having large grain size with high mobility charge carriers and high absorption in the visible region. Ag_2S films formed at the interface of aqueous $AgNO_3$ solution and H_2S gas (solution-gas interface technique) meet these conditions. Negative photoconductivity is known to occur in Ag_2S films [15]. Therefore some workers have tried to activate the properties of Ag_2S films by doping with impurities [15–17]. Only in Au(III) and Hg(II), the doping beneficial effect is observed. However, little study has been made with Bi(III) doping. The aim of the present investigation is mainly to use silver sulphide cells as photoconductive devices, that requires a lowering of the dark resistance without affecting the photosensitivity. With this in view Bi(III) and nitrate ions have been tried as dopants.

2. Experimental

Figure 1 shows the experimental set-up used for Ag_2S film preparation. A dish with 100 cc of 1% $AgNO_3$ solution was placed in an atmosphere of H_2S gas. The Ag_2S film formed at the interface of solution and gas was picked up on ultrasonically

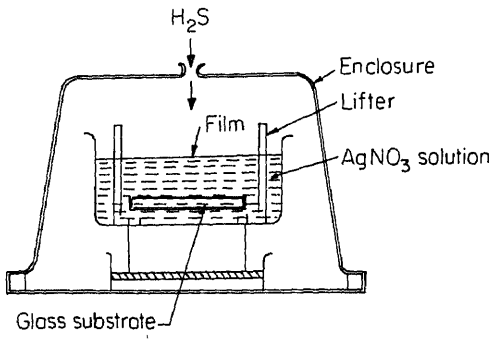

Figure 1. Experimental set up for film formation.

cleaned glass substrate already dipped in solution. The film was washed 2 to 3 times in distilled water to remove traces of impurities present in the film. The film was dried in vacuo of $\sim 10^{-2}$ torr. Dried films were annealed at 200°C for 8 h in dark and stored in vacuum desiccator covered with black paper. The Ag_2S films, had thickness varying between 500–4000 Å, depending upon the time of exposure of $AgNO_3$ solution to H_2S gas. Various concentrations of Bi(III) were added to Ag_2S films by adding 0·5, 1, 1·5, 2, 3 and 55 ml of 1% $Bi(NO_3)_2$ solution in 100 ml of 1% $AgNO_3$ solution.

The composition and hence stoichiometry of Ag_2S film was determined by absorptiometric spectroscopy at 620 μm [18] which revealed that silver sulphide films were nearly stoichiometric corresponding to Ag_2S formula. Rough estimates showed that grain diameter varied between 0·04 and 0·1 μm.

Methods employed to measure film thickness by gravimetric method and dark conductivity at various temperatures employing two-probe technique using pressure contacts, were similar to those reported earlier [18].

For photoconductivity measurements, the film was sandwiched between evaporated aluminium electrodes. Film along with pressure contacts was placed in a transparent glass tube with provision of microheater to heat the sample. Light of a 100 W lamp was used as a source of illumination. A proper focussing arrangement of light on the sample was made by using a collimating system. The area of the film exposed to light was $1{\cdot}5 \times 1\ cm^2$. The whole arrangement was enclosed in light-tight box which acted as a shield for stray radiations. The light intensity over the film surface was varied by changing sample to light source distance and measured with a lux meter. Different excitation wavelengths were obtained by using filters. Photo currents from Ag_2S and Ag_2S:Bi films of different thicknesses, at various light intensities with different excitation energies, and at different temperatures were measured with the help of a nanometer.

3. Results and discussion

Figures 2 and 3 show variation of log R versus $1/T$ for Ag_2S and Ag_2S:Bi films respectively. Resistance of the films decreases reversibly with increase of temperature, which is characteristic of semiconducting behaviour. Films show two phases (i) low temperature β-phase below 450 °K, and (ii) high temperature α-phase above 450 °K. Similar results are reported by Paul *et al* [19]. Figures 4 and 5 represent the energy

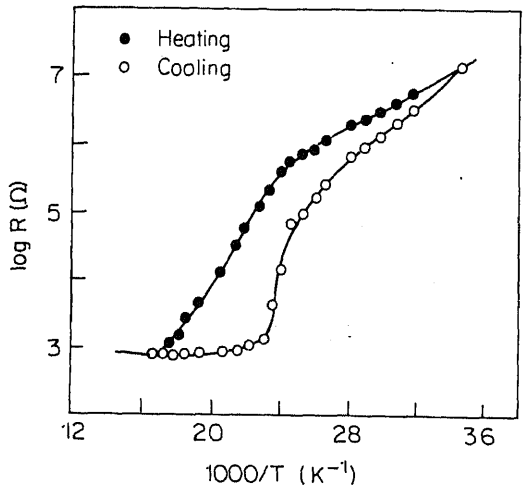

Figure 2. Log R vs $1/T$ for Ag_2S film of thickness ~ 1439 Å.

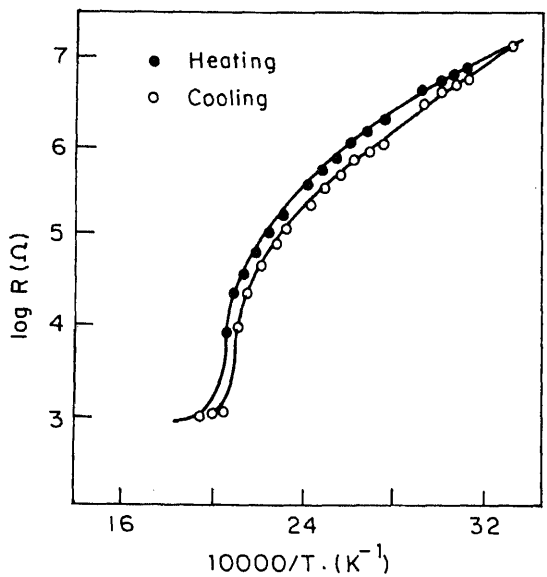

Figure 3. Log R vs $1/T$ for Ag_2S:Bi film of thickness ~ 2481 Å.

variation of activation (ΔE) with thickness (d) of Ag_2S and Ag_2S:Bi films respectively. The dependence of ΔE on d is quadratic. Thicker films have lower values of ΔE. Thickness dependence of ΔE is a result of combined effect [20]: (i) the change in the barrier height due to the size of the grains in a polycrystalline films; (ii) a large density of dislocations; (iii) changes in stoichiometry and (iv) quantum size effects.

According to Slater's model [21], ΔE is given by

$$\Delta E = \Delta E_0 + C(X - fD)^2, \tag{1}$$

where ΔE_0 is the original barrier height, C is a term depending on density of charge

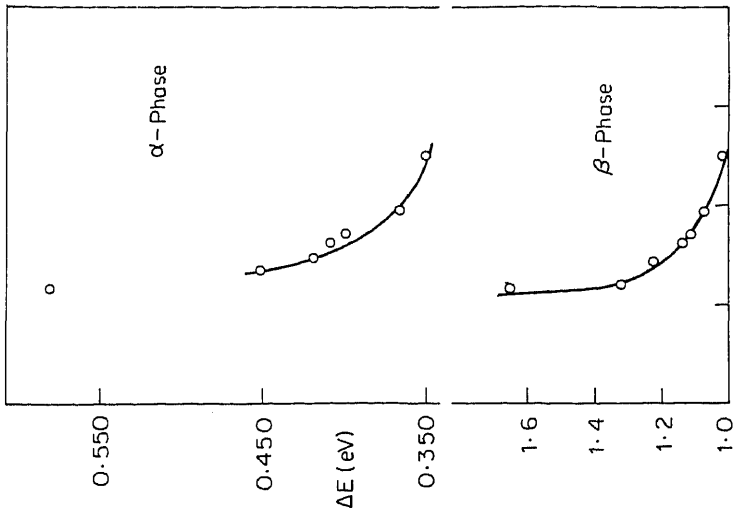

Figure 5. ΔE vs d for Ag_2S:Bi films.

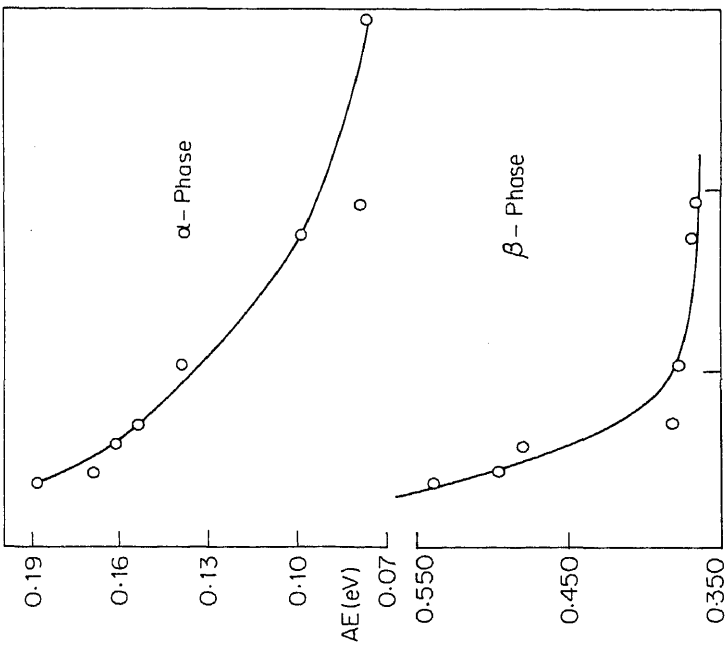

Figure 4. ΔE vs d for Ag_2S films.

carriers, electronic charge, and dielectric constant of the material. D is the dimension of the grain, and f is a fraction of the order of 1/15 to 1/50 depending on the charge accumulation at the grain boundaries. It is known from literature [22] that the grain size (D) is approximately proportional to thickness (d); and hence increases as thickness increases. Therefore ΔE should be proportional to $(X - fD)^2$.

The films studied are mostly stoichiometric with lesser density of dislocations, and hence observed ΔE variation with thickness cannot be attributed to second and third effects.

In quantum size effects [22] in semimetals and semiconductors ΔE is given by

$$\Delta E \sim \frac{h^2}{8m^* d^2}, \tag{2}$$

where m^* is the effective carrier mass. Equation (2) is found valid qualitatively as well as quantitatively for Ag_2S and Ag_2S:Bi films.

Thus we can say that increase of ΔE with decreasing thickness of Ag_2S and Ag_2S:Bi films may possibly be due to the combined effects of varying barrier heights with varying thicknesses and quantum size effects in films.

An alternative explanation for the higher values of ΔE for thinner films may be explained qualitatively on the basis of island structure theory of Neugebauer and others. Accordingly ΔE is given by

$$\Delta E = \frac{e^2}{D.r} + \frac{E_g}{2}. \tag{3}$$

The terms involved in (3) has been explained previously [18]. Hence ΔE varies inversely with d. Since plots of ΔE vs $1/d^2$ (not shown) are more or less linear, the dependence of ΔE on d is closer to quantum size effects in the present investigation.

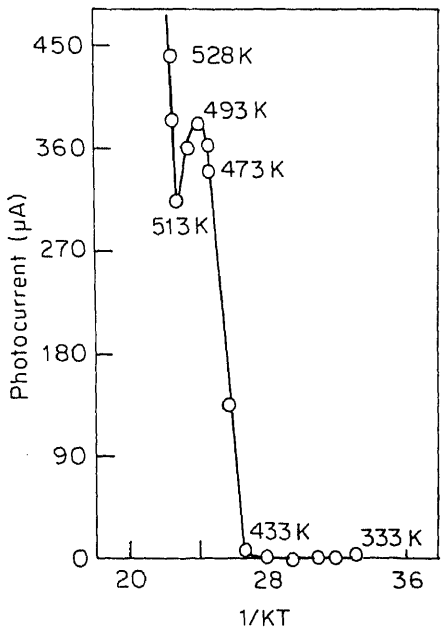

Figure 6. Photocurrent vs $1/KT$ for Ag_2S film of thickness ~ 1058 Å.

Figure 6 shows temperature (T) dependence of photo current (I_{ph}) for a fixed incident photoflux. Similar curves are obtained at other light intensities. The results obtained are highly reproducible for all radiations of different wavelengths. The photocurrent (I_{ph}) versus $1/KT$ curve for Ag_2S film shows four different regions (i) in high temperature region (510–528 K), the photocurrent decreases with decrease of temperature and reaches to minium at 510 K. In this region, all charge carriers are thermally generated and there are no photo-excited carriers. (ii) in the temperature region (493–510 K), photocurrent increases with decrease of temperature and reaches to maximum at 493 K (T_m). The photocurrent is carried in extended states on either side of the maxima, but the character of the recombination kinetics changes on passing through the maximum. Above T_m, the number of thermally generated carriers is larger than the number of photoexcited carriers and the recombination is mono molecular. (iii) in the intermediate temperature region (433–493 K), immediately below the maximum, the photocurrent decreases exponentially with $1/KT$. Below T_m, a bimolecular recombination mechanism dominates, because in this region, the number of thermally generated carriers is negligibly small. (iv) in the low temperature region (333–433 K), the photocurrent is much larger than thermal current, and photocurrent increases with temperature in this region. This indicates that the Fermi level is moving in the midst of an exponential trap distribution [23].

The dependence of photocurrent (I_{ph}) on light intensity (L) for α and β phases of Ag_2S films is plotted in figures 7–10. It has the form

$$I_{ph} = L^r \tag{4}$$

It is evident that $r = 1$ at low light intensity indicating first order type of recombination, while $r = 0{\cdot}5$ at higher light intensities, suggesting second order type of recombination process. According to the Rose model [24], the two steady state Fermi levels are shifted towards their respective band edges with an increase in the intensity of illumination. During this shifting of Fermi levels a large number of traps are converted to recombination centres.

In an attempt to explain dependence of photocurrent on light intensity in the various temperature ranges, we assume the model proposed by Miccoci *et al* [25]. Briefly it is assumed that a semiconductor contains, in addition to the extended

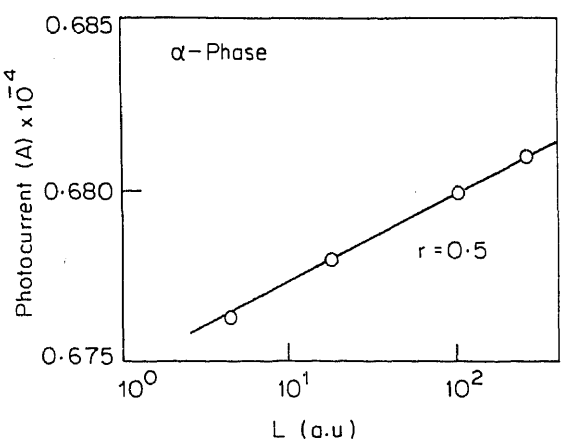

Figure 7. Log–log plot of light intensity vs photocurrent for α-phase ($r = 0{\cdot}5$).

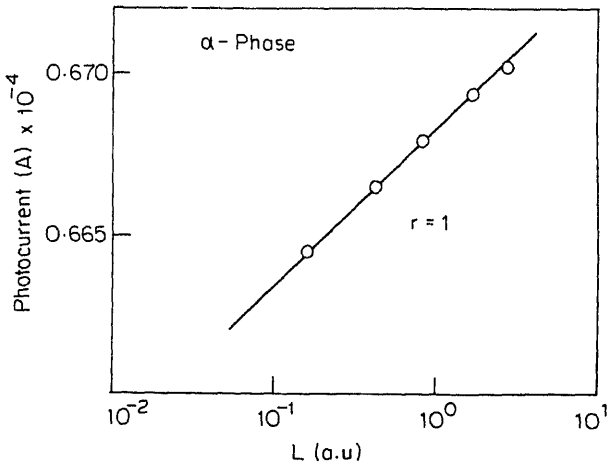

Figure 8. Log–log plot of light intensity vs photocurrent for α-phase ($r = 1$).

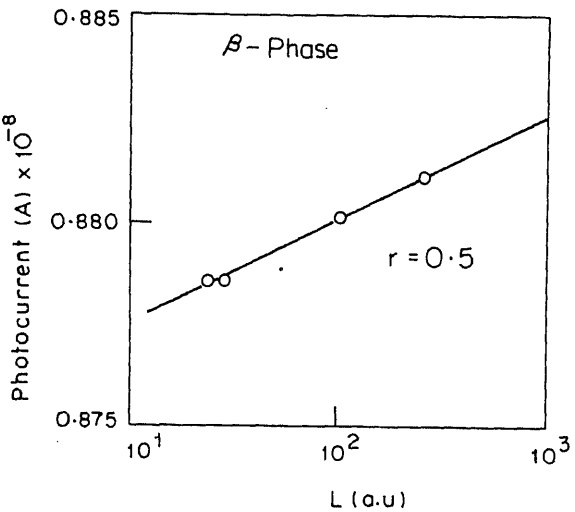

Figure 9. Log–log plot of light intensity vs photocurrent for β-phase ($r = 0.5$).

electron and hole states, two types of imperfections confined in relatively narrow bands such that discrete levels can be considered (figure 11). The type t imperfection is a shallow hole trap, while type r imperfection is a slow recombination centre. According to Shockley–Read [26], the expression for the recombination rate is

$$F = [\alpha_r \beta_r N_r/(\alpha_r n + \beta_r p + P_r)]np, \tag{5}$$

where

$$P_r = \alpha_r N_c \exp[-(E_c - E_r)/kT]$$

and F is the rate of electron-hole pair generation caused by light.

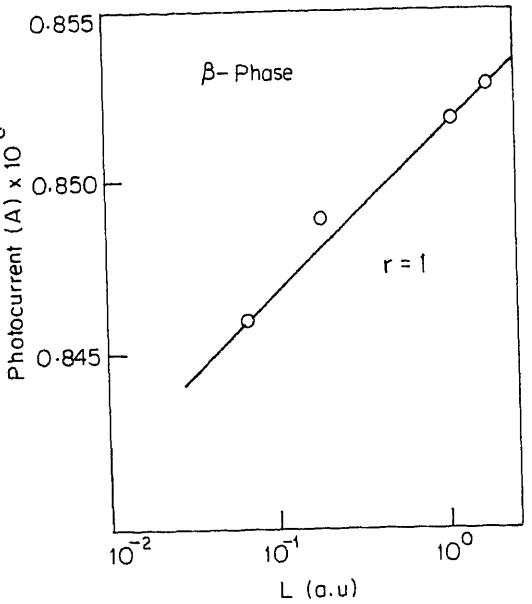

Figure 10. Log–log plot of light intensity vs photocurrent for β-phase ($r = 1$).

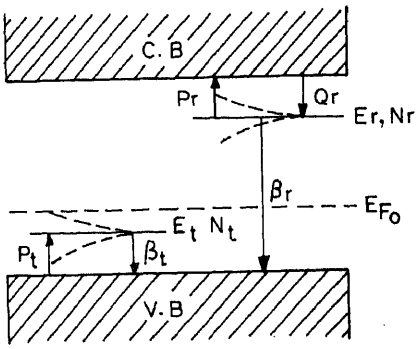

Figure 11. Energy level model of photocurrent curves.

Now, assuming that the captured carrier density is much greater than the free carrier density, the condition of charge neutrality yields

$$\alpha_r N_r[n/(\alpha_r n + \beta_r p + P_r) - n_0/(\alpha_r n_0 + \beta_r p_0 + P_r)] = \beta_t N_t[p/(\beta_t p + P_t) - p_0(\beta_t p_0 + P_t)] \quad (6)$$

where

$$P_t = \beta_t N_v \exp[-(E_c - E_v)/kT]$$

n_0 and p_0 represent the dark carrier concentrations.

Since chemically deposited Ag_2S films exhibit P-type conduction [27], it is possible to calculate Δp from (5) and (6) and hence the dependence of the photocurrent on temperature and light intensity.

The dependence of photocurrent on the excitation energy (from 5700–6500 Å) of

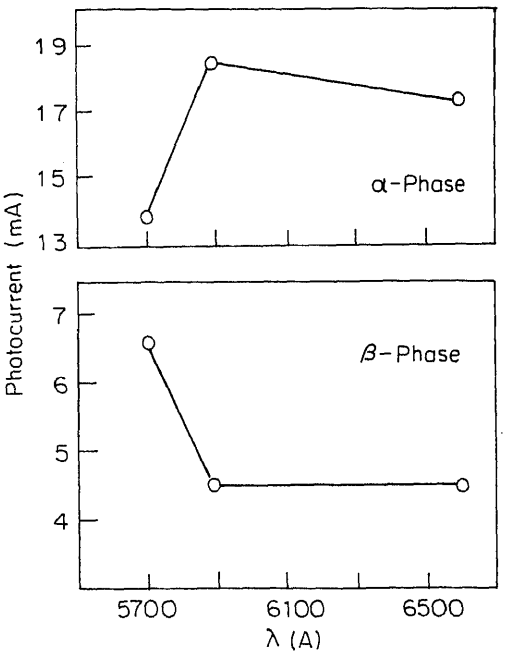

Figure 12. Plot of photocurrent vs wavelength.

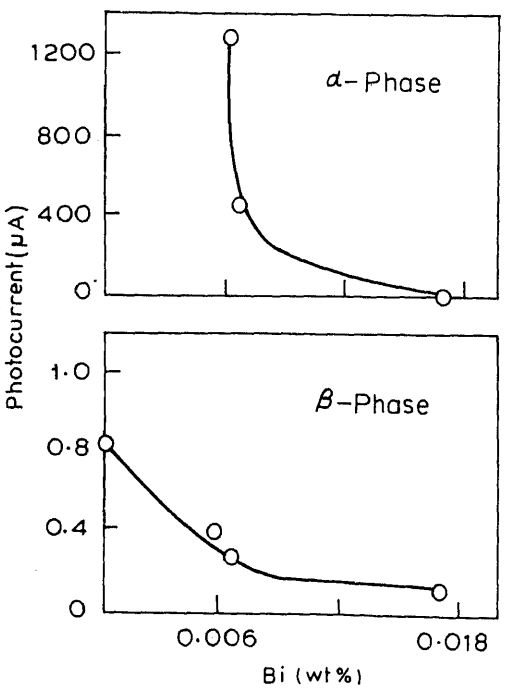

Figure 13. Photocurrent vs Bi concentration.

light is shown in figure 12. The different wavelengths were obtained from a tungsten lamp using filters and the measurements were made for a fixed incident photoflux. The photocurrents are maximum at 5700 Å and 5900 Å for β and α phases respectively. It is common for spectral response curves of photoconductivity to show a fairly sharp maximum at a wavelength slightly longer than that corresponding to the absorption edge. For wavelengths longer than the maximum, the excitation decreases sharply, because the absorption producing free carriers are decreasing for wavelengths longer than maximum, the radiation is being strongly absorbed and produces excitation only near the surface. The surface imperfections are characterised by rapid non-radiative recombination. The excitation of photoconductivity is less when limited to the surface.

Mangalam *et al* [15] have reported that silver sulphide is *n*-type photoconductor. Negative photoconductivity is known to occur (i) due to ionic conductivity and (ii) due to non ohmic contacts [27]. With Bi(III) doping, negative photoconductivity is expected to be absent in Ag_2S:Bi films. Photocurrent decreased with increase of concentration of Bi(III) (figure 13), probably due to the fact that Bi(III) ions act as trap centres in the midst of energy gap of Ag_2S film. This is further visualised from higher values of ΔE of Ag_2S:Bi films than those for Ag_2S films.

4. Conclusions

Large area Ag_2S films formed at solution-gas interface have high temperature (α) and low temperature (β) phases. Doping of Bi(III) in Ag_2S films decreased photoconductivity, acting as trap centres for carriers.

References

[1] A S Okhotin and A S Pushkarskii, *Dokl. Akad. Nauk. SSSR* **203**, 336 (1972)
[2] B D Talya, P Tonnies and C Benzion, *Water Res.* **103**, 983 (1985)
[3] V V Galavano and Zlatkin, *Instrum. Expt. Technol.* **69**, 1471 (1966)
[4] T Y Hsu, H Buhay and N P Murarka, *Proc. Soc. Photo-Opt. Instrum. Eng.* **59**, 38 (1981)
[5] A J Vorkey, *Sol. Energy Mater.* **21**, 291 (1991)
[6] L Constantinescu, *Stud. Cercet Fiz.* **25**, 1221 (1973)
[7] D K Burge, J M Bennett, R L Peck and H E Bennett, *Surf. Sci.* **16**, 303 (1969)
[8] P Bruesch and J Wallschleger, *Solid State Commun.* **13**, 9 (1973)
[9] T Fleisch and R Aberman, *Thin Solid Films*, **42**, 255 (1977)
[10] D L Douglass, *Sol. Energy Mater.* **10**, 1 (1984)
[11] A Kunugi, M Fujimoto and T Hiraj, *Mem. Fac. Eng. Osaka City Univ.* **26**, 79 (1985)
[12] S P Sharma and J H Thomas (III), *J. Appl. Phys.* **47**, 1808 (1976)
[13] S S Dhumure and C D Lokhande, *Mater. Chem. Phys.* **27**, 321 (1991)
[14] D P Amalnerkar, M S Setty, N R Pavaskar and A P B Sinha, *Bull. Mater. Sci.* **2**, 2 (1980)
[15] M J Mangalam, K N Rao, N Rangarajan and C V Suryanarayana, *Indian J. Pure Appl. Phys.* **7**, 629 (1969
[16] M J Mangalam, K N Rao, N Rangarajan and C V Suryanarayana, *Phys. Status Solidi*, **A2**, K-17 (1970)
[17] S S Dhumare and C D Lokhande, *Indian J. Pure Appl. Phys.* **30**, 71 (1982)
[18] P S Nikam and H S Aher, *Indian J. Pure Appl. Phys.* **31**, 79 (1993)
[19] N Paul, M G K Pillai and K B Joseph, *Indian J. Pure Appl. Phys.* **18**, 311 (1980)
[20] V Damodara Das and D Karunakaran, *Phys. Rev.* **B39**, 10872 (1989)
[21] J C Slater, *Phys. Rev.* **103**, 1631 (1956)
[22] K L Chopra, *Thin film phenomenon* (McGraw-Hill, New York, 1969)

[23] P K C Pillai, N Schroff, N Nandkumar and A K Tripathi, *Phys. Rev.* **32**, 8228 (1985)
[24] A Rose, *Concepts of photoconductivity and allied problems* (Wiley, New York, 1963) p. 43
[25] G Miccoci, A Rizzo and A Tepore, *Phys. Status Solidi* **A85**, 609 (1984)
[26] W Shickley and W T Read, *Phys. Rev.* **87**, 835 (1952)
[27] K A Pathan, Ph D Thesis, Poona University, (1993)

PRAMANA
— journal of
physics

© Printed in India

Vol. 43, No. 1,
July 1994
pp. 67–72

Enhanced bistability with the line-narrowed modes in a nonlinear modulated index Fabry–Perot cavity

S DUTTA GUPTA
School of Physics, University of Hyderabad, Hyderabad 500 134, India

MS received 25 March 1994

Abstract. We exploit the recently reported line narrowed modes [1] for observation of bistability in a nonlinear Fabry–Perot cavity with intracavity index modulation. We show that the frequency response of the structure exhibits larger bistability loops for the line narrowed modes.

Keywords. Bistability; multi stability.

PACS No. 42·65

In the past two decades there has been a lot of interest in distributed feedback structures in the context of lasing [2, 3] and other applications [[4], Chapters 7 and 10]. Nonlinear distributed feedback structures have been exploited to show the existence of optical bistability [5] and localized solutions in them [6–11]. Chaotic response of such structures has also been reported [12–14]. Very recently it was demonstrated that one can narrow down the resonances if the distributed feedback medium is enclosed in a Fabry–Perot (FP) cavity [1]. The interplay of the distributed feedback and the localized feedback due to the FP mirrors can diversely affect the various resonances leading to line narrowing of some selective modes. The line narrowing was shown to be quite useful in the context of cavity quantum electrodynamics applications, in particular, for vacuum field Rabi splitting [1]. The line narrowing effect can also be exploited for optical bistability since it is well established that the narrower the resonances the easier it is to deform them to obtain bistable/multistable output. In this paper we consider a FP cavity with intracavity index modulation and with Kerr type nonlinearity. In the framework of a coupled wave theory [[4] pp 189–199] we obtain the equations for the forward and backward propagating waves. These equations are integrated to calculate the frequency response of the structure in the domain which encompasses the line narrowed resonance along with others. We show that the nonlinearity induced bending of the line narrowed resonance dominates over those of other resonances leading to a larger bistability loop. We also study the power dependence of the transmission coefficient when the frequencies are chosen to be detuned by the same amount from the centre of the mode resonances. We demonstrate that the line narrowed modes offer well defined multistable behaviour.

We consider a FP cavity of length L with intracavity index modulation. The intracavity medium is assumed to possess Kerr type nonlinearity. Thus, in the approximation that depth of modulation n_1 is much smaller than background

refractive index n_0 the dielectric function for the intracavity medium can be written as

$$\varepsilon(z, E) = n_0^2 + 2n_0 n_1 \cos(Kz + \theta) + 4\pi\chi_n |E|^2, \tag{1}$$

where K is the grating constant ($= 2\pi/\Lambda, \Lambda$ is the grating period). Phase θ can be adjusted to have sine or cosine modulation and χ_n is the nonlinearity parameter. The smallness of the modulation amplitude enables one to develop a coupled mode theory, whereby the field inside the cavity can be expressed as a sum of counter propagating terms as follows:

$$E(z) = E_f + E_b = \mathscr{E}_f(z)e^{ikz} + \mathscr{E}_b(z)e^{-ikz}, \tag{2}$$

with $k = \dfrac{\omega}{c} n_0$.

Henceforth, it is assumed that the grating vector K is close to twice the momentum of the field in order to have efficient coupling between the forward and backward propagating waves. On substituting (2) in the wave equation and making slowly varying envelope approximation the coupled amplitude equations can be obtained and can be written as follows:

$$\frac{d\mathscr{E}_f}{dz} = i\beta\mathscr{E}_b e^{-i\delta z + i\theta} + i\alpha\mathscr{E}_f(|\mathscr{E}_f|^2 + 2|\mathscr{E}_b|^2), \tag{3}$$

$$\frac{d\mathscr{E}_b}{dz} = -i\beta\mathscr{E}_b e^{i\delta z - i\theta} - i\alpha\mathscr{E}_b(|\mathscr{E}_b|^2 + 2|\mathscr{E}_f|^2). \tag{4}$$

In eqs (3), (4)

$$\delta = 2\frac{\omega}{c} n_0 - K, \quad \beta = \frac{\omega n_1}{c}, \quad \alpha = 2\pi\omega\chi_n / cn_0.$$

In writing (3)–(4) we ignored the quickly oscillating spatial components like $e^{\pm i3kz}$. For the set of equations (3), (4) a closed form solution could not be obtained and we resort to numerical methods to solve them. In order to obtain transmission characteristics of the structure eqs (3), (4) are to be supplemented by the FP boundary conditions. Assuming that both the mirrors of the FP cavity are identical with amplitude reflection and transmission coefficients r and t, respectively, with $|r|^2 + |t|^2 = 1$ (mirrors are lossless) the boundary conditions can be written as follows

$$\mathscr{E}_f(0) = t\mathscr{E}_i + r\mathscr{E}_b(0), \tag{5}$$

$$\mathscr{E}_b(L)e^{-ikL} - r\mathscr{E}_f(L)e^{ikL} = 0, \tag{6}$$

$$\mathscr{E}_t = t\mathscr{E}_f(L), \tag{7}$$

$$\mathscr{E}_r = t\mathscr{E}_b(0) - r\mathscr{E}_i. \tag{8}$$

We now switch to dimensionless quantities as follows:

$$K \to KL = \tilde{K}, \quad \beta \to \beta L = \tilde{\beta}, \quad \delta \to \delta L = \tilde{\delta}$$

$$\mathscr{E}_{f,b} \to \sqrt{\alpha L}\mathscr{E}_{f,b} = \tilde{\mathscr{E}}_{f,b}, \quad z \to z/L = \tilde{z}.$$

Restricting to cosine modulation ($\theta = 0$), eqs (3) and (4) can be written in terms of the dimensionless quantities as follows

$$\frac{d\tilde{\mathscr{E}}_f}{d\tilde{z}} = i\tilde{\beta}\tilde{\mathscr{E}}_b e^{-i\tilde{\delta}\tilde{z}} + i\tilde{\mathscr{E}}_f(|\tilde{\mathscr{E}}_f|^2 + 2|\tilde{\mathscr{E}}_b|^2), \tag{9}$$

$$\frac{d\tilde{\mathscr{E}}_b}{d\tilde{z}} = -i\tilde{\beta}\tilde{\mathscr{E}}_b e^{-i\tilde{\delta}\tilde{z}} - i\tilde{\mathscr{E}}_b(|\tilde{\mathscr{E}}_b|^2 + 2|\tilde{\mathscr{E}}_f|^2). \tag{10}$$

Henceforth, we treat $\tilde{\mathscr{E}}_t (= \sqrt{\alpha L}\mathscr{E}_t)$ as a parameter in terms of which both $\tilde{\mathscr{E}}_f$ and $\tilde{\mathscr{E}}_b$ can be specified at $\tilde{z} = 1$ ($z = L$) as follows

$$\tilde{\mathscr{E}}_f(1) = \tilde{\mathscr{E}}_t/t, \tag{11}$$

$$\tilde{\mathscr{E}}_b(1) = r\tilde{\mathscr{E}}_f(1)e^{i(\tilde{K}+\tilde{\delta})}. \tag{12}$$

Equations (9) and (10) can be solved with initial conditions (11) and (12) and the solution can be obtained at $\tilde{z} = 0$. In terms of $\tilde{\mathscr{E}}_f(0)$ and $\tilde{\mathscr{E}}_b(0)$ the scaled incident and reflected amplitudes can be evaluated by using the following equations:

$$\tilde{\mathscr{E}}_i = \frac{\tilde{\mathscr{E}}_f(0) - r\tilde{\mathscr{E}}_b(0)}{t}, \tag{13}$$

$$\tilde{\mathscr{E}}_r = t\tilde{\mathscr{E}}_b(0) - r\tilde{\mathscr{E}}_i. \tag{14}$$

For a given $\tilde{\mathscr{E}}_t$ once the incident and reflected amplitudes, $\tilde{\mathscr{E}}_i$ and $\tilde{\mathscr{E}}_r$ are known, it is straightforward to calculate the intensity transmission and reflection coefficients. Note that the above procedure can lead to a simple calculation of the power dependence of the transmission/reflection coefficients. However, for a given input power and given frequency of the incident radiation calculation of the transmission coefficient is not straightforward. One has to solve a nonlinear equation to obtain the value of $\tilde{\mathscr{E}}_t$ which corresponds to the given $\tilde{\mathscr{E}}_i$.

In what follows we present the results of numerical calculations. The following system parameters were chosen for calculation: $KL/2 = 439\pi$, $r^2 = 0{\cdot}7$, $n_0 = 2{\cdot}3$, $n_1 = 10^{-2}$. We first present the results pertaining to the frequency response of the system for given input fields. In figure 1 we have shown the transmission coefficient for two different values of $|\tilde{\mathscr{E}}_i|^2$ namely $|\tilde{\mathscr{E}}_i|^2 = 1{\cdot}0 \times 10^{-5}$ (dashed curve) and 0·1 (solid curve), as functions of dimensionless $\tilde{\delta}$. Various peaks for the case of low input intensity are labelled by the corresponding mode indices (see Dutta Gupta *et al* [1]). Since the input intensity for this case is vanishingly small the response agrees quite well with response of a linear structure (with $\alpha = 0$). As was shown in ref. 15, the mode labelled by $+1$ is the line narrowed mode and the resonance corresponding to it is the narrowest one. We now concentrate on the case when the incident intensity is increased to 0·1. The nonlinearity comes into play and bends all the resonances leading to a shift of their peaks. The broader the resonance (e.g., -2, -1 modes) the less is the effect on them. The bending is maximum for the $+1$ mode which has the highest quality factor compared to all others. Thus, the line narrowed mode exhibits the largest bistability loop demonstrating its potentials for various applications. In other words, for moderate incident powers when other modes cannot exhibit bistability the line narrowed mode can show well defined and well separated multivalued output.

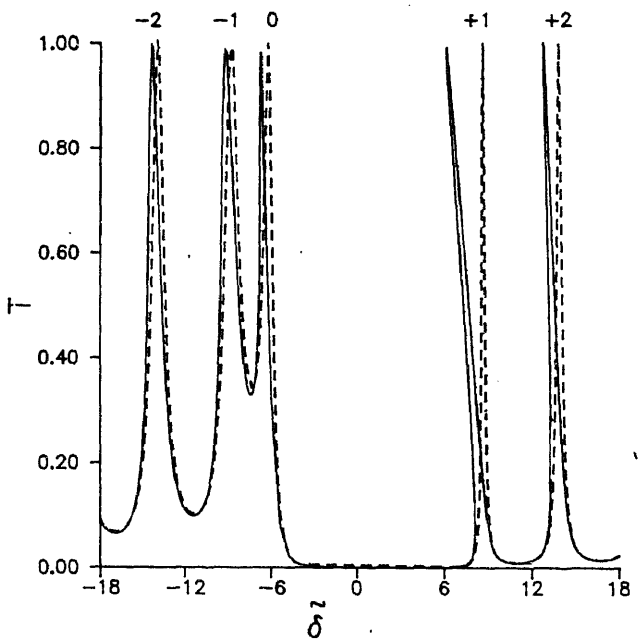

Figure 1. Transmission coefficient T as a function of dimensionless detuning $\tilde{\delta}$ for a cosine modulated FP cavity. The dashed curve corresponds to low input intensity ($|\tilde{\mathscr{E}}_i|^2 = 1{\cdot}0 \times 10^{-5}$) and is almost identical with the linear response. Various resonances are labelled by their corresponding mode numbers [1]. The solid curve shows the response for a large input intensity ($|\tilde{\mathscr{E}}_i|^2 = 0{\cdot}1$). Other parameters are as follows: $r^2 = 0{\cdot}7$, $KL/2 = 439\pi$, $n_0 = 2{\cdot}3$, $n_1 = 0{\cdot}01$.

We now turn to the bistability in the input-output characteristics of the system. In figure 2 we have shown the transmission coefficient as a function of incident intensity $|\tilde{\mathscr{E}}_i|^2$ for fixed frequencies (fixed $\tilde{\delta}$). Results for $\tilde{\delta} = -9{\cdot}12$ ($= 5{\cdot}69$) are shown in figure 2a (2b). The chosen values of $\tilde{\delta}$ correspond to an equal amount of offset in the same direction from the 0 and the $+1$ mode resonances of the linear structure. It is clear from a comparison of figures 2a and 2b that the high-to-low switching threshold is an order of magnitude lower in the case of $+1$ mode. However, one has to drive the system stronger for the $+1$ mode in order to go to the upper transmission branch. Besides, one has the possibility of multistability with $+1$ and $+2$ modes, whereas, multistability is not exhibited in figure 2a.

In conclusion, we studied an index modulated Fabry–Perot cavity with Kerr type nonlinearity. We obtained the frequency response of the structure for given input intensities. In the frequency response the line narrowed modes are shown to lead to larger bistability loops. Moreover, we studied the power dependence of the transmission coefficient at given frequencies and demonstrated multistability with line narrowed modes.

The author would like to thank R W Boyd for the hospitality at Institute of Optics, University of Rochester, where the work was carried out under the NSF Project no. INT910085.

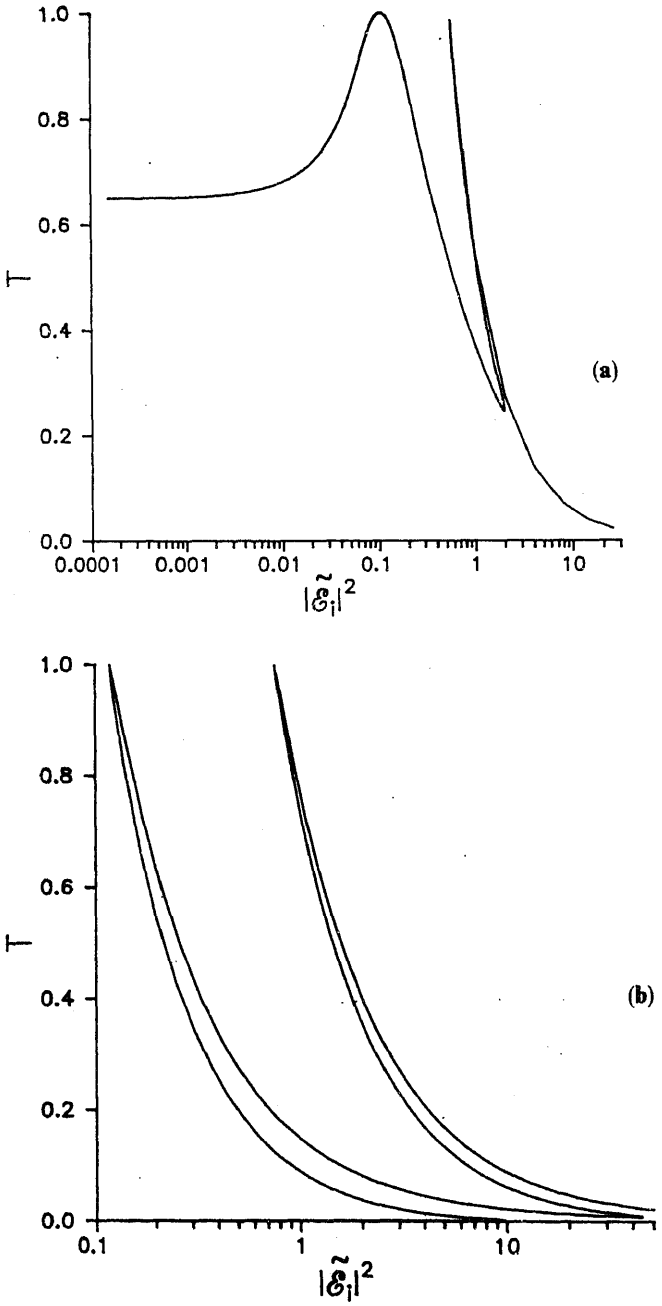

Figure 2. Transmission coefficient T as a function of incident intensity $|\tilde{\mathcal{E}}_i|^2$ for (**a**) $\tilde{\delta} = -9{\cdot}12$ and for (**b**) $\tilde{\delta} = 5{\cdot}69$. Other parameters are as in figure 1. The cases (a) and (b) correspond to an equal amount of shift from the linear 0 and + 1 mode resonances, respectively.

References

[1] S Dutta Gupta and G S Agarwal, *Opt. Commun.* **103**, 122 (1993)
[2] H Kogelnik and C V Shank, *J. Appl. Phys.* **43**, 2327 (1972)
[3] M Sargent III, W H Swatner and J D Thomas, *IEEE J. Quant. Electron.* **QE-16**, 465 (1980)
[4] P Yeh, *Optical waves in layered media* (Wiley, New York, 1988)
[5] H G Winful, J H Marburger and E Garmine, *Appl. Phys. Lett.* **35**, 379 (1979)
[6] W Chen and D L Mills, *Phys. Rev. Lett.* **58**, 160 (1987)
[7] J Coste and J Peyreud, *Phys. Rev.* **B39**, 13086 (1989)
[8] J Coste and J Peyreud, *Phys. Rev.* **B39**, 13096 (1989a)
[9] C M de Sterke and J E Sipe, *Phys. Rev.* **A38**, 5149 (1988)
[10] C M de Sterke and J E Sipe, *Phys. Rev.* **B39**, 5163 (1989)
[11] C M de Sterke and J E Sipe, *Phys. Rev.* **A42**, 550 (1990)
[12] M Grabowski and P Hawrylak, *Phys. Rev.* **B41**, 5783 (1990)
[13] P Hawrylak, M Grabowski and P Wilson, *Phys. Rev.* **B40**, 6398 (1989)
[14] C M de Sterke and J E Sipe, *Phys. Rev.* **A42**, 2858 (1990a)

PRAMANA
— journal of
physics

© Printed in India

Vol. 43, No. 1,
July 1994
pp. 73–80

New band system of MnSe molecule

K N UTTAM, R GOPAL and M M JOSHI
Saha's Spectroscopy Laboratory, Physics Department, University of Allahabad, Allahabad 211 002, India

MS received 19 February 1994

Abstract. Thermal emission spectrum of MnSe molecule, excited in high temperature graphite furnace, has been photographed in the spectral region $\lambda\lambda$ 4150–5800 Å at a reciprocal linear dispersion of 7·3 Å/mm. The study reveals the presence of two band systems viz. $A—X$ and $B—X$ in which $B—X$ is entirely new. While the system $A—X$ consists of 29 bands, the new system $B—X$ comprises of 24 single headed and red degraded bands. Vibrational analysis performed suggested that both the systems involve ground state $^6\Sigma$ with a vibrational frequency $\omega''_e = 361{\cdot}0\,\text{cm}^{-1}$. Transition responsible for MnSe spectrum appears to be of the type $^6\Sigma—^6\Sigma$.

An estimation of the ground state vibrational frequency for MnTe molecule gives rise to its value as $280\,\text{cm}^{-1}$.

Keywords. Thermal emission; molecular spectra; vibrational analysis; spectra of inorganic diatomic molecule; transition elements.

PACS No. 33·20

1. Introduction

Electronic spectrum of MnSe was observed by Monjajeb [1] for the first time twenty years ago from thermal emission in a King's furnace by heating a mixture of manganese and selenium or cadmium selenide or zinc selenide at 1800°C in argon atmosphere. Single headed bands shaded to red, occurring in the visible region $\lambda\lambda$ 4970–5600 Å, were attributed to a single system. However the analysis is based on the spectrograms taken under low dispersion (12–40 Å/mm) with Hilger E-492 spectrograph. Because MnSe has the same electronic structure as MnS, one can therefore assume that this system corresponds to the $A^6\Sigma—X^6\Sigma$ visible system of MnS molecule. Since the study of MnS molecule in thermal emission by Uttam *et al* [2] reveals the presence of two band systems viz. $A—X$ and $B—X$ in the visible region, we expect a new band system in the visible spectra of MnSe. Further the spectrum of MnSe is congested due to the presence of large number of isotopic abundance of selenium. Therefore we examined the thermal emission spectrum of MnSe molecule using high temperature graphite furnace at a comparatively higher dispersion (7·3 Å/mm) and higher resolution (0·1 Å) than that of Monjajeb [1].

Here we report the fresh results for MnSe molecule in the visible region $\lambda\lambda$ 4150–5800 Å.

2. Experimental details

A small quantity of intimate mixture of manganese metal power (BDH) with selenium or some solid selenide like CdSe or ZnSe was put in the graphite tube of the Saha's

high temperature furnace [3]. After making necessary routine adjustments and evacuation of the furnace chamber, argon gas was filled at about pressure of 50 cm of mercury. The tube was heated electrically to around 1800°C. A host of well marked bands, all degraded to the red, appeared in the blue-green region. A two meter Plane Grating Spectrograph with a grating blazed at λ 5600 Å and total lines ruled 45600 was used to photograph these bands in first order at a reciprocal linear dispersion of 7·3 Å/mm. An exposure time of about 6–8 min was sufficient to record the spectrogram on ORWO 400 ASA black and white films. An iron dc arc spectrum was recorded for comparison. The measurements were made using CZ Abbe Comparator with a least count of 0·0001 cm.

3. Results and Analyses

The bands appear in two groups in the spectral region $\lambda\lambda$ 4800–5800 Å and $\lambda\lambda$ 4150–4600 Å. Each group consists of a single system. All the bands are red degraded. Because of the higher resolution and dispersion, a partial rotational structure has been resolved. The complete reproduction of the spectrum is given in figure 1. The following is the system wise description:

3·1 *A—X system ($\lambda\lambda$ 4800–5800 Å)*

This system appears in the region $\lambda\lambda$ 4800–5800 Å and is constituted of 29 red degraded bands. The (0,0) of the system lies at λ5316 Å and is marked in figure 1. Observed band head data, their vibrational assignments and relative visual estimates of intensities are collected in table 1. The following equation [ref. 4] was found satisfactory to represent the wave numbers of the different band heads observed.

$$\nu = 18850{\cdot}7 + 270{\cdot}5\,(v' + 1/2) - 1{\cdot}75(v' + 1/2)^2 - 361{\cdot}0(v'' + 1/2) + 2{\cdot}25(v'' + 1/2)^2.$$

3.2 *B—X system ($\lambda\lambda$ 4150–4600 Å)*

This system lies in the region $\lambda\lambda$ 4150–4600 Å and consists of 24 single headed, red degraded relatively faint bands. The (0,0) of the system was located at λ 4293·9 Å. Table 2 provides the observed wave numbers in vacuum, visual estimates of their intensities and the vibrational assignments to the attributed bands. The following equation [ref. 4] accounts fairly well for the wave numbers of the different band heads forming this system.

$$\nu = 23323{\cdot}1 + 278{\cdot}0(v' + 1/2) - 1{\cdot}00(v' + 1/2)^2 - 361{\cdot}0(v' + 1/2) + 2{\cdot}25(v'' + 1/2)^2.$$

4. Discussion

The thermal emission spectrum of MnSe molecule consists of two systems designated as *A* and *B* in the visible region. As already mentioned, Monjajeb [1] had proposed only a tentative analysis of system *A* and suggested the probable value of the ground state vibrational frequency to be 360·0 cm^{-1}. The ω_e'' value obtained here is 361·0 cm^{-1}, which agrees with that of Monjajeb [1]. The remaining system *B* is faint. However,

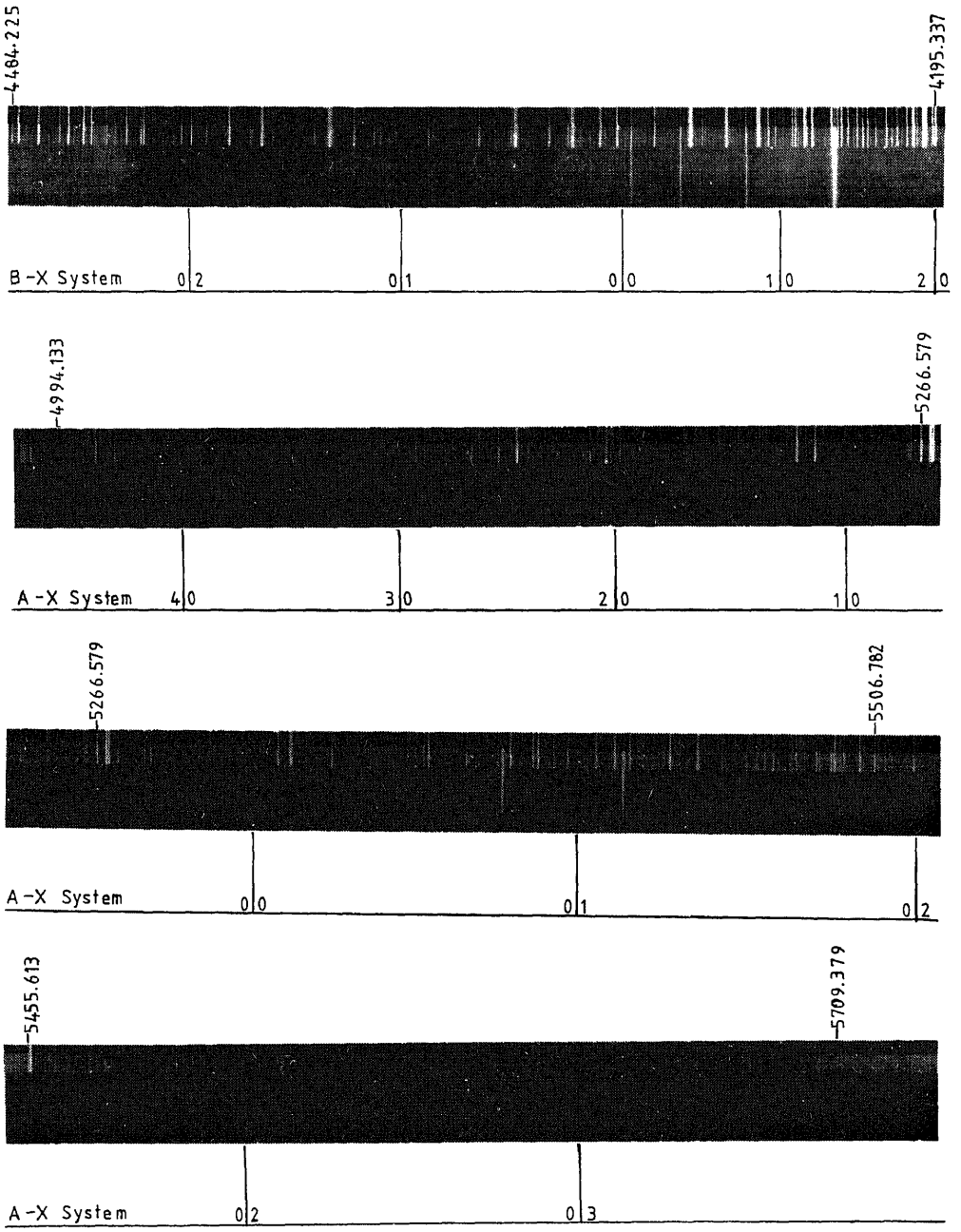

Figure 1. Thermal emission spectrum of MnSe molecule at a reciprocal linear dispersion of 7·3 Å/mm.

well marked and intense $\Delta v = 0$ and ± 1 sequences are present. This situation is helpful in determining the ground state vibrational constants with reasonable certainty. Figure 2 displays a smooth curve demonstrating the variation of ω_e'' values for diatomic MnO, MnS and MnSe with the number of electrons in these molecules.

Table 1. Band head data of MnSe molecule: $A—X$ system.

$\nu_{obs}(cm^{-1})$	$\Delta\nu(cm^{-1})$ (Obs–Cal)	Int.	Analysis (v', v'')	$\nu_{obs}(cm^{-1})$	$\Delta\nu(cm^{-1})$ (Obs–Cal)	Int.	Analysis (v', v'')
17749·8	0·2	1	(0, 3)	19072·3	−0·3	3	(1, 0)
17675·0	1·4	1	(1, 4)	18978·8	−0·8	1	(2, 1)
18098·3	1·2	2	(0, 2)	18886·8	−0·8	1	(3, 2)
18917·2	0·6	2	(1, 3)	19335·8	−0·3	3	(2, 0)
18936·2	−0·9	3	(2, 4)	19239·9	0·3	2	(3, 1)
18450·2	1·1	4	(0, 1)	19143·2	−0·9	1	(4, 2)
18365·2	1·1	1	(1, 2)	19597·1	1·0	2	(3, 0)
18280·4	0·3	1	(2, 3)	19496·8	0·7	1	(4, 1)
18198·2	1·1	1	(3, 4)	19398·5	1·4	1	(5, 2)
18805·6	0	4	(0, 0)	19853·0	0·4	2	(4, 0)
18715·8	−0·3	1	(1, 1)	19751·0	1·0	1	(5, 1)
18627·5	−0·1	1	(2, 2)	19647·5	0·9	1	(6, 2)
18539·8	−0·3	1	(3, 3)	20106·8	1·2	1	(5, 0)
18454·2	0·6	1	(4, 4)	20099·6	1·0	1	(6, 1)
				19891·4	−1·2	1	(7, 2)

Table 2. Band head data of MnSe molecule: $B—X$ system.

$\nu_{obs}(cm^{-1})$	$\Delta\nu(cm^{-1})$ (Obs–Cal)	Int.	Analysis (v', v'')	$\nu_{obs}(cm^{-1})$	$\Delta\nu(cm^{-1})$ (Obs–Cal)	Int.	Analysis (v', v'')
22226·2	0·3	1	(0, 3)	22635·3	−1·1	1	(4, 5)
22157·3	−1·6	1	(1, 4)	23281·9	0	3	(0, 0)
22093·5	−0·9	1	(2, 5)	23200·9	−0·5	2	(1, 1)
22032·0	−0·4	1	(3, 6)	23123·3	−0·1	2	(2, 2)
22574·2	0·8	2	(0, 2)	23048·7	0·8	2	(3, 3)
22502·6	0·7	1	(1, 3)	22973·6	−1·3	2	(4, 4)
22432·8	−0·1	2	(2, 4)	23557·4	−0·5	1	(1, 0)
22365·5	−0·9	1	(3, 5)	23474·7	−0·7	2	(2, 1)
22924·3	−1·1	2	(0, 1)	23396·3	0·9	2	(3, 2)
22848·7	−0·7	2	(1, 2)	23832·3	0·4	2	(2, 0)
22774·4	−1·5	2	(2, 3)	23746·3	−1·1	2	(3, 1)
22703·5	−1·4	2	(3, 4)	23666·1	0·7	1	(4, 2)

The present ω_e'' value for MnSe fits in the curve very well. Thus the ground state vibrational frequency for MnSe can be accepted as 361 cm^{-1}.

It is clear from the analysis that the vibrational constants of the lower state of the proposed system (B system) are identical with those of the ground state of the MnSe molecule. Further the general appearance of the bands and the simultaneous recording of the well-known visible system of MnSe are also strongly in favour of attributing these bands to the diatomic MnSe molecule. This evidently confirms that the carrier of the bands has been rightly identified as MnSe.

The $\Delta v = 0$ sequence is easily identified among the observed bands and those involving higher vibrational levels are found to be diffuse in appearance. The diffuseness increases as one moves away from the system origin and can be explained to

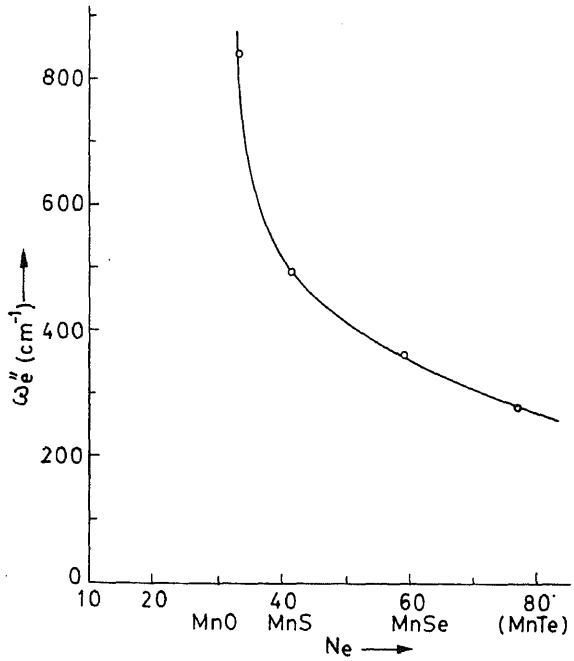

Figure 2. Variation of ground state frequency (ω_e'') vs number of electrons (Ne).

be due to the presence of large number of isotopes of selenium. The separate identification of the isotopic heads is not possible due to the faint spectrum.

The normal state electronic configurations of Mn and Se are given by:

$$_{25}\text{Mn} = 1s^2, 2s^2 2p^6, 3s^2 3p^6 3d^5, 4s^2 \text{ — } {}^6S_{5/2}$$

$$_{33}\text{Se} = 1s^2, 2s^2 2p^6, 3s^2 3p^6 3d^{10}, 4s^2 4p^4 \text{ — } {}^3P_2.$$

Our study of MnS molecule [2] reveals that the ground state is $^6\Sigma$. Since MnSe has the same electronic structure (isovalent) as MnS and the chances of observing the transition which involves the ground state are higher in thermal emission, it is reasonable to assume that the ground state of MnSe is also $^6\Sigma$. Thus the optically allowed transitions are $^6\Sigma$—$^6\Sigma$ and $^6\Pi$—$^6\Sigma$. Since in the present study systems A—X and B—X consist of single headed bands analogous to MnS [2] molecule, therefore these systems involve $^6\Sigma$—$^6\Sigma$ transition.

The dissociation energy, using Birge–Sponer extrapolation formula, is given by

$$D_0 = \omega_e''^2/4\omega_e'' x_e''.$$

Substituting the constants we find $D_0 = 14480{\cdot}1\,\text{cm}^{-1} = 1{\cdot}80\,\text{eV}$ which is quite reasonable.

The VI sub-group of the periodic table consists of five elements viz. O, S, Se, Te and Po. The diatomics with manganese of each one of them have been investigated spectroscopically except MnTe and MnPo. The transition A—X has been observed in each case of MnO, MnS and MnSe. This transition is characterized by well marked sequences. Table 3 displays the relevant data for these molecules with reference to system A—X. The ω_e'/ω_e'' and D_0 values for MnO, MnS and MnSe have been

Table 3. Spectroscopic constants for the A—X system.

	MnO	MnS	MnSe
$\omega_e''(cm^{-1})$	839·6	490·6	361·0
$\omega_e'(cm^{-1})$	762·8	371·8	270·5
ω_e'/ω_e''	0·9085	0·7579	0·7493
$D_0(cm^{-1})$	29842·2	33428·9	14480·1
$\nu_{00}(cm^{-1})$	17909·0	18858·1	18805·6

Table 4. Comparative data for the different diatomic molecules.

Molecule	Ne	ω_e''	$\omega_e''^{-2} \times 10^{-7}$	Molecule	Ne	ω_e''	$\omega_e''^{-2} \times 10^{-7}$
PbO	90	721·0	19·2	BiO	91	692·4	20·9
PbS	98	429·4	54·2	BiS	99	408·7	59·9
PbSe	116	277·6	129·8	BiSe	117	265·6	141·8
PbTe	134	211·9	222·7	BiTe	135	208·5	230·0
SbO	59	816·0	15·0	SnO	58	822·1	14·8
SbS	67	482·4	43·0	SnS	66	487·3	42·1
SbSe	85	326·1	94·1	SnSe	84	331·2	91·2
SbTe	103	284·4	123·6	SnTe	102	259·5	148·5
AlO	21	979·2	10·4	MnO	33	839·6	14·2
AlS	29	617·1	26·6	MnS	41	490·6*	41·6
AlSe	47	467·6	45·7	MnSe	59	361·0&	76·7
AlTe	65	415·0	58·1	MnTe	77	280·0#	124·9

(All ω_e'' values are in cm^{-1} units),
(Ne: Number of electrons; #: expected value; &: present value, *: ref. [2]. All other values taken from ref. [5]

calculated on the basis of molecular constants taken from [5], [2] and present study respectively.

The behaviour of ground state vibrational frequencies is quite satisfactory and the plot of the number of electrons (Ne) against (ω_e'') values is a smooth curve (figure 2). According to Howell [6], the similarity of the ratio ω_e'/ω_e'' in such cases indicates that the same type of relative loosening takes place in the molecular binding on examination. That a similar situation exists in the present case of MnS and MnSe also can be readily inferred from table 4 where the ratio ω_e'/ω_e'' is strikingly similar for MnS and MnSe. The dissociation energy D_0 has been calculated for these molecules with the help of vibrational constants. Since sufficient vibrational quanta have been observed in the ground state, the extrapolated values described in the table appear to be reasonably accurate.

Our attempts fail to record the electronic band spectra due to MnTe molecule and hence, we do not have much information about this molecule. However, from the information available for MnO, MnS and MnSe some predictions can be made for MnTe.

The plot of $\omega_e''^{-2}$ values versus electron number for different diatomics of this

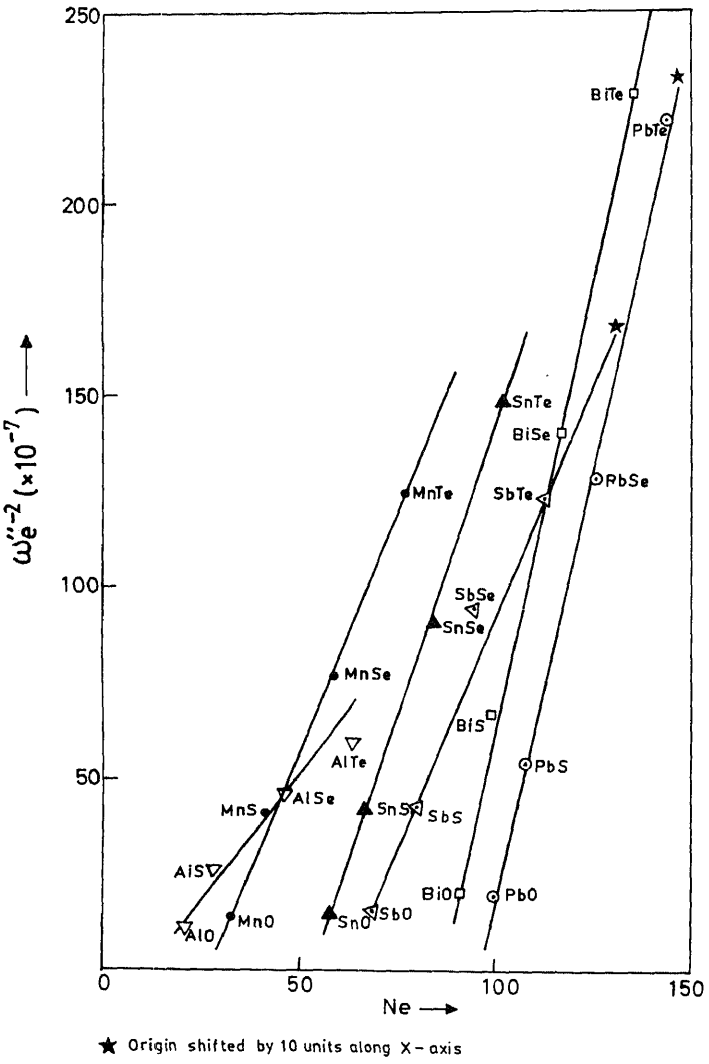

Figure 3. Variation of $\omega_e''^{-2}$ vs number of electrons (Ne).

molecular group involving manganese gives rise to a straight line. Spectroscopic constants for the diatomic combinations of many other atoms with O, S, Se and Te were also reviewed in this connection and table 4 presents the comparative data. If one plots $\omega_e''^{-2}$ values versus electron numbers straight lines are obtained for such of these molecular group vide figure 3. According to this trend in the group wise behaviour of molecular constants one can safely expect the ω_e'' value for MnTe to be around 280 (cm^{-1}).

Acknowledgements

The authors are thankful to Prof. B N Mishra for the fruitful discussion. One of the authors (KNU) is also thankful to CSIR, New Delhi for the financial support.

References

[1] A Monjajeb, '*Electronic spectra of certain transient gaseous diatomics at high temperature*' D. Phil Thesis, University of Allahabad, Allahabad, India, (1973)
[2] K N Uttam, R Gopal and M M Joshi, *Indian J. Phys.* **B67**, 183 (1993)
[3] M N Saha, N K Sur and K Majumdar, *Z. Phys.* **40**, 648 (1927)
[4] G Herzberg, *Molecular spectra and molecular structure* (Spectra of Diatomic Molecules, D Van Nostrand Company, New York, 1950) Vol. I pp 151
[5] K P Huber and G Herzberg, *Molecular spectra and molecular structure* (Constants of Diatomic Molecules, D Van Nostrand Company, New York, 1979) Vol. IV
[6] H G Howell, *Proc. R. Soc.* (*London*), **A153**, 683 (1936)

PRAMANA
— journal of
physics

© Printed in India

Vol. 43, No. 1,
July 1994
pp. 81–89

Thermal diffusion factors of hydrogenic trace mixtures with helium by column calibration factor

G DASGUPTA, A K DATTA and S ACHARYYA
Department of Physics, University College, Raiganj 733 134, India

MS received 20 July 1993; revised 11 March 1994

Abstract. Using column calibration factor (CCF) F_s for a given column, the temperature dependence of experimental thermal diffusion factors α_T of hydrogenic trace mixtures in helium are accurately determined. This study, however, observes the inelastic collision effect in these trace mixtures when α_T by our CCF method are compared with those by the existing methods and theoretical ones respectively.

Keywords. Column calibration factor; thermal diffusion factor; thermal diffusion column; inelastic and elastic collisions.

PACS No. 44·90

1. Introduction

In the existing column theory as developed by Furry and others [1–3] the column geometry plays an important role in determining the exact value of thermal diffusion factor α_T of a binary gas mixture. The column as such cannot yield the actual α_T values both in trend and in magnitude with respect to temperature and composition as the binary molecular interactions are often called into play. Thermal diffusion column is still far superior to any other α_T measuring instruments as the equilibrium separation factor q_e defined by

$$q_e = \frac{(\chi_i/\chi_j)_{\text{top}}}{(\chi_i/\chi_j)_{\text{bot}}}$$

is very large even in the case of small mass difference between the components of a mixture. Here, χ_i and χ_j are the mass fractions of the lighter and the heavier components respectively. Hence for a binary mixture of almost identical masses, shapes and sizes a calibrated TD column can safely be used to measure a reliable relative and small α_T values. For this reason we have calibrated the given column of Slieker and de Vries [4] with known and reliable α_T of He – T_2 mixture to arrive at the column calibration factor (CCF) F_s from the relation:

$$\ln q_{\max} = \alpha_T F_s(r_c, r_h, L, \bar{T}) \tag{1}$$

where $\bar{T}$ is the mean temperature of T_h and T_c, T_h and T_c being the hot and cold wall temperatures in K. r_c and r_h are the radii of cold and hot wall of a column of geometrical length L. F_s is supposed to be an independent molecular model solely dependent on the column geometry at any mean temperature $\bar{T}$ in K.

A number of studies by Acharyya *et al* [5–7] and Navarro *et al* [8] on F_s enabled us to study the temperature dependence of α_T of DT and HT in helium only to explore the fact that the TD column is a reliable relative α_T measuring instrument and to observe the inelastic collision effects in them. In this study, we estimate the experimental parameters a' and b' governing the very nature of variation of the available experimental $\ln q_e$ against pressure p of He–DT and He–HT gas mixtures [4], the hydrogenic components were never becoming larger than 5% in helium at three experimental temperatures.

The computed data of $\ln q_e$ of He–DT and He–HT against pressure in atmosphere are shown in figures 1 and 2 respectively to ensure that the least square fitted curves agree excellently with the experimental ones. For He–HT an interesting feature is that unlike the usual behaviour, $\ln q_e$ becomes smaller with temperatures, not noticed earlier [7].

The hydrodynamical part of the column theory is excellently obeyed by He–DT and for some selected experimental points of He–HT as their $p^2/\ln q_e$ against p^4 were found out to be

$$p^2/\ln q_e = 0{\cdot}7758 + 0{\cdot}8161\ p^4 \text{ at } 338\text{ K.}$$
$$= 0{\cdot}4938 + 0{\cdot}7294\ p^4 \text{ at } 378\text{ K}$$
$$= 0{\cdot}3964 + 0{\cdot}6024\ p^4 \text{ at } 423\text{ K}$$

and

$$p^2/\ln q_e = 9{\cdot}0749 + 14{\cdot}8368\ p^4 \text{ at } 338\text{ K}$$
$$= 13{\cdot}5999 + 64{\cdot}6412\ p^4 \text{ at } 378\text{ K}$$
$$= 14{\cdot}6461 + 411{\cdot}5226\ p^4 \text{ at } 423\text{ K respectively.}$$

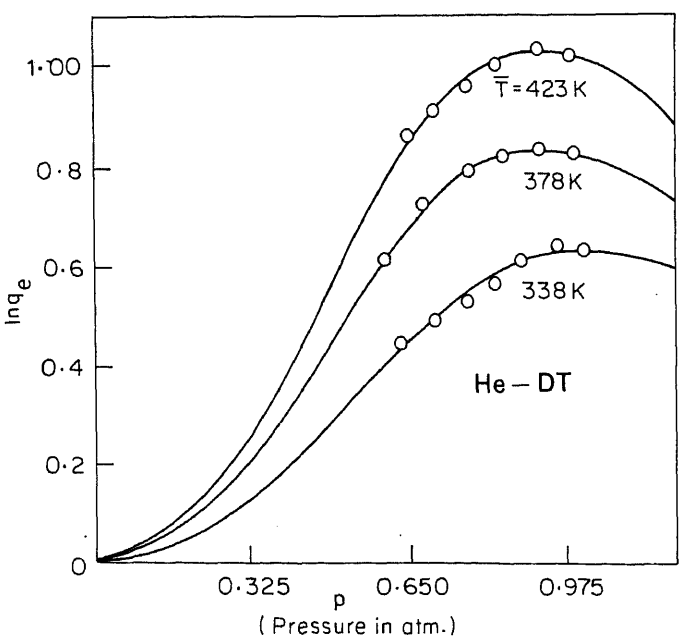

Figure 1. $\ln q_e$ against pressure p in atmosphere for He–DT trace mixture, at $\bar{T}$= 338, 378 and 423 K, 'O' experimental points.

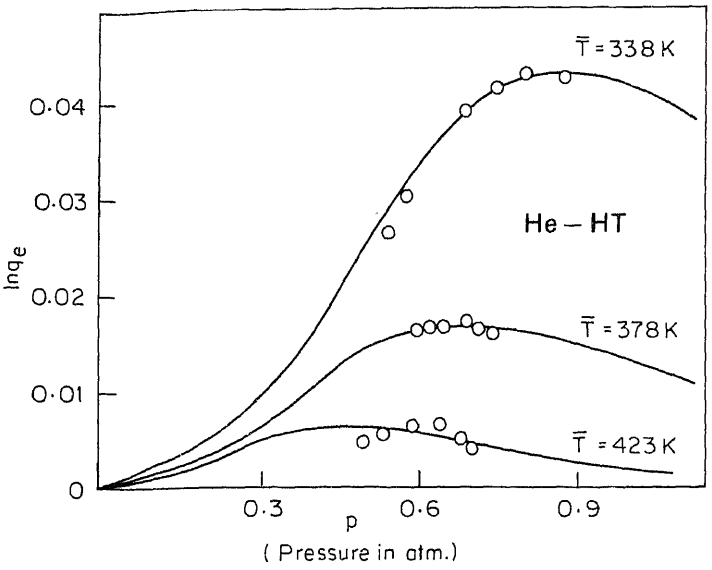

Figure 2. $\ln q_e$ against pressure p in atmosphere for He–HT trace mixture at $\bar{T} = 338$, 378 and 423 K, 'O' experimental points.

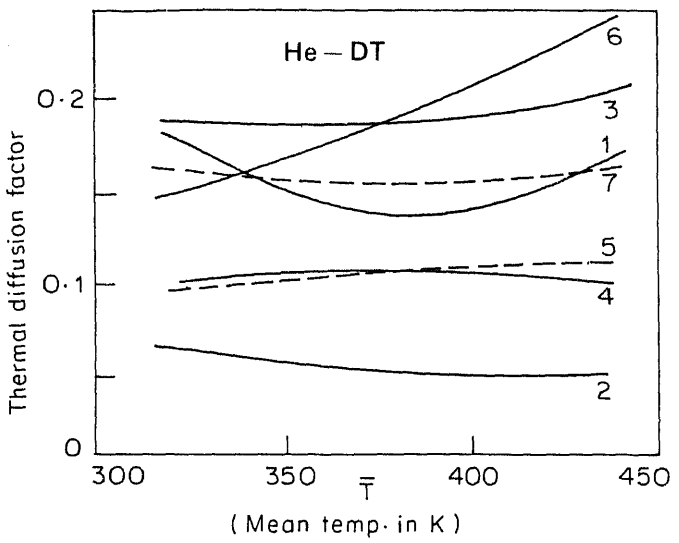

Figure 3. Variation of α_T with $\bar{T}$ of He–DT trace mixture, 1. Our expt α_T from $\ln q_{max}$ and F_s; 2. Expt α_T(Maxwell case); 3. Expt α_T(Slieker case); 4. Theor α_T(elastic) from Eq (7); 5. Theor α_T(inelastic) with $Z_{rot} = 300$ from Eq (7); 6. Theor α_T(inelastic) with Z_{rot} calculated from Barua *et al* (1970) from Eq (8); 7. Theor α_T(inelastic) with Z_{rot} calculated from Parkers [12] formula with adjustable $Z^a_{rot} = 7{\cdot}08$ [13].

In the absence of any reliable possibility to estimate the actual experimental α_T of a mixture through the use of molecular model we used the values of F_s already obtained for the column [7]:

$$F_s = -66{\cdot}52202 + 0{\cdot}3502286\,\bar{T} - 4{\cdot}1879 \times 10^{-4}\,\bar{T}^2.$$

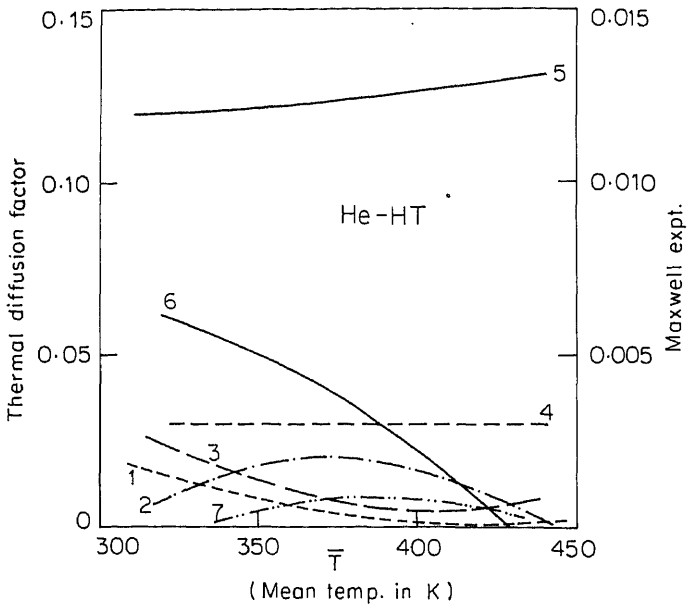

Figure 4. Variation of α_T with $\bar{T}$ of He–HT trace mixture
1. Our expt α_T from $\ln q_{max}$ and F_s; 2. Expt α_T(Maxwell); 3. Expt α_T(Slieker); 4. Theor α_T(elastic) from Eq (7); 5. Theor α_T(inelastic) with $Z_{rot} = 300$ from Eq (8); 6. Theor α_T(inelastic) with Z_{rot} calculated from Barua *et al* [12] from Eq (8); 7. Theor α_T(inelastic) with Z_{rot} calculated from Parker [13] formula with adjustable $Z^{\alpha}_{rot} = 12{\cdot}15$.

Now α_T's of He–DT and He–HT were obtained from (1) and compared with those by the existing methods using column theory as well as the theoretical α_T's based on elastic and inelastic [9] collisions in figures 3 and 4 respectively in order to reveal the existence of inelastic collisions in these mixtures.

2. Theoretical formulation to estimate experimental α_T

Both ends being closed for the ideal column of length L, $\ln q_e$ of a gas mixture at any mean temperature $\bar{T}$ is given by

$$\ln q_e = \frac{HL}{K_c + K_d} \tag{2}$$

where H, K_c and K_d are the functions of transport coefficients of a gas mixture and proportional to p^2, p^4 and p^0 respectively, p being pressure in atmosphere.

In order to remove parasitic remixing effect, Furry and Jones [2] simply added a term K_p proportional to p^4 to the denominator when (2) becomes

$$\ln q_e = \frac{a' p^2}{b' + p^4} \tag{3}$$

which is also written as

$$p^2/\ln q_e = b'/a' + (1/a')p^4 \tag{4}$$

a' and b' are however related by

$$(HL/K_c)p^2 = a'(1 + K_p/K_c) \text{ and } (K_d/K_c)p^4 = b'(1 + K_p/K_c)$$

H, K_c, K_d are the functions of the transport coefficient of a mixture and K_p is the remixing coefficient.

Again if c represents the intercept of the straight line of (4) we have

$$H = (K_d/Lc) \tag{5}$$

the exact expressions for H, K_c and K_d are given in our previous publications [5–7].

The estimation of the experimental α_T through the existing formulations involved the shape factors taking account of the inherent asymmetry of the column geometry. The mass density ρ, the viscosity coefficient η and the diffusion coefficient D were calculated from MTGL of Hirschfelder *et al* [10], the column shape factors and the force parameters required had already been reported earlier [7].

It is observed in figures 1–2 that as the pressure increases $\ln q_e$ increases and becomes maximum when $p = (b')^{1/4}$ for which $(\delta \ln q_e/\delta p) = 0$.

We then have from (3)

$$\ln q_{\max} = (a'/2\sqrt{b'}) \tag{6}$$

It is also observed in He–HT, unlike He–DT, that some experimental data of $\ln q_e$ are not in fit with the hydrodynamical part of the column theory as they have tendency to yield the negative intercept of $p^2/\ln q_e$ against p^4 which is absurd unless inversion of α_T would take place. Hence we are bound to select some six or seven data from the reported graph to fix the values of $\ln q_{\max}$ from the (6).

Table 1 and the graphs of figures 1–2, revealed that $\ln q_{\max}$ from (6) in terms of a' and b' are in good agreement with the graphically determined values earlier [7]. This establishes the fact that our choice of the $\ln q_e$ data with pressure particularly for the He–HT mixture where the mass difference between the components is practically nil, is almost right.

3. Theoretical formulations to calculate α_T

Theoretical α_T can, however, be estimated from

$$\alpha_T = \frac{1}{6[\lambda_{ij}]_1} \frac{S^{(i)}\chi_i - S^{(j)}\chi_j}{[X_\lambda + Y_\lambda]} (6C^*_{ij} - 5) \tag{7}$$

where $(6C^*_{ij} - 5)$ depends mainly on the temperature while the other factors involved in (7) are the complicated functions of composition, masses and thermal conductivities of gases and gas mixtures. The α_T, calculated from (7), is presented in the 12th column of table 1, and shown graphically in figures 3–4 for He–DT and He–HT respectively.

Table 1. Experimental and Theoretical α_T values of binary gas mixtures with temperature.

System	Hot wall temp T_h in K	Cold wall T_c in K	Mean Temp $\bar{T}$ in K	a' in $(atm)^2$	b' in $(atm)^4$	In q_{max} computed from Eq (5)	Expt F_s Ref (6)	Expt α_T with: Our calibration factor method Eq. (1)	Expt α_T with: Maxwell shape factor	Expt α_T with: Slieker shape factor	Theor. α_T from Eq (6) elastic theor. method	Theoretical α_T from Eq (7) with Z_{rot}: 300	Barua *et al*	Parker
He–HT	393	283	338	0·0674	0·6116	0·0431	4·001	0·0107	0·0014	0·0017	0·030	0·121	0·055	0·002
	473	283	378	0·0155	0·2104	0·0169	6·026	0·0020	0·0028	0·0007	0·030	0·124	0·037	0·009
	563	283	423	0·0024	0·3559	0·0064	6·691	0·0009	0·0010	0·0006	0·030	0·129	0·005	0·005
He–DT	393	283	338	1·289	1·0519	0·6284	4·001	0·1567	0·060	0·186	0·105	0·100	0·158	0·158
	473	283	378	1·371	0·6670	0·8331	6·026	0·1382	0·054	0·187	0·104	0·105	0·188	0·154
	563	283	423	1·660	0·6580	1·0232	6·691	0·1529	0·050	0·194	0·103	0·109	0·226	0·159

Thermal diffusion factors

The inelastic thermal diffusion factor α_{ij} is given by according to Monchick *et al* [11]

$$\alpha_T = \frac{(6C_{ij}^* - 5)\mu_{ij}}{5nk[D_{ij}]_1}\left(\frac{\lambda_{j\,\text{trans}}^{\alpha}}{\chi_j m_j} - \frac{\lambda_{i\,\text{trans}}^{\alpha}}{\chi_i m_i}\right) + \frac{1}{5nk[D_{ij}]_1}$$
$$\left[\frac{(6\tilde{C}_{ji} - 5)\lambda_{j\,\text{int}}^{\alpha}}{\chi_j} - \frac{(6\tilde{C}_{ij} - 5)\lambda_{i\,\text{int}}^{\alpha}}{\chi_i}\right] \tag{8}$$

where the symbols have their usual meanings only the collision integral ratio $\tilde{C}_{ij}$ differs from C_{ij}^*. In fact $\tilde{C}_{ij}$ is not symmetric with respect to the interchange of the indices i and j and is very sensitive to inelastic collision.

For a pure gas the exact values of $\lambda_{j\,\text{trans}}^{\alpha}$ and $\lambda_{i\,\text{trans}}^{\alpha}$ is given by

$$\lambda_{i\,\text{trans}} = \frac{\eta}{M}\left[\left(\frac{5}{2}C_{v\,\text{trans}} + \frac{\rho D_{\text{int}}}{\eta}C_{\text{int}}\right) - \left(\frac{2}{\pi}\frac{C_{i\,\text{int}}}{Z_{\text{rot}}}\right)\left(\frac{5}{2} - \frac{\rho D_{\text{int}}}{\eta}\right)^2\right.$$
$$\left.\left\{1 + \frac{2}{\pi Z_{\text{rot}}}\left(\frac{5}{3}\frac{C_{\text{int}}}{R} + \frac{\rho D_{\text{int}}}{\eta}\right)\right\}^{-1}\right]. \tag{9}$$

Here $C_{v\,\text{trans}} = 3R/2$, the constant value of translational heat capacity, Z_{rot} is the rotational translational collision number for inelastic collision.

The nonspherical terms of (8) we used Hirchfelder–Euken expression [10] to calculate the thermal conductivity $\lambda_{i\,\text{int}}^{\alpha}$ from

$$\lambda_{i\,\text{int}}^{\alpha} = \frac{n[D_{ii}]_1 C_{\text{int}}}{1 + (\chi_j/\chi_i)(D_{ii}/D_{ij})_1} \tag{10}$$

Theoretical inelastic α_T's for He–DT and He–HT thus calculated from (8) with the help of (9) and (10) are shown in table 1 and also in figures 3–4 respectively for comparison with other experimental α_T values.

4. Results and discussion

The inherent asymmetry in the column geometry is however, taken into account by Maxwell, Slieker and Lennard–Jones dimensionless shape factors [7]. We calculated the experimental α_T's of He–HT and He–DT trace mixtures at $T = 338$, 378 and 423 K respectively from (5) using those shape factors. Slieker's case does not involve any molecular model and it gives rather a rough estimation of the experimental α_T while the former includes inverse fifth power potential. As the cold wall temperature T_c was held fixed experimental α_T due to L–J case cannot be applicable here. The α_T thus obtained due to Maxwell and Slieker cases is presented in table 1 and shown graphically by the curves 2 and 3 respectively of figures 3 and 4.

The experimental α_T from (1) as obtained in terms of $\ln q_{\max}$ of (6) and F_s is shown by curve 1 in figures 3 and 4. When they are compared with those due to Maxwell (curve 2) and Slieker (curve 3) it is found that so far as the trend is concerned the data due to Slieker agree better than those due to Maxwell's shape factors. This is perhaps due to the fact that both Slieker and our method are free from any binary molecular model. As the mass difference between the components of a binary mixture decreases as in the case of He–HT the agreement is more close.

The theoretical α_T based on elastic collision theory, (7), as shown by curve 4 in

figures 3–4 appears to be temperature independent. Unlike He–HT, He–DT however show slightly lower value at higher temperature. The inelastic α_T as calculated from (8) with $Z_{rot} = 300$, show its positive temperature dependence as represented by curve 5 in figures 3–4.

When α_{ij} were calculated with the available rotational translational collision number of Barua *et al* [12] an interesting feature is that the curve 6 of figures 3–4 coincide with α_T's of our CCF method. This fact prompted us to adjust Z_{rot} from Parker's formula [13]. Using $Z_{rot} = 2{\cdot}78$, 2·91 and 3·05 for HT and $Z_{rot} = 4{\cdot}78$, 5·01 and 5·23 for DT at 338, 378 and 423 K respectively inelastic α_{ij}'s are then estimated for both He–DT and He–HT trace mixtures and were shown by curve 7 in figures 3–4 respectively for comparison with other α_T's.

With Z_{rot} determined by us inelastic theoretical α_T's curve 7 (15th column of table 1) so far as the magnitude and trend are concerned in the case of He–DT, support our α_T's curve 1 (9th column of table 1) and only in trend with α_T's due to Slieker (11th column of table 1). In the case of He–HT these theoretical α_T's almost coincide with our α_T's, but in trend with the experimental α_T's due to Maxwell.

All these comparison of α_T's so far obtained thus reveal that inelastic collisions play an important role in such trace mixtures. Again the variation of $\ln q_{max}$ against $\bar{T}$ for He–HT is given by

$$\ln q_{max} = 0{\cdot}89879 - 4{\cdot}2097 \times 10^{-3}\ \bar{T} + 4{\cdot}9647 \times 10^{-6}\ \bar{T}^2$$

showing that at $\bar{T} \simeq 429$ K, $\ln q_{max}$ may be zero as shown in figure 5. The isobaric He–HT mixture may yield an interesting phenomenon of inversion of both $\ln q_{max}$ and α_T with respect to temperature like isobaric system N_2–CO as studied in our recent publication of Saha *et al* [14]. The system He–HT deserves a detailed study of measurements of $\ln q_e$ against pressure for its different composition and temperatures.

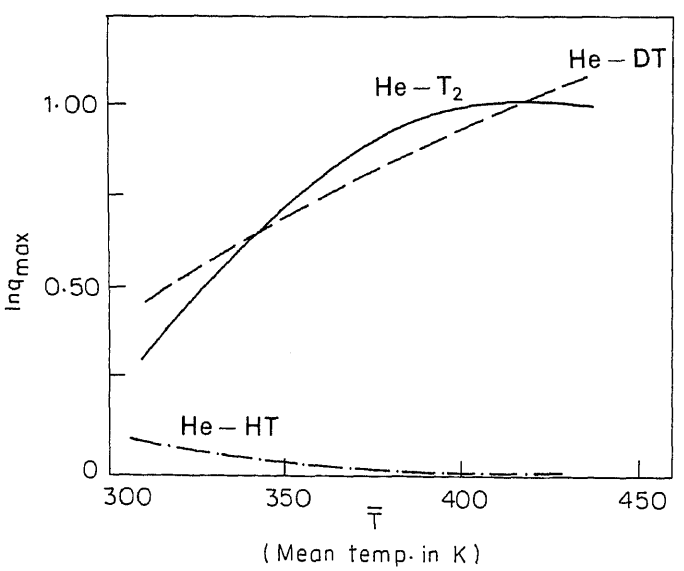

Figure 5. Variation of $\ln q_{max}$ with temperature $\bar{T}$ in K for He–DT He–T_2 and He–HT mixtures.

We are, therefore, now in a position to conclude that CCF is an accurate α_T determining factor of isotopic, nonisotopic and isobaric α_T's of binary gas mixtures. The functional relationship of F_s with r_c, r_h, L and $\bar{T}$ should be studied both from the theoretical and experimental viewpoints.

References

[1] W H Furry, R C Jones and L Onsager, *Phys. Rev.* **55**, 1083 (1939)
[2] W H Furry and R C Jones, *Phys. Rev.* **60**, 459 (1946)
[3] R C Jones and W H Furry, *Rev. Mod. Phys.* **18**, 151 (1946)
[4] C J G Slieker and A E deVries, *J. Chim. Phys.* **60**, 172 (1967)
[5] S Acharyya, A K Das, P Acharyya, S K Datta and I L Saha, *J. Phys. Soc. Jpn.* **50**, 1603 (1981)
[6] S Acharyya, I L Saha, P Acharyya, A K Das and S K Datta, *J. Phys. Soc. Jpn.* **51**, 1469 (1982)
[7] S Acharyya, I L Saha, A K Datta and A K Chatterjee, *J. Phys. Soc. Jpn.* **56**, 105 (1987)
[8] J L Navarro, J A Madariage and J M Saviron, *J. Phys. Soc. Jpn.* **52**, 478 (1983)
[9] T K Chatterjee and S Acharyya, *J. Phys.* **B7**, 2277 (1974)
[10] J O Hirschfelder, C F Curtiss and R B Bird, *Molecular theory of gases and liquids*, (John Wiley, New York, 1964)
[11] L Monchick, S I Sandler and E A Mason, *J. Chem. Phys.* **49**, 1178 (1968)
[12] A K Barua, A Manna, P Mukhopadhyay and A Dasgupta, *J. Phys.* **B3**, 619 (1970)
[13] J G Parker, *Phys. Fluids* **2**, 449 (1959)
[14] I L Saha, A K Datta, A K Chatterjee and S Acharyya, *J. Phys. Soc. Jpn.* **56**, 2381 (1987)

PRAMANA
— journal of
physics

© Printed in India

Vol. 43, No. 1,
July 1994
pp. 91–99

Construction of broadband homonuclear TOCSY sequences via numerical optimization

N SAMBASIVA RAO and NARSIMHA REDDY
NMR Laboratory, Indian Institute of Chemical Technology, Hyderabad 500007, India

MS received 17 September 1993; revised 19 May 1994

Abstract. Some new isotropic mixing sequences have been designed via numerical optimization procedure. The performance of the isotropic mixing sequences generated here, has been assessed and compared with other existing sequences by computer simulation. The global quality factors for some of the present sequences are better, when compared to the sequences that are routinely used in the literature for TOCSY experiments.

Keywords. Isotropic mixing; in-phase coherence transfer; numerical optimization; quality factor.

PACS No. 33·25

1. Introduction

Homonuclear coherence transfer (CT) techniques constitute an important class of experiments that facilitate the spectral assignment of complex biomolecules in the liquid state [1–3]. The two dimensional isotropic mixing experiment (TOCSY/HOHAHA) [4, 5] provides a most effective homonuclear coherence transfer mechanism. In contrast to the COSY type experiments [2, 6], this experiment effects a transfer of in-phase coherence throughout the coupling network and pure phase spectra can be obtained. The resulting in-phase cross-peak multiplets give rise to a higher sensitivity, if the line widths are larger than or on the order of the coupling constants. Hence the TOCSY experiment has many useful applications in the study of biological macromolecules [7]. A number of theoretical treatments of the isotropic mixing experiment have appeared in the literature which discuss the ideal isotropic mixing process [4, 8, 9].

Keeping in view of the incredible power of this experiment, efforts were made in the past [7c, 9, 10] to improve the efficiency of this experiment in maximizing the cross-peak intensity over a wide band width of resonance frequencies. Most of the initial sequences employed for this purpose were originally developed for broadband heteronuclear decoupling. The suppression of chemical shift terms in a zero order Magnus expansion [11] over a relatively broad spectral range makes these sequences good candidates for homonuclear isotropic mixing. However, as pointed out earlier [12, 13], these sequences also produce combinations of bilinear operator terms of the type $I_{1\alpha}I_{2\beta}$ (with $\alpha, \beta = x, y, z$), apart from the ideal isotropic mixing Hamiltonian. Even with the decoupling sequences such as DIPSI [13], which have been optimized for minimal production of bilinear cross terms, the in-phase CT is not uniform for all the orthogonal magnetization components. Also the present tendency is to undertake

studies on macromolecules at highest possible magnetic fields. Hence, there is a necessity to construct newer homonuclear TOCSY sequences for efficient coherence transfer over a wide range of offsets and at the same time provide uniform transfer of CT for all the orthogonal components of magnetization.

Recently Kadkhodaie *et al* [10] have designed a new pulse sequence, called FLOPSY, for broadband homonuclear CT via numerical optimization procedure. In this paper, we present an alternative approach to construct broadband isotropic mixing sequences using numerical optimization. The approach involves maximization of coherence transfer, for all the initial components of magnetization, employing Nelder–Mead [14] optimization procedure. The performance of our numerically optimized isotropic mixing sequences (NOIS) has been assessed employing the procedure described by Glaser and Drobny [9] and also by performing experiment using NOIS sequence.

2. Numerical design of TOCSY sequences

The numerical optimization is based on a system consisting of two spin 1/2 nuclei I_k and I_l with resonance offsets, δ_k and δ_l respectively. The Hamiltonian during the application of RF pulses is given by

$$\mathbf{H} = \delta_k \mathbf{I}_{kz} + \delta_l \mathbf{I}_{lz} + 2\pi J \mathbf{I}_k \mathbf{I}_l + \omega_1[\cos\phi(\mathbf{I}_{kx} + \mathbf{I}_{lx}) + \sin\phi(\mathbf{I}_{ky} + \mathbf{I}_{ly})] \tag{1}$$

where J_{kl} is the coupling constant of the spins k and l, ω_1 is the RF field strength (in frequency units) and ϕ is the phase of the RF field. The efficiency of CT during the mixing sequence can be calculated numerically using the procedure outlined in ref. [9].

The isotropic mixing sequences to be constructed are assumed to consist of a basic pulse cycle with duration τ_{cyc}, which is repeated m times in order to create an isotropic mixing period of duration $\tau_{mix} = m\tau_{cyc}$. Each basic cycle of the mixing sequence has been considered to be a super cycle (S) of the form $\overline{RRRR}$ or $\overline{RRRR}$ $\overline{RRRR}$. R in the super cycle is a composite 180° pulse consisting of n pulses with flip angles α_i and phases ϕ_i. The super cycle of the above type has been considered for the optimization as they are known for their pulse error compensation [15]. In our numerical design, Nelder–Mead optimization procedure [14] has been adopted to minimize the error function,

$$f_e = \sum_{\alpha=x,y,z} \sum_{\delta_k \delta_l} |(1 - \Gamma^{(kl)}_{\alpha\alpha}(\tau_{mix}, \delta_k, \delta_l))| \tag{2}$$

where $\Gamma^{(kl)}_{\alpha\alpha}(\tau_m, \delta_k, \delta_l)$ is the normalized coherence transfer function defined by

$$\Gamma^{(kl)}_{\alpha\alpha}(\tau_{mix}, \delta_k, \delta_l) = \frac{\mathrm{Tr}[\mathbf{I}_{k\alpha}\mathbf{U}_{eff}(\tau_{mix}, \delta_k, \delta_l)\mathbf{I}_{l\alpha}\mathbf{U}^{\dagger}_{eff}(\tau_{mix}, \delta_k, \delta_l)]}{\mathrm{Tr}[\mathbf{I}_{k\alpha}\mathbf{U}_{eff}(\tau_{mix}, 0, 0)\mathbf{I}_{l\alpha}\mathbf{U}^{\dagger}_{eff}(\tau_{mix}, 0, 0)]} \tag{3}$$

where U_{eff} is calculated using (3) and (4) of ref. [9]. The transfer efficiency function is determined at the mixing time of 1/2 J, where the coupling constant J has been fixed at 10 Hz. The parameters, n flip angles α_i and n phase ϕ_i of composite element R of the super cycle S have been optimized to get the minimum error function for the range of offset values $-5\,\mathrm{kHz} < \delta_k, \delta_l < 5\,\mathrm{kHz}$. An RF field amplitude of 10 kHz has been employed for calculations. During the optimization procedure only those combinations of α's and ϕ's are chosen for which the error function is almost zero

Table 1. Numerically optimized isotropic mixing sequences (NOIS) along with some of the existing sequences and their global quality factors (calculated with $\delta_{max} = 4$ kHz).

Name	No. of pulses	Sequence (R)	Super-cycle used	Global quality factors		
				Q_x	Q_y	Q_z
FLOPSY	9	46(0) 96(45) 164(67·5) 159(315) 130(22·5) 159(315) 164(67·5) 96(45) 46(0)	$\overline{RRRR}$ $RR\overline{RR}$	0·61	0·53	0·59
DIPSI-2	9	320(0) 410(180) 290(0) 285(180) 30(0) 245(180) 375(0) 265(180) 370(0)	$R\overline{RRR}$	0·68	0·44	0·46
WALTZ-16	9	270(180) 360(0) 180(180) 270(0) 90(180) 180(0) 360(180) 180(0) 270(180)	$R\overline{RRR}$	0·31	0·03	0·04
MLEV-16	3	90(0) 180(90) 90(0)	$R\overline{RR}\,\overline{R}R\overline{RR}$ $\overline{RR}\,RR\,R\overline{RR}$	−0·31	−0·31	0·16
NOIS-1	9	326(0) 346·5(0) 279(185) 68(0) 298·5(183) 311·5 (0) 325·5(180) 32·5(0) 4(65)	$R\overline{RRR}$	0·70	0·46	0·59
NOIS-2	8	254(0) 404(0) 286(240) 65(0) 279(232) 339(0) 321·3(176·5) 31·4(0)	$\overline{RRR}$ $RR\overline{RR}$	0·62	0·55	0·60
NOIS-3	5	159·3(229·3) 328(219·3) 181·5(289·2) 334(201·6) 154·6(229·5)	$R\overline{RRR}$ $RR\overline{RR}$	0·50	0·59	0·59
NOIS-4	8	79(175) 180(146) 76(160) 131(156·6) 177·6(110·6) 81·6(186·7) 206(210·5) 171(194·6)	$\overline{RRR}$ $RR\overline{RR}$	0·54	0·53	0·60

for the zero values of δ_k and δ_l. During the optimization, the pulse widths α_i and phases ϕ_i have been allowed to vary between 0° and 520°. A computer program has been developed for the numerical optimization in FORTRAN-77 and implemented on our SUN SPARK station 330 running under UNIX operating system. Offset compensated 180° pulse sequences have been chosen as starting values for the composite element R. Some of these starting composite 180° sequences have been taken from the literature [16] and some of them have been constructed by us using Nelder–Mead optimization procedure. Typically, for obtaining an isotropic mixing sequence with 8 pulses in its R element, the optimization takes about 6–8 hr. A list of numerically optimized isotropic mixing sequences (NOIS) is given in table 1. The sequence R in table 1 consists of a series of pulses. Each pulse is represented in the form of flip angle (phase). The global quality factors for these sequences along with the sequences reported in the literature are also given in this table.

3. Performance assessment

Waugh [10] represented the resonance offset effects on the performance of isotropic mixing sequences by plotting the Fourier transform (FT) of $[\langle I_k \rangle - \langle I_l \rangle](\tau_{mix})$ as a function of the chemical shift of one of the spins, while fixing that of the other. Such a plot yields two peaks at $\pm J_{kl}$ values [12]. An ideal isotropic mixing sequence gives such FT spectrum that is independent of the chemical shifts of the spins. However, the Waugh's plot for practical sequences shows that the coherence transfer frequencies fall as a function of resonance offset. In order to assess the effectiveness of coherence transfer in a 2D TOCSY experiment, it is necessary to investigate the full range of the independent chemical shifts δ_k and δ_l. As it is difficult to undertake such an analysis for the full range of resonance offsets of both the spins involved, Glaser and Drobny [9] have therefore introduced the concept of quality factors for assessing the performance of isotropic mixing sequences. They defined two types of quality factors, namely, local and global. The value of the local quality factor (q_α) gives the information about the efficiency of coherence transfer over a range of J_{kl} values for particular offset values (δ_k and δ_l). The global quality factor (Q_α) of a particular mixing sequence is the minimum value of local quality factor over a particular range of offset values. Mathematically, for a two-spin system, these can be defined as

$$q_\alpha = C \min_{0{\cdot}8\tau_{max} \leqslant \tau_{mix} \leqslant 1{\cdot}2\tau_{max}} [\Gamma^{kl}_{\alpha\alpha}(\tau_{mix})] \tag{4}$$

$$Q_\alpha = \min_{|\delta_k|,|\delta_l| \leqslant \delta_{max}} q_\alpha \tag{5}$$

q_α is the local quality factor for the $\alpha(x, y \text{ or } z)$ component of initial magnetization; Q_α represents the global quality factor for $\alpha(x, y \text{ or } z)$ component, C is the normalization constant given by $1/\sin^2(0{\cdot}8\pi/2)$ and normalizes q_α to 1 for the ideal isotropic mixing case ($\tau_{max} = 1/2J_{kl}$); and $\Gamma^{kl}_{\alpha\alpha}$ is the coherence transfer function δ_k and δ_l are the offsets of the spins k and l. Though the single value of the global quality factor represents the quality of a mixing sequence over a range of offsets, the two dimensional plots, of local quality factor $q_\alpha(\delta_k, \delta_l)$, give the comprehensive picture of the efficiency of an isotropic mixing sequence for coherence transfer.

The performance of our numerically optimized isotropic mixing sequences (NOIS) has been assessed using both the procedures described by Waugh [12] and Glaser-

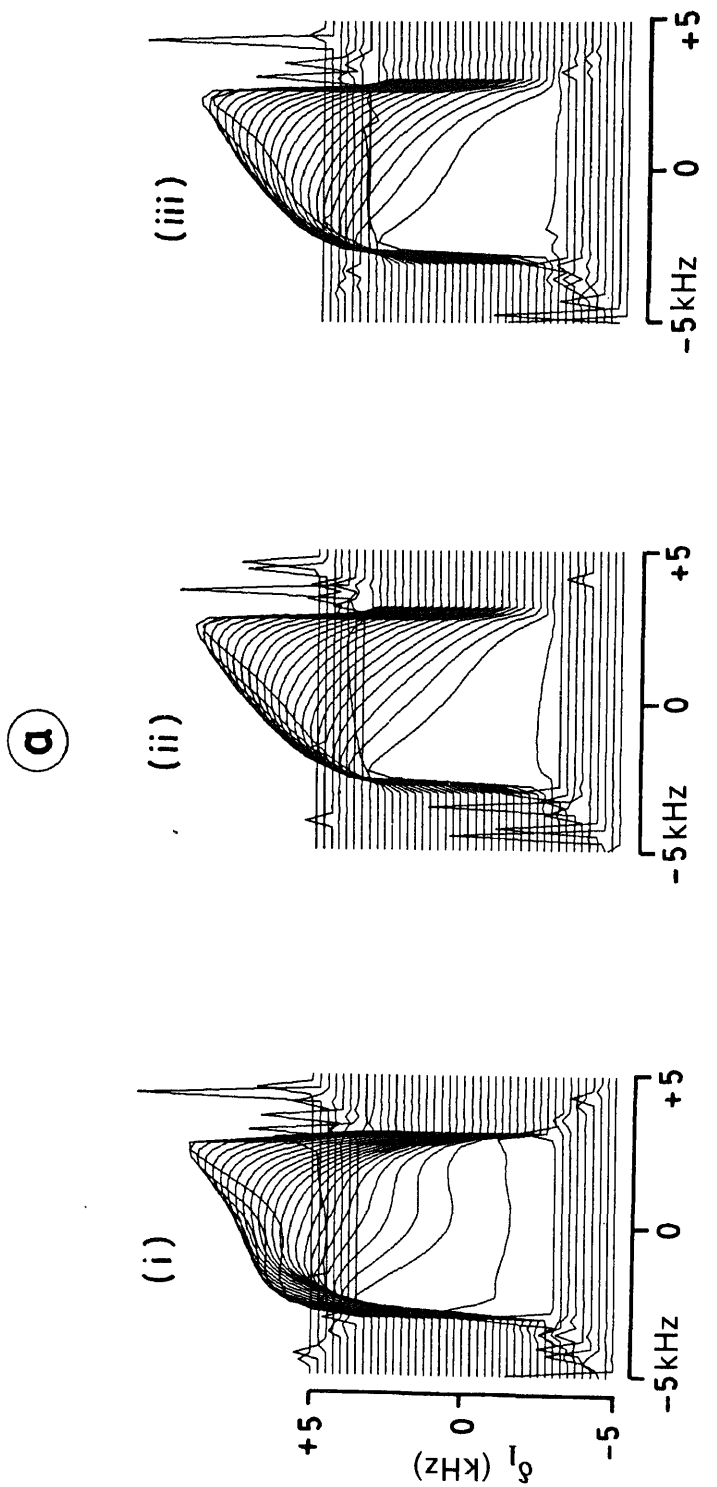

Figure 1(a). The theoretical assessment of the performance of NOIS-1 sequence. The two dimensional maps of local offset quality factor (i) $\langle I_{kx} \rangle - \langle I_{Ix} \rangle$, (ii) $\langle I_{ky} \rangle - \langle I_{Iy} \rangle$, (iii) $\langle I_{kz} \rangle - \langle I_{Iz} \rangle$ displayed in the form of stacked plots.

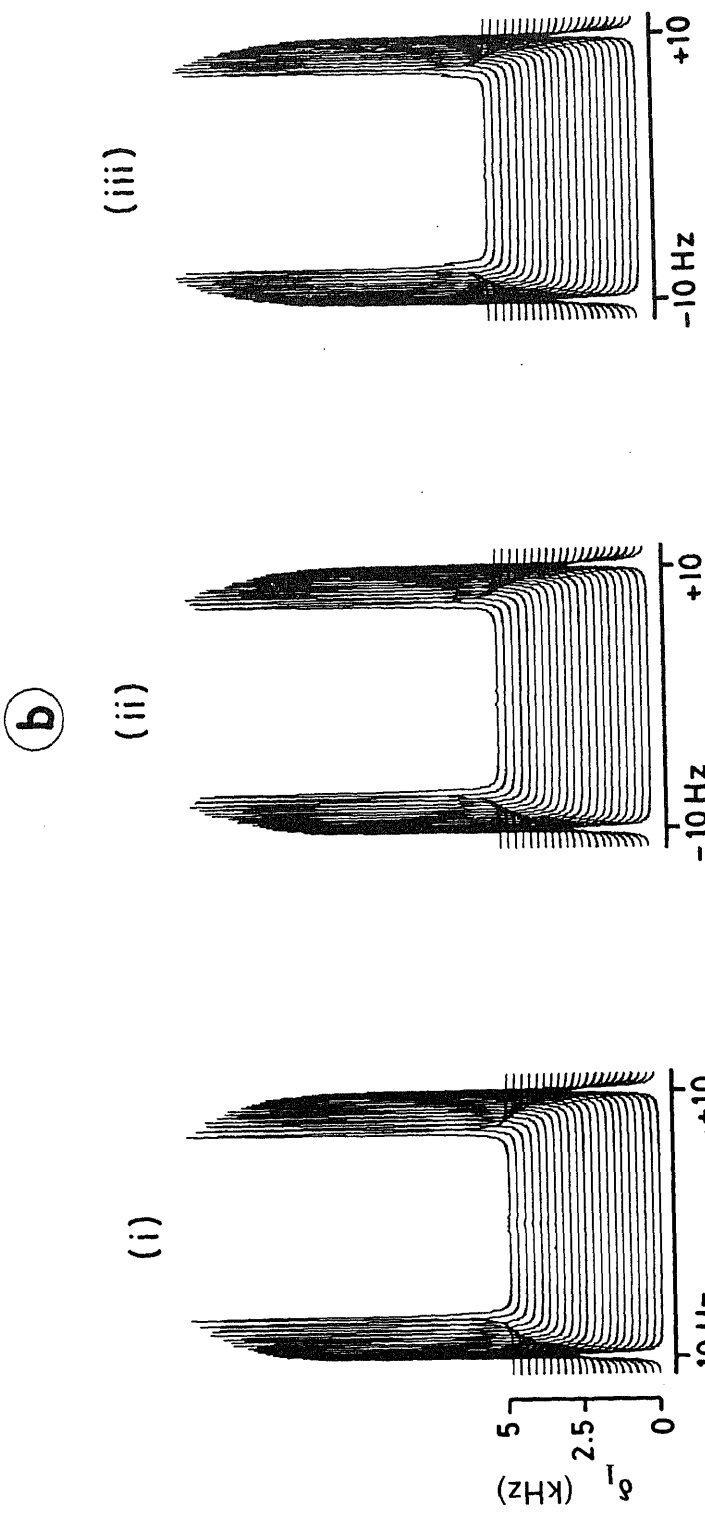

Figure 1(b). The theoretical assessment of the performance of NOIS-1 sequence. The Fourier spectra of the difference magnetization (i) $\langle I_{kx}\rangle - \langle I_{ix}\rangle$, (ii) $\langle I_{ky}\rangle - \langle I_{iy}\rangle$, (iii) $\langle I_{kz}\rangle - \langle I_{iz}\rangle$ as a function of δ_1 offset with $\delta_k = 0$, $J = 10$ Hz, $\omega_1 = 10$ kHz have been used for the generation of the plots (a) and (b).

Drobny [9]. The global quality factors Q_α for the NOIS sequences along with those sequences reported in the literature are presented in table 1. A close comparison of global quality factors of NOIS-1 and NOIS-2 with DIPSI-2 and MLEV-16 clearly shows that our sequences are better. Also our sequences have more uniform transfer efficiency for x, y and z magnetization components. NOIS-2 sequence generated in the present work has also got better quality factors than even the FLOPSY sequence. The two dimensional plots of local quality factors $q_\alpha(\alpha = x, y, z)$ and the Waugh's type of plots have been exemplified in figure 1 for the isotropic mixing sequence NOIS-1. Similar performance has been found for other NOIS sequences generated by us (figures not shown). Clearly, these plots indicate superior performance of NOIS sequences for TOCSY experiments with uniform transfer efficiency for all the three orthogonal magnetization components for a given chemical shift values (δ_k and δ_l). Flip angle errors of $\pm 3\%$ and phase errors of $\pm 5\%$ do not cause appreciable change

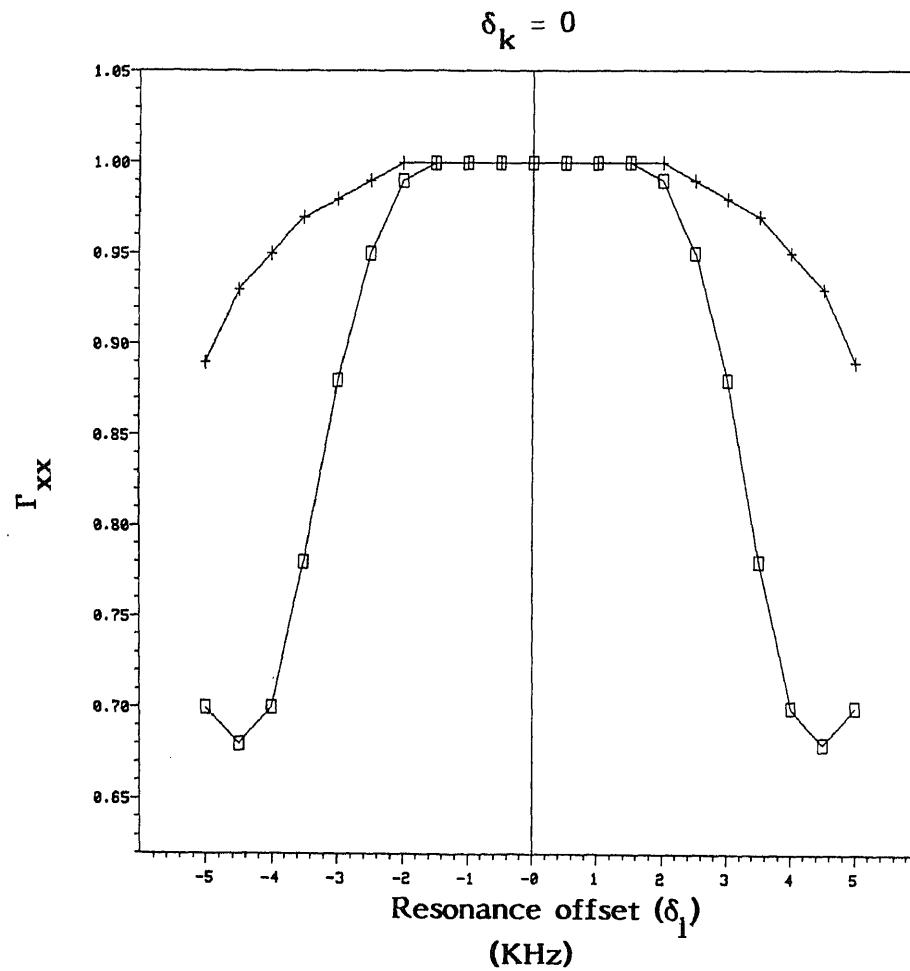

Figure 2. Computed coherence transfer efficiency $\Gamma_{xx}^{(kl)}(\tau_{mix}, \delta_k, \delta_l)$ for mixing sequence MLEV-16 (□) and NOIS-1 (+) as a function of resonance offsets of spin 1 (with $\delta_k = 0$). An RF field strength of 10 kHz and coupling constant, J of 10 Hz are used. A mixing time, τ_{mix} of 1/2 J has been used in the calculation.

in the performance of NOIS sequences. The experimental TOCSY spectra of vancomycin with MLEV-16 and our mixing sequence NOIS-1 (results not presented) are comparable at the H_0 field strengths employed in the experiment (400 MHz for ^{1}H). The real performance of our sequence (NOIS-1) can be expected to be better than MLEV-16 at higher H_0 field strengths, because the global quality factors, for the off-set range of $\pm$ 4 kHz, of our sequence (NOIS-1) are much better than MLEV-16. This is clear from the computed coherence transfer efficiency function $\Gamma_{xx}^{(kl)}$ (eq. 3) for a two spin system, as a function of resonance off-set (δ_1) with NOIS-1 and MLEV-16 sequences (figure 2).

4. Conclusion

New broadband homonuclear isotropic mixing sequences (NOIS) have been designed, by maximizing the coherence transfer efficiency employing numerical optimization procedure. Some of the numerically designed sequences reported in this work have uniform coherence transfer efficiency in all the x, y and z directions. Such sequences are of great use as they can be employed for inducing coherence transfer starting from any component of the spin magnetization. The global quality factors for NOIS-1 and NOIS-2 sequences are superior than the sequences that are routinely used in the literature for isotropic mixing (see table 1).

Global optimization procedures like simulated annealing, genetic algorithms etc can be employed instead of local optimization procedures (eg. Nelder–Mead) to obtain the best possible isotropic mixing sequences. Work in this direction is in progress in our laboratory.

Acknowledgements

We thank Dr R Ramachandran, IMB, Jena, Germany for several useful discussions. NSR thanks CSIR for research fellowship. We thank the referee for his valuable comments.

References

[1] R R Ernst, G Bodenhausen and A Wokaun, *Principles of nuclear magnetic resonance in one and two dimensions* (Clarendon Press, Oxford, 1987)
[2] W P Aue, E Bartholdi and R R Ernst, *J. Chem. Phys.* **64**, 2229 (1976)
[3] K Wuthrich, *NMR of proteins and nucleic acids* (John Wiley and Sons, NY, 1986)
[4] L Braunschweiler and R R Ernst, *J. Magn. Reson.* **53**, 521 (1983)
[5] D G Davis and A Bax, *J. Am. Chem. Soc.* **107**, 2820 (1985)
[6] G Eich, G Bodenhausen and R R Ernst, *J. Am. Chem. Soc.* **104**, 3732 (1982)
[7] R E Klevit and G P Drobny, *Biochemistry* **25**, 7770 (1986)
C Grienger, G Otting, K Wuthrich and R R Ernst, *J. Am. Chem. Soc.* **110**, 7870 (1988)
A Bax, *Methods Enzymol.* **176**, 151 (1989) and references therein
B Celda and G T Montelione, *J. Magn. Reson. Ser.* **B101**, 189 (1993)
Ted T, Sakai, M J Jablonsku, Paul A DeMuth and N Rama Krishna, *Biochemistry* **32**, 5650 (1993)
[8] K Bazzo and J Boyd, *J. Magn. Reson.* **75**, 452 (1987)
N Chandrakumar, *J. Magn. Reson.* **71**, 322 (1987) and the references therein
A Ramamoorthy and N Chandrakumar, *J. Magn. Reson.* **100**, 60 (1992)
J Briand and R R Ernst, *J. Magn. Reson.* **A104**, 54 (1993)

[9] S J Glaser and G P Drobny, *Advances in magnetic resonance*, edited by W S Warren (Academic Press, 1990) Vol. 14, p. 35
[10] M Kadkhodaie, O Rivas, M Tan, A Mohebbi and A J Shaka, *J. Magn. Reson.* **91**, 437 (1991)
[11] U Haeberlen and J S Waugh, *Phys. Rev.* **175**, 453 (1965)
[12] J S Waugh, *J. Magn. Reson.* **68**, 189 (1986)
[13] A J Shaka, C J Lee and A Pines, *J. Magn. Reson.* **77**, 274 (1988)
[14] J A Nelder and R Mead, *Comput. J.* 7, 308 (1964)
[15] M H Levitt, *Prog. Nucl. Magn. Reson. Spectrosc.* **18**, 61 (1986)
[16] D J Lurie, *J. Magn. Reson.* **70**, 11 (1986)

Note added in proof

Recently some new Homo-TOCSY sequences have been designed in the literature [N Sunitha Bai and R Ramachandran, *J. Magn. Reson.* **A105**, 298 (1993)] using a different procedure.

PRAMANA
— journal of
physics

© Printed in India

Vol. 43, No. 1,
July 1994
pp. 101–115

Design and fabrication of a high temperature X-ray powder diffraction camera

MOHD. ATEEQUDDIN, K A HUSSAIN, K G SUBHADRA and
D B SIRDESHMUKH
Department of Physics, Kakatiya University, Warangal 506 009, India

MS received 2 February 1994; revised 16 May 1994

Abstract. A high temperature X-ray powder diffraction camera has been designed and fabricated with indigenous material. The camera design is similar to the Unicam model but overcomes some inconvenient features of the latter. The camera incorporates a miniheater which is inexpensive and easily replaceable. The camera enables determination of lattice parameters with an accuracy of $\pm 0{\cdot}0002$ Å up to 800°C.

Keywords. X-ray powder camera; lattice constants.

PACS Nos 61·10; 65·70

1. Introduction

The lattice constants are basic crystallographic parameters as they define the dimensions of the unit cell. From lattice constants the other crystal parameters like the molar volume, the density and, in simple structures, the ionic radii can be estimated. The variations in lattice constants with temperature and pressure yield values of the thermal expansion coefficient and compressibility respectively. The effects of thermally generated defects, doping and radiation-induced defects can be followed through small but significant changes in the lattice constants. When determined with accuracy, the lattice constant provides rich information about the crystal and is a powerful solid state probe [1].

The lattice constants can be determined with accuracy by employing a combination of well designed cameras and well developed processing of data. For over two decades, several studies have been made in this laboratory using a 11·46 cm Rigaku Denki Debye–Scherrer camera and a laboratory built symmetric focusing camera [2] useful up to about 300°C.

For some problems on hand, like phase transitions, a camera capable of higher resolution and useful at higher temperatures was considered necessary. Designs of various high temperature cameras reviewed by Peiser *et al* [3], Klug and Alexander [4] and Kaelble [5] were examined on a comparative basis. The Unicam cylindrical high temperature camera with its large diameter of 19 cm appeared most suitable. But, this camera is prohibitively expensive. Further, a critical study revealed that it has the following drawbacks.

i) It employs the Bradley–Jay mounting with two film strips. The centre of the ring system is not included on either strip making the use of knife edges unavoidable.

ii) The specimen centering device is not convenient to operate and is not easily accessible. In the original design, the specimen is suspended from above.
iiii) The platinum-wound heater is excellent but its spherical design makes any repair impossible and replacement is, again, too expensive.

As an experiment in indigenous instrumentation, we designed and fabricated a 19 cm cylindrical camera. While this design is essentially similar to the Unicam model, we have overcome some drawbacks observed in it.

2. Design and description of the camera

2.1 *Geometry of the camera*

The principle of a cylindrical camera is shown in figure 1. The film forms a cylinder at the axis of which the powder sample in the form of a thin cylindrical rod is located; for thoroughly random orientation of the crystallites, the specimen is rotated about its own axis. The incident rays enter through a collimator and the direct ray is stopped by a beam stopper. In a back reflection camera, the diffracted rays travel backward (with respect to the incident beam) along a cone of angle 4ϕ.

2.2 *Design of camera*

The design of the camera is quite similar to that of the Unicam camera [5] with certain modifications. The essential parts of the camera are shown in figure 2. These are: the main base (A), the base plate (B), the specimen holder (C), the central brass cylinder (D), the heater (E) (not shown in the figure), the evacuation chamber (F) and the film cassette (G). These are now described in detail.

2.2a *Main base*: The main base (figure 3) is a trapezoidal hollow box of height 9·5 cm with dimensions 28 cm × 20·5 cm and 30 cm × 22 cm at the top and bottom respectively. This box is an aluminium casting provided with levelling screws (1). A hole (2) of diameter 15 cm is cut at the top of the box. There are four columns (3, 4, 5, 6) of 30 mm × 20 mm × 25 mm touching the circumference of the hole. At the top of each column a step is machined for mounting the film holder. A metal bracket (7) is fixed on the front face of the box to hold a microscope for observing the sample alignment. A spirit level is fixed at the top surface for levelling of the camera.

2.2b *Base plate*: The base plate (figure 4) is a stainless steel disc fixed in the hole at the top surface of the main base. There is a small circular hole (1) at the centre of this plate through which a shaft supporting the specimen holder passes down and is coupled to a synchronous motor inside the main base. The shaft is carried on ball bearings and rotates at the rate of 1 rpm. Eight terminals (2 to 9) are connected on

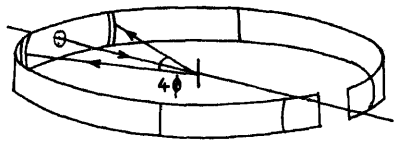

Figure 1. Principle of a cylindrical camera.

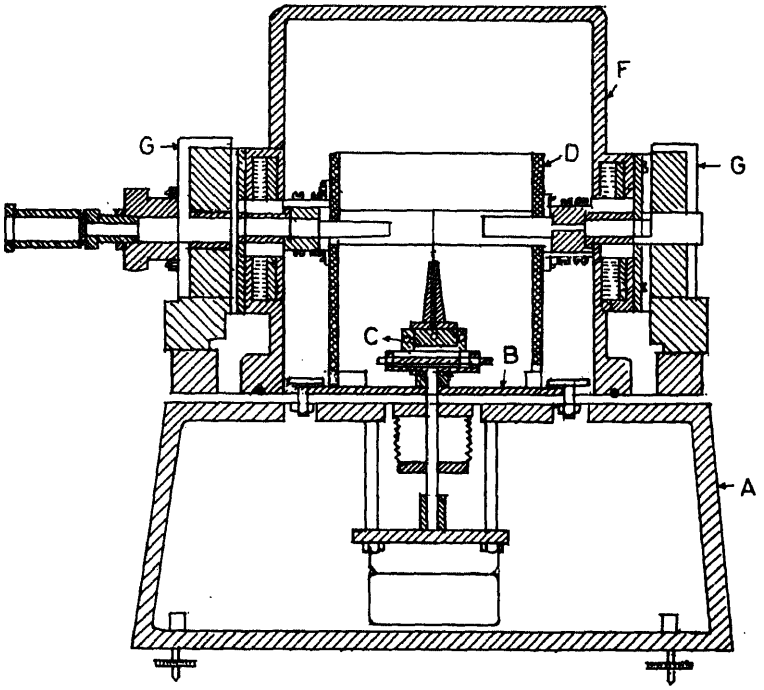

Figure 2. Essential parts of the high temperature powder diffraction camera.

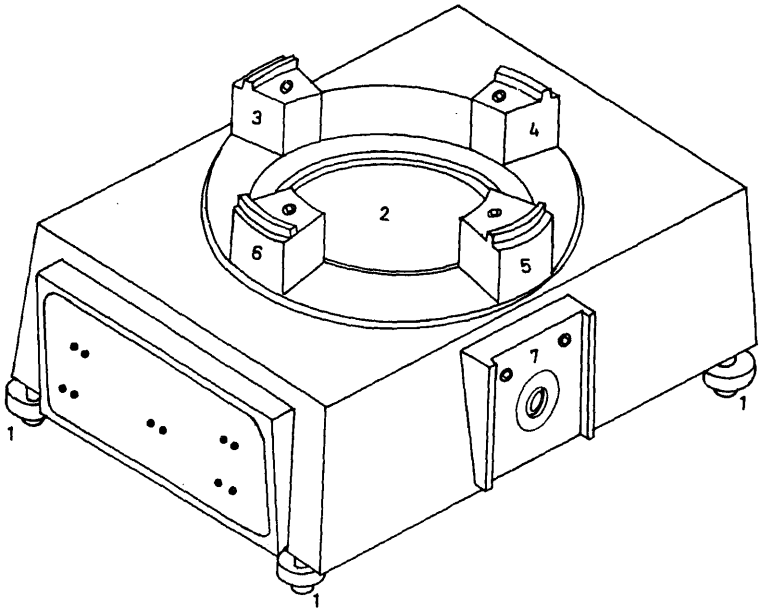

Figure 3. Main base of the camera.

the surface to connect the heater and the thermocouple leads. Teflon rings are fixed between the terminals and the plate for insulation. The terminals and central shaft are made vacuum tight with 'O' rings placed in the connecting screws. A groove (10)

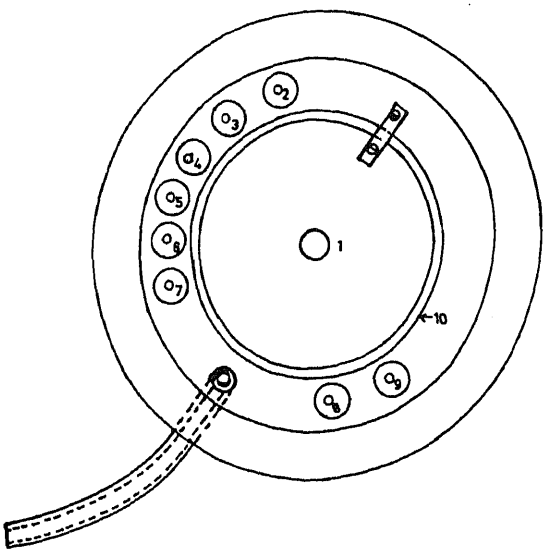

Figure 4. The base plate of the camera.

is machined on the top of the plate to hold the central brass cylinder (figure 2D). A pipe (11) comes out from the lower side of the plate which is connected to a vacuum pump to evacuate the vacuum chamber.

2.2c *Specimen holder*: The centering of the specimen is accomplished by the device shown in figure 5a (top view) and figure 5b (cross section). The specimen is mounted in a cavity drilled in the top portion of a thin brass rod (1) which has a circular base (2). The base is rigidly fixed over a small horizontal table (3) which is fixed in a slot by means of a screw (4) with stoppers at the ends. To obtain transverse motion of table (3) another similar table (5) is fixed below (3). Table (5) is fixed with screw (6). The two screws (4) and (6) are at right angles to each other and enable the specimen to be moved linearly. A brass bush is fixed at the bottom of the lower table (5). The entire arrangement is mounted on a shaft with a provision to lock it on to the shaft or to release it. The sample filled in a thin capillary tube is fixed in the cavity of rod (1), using dental cement. Centering of the specimen is checked by viewing it through a microscope fixed to the main base. The sample holder is released from the shaft and rotated to bring screw (4) to the right of the viewer. If the sample does not coincide with the vertical cross wire in the microscope, screw (4) is manipulated suitably. The sample holder is then rotated through a right angle such that screw (6) is on the right and the specimen is again centred using screw (6). This process is repeated until no displacement is observed from the axis of rotation. The specimen holder is now locked on to the shaft. The other end of the shaft connects with the spindle of a 1 rpm motor. When the film cassette is in position, the sample may be observed by its shadow on the fluorescent screen of the beam stop.

2.2d *Central brass cylinder*: The central brass cylinder (top view figure 6a, side view figure 6b) consists of two short cylinders (1) and (2) connected by two blocks (3) and (4). A gap of 1·2 cm is provided between (1) and (2) for the passage of diffracted X-rays. A hole of diameter 6 mm is drilled in each block to allow the passage of the main

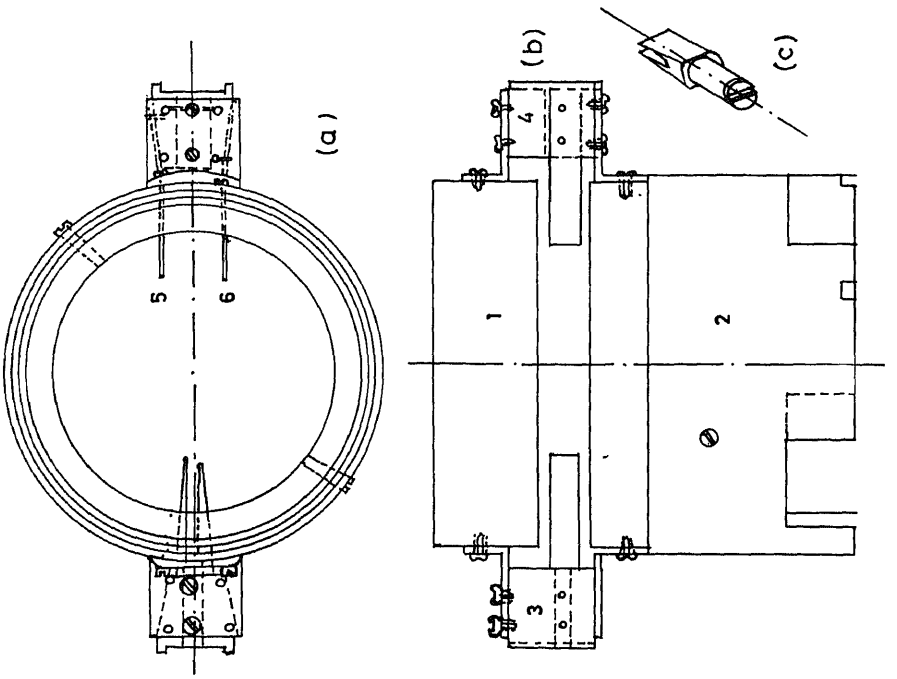

Figure 6 The central brass cylinder. (**a**) top view, (**b**) side view and (**c**) collimator.

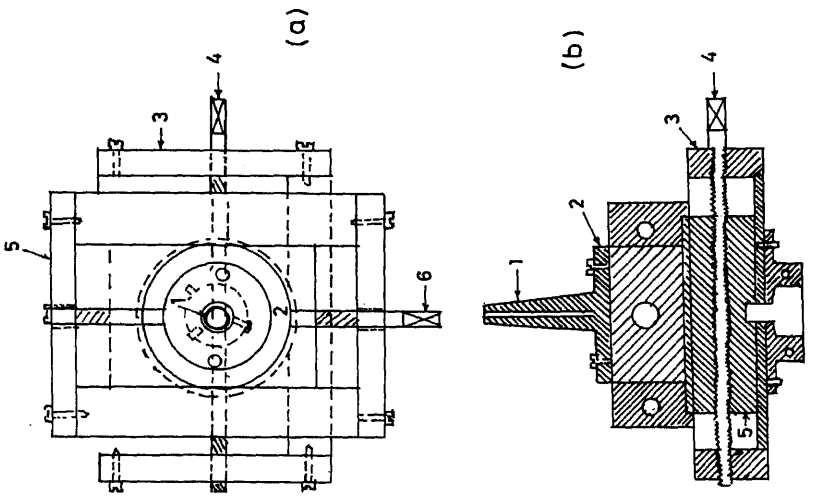

Figure 5. The specimen centering device. (**a**) top view, (**b**) cross section.

beam. A collimator (figure 6c) is fixed in the hole drilled in (3). The collimator is a separate unit with a rectangular aperture which can be easily detached from the supporting block (3). The cylinder is placed on the base plate such that it exactly fits into a groove machined in it. The cylinder is brought into correct position with the help of a guide fixed in the groove. A slot is provided in each of the blocks (3, 4) which serve as guides for the correct positioning of the steel chamber (to be discussed below). Two metal strips (5, 6) are connected to block (4) to minimize the scattering of X-rays which are reflected after striking the block (4).

2.2e *Heater*: The high temperature diffraction problems demand the fabrication of a suitable heating unit. The chief requirements of high temperature operation are the temperature stability over a period of 6 to 10 hours and the measurement of specimen temperature. Several different sets of electric resistance heaters were designed and fabricated and trial-tested for our requirements. The design finally chosen is shown in figure 7.

A hollow brass tube (1) of length 6 cm and diameter 1·5 cm with a slot (2) and a hole (3) at the centre is brazed at its top to a circular disc (4). The slot is of width 10 mm extending around the tube over an angle of 220° and is at right angles to the axis of the tube. The hole permits the incident X-ray beam to strike the specimen and the slot allows the diffracted beam to pass out to the film. A refractory hollow tube (5) of thickness 1 cm with a similar slot and hole is compounded with the brass tube. The refractory tube snugly fits over the brass tube. The refractory tube has linear holes all round through which a coiled super-kanthal wire (7) is passed. A thin circular asbestos plate (8) with a central hole of diameter 2 cm is fixed on the lower side of the disc (4) to prevent heat losses due to conduction. The lead wires of the coils are brought out to the terminals through a small two-holed ceramic tube (9) fixed in a hole drilled in the brass disc. There is a hole at the centre of the disc

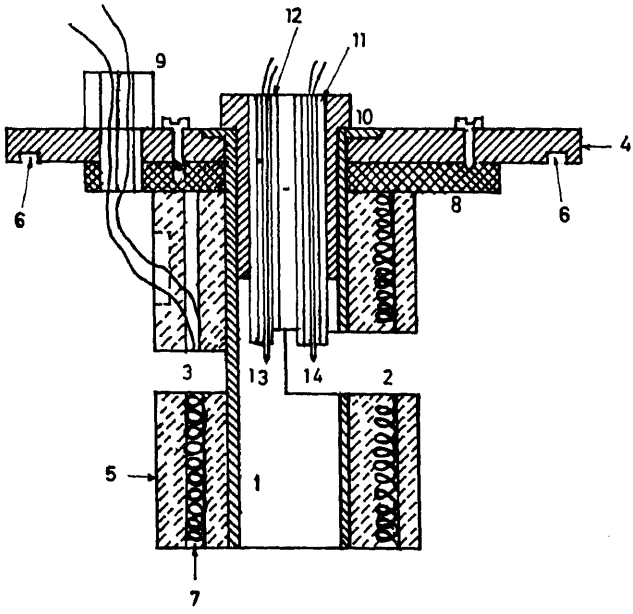

Figure 7. Design of the heater.

through which a brass bush (10) of length 2·7 cm is press-fitted into the brass tube. Two two-holed ceramic tubes (11, 12) are rigidly fixed vertically in the holes drilled at the bottom of the bush. The lower ends of the ceramic tubes just enter into the gap provided for the passage of diffracted X-rays. Chromel-alumel thermocouple wires are passed through the ceramic tubes such that their junctions (13, 14) lie very close to the specimen on either side of the portion of the sample exposed to X-rays.

The entire assembly is inserted in the central brass cylinder. A circular groove (6) is engraved in the disc (4) on the side facing the base of the camera and fits on the top of the central brass cylinder. The disc can be rotated horizontally about the axis of rotation of the sample holder and can be fixed such that the incident X-ray beam after passing through the hole in the heater strikes the sample and diffracted X-rays reach the film arranged to receive backward reflection. The heater wire and thermocouple wires outside the heater are passed through ceramic beads. The free ends of the heater and thermocouple wires are connected to the terminals on the base plate (figure 4) of the camera. The thermocouples are connected to two separate millivoltmeters. The heater is fed from an AC supply through a stabilizer and a variac. A temperature of about 800°C can be attained within 20 min. The temperature stability is obtained by adjusting the output of the variac to give a constant voltage. The temperature distribution in the heater was investigated by positioning the thermocouple along the exposed length of the specimen. It was observed that the temperature remains fairly steady along the length of the specimen exposed to X-rays. The temperature recorded by the two thermocouples always agreed within 0·5°C. The constancy of temperature with time is excellent once the equilibrium is reached. The fluctuation in temperature during exposure was $< \pm 1$°C up to 400°C and $< \pm 2$°C at higher temperatures.

The heater is so designed that it can be lifted in and out of the camera as a single unit during the sample mounting and alignment procedure. Also if the heater element is burnt out it can be replaced easily.

2.2f *Evacuation chamber*: The evacuation chamber (figure 8) is a double-walled stainless steel cylinder 14 cm in height and 13 cm in diameter with inlet (1) and outlet (2) ports for the direct X-ray beam. Two small hollow cylinders (3, 4) of inner diameter 6 mm slightly protruding inside are rigidly fixed at the inlet and outlet ports which exactly fit into the slots provided in the blocks (1) and (2) of the central brass cylinder (figure 5b). The chamber has two slots 15 mm in breadth on the two sides of inlet and outlet ports which permit the passage of diffracted X-rays. These slots are covered by a Mylar sheet. Water channels (5) are provided between two walls for water circulation during the high temperature work. These channels are connected to two tubes (6, 7) which serve as inlet and outlet for the flow of water. The bottom of the chamber is machined, grooved and fitted with neoprene *O* ring (8) to produce an adequate air seal. The chamber can be evacuated by connecting the tube which projects from the lower side of the camera base to an evacuating pump. Rectangular metal strips (9, 10) are fixed over the exit and entry ports with holes for the passage of the X-ray beam. These strips also act as guides for the correct positioning of the film cassette. While the vacuum is optional, the evacuation chamber is an integral part of the camera.

2.2g *Film cassette*: The film cassette (figure 9a) consists of a circular base (1) in the form of a ring carrying a short vertical cylinder (2) of outer diameter 19 cm and inner

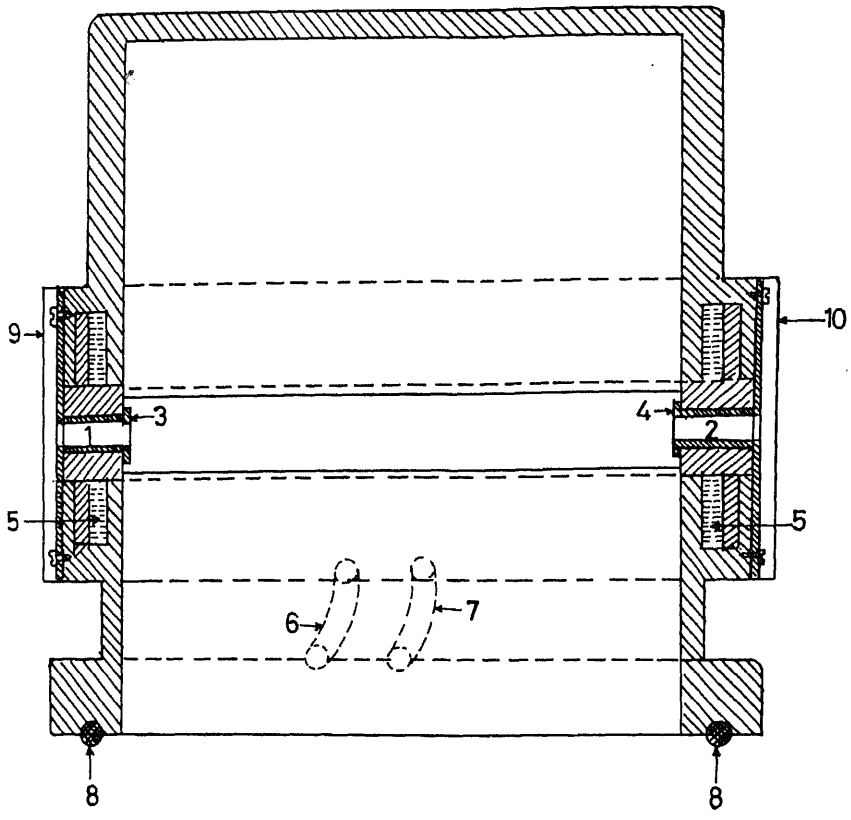

Figure 8. The evacuation chamber.

diameter 17·6 cm with two slots 1·5 cm wide over a Bragg angle range of 5°–85°. A photographic film punched at the centre can be clamped by means of a strap (3) against the outer surface of the cylinder. The free end of the strap is held in clip (4). The inside of the film holder is covered with black paper to prevent exposure of the film. The cover (figure 9b) is brought into correct position with the help of a projection in the groove which fits into a gap (5) at the bottom edge. On the outside of the cover a slit (6) of adjustable width is fixed which limits the width of the incident X-ray beam. The slit system consists of a curved brass strip which extends over about 3·5 cm of the circumference of the cassette cover. A tube (7) is fixed on the cover opposite to the slit into which a beam—stop with lead glass and fluorescent screen can be inserted. The cassette is brought into the correct position using guides provided at the exit and entry ports of the evacuation chamber. The base of the cassette has a step of 5 mm × 5 mm which fits exactly into the steps provided on the four columns of the main base. The cassette is entirely independent of the vacuum chamber and may be removed and reloaded without disturbing the vacuum condition, water cooling and orientation of the specimen.

Unlike the Unicam camera which employs Bradley–Jay film mounting, Van Arkel type of mounting is employed in this camera. With this mounting, both sides of the ring system are recorded and the ring diameters can be measured without the need for knife-edge or any other calibration.

A photograph of the camera in the assembled form is shown in figure 10.

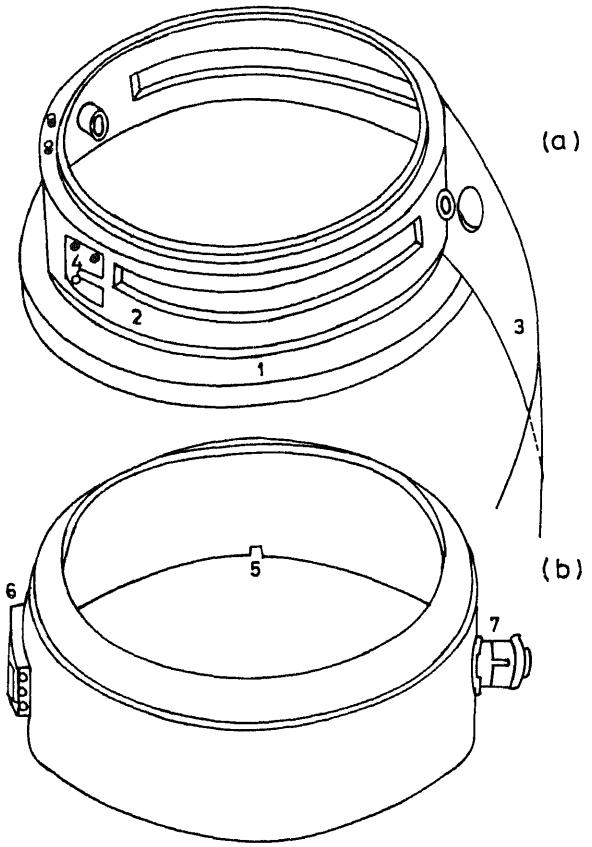

Figure 9. The film cassette (**a**) and the cassette cover (**b**).

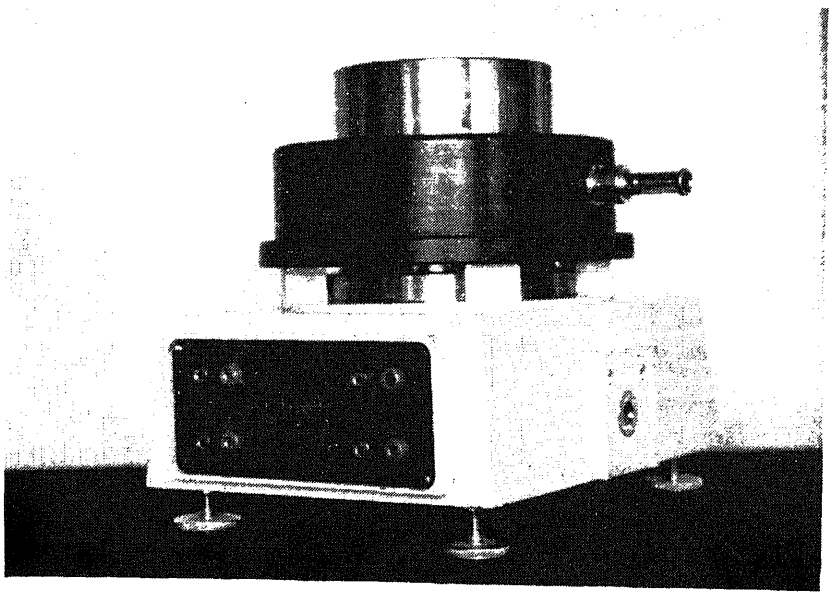

Figure 10. Photograph of the assembled high temperature camera.

3. Standardization

3.1 *Accurate determination of lattice constants*

The Bragg angle θ is obtained from the relations

$$\theta = ((\pi/2) - \phi); \quad \phi = (S/4R) \tag{1}$$

where S is the diameter of a ring in the back reflection region and R the camera radius. For simplicity, we shall consider a cubic crystal. The lattice constant is calculated for each reflection using the relation:

$$a = \frac{(\lambda/2)(h^2 + k^2 + l^2)^{1/2}}{\sin\theta} \tag{2}$$

where h, k and l are the Miller indices and λ is the wavelength of the X-radiation. Filtered Cu radiation was employed. The wavelengths used for calculating lattice constants are

$$\lambda_{k\alpha_1} = 1{\cdot}54050\,\text{A} \quad \text{and}$$

$$\lambda_{k\alpha_2} = 1{\cdot}54434\,\text{A}.$$

The lattice constant values are affected by systematic as well as random errors. The systematic errors associated with a cylindrical camera have been discussed by Peiser *et al* [3]. Klug and Alexander [4] and Kaelble [5]. The main sources of error are (i) sample eccentricity (ii) error in camera radius and film shrinkage and (iii) absorption. Nelson and Riley [6] and Taylor and Sinclair [7] have independently shown that the total error $f(\theta)$ due to these sources is given by

$$f(\theta) = (1/2)[(\cos^2\theta/\sin\theta) + (\cos^2\theta/\theta)] \tag{3}$$

$f(\theta)$ is called the error function. The values of the lattice constant obtained from (2) for different reflections are plotted against the error function $f(\theta)$. The linear plot obtained is extrapolated to $f(\theta) = 0$. The intercept gives the value of the accurate lattice constant.

Random errors are minimized by measuring the ring diameters repeatedly and independently and taking their mean value. Even after this, random errors persist and show up in the form of scattering of data points on the extrapolation plot. The random errors are further minimized by following the least squares procedure for drawing the extrapolation line.

3.2 *Room temperature standardization*

For room temperature standardization of the camera the lattice constants of MgO, PbF_2, CaF_2, CdO, NaCl and Al were determined. Typical X-ray diffraction photographs are shown in figure 11. Typical extrapolation plots obtained by the procedure discussed in § 3.1 are shown in figure 12. The values of the lattice constants obtained in the present experiments are given in table 1. For comparison, values reported by other investigators are also given. Wherever there was a difference in the temperatures of measurement, a correction was applied using thermal expansion data from literature. Agreement is close to the limits of the combined errors.

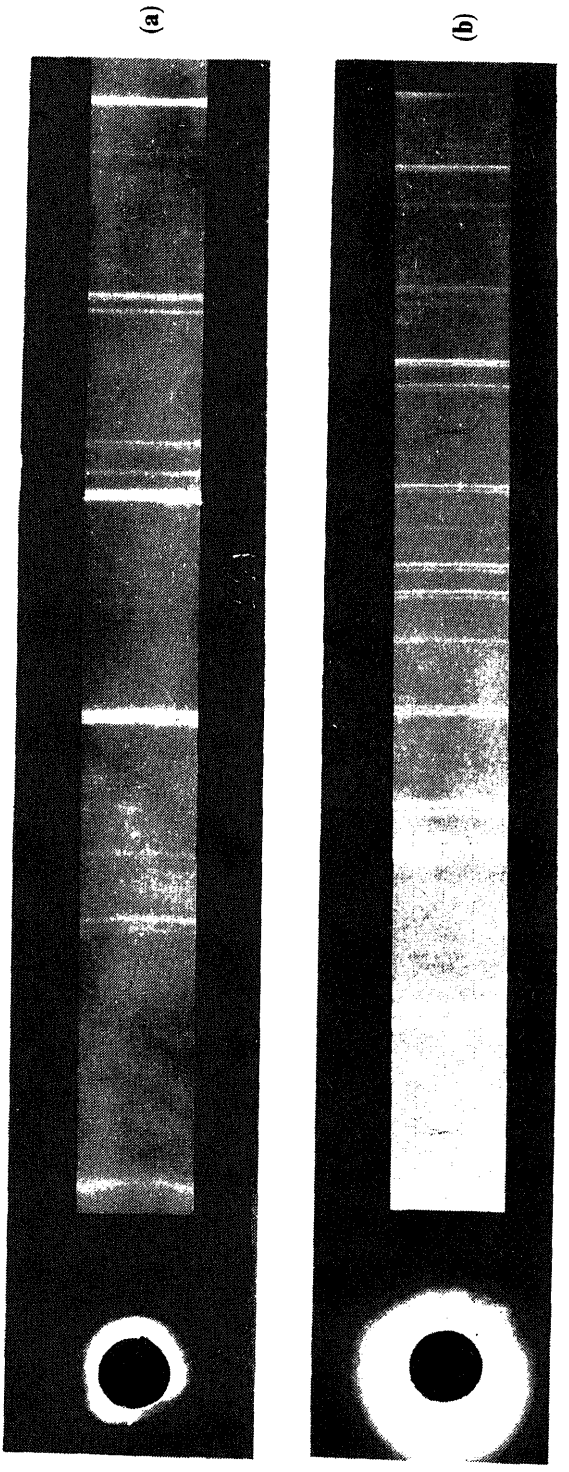

Figure 11. Typical X-ray diffraction photographs. (**a**) MgO, (**b**) PbF_2. Although the camera records both sides of the rings, only one side is reproduced for convenience.

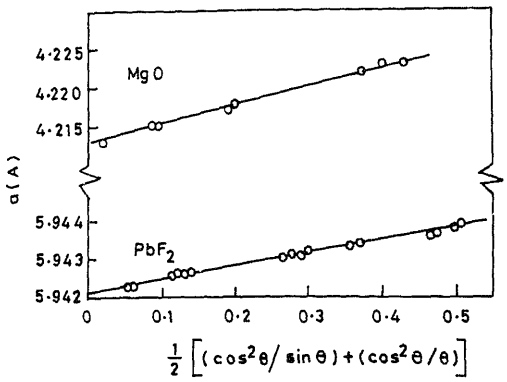

Figure 12. Typical extrapolation plots. (**a**) MgO, (**b**) PbF_2.

Table 1. Room temperature lattice constants.

	Present work		By others	
Substance	*a* (A)	Temp. (°C)	*a* (A)	Reference
MgO	4·2128 ± 0·0002	34	4·2132 ± 0·0001	Merryman [8]
PbF_2	5·9421 ± 0·0002	37	5·9425 ± 0·0002	Palchoudhuri and Bichile [9]
CaF_2	5·4650 ± 0·0002	31	5·4645 ± 0·0002	Sirdeshmukh and Deshpande [10]
CdO	4·6954 ± 0·0003	32	4·69606 ± 0·00002	Swanson *et al* [11]
NaCl	5·6407 ± 0·0004	29·5	5·6410 ± 0·0001	Swanson and Fuyat [12]
Al	4·0504 ± 0·0002	32	4·0503 ± 0·0002	Smakula and Kalnajs [13]

3.3 *High temperature standardization*

For high temperature standardization of the camera, MgO was studied. Photographs of MgO were taken at several elevated temperatures using CuKα radiation. Some of the high temperature photographs are shown in figure 13. The lattice parameters obtained at different temperatures are shown in figure 14 along with the values obtained by Merryman [8] and Dutta [14]. By and large, the value obtained in the three independent investigations are close to a single common curve indicating that the present results are consistent with earlier results.

The above analysis helps us to compare the present high temperature results with those obtained by others using X-ray technique. It is also possible to compare the X-ray results with the results obtained by other techniques by a comparison of the values of the per cent expansion defined as:

$$\% \text{expansion} = \frac{(a_t - a_0)}{a_0} \times 100 \quad \text{(X-ray method)}$$

$$= \frac{(L_t - L_0)}{L_0} \times 100 \quad \text{(other methods)} \qquad (4)$$

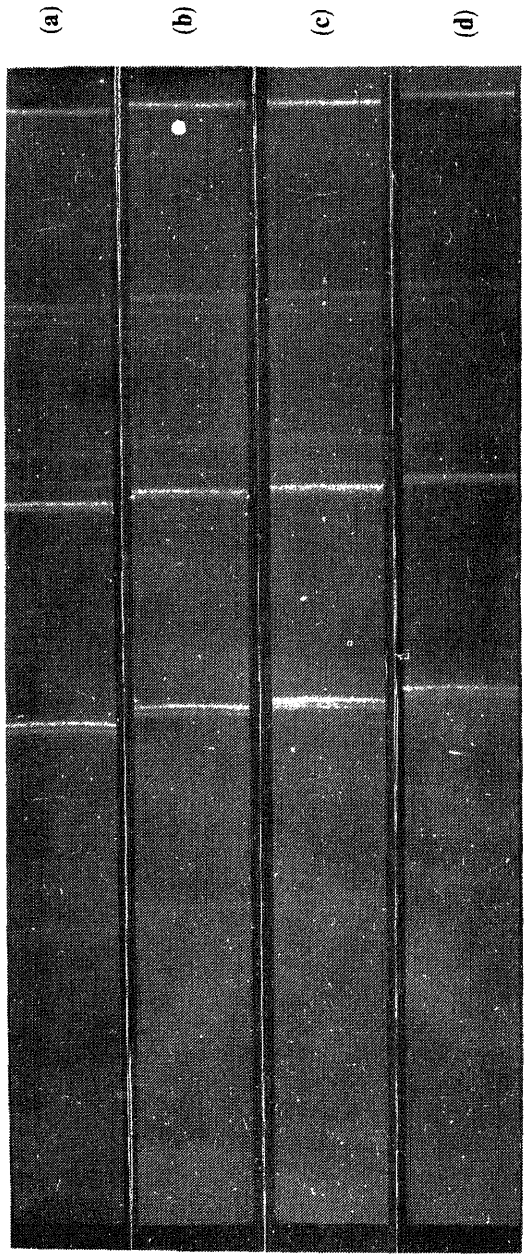

Figure 13. X-ray diffraction photographs of MgO at different temperatures (**a**) 34°C (**b**) 298°C (**c**) 402°C and (**d**) 600°C.

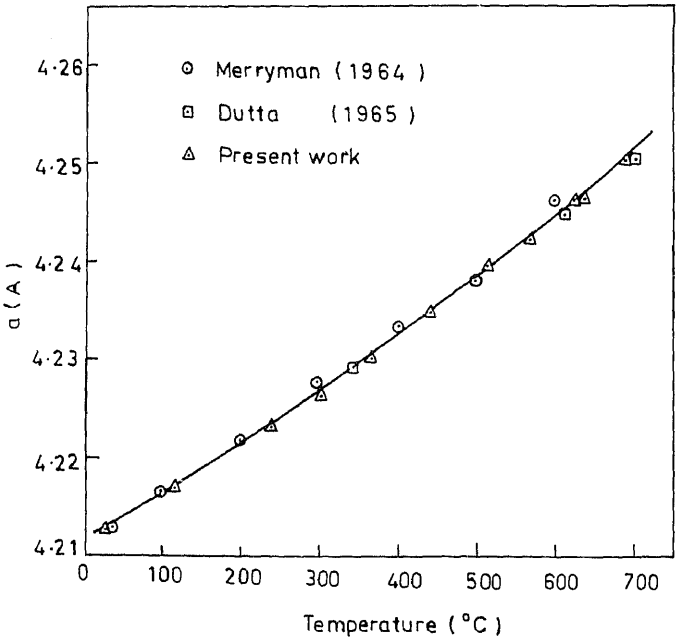

Figure 14. Temperature variation of the lattice parameter of MgO.

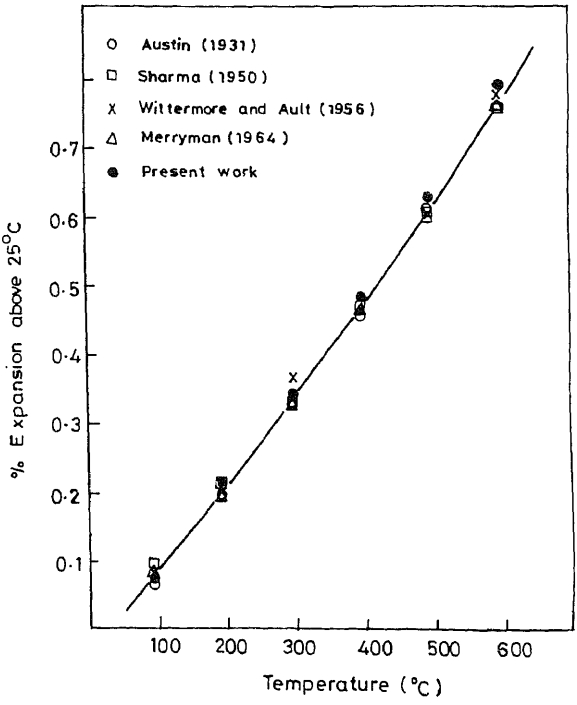

Figure 15. The per cent expansion of MgO.

where a_t and a_0 are the lattice constants at temperature t and a reference temperature and, similarly, L_t and L_0 are lengths of bulk sample at temperature t and at the reference temperature respectively. The per cent expansion values obtained in the present work and from data reported by other workers using different techniques are shown in figure 15. The present results are consistent with those of other workers and all the data points are close to a single smooth curve.

4. Discussion

As this was an experiment in indigenous instrumentation undertaken at an institution with modest facilities, a few aspects related to the actual fabrication are mentioned. With regards to the fabrication aspect, the bulk of the components have cylindrical geometry and good turning facility was required. A modest workshop with foundry and a medium capacity lathe was entrusted with the work. The actual fabrication took a little more than a year and costed Rs. 50,000/- whereas the imported camera will cost 5–6 times higher. In the commissioning stage, certain defects and drawbacks were observed, which had to be rectified. Nearly eighty films were recorded to make sure that these defects were rectified. Thus, commissioning and standardization took another one year.

Acknowledgements

This contribution (No. 96) is dedicated to the memory of (late) Prof. V T Deshpande. Thanks are due to the Council of Scientific and Industrial Research for the sanction of a research project. The authors place on record the contribution of Shri Narasimha Reddy of Pushpa Scientific Works in the efficient fabrication of the camera as per the design provided.

References

[1] D B Sirdeshmukh, *Proc. Third Natl. Seminar on crystal growth* (Anna University, Madras, 1987)
[2] D B Sirdeshmukh and V T Deshpande, *Proc. Indian Natl. Sci. Acad.* **A38** 167 (1972)
[3] H S Pieser, H P Rooksby and A J C Wilson, *Diffraction of polycrystalline materials* (Inst. of Phys. London, 1955)
[4] H P Klug and L E Alexander, *X-ray diffraction procedures* (John Wiley, New York, 1954)
[5] E F Kaelble, *Hand book of X-rays* (Mcgraw Hill, New York, 1967)
[6] J B Nelson and D P Riley, *Proc. Phys. Soc. (London)* **57**, 160 (1945)
[7] A Taylor and H Sinclair, *Proc. Phys. Soc. (London)* **57**, 126 (1945)
[8] R G Merryman, Report La-2687 (University of California, Los Alamos, New Mexico, 1964)
[9] S Palchoudhuri and G K Bichile, *J. Mater. Sci. Lett.* **6**, 945 (1987)
[10] D B Sirdeshmukh and V T Deshpande *Indian J. Pure Appl. Phys.* **2**, 405 (1964)
[11] H E Swanson, H F McMurdie, Mc Morris, E H Evans and B Paretzkin, NBS Monograph 25 Section 10 (1972)
[12] H E Swanson and A Fuyat, NBS Circular No. 539 (2) 41 (1953)
[13] A Smakula and J Kalnajs, *Phys. Rev.* **99**, 1737 (1955)
[14] B N Dutta, *J. Sci. Res. (BHU)* **15**, (1964–65)
[15] J B Austin, *J. Am. Chem. Soc.* **14**, 795 (1931)
[16] S S Sharma, *Proc. Indian Acad. Sci.* **32**, 268 (1950)
[17] O J Wittermore Jr and N J Adult, *J. Am. Ceram. Soc.* **39**, 443 (1956)

PRAMANA
— journal of
physics

© Printed in India

Vol. 43, No. 2,
August 1994
pp. 117–128

Stationary anharmonic oscillators in the particle-in-a-box basis: Near-exact results

A K CHANDRA and K BHATTACHARYYA
Department of Chemistry, Burdwan University, Burdwan 713 104, India

MS received 18 April 1994

Abstract. Variational studies employing the basis functions of the quantal particle-in-a-box model are shown to lead to accurate estimates of eigenvalues, various expectation values and eigenfunctions of the stationary anharmonic oscillator problem. Calculations involve both $zx^{2\alpha}$ and $(x^2 + zx^{2\alpha})$-type oscillators, with $\alpha = 2$, 3 and 4, both in weak and strong coupling regime. Apart from its recommendable computational simplicity, convergence of the present recipe has also been demonstrated to be quite fast. Results for the first ten states are reported. A few goodness tests for the approximate wavefunctions and consistency requirements for some properties are also performed.

Keywords. Linear variations; anharmonic oscillators; eigenvalues; eigenfunctions; basis sets.

PACS Nos 03·65; 02·60; 02·70

1. Introduction

Studies on the energy-eigenvalue problem of quantum anharmonic oscillators have become important over decades. Such calculations have relevance to molecular vibrations [1], solid state and statistical physics [2] and nonlinear quantum field theory [3, 4]. Keeping aside the practical significance, strategies of obtaining accurate estimates of eigenvalues, expectation values and wavefunctions of these oscillators have attracted considerable attention recently [5–24], both from mathematical and computational standpoints, and it is here that standard quantum-theoretical methods find extensive use and their efficiencies tested. The primary reason behind a general interest on this simple problem is that the most natural choice of perturbation theory as a candidate of finding approximate but reliable results fails here miserably [4, 7]. This is because of divergence of the corresponding perturbation series that owes its origin to the more singular nature of the perturbing potential. On the other hand, variational calculations usually involve a substantially large number of basis functions and, in most cases, convergence of the process with increasing size of the matrix Hamiltonian is not quite encouraging, especially in the strong-coupling regions and for excited states.

In perturbative approaches, divergent power-series expansions are converted to convergent forms. This is accomplished in various ways, e.g. via continued fractions [5, 6], Pade' approximants [8, 9], etc. Other ways of bypassing the divergence problem, in general, also appeared [10].

Variationally, early works by using harmonic-oscillator bases [11] and the so-called Hill determinantal method [12] were poorly convergent. But, use of scaled bases [13]

has improved the accuracy remarkably. Variants of this scheme are also known [14]. A faster convergent algorithm was next put forward [15, 16] in the Bargmann representation. Other attempts to obtain reliable results include uses of Chebyshev polynomials [17], hypervirial theorems [18] and the coherent-state ansatz [19]. Variation-perturbation approaches [20] were also pursued and some kind of effective Hamiltonian scheme or renormalization is implicit in quite a few works [21–23]. A local energy method involving Wronskians [24] has recently found notable success, however. Bounds to the eigenvalues were reported in some works as well [25, 26].

While the list of works cited above is by no means complete, the intricacies, relevance of quantum-chemical methods and immense interest on this problem are very apparent now. More important, amidst such a wide variety of approaches, a question that still remains pertinent is, whether there exists any simple yet fast-convergent algorithm of obtaining gradually improved approximate solutions to this eigenvalue problem that applies to the entire coupling range. Particularly in a variationl context, such a query becomes very relevant in view of quite a few works. For example, the coupled hypervirial-WKB approach [22], matrix-folding algorithm [23] and the method based on Riccati equation [25] are all unsuitable at large coupling strengths. Moreover, well-known consistency conditions are rarely checked in most studies. Thus, one fails to gain any clear idea about the general quality of the approximate wavefunctions, the more so in small-basis computations.

That the crux of the problem lies in the choice of a suitable basis-set in variational calculations is now transparent from what has been stated above. So, in the present communication, we take the opportunity to put forward a recipe that is (i) simple, (ii) fast-convergent, (iii) applicable to both even and odd states and (iv) works over a wide coupling range with almost equal facility. To this end, a variationl route [27–28] will be chosen by employing the trigonometric bases. These are actually the particle-in-a-box (PB) eigenstates. In a very general context, the Sturm–Liouville problem, we have recently [29] noted their advantages. Pilot calculations to the ground quartic anharmonic oscillator state has also been found to be quite encouraging, though there is neither a Gaussian prefactor nor any imposed coordinate scaling. Here, we like to report a thorough investigation and extend applications to both excited states and higher anharmonicities, including property calculations and a few checks of consistency.

The paper is organized as follows. The scheme is outlined in § 2. Desirable convergence properties are discussed in § 3, with attention to the character of the optimized wavefunction. Computational results are mainly summarized in § 4. Section 5 is reserved for a few goodness tests to emphasize the quality of computed data. Finally, conclusions of this survey are presented in § 6.

2. The method

We consider any 1-dimensional Hamiltonian of the form

$$H = -\nabla^2 + V(x), \tag{1}$$

with $V(x) = V(-x)$, and $V(x) = 0$ at $x = 0$, while $V(x) = \infty$ as $x \to \infty$. Also, here we shall be concerned only with positive semidifinite $V(x)$. The observations below then follow immediately. (i) For a given value of total energy (positive), there should exist classical turning points $\pm L_c$. (ii) In regions $|x| \gg L_c$, the quantal probability density

$[\rho_n(x) = \psi_n^*(x)\psi_n(x)]$ for some nth eigenstate would obey $\rho_n(x) \approx 0$. (iii) In view of the symmetry of the problem, the odd and even states can be treated separately.

Now, we choose the particle-in-a-box (PB) bases. Extending the usual domain $[0, L]$ to $[-L, L]$ by a change of variable, one finds two sets $\{\cos(2k-1)\pi x/2L\}$ and $\{\sin k\pi x/L\}$ of basis functions ($k = 1, 2, 3, \ldots$). These bases are symmetry-adapted. So, if it is ensured that $L \gg L_c$ which may be checked a posteriori, we may well choose the following trial function for even n:

$$\tilde{\psi}_n(N) = \sum_{k=1}^{N} C_{kn} \cos(2k-1)\pi x/2L \quad (-L \leqslant x \leqslant L). \tag{2}$$

For odd n, one would likewise employ

$$\tilde{\psi}_n(N) = \sum_{k=1}^{n} D_{kn} \sin k\pi x/L \quad (-L \leqslant x \leqslant L). \tag{3}$$

In (2) and (3), N refers to the number of bases employed while L appears as a non-linear variational parameter along with the linear ones (viz. the C's and D's). Optimization with respect to $L(L_0)$ is obviously based on the minimum-energy criterion for respective lowest states, $n = 0$ (even) and $n = 1$ (odd). One may further note, although such trial functions vanish for any $|x| \geqslant L$, they should be adequate in view of remark (ii) quoted above.

That there should exist some optimal L_0 is also clear from (2) or (3). This is due to the approach of the average potential energy towards infinity as $L \to \infty$; on the contrary, the average kinetic energy behaves in the same manner as $L \to 0$. Certainly then, a balanced finite estimate of each of these quantities would necessitate some nonzero finite L-value. Notably, L in (2) or (3) appears thus also as a natural scaling parameter.

Here, we concentrate on two cases. The first one $[H_1(\alpha)]$ refers to anharmonic effects on a harmonic oscillator potential:

$$H_1(\alpha) = -\nabla^2 + x^2 + zx^{2\alpha}, \quad \alpha = 2, 3, 4. \tag{4}$$

Pure anharmonic potential, defined by

$$H_2(\alpha) = -\nabla^2 + zx^{2\alpha}, \quad \alpha = 2, 3, 4 \tag{5}$$

is our other choice.

The method is simple to employ. We choose the Hamiltonian, take the appropriate bases from (2) and (3), fix the N-value, construct the Hamiltonian matrix and diagonalize it at a preassigned value of L. Then, in small steps, we change the value of L to find L_0 where the lowest eigenvalue attains a minimum. At this point, the eigenspectrum and properties of interest are recorded. The procedure is repeated by changing N. A major simplicity of the whole endeavour is provided by the integrals involved; these are extremely easy to evaluate.

3. Adequacy of the choice

Basically, the present scheme employs at each stage, i.e. for a given L, a straightforward linear variation. The success of such a strategy is surely dependent on the choice of

Table 1. Convergence of the expansion coefficients $\{C_{k0}\}$ for the H_1 (α)-eigenvalue problem at $L = L_0$ in selected situations ($n = 0, N = 10$).

	C_{k0}	
k	$\alpha = 2, z = 40{,}000$	$\alpha = 4, z = 1$
1	−0·859 461 802	0·934 413 138
2	−0·493 080 486	0·355 774 948
3	−0·134 353 345	−0·006 133 336
4	0·004 500 039	−0·014 402 461
5	0·011 161 056	0·007 074 015
6	0·001 100 014	−0·000 967 240
7	−0·000 439 783	−0·000 407 236
8	−0·000 039 515	0·000 274 333
9	0·000 013 795	−0·000 086 742
10	0·000 000 073	0·000 015 606

Table 2. Behaviour of L_0 as functions of N and z for $\bar{E}_1$ (2).

z	N	L_0/π	N	z	L_0/π
1	4	0·832	10	10	0·797
	6	0·937		100	0·547
	8	1·095		1000	0·374
	10	1·129		10000	0·303
	20	1·370		100000	0·173

the trial bases and it is here that the present recipe possesses an edge over a number of other similar approaches. So, novelty of the choice (2) or (3) as variational trial functions for the problems in hand will now be briefly considered. In this respect, the first important point is, how fast the coefficients (C's or D's) decay as k increases in (2) or (3). Table 1 shows the behaviour in two selected situations. The rate of decay, one may note, is quite fast. Secondly, an extensive search for L_0 may be avoided. This is because, L_0 follows a systematic trend. Table 2 reveals the increase with N and decrease with z of L_0 by considering a specific case. While these changes are expected on physical grounds or intuitively, what table 3 shows concerning variation with α is apparently difficult to comprehend. The decrease of L_0 with increasing α is understandable here. But, this is obeyed only in the small-z regime; for large z, one observes the reverse trend. A close scrutiny on this point is hence necessary.

An explanation emerges on the obvious assumption that L_0 increases with L_c. It becomes then transparent that the potential rises more steeply as α increases, and this is why both L_c and L_0 decrease. When z is large, however, the simple picture breaks down. Primarily, this is because of the asymptotic z-dependence of $E_n(\alpha, z)$ that goes as [8].

$$E_n(\alpha, z) = e_n(\alpha) z^{1/(\alpha+1)} (z \to \infty). \tag{6}$$

Table 3. Variation of L_0/π with α at fixed $N(N = 10)$ for the two systems.

	$H_1(\alpha)$		$H_2(\alpha)$	
α	$z = 1$	$z = 40000$	$z = 1$	$z = 40000$
2	1·1416	0·1872	1·2039	0·1873
3	0·8397	0·2252	0·8470	0·2252
4	0·6980	0·2425	0·6997	0·2425

It then follows from preliminary calculations of turning points, either for $H_1(\alpha)$ or $H_2(\alpha)$, that L_c is required to satisfy at large z

$$L_{c^2} \approx e_0(\alpha)/z^{1/(\alpha+1)}. \tag{7}$$

Now, (7) explains why L_0 increases with α for large values of z.

Two more clarifications are still required. One is, whether $L_0 \gg L_c$ is valid always in the course of the present analysis. This is very easy to check. So, for brevity, these results are not displayed. A positive answer is found in every case. Indeed, had such an inequality not been followed, results would never turn out to be so impressive. Thus, success of the recipe indirectly hints satisfaction of the above starting assumption. Another point that we wish to comment on is, how the numerical optimization of L to third or, at best, fourth decimal place (see, e.g. tables 2 and 3) affects the energy or other properties, in general. A weak dependence in this respect should be computationally convenient. But, here we refrain from a thorough discussion on this aspect. As this question is intimately connected to the quality of the optimized variational function, coverage on this point will be found in § 5.

4. Results

Tables 4 and 5 display the energy-eigenvalues $\bar{E}_n(\alpha)$ for the two classes of potentials (4) and (5). Results are remarkably accurate and comparable with the oft-quoted near-exact values of Ref. [13]. As the accuracy gradually decreases with increasing n, characteristic of linear variations, we report here data up to which agreement with standard [13] results are obtained. In all cases, however, stability to approximately 10 decimal places is always retained though we employ only 20 basis functions. For further accuracy, one only needs to increase the size of the Hamiltonian matrix—a routine numerical job.

Values for properties like $\langle x^2 \rangle$ and $\langle -\nabla^2 \rangle$ are presented in tables 6 and 7. They also agree with literature values, wherever obtained [13]. But, such results are not generally available. So, we have quoted here estimates up to 13 to 14 digits. The efficiency of our simple variational scheme is pretty apparent now. We hope, these results may be important as standard benchmark work.

5. Goodness tests

A few goodness tests are now in order. These would indicate correctness of data displayed in tables 4 to 7. Also, one would find here an opportunity to assess how

Table 4. Computed $\bar{E}_n(\alpha)$ values of anharmonic oscillators $[H_1(\alpha)]$ at $N = 20$.

n	$\alpha = 2$	$\alpha = 3$	$\alpha = 4$
$(z = 1)$			
0	1·392 351 641 530 291 856	1·435 624 619 003 392 316	1·491 019 895 662 205 177
1	4·648 812 704 212 077 536	5·033 395 937 720 266 477	5·368 778 061 748 130 171
2	8·655 049 957 759 309 688	9·966 621 999 718 110 285	10·993 737 335 502 964 04
3	13·156 803 898 049 875 08	15·989 440 787 825 731 07	18·191 100 018 514 932 45
4	18·057 557 436 303 252 90	22·910 180 430 728 544 76	26·743 448 558 041 7
5	23·297 441 451 223 189 09	30·622 590 570 533 258 64	36·509 236 308 241 9
6	28·835 338 459 504 248 87	39·051 906 854 386 110 73	47·393 379 092 02
7	34·640 848 321 111 332 59	48·141 305 571 449 512 35	59·323 544 225 67
8	40·690 386 082 106 446 90	57·845 728 456 325 8	72·241 637 072 8
9	46·965 009 505 675 533 54	68·128 291 836 139	86·099 541 860 5
$(z = 40000)$			
0	36·274 458 133 736 835 47	16·211 718 264 749 243 62	10·238 868 235 479 041 60
1	129·973 351 403 293 737 9	61·407 828 604 359 446 05	39·670 505 945 098 289 20
2	255·017 677 289 573 991 3	128·376 742 015 189 214 9	85·384 995 313 355 091 00
3	398·290 246 956 059 026 2	211·290 344 511 508 045 9	144·492 517 309 256 575 7
4	556·200 474 630 525 35	307·169 772 116 720 73	214·986 131 730 878
5	726·403 686 448 354 09	414·453 587 749 839 37	295·660 523 015 272
6	907·329 749 584 430 3	532·031 545 974 230 4	385·708 384 533 62
7	1097·832 281 319 199	659·065 528 349 994 5	484·514 056 324 43
8	1297·030 657 029 7	794·894 932 499 66	591·584 145 929 7
9	1504·223 045 054 7	938·981 406 361 52	706·511 061 163 9

Table 5. Computed $\bar{E}_n(\alpha)$ values for pure oscillators $[H_2(\alpha)]$ at $N = 20$.

n	$\alpha = 2$	$\alpha = 3$	$\alpha = 4$
$(z = 1)$			
0	1·060 362 090 484 182 900	1·144 802 453 797 052 764	1·225 820 113 800 492 589
1	3·799 673 029 801 394 169	4·338 598 711 513 981 192	4·755 874 413 960 760 520
2	7·455 697 937 986 738 392	9·073 084 560 921 433 861	10·244 946 977 236 870 80
3	11·644 745 511 378 162 02	14·935 169 634 910 736 03	17·343 087 970 585 609 98
4	16·261 826 018 850 225 94	21·714 165 422 196 722 80	25·809 006 751 297 9
5	21·238 372 918 235 940 03	29·299 645 937 401 893 78	35·497 898 805 171 8
6	26·528 471 183 682 518 27	37·613 086 560 895 194 00	46·312 770 495 05
7	32·098 597 710 968 326 86	46·595 211 448 551 772 09	58·179 649 949 71
8	37·923 001 027 033 986 79	56·199 300 852 500 4	71·039 257 676 3
9	43·981 158 097 289 736 50	66·387 281 706 593	84·842 624 592 7
$(z = 40000)$			
0	36·263 873 389·915 441 73	16·189 951 563 977 905 42	10·205 604 674 423 291 48
1	129·946 989 723 931 049 7	61·357 051 395 175 074 53	39·595 184 973 435 355 93
2	254·981 282 792 887 419 8	128·312 792 386 130 299 1	85·294 634 655 606 736 20
3	398·244 694 592 561 819 1	211·215 194 540 335 894 0	144·390 435 161 638 914 9
4	556·146 626 825 504 84	307·084 672 356 835 09	214·873 713 506 492
5	726·342 136 734 665 83	414·359 566 574 035 14	295·538 895 062 724
6	907·260 952 524 099 9	531·929 371 371 311 8	385·578 456 193 11
7	1097·756 600 156 166	658·955 799 721 840 2	484·376 541 711 32
8	1296·948 391 643 0	794·778 134 614 92	591·439 618 295 2
9	1504·134 449 069 7	938·857 941 585 47	706·359 992 287 2

Table 6. Mean square displacements and average kinetic energies for the first ten states of $H_1(\alpha)$ at $N = 20$.

		$\langle x^2 \rangle$		$\langle -\nabla^2 \rangle$	
α	n	$z = 1$	$z = 40000$	$z = 1$	$z = 40000$
2	0	0·305 813 650 718	0·010 583 881 287	0·826 296 544 114	24·179 444 128 73
	1	0·801 250 595 541	0·026 360 242 520	2·832 124 937 628	86·640 114 188 02
	2	1·155 440 519 200	0·036 393 331 691	5·384 886 465 440	169·999 653 749 2
	3	1·467 523 215 391	0·045 551 185 855	8·282 028 193 570	265·511 647 575 4
	4	1·750 939 501 761	0·053 846 632 183	11·454 725 123 62	370·782 367 542 9
	5	2·014 067 745 278	0·061 548 542 567	14·860 271 719 06	484·248 608 118 0
	6	2·261 703 958 855	0·068 795 890 247	18·469 657 653 38	604·863 567 758 6
	7	2·496 957 081 437	0·075 679 993 598	22·261 579 853 60	731·862 960 881 1
	8	2·721 984 850 987	0·082 264 217 733	26·219 595 771 08	864·659 683 287 5
	9	2·938 362 108 797	0·088 594 816 340	30·330 552 300 85	1002·785 831 762
3	0	0·275 058 719 125	0·021 760 150 814	0·939 189 104 690	12·147 908 623 15
	1	0·672 320 074 176	0·050 768 587 541	3·438 886 916 202	46·030 487 159 50
	2	0·882 083 484 881	0·063 946 002 760	7·033 924 757 348	96·250 583 510 01
	3	1·045 462 539 517	0·075 147 043 401	11·469 349 321 11	158·430 184 861 9
	4	1·188 346 123 442	0·085 097 160 029	16·588 462 261 32	230·334 780 507 5
	5	1·316 082 578 838	0·094 018 831 047	22·308 901 638 48	310·793 181 396 9
	6	1·432 555 255 303	0·102 172 450 727	28·572 652 513 14	398·972 573 255 3
	7	1·540 292 104 466	0·109 726 627 310	35·335 833 126 35	494·244 282 948 8
	8	1·640 998 542 235	0·116 796 007 033	42·563 797 071 13	596·112 801 371 2
	9	1·735 889 945 138	0·123 463 001 099	50·228 273 904 52	704·174 323 270 5
4	0	0·253 957 749 812	0·033 241 708 529	1·040 441 266 642	8·171 149 563 27
	1	0·598 857 545 807	0·075 295 431 260	3·935 707 921 914	31·691 227 497 32
	2	0·744 787 196 663	0·090 355 310 117	8·348 117 550 403	68·253 783 064 62
	3	0·845 935 134 230	0·102 079 152 686	14·045 318 934 27	115·532 766 355 79
	4	0·932 834 785 354	0·112 415 736 233	20·835 057 975 23	171·921 455 943 03
	5	1·009 985 263 283	0·121 625 795 626	28·601 397 888 63	236·455 442 934 85
	6	1·079 440 668 553	0·129 926 447 414	37·267 038 872 59	308·488 751 759 53
	7	1·142 863 779 829	0·137 512 924 652	46·773 117 112 73	387·528 737 304 96
	8	1·201 454 698 458	0·144 526 104 338	57·072 436 839 68	473·180 601 086 89
	9	1·256 076 644 509	0·151 067 479 828	68·125 987 501 79	565·118 208 446 54

far the accuracy in estimating L_0 affects the computed data for observables, a question that has been raised towards the end of § 3.

The virial theorem [30] will be considered first. For $H_1(\alpha)$, it states that

$$\langle -\nabla^2 \rangle = \langle x^2 \rangle + \alpha z \langle x^{2\alpha} \rangle, \tag{8}$$

by virtue of which the average energy for any state would satisfy

$$\langle H \rangle = 2\langle x^2 \rangle + (\alpha + 1) z \langle x^{2\alpha} \rangle = E_v. \tag{9}$$

So, if $\bar{E}_n$ refers to the eigenvalue of the matrix problem and E_v is the energy obtained from (9) by computing the relevant moments for state n, we should have

$$|\bar{E}_n(\alpha)/E_v(\alpha) - 1| = 0. \tag{10}$$

Table 7. Mean square displacements and average kinetic energies for the first ten states of $H_2(\alpha)$ at $N = 20$.

		$\langle x^2 \rangle$		$\langle -\nabla^2 \rangle$	
α	n	$z = 1$	$z = 40000$	$z = 1$	$z = 40000$
2	0	0·362 022 648 789	0·010 585 606 467	0·706 908 060 323	24·175 915 593 28
	1	0·901 605 895 820	0·026 363 116 323	2·533 115 353 201	86·631 326 482 62
	2	1·244 714 121 511	0·036 395 661 703	4·970 465 291 991	169·987 521 861 9
	3	1·557 909 193 537	0·045 553 541 164	7·763 163 674 252	265·496 463 061 7
	4	1·841 609 138 552	0·053 848 977 879	10·841 217 345 90	370·764 417 883 7
	5	2·105 010 651 065	0·061 550 884 828	14·158 915 278 82	484·228 091 156 4
	6	2·352 866·384 212	0·068 798 230 431	17·685 647 455 79	604·840 635 015 1
	7	2·588 299 362 716	0·075 682 332 484	21·399 065 140 65	731·837 733 437 0
	8	2·813 476 631 178	0·082 266 555 751	25·282 000 684 69	864·632 261 102 2
	9	3·029 980 037 256	0·088 597 153 750	29·320 772 064 86	1002·756 299 377
3	0	0·307 920 303 733	0·021 773 253 483	0·858 601 840 348	12·142 463 672 98
	1	0·718 220 132 308	0·050 785 832 594	3·253 949 033 635	46·017 788 546 38
	2	0·904 435 592 147	0·063 953 254 035	6·804 813 420 691	96·234 594 289 59
	3	1·062 822 482 158	0·075 152 898 433	11·201 377 226 18	158·411 395 905 3
	4	1·203 529 109 137	0·085 102 359 443	16·285 624 066 65	230·313 504 267 6
	5	1·329 693 376 533	0·094 023 520 345	21·974 734 453 05	310·769 674 930 5
	6	1·444 997 526 013	0·102 176 754 944	28·209 814 920 66	398·947 028 528 5
	7	1·551 825 435 504	0·109 730 628 866	34·946 408 586 41	494·216 849 791 4
	8	1·651 798 079 925	0·116 799 762 347	42·149 475 639 39	596·083 600 961 1
	9	1·746 080 708 075	0·123 466 550 918	49·790 461 279 93	704·143 456 189 0
4	0	0·277 118 934 339	0·033 285 432 315	0·980 656 091 040	8·164 483 739 54
	1	0·627 299 876 815	0·075 346 520 948	3·804 699 531 169	31·676 147 978 75
	2	0·752 344 968 196	0·090 365 992 408	8·195 957 581 785	68·235 707 724 48
	3	0·849 913 091 187	0·102 085 138 058	13·874 470 376 47	115·512 348 129 31
	4	0·935 962 229 723	0·112 420 710 340	20·647 205 401 05	171·898 970 805 21
	5	1·012 635 366 092	0·121 630 108 093	28·398 319 044 14	236·431 116 050 19
	6	1·081 738 316 981	0·129 930 232 371	37·050 216 396 17	308·462 764 954 66
	7	1·144 896 373 375	0·137 516 300 845	46·543 719 959 89	387·501 233 369 27
	8	1·203 282 142 484	0·144 529 158 241	56·831 406 141 69	473·151 694 638 50
	9	1·257 740 403 671	0·151 070 273 055	67·874 099 674 36	565·087 993 833 11

Table 8 shows how far (10) is obeyed in our scheme. We happily note, accuracy to 10 decimal places always persists. This implies, dependence of results on accuracy in L_0 is very feeble, as wanted. Also, it is now clear that if we compute $\langle x^{2\alpha} \rangle$ on the basis of (8) and table 6, results should be correct up to 10 decimal places at least. This is precisely why we have not separately displayed data for the said property. A similar error level is likely when $\langle x^{2\alpha} \rangle$ will be estimated through the virial theorem and table 7 for $H_2(\alpha)$. So, these values also are not tabulated, for brevity.

In the above context, let us finally notice that satisfaction of (8) does not follow directly on the ground that (2) or (3) is ultimately optimally scaled. This assertion [30] is true only when one optimizes the scale parameter analytically. As we have performed a numerical optimization here, which is partial, significance of goodness test via (8) or (9) is still retained.

Another criterion of accuracy of data is provided by (6). Table 9 presents demonstrative calculations in this regard for ground states. With $N = 10$, we already obtain stability

Table 8. Satisfaction of the virial theorem for $H_1(\alpha)$ in the form $|\bar{E}_n(\alpha)/E_v(\alpha) - 1| = 0$. Results refer to the lhs in 20-basis calculations. Values beyond $10^{-14}(\equiv E\text{-}14)$ are considered zero.

	$\alpha = 2$		$\alpha = 3$		$\alpha = 4$	
n	$z = 1$	$z = 40000$	$z = 1$	$z = 40000$	$z = 1$	$z = 40000$
0	0·0	0·0	0·0	0·0	0·0	0·0
1	0·0	0·0	0·0	0·0	0·0	0·0
2	0·0	0·0	6·0 E-13	1·9 E-13	6·3 E-13	1·0 E-13
3	0·0	0·0	1·6 E-14	0·0	2·5 E-13	9·9 E-14
4	0·0	1·0 E-13	2·7 E-12	1·9 E-13	1·4 E-12	1·5 E-12
5	0·0	6·8 E-14	1·1 E-13	0·0	2·5 E-13	1·3 E-13
6	0·0	3·3 E-12	1·0 E-13	1·0 E-13	1·1 E-11	1·4 E-11
7	0·0	1·3 E-12	3·0 E-13	2·3 E-14	2·0 E-12	2·2 E-12
8	0·0	1·6 E-11	8·0 E-13	3·9 E-13	3·6 E-11	4·9 E-11
9	0·0	8·0 E-12	6·4 E-13	2·9 E-13	7·7 E-12	2·3 E-11

Table 9. Convergence of $\bar{E}_0(\alpha)/z^{1/(\alpha+1)}$ towards a constant value for $H_1(\alpha)$ at $N = 10$.

z	$\alpha = 2$	$\alpha = 3$	$\alpha = 4$
10000	1·061	1·148	1·233
20000	1·060 9	1·147	1·231
40000	1·060 7	1·146 3	1·229 8
60000	1·060 60	1·146 1	1·229 2
80000	1·060 56	1·145 89	1·228 85
100000	1·060 53	1·145 78	1·228 59

to 3rd or 4th decimal place. Naturally, results would converge better for $N = 20$. The actual relation

$$E_n(\alpha)/z^{1/(\alpha+1)} = e_n(\alpha) + O(z^{-2/(\alpha+1)}) \quad (z \to \infty), \tag{11}$$

obtained by Symanzik scaling argument [8], also implies that neglected terms are likely to affect 3rd place of decimal or beyond for the region of z considered. So, our results are quite accurate.

While the credibility of energy-eigenvalues is thus justified above, now we shall see whether the average values also obey the asymptotic (large-z) behaviour properly. Noting for $H_1(\alpha)$ that

$$\langle x^{2\alpha} \rangle = \mathrm{d}E_n(\alpha)/\mathrm{d}z, \tag{12}$$

we use (11) to arrive at the following relation

$$z\langle x^{2\alpha} \rangle / E_n(\alpha) = 1/(\alpha + 1) + O(z^{-2/(\alpha+1)}) \quad (z \to \infty). \tag{13}$$

Table 10 shows how well (13) is satisfied. Here, we see betterment for smaller α-value. This is expected. Generally, accuracy decreases as α increases. Of interest is to also

Table 10. Verification of $z\langle x^{2\alpha}\rangle/\bar{E}_n(\alpha) = 1/(1+\alpha)$ at $z = 40000$ with different N for a few even states.

		n		
α	N	0	2	4
2	5	0·333 139	0·334 125	0·370 553
	10	0·333 139	0·333 238	0·333 269
	20	0·333 139	0·333 238	0·333 269
4	5	0·198 703	0·198 290	0·192 076
	10	0·198 701	0·199 577	0·199 789
	20	0·198 701	0·199 577	0·199 791

Table 11. Dependence of $z\langle x^{2\alpha}\rangle/\bar{E}_n(\alpha)$ on n at $\alpha = 3$, $N = 20$, $z = 40000$.

n	$z\langle x^{2\alpha}\rangle/\bar{E}_n(\alpha)$
0	0·249 329
1	0·249 587
2	0·249 751
3	0·249 822
4	0·249 861
5	0·249 887
6	0·249 904
10	0·249 941
15	0·249 960

note that, while results become worse with n for smaller N, a gradual betterment is observed with increasing n at large N. Since small-N data are not dependable because of inherent errors in both $\langle x^{2\alpha}\rangle$ and $\bar{E}_n(\alpha)$, we value the latter part more and presume that results would improve systematically with n for accurate data. This is exactly what a sample calculation in table 11 reveals. Thus, a sort of classicality, i.e. better results for larger n, may be hidden in the present scheme.

6. Final remarks

Summarizing, we have put forward a very simple scheme of obtaining quite accurate results of various anharmonic oscillators. Major advantages of the present endeavour are fast convergence and simplicity. Energies and important average values of the first ten states are reported here for all the anharmonic oscillators usually considered in the literature. These tabulated data satisfy a number of criteria which the 'exact' results should obey, providing additional testimony of the reliability of our computations. Still more accuracy may be gained just by increasing N.

Only anharmonic oscillators are chosen here as examples. But, our recipe is likely to be equally efficient in solving any bound-state 1-dimensional polynomial potential problem which may correspond to physically relevant situations, e.g. double wells. Here lies its generality. Further work along this direction is in progress.

Acknowledgements

Financial assistance of CSIR, India, is gratefully acknowledged. One of us (AKC) is also thankful to CSIR for providing a research associateship.

References

[1] G Herzberg, *Molecular spectra and molecular structure* (Van Nostrand Reinhold, NY, 1950) **Vol 1**
[2] C Kittel, *Introduction to solid state physics* (Wiley, NY, 1986)
R K Pathria, *Statistical mechanics* (Pergamon, Oxford, 1986)
[3] C M Bender and T T Wu, *Phys. Rev. Lett.* **21** 406 (1968)
S J Chang, *Phys. Rev.* **D12**, 1071 (1975)
C Itzykson and J B Zuber, *Quantum field theory* (McGraw-Hill, NY, 1980)
[4] F J Dyson, *Phys. Rev.* **85**, 631 (1952)
[5] C E Reid, *Int. J. Quantum Chem.* **1**, 521 (1967)
[6] J Cizek and E R Vrscay, *Phys. Rev.* **A30**, 1550 (1984)
[7] C M Bender and T T Wu, *Phys. Rev.* **184** 1231 (1969)
[8] B Simon, *Ann. Phys. (NY)* **58**, 79 (1970)
B Simon, *Int. J. Quantum Chem.* **21**, 3 (1982)
[9] S Graffi and V Grecchi, *J. Math. Phys.* **19**, 1002 (1978)
K Bhattacharyya, *Phys. Rev.* **A39**, 6124 (1989)
A K Chandra and K Bhattacharyya, *Int. J. Quantum Chem.* **45**, 251 (1993)
[10] R Seznec and J Zinn-Justin, *J. Math. Phys.* **20**, 1398 (1979)
I G Halliday and P Suranyi, *Phys. Rev.* **D21**, 1529 (1980)
J E Drummond, *J. Phys.* **A14**, 1651 (1981)
G A Arteca, F M Fernandez and E A Castro, *J. Math. Phys.* **25**, 2377, 3492, (1984)
E J Weniger, J Cizek and F Vinette, *Phys. Lett.* **A156**, 169 (1991)
E J Weniger, J Cizek and F Vinette, *J. Math. Phys.* **34**, 571 (1993)
[11] C E Reid, *J. Mol. Spectrosc.* **36**, 183 (1970)
[12] S N Biswas, K Datta, R P Saxena, P K Srivastava and V S Varma, *Phys. Rev.* **D4**, 3617 (1971)
S N Biswas, K Datta, R P Saxena, P K Srivastava and V S Varma, *J. Math. Phys.* **14**, 1190 (1973)
[13] K Banerjee, S P Bhatnagar, V Choudhry and S S Kanwal, *Proc. R. Soc. London* **A360**, 575 (1978)
K Banerjee, *Proc. R. Soc. London* **364**, 265 (1978)
K Banerjee, *Proc. R. Soc. London* **368**, 155 (1979)
[14] J Killingbeck, *Phys. Lett.* **A84**, 95 (1981)
K Banerjee and J K Bhattacharyya, *Phys. Rev.* **D29**, 1111 (1984)
R N Chaudhuri and M Mondal, *Phys. Rev.* **A40**, 6080 (1989)
R N Chaudhuri and M Mondal, *Pramana – J. Phys.* **37**, 13 (1991)
[15] F T Hioe and E W Montroll, *J. Math. Phys.* **16**, 1945 (1975)
[16] F T Hioe, D MacMillen and E W Montroll, *J. Math. Phys.* **17**, 1320 (1976)
F T Hioe, D MacMillen and E W Montroll, *Phys. Rep.* **43**, 305 (1978)
[17] J P Boyd, *J. Math. Phys.* **19**, 1445 (1978)
[18] R J Swenson and S H Danforth, *J. Chem. Phys.* **57**, 1734 (1972)
K Banerjee, *Phys. Lett.* **A63**, 223 (1977)
J Killingbeck, *Phys. Lett.* **A65**, 87 (1978)
J L Richardson and R Blakenbecler, *Phys. Rev.* **D19**, 496 (1979)
C S Lai and M P Madan, *Mol. Phys.* **54**, 669 (1985)
S Srivastava and Vishwamitter, *Mol. Phys.* **72**, 1285 (1991)
S Srivastava and Vishwamitter, *Chem. Phys. Lett.* **176**, 266 (1991)
[19] C-S Hsue and J L Chern, *Phys. Rev.* **D29**, 643 (1984)
P K Patnaik, *Phys. Rev.* **33**, 3145 (1986)

[20] K Schonhammer and L S Cederbaum, *Phys. Lett.* **A51**, 325 (1975)
J Killingbeck, *Phys. Lett.* **62**, 285 (1977)
[21] J Killingbeck, *J. Phys.* **A14**, 1005 (1981)
L Friedlander, *J. Math. Phys.* **26**, 961 (1985)
S C Chhajlany, D A Letov and V N Malnev, *J. Phys.* **A24**, 2731 (1991)
[22] J Killingbeck, *J Phys.* **A20**, 601 (1987)
[23] J Killingbeck and G Jolicard, *Phys. Lett.* **A166**, 159 (1992)
[24] H Taseli and M Demiralp, *J. Phys.* **A21**, 3903 (1988)
[25] F M Fernandez, Q Ma and R H Tipping, *Phys. Rev.* **A39**, 1605 (1989)
[26] F Vinette and J Cizek, *J. Math. Phys.* **32**, 3392 (1991)
[27] J K L Macdonald, *Phys. Rev.* **43**, 830 (1933)
[28] S T Epstein, *The Variation method in quantum chemistry* (Academic, NY, 1974)
[29] R K Pathak, A K Chandra and K Bhattacharyya, *Phys. Rev.* **A48**, 4097 (1993)
[30] See, e.g., P O Lowdin, *J. Mol. Spectrosc.* **3**, 46 (1959) and refs. therein

PRAMANA
— journal of
physics

© Printed in India

Vol. 43, No. 2,
August 1994
pp. 129–137

First-order transition in a 2D classical XY-model using microcanonical Monte Carlo simulations

SMITA OTA and S B OTA
Institute of Physics, Sachivalaya Marg, Bhubaneswar 751 005, India

MS received 30 December 1993; revised 12 April 1994

Abstract. We have simulated two-dimensional classical XY-model in a microcanonical ensemble using the Monte Carlo technique. Simulations were carried out on a square lattice having 25, 100 or 900-spins with periodic boundary conditions. The nearest neighbour interaction potential was taken to be $V(\theta) = 2J[1 - \cos^{100}(\theta/2)]$. The system energy, mean square magnetization and vortex-density were calculated as functions of temperature. A sudden change in the system energy, vortex density and mean square magnetization was observed at the first-order transition which is associated with this choice of the nearest neighbour interaction potential. The transition temperature increases with decrease in the system size. It is found that the creation of a vortex-antivortex pair costs more energy during the first-order transition than the energy associated with a tightly bound vortex-antivortex pair.

Keywords. XY-model; microcanonical Monte Carlo.

PACS Nos 05·20; 75·10; 64·60; 05·40

1. Introduction

Computer experiments have become one of the most powerful branches in statistical physics to study model spin systems [1]. The usual Monte Carlo method of computer simulation is based on the Metropolis technique [2] which operates in a canonical ensemble. Here the temperature is used as the input parameter and other physical variables are obtained as outputs of the simulations. The stochasticity of the technique gives rise to the ergodicity of the process under investigation. Creutz [3] developed a parallel Monte Carlo technique which operates in a microcanonical ensemble. This technique found application in a number of ways in different fields of physics immediately after its formulation. The full potential of this simulation method is still being explored. In this technique, an extra degree of freedom called the demon (after Maxwell's demon) moves around the system transferring energy as it changes the microstates. This technique is deterministic in principle. The system complexity is expected to give rise to ergodicity. Some amount of randomness is generally incorporated in the simulation procedure, which also helps in achieving ergodicity [4]. Ergodicity of the technique is demonstrated for Ising model [4] by comparing the results of the simulation with the existing canonical Monte Carlo result. Of late, this technique was extended for the simulation of the classical two-dimensional (2D) XY-model [5]. Ergodicity in the case of classical 2D XY-model was achieved with ease because it is more complex a system than the Ising model. Since a rigorous proof is lacking, the ergodicity was demonstrated for the classical 2D XY-model [5] from the comparison of results with the canonical Monte Carlo and the Molecular

dynamics simulations results. The algorithm has energy as the input parameter unlike the canonical Monte Carlo simulation method. Since the physical quantities depend on a smoother way on the energy than on the temperature, the selection of energy as the input parameter is a strategic choice for some cases. This situation arises in a first order transition which is associated with a 'sudden jump' of the system energy from one value to another at the transition temperature. Therefore, it is difficult to study the transition region by the canonical Monte Carlo technique where temperature is the input parameter. Whereas the choice of energy as the input parameter in the case of microcanonical Monte Carlo technique makes it possible to study the system at the transition temperature of a first order transition.

Microcanonical Monte Carlo simulation technique was used by Harris [6] to study the first and second order transitions in a discrete Ising-like model. In an attempt to study the first order transition in a spin system with continuous symmetry, we considered the classical 2D XY-model [7]. The classical 2D XY-model is known to undergo a topological transition. Domany *et al* [8] suggested a modification of the nearest neighbour interaction potential in this model. By appropriate choice of parameters in this potential a first-order transition is observed. Several canonical Monte Carlo simulations have been carried out to study the first order transition in this spin model. In this work, we report the study of the first order transition in a 2D classical XY-model with the nearest neighbour interaction potential suggested by Domany *et al* in a microcanonical ensemble. Using this algorithm, we clearly demonstrate the potential of the microcanonical Monte Carlo simulations for the study of the coexistence region in first order transition.

This paper is organized as follows. In § 2, we discuss the Hamiltonian of the classical 2D XY-model. The simulation procedure is outlined in § 3. Section 4 contains the results of the simulation. Finally, the discussion and conclusion are given in § 5.

2. The classical 2D XY-model

The Hamiltonian of the 2D classical XY-model with the spins constrained to lie in a plane is given by

$$H = -J \sum_{\langle i,j \rangle} \cos(\theta_i - \theta_j) \tag{1}$$

where $J > 0$ is the coupling constant and θ_i is the angle made by the spin at site i with respect to some fixed axis in the plane. The sum $\langle i,j \rangle$ is over the nearest neighbours. The absence of long range order, presence of topological defects called the 'vortices' and the Kosterlitz–Thouless (KT) transition are some of the important properties of the XY-model for which it is distinctly different from other 2D classical systems [7, 9–12]. The presence of vortices in the 2D classical XY-model, which was postulated theoretically, has been examined in several computer simulations [13–18]. At low temperatures vortices are observed in the form of bound vortex-antivortex pairs. With increase in temperature the vortex-antivortex pair unbind at the KT transition. However, no specific heat anomaly is observed at the KT transition. Several Monte Carlo and molecular dynamics simulations have been carried out to study the nature of the KT transition [13–20].

There have been investigations on the possibility of a first order transition in the classical 2D XY-model without changing the essential symmetry [21]. Domany *et al*

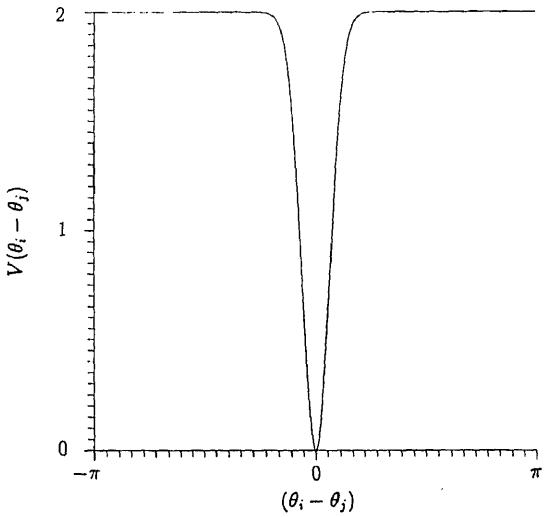

Figure 1. The nearest neighbour interaction potential causing the first order transition as a function of $\theta_i - \theta_j$ for $2p^2 = 100$.

[8] suggested a modified nearest neighbour interaction potential, which is given by:

$$H = 2J \sum_{\langle i,j \rangle} [1 - \cos^{2p^2}((\theta_i - \theta_j)/2)], \quad J > 0, \tag{2}$$

where the notations used have their usual meanings. For $p^2 = 1$ the Hamiltonian reduces to that of the usual classical 2D XY-model. This potential retains the essential symmetry of the 2D XY-model and the potential well can be made narrower by increasing the value of the parameters p^2 (figure 1). Several canonical Monte Carlo simulations have been carried out to study the nature of the transition in this system [8, 22–25]. It is observed that for $p^2 \gtrsim 10$, the transition becomes first order in nature. We have studied this model using the microcanonical Monte Carlo simulation technique [3, 5]. The simulation procedure is described in the following section.

3. The simulation procedure

We consider a 2D square lattice having 25, 100 or 900 spins with periodic boundary conditions. For simplicity and faster computational speed, the continuous θ is discretized. We used 300 discrete states; $\theta_i = 2\pi n/300$, where $n = 1, 2, 3, \ldots, 300$. The microcanonical Monte Carlo simulations were carried out as follows. Initially all the spins are aligned in one direction i.e. all θ_i's $= 2\pi$ with respect to the fixed axis in the plane. An extra degree of freedom called the 'demon' is allowed to move from one spin-site to the other sequentially on the lattice as it exchanges energy with spins changing the microstates. The alignment of the spins in one direction, corresponds to the lowest energy state of the spin-system. The simulation begins with the demon having a fixed amount of energy (E_d). This demon energy when added to the system energy (E_s) corresponds to the energy of the system at the highest desired temperature.

At a particular total system energy ($E_T = E_s + E_d$), the algorithm starts by generating a random integer in the interval $[-150, 150]$, when the demon reaches

a particular site. This corresponds to the change in spin angle θ_i in the range $[-\pi, \pi]$. The change in energy is calculated corresponding to this change in angle. A positive change in energy is allowed if the demon has sufficient amount of energy to effect this change. Otherwise, the old spin state is retained. A negative or zero change in energy is always accepted and the demon recieves this amount of energy from the spin system. The energy of the demon remains positive when it is in equilibrium with the spin system. The demon moves to the next site on the lattice in a sequential manner. The above procedure is repeated till the demon visits all the sites of the lattice. This constitutes one Monte Carlo step per spin (MCSS) of the simulation. The criteria of chosing the random number and accepting the change of configuration as described above satisfies a restricted form of detailed balance [3].

We now mention a few computational advantages of this simulation method. Firstly, the increment in the number of discrete states of the spin angle practically does not increase the computational time more than calling a random number from those many number of discrete states. Secondly, the quality of the random numbers is not the main concern in this case since the ergodicity of the simulation is attained primarily by the system complexity. Finally, the algorithm is computationally simpler and faster than its canonical counterpart (comparing the CPU time per MCSS of the simulation).

The simulation constitutes a cooling run followed by a heating one. At the highest energy state 1×10^5 MCSS (for 900 spin system) were discarded in order to allow for equilibration. The physical variables such as mean square magnetization and vortex density were obtained by averaging the corresponding quantities over 6×10^4 MCSS in 12 blocks (5×10^3 per block). These block averages were taken to calculate the standard deviation of the physical variables which is a measure of the accuracy of the computed quantities. The final spin configuration and the final demon energy was retained and then the system was allowed to cool down to the next lower energy state. This is achieved by removing some energy from the system through the demon. The simulation then proceeds with 4×10^4 MCSS for equilibration and 6×10^4 MCSS for averaging. This way the system is allowed to cool down in steps until the lowest energy state is reached. The final system configuration and the final demon energy straightaway enters the heating run and the physical variables were computed in the manner mentioned before. Then to the final system configuration some amount of energy is added through the demon with the demon having the final energy of the previous run. This way the system is heated back to its highest energy state in steps from which it was cooled. The system goes through the same total energy states $(E_s + E_d)$ in both the cooling and heating runs. The physical quantities computed are an average of the heating and the cooling runs. We present the results obtained from the simulations in the following section.

4. Results

In equilibrium, the energy distribution of E_d follows the Boltzmann distribution function [3]. The system temperature is directly related to the average demon energy $\langle E_d \rangle$:

$$k_B T = \langle E_d \rangle, \tag{3}$$

where k_B is the Boltzmann constant. (Hereafter we replace $k_B T/J$ by T and E/J by

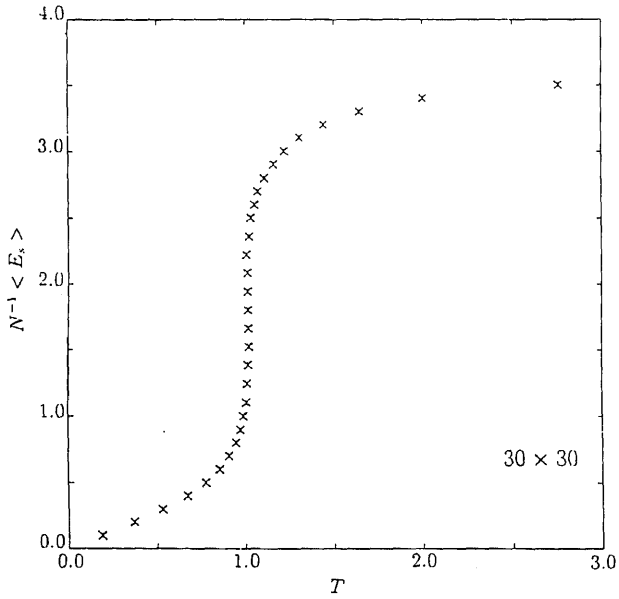

Figure 2. Average system energy per spin as a function of temperature for 900 spin system.

E for simplicity). We note that eq. (3) is valid when E_d takes continuous positive values. Although the change in spin angle is discrete in the present simulations, E_d takes continuous value. We used only the final E_d after each MCSS to calculate the corresponding temperature for the Boltzmann distribution. The average of physical quantities were computed from the corresponding quantities obtained at the end of a MCSS over the total number of MCSS used for the averaging. The results of the cooling run and the heating run did not differ by more than 2 per cent.

The temperature dependence of the system energy (E_s) is displayed in figure 2. The standard deviation of the estimated temperature is less than 0·5 per cent. The linear temperature dependence of E_s seen at low temperatures is due to the spin wave behaviour. The spin wave behaviour is ensured since the nearest neighbour interaction potential can be approximated by $Jp^2\theta^2/2$ near the minimum.

The mean square magnetization per spin is calculated from the following equation:

$$N^{-1}\langle M^2\rangle = N^{-1}\left\langle \left(\sum_{i=1}^{N}\cos\theta_i\right)^2 + \left(\sum_{i=1}^{N}\sin\theta_i\right)^2 \right\rangle, \tag{4}$$

where N is the total number of spins. Figure 3 displays $N^{-1}\langle M^2\rangle$ as a function of temperature. The standard deviation of the calculated $N^{-1}\langle M^2\rangle$ is less than 2 per cent.

The Kosterlitz-Thouless theory defines the vorticity q of a given region as follows

$$q = \frac{1}{2\pi}\oint \mathrm{d}\theta(r). \tag{5}$$

Here the integral is taken round the boundary of that region and $\theta(r)$ is the angle which a spin situated at r makes with the fixed axis. We used a discrete version of

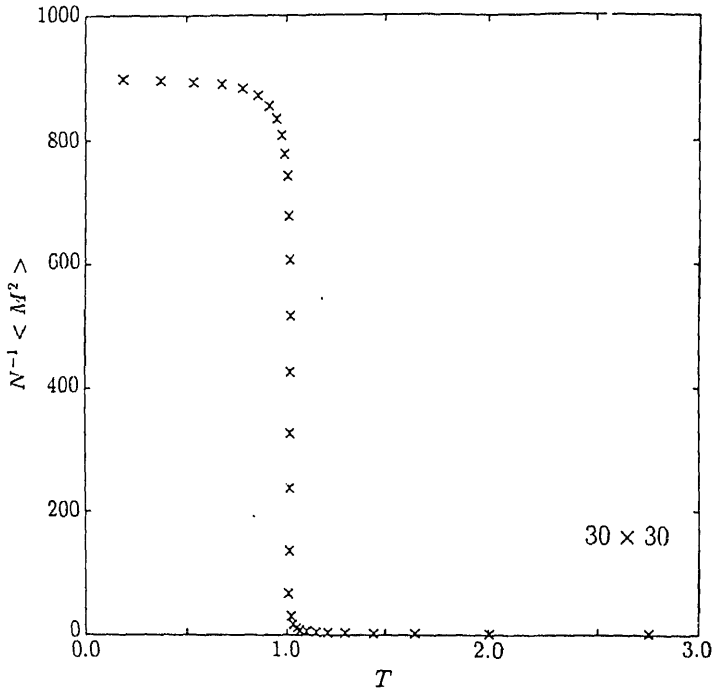

Figure 3. The mean square magnetisation per spin as a function of temperature for 900 spin system.

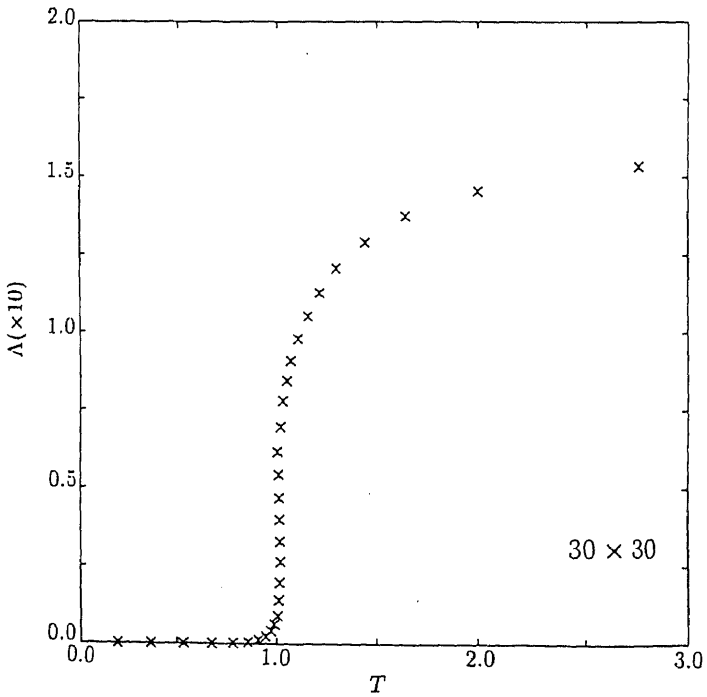

Figure 4. Vortex density as a function of temperature for 900 spin system.

the above definition of q to calculate the vorticity in each elementary square plaquette consisting of four spins at the corners. The total number of positive vortices was found to be equal to the total number of negative vortices, which is a consequence of the periodic boundary conditions [15]. We define the vortex density Λ as the total number of positive (or negative) vortices divided by the number of spins. Figure 4 displays the temperature dependence of vortex density. The standard deviation of the calculated vortex density is typically less than 1 per cent.

It is seen that the temperature dependence of E_s, $N^{-1}\langle M^2\rangle$, and Λ show a 'jump' at 1·01 which corresponds to the first order transition temperature T_c (figures 2–4). The latent heat was found to be 1·15 from the temperature dependence of E_s. For this purpose the E_s versus T data were least squares fitted to a second order polynomial above and below T_c. The least squares fitted polynomials were then extrapolated to T_c to obtain the latent heat. This is in good agreement with the latent heat value of 1·2 obtained by the canonical Monte Carlo simulations of Domany *et al* [8]. Simulations on 25 and 100 spin systems, were carried out with 2×10^4 MCSS for equilibration and 3×10^4 MCSS for averaging (in 12 blocks with 2500 MCSS per block). Average over three energy values was taken to obtain the transition temperature. We obtain T_c of 1·11 (1·04) for 25 spin (100 spin) system. We note that T_c increases with decrease in system size. This value of T_c can be compared with that obtained from the previous canonical MC simulation results (1·01 for 600 spins [22] and 1·01 for 4096 spins [8]). It is seen that T_c obtained from the present simulations agrees well with that obtained from canonical MC simulations.

5. Discussion and conclusion

Several canonical MC simulations have been carried out to study the first order transition in the classical 2D XY-model. In the present simulation, physical quantities have been obtained in the coexistence region, which were absent in the earlier canonical MC simulations. The physical variables, e.g. system energy, vortex density and the square of magnetization show a 'jump' at $T = 1{\cdot}01$ corresponding to the first order transition. The origin of the first-order transition can be understood as follows. For small value of p in eq. (2), the potential well of the nearest neighbour interaction is rather wide, so that vortices and antivortices enter the system gradually as the temperature is increased and at the Kosterlitz–Thouless transition temperature there is a dissociation of the bound vortex-antivortex pair. As the value of p increases, the potential well becomes increasingly narrow with a width of order π/p and there is an insufficient increase of vortex density at low temperature. Then at a fixed higher temperature there is a sudden appearance of large number of vortices, resulting in a first-order transition. This feature is clearly seen in figure 4. From the energy dependence of vortex density of the 900-spin system, we estimate that the creation of a vortex-antivortex pair costs about 19 units of energy in the coexistence region, which is larger than the energy associated with a tightly bound vortex-antivortex pair. We also observed that the value of vortex density for a fixed system energy in the heating cycle is lower than the corresponding value in the cooling cycle. This difference is due to the metastability of the system in a first-order transition. It is important to note that, in an experimental study of the first order transition, energy is added to (removed from) the system and the resulting physical quantities are measured. During the transition, the temperature remains constant. The micro-

canonical Monte Carlo simulations closely represents this situation and therefore, is expected to give reliable results of the transition.

In conclusion, we have demonstrated the potential of the microcanonical Monte Carlo simulations for the study of first order transition in spin systems with continuous symmetry. Specifically, we have considered the modified nearest neighbour interaction potential suggested by Domany *et al* for the 2D classical XY-model. We have obtained the vortex density and mean square magnetization in the coexistence region of the first order transition. The latent heat was found to be 1·15. The first order transition temperature obtained from this simulation shows good agreement with that obtained from previous canonical MC simulations. It is observed that the creation of a vortex antivortex pair costs about 19 units of energy in the coexistence region. This is considerably larger than the energy associated with a tightly bound vortex-antivortex pair.

Acknowledgements

This investigation was initiated in the Max-Planck-Institut für Metallforschung and Max-Planck-Institut für Festkörperforschung, Stuttgart, Germany. One of us (SO) would like to thank the Council of Scientific and Industrial Research for the award of fellowship.

References

[1] D G Mountsen, *Computer studies of phase transitions and critical phenomena* (Springer Series in Computational physics) (Springer Berlin, 1984)
K Binder and D Stauffer, *Applications of the Monte Carlo method in statistical physics* (Topics in Current Physics 36) edited by K Binder (Springer, Berlin, 1984) p1
K Binder and D W Heermann, *Monte Carlo simulation in statistical physics* (Springer Series in Solid State Sciences 80) edited by P Fuldè (Springer, Berlin, 1988)
[2] N Metropolis, A Rosenbluth, M Rosenbluth, A Teller and E Teller, *J.Chem. Phys.* **21**, 1087 (1953)
[3] M Creutz, *Phys. Rev. Lett.* **50**, 1411 (1983)
[4] G Bhanot, M Creutz and H Neuberger, *Nucl. Phys.* **B235**, 417 (1984)
[5] S Ota, S B Ota and M Fähnle, *J. Phys. Condens. Matter* **4**, 5411 (1992)
[6] R Harris, *Phys. Lett.* **A111**, 299 (1985)
[7] S K Ma, *Statistical mechanics* (World Scientific, Singapore, 1985) ch 29, 495
[8] E Domany, M Schick and R H Swendsen, *Phys. Rev. Lett.* **52**, 1535 (1984)
[9] N D Mermin and H Wagner, *Phys. Rev. Lett.* **17**, 1133 (1966)
[10] V L Berezinskii, *Sov. Phys.-JETP* **32**, 493 (1970)
[11] J M Kosterlitz and D J Thouless, *J. Phys.* **C5**, L124 (1972); *J. Phys.* **C16**, 1181 (1973)
[12] J M Kosterlitz, *J. Phys.* **7**, 1046 (1974)
[13] C Kawabata and K Binder, *Solid State Commun.* **22**, 705 (1977)
[14] S Miyashita, H Nishimori, A Kuroda and M Suzuki, *Prog. Theor. Phys.* **60**, 1669 (1978)
[15] J Lobochnik and G V Chester, *Phys. Rev.* **B20**, 3761 (1979)
[16] H Betsuyaku, *Physica* **A106**, 311 (1981)
[17] U Wolff, *Nucl. Phys* **B322**, 759 (1989)
[18] J Kogut and J Polonyi, *Nucl. Phys.* **B265**, [FS15], 313 (1986)
[19] J F Fernandes, M F Ferreira and J Stankiewicz, *Phys. Rev.* **B34**, 292 (1986)
[20] R Gupta, J Delapp, G G Batrouni, G C Fox, C F Baillie and J Apostolakis, *Phys. Rev. Lett.* **61**, 1996 (1986)

[21] R H Swendsen, *Phys. Rev. Lett.* **49**, 1302 (1982)
[22] J E van Himbergen, *Phys. Rev. Lett.* **53**, 5 (1984)
[23] H J F Knops, *Phys. Rev.* **B30**, 470 (1984)
[24] J E van Himbergen, *Solid State Commun.* **55**, 289 (1985)
[25] A Jonsson, P Minnhagen and M Nylén, *Phys Rev. Lett.* **70**, 1327 (1993)

PRAMANA
— journal of
physics

© Printed in India

Vol. 43, No. 2,
August 1994
pp. 139–153

Perturbative and nonperturbative quark masses in structure functions

D K CHOUDHURY and RANJITA DEKA*
Department of Physics, University of Gauhati, Guwahati 781014, India
*On leave from Pragjyotish College, Guwahati, India

MS received 6 August 1992; revised 30 March 1994

Abstract. Flavour symmetry breaking is introduced in the approximate formula for quark mass reported earlier. We use SLAC-MIT as well as NMC data to estimate the up, down and strange quark masses from structure functions. Using the approximate Q^2 evolutions of Altarelli–Parisi equations, we also estimate its perturbative and nonperturbative components.

Keywords. Quark mass; structure function; quantum chromodynamics.

PACS Nos 12·35; 13·60

1. Introduction

Some time back [1], we derived an approximate formula for the quark mass which occurred in the ξ-formalism [2], and studied its phenomenological application to the SLAC-MIT data [3]. To that end, we used the approximate QCD model of $F_2^{ep}(x, Q^2)$ as given by Buras and Gaemers [4] for numerical analysis. In that work, we studied the sensitivity of our results with QCD scale parameter Λ, gluon distribution, intrinsic charm component of the proton wave function [5, 6]; and higher twist (HT) effects [7–12] in the structure function.

One of the limitations of the earlier work was that we could only measure the average quark mass in the explored Q^2 range under study, but not the quark mass of individual flavour. Nor could we study the Q^2 running of the quark mass. The reasons are understandable: we did not have suitable method of introducing flavour symmetry breaking in the model, neither did we explore the asymptotic behaviour of the quark mass formula so that $\underset{Q^2 \to \infty}{\text{Lt}}\ m(Q^2)$ vanishes.

In recent years we reported [13, 14] approximate solutions of Altarelli–Parisi equations [15] valid for intermediate x and it was tested for considerable high Q^2: $Q^2 < 90\,\text{GeV}^2$ [16].

It is therefore meaningful to study the mass problem as well with these approximate solutions rather than with the moment methods of Buras Gaemers [4]. The advantage of the approximate method over the moment method is that for each value of x, we require input information only for larger values of x, and not over the full range from 0 to 1. This is important in practice, because structure functions are poorly known at small values of x.

While addressing to the mass problem one encounters three kinds of quark mass: current, dynamical and constituent quark mass [17–22]. In QCD, current quark

mass is perturbative while the dynamical quark mass is non-perturbative [19]. In the present method, since quark mass is expressed in terms of structure function $F_2(x, Q^2)$, the non-perturbative input for $F_2(x, Q_0^2)$ generates dynamical quark mass while the rest, the perturbative piece. The present paper will deal with this aspect of the problem as well.

Section 2 discusses the theory while § 3 deals with results and discussion.

2. Formalism

2.1 *Formula for quark mass*

In an earlier communication [1] we derived an approximate formula for quark mass from ξ formalism [2]. In this formalism the structure function with target and quark mass correction has the form

$$\bar{F}_2(x, Q^2) = \frac{x^2 V^3 F_2(\xi, Q^2)}{\xi^2} + \frac{6M^2 x^3 V^4}{Q^2} \int_\xi^1 \frac{dx' F_2(x', Q^2)}{x'^2} + \frac{12M^4 x^4 V^5}{Q^4} \int_\xi^1 dx' \int_{x'}^1 \frac{dx'' F_2(x'', Q^2)}{x''^2} \tag{2.1}$$

where

$$\xi = \frac{x[1 + (1 + 4mq^2/Q^2)^{1/2}]}{1 + (1 + (4M^2 x^2/Q^2))^{1/2}} \tag{2.2}$$

and

$$V = \left(1 + \frac{4M^2 x^2}{Q^2}\right)^{-1/2}. \tag{2.3}$$

Here $m_q = m_q(x, Q^2)$ is the momentum dependent running quark mass, M is the target mass while $\bar{F}_2$ is the experimental structure function incorporating the target and quark mass effects.

Taking form $O\left(\frac{1}{Q^2}\right)$ only, (2.1) is reduced to [1]

$$\bar{F}_2(x, Q^2) = F_2(x, Q^2)\left[1 + \frac{1}{Q^2}\left\{-2(m_q^2 + 2M^2 x^2) - (m_q^2 - x^2 M^2) \frac{\tilde{f}(x, Q^2)}{F_2(x, Q^2)} + 6M^2 x^3 \frac{F_2'(x, Q^2)}{F_2(x, Q^2)}\right\}\right] \tag{2.4}$$

which yields

$$m_q^2(x, Q^2) = \left[\frac{Q^2}{2 + [\tilde{f}(x, Q^2)/F_2(x, Q^2)]}\right]\left(\frac{F_2(x, Q^2) - \bar{F}_2(x, Q^2)}{F_2(x, Q^2)}\right) - \frac{[M^2 x^2(4 - [\tilde{f}(x, Q^2)/F_2(x, Q^2)]) - 6M^2 x^3 (F_2'(x, Q^2)/F_2(x, Q^2))]}{2 + f(x, Q^2)/F_2(x, Q^2))}. \tag{2.5}$$

In (2·4) or (2·5), $\tilde{f}(x, Q^2)$ and $F_2'(x, Q^2)$ can be explicitly obtained from the structure

function $F_2(x, Q^2)$ since

$$F_2(\xi, Q^2) \simeq F_2(x, Q^2) - (m_q^2 - x^2 M^2)\frac{\tilde{f}(x, Q^2)}{Q^2} \tag{2.6}$$

and

$$F'_2(x, Q^2) = \int_x^1 \mathrm{d}x' \frac{F_2(x', Q^2)}{x'^2}, \tag{2.7}$$

where

$$\xi = x + \frac{x}{Q^2}(m_q^2 - x^2 M^2). \tag{2.8}$$

We note that in the limit $M \to 0$ and $m_q \to 0$, $\bar{F}_2(x, Q^2)$ and $F_2(x, Q^2)$ are identical.

We take the absolute value of the RHS of (2.5) so that $m_q^2 > 0$ for $0 < x < 1$ and $0 < Q^2 < \infty$.

If we include the higher twist (HT) term [8] with the following form

$$F_2^{\mathrm{QCD}}(x, Q^2) = F_2^{\mathrm{LT}}(x, Q^2)\left(1 + \frac{\mu_4^2 x^\alpha}{(1-x)Q^2}\right) \tag{2.9}$$

with $\alpha = 3{\cdot}1 \pm 0{\cdot}05$ and $\mu_4^2 = 1{\cdot}7 \pm 0{\cdot}05\,\mathrm{GeV}^2$, then m_q^2 of (2.5) is modified to

$$m_q^2 \to m_q^2 + \frac{\mu_4^2 x^\alpha}{(1-x)} \Big/ \left(2 + \frac{\tilde{f}(x, Q^2)}{F_2(x, Q^2)}\right). \tag{2.10}$$

In (2.9) F_2^{LT} denotes the leading twist contribution.

More recently, HT effects have been reported in tabular form [11, 12] instead of the explicit model dependent form (2.9). The parametrization then has the general form

$$F_2^{\mathrm{QCD}}(x, Q^2) = F_2^{\mathrm{LT}}(x, Q^2)\left(1 + \frac{C_i(x)}{Q^2}\right) \tag{2.11}$$

where the coefficients $C_i(x)$ is x-dependent numericals. For small $x (x < 0{\cdot}40)$ they are small ($\sim 0{\cdot}05$) while for large $x (x > 0{\cdot}40)$ they increase as expected in models like (2·9). Equation (2.10) is then modified to

$$m_q^2 \to m_q^2 + C_i(x) \Big/ \left(2 + \frac{\tilde{f}(x, Q^2)}{F_2(x, Q^2)}\right) \tag{2.12}$$

where $C_i(x)$ for hydrogen target of ref. [12] are given in table 2.

In our analysis, we will test both (2.10) and (2.12). Let us now derive the asymptotic condition on $\bar{F}_2(x, Q^2)/F_2(x, Q^2)$ as $Q^2 \to \infty$. As $m_q^2 \to 0$ asymptotically, (2.5) predicts

$$\operatorname*{Lt}_{Q^2 \to \infty} \frac{\bar{F}_2(x, Q^2)}{F_2(x, Q^2)} = 1 - \frac{1}{Q^2}\left[M^2 x^2\left(4 - \frac{\tilde{f}(x, Q^2)}{F_2(x, Q^2)}\right) - 6M^2 x^3 \frac{F'_2(x, Q^2)}{F_2(x, Q^2)}\right]. \tag{2.13}$$

Table 1. Dynamical quark mass.

Quark flavour	Data	Inputs		
		Gluck *et al* ($Q_0^2 = \text{GeV}^2$)	ELHQ $Q_0^2 = \text{GeV}^2$	EHQ $Q_0^2 = \text{GeV}^2$
m_u	SLAC-MIT	$0{\cdot}126 \pm 0{\cdot}01$ GeV	$0{\cdot}366 \pm 0{\cdot}02$ GeV	$0{\cdot}410 \pm 0{\cdot}01$ GeV
	NMC	$0{\cdot}410 \pm 0{\cdot}12$ GeV	$0{\cdot}467 \pm 0{\cdot}13$ GeV	$0{\cdot}456 \pm 0{\cdot}21$ GeV
m_d	SLAC-MIT	$0{\cdot}434 \pm 0{\cdot}03$ GeV	$0{\cdot}373 \pm 0{\cdot}01$ GeV	$0{\cdot}381 \pm 0{\cdot}11$ GeV
	NMC	$0{\cdot}544 \pm 0{\cdot}11$ GeV	$0{\cdot}436 \pm 0{\cdot}12$ GeV	$0{\cdot}564 \pm 0{\cdot}15$ GeV

2.2 Q^2 *evolution of structure functions*

As mentioned in the introduction we will use the approximate form of structure function [13]

$$F_2(x,t) = \frac{5}{18}F_2^S(x,t_0)\left(\frac{t}{t_0}\right)^{H^S(x)} + \frac{3}{18}F_2^{NS}(x,t_0)\left(\frac{t}{t_0}\right)^{H^{NS}(x)} \tag{2.14}$$

with

$$H^S(x) = \frac{4}{25}[3 + 4\ln(1-x) + 2I^S(x) + 6g(x)] \tag{2.15}$$

$$H^{NS}(x) = \frac{4}{25}[3 + 4\ln(1-x) + 2I^{NS}(x)] \tag{2.16}$$

where $I^S(x)$, $I^{NS}(x)$ and $g(x)$ are the integrals [13] defined as

$$I^S(x) = \int_x^1 \frac{dw}{(1-w)}\left\{(1+w^2)\frac{F_2^S(x/w,t_0)}{F_2^S(x,t_0)} - 2\right\} \tag{2.17}$$

$$I^{NS}(x) = \int_x^1 \frac{dw}{(1-w)}\left\{(1+w^2)\frac{F_2^{NS}(x/w,t_0)}{F_2^{NS}(x,t_0)} - 2\right\} \tag{2.18}$$

$$g(x) = \int_x^1 \left\{dw(w^2+(1-w)^2)\frac{G(x/w,t_0)}{F_2^S(x,t_0)}\right\} \tag{2.19}$$

We evaluate the integrals using Taylor approximation method reported earlier [23, 14].

2.3 *Flavour symmetry breaking*

In order to evaluate quark mass of definite flavour in (2.5) or (2.10) we have to identify m_q with the definite flavour. Similarly, the contribution to $F_2(x,Q^2)$ of an individual flavour, $F_2(x,Q^2)$, $F_2'(x,Q^2)$ and $\tilde{f}(x,Q^2)$ needs to be identified. We therefore write the standard form of structure function neglecting the heavy flavour contents as

$$F^{ep}(x,Q^2) = F^u(x,Q^2) + F^d(x,Q^2) + F^S(x,Q^2) \tag{2.20}$$

where

$$F^u(x,Q^2)=\tfrac{4}{9}[u_v(x,Q^2)+2u_s(x,Q^2)], \tag{2.21}$$

$$F^d(x,Q^2)=\tfrac{1}{9}[d_v(x,Q^2)+2d_s(x,Q^2)], \tag{2.22}$$

$$F^S(x,Q^2)=\tfrac{2}{9}S(x,Q^2). \tag{2.23}$$

Using (2.20)–(2.23) one obtains $F'_2(x,Q^2)$ and $\tilde{f}(x,Q^2)$ for individual flavour.

In order to obtain $\bar{F}_2(x,Q^2)$ for individual flavours, we use the flavour contents of F_2 as defined in the quark model.

To proceed further we need information on input structure function. There are several inputs [24–26] in the literature. Each of them has the generic form

$$x_{q_v}(x,Q_0^2)=\sum_{i=1}^{n} a_i^q x^{p_i^q}(1-x^{\alpha_i^q})^{l_i^q}, \quad (q=u,d,s) \tag{2.24}$$

Numerical values of a_i^q, p_i^q, α_i^q and l_i^q are given in Appendix A.

2.4 *Determination of* $\tilde{f}(x,Q^2)$

Let us illustrate it with explicit evaluation of $\tilde{f}_{u_v}(x,Q^2)$:
From (2.6)

$$\tilde{f}_{u_v}(x,Q^2)=\frac{Q^2}{(mq^2-x^2M^2)}[U_v(x,Q^2)-U_v(\xi,Q^2)] \tag{2.25}$$

where ξ is defined in (2.8).

Determination of $\tilde{f}_{u_v}(x,Q^2)$, therefore needs $u_v(x,Q^2)$ as well as $u_v(\xi,Q^2)$.

To that end we use the evolution

$$u_v(x,Q^2)=u_v(x,Q_0^2)\left(\frac{t}{t_0}\right)^{H^{NS}}(x) \tag{2.26}$$

where $H^{NS}(x)$ is given by (2.16). $I^{NS}(x)$ occurred in (2.16) and defined in (2.18) should correspond to single quark species, and has approximate analytical form [16]

$$I^{NS}_{u_v}(x)=2x(1-x)\frac{u'_v(x)}{u_v(x)}-2(1-x)-x(1-x)^2\frac{u'_v(x)}{u_v(x)}+\frac{(1-x)^2}{2}+\frac{x(1-x)^3}{3}\frac{u'_v(x)}{u_v(x)} \tag{2.27}$$

By using (2.27) $I^{NS}_{u_v}(x)$ can then be explicitly calculated once $u_v(x)$ is known from (2.24).

By making the replacement $x\to\xi$ as defined in eq. (2.8) $I^{NS}(\xi)$ and $\ln(1-\xi)$ occurred in $H^{NS}_{u_v}(\xi)$ then take the forms

$$I^{NS}(\xi)=I^{NS}(x)+\frac{m_q^2-x^2M^2}{Q^2}R^{NS}(x) \tag{2.28}$$

$$\ln(1-\xi)=\ln(1-x)-x\frac{(m_q^2-x^2M^2)}{(1-x)Q^2} \tag{2.29}$$

where

$$R^{NS}(x) = 2x - \frac{x(1-x)}{2} + \frac{\sum_i a_i x^{p_i}(1-x^{\alpha_i})^{l_i}}{\sum_j a_j x^{p_j}(1-x^{\alpha_j})^{l_j}} \left[p_i(1-x)\left\{(p_i - p_j)M(x) - \frac{\alpha_i l_i x^{\alpha_i}}{(1-x^{\alpha_i})} M(x)\frac{x}{1-x} N(x) + \frac{\alpha_j l_j x^{\alpha_j}}{(1-x^{\alpha_j})} M(x)\right\} - l_i \alpha_i x^{\alpha_i} \frac{(1-x)}{(1-x^{\alpha_i})} \left\{(\alpha_i + p_i - p_j)M(x) - \frac{(l_i - 1)\alpha_i x^{\alpha_i}}{(1-x^{\alpha_i})} M(x) - \frac{x}{1-x} N(x) + \frac{\alpha_j l_j x^{\alpha_j}}{(1-x^{\alpha_j})} M(x)\right\}\right]. \tag{2.30}$$

$$M(x) = 2 - (1-x) + \frac{(1-x)^2}{3} \tag{2.31}$$

and

$$N(x) = 2 - 2(1-x) + (1-x)^2. \tag{2.32}$$

These result in

$$H_{u_v}^{NS}(\xi) = H_{u_v}^{NS}(x) - \frac{(m_q^2 - x^2 M^2)}{Q^2}\left[\frac{16x}{25(1-x)} - 8R^{NS}(x)\right] \tag{2.33}$$

so that

$$\left(\frac{t}{t_0}\right)^{H_{u_v}^{NS}(\xi)} \approx \left(\frac{t}{t_0}\right)^{H_{u_v}^{NS}(x)}\left[1 - \frac{(m_q^2 - x^2 M^2)}{Q^2}\left(\frac{16x}{25(1-x)} - 8R^{NS}(x)\right)\right]. \tag{2.34}$$

This yields

$$u_v(\xi, Q^2) = u_v(x, Q^2) - \sum_i a_i x^{p_i}(1-x^{\alpha_i})^{l_i}\left(\frac{t}{t_0}\right)^{H_{u_v}^{NS}(x)} \frac{(m_q^2 - x^2 M^2)}{Q^2} \times \left[\left\{\frac{16x}{25(1-x)} - 8R^{NS}(x)\right\}\ln\frac{t}{t_0} + (p_i + l_i \alpha_i x^{\alpha_i})\right]. \tag{2.35}$$

Using it in (2.2), we then obtain

$$\tilde{f}_{u_v}(x, Q^2) = \sum_i a_i x^{p_i}(1-x^{\alpha_i})^{l_i}\left(\frac{t}{t_0}\right)^{H_{u_v}^{NS}(x)} \times \left\{\left(\frac{16x}{25(1-x)} - 8R^{NS}(x)\right)\ln\frac{t}{t_0} + (p_i + l_i x^{\alpha_i}\alpha_i)\right\}. \tag{2.36}$$

For the sea components, $H^{NS}(x)$ occurring in (2.26) is to be replaced by $H^S(x)$ given in eq. (2.15) and $\tilde{f}_{us}(x, Q^2)$ follows from (2.37) with replacement $H_{u_v}^{NS}(x) \to H_{us}^{S}(x)$.

2.5 *Perturbative and non-perturbative quark masses*

Elias and Scadron [19] pursues a theoretical model where the total quark mass is the sum of a flavour dependent current mass and a flavour independent dynamical mass, away from the chiral limit

$$m(Q^2) = m_{\text{current}}(Q^2) + m_{\text{dyn}}(Q^2). \tag{2.37}$$

In the chiral limit $m_{\text{current}}(Q^2) \to 0$, $m_{\text{dyn}}(Q^2)$ is identified with the constituent quark mass. As the current quark mass is perturbative while the dynamical quark mass is non-perturbative [19] in QCD, we identify the quark mass at $Q^2 = Q_0^2$ to be of dynamical origin. It will contain two pieces, the flavour dependent piece coming from input $F_2(x, Q_0^2)$ and the flavour independent one from HT term. The Q^2 dependence of the dynamical mass is solely due to HT so that without HT, it corresponds to the constituent mass. The perturbative quark mass $m_{\text{current}}(Q^2)$ can then be obtained from (2.37). We note that $m_{\text{dyn}}(x, Q^2)$ will critically depend on the inputs used. We will therefore test the sensitivity of our results with the inputs of Glück *et al* [24], ELHQ [25] and EHQ [26] as representative samples.

If the additivity relation (2.37) is extrapolated down to $Q^2 \to Q_0^2$, $m_{\text{current}}(Q^2)$ should tend to zero, on the other hand, as $Q^2 \to \infty$, $m_{\text{current}}(Q^2)$ should also have a vanishing limit [27] in QCD:

$$m_{\text{current}}(Q^2) = \frac{\hat{m}}{(1/2 \ln Q^2/\Lambda^2)^{-\gamma_1/\beta_1}} \tag{2.38}$$

where $\hat{m}$ is the scale invariant mass, $\gamma_1 = 2$ for three colours and $\beta_1 = -11/2 + n_{f/3}$, n_f being the number of flavours. Equations (2.37) and (2.38) then determine the behaviour of $m_{\text{current}}(Q^2)$ down to $Q^2 = Q_0^2$. In the next section we will discuss its behaviour graphically.

3. Results and discussion

In the present work, we report our analysis for up, down and strange quark. In figure 1(a–d) we present our results (denoted by solid points with bars) for x-averaged m_u and m_d using representative data samples of SLAC-MIT [3] (figure 1(a), 1(c)) and NMC [28] (figure 1(b), 1(d)) respectively, using the inputs of Glück *et al* [24], ELHQ [25] and EHQ [26]. To obtain these representative results, we need $\bar{F}_u$ and $\bar{F}_d$, the structure function contributions due to u and d quarks respectively. This can be estimated in a quark parton model as described in appendix B. In table 1, we record the values of dynamical quark masses (m_u and m_d) with the three inputs; (Glück *et al* [24], ELHQ [25] and EHQ [26]. In figure 2(a–d) we plot $m_{\text{cur}}(Q^2)$ vs Q^2 using SLAC-MIT [3] and NMC [28] data. In figure 3(a–b) we also plot $\bar{F}^u(x, Q^2)/F^u(x, Q^2)$ as Q^2 using (2.13) for $x = 0{\cdot}225$ and $0{\cdot}5$ respectively. Using SLAC-MIT [3] and NMC [28] data, similar curve can be drawn for d quark as well.

We have also made similar analysis for S-quark. The results are found to be much more sensitive to the values of x as well as inputs. Its magnitude is also relatively high. As an illustration with $x \sim 0{\cdot}18$ from NMC data and inputs of Glück *et al* [24] ELHQ [25] and EHQ [26] yields n_s the dynamical s quark to be $0{\cdot}75$, $0{\cdot}87$, $0{\cdot}9$ respectively. This is rather an unfortunate feature of the present formalism.

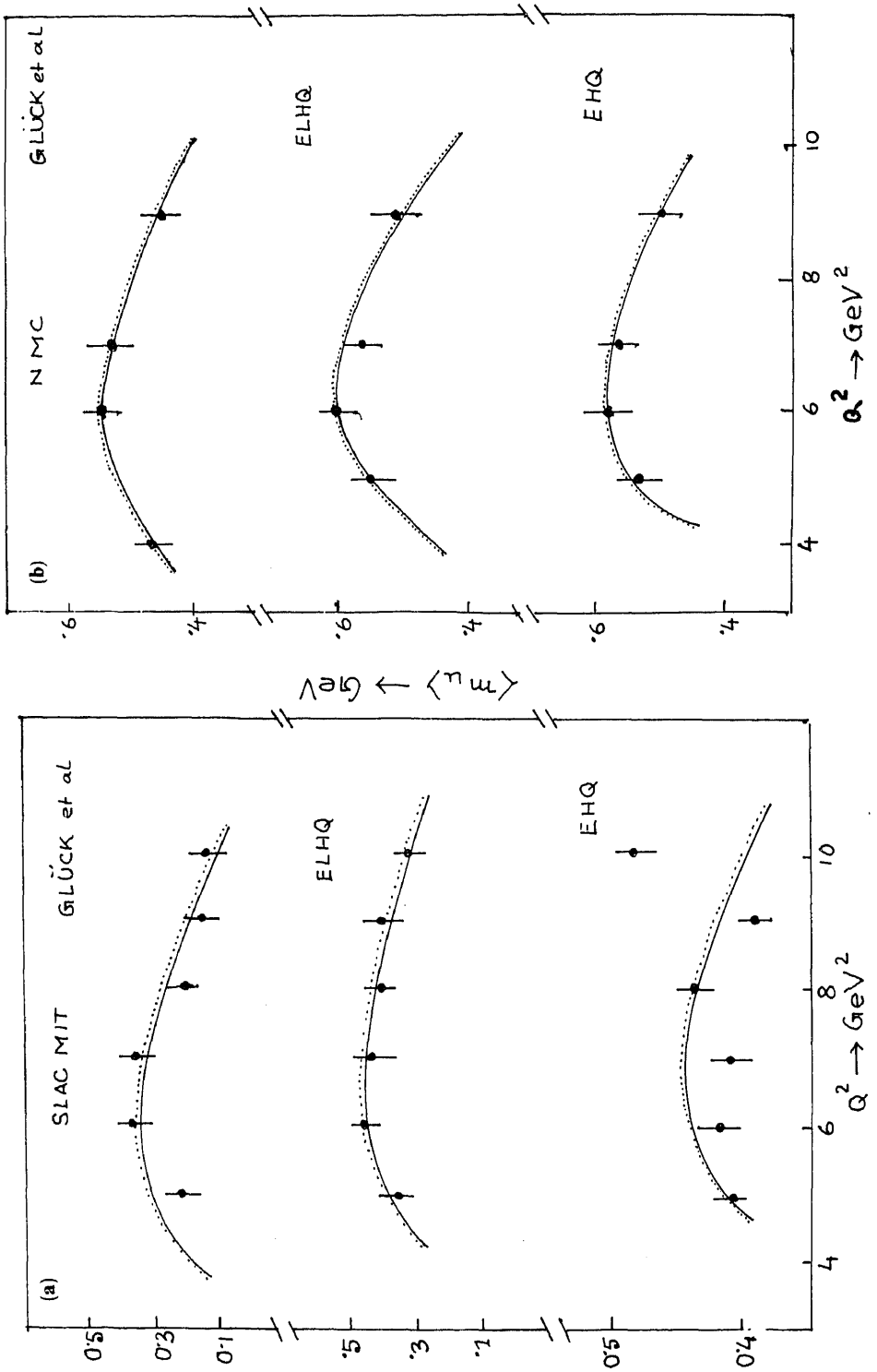
(a)
SLAC MIT
GLÜCK et al
ELHQ
EHQ
$\langle \pi_v \rangle \rightarrow$ GeV
$Q^2 \rightarrow$ GeV^2
(b)
NMC
GLÜCK et al
ELHQ
EHQ
$\langle \pi_v \rangle \rightarrow$ GeV
$Q^2 \rightarrow$ GeV^2

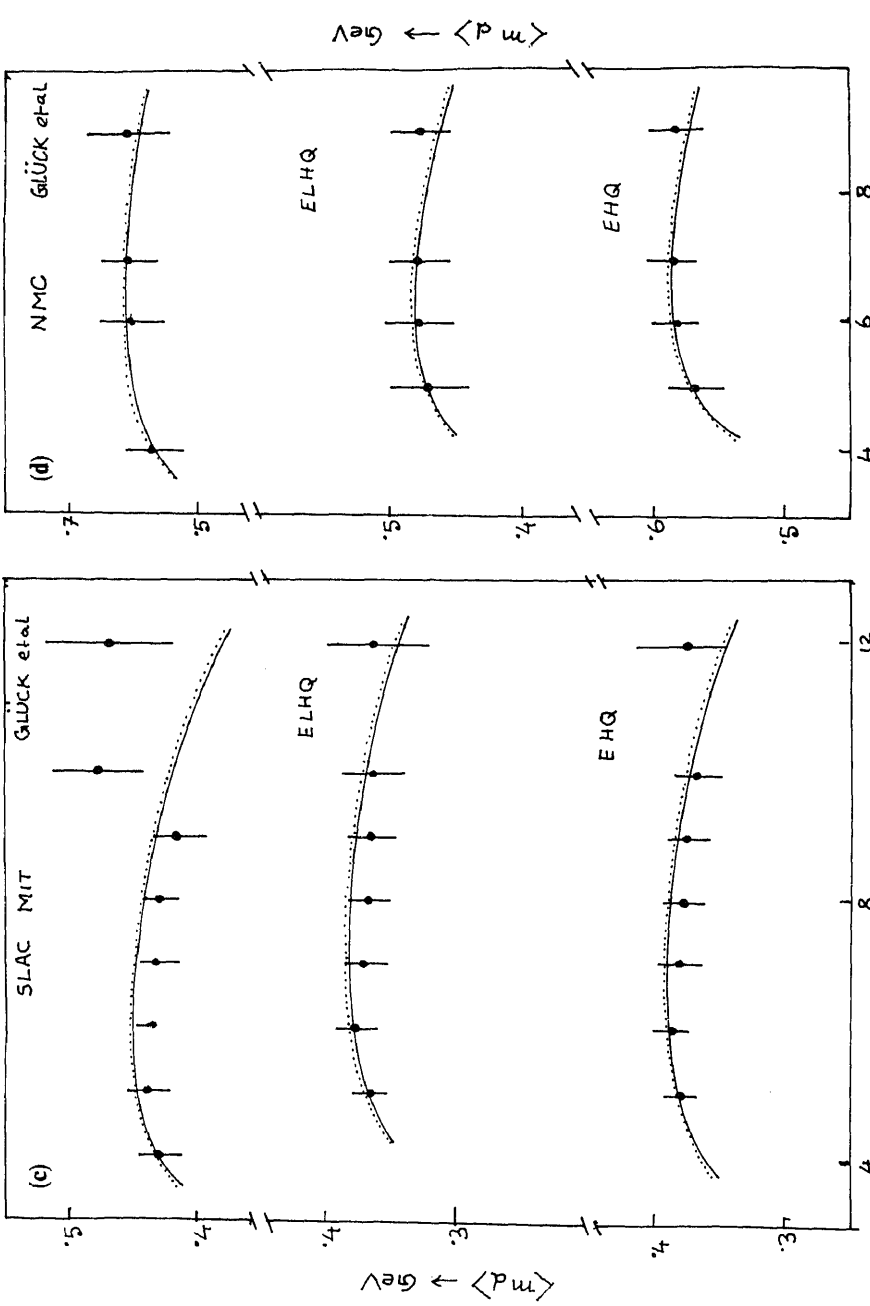

Figure 1(a–d). x averaged $m_u(Q^2)$ vs Q^2 using the inputs of Glück *et al* [24], ELHQ [25] and EHQ [26]. Data taken from SLAC-MIT [3] and NMC [28] respectively. Dotted lines represent HT effect.

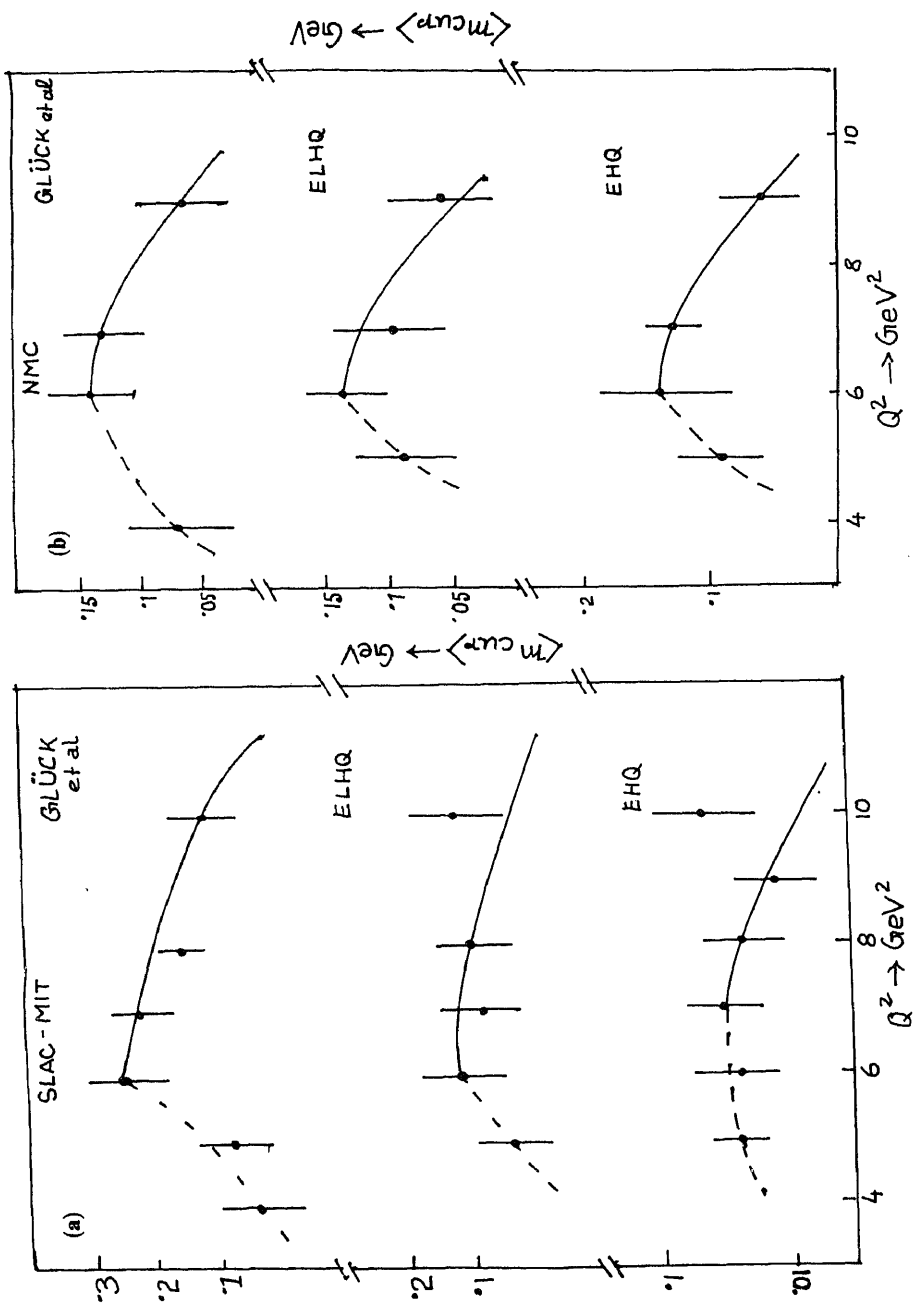
(a)
SLAC - MIT
GLÜCK et al
ELHQ
EHQ
(b)
NMC
GLÜCK et al
ELHQ
EHQ
$\langle m_{cur} \rangle \rightarrow$ GeV
$Q^2 \rightarrow$ GeV^2

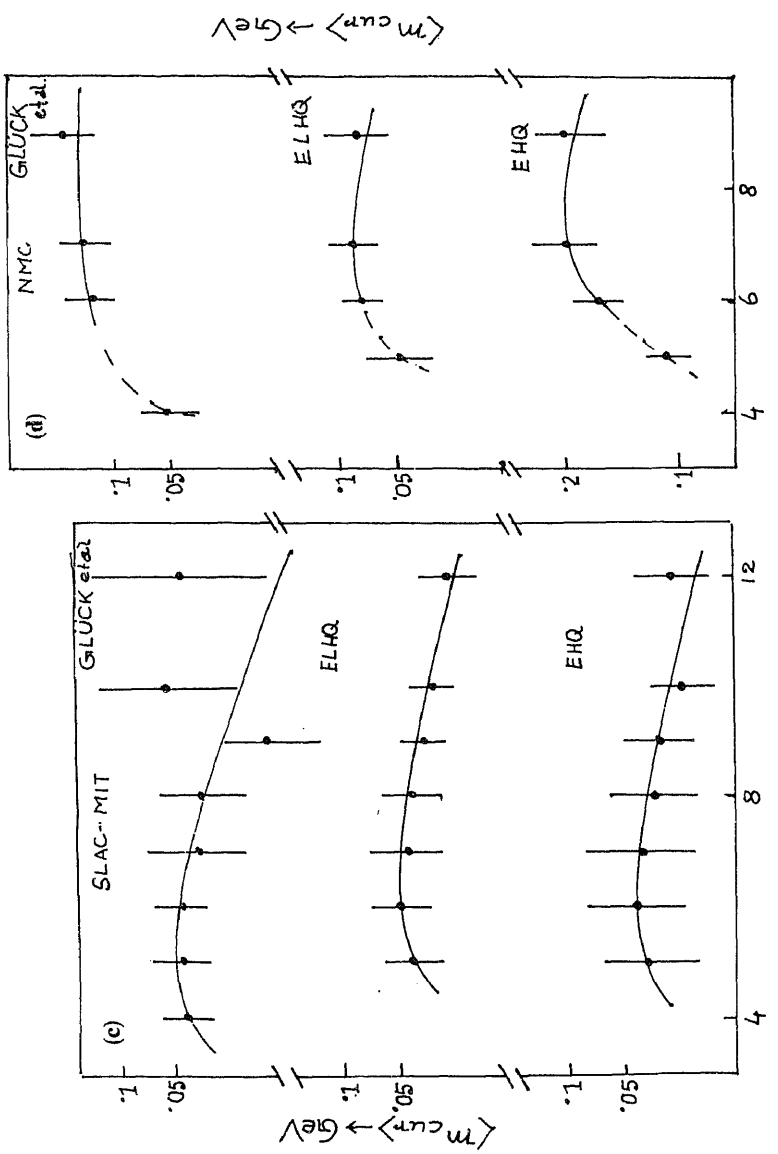

Figure 2(a–d). x averaged current quark mass vs Q^2 using the inputs of Glück *et al* [24], ELHQ [25] and EHQ [26]. Data taken from SLAC-MIT [3] and NMC [28] respectively. The dashed section of the curves represents m_{current} extrapolated down to $Q^2 \sim Q_0^2$.

These curves and the table demonstrate the following features of the quark mass.

(i) The dynamical quark mass depends on the inputs as well as on data. But such variation does not change its order of magnitude. We find $m_u \sim 0{\cdot}126 - 0{\cdot}656$ GeV while $m_d \sim 0{\cdot}373 - 0{\cdot}664$ GeV.
(ii) Inclusion of HT enhances the dynamical mass slightly but it falls to its constituent limit as Q^2 increases.
(iii) Figure 2 (a–d) shows that away from $Q^2 \sim Q_0^2$, the current mass falls. But if they are extrapolated down to $Q^2 \sim Q_0^2$ (shown by dashed section of the curves), they acquire maxima at around 6–7 GeV^2.

This peculiar feature of current quark mass is due to the following reasons:

(a) The dynamical and current quark masses are additive even in the limit $Q^2 \to Q_0^2$
(b) Both $m_{dyn}(Q^2)$ and $m_{cur}(Q^2)$ are positive definite
(c) $m_{current}(Q^2)$ should vanish both at $Q^2 \approx Q_0^2$ and $Q^2 \to \infty$.

Any deviation of the behaviour of current quark mass from figure 2(a–d) represents the breakdown of the naive additivity relation (Equation 2.37).

Finally, in figure 3(a, b), we show representative estimates of log $\bar{F}_u/F^u$ using eq. (2.13) with NMC data and ELHQ inputs. Theoretically one expects a decrease of m_q as Q^2 increases (represented by solid lines) while asymptotically it should vanish [represented by dashed line]. The representative results of figure 3(a, b) are compatible with this expectation.

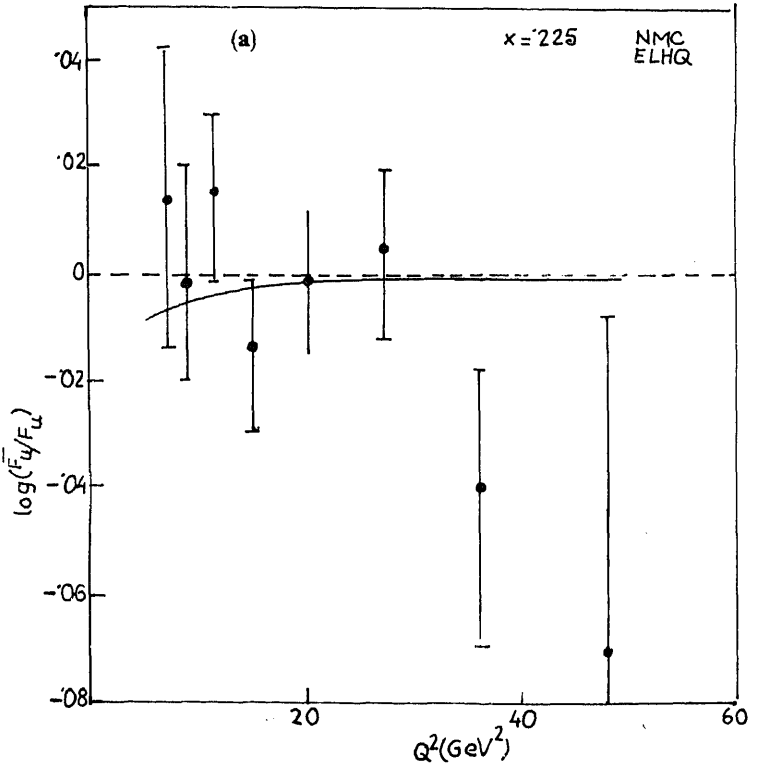

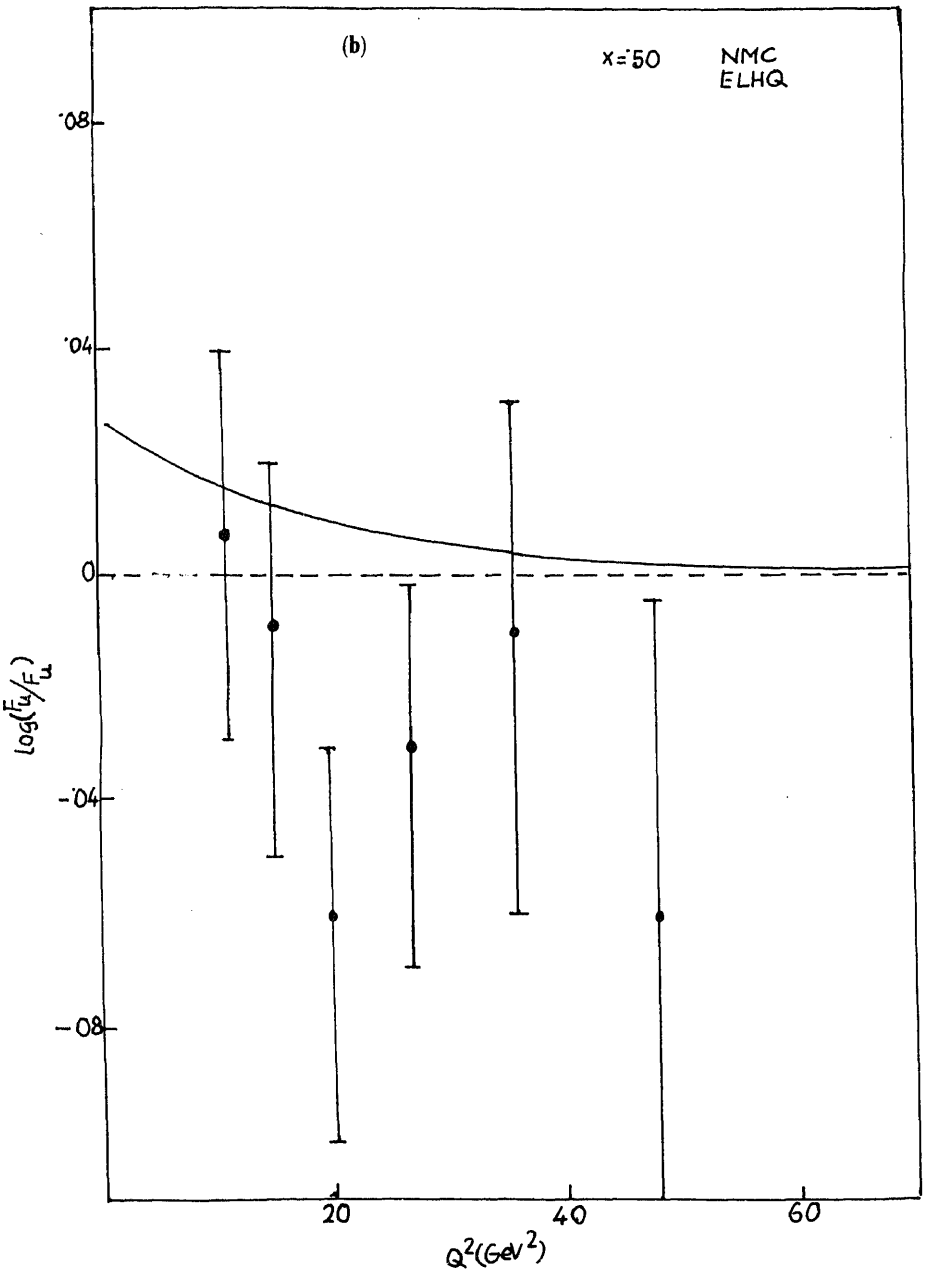

Figure 3(a–b). $F^u(x, Q^2)/F^u(x, Q^2)$ vs Q^2 for $x = 0{\cdot}225$ and $0{\cdot}5$ respectively using NMC data and ELHQ input.

4. Conclusions

We have thus shown that the dynamical and the current quark masses for each flavour can be extracted from structure functions by improving the formalism reported earlier [1]. For up and down quark, the results are reasonable but for s quark the results are more sensitive to x values and inputs used.

Acknowledgements

The authors are grateful to Drs N Nimai Singh, A Saikia, J K Sarma and Mrs P Das of University of Gauhati for stimulating discussions. One of us (RD) acknowledges UGC, New Delhi for financial support.

Appendix A

We record below the parameters of eq. (2.24) occurring in the inputs of Glück *et al* [24] ELHQ [25] and EHQ [26]

Glück et al [24] *distribution* $Q_0^2 = 4\,\mathrm{GeV}^2$

$$n^u = 1, \quad a_1^u = 1{\cdot}230, \quad p_1^u = 0{\cdot}421, \quad \alpha_1^u = 2, \quad l_1^u = 3{\cdot}37,$$
$$n^d = 1, \quad a_1^d = 0{\cdot}541, \quad p_1^d = 0{\cdot}364, \quad \alpha_1^d = 2, \quad l_1^d = 5{\cdot}09,$$
$$n^s = n^{\bar{s}} = 1, \quad a_1^s = 0{\cdot}25, \quad p_1^s = 0, \quad \alpha_1^s = 1, \quad l_1^s = 7,$$

ELHQ [25] *distribution* $Q_0^2 = 5\,\mathrm{GeV}^2$

$$n^u = 1, \quad a_1^u = 1{\cdot}78, \quad p_1^u = 0{\cdot}5, \quad \alpha_1^u = 1{\cdot}51, \quad l_1^u = 3{\cdot}5,$$
$$n^d = 1, \quad a_1^d = 0{\cdot}67, \quad p_1^d = 0{\cdot}4, \quad \alpha_1^d = 1{\cdot}51, \quad l_1^d = 4{\cdot}5,$$
$$n^{u_s} = n^{d_s} = 1, \quad a_1^{u_s} = a_1^{d_s} = 0{\cdot}182, \quad p_1^{u_s} = p_1^{d_s} = 0, \quad \alpha_1^{u_s} = \alpha_1^{d_s} = 1, \quad l_1^{u_s} = l_1^{d_s} = 8{\cdot}54,$$
$$n^{s_s} = 1, \quad a_1^s = 0{\cdot}081, \quad p_1^s = 0, \quad \alpha_1^s = 1, \quad l_1^s = 8{\cdot}54$$

EHQ [26] *distribution* $Q_0^2 = 5\,\mathrm{GeV}^2$

$$n^u = 1, \quad a_1^u = 2{\cdot}406, \quad p_1^u = 0{\cdot}60, \quad \alpha_1^u = 1, \quad l_1^u = 3{\cdot}1,$$
$$n^d = 1, \quad a_1^d = 2{\cdot}144, \quad p_1^d = 0{\cdot}70, \quad \alpha_1^d = 1{\cdot}2, \quad l_1^d = 4{\cdot}8,$$
$$n^{\bar{s}} = 1, \quad a_1^{\bar{s}} = 0{\cdot}086, \quad p_1^{\bar{s}} = 0, \quad \alpha_1^{\bar{s}} = 1, \quad l_1^{\bar{s}} = 8{\cdot}5,$$
$$n^{\bar{u}} = 1, \quad a_1^{\bar{u}} = 0{\cdot}20, \quad p_1^{\bar{u}} = 0, \quad \alpha_1^{\bar{u}} = 1, \quad l_1^{\bar{u}} = 11{\cdot}2,$$
$$n^{\bar{d}} = 1, \quad a_1^{\bar{d}} = 0{\cdot}20, \quad p_1^{\bar{d}} = 0, \quad \alpha_1^{\bar{d}} = 1, \quad l_1^{\bar{d}} = 5{\cdot}8.$$

Appendix B

Extraction of F^u, F^d in the experimental data.

We show the extraction of F^u and F^d from SLAC MIT data [3] with ELHQ input at $x = 0{\cdot}25$, $Q_0^2 = 5\,\mathrm{GeV}^2$. Similar analysis can be done for other representative points for different inputs as well:

From equations (2.21), (2.22) and (2.23) of the text and using ELHQ inputs (Appendix A) one obtains at $x = 0{\cdot}25$

$$F^u \to 0{\cdot}236; \; F^d \to 0{\cdot}027; \; F^s \to 0{\cdot}002.$$

It leads to the theoretical value of structure function at $x = 0{\cdot}25$ and $Q_0^2 = 5\,\mathrm{GeV}^2$ to be

$$F(x = 0{\cdot}25, \quad Q^2 = 5\,\mathrm{GeV}^2) \approx 0{\cdot}292.$$

It gives

$$\left.\frac{F^u}{F}\right|_{x=0\cdot25} \approx 0\cdot902.$$

The experimental value of structure function from SLAC-MIT data at the corresponding values of x and Q^2 is

$$\bar{F} = 0\cdot2959 \pm 0\cdot0112.$$

This yields

$$F^u \simeq 0\cdot902 \times \bar{F} \approx 0\cdot27 \pm 0\cdot01.$$

Similarly for d quark at the same x and Q^2 yield

$$\left.\frac{F^d}{F}\right|_{x=0\cdot25} \approx 0\cdot09 \quad \text{so that } \bar{F}^d \simeq 0\cdot09 \times \bar{F}$$

$$\simeq 0\cdot026 \pm 0\cdot001$$

and so on.

References

[1] D K Choudhury and A K Misra, *Pramana – J. Phys.* **31**, 479 (1988)
[2] H Georgi and H D Politzer, *Phys. Rev.* **D14**, 1829 (1976)
[3] A Bodek *et al* (SLAC MIT), *Phys. Rev.* **D20**, 1471 (1979)
[4] J Buras and K J F Gaemers, *Nucl. Phys.* **B132**, 249 (1978)
[5] S J Brodsky, P Hoyer, C Peterson and N Sakai, *Phys. Lett.* **B93**, 451 (1980)
[6] D P Roy, *Phys. Rev. Lett.* **B93**, 451 (1980)
[7] L F Abbott, W B Atwood and R M Barnett, *Phys. Rev.* **D22**, 582 (1980)
[8] J J Aubert *et al*, *Nucl. Phys.* **B259**, 189 (1985)
[9] D Bollini *et al*, *Phys. Lett.* **B104**, 403 (1981)
[10] R Godbole and D P Roy, *Z. Phys.* **C15**, 39 (1982)
[11] A Ouraou, in *Proceedings of the 25th International Conference on high energy physics* edited by K K Phua and Y Yamaguchi (South East Asia Theoretical Physics Association, Physical Society of Japan, 1991) **Vol. 1** p. 634
[12] M Virchaux and A Milsztajn, *Phys. Lett.* **B274**, 22 (1992)
[13] D K Choudhury and A Saikia, *Pramana – J. Phys.* **33**, 359 (1989)
[14] D K Choudhury, in *Plots, Quarks and Strange Particles Proc. of the Dalitz Conference* 1990, edited by I J R Aitchison, C H Llewellyn Smith and J E Paton, (World Scientific, Singapore, 1991) p. 194
[15] G Altarelli and G Parisi, *Nucl. Phys.* **B126**, 298 (1977)
[16] D K Choudhury and R Deka, *Indian J. Phys.* **A66**, 801 (1992)
[17] M D Scadron, *Rep. Prog. Phys.* **44**, 213 (1981)
[18] M D Scadron, *Ann. Phys. (N. Y).* **148**, 257 (1983)
[19] V Elias and M D Scadron, *Phys. Rev.* **D30**, 647 (1984)
[20] J Thakur, *Phys. Rev.* **D39**, 873 (1989)
[21] D B Lichtenberg, *Phys. Rev.* **D40**, 3675 (1989)
[22] D Atkinson and P W Johnson, *Phys. Rev.* **D41**, 1661 (1990)
[23] D K Choudhury and A Saikia, *Pramana – J. Phys.* **34**, 85 (1990)
[24] M Gluck, E Hoffmann and E Reya, *Z. Phys.* **C13**, 119 (1982)
[25] E Eichten, I Hinchliffe, K Lane and C Quigg, *Rev. Mod. Phys.* **56**, 579 (1984), Hereafter referred ELHQ
[26] E Eichten, I Hinchliffe and C Quigg, *Phys. Rev.* **D45**, 2269 (1992), Hereafter referred EHQ
[27] T N Truong, *Determination of light quark masses CDRN* TH3277 (unpublished) (1982)
[28] P Amaudruz *et al* (NMC), CERM-PPE **92–124**, (1992)

PRAMANA
— journal of
physics

© Printed in India

Vol. 43, No. 2,
August 1994
pp. 155–163

Electromagnetic mass differences of t-flavored hadrons in modified bag model

BISHWARANJAN DASH[1], SRIPATI KUMAR NAYAK[2] and
LAMBODAR P SINGH[3]
[1] Physics Department, Banki College, Banki, Cuttack, India
[2] Physics Department, S.V.M College, Jagatsingpur, Cuttack, India
[3] Physics Department, Utkal University, Vanivihar, Bhubaneswar 751 004, India

MS received 16 February 1994; revised 6 June 1994

Abstract. Mass difference of t-flavored hadrons is calculated using bag model modified for considering heavy quarks inside the bag. Both electric and magnetic contributions to mass differences are evaluated without the assumption of degenerate intermediate state. Mass differences between up and down quarks inside the bag is taken to be a constant in the absence of a dynamical calculations for the same.

Keywords. Bag model; t-flavoured hadrons; electromagnetic mass differences.

PACS Nos 12·40; 13·40

1. Introduction

A new era was started in the theoretical understanding of particle properties when Gell-mann and Zweig [1] introduced quarks as fundamental constituents of hadrons. Basing on the symmetry group global SU(3), three quark-model with fractionally charged quarks was proposed. These are commonly known as u, d, s quarks and are said to represent three quark flavors. Discovery [2] of mesons like ψ and Υ required the existence of additional flavors like c and b. There are also two independent evidences for the existence of the heaviest top quark t, coming from forward-backward asymmetry in $e^+ e^- \to b\bar{b}$ [3] and the absence of flavor changing neutral current decay $b \xrightarrow{z} s, d$ [4]. Besides, aesthetics of quark-lepton symmetry and the resulting three quark family structure have led many to believe in the existense of sixth quark t.

The precision of electroweak data has made it possible to estimate indirectly the masses of the top quark via their contributions to the radiative corrections. A global fit to all data of standard model yield, $m_t = 150^{+23}_{-26} \pm 16$ GeV [5] where the central value is for Higgs mass $m_H = 250$ GeV. A new update precision LEP data are analysed to predict $m_t = 126^{+26}_{-28}$ GeV [6] for Higgs mass unconstrained. If these predictions are correct, the top quark should be discovered during the new run of Fermilab $p\bar{p}$ collider.

Thus, on the eve of a possible of discovery of t-quark, assumed to live long enough to hadronise, a calculation [7] of masses of t-flavored hadrons was undertaken to facilitate comparison with the experimental results when the t-flavored hadrons are eventually discovered and shed light on the understanding of the confinement of heavy quarks to form hadrons drawn from the above comparison. The purpose of

the present work is to carry the above work to completion with the estimation of the electromagnetic mass differences between t-flavored mesons and baryons carrying spin 0, 1 and $\frac{1}{2}$, $\frac{3}{2}$ respectively.

The paper is organized as follows. In § 2 we have described the model used for our calculation. In § 3 we present our numerical results and in § 4 we conclude with a discussion.

2. The model

It is long identified that the strong interaction creates complications in calculating mass differences among hadrons in the same isospin multiplet. These problems, one assumes, may perhaps be avoided in a quark model, where the mass shift due to electromagnetic interaction has two parts; one from electric and magnetic interactions between different quarks and a second from the self energies of quarks themselves. The latter results in a mass difference between up and down quarks for which a thorough dynamical calculation has not been carried out so far [8]. The electric and the magnetic interactions on the other hand can be explicitly calculated [9] using, say, MIT bag model which provides us an explicit wavefunction for quarks constituting a hadron.

The MIT bag model, implementing quark and gluon confinement in a simple manner, has been very successful in description of ground state hadrons formed with light quarks [10]. But the application of this model to heavy quark states or nonspectroscopic calculation have been very limited, reflecting a lack of proper understanding of its two most important parameters like the bag pressure B and zero point energy Z_0. This has also resulted in poor agreement of model predictions with the experiment as one goes to heavier quark systems. Heavy quarks, in all likelihood, destroy the sphericity of the bag. However, a nonspherical bag has not yet been solved. Therefore Ponce [11] modified the spherical bag model by invoking mass-dependent series expansions for ω, the frequency of a quark inside a spherical bag and also for the zero point energy Z_0. The virtue of this expansion lies in the better agreement with experimental results in the c and b sectors. We, in the following, will use these expansions for heavy t-quark.

As stated before, we write the electromagnetic mass difference in a quark model as

$$\Delta M = (\Delta M)_{\text{el}} + (\Delta M)_{\text{mag}} + (\Delta M)_{\text{q}} \tag{1}$$

where $(\Delta M)_{\text{el,mag}}$ are contributions to ΔM from electric and magnetic interactions between quarks. $(\Delta M)_q$ is the up and down quark mass difference.

Electromagnetic self energy of a particle appropriate to a bag model can be written as [9]

$$\frac{e^2}{4\pi}\sum_N \int_{\text{bag}} \mathrm{d}^3x \mathrm{d}^3y \int_0^\infty \frac{\mathrm{d}k}{k+\Delta E} \frac{\sin k|\mathbf{x}-\mathbf{y}|}{|\mathbf{x}-\mathbf{y}|} \times \langle P|J_\mu(\mathbf{x},0)|N\rangle\langle N|J_\mu(\mathbf{y},0)|P\rangle \tag{2}$$

where ΔE is the mass of the intermediate state N minus the external state P, the k integration is the residual of photon propagator integral. The quark current J_μ is given by

$$J_\mu(x) = \sum_\alpha Q_\alpha \bar{q}_\alpha(x)\gamma_\mu q_\alpha(x) \tag{3}$$

where Q_α and q_α are the charge and field operators of the αth quark respectively. When (3) is substituted into (2) two types of terms originate; one where a virtual photon is emitted and absorbed by the same quark and another in which virtual photon is exchanged between two different quarks. The former gives self energy of a quark and finally leads to the mass difference between the up and down quark when confined inside the bag. But its explicit estimation needs more work [8]. We thus concentrate on evaluation of the electric and magnetic interaction between a pair of quarks using bag model wavefunctions.

The contribution to mass difference due to electric interaction involves J_0 and this being a diagonal operator the intermediate state (N) can only be same as the external state (P) and one gets

$$(\Delta M)_{\mathrm{el}} = \sum_{\alpha,\beta;\alpha>\beta} C_{\alpha\beta}[I_{\alpha\beta}(R) + I_{\beta\alpha}(R)] \tag{4}$$

where R is radius of bag,

$$C_{\alpha\beta} = Q_\alpha Q_\beta \tag{5}$$

is the product of charges of the two quarks and

$$I_{\alpha\beta}(R) = \left(\frac{e^2}{4\pi}\right) N_\alpha^2 N_\beta^2 \int_0^R y\,\mathrm{d}y \left[\left(\frac{w_\beta + m_\beta}{w_\beta}\right)\left[j_0\left(\frac{x_\beta y}{R}\right)\right]^2 + \left(\frac{w_\beta - m_\beta}{w_\beta}\right) \times \left[j_1\left(\frac{x_\beta y}{R}\right)\right]^2\right] \frac{R^2}{4x_\alpha^2}\left\{\left(\frac{w_\alpha + m_\alpha}{w_\alpha}\right)\left(2y - \frac{R}{x_\alpha}\sin\frac{2x_\alpha y}{R}\right) + \left(\frac{w_\alpha - m_\alpha}{w_\alpha}\right) \times \left[2y + \frac{R}{x_\alpha}\sin\left(\frac{2x_\alpha y}{R}\right) - 4\frac{R^2}{x_\alpha^2}\frac{\sin^2(x_\alpha y/R)}{y}\right]\right\} \tag{6}$$

where N_α is the normalization constant for the wavefunctions of the quark of type α and is given by

$$(N_\alpha^2)^{-1} = R^3 j_0^2(x_\alpha)\frac{2w_\alpha(w_\alpha - (1/R)) + (m_\alpha/R)}{w_\alpha(w_\alpha - m_\alpha)} \tag{7}$$

and j's are spherical Bessel functions. m_α and w_α are mass and frequency of the αth quark in the lowest mode, respectively. w_α is given by

$$w_\alpha = \frac{[x_\alpha^2 + (m_\alpha R)^2]^{1/2}}{R} \tag{8}$$

where x_α is the root of transcendental equation, generated by the linear boundary condition of the bag model.

$$\tan x_\alpha = \frac{x_\alpha}{1 - m_\alpha R - [(m_\alpha R)^2 + x_\alpha^2]^{1/2}}. \tag{9}$$

The magnetic interaction on the other hand involves the spatial part of the quark current which is not diagonal. Thus one can write the contribution to the mass-shift due to magnetic interaction as sum of contributions from the possible intermediate

states as

$$(\Delta M)_{\text{mag}} = \sum_{N} (\Delta M)^{PN}_{\text{mag}} \tag{10}$$

with

$$(\Delta M)^{PN}_{\text{mag}} = -\sum_{\alpha,\beta;\alpha>\beta} C^{PN}_{\alpha\beta}[J_{\alpha\beta}(\Delta E, R) + J_{\beta\alpha}(\Delta E, R)] \tag{11}$$

where $C^{PN}_{\alpha\beta}$ are co-efficients which are appropriate differences of the product of quark charges and spin operators and

$$J_{\alpha\beta}(\Delta E, R) = \frac{e^2}{4\pi}\frac{8}{3\pi} N_\alpha^2 N_\beta^2 \frac{[(w_\alpha^2 - m_\alpha^2)(w_\beta^2 - m_\beta^2)]^{1/2}}{w_\alpha w_\beta} \frac{R^2}{x_\alpha^3} \int_0^\infty \mathrm{d}k \frac{k}{k + \Delta E}$$
$$\times \int \mathrm{d}y y^2 j_0\left(\frac{x_\beta y}{R}\right) j_1\left(\frac{x_\beta y}{R}\right) j_1(ky)$$
$$\times \left(\int_0^{(x_z y/R)} \mathrm{d}z \frac{\sin^2 z}{z} \sin\left(\frac{kRz}{x_\alpha}\right) - j_1(ky)\sin^2\left(\frac{x_\alpha y}{R}\right)\right) \tag{12}$$

In the limit $\Delta E \to 0$ eq. (12) reduces to the form,

$$J_{\alpha\beta}(0, R) = \frac{e^2}{4\pi}\left(\frac{1}{9}\right) N_\alpha^2 N_\beta^2 \frac{[(w_\alpha^2 - m_\alpha^2)(w_\beta^2 - m_\beta^2)]^{1/2}}{w_\alpha w_\beta}$$
$$\times \int_0^R \mathrm{d}y\, j_0\left(\frac{x_\beta y}{R}\right) j_1\left(\frac{x_\beta y}{R}\right) \frac{R^3}{x_\alpha^3}$$
$$\times \left(4y - \frac{3R}{x_\alpha}\sin\left(\frac{2x_\alpha y}{R}\right) + 2y\cos\left(\frac{2x_\alpha y}{R}\right)\right). \tag{13}$$

For the heavy t-quark, as stated earlier, we will use the following expansion for w_α, as suggested by Ponce [11]

$$w_t = X_t + \frac{\pi^2}{2X_t} - \frac{\pi^2}{2X_t^2} + \cdots \tag{14}$$

where $X_t = m_t R$. The corresponding x_t will be obtained from

$$x_t = (w_t^2 - m_t^2)R \tag{15}$$

It is also worth mentioning here that in evaluating the magnetic interaction we have considered the contributions of the intermediate states whose wavefunctions are totally symmetric in flavor and spin. To be specific, we have omitted the contributions of T_0^+ hadron intermediate state with flavor structure as $t(ud)_{\text{antisym}}$ to $J_{\alpha\beta}$ and $J_{\beta\alpha}$ for T_1^+ and T_1^{*+} hadrons since the co-efficients $C_{\alpha\beta}$ will have only one non-zero value for heavy quark-light quark combinations. The contribution of T_0^+ intermediate state towards $(\Delta M)_{\text{mag}}$ for T_1^+ and T_1^{*+} will not, thus, significantly alter the values estimated here.

3. Numerical results

In tables 1 and 2 we have presented magnetic co-efficients for mesons and baryons repectively, which are appropriate difference of the product of charges and spin

Table 1. The magnetic co-efficients of the mesons.

Particle $P(q_1 q_2)$	Intermediate state N	Co-efficients $C_{\alpha\beta}^{PN}$
$T^+(t\bar{d})$	T^+	0
	T^{*+}	$-\frac{2}{3}$
$T^0(t\bar{u})$	T^0	0
	T^{*0}	$\frac{4}{3}$
$T^{*+}(t\bar{d})$	T^{*+}	$\frac{4}{9}$
	T^+	$-\frac{2}{9}$
$T^{*0}(t\bar{u})$	T^{*0}	$-\frac{8}{9}$
	T^0	$\frac{4}{9}$

Table 2. The magnetic co-efficients of baryons.

Particle $P(q_1 q_2 q_3)$	Intermediate state N	Co-efficients $C_{\alpha\beta}^{PN}$ $q_1 q_2$	$q_1 q_3$	$q_2 q_3$
$T_u^{++}(ttu)$	T_u^{++}	$\frac{16}{27}$	$-\frac{8}{27}$	$-\frac{8}{27}$
	T_u^{*++}	$\frac{8}{27}$	$-\frac{16}{27}$	$-\frac{16}{27}$
$T_d^{+}(ttd)$	T_d^{+}	$\frac{16}{27}$	$\frac{4}{27}$	$\frac{4}{27}$
	T_d^{*+}	$\frac{8}{27}$	$\frac{8}{27}$	$\frac{8}{27}$
$T_1^{++}(tuu)$	T_1^{++}	$-\frac{8}{27}$	$-\frac{8}{27}$	$\frac{16}{27}$
	T_1^{*++}	$-\frac{16}{27}$	$-\frac{16}{27}$	$\frac{8}{27}$
$T_1^{+}(tud)$	T_1^{+}	$-\frac{8}{27}$	$\frac{4}{27}$	$-\frac{8}{27}$
	T_1^{*+}	$-\frac{16}{27}$	$\frac{8}{27}$	$-\frac{4}{27}$
$T_1^{0}(tdd)$	T_1^{0}	$\frac{4}{27}$	$\frac{4}{27}$	$\frac{4}{27}$
	T_1^{*0}	$\frac{8}{27}$	$\frac{8}{27}$	$\frac{2}{27}$
$T_u^{*++}(ttu)$	T_u^{*++}	$\frac{20}{27}$	$\frac{20}{27}$	$\frac{20}{27}$
	T_u^{++}	$\frac{4}{27}$	$-\frac{8}{27}$	$-\frac{8}{27}$
$T_d^{*+}(ttd)$	T_d^{*+}	$\frac{20}{27}$	$-\frac{10}{27}$	$-\frac{10}{27}$
	T_d^{+}	$\frac{4}{27}$	$\frac{4}{27}$	$\frac{4}{27}$
$T_1^{*++}(tuu)$	T_1^{*++}	$\frac{20}{27}$	$\frac{20}{27}$	$\frac{20}{27}$
	T_1^{++}	$-\frac{8}{27}$	$-\frac{8}{27}$	$\frac{4}{27}$
$T_1^{*+}(tud)$	T_1^{*+}	$\frac{20}{27}$	$-\frac{10}{27}$	$-\frac{10}{27}$
	T_1^{+}	$-\frac{8}{27}$	$\frac{4}{27}$	$-\frac{2}{27}$
$T_1^{*0}(tdd)$	T_1^{*0}	$-\frac{10}{27}$	$-\frac{10}{27}$	$\frac{5}{27}$
	T_1^{0}	$\frac{4}{27}$	$\frac{4}{27}$	$\frac{1}{27}$

operators. Important parameters like bag radius and quark eigenvalues $x_\alpha, \alpha = u, d, t$ for each of the hadrons are given in table 3. We have calculated numerically the integrals $I_{\alpha\beta}(R)$ and $J_{\alpha\beta}(\Delta E, R)$ for various t-flavored hadrons taking $m_u = m_d = 0$ and $m_t = 150\,\text{GeV}$. The results are given in tables 4, 5 and 6. The consequent values of (i) $(\Delta M)_{\text{el}}$ (ii) $(\Delta M)_{\text{mag}}$ are given in table 7. Since an exact evaluation of $(\Delta M)_q$ part of eqn. (1) in the framework of bag model has not been done as of yet, we make the usual assumption of a constant up and down quark mass difference and determine the same from $m_{D^+} - m_{D^0}$. Thus we work with $(\Delta m)_q = -2{\cdot}06 \pm 0{\cdot}28$ MeV determined

Table 3. Radius R and quark eigenvalues x_α, $(\alpha = u, d, t)$ for each of the hadrons.

Particle	R (in GeV^{-1})	x_t	$x_u = x_d$
T_u^{++}	4·5045	3·1392827	2·04
T_d^{+}	4·5045	3·1392827	2·04
T_u^{*++}	4·5096	3·1392853	2·04
T_d^{*+}	4·5096	3·1392853	2·04
T_1^{++}	5·2826	3·1396230	2·04
T_1^{+}	5·2826	3·1396230	2·04
T_1^{0}	5·2826	3·1396230	2·04
T_1^{*++}	5·2868	3·1396246	2·04
T_1^{*+}	5·2868	3·1396246	2·04
T_1^{*0}	5·2868	3·1396246	2·04
T^0	4·4944	3·1392775	2·04
T^+	4·4944	3·1392775	2·04
T^{*0}	4·5045	3·1392827	2·04
T^{*+}	4·5045	3·1392827	2·04

Table 4. Evaluation of electric and magnetic integrals of mesons. The states within parantheses in column 3 denote the intermediate states. The integrals are defined in eqs (6), (12) and (13).

Particle	$I_{\alpha\beta} + I_{\beta\alpha}$ (in MeV)	$J_{\alpha\beta} + J_{\beta\alpha}$ (in $\text{MeV} \times 10^{-3}$)
T	2·3665	1·0075 (T) 1·7317 (T^*)
T^*	2·3610	1·0030 (T^*) 0·7770 (T)

Table 5. Electric interaction integrals $I_{\alpha\beta} + I_{\beta\alpha}$ for baryons.

Particle	Integrals q_1q_2	$I_{\alpha\beta}(R) + I_{\beta\alpha}(R)$ (in MeV) q_1q_3	q_2q_3
T_u^{++}	2·9680	2·3610	2·3610
T_d^{+}	2·9680	2·3610	2·3610
T_1^{++}	2·0137	2·0137	1·7560
T_1^{+}	2·0137	2·0137	1·7560
T_1^{0}	2·0137	2·0137	1·7560
T_u^{*++}	2·9640	2·3583	2·3583
T_d^{*+}	2·9640	2·3583	2·3583
T_1^{*++}	2·0123	2·0123	1·7548
T_1^{*+}	2·0123	2·0123	1·7548
T_1^{*0}	2·0123	2·0123	1·7548

Table 6. Magnetic interaction integrals $J_{\alpha\beta}(\Delta E, R) + J_{\beta\alpha}(\Delta E, R)$ for baryons.

Particle $P(q_1q_2q_3)$	Intermediate states $N(q_1q_2q_3)$	Integrals q_1q_2	$J_{\alpha\beta}(\Delta E, R) + J_{\beta\alpha}(\Delta E, R)$ (in MeV) q_1q_3	q_2q_3
T_u^{++}	T_u^{++}	$0{\cdot}5114 \times 10^{-5}$	$1{\cdot}003 \times 10^{-3}$	$1{\cdot}003 \times 10^{-3}$
	T_u^{*++}	$0{\cdot}5602 \times 10^{-5}$	$1{\cdot}135 \times 10^{-3}$	$1{\cdot}135 \times 10^{-3}$
T_d^{+}	T_d^{+}	$0{\cdot}5114 \times 10^{-5}$	$1{\cdot}003 \times 10^{-3}$	$1{\cdot}003 \times 10^{-3}$
	T_d^{*+}	$0{\cdot}5602 \times 10^{-5}$	$1{\cdot}135 \times 10^{-3}$	$1{\cdot}135 \times 10^{-3}$
T_1^{++}	T_1^{++}	$0{\cdot}7295 \times 10^{-3}$	$0{\cdot}7295 \times 10^{-3}$	0·1867
	T_1^{*++}	$0{\cdot}7971 \times 10^{-3}$	$0{\cdot}7971 \times 10^{-3}$	0·1952
T_1^{+}	T_1^{+}	$0{\cdot}7295 \times 10^{-3}$	$0{\cdot}7295 \times 10^{-3}$	0·1867
	T_1^{*+}	$0{\cdot}7971 \times 10^{-3}$	$0{\cdot}7971 \times 10^{-3}$	0·1952
T_1^{0}	T_1^{0}	$0{\cdot}7295 \times 10^{-3}$	$0{\cdot}7295 \times 10^{-3}$	0·1867
	T_1^{*0}	$0{\cdot}7971 \times 10^{-3}$	$0{\cdot}7971 \times 10^{-3}$	0·1952
T_d^{*+}	T_d^{*+}	$0{\cdot}5096 \times 10^{-5}$	$1{\cdot}001 \times 10^{-3}$	$1{\cdot}001 \times 10^{-3}$
	T_d^{+}	$0{\cdot}5326 \times 10^{-5}$	$1{\cdot}086 \times 10^{-3}$	$1{\cdot}086 \times 10^{-3}$
T_u^{*++}	T_u^{*++}	$0{\cdot}5096 \times 10^{-5}$	$1{\cdot}001 \times 10^{-3}$	$1{\cdot}001 \times 10^{-3}$
	T_u^{++}	$0{\cdot}5326 \times 10^{-5}$	$1{\cdot}086 \times 10^{-3}$	$1{\cdot}086 \times 10^{-3}$
T_1^{*++}	T_1^{*++}	$0{\cdot}7283 \times 10^{-3}$	$0{\cdot}7283 \times 10^{-3}$	0·1866
	T_1^{++}	$0{\cdot}7797 \times 10^{-3}$	$0{\cdot}7797 \times 10^{-3}$	0·1903
T_1^{*+}	T_1^{*+}	$0{\cdot}7283 \times 10^{-3}$	$0{\cdot}7283 \times 10^{-3}$	0·1866
	T_1^{+}	$0{\cdot}7797 \times 10^{-3}$	$0{\cdot}7797 \times 10^{-3}$	0·1903
T_1^{*0}	T_1^{*0}	$0{\cdot}7283 \times 10^{-3}$	$0{\cdot}7283 \times 10^{-3}$	0·1866
	T_1^{0}	$0{\cdot}7797 \times 10^{-3}$	$0{\cdot}7797 \times 10^{-3}$	0·1903

Table 7. Predicted mass difference for t-flavored hadrons.

Mass difference	$(\Delta M)_{el}$ (in MeV)	$(\Delta M)_{mag}$ (in MeV)	$(\Delta M)_q = m_u - m_d$ (in MeV)	$(\Delta M)_{total}$ (in MeV)
$T_u^{++} - T_d^{++}$	3·148	0·0029	$-2·06 \pm 0·28$	$1·0909 \pm 0·28$
$T_1^{++} - T_1^{+}$	2·513	$-0·2517$	$-2·06 \pm 0·28$	$0·2013 \pm 0·28$
$T_1^{+} - T_1^{0}$	0·7571	0·1274	$-2·06 \pm 0·28$	$-1·1755 \pm 0·28$
$T_u^{*++} - T_d^{*+}$	3·1444	$-0·0013$	$-2·06 \pm 0·28$	$1·0831 \pm 0·28$
$T_1^{*++} - T_1^{*+}$	2·5114	$-0·2498$	$-2·06 \pm 0·28$	$0·2016 \pm 0·28$
$T_1^{*+} - T_1^{*0}$	0·7566	0·1250	$-2·06 \pm 0·28$	$-1·1784 \pm 0·28$
$T^{+} - T^{0}$	1·5776	0·0035	$-2·06 \pm 0·28$	$3·6411 \pm 0·28$
$T^{*+} - T^{*0}$	1·574	$-0·0008$	$-2·06 \pm 0·28$	$3·6332 \pm 0·28$

from $m_{D^+} - m_{D^0}$, the error coming from the error in D-mass difference [5]. Good agreement of electromagnetic mass difference for b-mesons [5], [12] based on this value of $(\Delta M)_q$ encourages us to stick to it as a good working hypothesis also for the t-sector. Combining now three pieces of contributions $(\Delta M)_{el}$, $(\Delta M)_{mag}$ and $(\Delta M)_q$, we estimate mass differences of hadrons and have presented it in the last column of table 7.

4. Discussion

Keeping in view a possible t-quark discovery in $p\bar{p}$ collider run at Fermilab, we have extended our previous work on t-flavored hadron mass calculation to estimate electromagnetic mass differences for t-flavored mesons of spin 0 and 1 and t-flavored baryons carrying spin $\frac{1}{2}$ and $\frac{3}{2}$.

The MIT bagmodel and its modification have been used to estimate the electric and magnetic interactions of the quarks inside the hadron. The general feature of the magnetic interaction contribution staying small compared with the electric interaction is also persistent for the t-flavored hadrons. The up and down quark mass difference, however, has not lent itself to a bag model calculation so far. A parametric expression such as $(\Delta M)_q = (A/R) + Bn_s + Cn_c$ where n_s and n_c are the number of strange and charm quarks were used earlier [9]. The predictions of electromagnetic mass differences on two extreme parametrization like $C = B$ and $C = (m_c/m_s)B$ with A and B obtained by fitting with known electromagnetic mass differences does not produce reasonable agreement with the experimental values for charmed mesons in either case [9]. Thus we have carried the assumption of a constant $(\Delta M)_q = -2·06 \pm 0·28$ MeV, that yielded reasonable agreement for b-flavored mesons to the t-quark sector.

The degree of agreement of the results presented here, we believe, will provide a test of the model used and shed light on the nature of confinement of heavy quarks as well.

Acknowledgements

We gratefully acknowledge some useful discussions with Prof. N Barik and Dr A R Panda.

References

[1] M Gell-mann, *Phys. Lett.* **8**, 214 (1964)
G Zweig, CERN report no. 8419/TH-412 (1964)
[2] J J Aubert *et al*, *Phys. Rev. Lett.* **33**, 1404 (1974)
J E Augustin *et al*, *Phys. Rev. Lett.* **33**, 1406 (1974)
G Goldhaber *et al*, *Phys. Rev. Lett.* **37**, 255 (1976)
B Knapp *et al*, *Phys. Rev. Lett.* **37**, 882 (1976)
S W Herb *et al*, *Phys. Rev. Lett.* **39**, 252 (1976)
W R Innes *et al*, *Phys. Rev. Lett.* **39**, 1240 (1976)
[3] G Kane, *Modern elementary particle physics*, (Addison-Wesley, London, 1987)
JADE collaboration, W Bartoi *et al*, *Phys. Lett.* **B146**, 437 (1984)
[4] V Barger and S Pakvasa, *Phys. Lett.* **B81**, 195 (1979)
G L Kane and M E Peskin, *Nucl. Phys.* **B195**, 29 (1982)
[5] K Hikasa *et al Review of particle properties, Phys. Rev.* **D45**, 11 Part II (1992)
[6] J Ellis, G L Fogli and E Lisi, CERN preprint CERN-TH-6568 (1992)
[7] S K Nayak and L P Singh, *Int. J. Mod. Phys.* **A6**, 4331 (1991)
[8] See for example, A Chodos and C B Thorn, *Nucl. Phys.* **B104** 21 (1976)
W P Hays, Ph D Thesis, MIT, 1976 (unpublished)
[9] N G Deshpande, D A Dicus, K Johnson and V L Teplitz, *Phys. Rev. Lett.* **37**, 1305 (1976)
N G Deshpande, D A Dicus, K Johnson and V L Teplitz, *Phys. Rev.* **D15**, 1885 (1977)
[10] T DeGrand, R L Jaffe, K Johnson and J Kiskis, *Phys. Rev.* **D12**, 2060 (1975)
R L Jaffe and J Kiskis, *Phys. Rev.* **13**, 1355 (1976)
[11] W A Ponce, *Phys. Rev.* **D19**, 2197 (1979)
[12] L P Singh, *Phys. Rev.* **D22**, 2224 (1980)

PRAMANA
— journal of
physics

© Printed in India

Vol. 43, No. 2,
August 1994
pp. 165–168

Single nucleon distribution based on shell-model and matrix ensemble theory

NAZAKAT ULLAH
Tata Institute of Fundamental Research, Bombay 400 005, India

MS received 25 April 1994

Abstract. An expression for the density of single nucleons in a heavy spherical nucleus is derived using the shell-model and matrix ensembles. It is shown that the theoretical expression gives an excellent fit to the density of nucleons for the nucleus ^{197}Au obtained using *e*-scattering data.

Keywords. Distribution of single nucleons; heavy spherical nuclei.

PACS Nos 21·60; 21·90

Since the early days of nuclear structure, there has been much interest in the study of distribution of nucleons in a nucleus. The single nucleon distribution plays an important role in the study of many-nucleon system, e.g. the direct part of the two body matrix elements can be calculated in terms of it. Even though very good fits to experimental data have been obtained using the phenomenological forms of radial density distribution given by either a modified form of Fermi distribution [1] or by a Fourier-Bessel expansion [2] no attempt has been made to derive an analytic form of the density distribution for heavy nuclei using a more fundamental approach of employing the complete set of wave functions given by the shell model. In the analytic work, like the calculation of two-body matrix elements, one would like very much to have a radial distribution which not only gives a good fit but also could be used in deriving analytic expressions for other quantities of interest.

As the density distribution is an average quantity of a many-body system, matrix ensembles can be employed to derive analytic expressions for it. The matrix ensembles in many-body physics were first introduced by Wigner [3] who had studied the distribution of the eigenvalues of a random matrix. The N eigenvalues of a random Hermitian matrix behave the same way as N nucleons moving in one dimension in an average harmonic oscillator potential.

In the present work we would like to develop a theory of single nucleon distribution using shell model and matrix ensembles.

Let us consider a spherical nucleus in which single nucleons fully occupy the single particle levels up to the oscillator quanta N_0. The exact ground state wave function Ψ can then be written as

$$\Psi = \lambda\left[\Phi_0 + \sum_{\mu=1} a_\mu \Phi_\mu\right], \tag{1}$$

where Φ_0 is the closed shell wave function and Φ_μ are all the other particle-hole

wave functions. a_μ are the expansion coefficients and λ is the normalization constant. The single nucleon wave function is given by

$$N_{nl}\exp(-\tfrac{1}{2}\alpha^2 r^2) r^l L_{n-1}^{(l+(1/2))}(\alpha^2 r^2)$$

multiplied by a spherical harmonic Y_{lm} and a spin and isospin wave function, N_{nl} being normalization constant and α, the harmonic oscillator parameter, l the orbital angular momentum and n the radial quantum number.

We next calculate the Wigner transform $f(\bar{r}, \bar{p})$ for Φ_0. It is given by [4]

$$f(\bar{r}, \bar{p}) = K \frac{1}{2\pi i} \oint \frac{dZ}{Z^{N_0+1}} (1+Z)^{-3}(1-Z)^{-1} \exp\left[-\left(\frac{p^2}{\alpha^2} + \alpha^2 r^2\right)\left(\frac{1-Z}{1+Z}\right)\right], \tag{2}$$

where K is a constant.

By integrating over momentum $\bar{p}$, we can obtain an expression for the single nucleon radial density $\rho(r)$.

As was mentioned in the introductory part, new techniques have recently been given [5] to evaluate the contour integral given by expression (2) when N_0 is large for the one dimensional case. These approximations show that density has two parts, one part is the well-known Wigner semi circular distribution and the other is an exponential tail. One finds the same kind of behaviour in three dimensions also. Since our aim is to take care of most of the effects of configuration interaction, we write the density in a parametrized form. The density $\rho(r)$ for heavy spherical nuclei can thus be written as

$$\rho(r) = K[(b^2 + a^2 - r^2)^{3/2} + A\exp(-\lambda(r-b) - \beta(r-b)^2)], \tag{3}$$

where $K, b, a, A, \lambda, \beta$ are parameters. The range of the first part of the density is $0 \leqslant r \leqslant b$, while the tail part given by the exponential has the range $b \leqslant r \leqslant \infty$. In expression (3), there are only three independent parameters b, a, β. The parameter K is fixed by the normalization condition:

$$\int_0^\infty dr\, r^2 \rho(r) = 1. \tag{4a}$$

The parameters A, λ are connected to b, a by the condition that the value of $\rho(r)$ and its derivative be continuous at $r = b$, which gives

$$A = a^3, \tag{4b}$$

$$\lambda = \frac{3b}{a^2}. \tag{4c}$$

We point out here that in our earlier work [6] we had used the Fourier transform of density and were able to obtain only the dominant part. The present formulation based on the ideas of matrix ensemble theory has given us the complete expression including the tail of the distribution. As will be shown shortly, expression (3) gives excellent fit to the experimental density.

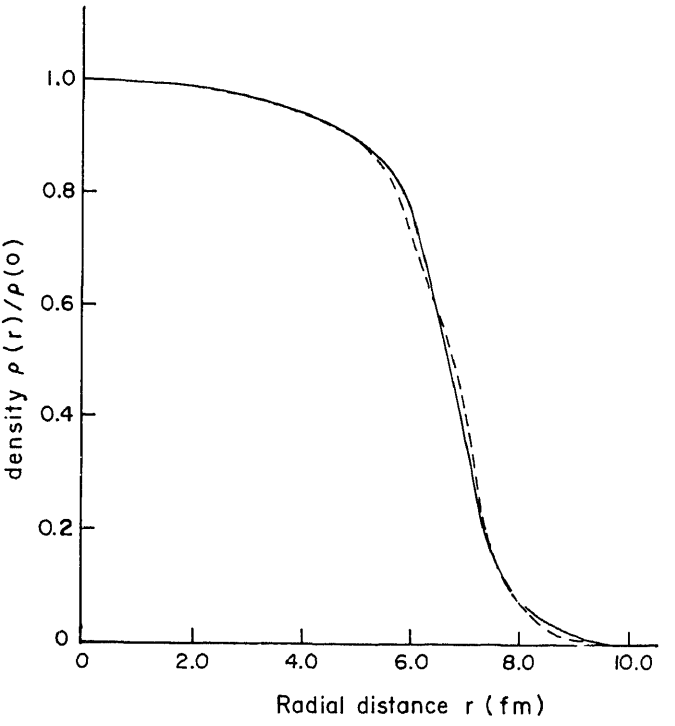

Figure 1. Nucleon density $\rho(r)/\rho(o)$ for ^{197}Au (i) using e-scattering data (smooth curve) and (ii) using theoretical expression (3) with parameters $a = 18{\cdot}53$, $b = 5{\cdot}00$, $\beta = 0{\cdot}217$ (---curve).

Before we apply expression (3) to an actual nucleus, we note that expression (3) can reproduce the general features of the single nucleon density distribution. If the parameter a is much larger than b, then it decreases slowly over the distance b. Beyond b it can decrease fairly rapidly because of the exponential function. Thus it reproduces the general form of the density in heavy nuclei. In order to see how good a fit we get for an actual nucleus we apply it to the density distribution in the nucleus ^{197}Au. In principle the best values of the three parameters b, a, β should be obtained by a least square fit, but in the present study, the parameters a, β have been obtained by comparing the measured $\rho(r)/\rho(0)$ with the calculated ones at $r = 5$ fm and $r = 8$ fm. The value of the parameter b which gives the range of the dominant component of the density is obtained by best fitting to be $b = 5{\cdot}0$. The values of a, β are: $a = 18{\cdot}531$ and $\beta = 0{\cdot}217$. We see from figure 1 that with these paremeters the theoretical expression (3) gives an extremely nice fit to the density of nucleons in the nucleus ^{197}Au. Further using these parameters we find that the equivalent uniform radius R of the nucleus ^{197}Au turns out to be 6·874 fm in excellent agreement with its experimented value of 6·87 fm.

Lastly we remark that because of the form of Wigner transform given by expression (2), the density of nucleons in the momentum space can be obtained by a scaling transformation. A detailed analysis of these features and further extension of this work to include higher correction terms to $\rho(r)$ is to be taken up shortly and intended to be published elsewhere later.

References

[1] D R Yennie, D G Ravenhall and R N Wilson, *Phys. Rev.* **95**, 500 (1954)
M A Preston, *Physics of the nucleus* (Addison-Wesley, Reading (Mass.), 1962)
[2] H Euteneuer, J Friedrich and N Voegler, *Nucl. Phys.* **A298**, 452 (1978).
[3] E P Wigner, *Can. Math. Cong. Proc.* (Toronto Univ. Press, 1957) p.174
[4] Nazakat Ullah, *Fortschr. Phys.* **37**, 838 (1989)
[5] J J M Verbaarschot, H A Weidenmüller and M R Zirnbauer, *Phys. Lett.* **B149**, 263 (1984)
[6] Nazakat Ullah, *Pramana-J. Phys.* **28**, 641 (1987)

PRAMANA
— journal of
physics

© Printed in India

Vol. 43, No. 2,
August 1994
pp. 169–174

Electron impact double ionization of Ba and Ba^+

L K JHA, S N CHATTERJEE and B N ROY
Department of Physics, B.B.A. Bihar University, Muzaffarpur 842001, India

MS received 9 March 1993; revised 15 March 1994

Abstract. Electron impact double ionization cross-sections for Ba and Ba^+ have been calculated in the binary encounter approximation. Hartree-Fock velocity distribution has been used for the first ejected electron and a hydrogenic velocity distribution for the second. For Ba^+ the focusing effects of the target ion on the incident electron have been incorporated in the calculations. Contributions from ionization-autoionization to the ionization cross-sections, as observed in experiments, have been included in the present work. The calculated results show structures as observed in recent experiments.

Keywords. Electron impact; single ionization; double ionization; ionization-autoionization.

PACS No. 34·50

1. Introduction

Electron impact single and multiple (particularly double) ionization processes of atoms and ions are of fundamental importance (see [1] and references quoted therein). In some experimental studies of electron impact ionization of heavy atoms and ions large anomalous features have been observed for double ionization of the systems close to $Z = 56$ (Ba) at electron energies less than two times the threshold [2]. These features have been interpreted as giant scattering resonances appearing in the scattered electron channel [3].

In many cases, besides direct ionization, electron impact double ionization of atoms and ions takes place due to several alternative mechanisms. In some cases these indirect ionization channels have been found to dominate over the direct ionization process. A single ionization event ejecting an inner shell electron can leave the product in an excited state which may subsequently cascade through several autoionizing levels resulting in relatively large net multiple (mainly double) ionization [4–6].

Due to complexities in quantal studies of direct double ionization the calculations are limited to a few lighter targets only [7–10]. Hence for heavy targets, the results of single ionization cross-sections for the inner shell involved are taken as a measure of total double ionization cross-sections. This cannot be strictly justified because the contributions from direct double ionization are small but not insignificant. On the other hand the modified binary encounter model proposed by Roy and Rai [11] based on Gryzinski's [12] double binary encounter model, has been successfully used for calculations of electron impact direct double ionization cross-sections of a number of atomic systems [13, 14]. Later on the contributions from inner shell ionization-autoionization to the electron impact double ionization of some atoms and ions were incorporated in the binary encounter calculations [1, 15, 16]. In the present work we extend the above calculations to more complex systems, namely Ba and Ba^+.

2. Calculation

The electron impact double ionization cross-section for an atomic system including the contribution from the inner shell ionization-autoionization process (Auger transition) is given by

$$Q^{ii}(T) = Q_{\mathrm{D}}^{ii} + Q_{\mathrm{A}}^{ii}$$

where Q_{D}^{ii} stands for the contribution to the double ionization cross-section from direct ejection of two electrons and Q_{A}^{ii} is that from the Auger emission. For Ba the expression for Q_{D}^{ii} is given by

$$Q_{\mathrm{D}}^{ii} = \frac{2n_e(n_e-1)}{4\pi\bar{r}^2}\int_{t=0}^{\infty}\int_{U_i}^{E_q-U_{ii}}\left\{\frac{2}{(s^2+t^2+1)U_i}\left[\left(\frac{1}{(\Delta E)^2}+\frac{4t^2U_i}{3(\Delta E)^3}\right)\right.\right.$$
$$+\left(\frac{1}{(s^2U_i+U_i-\Delta E)^2}+\frac{4t^2U_i}{3(s^2U_i+U_i-\Delta E)^3}\right)-\left.\frac{\phi}{\Delta E(s^2U_i+U_i-\Delta E)}\right]$$
$$\left.\alpha f(t)U_i^{1/2}\right\}\mathrm{d}(\Delta E)\mathrm{d}t \times 8{\cdot}797\times10^{-17}(\pi(a_0^2)) \qquad (1)$$

and that of Q_{A}^{ii} is given by

$$Q_{\mathrm{A}}^{ii} = an_e\int_0^{\infty}\left\{\frac{4}{(s^2+t^2+1)U_i^2}\left[\frac{s^2-1}{s^2}+\frac{2t^2}{3}\left(\frac{s^4-1}{s^4}\right)-\frac{\phi\ln s^2}{(s^2+1)}\right]\right\}$$
$$f(t)U_i^{1/2}\mathrm{d}t \qquad (2)$$

where the various symbols appearing in the above equations have already been defined by Roy and Rai [11] and Chatterjee and Roy [1].

In the case of Ba^+, as the electron reaches the neighbourhood of the positive ion its kinetic energy is increased and impact parameter is reduced due to Coulombic attraction. Thomas and Garcia [17] have shown that the effects of these two physical processes can be approximately incorporated in the ionization cross-section through the relation

$$\sigma_{\mathrm{I}}(E_1) = \sigma_{\mathrm{I}}(E_1')\left[\frac{1}{2}+\frac{1}{2}\left(1+\frac{Ze^2}{E_1\xi}\right)^{1/2}\right]^2$$

where E_1 is the incident energy, Ze is the charge on the target ion, $\sigma_{\mathrm{I}}(E_1')$ is the ionization cross-section at the increased electron energy E_1 and ξ is the collision radius whose value depends upon the ionic radius and electron–electron separation in the shell. Following the above prescription the expressions for Q_{D}^{ii} and Q_{A}^{ii} for Ba^+ are obtained after replacing s by s' in (1) and (2) and multiplying each of them by $(s+s')^2/4s^2$ where $s'^2 = s^2 + (2Z/\xi U_i)$.

In the derivation of Q_{D}^{ii} an accurate Hartree-Fock (HF) velocity distribution and a hydrogenic velocity distribution have been used while considering the ejection of the first and the second electron, respectively. The use of a HF velocity distribution in both cases would have been appropriate but this would give rise to complex numerical integration in the evaluation of Q_{D}^{ii}. Contributions of ionization from inner shells have also been included in the direct double ionization cross-section.

In the present work we have used the HF binding energy of shells as reported by Mclean and Mclean [18]. For shell radii of Ba the quantum mechanical values of points of maximum radial probability density reported by Desclaux [19] have been used. For Ba^+ the HF value of $\langle r \rangle$ reported by Mclean and Mclean [18] have been used for shell radii. Momentum distribution function for Ba and Ba^+ have been constructed using HF radial distribution reported in [18].

Here we point out that after the ejection of one electron the target becomes Ba^+ (for Ba) and Ba^{2+} (for Ba^+). Hence one would expect the use of the binding energies of Ba^+ and Ba^{2+} while considering the ejection of the second electron. However, we have used the binding energies of Ba and Ba^+ while considering the ejection of both the electrons. This consideration is physically justified at high impact energies so that the ejection of two electrons may be supposed to be simultaneous, leaving no time for the target to relax after the ejection of the first electron. This choice is expected to overestimate the cross-section close to the threshold but would be more appropriate with increase in impact energy.

At this stage we mention that correlation plays an important role in the double ionization process. In the direct double ionization calculations one should consider correlation of events called dynamic correlation as well as electron–electron correlation [10]. The present calculations, based on Gryzinski's [12] double binary encounter model, consider the correlation of events. Moreover, one of the two binary encounter processes suggested by Gryzinski in which the first ejected electron knocks out the second electron partly takes into account electron–electron correlation [20]. The electron–electron correlation is taken into account in the theoretical studies of double ionization process by the use of correlated wave functions for the target electrons e.g. configuration interaction approach based on Slater–Condon theory, multi-configuration Hartree Fock (HF) approach used by Fischer (see Griffin and Pindzola [21]). Calculations using these wave functions are difficult to perform, particularly for heavier targets, as they require extensive computational work. HF wave functions consider the electron-electron correlation to some extent through antisymmetrization [21]. Moreover, for fast projectiles the effects of electron-electron correlation may not be significant [10]. Therefore, the use of HF wave function in the studies of double ionization processes using the BEA is reasonable.

3. Results and discussion

Our results for barium have been presented in figure 1 along with the recent experimental observations of Dettmann and Karstensen [22] and calculation of McGuire [23]. Calculated results of McGuire are singly peaked and are lower than the experimental cross-sections throughout the energy range.

The maxima obtained in the experimental observations [22] have been attributed to the ionization processes involving O shell and N_4 or N_5 shell, respectively. The present direct double ionization cross-sections include, besides the valence shell ionization the contributions from the process in which one electron is ejected from the valence shell and the other from inner shell (5s or 5p). Besides this we have also included the contributions of ionization-autoionization from 4d subshell. In the latter calculations we have evaluated the electron impact single ionization cross-sections for the 4d subshell of Ba and taken the same as the contribution from ionization-autoionization to the double ionization cross-section assuming the branching ratio for the process equal to unity, due to non-availability of the same in literature.

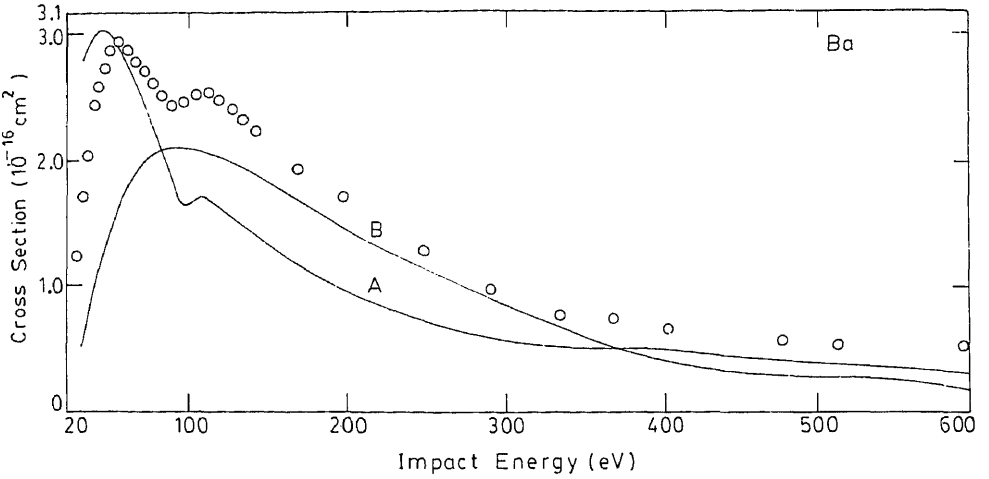

Figure 1. Results for Ba. A: Present results; B: Calculations of McGuire [23]; O: Experimental observations of Dettmann and Karstensen [22].

The present calculations also show two peaks at impact energies of 45 eV and 108 eV respectively. Positions of these peaks are close to those observed in experiments. The calculated cross-section (about $3{\cdot}0 \times 10^{-16}$ cm^2) at the first peak is slightly higher than its experimental counterpart (about $2{\cdot}85 \times 10^{-16}$ cm^2) but the present value of the second peak (about $1{\cdot}7 \times 10^{-16}$ cm^2) is lower than the corresponding measured value (about $2{\cdot}5 \times 10^{-16}$ cm^2). Moreover, below 50 eV impact energy calculated results are higher than the experimental observations whereas beyond this the present values are lower. The overestimation at low impact energies might be due to the use of binding energy of neutral barium for the ejection of both the electrons while evaluating direct double ionization cross-sections and use of a hydrogenic velocity distribution for the second ejected electron. In spite of these discrepancies the present results are always within a factor of 2 from the experimental observations. In the energy region of 80 eV to 370 eV the calculated results of McGuire are closer to experiment as compared to the present cross-sections. However, the calculations of McGuire fail to exhibit the structure in cross-section curve found in experiment as well as in the present study.

Figure 2 shows the results of Ba^+. Calculated cross-sections have been compared with the experimental measurements of Hirayama *et al* [24]. Experimental cross-section curve has a broad rise at about 50 eV and shows a steep rise around 85 eV impact energy.The cross-section has a sharp maximum at about 115 eV and exhibits a small but distinct shoulder around 200 eV. The structure in the ionization function above 85 eV has been attributed to 4d ionization followed by autoionization of the residual ion expressed as $Ba^+ (4d^{10}\,5s^2\,5p^6\,6s) \rightarrow Ba^{2+}(4d^9\,5s^2\,5p^6\,6s) + e \rightarrow Ba^{3+}(4d^{10}\,5s^2\,5p^5) + 2e$. The shoulder-like structure observed around 200 eV is considered to be due to the second maximum in the cross-section function for the 4d ionization (ionization energy of 114 eV). The broad rise ranging from 50 eV to 90 eV impact energy is a specific feature of Ba^+ ion. This structure is attributed to the ionization of the 5s-electron followed by autoionization expressed as $Ba^+ (5s^2\,5p^6\,6s) \rightarrow Ba^{2+}(5s\,5p^6\,6s) + e \rightarrow Ba^{3+}(5s^2\,5p^5) + 2e$ considering that the binding energy (46·3 eV) of

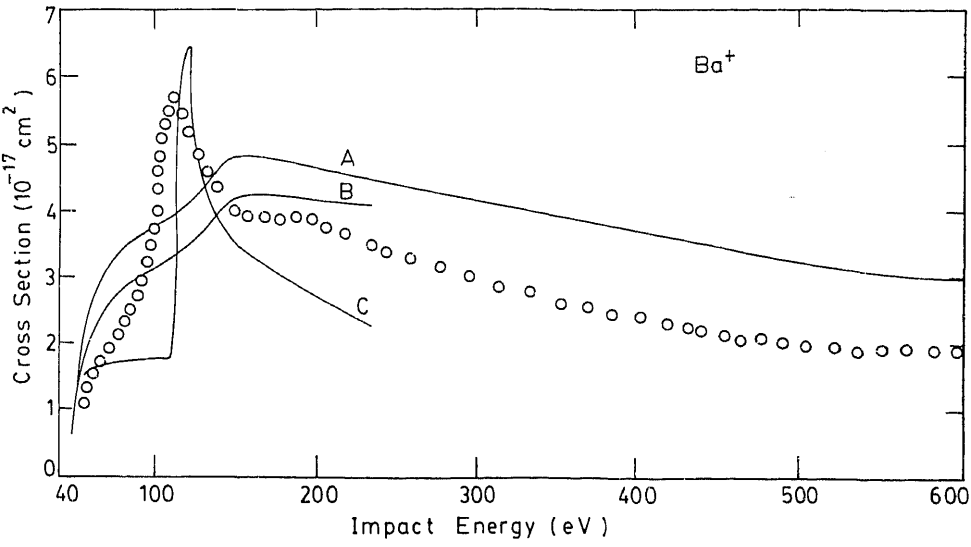

Figure 2. Results for Ba^+. A: Present results; B: Sum of the present values of single ionization cross-sections for 5s and 4d shells; C: The same as curve B calculated by Younger [25]; O: Experimental results of Hirayama *et al* [24].

5s electron in Ba^+ is close to threshold energy (about 45 eV as quoted by Hirayama *et al*) of double ionization of Ba^+.

In the present calculations of direct double ionization we have included the contribution from the processes in which one electron is ejected from the valence shell and the other from an inner shell (5p or 5s or 4d). We have also calculated the single ionization cross-sections for 5s and 4d and have taken the values obtained as the contributions of inner shell ionization-autoionization to electron impact double ionization cross-section. The present cross-section curve also shows two shoulder-like structures at impact energies of about 85 eV and 147 eV but it does not show the sharp peak at about 115 eV observed in experiment. The experimental peak has been attributed to the excitation of 4d-electron to states connected to the double autoionization e.g. $4d^{10}\,5s^2\,5p^6\,6s \rightarrow 4d^9\,5s^2\,5p^6\,6s\,nl \rightarrow 4d^{10}\,5s\,5p^6\,6s + e \rightarrow 4d^{10}\,5s^2\,5p^5 + 2e$. This process being quantum mechanical phenomenon, its contribution could not be included in the present work. Except in the energy range of 100 eV–135 eV the present cross-sections are higher than the experimental observations. The reasons for the discrepancies are similar to those discussed for Ba. Apart from the discrepancies mentioned above the calculated results are in reasonably good agreement with experiments, always being within a factor of 2 as compared with the measured cross-sections. We have also plotted the sum of the present single ionization cross-section for 5s and 4d subshell as well as the same calculated by Younger [25] in distorted wave Born exchange approximation. These plots indicate that inner shell ionization-autoionization dominates over direct double ionization for Ba^+.

4. Conclusions

From a close examination of our calculated results it is concluded that the present method gives reasonably accurate values of electron impact double ionization cross-

sections for Ba and Ba^+. The use of binding energy of Ba and Ba^+ respectively, while evaluating direct double ionization cross-section is reasonable at high impact energies. At low impact energy there is a partial rearrangement. If the effect of partial rearrangement could be incorporated, the present results would be lowered at low impact energies leading to a better agreement with experiments. In the case of heavy particle impact the concept of partial rearrangement of target has been incorporated by Chatterjee and Roy [26] but unfortunately, it is difficult to consider this for electron impact studies.

Acknowledgements

The authors (SNC) and (BNR) are grateful to CSIR, New Delhi for the award of a research associateship and research scheme respectively.

References

[1] S N Chatterjee and B N Roy, *J. Phys.* **B17**, 2527 (1984)
[2] K Tinschert, A Muller, G Hofmann, E Salzborn and S M Younger, *Phys. Rev.* **A43**, 3522 (1991)
[3] A Muller, K Tinschert, G Hofmann, E Salzborn and G H Dunn, *Phys. Rev. Lett.* **61**, 70 (1988)
[4] A Muller and R Frodl, *Phys. Rev. Lett.* **44**, 29 (1980)
[5] M S Pindzola, D C Griffin, C Bottcher, D H Crandall, R A Phaneuf and D C Gregory, *Phys. Rev.* **A29**, 1749 (1984)
[6] A Muller, K Tinschert, C Achenbach, R Becher and E Salzborn, *J. Phys.* **B18**, 3011 (1985)
[7] J H McGuire, *Phys. Rev. Lett.* **49**, 1153 (1992)
[8] J F Reading and A L Ford, *Phys. Rev. Lett.* **58**, 543 (1987)
[9] A L Ford and J F Reading, *J. Phys.* **B21**, L685 (1988)
[10] N C Deb and D S F Crothers, *J. Phys.* **B23**, L799 (1990)
[11] B N Roy and D K Rai, *J. Phys.* **B6**, 816 (1973)
[12] M Gryzinski, *Phys. Rev.* **A138**, 336 (1965)
[13] A Kumar and B N Roy, *Can. J. Phys.* **56**, 1255 (1978)
[14] S N Chatterjee, A Kumar and B N Roy, *J. Phys.* **B15**, 1415 (1982)
[15] S N Chatterjee and B N Roy, *J. Phys.* **B20**, 2291 (1987)
[16] L K Jha, S N Chatterjee and B N Roy, *Indian J. Phys.* **B67**, 1 (1993)
[17] B K Thomas and J D Garcia, *Phys. Rev.* **179**, 94 (1969)
[18] A D Mclean and R S Mclean, *At. Data Nucl. Data Tables* **26**, 197 (1981)
[19] J P Desclaux, *At. Data Nucl. Data Tables* **12**, 325 (1973)
[20] L Vriens, *Case studies in atomic collision physics* (North-Holland Publishing Company, Amsterdam) **1**, 358 (1969)
[21] D C Griffin and M S Pindzola, *Comm. At. Mol. Phys.* **13**, 1 (1983)
[22] J M Dettmann and F Karstensen, *J. Phys.* **B15**, 287 (1982)
[23] E J McGuire, *Phys. Rev.* **A20**, 445 (1979)
[24] T Hirayama, S Kobayashi, A Matsumoto, S Ohtani, T Takayanagi, K Wakiya and H Suzuki, *J. Phys. Soc. Jpn.* **56**, 851 (1987)
[25] S M Younger, *Phys. Rev.* **A34**, 1952 (1986)
[26] S N Chatterjee and B N Roy, *J. Phys.* **B18**, 4283 (1985)

PRAMANA
— journal of
physics

© Printed in India

Vol. 43, No. 2,
August 1994
pp. 175–179

Use of a diabatic molecular expansion in studies on electron capture by He^{2+} ions in helium at keV energies

C CHAUDHURI, S SANYAL (nee GANGULY) and T K RAI DASTIDAR
Atomic and Molecular Physics Section, Department of Materials Science, Indian Association for the Cultivation of Science, Jadavpur, Calcutta 700 032, India

MS received 21 April 1994.

Abstract. In this preliminary work, using a 3-state diabatic molecular expansion without any excited channels, we have studied within the semiclassical impact parameter approximation the single charge transfer process $He^{2+} + He(1s^2) \rightarrow He^+(1s) + He^+(1s)$. Our results agree very well with experiment, which demonstrates the usefulness of this type of diabatic molecular basis in doubly charged ion-atom collision systems.

Keywords. Diabatic molecular expansion; ion-atom collision.

PACS No. 34·70

In ion-atom collisions at low energies, a quasimolecular description of the collision complex is appropriate, and there have been many attempts (e.g. [1–8]) to define diabatic molecular states, although no unique definition still exists. We have recently initiated a programme of studying low-energy charge transfer collisions between atoms and doubly charged ions, using diabatic molecular wavefuntions constructed somewhat similarly as in an earlier work [9] devoted to He^+–He collisions. Before embarking on large-scale calculations, we decided to try out a simple 3-configuration basis on the He^{++}–He single charge transfer problem for which extensive data are avilable [10–12]. We found that this simple diabatic basis accounts extremely well for single charge transfer to the ground state [11] for the above system. We feel that this demonstrates the basic usefulness of this type of diabatic basis in collision problems, and we are now pursuing this approach with a larger, more state-of-the-art basis set including excited channels to study single as well as double charge transfer collisions; meanwhile, we report here our preliminary findings.

We are using atomic units throughout except where otherwise stated. Expand the total wavefunction of the collision complex in a truncated basis

$$\Psi(\mathbf{r}, \mathbf{R}(t)) = \sum_k c_k(t)\psi_k(\mathbf{r}, R). \tag{1}$$

Then in the semiclassical impact parameter approximation, the time-dependent Schrödinger equation becomes (see [9] for details)

$$i\frac{dc_j}{dt} = \sum_k (H_{jk} + P_{jk} + Q_{jk})c_k \tag{2}$$

where

$$H_{jk} = \langle \psi_j | H_{el} | \psi_k \rangle,$$

$$P_{jk} = \frac{vz}{R} \left\langle \psi_j \left| -i \frac{\partial}{\partial R} \right| \psi_k \right\rangle,$$

$$Q_{jk} = \frac{vb}{R^2} \left\langle \psi_j \left| -i \frac{\partial}{\partial \theta} \right| \psi_k \right\rangle$$

where $z = vt$, and b is the impact parameter. (There is an obvious misprint in the last line of eq. (7) in [9].)

For use in (1–2) we now define a diabatic molecular basis as in [9]:

$$\boldsymbol{\psi}(\mathbf{r}, R) = \mathbf{U}(R = \infty)\mathbf{S}(R)\boldsymbol{\phi}(\mathbf{r}, \xi(R = \infty); R) \tag{3}$$

where $\boldsymbol{\psi}$ and $\boldsymbol{\phi}$ are column vectors, ξ's are the orbital exponents, $\mathbf{S}(R)$ is the Schmidt orthonormalization matrix and $\mathbf{U}$ diagonalizes $\langle \mathbf{S}\boldsymbol{\phi} | H_{el} | \mathbf{S}\boldsymbol{\phi} \rangle$ at large R. The centre of mass coincides with the centre of charge for a symmetric system, and has been chosen as the origin of coordinates. Obviously, at large R, $\boldsymbol{\psi}$ coincides with the adiabatic basis. We are concerned with the low-energy region ($v < 1$ a.u), and for the present choose to omit the electron translation factors (ETF's).

In this work concentrating on electron capture into the ground state only, we choose a three-state expansion as follows (apart from normalization factors):

$$\phi_1 = 1\sigma_g^2 + 1\sigma_u^2 \qquad (^1\Sigma_g),$$

$$\phi_2 = 1\sigma_g^2 - 1\sigma_u^2 \qquad (^1\Sigma_g),$$

$$\phi_3 = |1\sigma_g 1\bar{\sigma}_u| + |1\sigma_u 1\bar{\sigma}_g| \qquad (^1\Sigma_u)$$

where the molecular orbitals $1\sigma_{g,u} = \frac{1}{\sqrt{2}}[1s(\mathrm{A}) \pm 1s(\mathrm{B})]$. Minimal (single-zeta) Slater-type functions were used as the atomic orbitals, the exponents being chosen to obtain variational minima of the eigenvalues at large R. Table 1 lists the exponents at $R = 50$ a.u., together with the energy values. Note that the ϕ's have gone over to the correct separated-atom energies [13].

We now freeze the exponents and the $\mathbf{U}$ matrix at $R = 50$ a.u. to form the diabatic basis (3) extending over all R. As shown in [9], this basis is a close approximation to the standard radial diabatic representation defined by Smith [3] in that $\mathbf{P}$ is negligible throughout; also, since (3) involves Σ-states only, the rotational coupling

Table 1. Basis functions used to construct the diabatic molecular wavefunctions (3).

Basis function	Separated atom limit	Atomic orbital exponent	Energy (a.u) at $R = 50$ a.u
ϕ_1, ϕ_3	$\mathrm{He_A}(1s^2) \pm \mathrm{He_B}^{++}$	1·6875	−2·847656*
ϕ_2	$\mathrm{He_A}^+(1s) + \mathrm{He_B}^+(1s)$	2·00	−3·980000

*Agrees exactly with the single-zeta energy for He (e.g. Clementi and Roetti [13]).

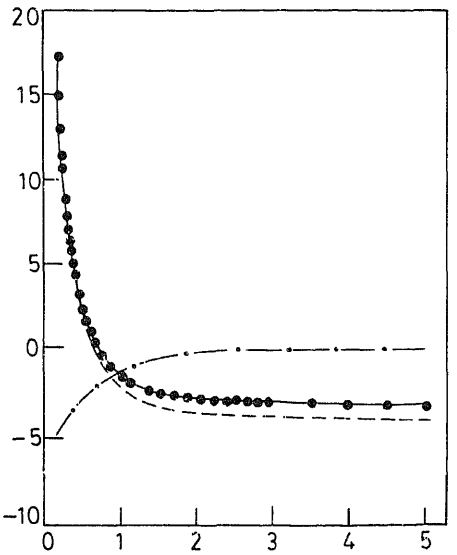

Figure 1. Diabatic Hamiltonian matrix elements for the basis (3) of text plotted against internuclear distance. Full-line curve, H_{11}; dots, H_{33}; dashed curve, H_{22}; dot-dashed curve, H_{12}.

matrix **Q** is identically zero. The coupled equations (2) now involve **H**-matrix elements only. One of the equations is uncoupled with the others and is trivially solved, and we solved the other two coupled equations by a variable-step fourth-order Runge-Kutta method which preserved unitarity to within 1 part in 10^4. The cross-sections for the charge transfer reaction

$$He_A + He_B^{+\,+} \rightarrow He_A^+(1s) + He_B^+(1s) \tag{4}$$

were then obtained by standard methods. Details of numerical procedures can be found elsewhere [14].

Figure 1 shows the frozen-orbital diabatic energies and the coupling term H_{12}. As table 1 shows, the diagonal terms go over to the correct separated-atom values. The off-diagonal coupling H_{12} decays exponentially, and from the figure it is obvious that we have a Demkov-type coupling here between the states ψ_1 and ψ_2. Space limitations do not permit displaying our results for the charge transfer probabilities; we found, however, that their velocity dependence follows the pattern predicted by Demkov [15].

Figure 2 shows our results for the total cross-section of the single capture process (4) as a function of collision energy. The results shown above 25 keV/amu ($v \sim 1$ a.u.) may be deemed simply an extrapolation of our code into the so-called "intermediate-energy region", and not really a "prediction" of our low-energy theory. Also displayed are the experimental results of Afrosimov *et al* [11] and the theoretical results of Fulton and Mittleman [16] and of Gramlich *et al* [21]. Although the $He^{+\,+}$–He collision has been theoretically treated by several groups [16–22], total cross-sections for the process (4) have been given only by three groups [16, 18, 21]. Fulton and Mittleman [16] used a three-state atomic orbital expansion; Harel and Salin [18] used a twelvestate adiabatic molecular expansion built with one-electron diatomic

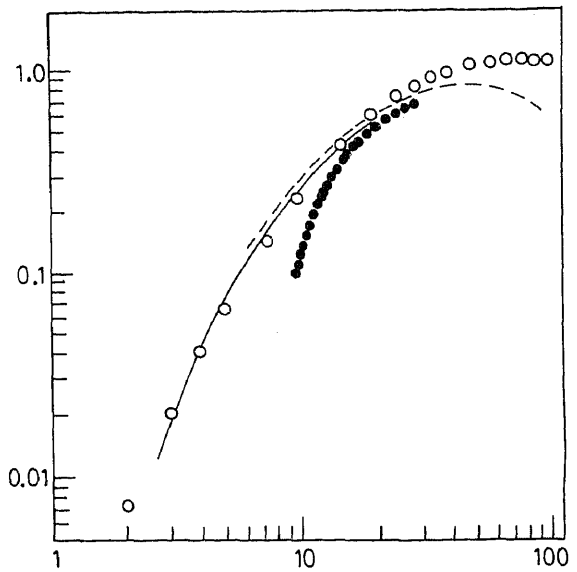

Figure 2. Single charge transfer cross-section for reaction (4) (10^{-16} cm^2) plotted against collision energy (keV/amu). Open circles, present results (see text); full-line curve, data of Afrosimov *et al* [11]; dashed curve, calculations of Fulton and Mittleman [16]; full circles, calculations of Gramlich *et al* [21].

molecular orbitals, while Gramlich *et al* [21] used a Gaussian atomic orbital expansion. ETF's were included in [16] and [21] but not in [18]. Comparison of our results with these experimental and theoretical works in figure 2 reveals the following features:

(1) Our results agree very well with the data of Afrosimov *et al* [11]. Although this is in accord with the observation of Zygelman *et al* [23] that a molecular-state expansion without electron translation factors is a valid low-energy approximation for charge transfer processes, we prefer to try out a larger basis before arriving at any conclusion on this point, inasmuch as this is linked with the question of origin-dependence of the results.

(2) The results of Fulton and Mittleman [16] and of Harel and Salin [18] (not shown) compare with experiment almost equally well as ours. Harel and Salin find, however, that leaving out excited-channel configurations (basis ϕ_5^g, ϕ_6^g and ϕ_4^u in their paper) yields theoretical results much lower than experiment, and from this they conclude that the ground level is populated principally through a complicated mechanism. Our results agree well enough with experiment to indicate that in the low energy regime, use of diabatic molecular expansions seems to allow us to ignore the excited channels. whereas use of adiabatic expansions does not. (The situation appears somewhat similar to Lichten's first use [1] of diabatic states in He^+–He collisions.) We, however, reserve our final judgement on this point till we try out a larger basis with excited channels. The results of Gramlich *et al* [21] do not compare well with our results in the energy range shown; however, their basis set was of a nature different from ours, and not much can be gained from this comparison. We note that Gramlich *et al* did not discuss the specific point above regarding the importance of the excited channels for the reaction (4).

Summarizing, we have demonstrated the usefulness of a very simple diabatic molecular basis in a doubly charged ion-atom collision system at low energies. Work is in progress to study charge transfer channels into excited states and also to check on what may be called the size-consistency of this basis set for the problem of charge transfer into the ground state.

One of the authors (S Sanyal) is thankful to the Council of Scientific and Industrial Research, New Delhi for support.

References

[1] W Lichten, *Phys. Rev.* **131**, 229 (1963)
[2] T F O'Malley, *Phys. Rev.* **162**, 98 (1967)
T F O'Malley, *J. Chem. Phys.* **51**, 322 (1969)
[3] F T Smith, *Phys. Rev.* **179**, 111 (1969)
[4] M Barat and W Lichten, *Phys. Rev.* **A6**, 211 (1972)
[5] J Eichler, U Wille, B Fastrup and K Taulbjerg, *Phys. Rev.* **A14**, 707 (1976)
[6] J B Delos, *Rev. Mod. Phys.* **53**, 287 (1981)
[7] T M Kereselidze and B I Kikiani, *Zh. Eksp. Teor. Fiz.* 87, 741 (1984)
T M Kereselidze and B I Kikiani, *Sov. Phys. JETP* **60**, 423 (1984)
[8] A Russek and R J Furlan, *Phys. Rev.* **A39**, 5034 (1989)
[9] T K Rai Dastidar and K Rai Dastidar, *Chem. Phys. Lett.* **85**, 229 (1982)
[10] J E Bayfield and G A Khayrallah, *Phys. Rev.* **A11**, 920 (1975)
[11] V V Afrosimov, A A Basalaev, G A Leiko and M N Panov *Zh. Eksp. Teor. Fiz.* **74**, 1605 (1978)
V V Afrosimov, A A Basalaev, G A Leiko and M N Panor, *Sov. Phys. JETP* **47**, 837 (1978)
[12] M B Shah, P McCallion and H B Gilbody, *J. Phys.* **B22**, 3037 (1989)
[13] E Clementi and C Roetti, *At. Data Nucl. Data Tables* **14**, 177 (1974)
[14] See e.g. T K Rai Dastidar and S S Bhattacharya, *J. Phys.* **B8**, 1522 (1975);
T K Rai Dastidar and S S Bhattacharya, *Indian J. Phys.* **50**, 731 (1976)
T K Rai Dastidar, K Rai Dastidar and M Guha, *Chem. Phys.* **43**, 189 (1979);
S Ganguly, K Rai Dastidar and T K Rai Dastidar, *Phys. Rev.* **A31**, 1171 (1985)
S Ganguly, K Rai Dastidar and T K Rai Dastidar, *Phys. Rev.* **A33**, 3060 (1986)
[15] Yu N Demkov, *Zh. Eksp. Teor. Fiz.* **45**, 195 (1963)
Yu N Demkov, *Sov. Phys. JETP* **18**, 138 (1964)
[16] M J Fulton and M H Mittleman, *Proc. Phys. Soc. (London)* **87**, 669 (1966)
[17] S C Mukherjee, K Roy and N C Sil, *J. Phys.* **B6**, 467 (1973)
[18] C Harel and A Salin, *J. Phys.* **B13**, 785 (1980)
[19] K R Sandhya Devi and J D Garcia, *J. Phys.* **B16**, 2837 (1983)
[20] M Kimura, *J. Phys.* **B21**, L19 (1988)
[21] K Gramlich, N Gruen and W Scheid, *J. Phys.* **B22**, 2567 (1989)
[22] R S Gao, C M Dutta, N F Lane, K A Smith, R F Stebbings and M Kimura, *Phys. Rev.* **A45**, 6388 (1992)
[23] B Zygelman, D L Cooper, M J Ford, A Dalgarno, J Gerratt and M Raimondi, *Phys. Rev.* **A46**, 3846 (1992)

PRAMANA
— journal of
physics

© Printed in India

Vol. 43, No. 3,
September 1994
pp. 181–187

Second order elastic anomalies in barium titanate from orthorhombic to rhombohedral phase transition

B SUBRAMANYAM
Department of Physics, Indian Institute of Technology, Madras 600036, India

MS received 4 May 1994; revised 21 July 1994

Abstract. The anomalies in second order elastic constants have been derived for barium titanate for the phase transition from orthorhombic to rhombohedral state. The equilibrium values of order parameter, strain variables and fluctuations in order parameter have been derived using stability conditions and Landau-Khalatnikov equations respectively. Expression for shift in specific heat is obtained. All the anomalies in second order elastic constants have been derived and relations among them reported. The numerical values of anomalies in the individual constants are calculated and their variation is represented graphically. Changes in elastic constants occur over a range of temperature of the order 10^{-2}K.

Keywords. Elastic anomalies; phase transition; barium titanate.

PACS Nos 64·70; 62·20; 64·60

1. Introduction

Barium titanate is a classical example of a substance undergoing a first order phase transition. The author in an earlier communication studied systematically [1] the anomalies of the second, third and fourth-order elastic constants arising from the cubic to the tetragonal phase and from tetragonal to the orthorhombic phase. Barium titanate undergoes yet another phase transition on cooling further below -70 C from orthorhombic to the rhombohedral $R_{3m}(C_{3v}^5)$ phase in which the polarization vector is directed along the [111] direction. This group is a subgroup of the parent (cubic) phase.

In this paper, the anomalies of the second-order elastic constants arising from the phase transition from the orthorhombic to rhombohedral phase are reported. The equilibrium values of the order parameter components and the strain variables are obtained from the stability conditions while the fluctuations in the order parameter are derived from Landau–Khalatnikov equation. In § 2 expressions for the equilibrium values of order parameter and strain variables are derived. In § 3 expressions for fluctuations in order parameter in terms of strain variables using Landau–Khalatnikov equations are obtained. Section 4 gives a single formula for all the second order elastic (SOE) anomalies in the rhombohedral phase. Relations among the SOE anomalies have been derived. The numerical equations for the anomalies of the individual SOE constants are given and their temperature variation is discussed.

2. Equilibrium values of the order parameters and the strain variables

The free energy of the crystal is given by

$$F = F_{ela} + F_L + F_c \tag{1}$$

where F_{ela} is the elastic energy, F_L is Landau energy and F_c is coupling energy. The expressions for the various energies are taken from the earlier publication [1]. In the present case $P_x = P_y = P_z \neq 0$. For the stability of the crystal, the partial derivatives of F with respect to strain variables and order parameter components must vanish. Using the expression for free energy and solving the nine equations for the stability of the crystal the equilibrium values of strain variables $\eta_{i0} (i = 1$ to $6)$ and order parameter components are obtained. They are

$$\eta_{10} = \eta_{20} = \eta_{30} = X_1 P_{z0}^2 \tag{2}$$

$$\eta_{40} = \eta_{50} = \eta_{60} = Z_1 P_{z0}^2 \tag{3}$$

where

$$P_{x0}^2 = P_{y0}^2 = P_{z0}^2 = \frac{-a}{b + 4C - 2X - 2Z} = -aP, \tag{4a}$$

$$X_1 = -\frac{g_{11} + 2g_{12}}{C_{11} + 2C_{12}}, \tag{4b}$$

$$Z_1 = -\frac{g_{44}}{C_{44}}, \tag{4c}$$

$$X = \frac{(g_{11} + 2g_{12})^2}{(c_{11} + 2c_{12})}, \tag{4d}$$

$$Z = \frac{g_{44}^2}{c_{44}}, \tag{4e}$$

$$a = a''(T - T_c). \tag{4f}$$

In the above equations (2) to (4) a'', b, C, g_{11}, g_{12} and g_{44} are constants. The numerical values of above constants except a'' and for the elastic constants C_{11}, C_{12} and C_{44} are taken as given by Devonshire [2] who first applied Landau theory to barium titanate. They are

$$b = 65{\cdot}6 \times 10^{-12},\ C = -0{\cdot}1 \times 10^{-12},\ g_{11} = -11{\cdot}2$$
$$g_{12} = 0{\cdot}8,\ g_{44} = -8,\ C_{11} = 6{\cdot}0 \times 10^{12}\ \text{dyne/cm}^2$$
$$C_{44} = C_{12} = 3{\cdot}0 \times 10^{+12}\ \text{dyne/cm}^2. \tag{5}$$

From the above numerical values we find that

$$P = +0{\cdot}151 \times 10^{12}, \tag{6a}$$

$$X = 7{\cdot}68 \times 10^{-12}, \tag{6b}$$

$$Z = 21{\cdot}6 \times 10^{-12}, \tag{6c}$$

3. Landau–Khalatnikov equations

As explained in an earlier communication [1] the three LK equations are

$$\dot{P}_x = -\Gamma_1 \frac{\partial F}{\partial P_x}, \tag{7a}$$

$$\dot{P}_y = -\Gamma_2 \frac{\partial F}{\partial P_y}, \tag{7b}$$

$$\dot{P}_z = -\Gamma_3 \frac{\partial F}{\partial P_z}. \tag{7c}$$

The symmetry of the rhombohedral phase requires $\Gamma_1 = \Gamma_2 = \Gamma_3 = \Gamma$. By expanding $\partial F/\partial P_i$ $(i = x, y, z)$ about the equilibrium values of the components of the order parameter and the strain variables and by ignoring product terms of higher order derivatives and further by writing P_i^* to be proportional to $e^{i\Omega t}$ where Ω is angular frequency of acoustic wave we arrive at the following expressions for the various derivatives

$$\left(\frac{\partial^2 F}{\partial P_k^2}\right)_0 = aP' \quad (k = x, y, z) \tag{8a}$$

where

$$P' = a(1 - 3b\,P - 4CP + 2PX] \tag{8b}$$

$$\left(\frac{\partial^2 F}{\partial P_x \partial P_y}\right)_0 = \left(\frac{\partial^2 F}{\partial P_y \partial P_z}\right)_0 = \left(\frac{\partial^2 F}{\partial P_z \partial P_x}\right)_0 = aP[Z - 4C] \tag{8c}$$

$$\left(\frac{\partial^2 F}{\partial \eta_1 \partial P_x}\right)_0 = \left(\frac{\partial^2 F}{\partial \eta_2 \partial P_y}\right)_0 = \left(\frac{\partial^2 F}{\partial \eta_3 \partial P_z}\right)_0 = 2g_{11}(-aP)^{1/2} \tag{8d}$$

$$\left(\frac{\partial^2 F}{\partial \eta_i \partial P_x}\right)_0 = \left(\frac{\partial^2 F}{\partial \eta_j \partial P_y}\right)_0 = \left(\frac{\partial^2 F}{\partial \eta_k \partial P_z}\right)_0 = 2g_{12}(-aP)^{1/2}$$

for

$$i = 2 \text{ and } 3 \text{ for } j = 1 \text{ and } 3 \text{ for } k = 1 \text{ and } 2 \tag{8e}$$

$$\left(\frac{\partial^2 F}{\partial \eta_i \partial P_x}\right)_0 = \left(\frac{\partial^2 F}{\partial \eta_j \partial P_y}\right)_0 = \left(\frac{\partial^2 F}{\partial \eta_k \partial P_z}\right)_0 = g_{44}(-aP)^{1/2}$$

and

$$\text{for } i = 5 \text{ and } 6 \text{ for } j = 4 \text{ and } 6 \text{ for } k = 4 \text{ and } 5 \tag{8f}$$

and all other second order derivatives are zero.

By substituting above relations in LK equations and solving for the fluctuations in order parameter components in terms of strain variables the following relations are obtained.

$$P_k^* = \alpha_{ki}\eta_i^*, \; k = x, y, z \text{ and } i = 1 \text{ to } 6. \tag{9}$$

The values of

$$\alpha_{x1} = \alpha_{y2} = \alpha_{z3} = -\frac{\Gamma P_{z0} A}{(a' - b')(a' + 2b')}, \tag{10a}$$

$$\alpha_{x2} = \alpha_{x3} = \alpha_{y1} = \alpha_{y3} = \alpha_{z1} = \alpha_{z2} = -\frac{\Gamma P_{z0} B}{(a'-b')(a'+2b')}, \tag{10b}$$

$$\alpha_{x4} = \alpha_{y5} = \alpha_{z6} = \frac{2\Gamma P_{z0} g_{44} b'}{(a'-b')(a'+2b')}, \tag{10c}$$

$$\alpha_{x5} = \alpha_{x6} = \alpha_{y4} = \alpha_{y6} = \alpha_{z4} = \alpha_{z5} = -\frac{\Gamma P_{z0} g_{44} a'}{(a'-b')(a'+2b')} \tag{10d}$$

where

$$a' = aP'\Gamma(1 + i\Omega\tau], \tag{11a}$$

$$b' = aP\Gamma[-Z + 4C], \tag{11b}$$

$$A = 2g_{11}a' + 2g_{11}b' - 4g_{12}b', \tag{11c}$$

$$B = 2g_{12}a' - 2g_{11}b'. \tag{11d}$$

The relaxation time

$$\tau = \left[\Gamma\left(\frac{\partial^2 F}{\partial P_z^2}\right)_0\right]^{-1}. \tag{11e}$$

4. Elastic anomalies in rhombohedral phase

Substituting $\eta_i = \eta_{i0} + \eta_i^*$ and $P_j = P_{j0} + P_j^*$ ($i = 1$ to 6 and $j = x, y$ and z), the expression for free energy becomes,

$$\begin{aligned}
&1/2C_{ij}(\eta_{i0} + \eta_i^*)(\eta_{j0} + \eta_j^*) + \frac{a}{2}[(P_{z0} + P_x^*)^2 + (P_{z0} + P_y^*)^2 + (P_{z0} + P_z^*)^2] \\
&+ \frac{b}{4}[(P_{z0} + P_x^*)^4 + (P_{z0} + P_y^*)^4 + (P_{z0} + P_z^*)^4] \\
&+ C[(P_{z0} + P_x^*)^2(P_{z0} + P_y^*)^2 + (P_{z0} + P_y^*)^2(P_{z0} + P_z^*)^2 \\
&+ (P_{z0} + P_z^*)^2(P_{z0} + P_x)^2] \\
&+ g_{11}[(\eta_{10} + \eta_1^*)(P_{z0} + P_x^*)^2 + (\eta_{20} + \eta_2^*)(P_{z0} + P_y^*)^2 \\
&+ (\eta_{30} + \eta_3^*)(P_{z0} + P_z^*)^2] \\
&+ g_{12}[(\eta_{10} + \eta_1^*)\{(P_{z0} + P_y^*)^2 + (P_{z0} + P_z^*)^2\} \\
&+ (\eta_{20} + \eta_2^*)\{(P_{z0} + P_z^*)^2 + (P_{z0} + P_x^*)^2\} \\
&+ (\eta_{30} + \eta_3^*)\{(P_{z0} + P_x^*)^2 + (P_{z0} + P_y^*)^2\}] \\
&+ g_{44}[(\eta_{40} + \eta_4^*)(P_{z0} + P_y^*)(P_{z0} + P_z^*) \\
&+ (\eta_{50} + \eta_5^*)(P_{z0} + P_z^*)(P_{z0} + P_x^*) + (\eta_{60} + \eta_6^*)(P_{z0} + P_x^*)(P_{z0} + P_y^*)]
\end{aligned} \tag{12}$$

In the above expression for free energy the linear terms in η_i^* vanishes in view of the stability conditions. F_0 and F_2 correspond to terms of order zero and two in the strain variables respectively. F_0 gives the shift in zero point energy at the transition temperature. Its derivative with respect to temperature will give the specific heat

anomaly at the transition temperature.

$$F_0 = -\frac{3}{4}a^2 P = -\frac{3}{4}[a''^2(T - T_c)^2]P, \tag{13}$$

$$\Delta C_v = \left(\frac{\partial F_0}{\partial T}\right)_v = -\frac{3}{2}a''^2 P(T - T_c)$$
$$= -0{\cdot}227a''^2(T - T_c) \times 10^{12}. \tag{14}$$

The change in specific heat is proportional to $(T - T_c)$.

By collecting all the terms which are quadratic in strain variables, the expression for F_2 is

$$F_2 = \frac{1}{2}\sum_{ij} C_{ij}^* \eta_i^* \eta_j^* \tag{15}$$

where C_{ij}^* represents the modified SOE constants.

Let us write

$$C_{ij}^* = C_{ij} + \Delta C_{ij}^* \tag{16}$$

ΔC_{ij}^* then gives the anomalies in SOE constants arising from the phase transition. Substituting the expressions for $P_k^*(k = x, y, z)$ in (12) from (9) and (10) and collecting all terms containing $\eta_i^* \eta_j^*$ the expression for SOE anomalies is

$$\frac{\Delta C_{ij}^*}{2}\eta_i^* \eta_j^* = (\alpha_{xi}\alpha_{xj} + \alpha_{yi}\alpha_{yj} + \alpha_{zi}\alpha_{zj})P_{z0}^2\left[\frac{a}{2P_{z0}^2} + \frac{3b}{2} + 2C - X\right]\eta_i^* \eta_j^*$$
$$+ (\alpha_{xi}\alpha_{yj} + \alpha_{yi}\alpha_{zi} + \alpha_{zi}\alpha_{xj})P_{z0}^2(4C - Z)\eta_i^* \eta_j^*$$
$$+ 2P_{z0}g_{11}[\alpha_{xi}\eta_1^*\eta_i^* + \alpha_{yi}\eta_2^*\eta_i^* + \alpha_{zi}\eta_3^*\eta_i^*]$$
$$+ [2P_{z0}g_{12}(\eta_1^* + \eta_2^*) + g_{44}P_{z0}(\eta_4^* + \eta_5^*)]\alpha_{zi}\eta_i^*$$
$$+ [2P_{z0}g_{12}(\eta_3^* + \eta_1^*) + g_{44}P_{z0}(\eta_4^* + \eta_6^*)]\alpha_{yi}\eta_i$$
$$+ [2P_{z0}g_{12}(\eta_2^* + \eta_3^*) + g_{44}P_{z0}(\eta_5 + \eta_6)]\alpha_{xi}\eta_i^*. \tag{17}$$

The following relations among the elastic anomalies can easily be verified by giving integral values for the indices i and j ranging from 1 to 6

$$\Delta C_{11}^* = \Delta C_{22}^* = \Delta C_{33}^*, \tag{18a}$$

$$\Delta C_{44}^* = \Delta C_{55}^* = \Delta C_{66}^*, \tag{18b}$$

$$\Delta C_{12}^* = \Delta C_{13}^* = \Delta C_{23}^*, \tag{18c}$$

$$\Delta C_{14}^* = \Delta C_{25}^* = \Delta C_{36}^*, \tag{18d}$$

$$\Delta C_{15}^* = \Delta C_{16}^* = \Delta C_{24}^* = \Delta C_{26}^* = \Delta C_{34}^* = \Delta C_{35}^*, \tag{18e}$$

$$\Delta C_{45}^* = \Delta C_{46}^* = \Delta C_{56}^*. \tag{18f}$$

The anomalies in SOE constants show that the velocities of the sound waves undergo a change during the phase transition. The complex nature of the anomalies indicates

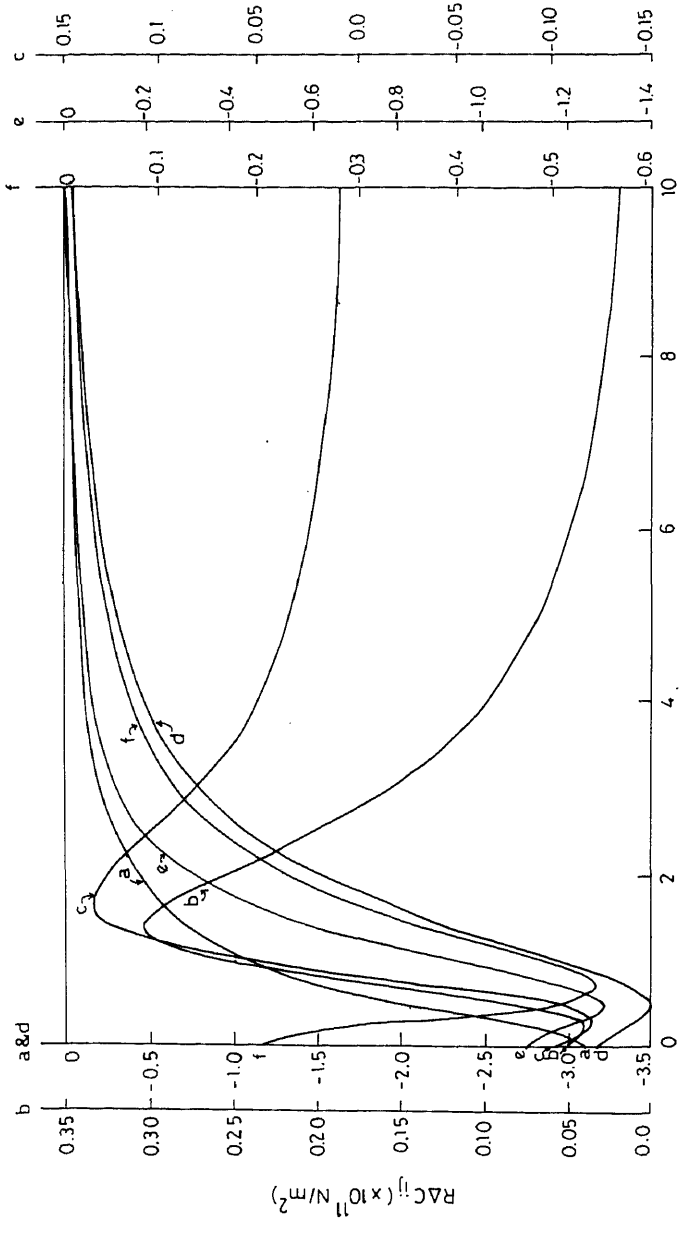

Figure 1. Variation of real part of $\Delta C^*_{ij} = R\Delta C^*_{ij}$ with respect to product of circular frequency and relaxation time $\Omega\tau$ according to Landau theory. a) $R\Delta C^*_{44}$ vs $\Omega\tau$; b) $R\Delta C^*_{12}$ vs $\Omega\tau$; c) $R\Delta C^*_{14}$ vs $\Omega\tau$; d) $R\Delta C^*_{11}$ vs $\Omega\tau$; e) $R\Delta C^*_{15}$ vs $\Omega\tau$; f) $R\Delta C^*_{45}$ vs $\Omega\tau$.

that the waves are attenuated in this region. Using the numerical values of the different constants given in (8) the real part of the anomalies in the individual SOE constants are given by

$$R\Delta C_{11}^{*} = -\frac{[3{\cdot}18 + 20{\cdot}17\Omega^2\tau^2 + 33{\cdot}44\Omega^4\tau^4 + 17{\cdot}8\Omega^6\tau^6]}{[1 + 2{\cdot}6\Omega^2\tau^2 + 1{\cdot}44\Omega^4\tau^4]^2} \times 10^{12}, \tag{19a}$$

$$R\Delta C_{44}^{*} = -\frac{[3{\cdot}1 + 7{\cdot}7\Omega^2\tau^2 + 10{\cdot}2\Omega^4\tau^4 + 4{\cdot}5\Omega^6\tau^6]}{[1 + 2{\cdot}6\Omega^2\tau^2 + 1{\cdot}44\Omega^4\tau^4]^2} \times 10^{12}, \tag{19b}$$

$$R\Delta C_{12}^{*} = +\frac{[0{\cdot}05 - 0{\cdot}15\Omega^2\tau^2 + 3\Omega^4\tau^4 + 3{\cdot}9\Omega^6\tau^6]}{[1 + 2{\cdot}6\Omega^2\tau^2 + 1{\cdot}44\Omega^4\tau^4]^2} \times 10^{12}, \tag{19c}$$

$$R\Delta C_{14}^{*} = +\frac{[-0{\cdot}1 - 1{\cdot}8\Omega^2\tau^2 + 1{\cdot}06\Omega^4\tau^4 + 2{\cdot}125\Omega^6\tau^6]}{[1 + 2{\cdot}6\Omega^2\tau^2 + 1{\cdot}44\Omega^4\tau^4]^2} \times 10^{12}, \tag{19d}$$

$$R\Delta C_{15}^{*} = -\frac{[1{\cdot}1 + 8\Omega^2\tau^2 + 12{\cdot}5\Omega^4\tau^4 + 1{\cdot}65\Omega^6\tau^6]}{[1 + 2{\cdot}6\Omega^2\tau^2 + 1{\cdot}44\Omega^4\tau^4]^2} \times 10^{12}, \tag{19e}$$

$$R\Delta C_{45}^{*} = -\frac{[0{\cdot}2 + 3{\cdot}7\Omega^2\tau^2 + 6\Omega^4\tau^4 + 2{\cdot}4\Omega^6\tau^6]}{[1 + 2{\cdot}6\Omega^2\tau^2 + 1{\cdot}44\Omega^4\tau^4]^2} \times 10^{12}. \tag{19f}$$

The relaxation time τ has a temperature dependence given by Lemanov [3]

$$\tau = \tau_0/|T_c - T| \tag{20}$$

where τ_0 has a value of the order 10^{-11} to 10^{-10}sK. Under experimental conditions the acoustic frequency Ω is chosen in the range 10^8–10^9Hz. Hence $\Omega\tau_0$ has a value of the order of 10^{-2} to 10^{-3}. The temperature dependence of anomalies can now be easily understood by writing $C_{ij}^{*} = C_{ij} + R\Delta C_{ij}^{*}$. The variation of real part of the anomalies is shown in figure 1. At $T = T_c$, $\tau \to \infty$ and all the anomalies vanish. It is seen from figure that the anomalies occur over a range of temperature 10^{-2}K below the transition temperature. The real part of ΔC_{44}^{*} falls to the value in rhombohedral phase. On the other hand the real parts of ΔC_{12}^{*} and ΔC_{14}^{*} reach maximum values and have a dip and rise again to the values in the rhombohedral phase. The real parts of ΔC_{11}^{*}, ΔC_{15}^{*} and C_{45}^{*} have a dip and rise again to the values in the rhombohedral phase. Unfortunately no experimental data are available as yet for comparison. Hopefully the present work will stimulate experimental investigations.

Acknowledgement

The author would like to thank Dr K S Viswanathan for his constant advice and discussion during the course of this work.

References

[1] B Subramanyam and K S Viswanathan, *J. Appl. Phys.* **74**, 945 (1993)
[2] A F Dovenshire, *Philos. Mag.* **40**, 1040 (1949)
[3] V V Lemanov, *Proc. Second Inter. Conf. Condensed Matter Physics* edited by M Brikov (Varna, Bulgaria) (World Scientific, Singapore, 1982) pp. 190–228

PRAMANA
— journal of
physics

© Printed in India

Vol. 43, No. 3,
September 1994
pp. 189–192

High pressure studies on $AgI–Ag_2O–MoO_3$ glasses

B VAIDHYANATHAN, S ASOKAN* and K J RAO**
Solid State and Structural Chemistry Unit,
*Instrumentation and Services Unit, Indian Institute of Science, Bangalore 560012, India
**To whom correspondence should be addressed.

MS received 20 April 1994; revised 7 June 1994

Abstract. The effect of pressure on the conductivity of $AgI–Ag_2O–MoO_3$ glasses has been reexamined. A conductivity maximum is observed around 0·7 GPa. No variation of the sample temperature is noted under pressure. The results are found to agree well with the cluster-tissue model.

Keywords. Conductivity; cluster model; ionic glasses; high pressure transport behaviour.

PACS Nos 61·40; 62·50; 72·20

The effect of pressure on the conductivity of $AgI–Ag_2O–MoO_3$ glasses has been studied a decade ago by Senapati *et al* [1], using a 4 mm Bridgman anvil set up with steatite as the pressure transmitting medium. It was reported that these glasses exhibit a conductivity maxima at high pressures around 1 GPa. The authors have explained the observed results on the basis of the cluster-tissue model [2, 3], according to which the glass is composed of quasi-ordered clusters which are connected by the disordered tissue. The initial increase in conductivity with pressure, is attributed to the transformation of the low density tissue regions to the high density clusters. The existing clusters in the material serve as a ready template for this transformation. The high pressure-low temperature conductivity measurements, undertaken by these authors, also provided a supporting evidence for the cluster-tissue description of these glasses [4].

Recently, Hutchinson *et al* [5] have studied the effect of pressure (up to 1 GPa) on the conductivity of $AgI–Ag_2O–MoO_3$ glasses using a piston-cylinder apparatus with castor oil as the pressurizing medium. These studies indicate a monotonic decrease in the normalized conductivity as a function of pressure. Experiments of Oyama and Kawamura [6], conducted on a piston-cylinder type high pressure vessel with silicone oil as the hydrostatic pressure fluid, also show a linear decrease in the conductivity of $AgI–Ag_2O–MoO_3$ glasses under pressure.

In this background, high pressure conductivity studies have been performed again on a few $AgI–Ag_2O–MoO_3$ glass compositions, to examine the reproducibility of the results of Senapati *et al* [1]. The present experiments have been carried out in a 12 mm tungsten carbide opposed anvil system. Pyrophyllite is used as the gasket material and steatite as the pressure transmitting medium. In situ calibration with Bi has been adopted, for accurate measurement of pressures. A chromel-alumel thermocouple is mounted inside the cell along with the sample, to monitor any change in sample temperatures under pressure. Pressurization of the samples has been carried

out very slowly, to enable the samples to reach equilibrium conditions. Experiments have also been repeated several times to ensure repeatability.

Figure 1 shows the variation of conductivity with pressure of $60\,AgI–20\,Ag_2O–20\,MoO_3$ and $50\,AgI–25\,Ag_2O–25\,MoO_3$ glasses. The inset in figure 1 gives the pressure dependence of resistivity of the in situ calibrant (Bi). It is seen from the figure that in both the glasses studied, a maximum in normalized conductivity is observed. It is found that the conductivity maximum with pressure is repeatable, with a small variation in the peak conductivity value. Also there is no appreciable change in the sample temperature with pressure (figure 2).

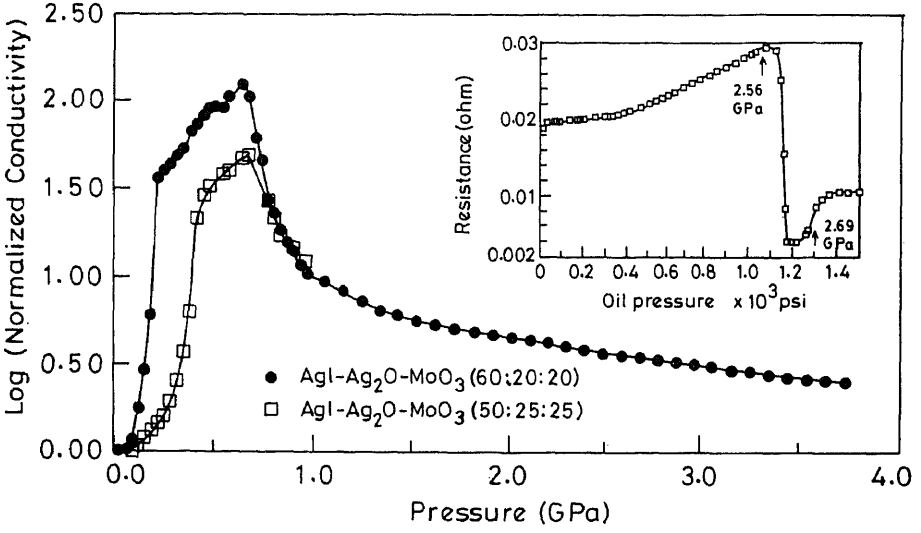

Figure 1. Variation of log of normalized conductivity with pressure for the $AgI–Ag_2O–MoO_3$ glasses. **Inset**: Plot of resistance versus pressure for the in situ Bi calibrant.

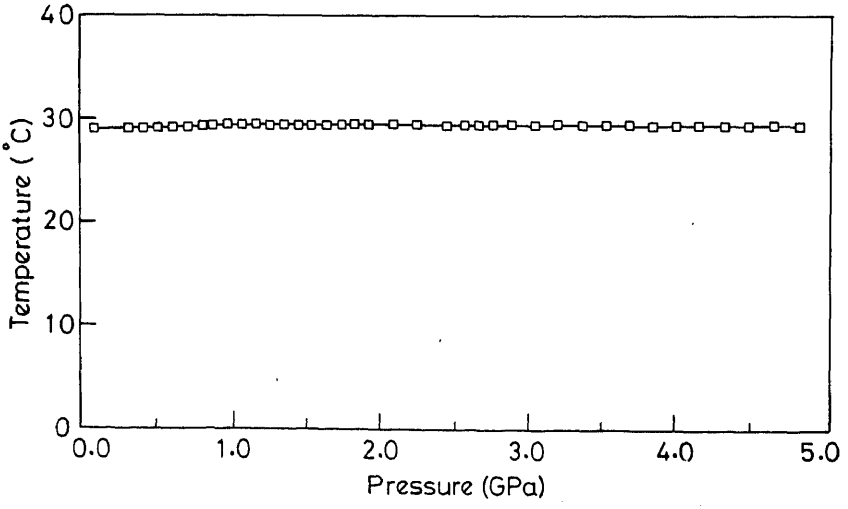

Figure 2. Temperature changes in the pressure chamber measured in situ using a chromel-alumel thermocouple.

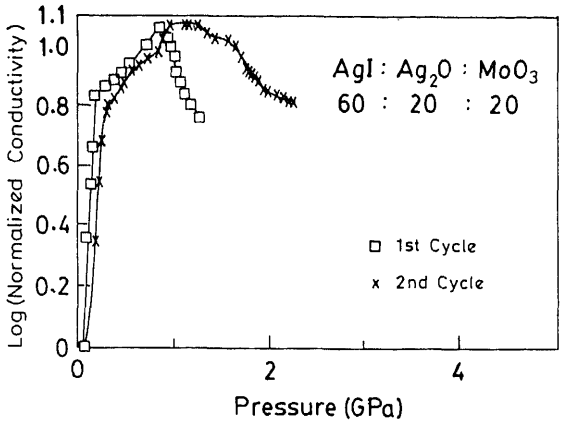

Figure 3. Pressure dependence of normalized conductivity of 60 AgI–20 Ag_2O–20 MoO_3 glass during the first and the second cycle.

The pressure dependence of conductivity observed in the present studies matches well with the results of Senapati *et al* [1]. The transformation pressure of 60 AgI–20 Ag_2O–20 MoO_3 sample is around 0·7 GPa in the present studies, whereas it was reported to be around 1 GPa earlier. The marginal difference in the transformation pressure, may be due to the fact that smaller anvils were used and in situ calibration was not employed in the earlier investigations (Senapati *et al* [1]).

It is possible to suspect that spurious conductivity maxima could have been observed by us in single-pass pressure experiments, particularly since the conductivity maxima occur around a relatively low pressure of 0·7 GPa. Hence, the conductivity measurements were repeated with pressure cycling up to 2·0 GPa. The results are shown in figure 3. Except for a slight increase in the pressure corresponding to the conductivity maximum and a slight broadening of the peak, the essential features are completely reproduced in the second cycle also.

As the earlier results of Senapati *et al* [1] have now been reconfirmed, the different results observed by Hutchinson *et al* [5] and Oyama and Kawamura [6] can only be due to the inherent differences in the Bridgman anvil and the piston-cylinder techniques. The large compressibility of the fluid transmitting media in a piston-cylinder set up, results in a Joule–Thomson heating (of up to 10 K) which in turn may affect the sample behaviour. The combined effect of applied pressure and local increase in temperature may bring about an accelerated tissue-cluster conversion which suppresses the conductivity maximum. However, we do not intend to explain completely the observations made in the piston-cylinder experiments. It is also possible that the shear component of the quasi-hydrostatic pressure generated in the Bridgman anvil technique, is partially responsible for causing the observed difference in the pressure behaviour.

At present, the cluster-tissue model seems to provide the only available appropriate explanation for the conductivity behaviour of $AgI-Ag_2O-MoO_3$ glasses, observed in Bridgman anvil high pressure experiments. It would be interesting to examine the role of shear component of pressure in the tissue-cluster transformation suggested in the model.

References

[1] H Senapati, G Parthasarathy, S T Lakshmikumar and K J Rao, *Philos. Mag.* **B47** 291 (1983)
[2] K J Rao and C N R Rao, *Mater. Res. Bull.*, **17**, 1337 (1982)
[3] K J Rao, *Proc. Indian Acad. Sci.* (*Chem. Sci.*), **93**, 389 (1984)
[4] S Hemlata, G Parthasarathy, K J Rao and E S R Gopal, *Pramana – J. Phys.* **23**, 269 (1984)
[5] J M Hutchinson, M D Ingram and A H J Robertson, *Philos. Mag.* **B66**, 449 (1992)
[6] Y Oyama and J Kawamura, *Solid State Ionics*, **53–56**, 1221 (1992)

PRAMANA
— journal of
physics

© Printed in India

Vol. 43, No. 3,
September 1994
pp. 193–199

Investigation of phonon anomalies in intermediate valence compounds SmS and $Sm_{0.75}Y_{0.25}S$

PRAFULLA KUMAR JHA and SANKAR P SANYAL
Department of Physics, C V Raman Building, Barkatullah University, Bhopal 462026, India

MS received 2 April 1994; revised 4 July 1994

Abstract. Phonon anomalies in two intermediate valence compounds (IVC), SmS and $Sm_{0.75}Y_{0.25}S$ have been investigated using breathing shell model (BSM). The BSM includes breathing motion of electron shells of the rare earth atom due to $f-d$ hybridization. The phonon dispersion curves of IVC, calculated from the present model, agree well with the measured data. One-phonon density of states calculated from the present model compares well with the Raman spectra.

Keywords. Phonons; phonon dispersion curves; dynamical matrix; density of states.

PACS Nos 63·20; 63·10

1. Introduction

The valence instability of the intermediate valence (IV) systems due to fluctuations between the $4f^n$ and $4f^{n+1}$ electronic configurations gives rise to peculiar phonon properties [1–11]. Because of this large volume difference in the two electronic states, strong electron-phonon interactions have been observed in these systems [1, 4, 8–9]. These volume fluctuations or the breathing motion of the electron shells of rare earth atoms occur on a time scale comparable with lattice response time, which influence on the phonon properties such as damping or softening of the phonon modes and elastic constants. Some of the IV compounds (IVC) for which phonon properties have been studied are sulfides and selenides of samarium (Sm), thulium (Tm) and yttrium (Y) and their alloys [5, 8–9, 11–14].

The phonon anomalies common to almost all the IVCs consist of softening of the zone boundary longitudinal phonon modes. For SmS in its semiconductor state, it is the longitudinal optical (LO) branch which gets soft at the zone boundary [8–9] while for $Sm_{0.75}Y_{0.25}S$ and YS both LO and LA show softening near the zone boundary. Similar situation is also observed in TmSe [1, 4]. The strong electron-phonon interactions which arise due to volume fluctuations affect the elastic properties of the IVCs. In SmS, C_{12} is small [6, 15] while in TmSe, YS and $Sm_{0.75}Y_{0.25}S$ it is negative [8, 9].

Recently much effort has been put in to interpret the electron-phonon interactions in IVCs namely SmS, $Sm_{0.75}Y_{0.25}S$, YS and TmSe [8–11]. Guntherodt *et al* [8] have examined the phonon anomalies in SmS, $Sm_{0.75}Y_{0.25}S$ and YS by using a lattice dynamical theory which considers the interionic charge deformabilities [8]. This theory satisfactorily explained the mode softening and Raman spectrum in these solids. The phonon dispersion curves (PDC) for YS and TmSe were measured long

back [2] where the PDC has been analysed using the rigid ion model. Only limited information is available for the optical modes in TmSe while no complete measurements of PDC for SmS is reported so far [1]. These authors have emphasized the necessity of a model theory which considers the charge deformabilities [2]. The phenomenological approach of Bilz *et al* [9] based on adiabatic cluster deformation of RE ion site seems to be the most successful one but the drawback with this approach is the fitting of the parameters with the PDC. In a recent paper Mischenko and Kikoin [11] have considered the contribution from charge density deformation and microscopic theory of electron-phonon interaction in IVCs. We have also reported the calculated results on PDC and one-phonon density of states using three-body force rigid ion model (TRIM) [1], which considers the long range many body interactions arises due to charge transfer between neighbor ions. This model explain the optical branches but fails to explain the acoustic anomalies in TmSe.

The phonon models mentioned above have considerable drawback, as far as their predictions are concerned. All the model theories fit their model except our own TRIM [1] to the measured dispersion curves to achieve a least square fit without taking care of the physical significance of the magnitudes of the fitted parameters.

In the present paper we report the results of the theoretical calculations of the PDC and one phonon density of states of SmS and $Sm_{0.75}Y_{0.25}S$ using a lattice dynamical model theory which includes the breathing motion of the valence electrons of the RE ions. This breathing motion of electron shells arises due to $f-d$ hybridization. This model has already been used to interpret the phonon properties in U-compounds which show similar phonon anomalies [16, 17].

2. Theory

The breathing shell model (BSM) considers phenomenologically the short range electron–phonon interactions in terms of electron shell deformations. Depending upon symmetry, it includes dipolar, quadrupolar and breathing deformabilities of the electron shells of the polarizable ions. A detailed review of this model can be obtained from [15, 18].

The dynamical matrix derived from the interaction hamiltonian can be written as [15]

$$D(q) = (R' + \mathrm{ZCZ}) - (R' + \mathrm{ZCY})(R' + K + \mathrm{YCY})^{-1}(R' + \mathrm{YCZ}) \tag{1}$$

where

$$R' = (R - QH^{-1}Q^{+}). \tag{2}$$

Here C and R are the coulomb and short range repulsive interaction matrices. Q is a (6×2) matrix representing the breathing mode variable while H is a (2×2) matrix specifying the interactions between the breathing mode variables of different ions in the lattice. K and Y are the diagonal matrices and represent the core–shell interaction and shell charge respectively.

The present version of the BSM has altogether eight parameters, which can be self consistently determined from elastic, dielectric and zone centre phonon properties. However, since we have not made any attempt to obtain the least square fit to the phonon data, we have assumed $Y = Y_1 = Y_2$ to minimize the number of parameters. The input and model parameters are listed in tables 1 and 2.

Table 1. Input parameters for SmS and $Sm_{0.75}Y_{0.25}S$.

Property	Value	
	SmS	$Sm_{0.75}Y_{0.25}S$
a	5·975	5·695
C_{11}	1·25	1·129 ± 0·70
C_{12}	0·12	− 0·491
C_{44}	0·31	0·299
$\nu_{TO}(\Gamma)$	5·33	7·900
α_1	0·41	0·45
α_2	5·50	6·50
ε_0	3·55	6·45
ε_∞	9·69	6·45

Elastic constants are in 10^{12} dyn/cm^2, frequency in THz, a in Å and polarizability in Å^{-3} [2, 8, 14].

Table 2. Model parameters for IVC using BSM. All are in units of $e^2/2V$ except Y which is in units of e.

Parameters	Value	
	SmS	$Sm_{0.75}Y_{0.25}S$
A_{12}	50·17260	15·53927
B_{12}	− 8·66930	2·76889
A_{11}	12·77000	− 1·70398
B_{11}	− 3·17000	0·40826
B_{22}	− 10·36000	3·63200
G_1	826·45000	11130·43900
G_2	33·04620	926·11500
Y	− 2·49000	− 9·82170

3. Results and discussion

The calculated phonon dispersion curves for SmS and $Sm_{0.75}Y_{0.25}S$ are plotted in figures 1 and 2 and compared with experimental results [2, 8, 11]. In figure 1 we have presented the PDC for SmS using BSM. The figure reveals that the BSM can explain satisfactorily the measured acoustic branches all along the Brillouin zone. The optical branches particularly in Δ and Λ directions are reproduced well by the present model while it fails in predicting the phonon modes in Σ direction. Since the information about the longitudinal optical branches is limited, appropriate comment cannot be made.

The calculated phonon dispersion curves for $Sm_{0.75}S_{0.25}S$ obtained from the present model are presented in figure 2 and compared with the neutron scattering measurements [8]. Since the model does not consider the doping effect of yttrium hence the local mode at 5·2 THz has not been shown in the figure, similar to what has been

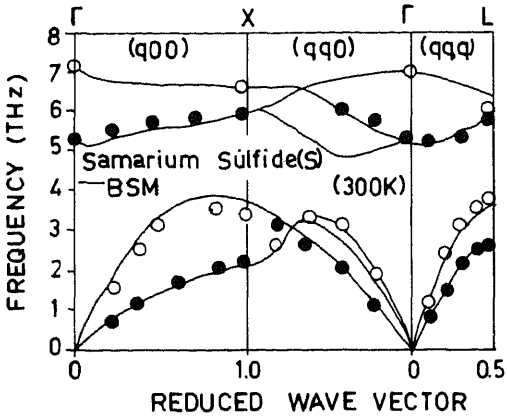

Figure 1. Phonon dispersion curves for SmS. Experimental points are taken from ref. [2, 8, 11].

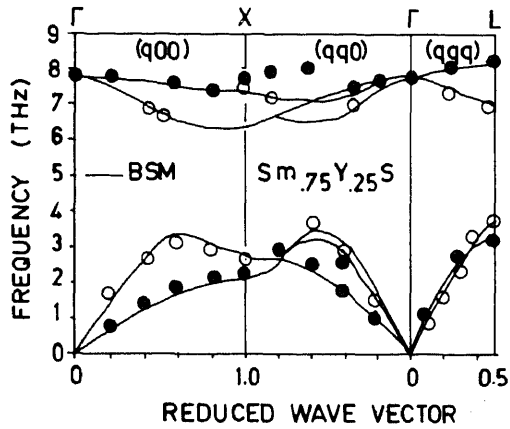

Figure 2. Same as in figure 1 for $Sm_{0.75}Y_{0.25}S$. Experimental points are taken from [2, 8].

reported by Mischenko and Kikoin [11]. Figure 2 reveals that the acoustic branches in $Sm_{0.75}Y_{0.25}S$ alloy have been fairly well reproduced by the present model. In this compound the BSM has predicted fairly well the longitudinal acoustic phonon anomalies throughout the Brillouin zone (BZ). The softening of LA branch at X-point, fairly close magnitude of LA and TA_2 modes along Σ direction particularly at lower wave vectors, softening of LA branch and crossing over TA around (0·4, 0·4, 0·4) have been explained satisfactorily. On the other hand the present model fails to predict the optical branches satisfactorily.

The force constants presented in table 2 for SmS and $Sm_{0.75}Y_{0.25}S$ are reasonably physical. The parameters are physically significant, in the sense that they correctly reproduce the short-range interactions and the crystal properties of these solids. These physically reasonable force constants have been obtained from the macroscopic properties of these compounds. From table 2 it is clear that the positive and negative ion interaction is dominant. The positive–positive ion and negative–negative ion

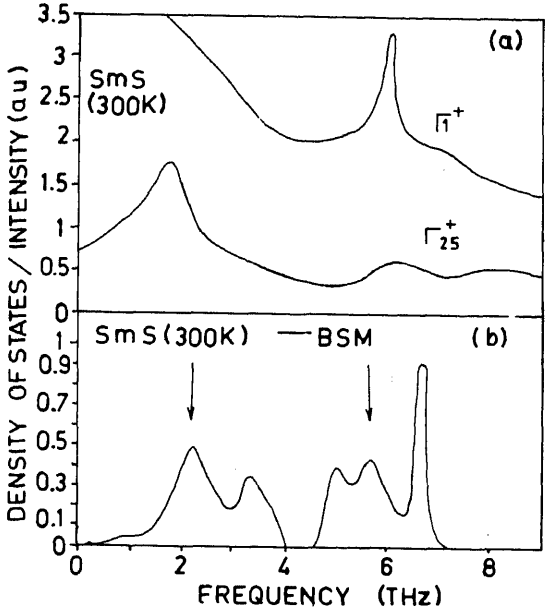

Figure 3. (a) One phonon Raman spectrum of SmS [2, 8]. (b) One phonon density of States of SmS.

interactions are small in magnitude. The $Sm_{0.75}Y_{0.25}S$, however do not follow the trend as SmS. This can be justified from the fact that the dispersion curves for $Sm_{0.75}Y_{0.25}S$ quantitatively reveal metallic nature and zone centre LO and TO phonons degenerate, while the same for SmS are different.

In figure 3, we have presented the one-phonon density of states (DOS) for SmS and compared with Raman spectrum [8]. The experimental Raman spectrum excludes the contribution due to quadrupolar deformability (Γ_{12}^+). Guntherodt *et al* [8] have observed a peak at 6 THz (200 cm^{-1}), contributed by zone boundary LO phonons due to breathing deformabilities. In our DOS, we have also observed similar peak at 6·25 THz contributed by the longitudinal phonons only. The largest contributions arise from the L point of the Brillouin Zone. This result is similar to EuS [20]. However, $q = 0$ phonons are observed at 300 K in EuS due to spin disorder, whereas due to lattice defects in SmS [7]. Another peak in the higher frequency side is due to TO branches. The broad band below 4 THz in figure 3 is from acoustic phonons and can be verified from the experimental Raman spectrum which is attributed to first order defect induced Raman scattering from acoustic phonons. It seems, therefore, the present model has predicted the gross features of the density of states for SmS.

In figure 4, we compare the DOS and Raman spectrum for $Sm_{0.75}Y_{0.25}S$. The Raman spectra of $Sm_{0.75}Y_{0.25}S$ show two sharp peaks at 2·5 THz and 7·0 THz which are due to the Sm- breathing deformability. The density of states of $Sm_{0.75}Y_{0.25}S$ calculated from the present model predicts the peaks at 7·0 THz contributed by LO phonons. This peak could be verified from the Raman spectrum. In our calculated density of states, we have also observed a peak at 6·25 THz due to TO phonons. In $Sm_{0.75}Y_{0.25}S$ the DOS shows a gap between 3·75 THz and 5·75 THz due to the separation between optical and acoustical branches. The peak at 2·55 THz in the

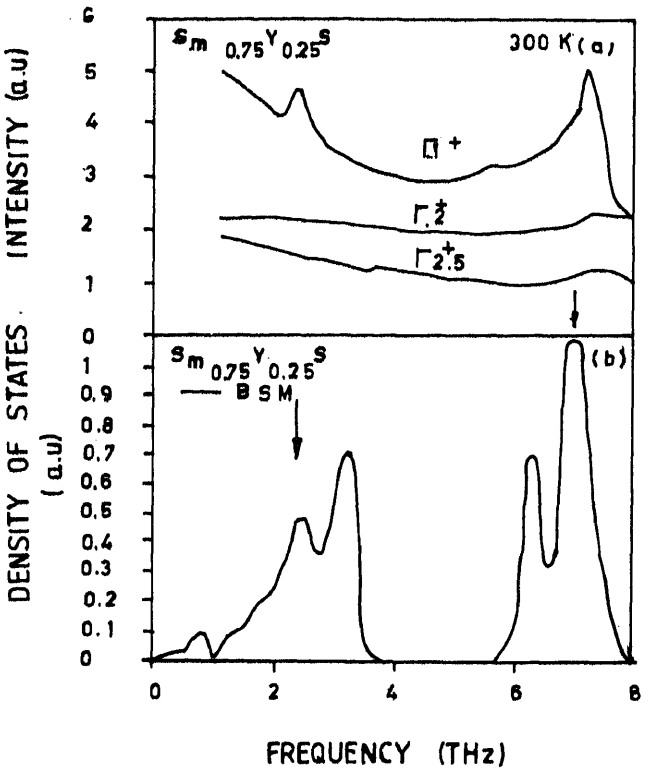

Figure 4. Same as in figure 3 for $Sm_{0.75}Y_{0.25}S$ [8].

lower frequency region of the Raman spectrum could also be obtained from our calculated DOS.

Therefore, from figures 3 and 4 it seems that the breathing deformability of Sm ion is responsible for the dominant contributions of Γ_2^+ Raman scattering and LO(L) phonons in the SmS and LO(L) and LA(L) in $Sm_{0.75}Y_{0.25}S$ to the peak at higher frequency side of the DOS.

Finally, in the present paper we have presented the results of a systematic study of phonon properties of SmS and $Sm_{0.75}Y_{0.25}S$. The calculated results bring out the views that the phonon anomalies in these compounds, in general originates from the breathing motion of the electron shells of rare earth ions. The breathing shell model satisfactorily reproduces the gross feature of the PDC. These predictions reveal that the short range deformations due to breathing motion of the electron shells of RE ions contribute significantly to the phonon anomalies in IVCs.

Acknowledgements

The work is financially supported by DAE, Government of India. One of us (PKJ) acknowledges the award of Research Associateship from CSIR, New Delhi.

References

[1] P K Jha and S P Sanyal, *Indian J. Pure Appl. Phys.* **31**, 469 (1993)
[2] H A Mook and F Holtzberg, *Valence fluctuations in solids*, edited by L M Falicov, W Hanke and M B Maple (North Holland, Amsterdam, 1981), p 113 and references therein
[3] H A Mook and R M Nicklov, *Phys. Rev.* **B20**, 1656 (1977)
[4] H A Mook, R M Nicklov, T Penny, F Holtzberg and W Shafer, *Phys. Rev.* **B18**, 2925 (1979)
[5] H A Mook, D B Mc Wahn and F Holtzberg, *Phys. Rev.*, **B25**, 4321 (1982)
[6] A Jayaraman, V Narayanamurti, E Bucher and R G Mains, *Phys. Rev. Lett.* **24**, 1430 (1970)
[7] G Guntherodt, R Merlin, A Frey and M Cardona, *Solid State Commun.* **27**, 251 (1978)
[8] G Guntherodt, A Jayaraman, W Kress and H Bilz, *Phys. Rev. Lett.* **20**, 824 (1981)
[9] H Bilz, G Guntherodt, W Klippmann and W Kress, *Phys. Rev. Lett.* **43**, 1998 (1979)
[10] P Roedhammer, W Reichardt and F Holtzberg, *Phys. Rev. Lett.* **40**, 465 (1978)
[11] A S Mischenko and K A Kikoin, *J. Phys. Condensed Matter.* **3**, 5937 (1991)
[12] H Boppart, A Treindl and P Wachter, *Valence Fluctuations in Solids*, edited by L M Falicov, W Hanke and M B Maple (North Holland, Amsterdam, 1981), p 103 and references therein
[13] P K Jha and S P Sanyal, *Indian J. Pure Appl. Phys.* **31**, 762 (1993)
[14] S P Sanyal and V Mishra, *Indian J. Pure Appl. Phys.* **26**, 624 (1988)
[15] V Nusslein and U Schroder, *Phys. Status Solidi.* **B21**, 309 (1967)
[16] P K Jha and S P Sanyal, *Phys. Rev.* **B** (1993) (in press)
[17] P K Jha and S P Sanyal, *Pramana – J. Phys.* **42**, 9 (1993)
[18] R K Singh, *Phys. Rep.* **85**, 259 (1982)
[19] T Hailing, G S Saunders and H Back, *Phys. Rev.* **B29**, 1848 (1984)
[20] R Merlin, R Zeyher and G Guntherodt, *Phys. Rev. Lett.* **39**, 1215 (1977)

PRAMANA
— journal of
physics

© Printed in India

Vol. 42, No. 3,
September 1994
pp. 201–209

Computation of collective modes and acoustic investigations at different temperatures of vitrous silica

R V GOPALA RAO and R VENKATESH
Division of Physical Chemistry, Jadavpur University, Calcutta 700 032, India

MS received 6 May 1994

Abstract. This paper is mainly concerned with elastic and acoustic properties of vitrous silica besides the computation of phonon frequencies. Thus the phonon frequencies of vitrous silica have been calculated assuming the electronic bulk modulus, K_e, as equal to zero. New equations have been derived to relate the pressure derivatives of second order elastic constants to the acoustic Gruneisen's parameters using both Bhatia–Singh's parameters and Schofield's equations. The calculated longitudinal and transverse Gruneisen's parameters and the predicted absorption band spectra from Nagendranath's equation and Bhatia Singh's parameters are in good agreement with experiment. The calculated mean acoustic mode Gruneisen's parameter evaluated from the pressure derivative of Nagendranath's equation is also in good agreement with experiment.

Keywords. Phonon frequencies; pressure derivatives of elastic constants; longitudinal and transverse Gruneisen's constants; absorption band.

PACS No. 62·20

1. Introduction

Recently, various aspects of vitrous silica have been investigated [1–5]. Some of the important properties that have been investigated are the acoustic properties [1], neutron diffraction studies [2–4], velocity measurements [5] of densified a-SiO_2 etc. Vitrous silica is of great technical importance. It is a pure, single-phase glass and its non-linear acoustic properties are singularly anomalous. The temperature dependence of elastic stiffness constants, as measured by Wang *et al* [6] are negative up to 70 K and then become positive. Recently the pressure dependence of longitudinal sound wave velocity in vitrous silica has been measured [7] through Brillouin spectroscopy between 50 K and room temperature. It is found that there is a reduction in velocity by the application of pressure. Negative pressure derivatives of second order elastic stiffness tensor components and positive third order elastic constants (TOEC) reveal anamolous effects in the vibrational anharmonicity while the mode Gruneisen's parameter's are negative [6]. Hence a knowledge of acoustic mode Gruneisen constant is important in understanding low temperature thermal expansion. Hence we felt a theoretical investigation of phonons, acoustic and elastic properties of vitrous silica is important. As pointed out earlier SiO_2 is remarkable in the sense that the pressure derivatives of second order elastic constants (SOEC) and also that of bulk modulus is negative unlike in normal substances like TeO_2 glass [8], amorphous As [9] and As_2S_3 [10]. Even though the SOEC pressure derivatives are negative it is remarkably isotropic over a wide temperature range. Vitrous silica has been shown to possess tetra-

hedral structure [11, 12] and the average number of nearest neighbours has been estimated [11] to be 4.3. Extensive elastic and acoustic work has been done on vitrous silica. We give only the reference to the recent studies of Wang *et al* [6] in which other references can be found. Wang *et al* made a detailed experimental study of the SOECs, their pressure derivatives as well as the acoustic Gruneisen's constants as a function of temperature. We also derive the phonon frequencies through Bhatia–Singh's (BS) method [13].

2. Theory

A. *Computation of phonon frequencies*

Bhatia and Singh [13] derived the following expressions for the longitudinal and transverse phonon frequencies

$$\rho\omega_L^2(k) = \frac{2n_c}{a^2}(\beta I_0 + \delta I_2) + \frac{K_e K_{TF}^2 k^2 [G(kr_s)]^2}{k^2 + K_{TF}^2 \tilde{g}(k)}. \tag{1}$$

$$\rho\omega_T^2(k) = \frac{2n_c}{a^2}\left[\beta I_0 + \frac{\delta}{2}(I_0 - I_2)\right]. \tag{2}$$

Here n_c stands for the number of nearest neighbours, a is the nearest neighbour distance, K_{TF} is the Thomas–Fermi inverse screening length, K_e is the electronic bulk modulus. r_s the Wigner–Seitz radius, $G(kr_s)$ is the shape factor and $\tilde{g}(k)$ is the Linhard–Langer–Vasko expression for the k dependent dielectric constant. Since these expressions have been discussed earlier [14, 15] we do not give any more details here. Since vitrous silica is not a semiconductor and is a dielectric we take K_e the electronic bulk modulus to be equal to zero and calculate $\omega_L(k)$ and $\omega_T(k)$ from (1) and (2). To evaluate β and δ we use the experimental values of C_{11} and C_{44} as given by Wang *et al* [6].

The equations are [13]

$$C_{11} = n_c\left[\frac{1}{3}\beta + \frac{1}{5}\delta\right], \tag{3}$$

$$C_{44} = n_c\left[\frac{1}{3}\beta + \frac{1}{15}\delta\right], \tag{4}$$

where

$$\beta = \frac{\rho a^2}{2M}\left[\frac{1}{r}\frac{d\phi}{dr}\right]_{r=a}, \tag{5}$$

$$\delta = \frac{\rho a^3}{2M}\left[\frac{d}{dr}\left\{\frac{1}{r}\frac{d\phi}{dr}\right\}\right]_{r=a}. \tag{6}$$

Here ϕ is the pair potential. We calculate the phonon frequencies at four different temperatures.

B. *Derivation of the pressure derivatives of elastic constants from Bhatia–Singh's β and δ parameters*

$$\frac{dC_{11}}{dP} = n_c\left[\frac{1}{3}\frac{d\beta}{dP} + \frac{1}{5}\frac{d\delta}{dP}\right]. \tag{7}$$

$$\frac{dC_{44}}{dP} = n_c\left[\frac{1}{3}\frac{d\beta}{dP} + \frac{1}{15}\frac{d\delta}{dP}\right]. \tag{8}$$

From (6) it can be shown that

$$\frac{d\delta}{dP} = -\frac{d\beta}{dP} + \frac{\rho a^2}{2M}\frac{d}{dP}\left(\frac{d^2\phi}{dr^2}\right)_{r=a} + \left(\frac{d^2\phi}{dr^2}\right)_{r=a}\frac{d}{dP}\left(\frac{\rho a^2}{2M}\right). \tag{9}$$

$$\frac{d}{dP}\left(\frac{d^2\phi}{dr^2}\right)_{r=a} = \left[\frac{d}{dV}\left(\frac{d^2\phi}{dr^2}\right)\frac{dV}{dP}\right]_{r=a}. \tag{10}$$

$$= \left[-\chi_T r\frac{d^3\phi}{3dr^3}\right]_{r=a}. \tag{11}$$

Here χ_T is the isothermal compressibility. Remembering that the Gruneisen's constant γ_g is given by [16, 17]

$$\gamma_g = \frac{-\frac{1}{6}a\left(\frac{d^3\phi}{dr^3}\right)_{r=a}}{\left(\frac{d^2\phi}{dr^2}\right)_{r=a}}, \tag{12}$$

one can show that

$$\left(\frac{d\delta}{dP}\right)_T = -\frac{d\beta}{dP} + 2\chi_T(\delta+\beta)\left(\gamma_g + \frac{1}{6}\right). \tag{13}$$

Similarly it can be shown that

$$\left(\frac{d\beta}{dP}\right)_T = -\frac{\rho a^2\chi_T}{6M}\left(\frac{d^2\phi}{dr^2}\right)_{r=a} + \frac{\rho a\chi_T}{3M}\left(\frac{d\phi}{dr}\right)_{r=a}. \tag{14}$$

Thus finally we obtain

$$\frac{d\delta}{dP} = 2\chi_T\left[\frac{\delta}{3} + (\beta+\delta)\gamma_g\right], \tag{15}$$

and

$$\frac{d\beta}{dP} = -\frac{\chi_T(\beta-\delta)}{3}. \tag{16}$$

Hence from (8) we get

$$\frac{dC_{11}}{dP} = n_c\chi_T\left[\frac{\delta+5\beta}{45} + \frac{2\gamma_g^L(\beta+\delta)}{5}\right]. \tag{17}$$

In an exactly similar way we obtain

$$\frac{dC_{44}}{dP} = n_c \chi_T \left[\frac{1}{9}(\beta - 0{\cdot}6\delta) + \frac{2}{15}\gamma_g^T(\beta + \delta) \right]. \tag{18}$$

Equations (17) and (18) are important and offer a method in the evaluation of the pressure derivatives of the SOECs. Vitrous silica is a highly isotropic substance and we can obtain dC_{12}/dP from the following equation

$$2\frac{dC_{44}}{dP} = \frac{dC_{11}}{dP} - \frac{dC_{12}}{dP}. \tag{19}$$

In this connection it is important to note that liquids in the high frequency region show rigidity which is a characteristic of solids [18, 19]. Hence it will be interesting and tempting to try the equations of Schofield [20] (Sch) to derive the pressure derivatives of SOECs. From Schofield's equations [20] we derive the following expressions for the pressure derivatives of SOECs as [21]

$$\frac{dC_{11}}{dP} = C_{11}\chi_T + 1.8(C_1 - 1). \tag{20}$$

$$\frac{dC_{44}}{dP} = C_{44}\chi_T + 0{\cdot}6(C_1 - 1). \tag{21}$$

$$\frac{dC_{12}}{dP} = C_{12}\chi_T + 0{\cdot}6(C_1 - 1). \tag{22}$$

Here

$$C_1 \equiv (dB/dP) \tag{23}$$

and B is the bulk modulus.

It is important to remember that C_1 is related to third order elastic constants [22]. Thus (20)–(22), even though can strictly be used for fluids can help us to estimate the pressure derivatives of the SOECs. Calculations for computing the pressure derivatives of SOECs have been made for vitrous silica at different temperatures using (17)–(22).

C. *Prediction of band absorption spectra of vitrous silica*

It was shown that [23–25]

$$\frac{8A(A + 8C_{11} - 16C_{44})}{(3A - 8C_{11} + 16C_{12})^2} = 1, \tag{24}$$

where

$$A = \omega^2 M/2a. \tag{25}$$

From (24) and (25) it is possible to solve for the frequency and hence predict the position of the absorption band.

From (6) we get

$$\delta = -\beta + \frac{\rho a^2}{2M}\left(\frac{d^2\phi}{dr^2}\right)_{r=a} \tag{26}$$

and we can calculate $(d^2\phi/dr^2)_{r=a} \equiv K_1$. With a three-force constant model it is possible to show that for a diamond type of lattice [25]

$$\omega^2 = \frac{4K_1}{M}, \tag{27}$$

and we have $1/\lambda = \omega/2\pi C$ where C is the velocity of light. Hence we can predict the position of the absorption band and can make a comparison of these results with experiment. Such calculations have been made for vitrous silica in these investigations.

D. *Methods of evaluation of acoustic Gruneisen's parameters* γ_g^T *and* γ_g^L

From (17) we get C_1 associated with γ_g^L the Gruneisen's constant of longitudinal wave while from (18) we get γ_g^T that of the transverse wave. Similarly we use (20) and (21).

The mean acoustic mode Gruneisen's parameter γ_g^{el} can be obtained [6] from the following equation

$$\gamma_g^{el}\left(\frac{\gamma_L}{V_L^3} + \frac{2\gamma_g}{V_L^3}\right)\left(\frac{1}{V_L^3} + \frac{2}{V_T^3}\right)^{-1}. \tag{28}$$

We now give a method of evaluation of γ_g^{el} using (24) and (25). We differentiate (24) with respect to pressure and solve for $(dA/dP)_T$. Thus we obtain

$$\frac{dA}{dP} = \left\{\frac{dC_{11}}{dP}[56A + 128C_{12} - 64C_{11}] - 64A\left(\frac{dC_{44}}{dP}\right) + \frac{dC_{12}}{dP}[128C_{11} - 48A - 256C_{12}]\right\}[A - 56C_{11} + 48C_{12} + 64C_{44}]^{-1}. \tag{29}$$

Now we eliminate dC_{12}/dP using the isotropy condition (vide (19)) and finally obtain

$$\frac{dA}{dP} = \left\{8\left(\frac{dC_{11}}{dP}\right)(3A - 8C_{11} + 16C_{12}) + 16\left(\frac{dC_{12}}{dP}\right)(8C_{11} - 16C_{12} - A)\right\}(A - 24C_{11} + 16C_{12})^{-1}. \tag{30}$$

Further we have

$$A = K_2\omega^2 \tag{31}$$

where

$$K_2 = M/2a \tag{32}$$

From (31) we get

$$\frac{dA}{dP} = \beta_T A\left[2\gamma_g^{el} + \frac{1}{3}\right], \tag{33}$$

where we assumed that $v = kr^3$. Here v is the volume and r is the radius. Hence from (30)–(33) we can solve the mean acoustic mode Gruneisen parameter γ_g^{el}.

3. Results and discussion

As pointed out already an application of the various equations derived above have been applied to vitrous silica. The experimental results used are those of Wang *et al* [6]. In figure 1 we give the phonon frequencies as obtained from (1) and (2) at two different temperatures namely 273 K and 77 K. As pointed out already vitrous silica is a dielectric and hence it is assumed that $K_e = 0$. The β and δ values calculated from (3) and (4) at the four temperatures are given in table 1. The position and maximum values of $\omega_L(k)$ and $\omega_T(k)$ are given in table 2. It may be noted from table 1 that

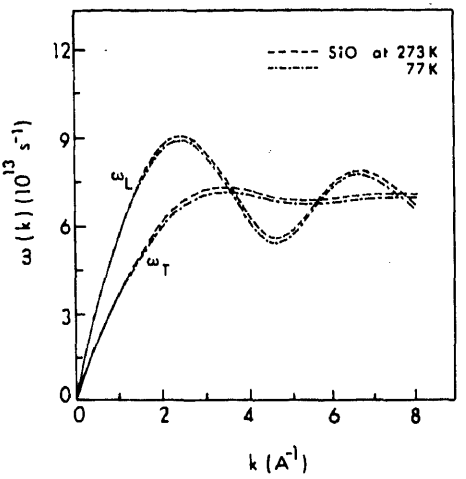

Figure 1. Phonon frequencies at 77 and 273 K.

Table 1. Parameters obtained for β and δ at different temperatures.

Temp. K	$\beta \times 10^{12}$ dyn/cm^2	$\delta \times 10^{12}$ dyn/cm^2
273	0·0469	0·835
233	0·0406	0·8383
123	0·0380	0·8311
77	0·0352	0·832

$K_e = 0$ and $\rho_w = 2{\cdot}202$ g/cm^3; n_c [11] = 4·3; a [11] = 1·61 Å

Table 2. Characteristics of phonon frequencies at different temperatures.

Temp. (K)	Position and maximum value k Å^{-1}	(ω_L) 10^{13}s^{-1}	Position and maximum values (k) Å^{-1}	ω_T 10^{13}s^{-1}
273	2·4	9·03	3·4	7·3
233	2·4	8·98	3·4	7·24
123	2·4	8·92	3·4	7·19
77	2·4	8·89	3·4	7·1

$\beta \neq 0$ and hence central forces are not alone operative. Evidently the tetrahedral angular forces are contributing and hence $(d\phi/dr)_{r=a} \neq 0$. The position of the maximum phonon frequency does not change with temperature both for $\omega_L(k)$ and $\omega_T(k)$. However with increase in temperature the frequency increases slightly. As expected $\omega_L(k)$ attains a maximum at a small value of k and oscillates showing collective mode propagation for larger values of k while $\omega_T(k)$ attains almost a constant value beyond the maximum. From β and δ given in table 1 and at a temperature 273 K we get $\omega = 11{\cdot}1 \times 10^3 s^{-1}$ through the use of (27) and the position of the absorption band should appear at $583\,cm^{-1}$. The value of A obtained from (24) is $31{\cdot}7 \times 10^{12}$ dyn/cm^2 and from (25) we get the absorption band of vitrous silica to appear at $536\,cm^{-1}$. The observed bands for vitrous silica as reported by Lippincot *et al* and Hass [26, 27] appear between $500\,cm^{-1}$ and $600\,cm^{-1}$ which are reasonably close to the calculated values obtained from A and $(d^2\phi/dr^2)_{r=a}$. The average value being $560\,cm^{-1}$. According to Bell and Dean [28] this vibrational mode arises from bond bending vibration in which the oxygen atoms move along the bisectors of Si–O–Si angles. In this connection the absorption band values of $536\,cm^{-1}$ and $583\,cm^{-1}$ correspond to a frequency $10 \times 10^{13} s^{-1}$ and $11{\cdot}0 \times 10^{13} s^{-1}$. These values can be considered to be close to each other. From the observed pressure derivatives we obtain (vide (20) and (21)) C_1^L corresponding to dC_{11}/dP and C_1^T to dC_{44}/dP. We now use the well-known Slater's equation [29]

$$C_1^{L,T} = 2\gamma_g^{L,T} + \frac{1}{3}. \tag{34}$$

We evaluate γ_g^L and γ_g^T at 273 and 77 K using (17) and (18) and also from (20) and (21). The values calculated are given in table 3. It is important to stress that γ_g^L and γ_g^T are related to third order elastic constants [30].

It is known that Bhatia–Singh equation is meant for amorphous solids and gives very good results in agreement with experiment both at low and high temperatures for which results are available. The application of Schofield's equations gives satisfactory results as well. It should be borne in mind that Schofield's equations are meant for liquids and hence the present agreement can be considered as very good.

We can calculate from (30)–(33) the mean acoustic mode Grüneisen's parameter γ_g^{el} at 273 K. Using the experimental values of SOECs we obtain a value of $31{\cdot}7 \times 10^{12}$ dyn/cm^2 for A from (24) and finally we get a value for $\gamma_g^{el} = -2{\cdot}2$ where we used (30)–(33). The experimental value is $-2{\cdot}0$. Thus the agreement is excellent.

Table 3. Gruneisen constants evaluated by different methods at different temperatures.

Temp. K	γ_g^L B.S eq. (17)	γ_g^L Sch eq. (20)	Expt[6]	γ_g^T B.S eq. (18)	γ_g^T Sch eq. (21)	Expt[6]
77	−5·4	−5·9	−5·5	−2·4	−3·6	−2·8
273	−2·4	−3·0	−2·5	−1·8	−2·9	−2·1

4. Conclusions

Using Bhatia–Singh's equation and assuming K_e, the electronic bulk modulus, equal to zero the phonon frequencies have been derived. A change of temperature over a wide range does not effect the position of the maximum while its magnitude decreases only slightly with decreasing temperature. Equations for the pressure derivatives of SOECs have been derived using both Bhatia–Singh's and Schofield's equations. Using the experimental values of the pressure derivatives of the SOECs the longitudinal and transverse Gruneisen's constants have been calculated at two extremely different temperatures for which accurate measurements are available. The results calculated from Bhatia–Singh's parameters give excellent results in agreement with experiment while those obtained from Schofield's equation are also in good agreement with experiment. Using (24) the absorption band spectrum of vitrous silica has been calculated and compared with that obtained from Bhatia–Singh's 'δ' parameter. Both the results are in fair agreement with experiment for SiO_2. Finally we calculate the mean acoustic mode γ_g^{el} from the pressure derivatives of (24). The value obtained is in excellent agreement with experiment.

Acknowledgements

The authors are thankful to the DST, CSIR, Government of India for financial support.

References

[1] R A Graham, *J. Acoust. Soc. Am.* **51**, 1576 (1972)
[2] A C Hannon, M Arai, R N Sinclair and A C Wright, *J. Non-Cryst. Solids* **150**, 239 (1992)
[3] J M Carpenter and D L Price, *Phys. Rev. Lett.* **54**, 441 (1985)
[4] S Susman, K J Volin, D L Price, M Grunsditch, J P Rino, R K Kalia, P Vashista, G Gwanmesia, Y Wang and R C Libermann, *Phys. Rev.* **B43**, 1194 (1991)
[5] A Polian and M Grunsditch, *Phys. Rev.* **B47**, 13979 (1993)
[6] Q Wang, G A Saunders, H B Senin and E F Lambson, *J. Non-Cryst. Solids* **143**, 65 (1992)
[7] D Tielburger, R Merz and S Hunklinger, in *Proceedings of the 3rd International Conference on Phonon Physics*, (World Scientific, Singapore, 1990) **Vol. 1** p. 447
[8] E F Lambson, G A Saunders, B Bridge and R A El-Mallawany, *J. Non-Cryst. Solids* **69**, 117 (1984)
[9] M P Brassington, W A Lambson, A J Miller, G A Saunders and Y K Yogurtan, *Philos. Mag.* **B42**, 127 (1980)
[10] M P Brassington, A J Miller, G A Saunders, *Philos. Mag.* **B43**, 1049 (1981)
[11] B E Warren, H Krutter and O Morningstar, *J. Am. Ceram. Soc.* **19**, 202 (1936)
[12] S R Elliott, *Physics of amorphous materials* (Longman, London and New York, 1984) p. 95–99
[13] A B Bhatia and R N Singh, *Phys. Rev.* **B31**, 4751 (1985)
[14] R V Gopala Rao and R Venkatesh, *Phys. Status Solidi* **B176**, 317 (1993)
[15] R V Gopala Rao and R Venkatesh, *Physica* **B190**, 417 (1993)
[16] P P M Meincke, *Can. J. Phys.* **40**, 283 (1962)
[17] C D Das, H V Keer and R V G Rao, *Z. Phys. Chem.* **224**, 377 (1963)
[18] S Takeno and M Goda, *Prog. Theor. Phys.* **15**, 331 (1971)
[19] A Rahaman, *Statistical mechanics: New concepts, new problems, new applications* edited by S A Rice, K F Freed and J C Light (University of Chicago Press, Chicago, 1972)
[20] P Schofield, *Proc. Phys. Soc.* **88**, 149 (1966)

[21] R V Gopala Rao and R Venkatesh, *J. Non-Cryst. Solids* (In press) 1994
[22] R N Thurston, *IEEE* **53**, 1320 (1965)
[23] N S Nagendra Nath, *Proc. Indian Acad. Sci.* **A1**, 333 (1934)
[24] H M J Smith, *Philos. Trans. R. Soc. (London)* **A241**, 105 (1948)
[25] J D Launay, in *Solid state physics*, edited by Frederick Seitz and David Turnbull (Academic Press, New York, 1956) **2**, 296
H B Huntington in *Solid State Physics* edited by Frederick Seitz and David Turnbull (Academic Press, New York, 1958) **7**, 301
[26] E R Lippincot, A V Valdenberg, C E Weir and E N Bunting, *J. Res. Natl. Bur. Stand.* **61**, 61 (1958)
[27] M Hass, *J. Phys. Chem. Solids* **31**, 415 (1970)
[28] R J Bell and P Dean, *Amorphous materials*, edited by R W Douglas and Bryan Ellis (Wiley Interscience, New York, 1972) p. 446
[29] S E Babb (Jr.), *J. Chem. Phys.* **38**, 2743 (1963)
[30] W T Yost and M A Breazeale, *J. Appl. Phys.* **44**, 1909 (1973)

PRAMANA
— journal of
physics

© Printed in India

Vol. 43, No. 3,
September 1994
pp. 211–217

Even harmonics of AC susceptibility in some sintered pellets of high temperature superconductors

A DAS, A BAJPAI, A BANERJEE and R SRINIVASAN
Inter University Consortium for DAE Facilities, University Campus, Khandwa Road, Indore 452001, India

MS received 13 May 1994

Abstract. The real (χ_n') and imaginary (χ_n'') parts of even harmonic susceptibility ($n \leqslant 6$) are measured as a function of external DC field (H_{dc}) in the field increasing ($H^{\uparrow}$) and decreasing ($H_{\downarrow}$) cycle. Hysteresis is observed between $H^{\uparrow}$ and $H_{\downarrow}$ cycles. In the $H_{\downarrow}$ cycle, at a field, $H_{comp} = 4{\cdot}2$ G, both χ' and χ'' of all the even harmonics vanish indicating a true cancellation of fields in the intergrain region ($H_{eff} \approx 0$) caused by the balance between H_{dc} and the remanent magnetization of the grains. The position of the extrema and the zero of the various harmonics undergo a shift proportional to the remanent magnetization of the grains at that particular field.

Keywords. AC Magnetic susceptibility; even harmonics; high T_c superconductors; thermomagnetic hysteresis; remanent magnetization.

PACS Nos 74·30; 74·60

1. Introduction

In sintered pellets of high temperature superconductors, the grains are interconnected through grain boundaries or weak links. AC susceptibility studies reveal interesting features linked with inter-grain and intra-grain flux penetration [1]. The observation of thermomagnetic hysteresis effects in $J_c(H)$ [2], harmonic voltages [3, 4] and minor loop magnetic hysteresis [5] in such materials have attracted attention.

One can understand the thermo-magnetic hysteresis in the following way. When a low value of external magnetic field, H_a, is applied, this field penetrates the weak links but is excluded from the grains, if it is below H_{c1} of the grains. The exclusion of the flux from penetrating the grains causes a concentration of flux in the intergrain region. This phenomenon termed flux compression causes the effective magnetic field in the intergrain region, H_{eff}, to be more than the applied field. When the applied field is reduced from a value large enough to ensure flux penetration within the grains, the remanent magnetization in the grains causes a field opposite in direction to the applied field in the weak link region. Thus the effective magnetic field is now lower than the applied field. Since J_c is a function of H_{eff} one sees hysteresis when J_c is plotted as a function of the applied field.

The occurrence of even harmonics in low amplitude AC susceptibility measurements requires (a) J_c to be a function of the effective magnetic field and (b) the presence of a non-zero DC magnetic field superposed on the AC field. In the decreasing cycle of the magnetic field one would reach a stage when H_{eff} will become zero. This will be signalled by the vanishing of all even harmonics at a non-zero value of the DC

magnetic field. Reitz *et al* [6] have used the amplitude of the second harmonic signal to detect when an exact compensation was achieved in the following two situations: (a) The sample is field-cooled (FC) in a large value of H_{dc}. After cooling the field is switched off. Then a small DC magnetic field is applied and its value is adjusted to get a minimum in the second harmonic signal; (b) The sample is zero-field cooled (ZFC); then a large DC field is applied for 100 s and switched off. After a delay of 100 s the second harmonic is monitored as a function of applied DC field till its amplitude vanishes. The two values of the field at which the second harmonic vanishes are different, the value in case (a) being larger than in the case (b). The value of the field at which the second harmonic vanishes is a measure of the remanent magnetization and this was verified by a direct determination of the remanent magnetization in FC and ZFC cases.

In the present study we have verified that the real and imaginary parts of all the even harmonics up to the sixth vanish at nearly the same value of H_{dc} indicating that the H_{eff} in the inter-granular region is really zero.

2. Experimental details

The sample studied is $Y_1Ba_2Cu_{2.8}Ag_{0.2}O_7$ prepared by the conventional ceramic route; and is in the form of a cylinder of about 2 mm diameter and 5 mm length. The T_c (onset) and $T_c(0)$ determined from χ_{ac} and resistivity measurements are 88 K and 87 K, respectively. The harmonic voltages are measured as a function of DC field (H_{dc}) at an excitation field of $H_{ac} = 1{\cdot}9$ G, using a lock-in amplifier (SRS 850), which is able to lock into the various harmonics of the fundamental frequency, without the requirement of any additional external circuitry. The fundamental frequency of measurement is kept at 66·666 Hz and the measurements are done at 77 K, having the sample, primary, balanced secondary and the coaxial DC coil assembly immersed in liquid nitrogen bath. The primary excitation field is a pure sine wave and no measurable harmonic voltages were found in the absence of sample and at the highest excitation fields. The phase adjustment is done by making $\chi_1'' = 0$ in 0·015 G AC field. All the measurements are done in the presence of the earth's magnetic field. When we are mentioning about ZFC measurements it is actually FC to 77 K in earth's magnetic field. The absolute magnitude of the even harmonics is very small but is much above the noise and experimental resolution. Since the measured voltages are not calibrated with respect to a standard sample the units are maintained as microvolt (μV).

3. Results and discussion

Figure 1 shows the variation of χ_2' and χ_2'' as a function of the applied DC field. Figure 1(a) shows the variation with increasing DC field ($H^{\uparrow}$) while figure 1(b) shows the results in the decreasing cycle ($H_{\downarrow}$). The maximum applied DC field is 53 G. In the $H^{\uparrow}$ cycle both χ_2' and χ_2'' exhibit a maximum around $H_{dc} \approx 5$ G. The maximum in χ_2' is broader than in the χ_2'' and appears to show some structure. The hysteresis in the values of χ_2' and χ_2'' with $H^{\uparrow}$ and $H_{\downarrow}$ is apparent from the figure. For the same value of applied field, χ_2' and χ_2'' are more in the decreasing cycle than in the increasing cycle and are also shifted to higher values of the applied field. As the field is reduced below the value at which the peaks are observed, both χ_2' and χ_2'' appear to go to zero (within the experimental uncertainty) at $H_{dc} \approx 4{\cdot}2$ G. The vanishing of the real

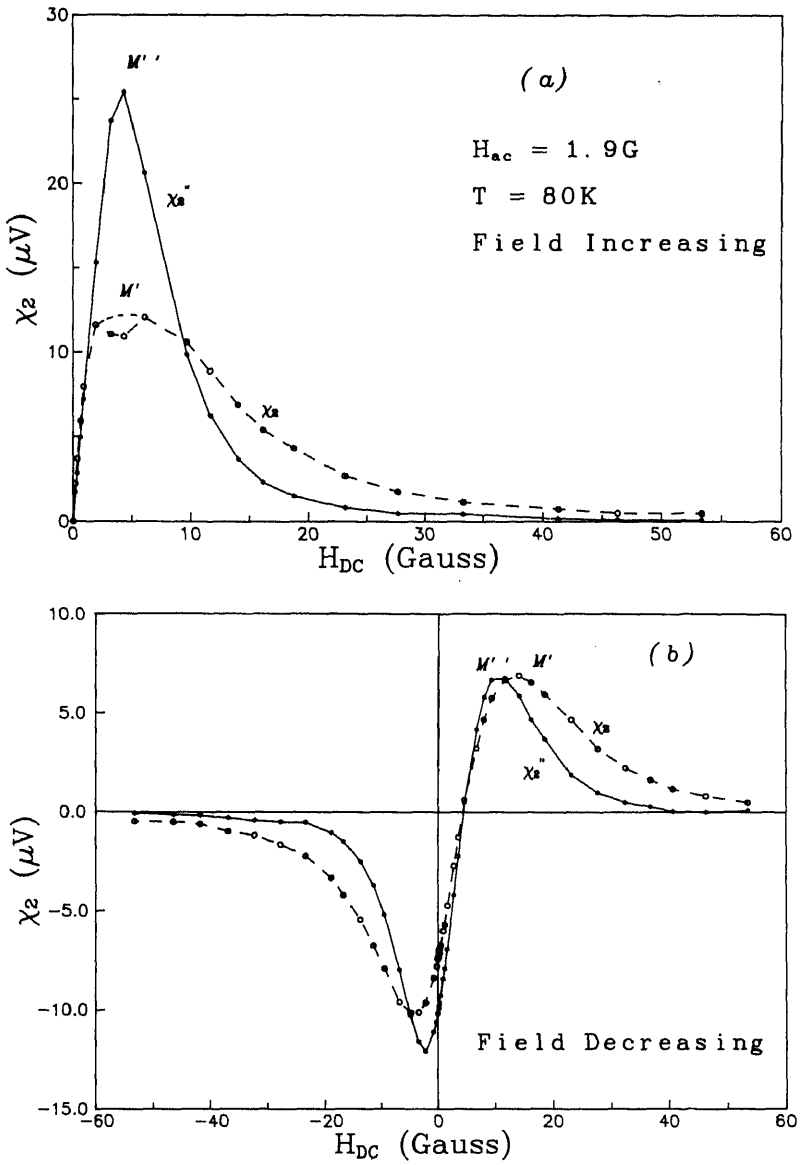

Figure 1. (**a**) The real (χ_2') and imaginary (χ_2'') component of the second harmonic susceptibility as a function applied DC field, H_{dc}, in the field increasing cycle (ZFC, $H^{\uparrow}$). (**b**) The same in the field decreasing cycle (ZFC, $H_{\downarrow}$).

and imaginary parts of the even harmonic susceptibility indicates that 4·2 G is the compensating field and is proportional to the remanent magnetization in the ZFC sample when it is exposed to a maximum field of 53 G. We find that the sign of both χ_2' and χ_2'' changes when H_{dc} is reduced below 4·2 G. With a spectrum analyzer, which will give only the amplitude, one could see a rise in amplitude below a minimum in the second harmonic signal [3]. However, the signal is not symmetric about the compensation field. The non-symmetric character can possibly be consequence of flux compression once the field in the intergrain region is reduced to zero and reversed.

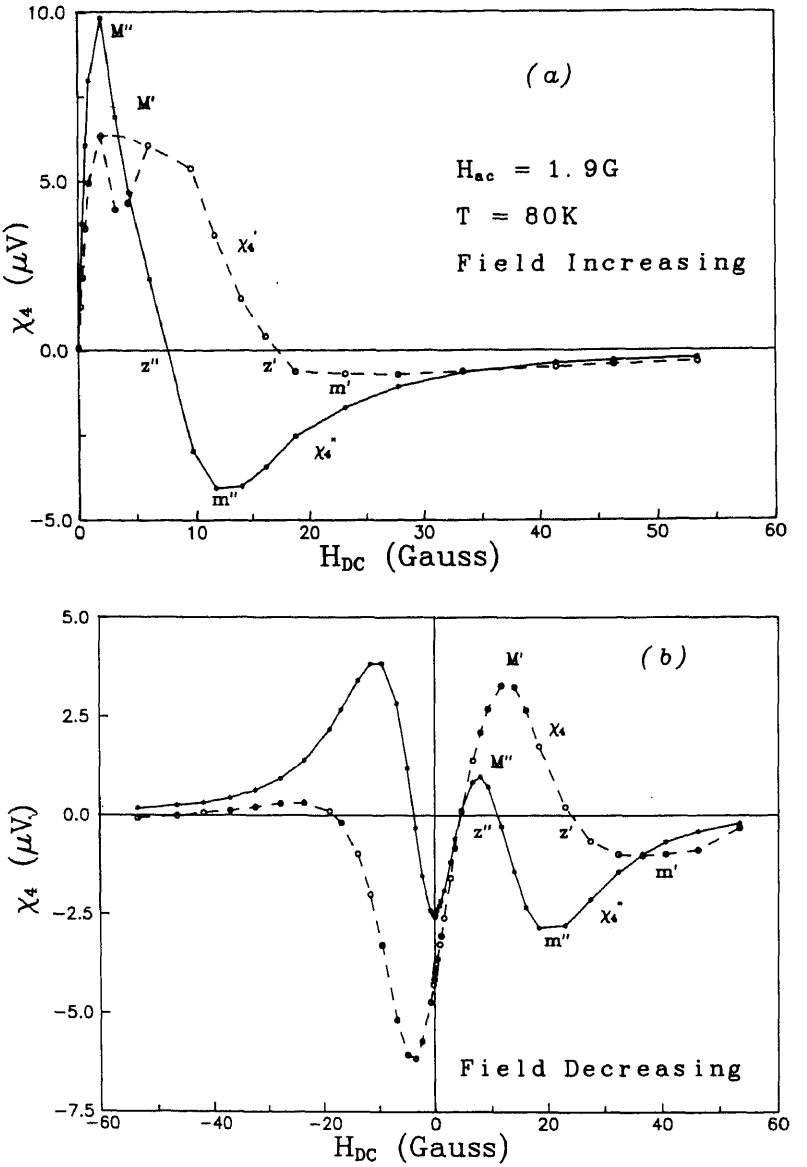

Figure 2. (**a**) The real (χ_4') and imaginary (χ_4'') component of the fourth harmonic susceptibility as a function applied DC field, H_{dc}, in the field increasing cycle (ZFC, $H^{\uparrow}$). (**b**) The same in the field decreasing cycle (ZFC, $H_{\downarrow}$).

Below H_{comp}, the effective field will be negative and as long as its magnitude is less than H_{c1} of the grain, there will be flux compression. So if we shift the origin of the magnetic field to the compensation point, the curve to the left will be compressed towards the y-axis resulting in an asymmetry. This is what is observed in the figure 1 (b).

Figures 2(a) and 2(b) depict the variation of χ_4' and χ_4'' as a function of H_{dc} in the increasing and decreasing magnetic cycles respectively. Figures 3(a) and 3(b) show the variation of χ_6' and χ_6'' with increasing and decreasing fields, respectively. Both

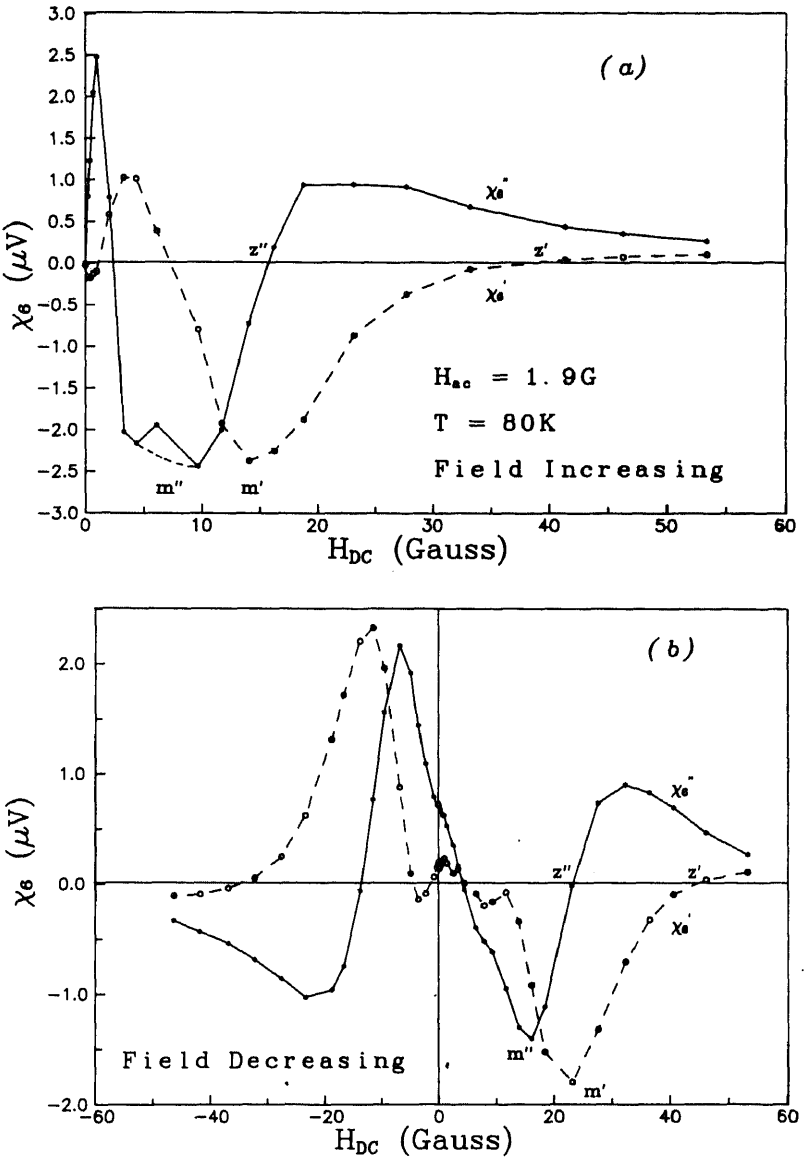

Figure 3. (**a**) The real (χ_6') and imaginary (χ_6'') component of the sixth harmonic susceptibility as a function applied DC field, H_{dc}, in the field increasing cycle (ZFC, $H^{\uparrow}$). (**b**) The same in the field decreasing cycle (ZFC, $H_{\downarrow}$).

χ_4' and χ_4'' change sign once in the increasing cycle. χ_6' and χ_6'' change signs twice with increasing field. However, the field at which the real part crosses the axis is different from that of the imaginary part both for χ_4 and χ_6. Whereas, on decreasing the field there is one value at which both real and imaginary parts vanish simultaneously. This occurs for χ_4 and χ_6 at 4·2 G which is the field at which the real and imaginary parts of χ_2 also vanish. This provides a clear indication that compensation of the intergrain field occurs when the magnetic field is at 4·2 G.

Table 1 gives the value of H_{dc} at which maxima, minima and zero of the real and imaginary parts of χ_2, χ_4 and χ_6 occur with increasing and decreasing fields. The difference in the position of either the extrema or zero, between increasing and decreasing field, at a particular field, is a measure of the remanent magnetization of the grains at that particular field. In figure 4 we plot these differences as a function

Table 1. DC fields at which maxima (M), minima (m) and zero values (z) occur in the real and imaginary parts of the even harmonics. The zero at the compensation field is omitted.
(Those fields which are larger than the compensation field and which can be reasonably well fixed are collected in the table).

Component	Figure	Field increasing	Figure	Field decreasing
2′	1a(M')	4·4	1b(M')	13·8
2″	1a(M'')	3·5	1b(M'')	10·0
4′	2a(M')	4·2	2b(M')	12·7
4′	2a(z')	17·6	2b(z')	24·2
4′	2a(m')	Broad	2b(m')	Broad
4″	2a(M'')	1·8	2b(M'')	7·9
4″	2a(z'')	7·8	2b(z'')	10·8
4″	2a(m'')	12·4	2b(m'')	20·0
6′	3a(m')	13·7	3b(m')	23·0
6′	3a(z')	38·1	3b(z')	44·0
6″	3a(m'')	7·0	3b(m'')	15·8
6″	3a(z'')	15·7	3b(z'')	23·0

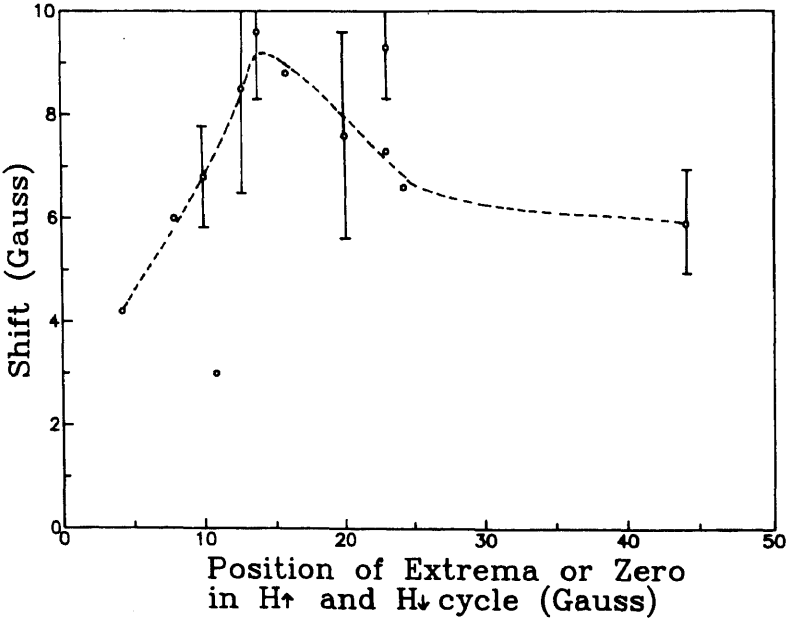

Figure 4. Plot of the shift in the position of the extrema and zero between $H^{\uparrow}$ and $H_{\downarrow}$ cycles as a function of the position of the extrema and zero in $H^{\uparrow}$ and $H_{\downarrow}$ cycles.

of the position of the extremum and zero. We find that the remanent magnetization shows a maximum at $H_{dc} \approx 15$ G. A similar behavior would be obtained if a plot of the difference in the magnetization $M(\text{ZFC}, H^{\uparrow})$ and $M(\text{ZFC}, H_{\downarrow})$ is made.

4. Conclusions

The even harmonics exhibit hysteresis between the field increasing and decreasing cycle. The hysteresis is due to $H_{\text{eff}}(\text{ZFC}, H^{\uparrow}) > H_{\text{eff}}(\text{ZFC}, H_{\downarrow})$. The vanishing of the real and imaginary parts of all the even harmonic susceptibilities at H_{comp} gives an unambiguous indication that H_{eff} in the intergrain region is truly zero at this field. The maximum cancellation of fields in the intergrain region occurs when H_{dc}, equals in magnitude, with the field caused by the trapped magnetization of the grains. The position of the extremum in the real and imaginary parts of the various harmonic susceptibility undergoes a shift which is proportional to the remanent magnetization of the grains at that particular field.

Acknowledgements

We thank Prof A K Majumdar of IIT, Kanpur for providing us with the sample on which basic characterization had been done. One of us (AD) gratefully acknowledges Dr P Chaddah of CAT, Indore for several discussions on these and other aspects relating to harmonics in HTSC materials.

References

[1] T Ishida and R B Goldfab, *Phys. Rev.* **B41**, 8937 (1990)
[2] J E Evetts and B A Glowacki, *Cryogenics* **28**, 641 (1988)
[3] Shailendra Kumar, S B Roy, P Chaddah, Ram Prasad and N C Soni, *Physica* **C191**, 450 (1992)
[4] D Sen, A Mitra and S K Ghatak, *Supercond. Sci. Technol.* **5**, 467 (1992)
[5] S B Roy, Shailendra Kumar, A K Pradhan, P Chaddah, Ram Prasad and N C Soni, *Physica* **C218**, 476 (1993)
[6] Th Ritzi, Ch Heinzel, Ch Neumann and P Ziemann, *Appl. Phys. Lett.* **60**, 2297 (1992)

PRAMANA
— journal of
physics

© Printed in India

Vol. 43, No. 3,
September 1994
pp. 219–229

Electric and dielectric properties of solution–gas interface grown amorphous AgCl films

P S NIKAM and K A PATHAN+
P G Department of Physical Chemistry, +Department of Physics, M S G College, Malegaon Camp 423 105, India

MS received 6 May 1994; revised 2 July 1994

Abstract. Electric and dielectric properties of solution–gas interface grown AgCl thin film capacitors (Al/AgCl/Al) of various thicknesses have been studied in the frequency range 10^1–10^6 Hz at various temperatures (303–393 K). I–V characteristics show ohmic, space-charge-limited, and thermionic emission conduction mechanisms to operate at low, intermediate and high voltages respectively. Capacitance decreases with increasing film thickness and applied frequency while it increases with increase of temperature. Loss factor ($\tan\delta$), which shows a pronounced minimum with frequency, increases with the rise of temperature and $(\tan\delta)_{min}$ shifts to a higher frequency. The large values of capacitance and dielectric constant (ε) in the low frequency region indicate the possibility of an interfacial polarization mechanism to operate in this region while electronic and ionic polarizations dominate in the high frequency region.

Keywords. I–V characteristics; space charge limited currents; thermionic emission; capacitance; dielectric constants; loss factor.

PACS No. 73·40

1. Introduction

Thin films of AgCl find applications in electrochemistry [1], ion sensitive membrane [2], coated wire electrodes [3] and in ion sensitive field transistor [4]. However, AgCl films formed by conventional thermal evaporation, sputtering and electrodeposition are impure, defective and nonstoichiometric [5–9]. Therefore, we have used, for the first time, solution–gas interface technique to give chemically and mechanically stable films of AgCl. The previous investigations of thin films of AgCl formed by using different techniques are restricted only to structural, optical and electric conductance studies [6, 9–18]. This is the only investigative study of I–V characteristics and dielectric properties of AgCl films formed at the interface of aqueous solution of 0·5% $AgNO_3$ and HCl gas.

2. Experimental

One hundred ml of 0·5% $AgNO_3$ aqueous solution in a dish was exposed to HCl gas atmosphere. The AgCl film formed on the surface of the solution was picked up on an ultrasonically cleaned glass substrate with evaporated (~ 2000 Å) aluminium base electrode. The film was washed 2–3 times by dipping it in warm distilled water to remove impurities followed by drying under a vacuum of $\sim 10^{-2}$ torr. Pure aluminium was again evaporated on the film to complete Al/AgCl/Al capacitor

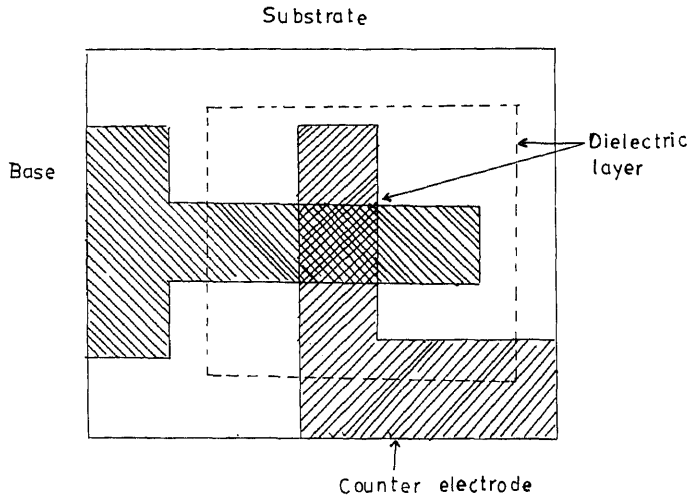

Figure 1. Configuration of Al/AgCl/Al capacitor.

(figure 1). All capacitors were of sandwich type. They were stabilized by keeping them at room temperature for several days in a vacuum desiccator, and later on annealing in vacuo of $\sim 10^{-5}$ torr at about 413 K for 6 h. Calorimetric analysis at 620 mμ wavelength [19] of AgCl films confirmed that films were more or less stoichiometric. The XRD study showed amorphous structure of the films. The dielectric thickness was measured with a multiple beam interferrometer with an accuracy of ± 20 Å. Capacitance and loss factor were measured at different frequencies (10^1–10^6 Hz), at different temperatures (303–393 K) for films of different thicknesses (2000–4000 Å), using a digital Agronic bridge (model-57) provided with internal as well as external generators along with a null detection system in a vacuo of $\sim 10^{-5}$ torr. Films of lower thicknesses (< 2000 Å) were discontinuous and those of higher thicknesses (> 4000 Å) peeled off.

Methods employed to measure electric conductivity and I–V characteristics of these capacitors of different dielectric thicknesses at various temperatures were similar to those reported earlier [20, 21].

3. Results and discussion

Figure 2 shows the variation of $\log R$ versus $1/T$ curves for AgCl film of thickness $\sim 2000 \pm 20$ Å. AgCl films exhibit semiconducting behaviour. Energy of activation (ΔE) values obtained from these curves (figure 2) are listed in table 1. Figure 3 shows typical I–V characteristics on a log–log scale. It is seen from these characteristics that, at low voltages I–V curves are ohmic ($I \propto V^1$), over intermediate voltage region, space charge limited ($I \propto V^2$) and at still higher voltage thermionic emission ($I \propto V^3$) conduction mechanisms. In order to analyse these curves (figure 3), we apply the model proposed by Rose [22] for defect insulators containing shallow traps. According to this model space charge limited (SCL) current is given by

$$I = \frac{9}{8}\frac{\mu_c \varepsilon V^2}{d^3}, \tag{1}$$

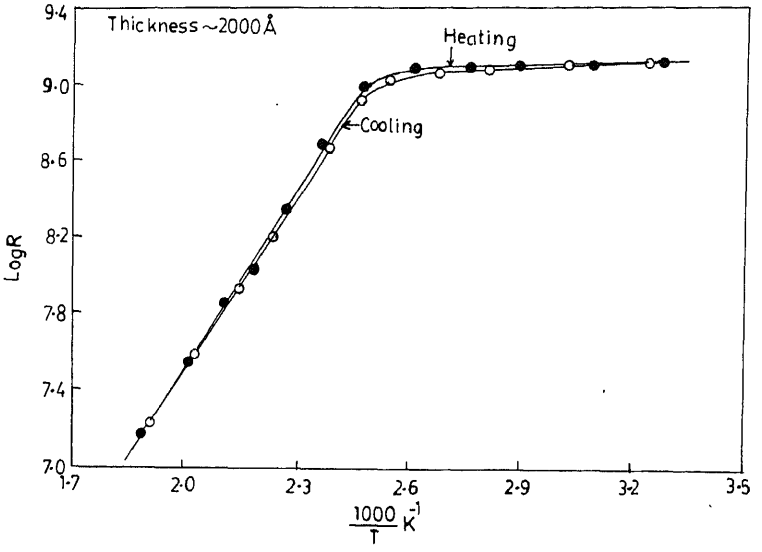

Figure 2. Log R vs $1/T$ for AgCl film of thickness ~ 2000 Å.

Table 1. ΔE values of AgCl films.

Thickness d (Å)	ΔE (eV) From resistance measurements	Thickness d (Å)	ΔE (eV) from capacitance measurements
2201	0·675	1958	0·690
2574	0·631	2314	0·649
2788	0·614	2812	0·583
3412	0·584	3210	0·566
3615	0·561	3539	0·539

where V is the applied voltage, d, the sample thickness, μ_c, the effective drift mobility of charge carriers in the presence of shallow traps, and ε is the dielectric constant of the material. In the present investigation SCL current has been found to vary directly with V^2 (figure 3) and inversely with d^3 (figure 4). It is also known that [23, 24], the voltage at which the transition from ohmic to SCL conduction occurs (V_{trans}) is

$$V_{trans} = \frac{8}{9}\frac{en_t d^2}{\varepsilon} \tag{2}$$

where n_t is the density of trapped carriers and other symbols have their usual meanings. In the present investigation, it has been found that V_{trans} is directly proportional to d^2 (figure 5). The constant value of energy of activation ($\Delta E \sim 0{\cdot}17$ eV) obtained from slopes of linear plots of $\log I$ versus $1/T$ (figure 6) suggests that energy level of traps to which the charge carriers are injected from electrodes does not vary with the applied field and the contact keeps injecting carriers all the time, which is the pre-requisite for SCL currents [25]. At higher voltages where $I \propto V^3$, conduction process is emission limited. This is the break away region preceding the break down.

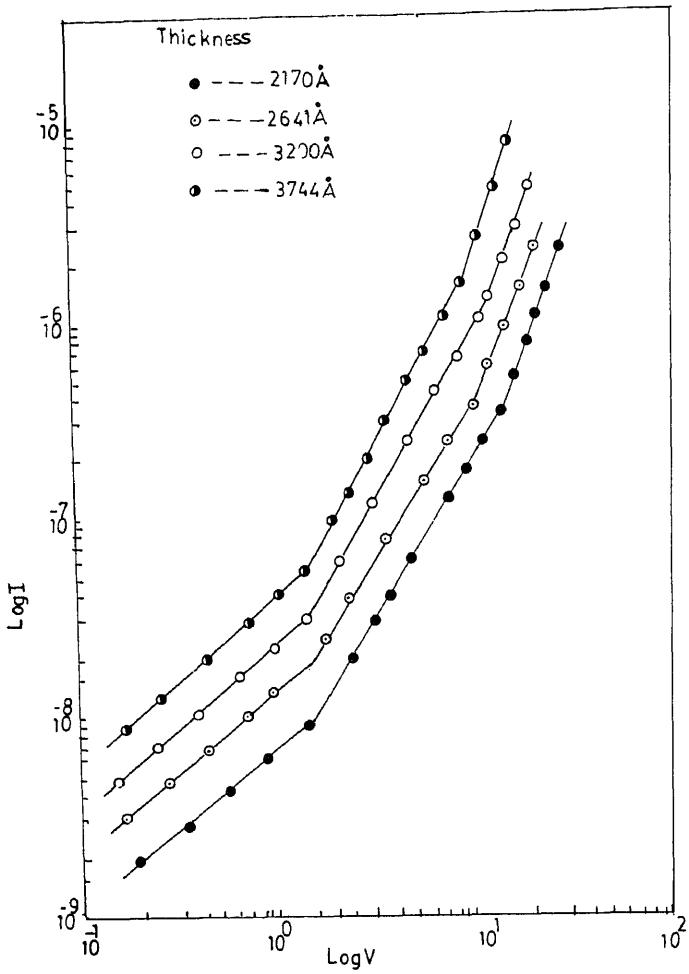

Figure 3. Log I vs log V for AgCl films at room temperature.

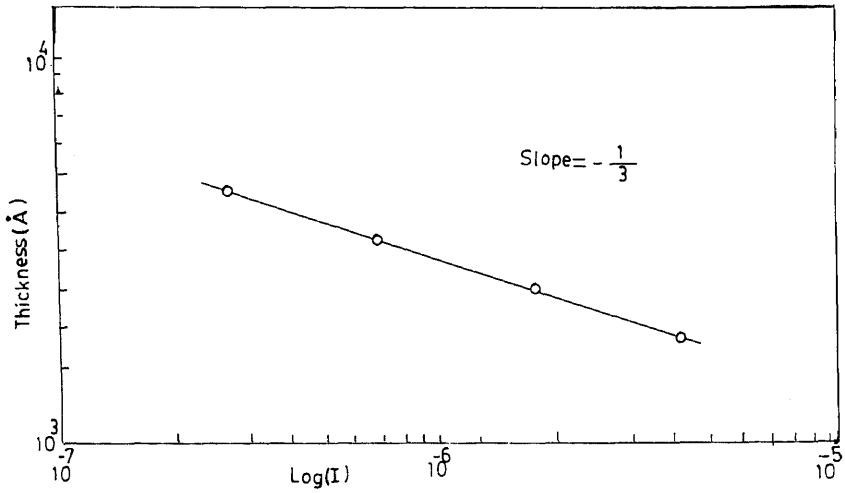

Figure 4. Log I vs d.

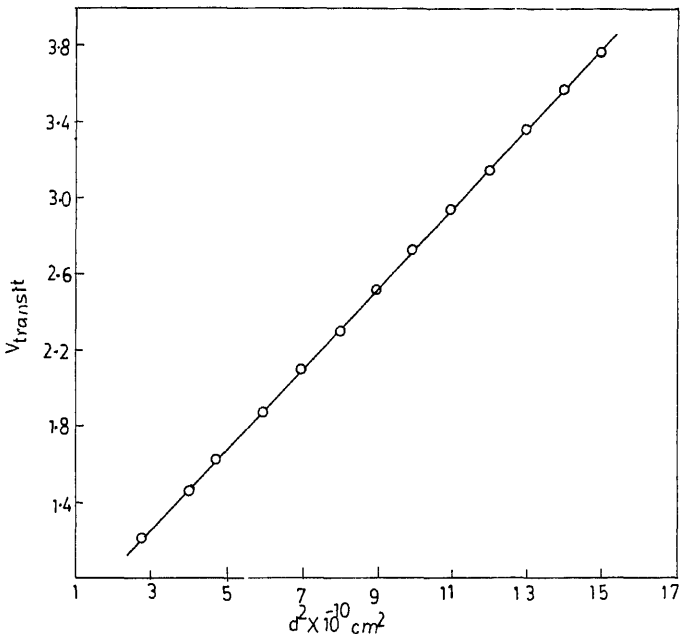

Figure 5. V_{trans} vs d^2.

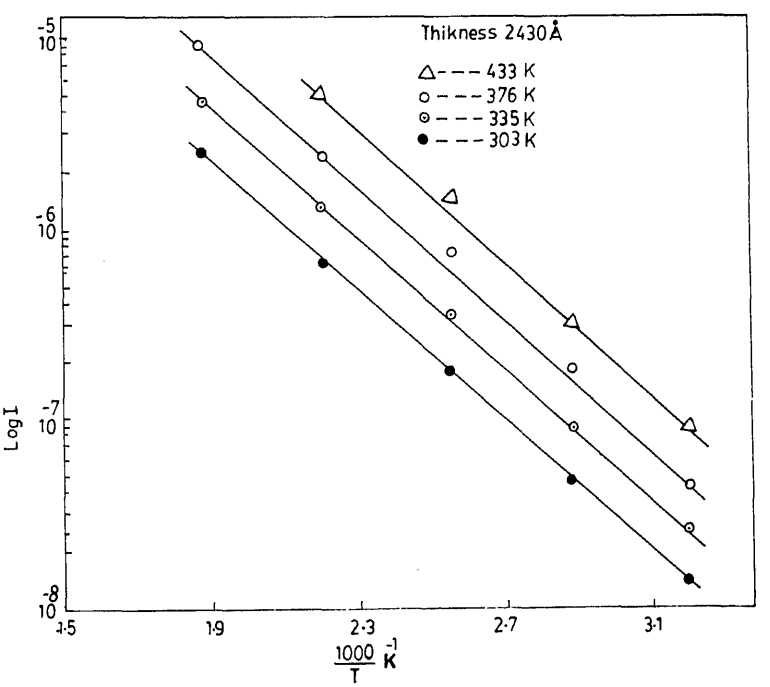

Figure 6. Log I vs $1/T$.

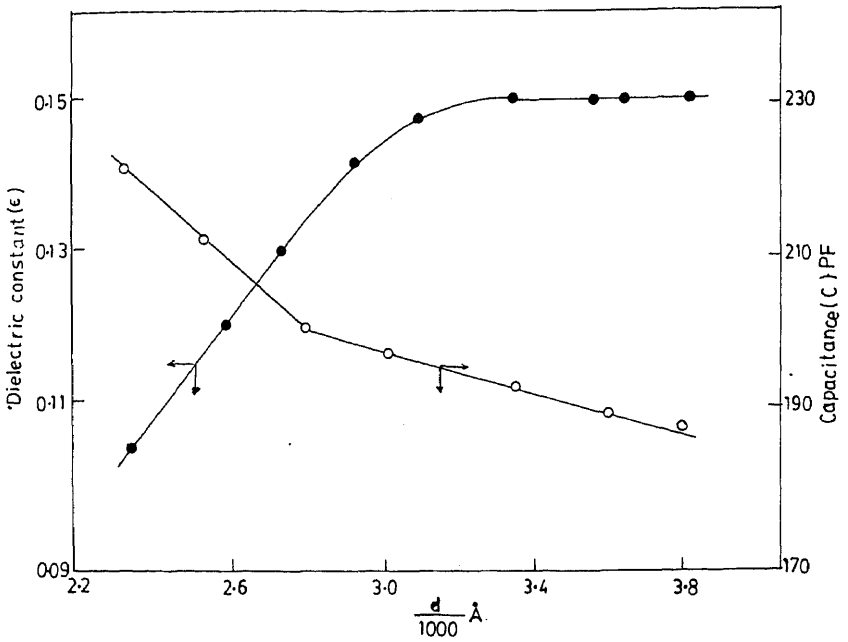

Figure 7. Capacitance and dielectric constant vs thickness.

Figure 7 shows the variation of capacitance and dielectric constant with film thickness at room temperature. It is seen that dielectric constant increases with increase of thickness and later on attains a constant value $\sim 0{\cdot}15$ at $d \sim 3200$ Å.

The values of C, ε, d, area (A) of the film and free space permitivity (ε_0) are interrelated by an equation [26]

$$C = \frac{\varepsilon \varepsilon_0 A}{d}. \tag{3}$$

Higher values of C at lower thickness can be attributed to a contribution to capacitance from a thin native oxide layer that is present on the lower aluminium electrode [27]. The increase of ε with increase of thickness can be related to the influence of grain size on dielectric constant. Grain size increases with thickness and dielectric constant increases with grain size and hence with thickness [28].

Since the dielectric constant is the material property, whereas capacitance is geometry dependent, the following interpretation would be the terms of ε and $\tan \delta$.

The variation of ε with f at various temperatures is presented in figure 8 for AgCl film of thickness 3800 ± 20 Å. In general, ε is found to decrease with frequency at all temperatures but this variation was less pronounced at lower temperatures. The manner in which ε varies with f, gives an indication as to which type of contribution is present [29]. The contribution from space charge polarization is mainly noticeable in the low frequency (0·01 Hz) region and depends on the purity and perfection of the films. In contrast, dipole orientation polarization can be exhibited by materials even up to 10^{10} Hz and is characterized by a Debye-type peak in the dielectric loss, while electronic and ionic polarization always exists below 10^{13} Hz. Since no relaxation effect (no $\tan \delta_{max}$) is observed in the frequency and temperature regions studied, the

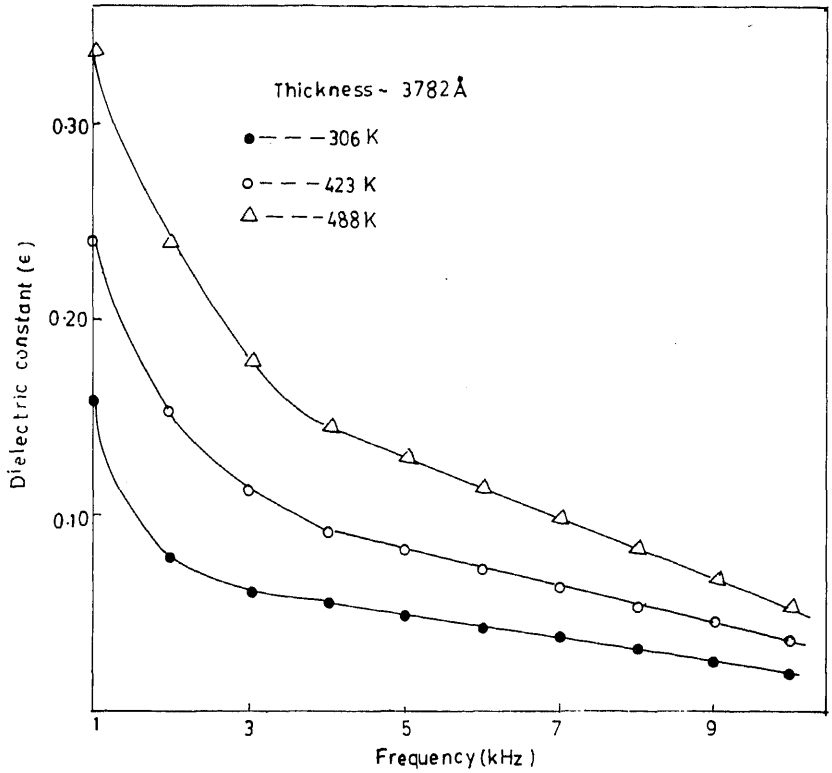

Figure 8. Dielectric constant vs frequency for a film of thickness ~ 3782 Å.

contribution from orientational polarization and possibly also that from interfacial polarization can be ruled out. Therefore only electronic and ionic polarizations contribute.

The most significant features of the ac behaviour of the AgCl film capacitors are the loss minimum ($\tan\delta_{min}$) in the frequency curve and its shift to higher values and to higher frequencies with increasing temperature and vice-versa (figure 9). This is true for all films. The appearance of the loss minimum in the $\tan\delta$ versus frequency curve is attributed to the effect of lead resistance. Goswami and Goswami [30] have proposed a parallel resistor-capacitor model in which an ideal capacitor element of capacitance C, independent of frequency and temperature is in parallel with a dielectric resistive element of R and in series with a small lead resistance r, such that $R \gg r$. The frequency at which $(\tan\delta)_{min}$ occurs is

$$\omega_{min} = 2\pi f_{min} = \frac{1}{C(rR)^{1/2}}, \tag{4}$$

where ω is the angular frequency and R is

$$R = R_0 \exp\left(\frac{\Delta E}{kT}\right). \tag{5}$$

Here R_0 is a constant and ΔE is the activation energy. Thus R would decrease when

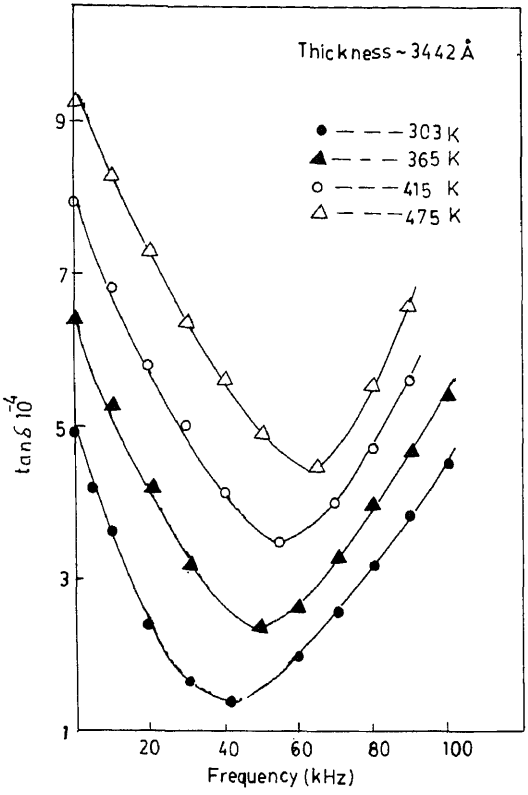

Figure 9. Tan δ vs frequency for a film of thickness ~ 3442 Å.

the temperature is raised and as a result f_{min} would shift towards the higher frequency region with rise in temperature. Recently Hino *et al* [27] proposed a capacitor model containing a capacitor with capacitance C and conductance σ. According to this model the minimum of tan δ appears at the frequency (f_{min}), satisfying the following relation

$$\omega_{min}^2 = (2\pi f_{min})^2 = \frac{\sigma(1 + R\sigma)}{C^2 R}. \tag{6}$$

Here R is the electrical resistance of native oxide layers formed on bottom Al electrodes. Since σ considerably increases with increase of temperature, R remaining practically unchanged, f_{min} will also be higher at high temperatures. Thus a shift of f_{min} would be to a higher frequency at higher temperatures and vice versa.

Figures 10 and 11 show variation of ε and tan δ with temperature respectively. The values of ε and tan δ increase with increase of temperature at all frequencies.

The temperature has a complicated influence on ε and tan δ, which in turn depend on electronic and ionic polarisation, dipole orientation polarisation, space charge polarisation etc. It may be pointed out that the dielectric conductivity is proportional to tan δ. Thus, as the temperature increases, the conductivity of the film and hence tan δ would increase. The large increase of ε and tan δ beyond 373 K may be assigned to ionic motion in the form of dipolar orientation.

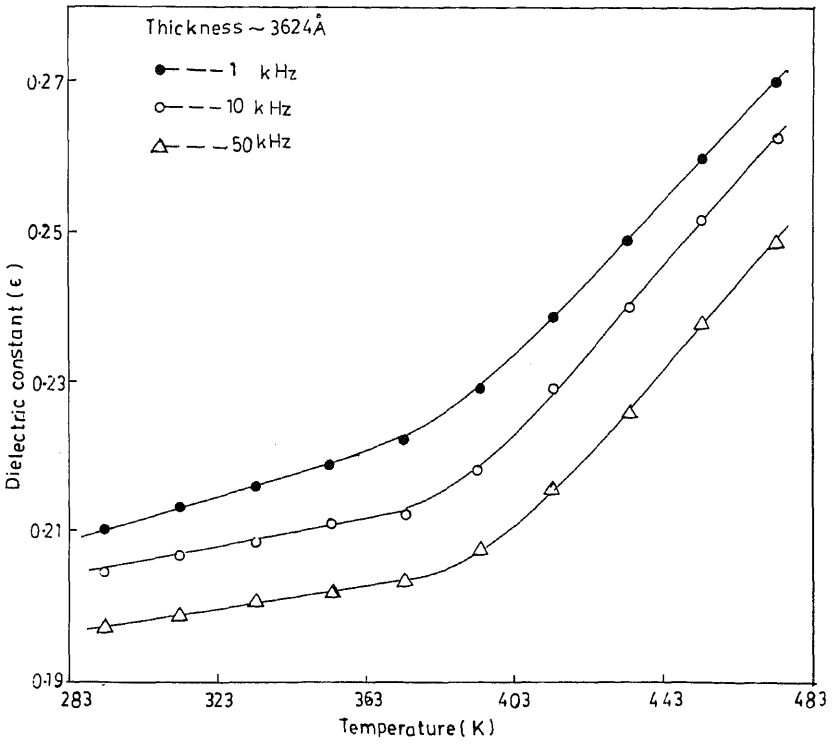

Figure 10. Dielectric constant vs temperature for a film of thickness ~ 3624 Å.

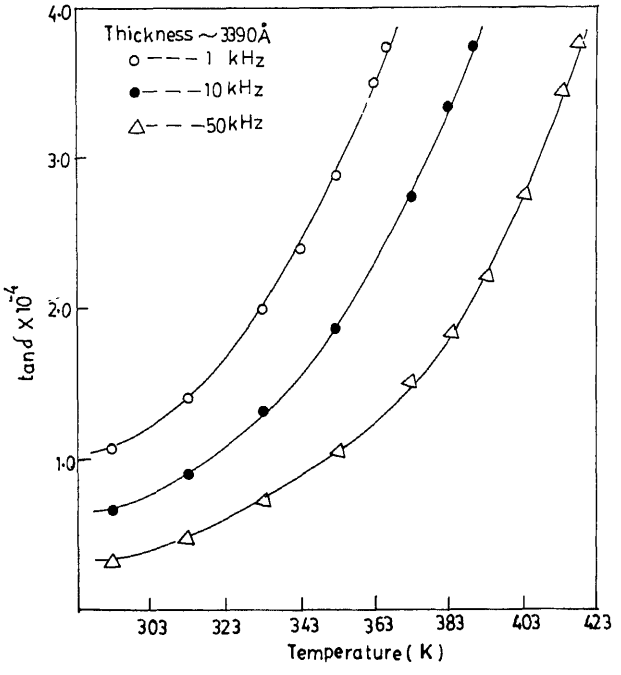

Figure 11. Tan δ vs temperature for a film of thickness ~ 3390 Å.

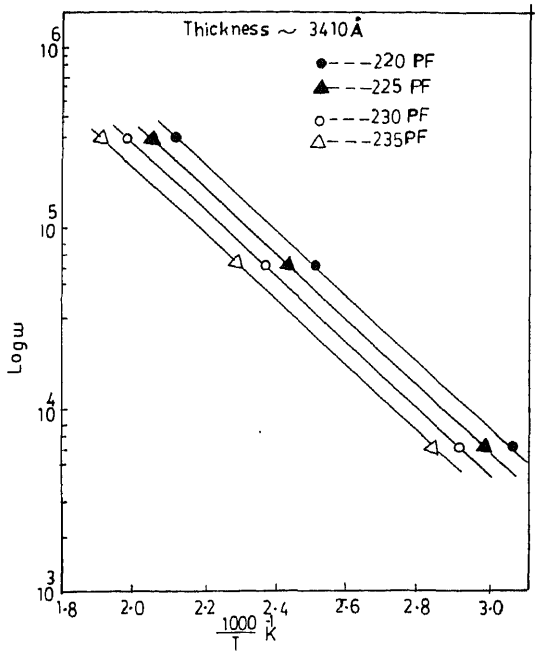

Figure 12. Log ω vs $1/T$ for a film of thickness ~ 3410 Å.

Therefore it can be said that in AgCl films major contributions to ε and $\tan\delta$ arise from the electronic and more probably from the ionic polarization due to the ionic nature of AgCl films.

According to Simmons *et al* [31] for any capacitor system with an inherent resistance, R_0,

$$\omega = 2\pi f = AR_0 \exp\left(\frac{-\Delta E}{kT}\right). \tag{7}$$

A is a constant whose magnitude depends on the particular selected value of constant capacitance. The variation of $\log\omega$ with $1/T$ for four constant capacitances for a film of thickness 3410 Å is represented in figure 12. The plots are found to be linear and parallel. Activation energies thus obtained from figure 12 are included in table 1 for comparison with those calculated from resistance measurements (figure 2). It is seen that ΔE from ε measurements and from resistance measurements are more or less identical.

4. Conclusions

Based on the experimental data presented and theoretical models discussed in this paper, it is concluded that amorphous AgCl films formed by using solution-gas interface technique are broad-band semiconductors exhibiting SCL and thermionic emission currents. Dielectric properties of these films indicate electronic and ionic polarization effects.

References

[1] D G J Ives and G J Janz, in *Reference electrodes: Theory and practice* (Pergamon, New York, 1961)
[2] J G Schindler, G Stork, H J Strub, W Scinid and M D Kaaraschinski, *Anal. Chem.* **295**, 248 (1979)
[3] J G Schindler and M V Gulich, *Biomed. Tech.* **26**, 43 (1981)
[4] J Janata and R J Huber, in *Ion-selective electrodes Reviews* edited by J D R Thomas, **Vol. 1**, 31 (1979)
[5] M S Indira and K S G Doss, *J. Electronal. Chem.* **17**, 145 (1968)
[6] P S Von Bacho, G P Ceasar, H M Saltsburg and R C Baetzoild, *J. Vac. Sci. Technol.*, **13**, 107 (1976)
[7] J W Coburn, E W Eckstein and E J Kay, *J. Vac. Sci. Technol.* **12**, 151 (1975)
[8] J W Coburn, *Thin Solid Films*, **64**, 371 (1979)
[9] H Haefke, M Krohn and V Panov, *J. Cryst. Growth*, **49**, 7 (1980)
[10] R C Baetzoild, *Appl. Phys. Lett.*, **26**, 709 (1975)
[11] Y Tu and J M Blakely, *Photogr. Sci. Eng.*, **20**, 59 (1976)
[12] T M Kelly and M G Mason, *J. Appl. Phys.*, **47**, 4721 (1976)
[13] R G Cooperthwaite and M Steinberg, *Solid State Commun.*, **28**, 915 (1978)
[14] J Sharma, P Dibona and D A Wiegand, *Appl. Surface Sci.*, **26**, 2070 (1982)
[15] H Saijo and T Tanaka, *Photogr. Sci. Eng.* **26**, 133 (1982)
[16] A Belkind and E Ezell, *Thin Solid Films*, **142**, 113 (1986)
[17] P G Aline, *Phys. Rev.* **105**, 406 (1957)
[18] J Maier, S Prill and B R Reichert, *Solid State Ion Diffusion React.* **28**, 1465 (1988)
[19] G Charlot, in *Colorimetric determination of elements*, (Elsevier, Amsterdam, 1964) p. 167
[20] P S Nikam and H S Aher, *Indian J. Pure Appl. Phys.* **31**, 79 (1993)
[21] P S Nikam and H S Aher, *Bull. Mater. Sci.* **17**, 41 (1994)
[22] R Rose, *Phys. Rev.* **97**, 1538 (1955)
[23] M A Lampert, *Phys. Rev.* **103**, 1648 (1956)
[24] M A Lampert, A Rose and R W Smith, *Phys. Chem. Solids*, **8**, 484 (1959)
[25] D R Lamb, in *Electrical conduction mechanism in thin insulating film* (Mehuen, London, 1967)
[26] D Peek, V C Guerra and R J Sladek, *J. Appl. Phys.* **57**, 4803 (1985)
[27] M Kushida, M Iwamato and T Hino, *Jpn. J. Appl. Phys.* **32**, 4709 (1993)
[28] T Horikawa, N Mikami, T Makita, J Tanimura, M Kataoka, K Sato and M Nunoshita, *Jpn. J. Appl. Phys.* **32**, 4126 (1993)
[29] V S Dharmadhikari and A Goswami, *Thin Solid Film* **87**, 119 (1982)
[30] A Goswami and A P Goswami, *Thin Solid Films* **16**, 175 (1973)
[31] J G Simmons, G S Nadkarni and M C Lancaster, *J. Appl. Phys.* **41**, 538 (1970)

PRAMANA
— journal of
physics

© Printed in India

Vol. 43, No. 3,
September 1994
pp. 231–236

Overtone spectroscopy of benzaldehyde

P K SRIVASTAVA, G ULLAS and S B RAI
Laser and Spectroscopy Laboratory, Department of Physics, Banaras Hindu University, Varanasi 221 005, India

MS received 18 January 1994; revised 20 May 1994

Abstract. The vibrational overtone spectra of aryl and alkyl C–H stretch vibrations in benzaldehyde have been studied using conventional IR and thermal lensing technique at room temperature. The stretching vibrational frequency ω_e, anharmonicity constant $\omega_e x_e$ and the dissociation energies of the two C–H bonds have been calculated. The bond length of C–H bond in aryl position has been estimated.

Keywords. Overtone spectroscopy; Benzaldehyde.

PACS No. 07·65

1. Introduction

Overtone spectroscopy of polyatomic molecules is of fundamental importance in understanding the photochemical reactions and non-radiative energy transfers. The normal coordinate description of molecular vibrations fail to describe satisfactorily the higher overtones in these molecules and the local mode model proposed by Henry [1] is used to describe the appearance of these bands. Recently we [2] have studied the higher harmonics of C–H stretch vibrations in several substituted benzenes using conventional IR and dual beam thermal lens technique. The carbon atom in the C–H bond in these molecules belong to the parent ring and C–H group known as aryl group have been studied. In the present note we have studied the overtone spectra of C–H stretch vibration in benzaldehyde which contains two C–H stretch vibrations, the aryl group and the other alkyl group (the C–H bond of the aldehyde group). A detailed study of the same are presented here.

2. Experimental

The experimental method used has been described in our earlier paper [2]. In brief, for IR spectrum we have used Perkin Elmer IR spectrophotometer (Model No. 883). The NIR spectra were recorded using Cary 2390, Varian Associates. The fifth overtone of aryl group and the sixth overtone of alkyl group lie in our dye laser region (17550–15650 cm^{-1}) and they have been studied using dual beam thermal lens technique. We have used benzaldehyde (Riedel) of 99·99% purity. Pure benzaldehyde shows beautiful needle-like crystals if left in the open. The liquid was doubly distilled and filtered with a 2–5 μm filter (Glaxo India) to avoid any dust or crystal in the sample. The fundamental, first, second and third overtones could be recorded using earlier mentioned spectrometers. The higher harmonics beyond this could not be recorded using spectrophotometers due to their weak intensities. This fifth overtone

of the aryl group and the sixth overtone of the alkyl group could be recorded using dual beam thermal lens technique. Several sets of spectra were recorded here. The maximum uncertainty in this case is $\sim 15\,cm^{-1}$ whereas the IR or NIR measurements involve large errors (up to $25\,cm^{-1}$).

3. Results

The structure of benzaldehyde molecule is shown in figure 1. The CHO group in the molecule lies in its molecular plane. The angle between C–H and C=O bond is of the order of 130°, so there is no interaction between oxygen and hydrogen atom. Thus there should not be any intermolecular O–H bond in the structure. However there may be intermolecular hydrogen bonding and a weak peak of small frequency due to this should appear in the structure. In fact peak due to weak O–H bond has been observed in the far IR region in this molecule. The aldehyde group C–H stretching fundamental band lies in between $2700–2750\,cm^{-1}$ and gives a very sharp peak in this region. The C–O-stretch vibration on the other hand, gives a quite broad peak near $1700\,cm^{-1}$. The IR spectrum also shows a strong broad peak with several components merged together in the range of $3000–3100\,cm^{-1}$. These peaks are due to aryl C–H vibrations.

The NIR spectrum corresponding to different harmonics of C–H aryl group is shown in figure 2. Whereas the first overtone peak appears to have several components, the higher overtones show only one peak. It appears that the intensity which is distributed in several CH modes are now localized in only one C–H mode (symmetric mode). This clearly indicates that whereas the fundamental and the first overtone of C–H stretch vibration can be described satisfactorily under normal mode description, for the second, third overtones, the local mode consideration is essential. The thermal lensing spectrum corresponding to fifth overtones of aryl group is also shown in the same figure.

The fundamental peak for alkyl group appears at $2730\,cm^{-1}$. This peak is very sharp and intense. A broad intense peak appears near $5332\,cm^{-1}$ and a weak peak at $5376\,cm^{-1}$. Initially it was thought that the intense peak belonged to second harmonics of alkyl group. However it is found that the weak peak fits better than the intense one. The intensity of the third harmonic peak is larger than the weak peak taken as second harmonic (see figure 3). It appears that the second harmonic peak of this is perturbed by some combination band. The fourth harmonics appear with very weak intensity. Though we could not observe the fifth and sixth harmonics, the seventh harmonics which lie in our dye laser region could be marked by dual beam thermal lens technique at $17018{\cdot}4\,cm^{-1}$. We noted that the intensity of the

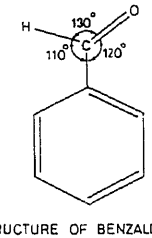

STRUCTURE OF BENZALDEHYDE

Figure 1. Structure of benzaldehyde.

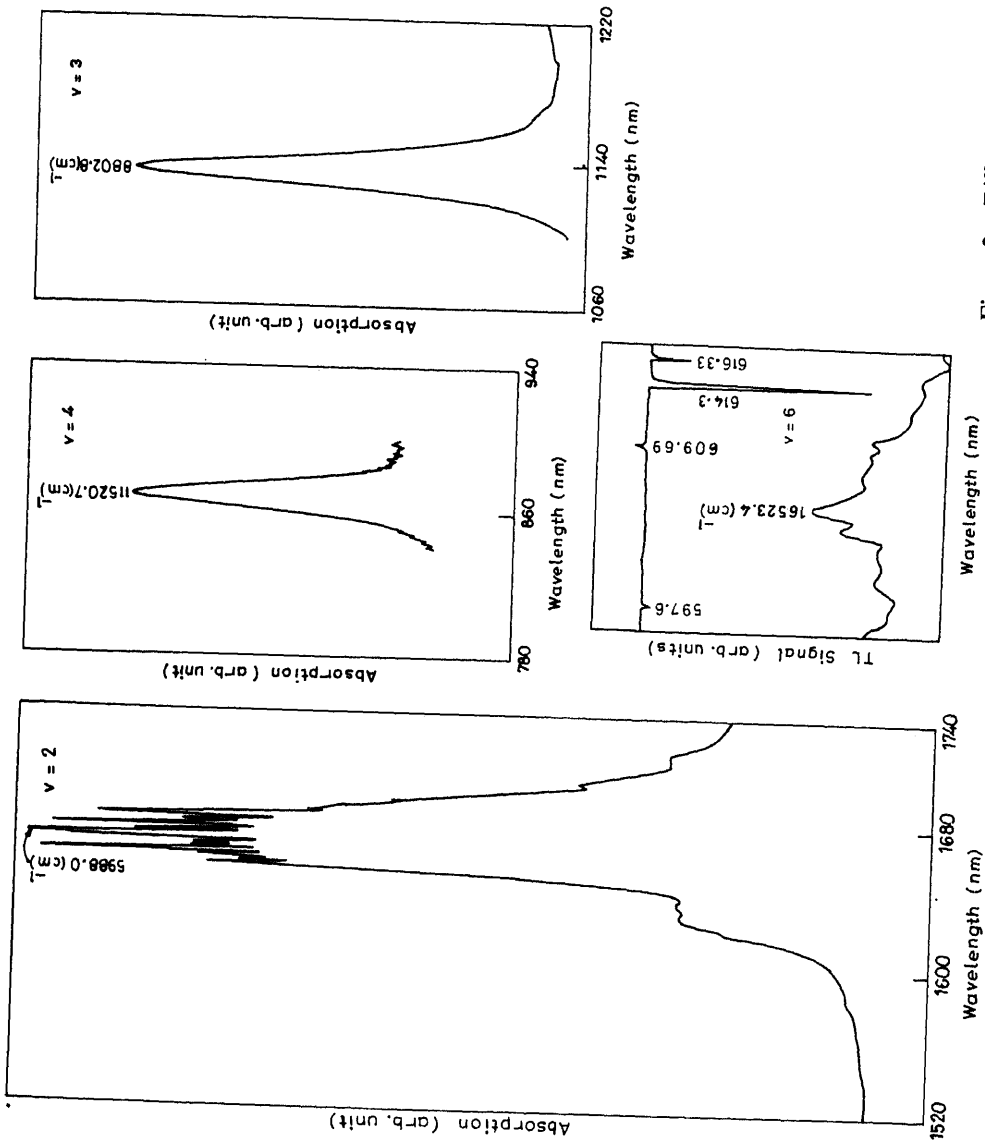

Figure 2. Different overtone spectra of CH aryl group.

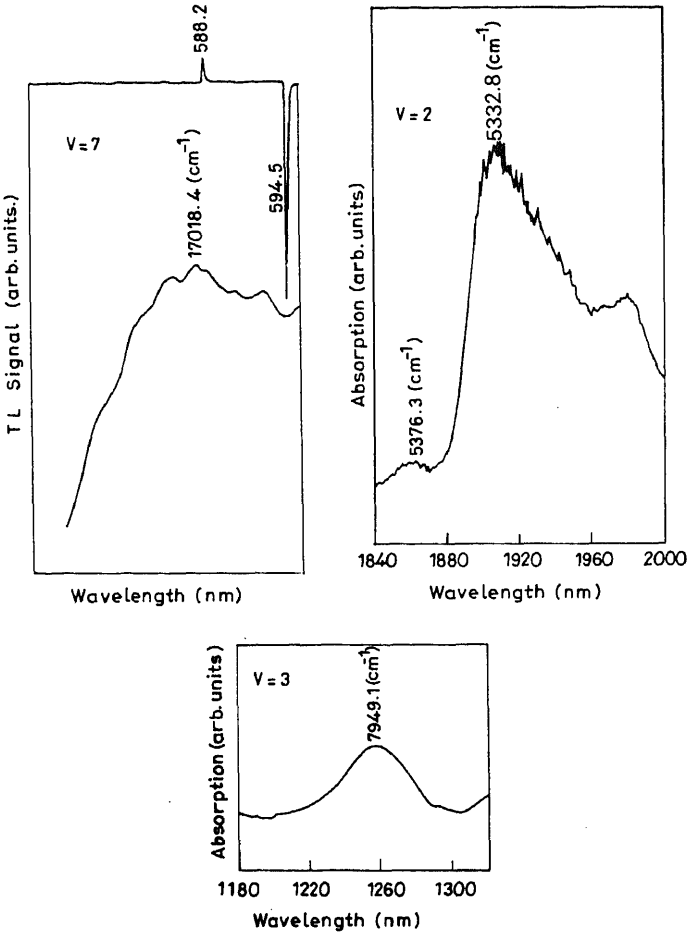

Figure 3. Different overtone spectra of CH alkyl group.

different peaks decreases rapidly as we go to higher harmonics. The intensities of the different peaks with respect to fundamental in the aryl group are 1/5, 1/50, 1/90, 1/200. This indicates that the absorption coefficients for higher harmonics decrease rapidly. We have also measured the width (FWHM) of different peaks in both the cases. The width of the peaks increases as we go to higher energies. The absorption frequencies corresponding to different peaks along with their full width at half maxima for both the C–H vibrations are given in table 1. Mizugai and Katayama [3] have also reported the lensing spectrum of this molecule and have given a value of $16525\,cm^{-1}$ for the fifth overtones or aryl group. We get this peak at $16523\,cm^{-1}$ in our thermal lensing spectrum which is the same. To determine the stretching frequency and anharmonicity constant, the frequencies corresponding to different harmonics for the two CH groups were fitted separately to the quadratic equation

$$E_{v,0} = Bv + Cv^2$$

where $E_{v,0}$ represents the energy separation of the vth level of CH vibration in the ground state from its 0th vibrational level. The terms B and C are the constants of

Table 1. Transition frequencies of different overtones in benzaldehyde for aryl and alkyl groups.

	Frequency (cm^{-1})						
	$v=1$	$v=2$	$v=3$	$v=4$	$v=5$	$v=6$	$v=7$
Aryl group	3075 (60)	5988·0 (122)	8802·8 (155)	11520·7 (186)	— —	16523·0 (126)	
Alkyl group	2730 (25)	5376·0 (26)	7949·1 (228)	10309·0 (254)	— —	— —	17018·4 (142)

Quantities in parentheses represent the FWHM of the peaks.

Table 2. Vibrational frequency and anharmonicity constant for the CH stretch vibration of benzaldehyde (cm^{-1}).

Group	B	$C(=\omega_e x_e)$	$B-C$ $(=\omega_e)$	$\Delta G_{1/2}$ $(\omega_e - 2\omega_e x_e)$	$\Delta G_{1/2}$ value from IR spectra
Aryl	3121·6 ± 6·2	−61·2 ± 1·2	3182·8 ± 7·4	3060·4 ± 8·7	3075
Alkyl	2791·6 ± 10·6	−51·6 ± 1·8	2843·2 ± 12·4	2740·1 ± 14·2	2730

fitting which are related to the vibrational frequency and the anharmonicity constant by

$$\omega_e = B - C \text{ and } \omega_e x_e = C.$$

In order to determine the values of B and C a least square fit procedure given by Birge [4] was used. The values of B and C for the CH stretch vibration for the alkyl and aryl groups are given in table 2. This enabled us to determine separately the ω_e and $\omega_e x_e$ values and the error in these for the alkyl and aryl CH stretch vibrations. The values thus obtained are also given in table 2. The two sets of values are very different from one another. The frequency of the first overtone of alkyl group calculated using present constants (5378 cm^{-1}) match very well with the weak band observed for this. It appears that the combination band lying near this at 5332 cm^{-1} has borrowed its intensity without shifting the second harmonic peak. We have also calculated the $\Delta G_{1/2}$ value using our ω_e and $\omega_e x_e$ values in the two cases. The $\Delta G_{1/2}$ values thus obtained are compared with the fundamental IR values in table 2. It is interesting to note that the two $\Delta G_{1/2}$ values are in good agreement with the first harmonic frequencies of the two CH groups. We also estimated the dissociation energy of the C–H bond in the two cases using Morse empirical relation $\omega_e^2/4\,\omega_e x_e$. The values of De thus obtained for the alkyl and aryl groups respectively are $39224{\cdot}69 \pm 1027\,cm^{-1}$ and $41388 \pm 648\,cm^{-1}$. The De value for aryl group is larger than that of free CH radical (28048 cm^{-1}, calculated using Morse relation) as well as of alkyl group. This indicates that the alkyl group CH bond is weaker compared to aryl group. However both are stronger than free CH radical.

The CHO group in benzaldehyde molecule is electron withdrawing type substituent. Thus when CHO is substituted on benzene ring by replacing hydrogen, it affects the charge-distribution at the neighbouring carbon atoms in the benzene ring. This influences the bond length of the aryl C–H bond. Mizugai and Katayama [5,6] has given an empirical relation to calculate the change in bond length of aryl type C–H bond with respect to benzene molecule. The aryl C–H bond length for fifth overtone in the new compound is

$$r_{CH} = 1{\cdot}084 - \frac{8 \times 10^{-5} \times \Delta\nu(\mathrm{cm}^{-1})}{\upsilon}$$

where 1·084 refers to the bond length of the C–H bond in benzene and $\Delta\nu$ is the shift in frequency of the particular overtone with respect to benzene, υ is the vibrational quantum number of the upper level involved in the transition. The bond length of the C–H aryl group in benzaldehyde is found to be (1·0833 ± 0·0001 Å).

References

[1] B R Henry, *Vibrational spectra and structure*, edited by J R Durig (Elsevier, Amsterdam, 1980) Vol. 10 p. 269

[2] J Vipin Prasad, S B Rai and S N Thakur, *Chem. Phys. Lett.* **164**, 69 (1989)

[3] Y Mizugai and M Katayama, *J. Am. Chem. Soc.*, **102**, 6424 (1980)

[4] R T Birge, *Rev. Mod. Phys.* **19**, 298 (1947)

[5] Y Mizugai and M Katayama, *Chem. Phys. Lett.*, **73**, 240 (1980)

[6] *Infrared and Raman spectroscopy*, Part B Edited by Edward G Brame Jr. and Jeanette G Grassetti (Marcel Dekker Inc., New York and Basel, 1977)

PRAMANA
— journal of
physics

© Printed in India

Vol. 43, No. 3,
September 1994
pp. 237–244

Fluorescence quenching in dyes under an optically thin approximation

GEORGE C CHENNATTUCHERRY*, G AJITHKUMAR and
N V UNNIKRISHNAN
School of Pure and Applied Physics, Mahatma Gandhi University, Kottayam 686 560, India
*Department of Physics, St. Berchmans' College, Changanacherry 686 101, India

MS received 27 December 1993; revised 13 June 1994

Abstract. Kinetic analysis of the energy level scheme of a dye molecule yields expression for the fluorescence quantum yield. The quantum yield is dependent on molecular parameters and laser pulse characteristics. Calculations show quenching of fluorescence quantum yield due to excited state absorption. Earlier studies on quenching of fluorescence have been discussed quantitatively under an optically thin approximation.

Keywords. Energy level scheme; fluorescence quantum yield; excited state absorption.

PACS Nos 42·55; 33·50

1. Introduction

Many workers, in an attempt to determine optimum configurations for nitrogen laser pumped tunable dye lasers, described that some dyes operate efficiently whether pumped transversely [1] or longitudinally [2] whereas others operate efficiently only in the transversely excited mode [3]. The primary differences between the two modes of excitation appear to be linked to the quenching of dye fluorescence yield at high pump intensity. This effect called photoquenching [4] comes about when molecules in their excited state absorb a photon. This photon, in general, through a radiationless process, is converted into heat and therefore does not contribute to the yield. This effect will usually be much more important at laser type intensities where other nonlinear processes can be neglected [5, 6]. In this report, expressions have been derived for the intensity dependent quantum yield and general nature of the yield on molecular parameters and laser characteristics has been discussed. Moreover, the results are discussed in relation to previous experiments on the fluorescence quenching of 7-DAMC and rhodamine 6G dye molecules.

2. Kinetic analysis and fluorescence yield

The energy level (figure 1) scheme represents the singlet manifold of a large molecule. The state X_1 can be excited at the rate $k_{12} = \sigma_{12} I, \sigma_{12}$ being the absorption cross section at the exciting laser frequency and I is the laser intensity. The excitation is to some vibronic level X_2' which relaxes at a rate k_{vib} into all other states X_2. The state X_2 can decay back to X_1 with a decay rate $k_{21} = k'_{21} + k''_{21}$, where k'_{21} and k''_{21} are the radiative and nonradiative decay rate constants respectively. Depending on

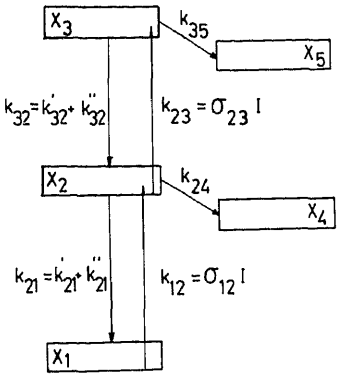

Figure 1. Kinetic energy level scheme for a dye molecule.

the value of the absorption cross section σ_{23}, the induced transition $X_2 \rightarrow X_3$ can compete with the $X_2 \rightarrow X_1$ decay process. This will be true as long as the pulse duration $\Delta t \gg 1/k_{vib}$ and the intensity satisfies the condition $\sigma_{12} I \ll k_{vib}$ so that stimulated emission from X_2' can be neglected. We will focus our attention to the situation where the laser pulses obey these relationships and the rate constants k_{24} and k_{35} for the intersystem crossing are negligibly small.

For calculation of the total fluorescence yield, the coupled differential equations corresponding to figure 1 in the optically thin approximation can be written in the matrix form

$$KX = \mathrm{d}X/\mathrm{d}t \tag{1}$$

or more explicitly, for the fluorescence case

$$\begin{bmatrix} -k_{12} & k_{21} & 0 \\ k_{12} & -(k_{21}+k_{23}) & k_{32} \\ 0 & k_{23} & -k_{32} \end{bmatrix} \begin{bmatrix} x_1 \\ x_2 \\ x_3 \end{bmatrix} = \frac{\mathrm{d}}{\mathrm{d}t} \begin{bmatrix} x_1 \\ x_2 \\ x_3 \end{bmatrix}. \tag{2}$$

Equation (2) can be solved analytically [7] by defining the concentration $X_i = A_i \exp(-\lambda t)$, here the A_i are constants and λ is a parameter to be determined. The corresponding set of algebraic equations for the A_i has a nontrivial solution only when the condition

$$\det(K_{ij} - \delta_{ij}\lambda) = 0 \tag{3}$$

is satisfied.

The resulting equation has the solutions

$$\lambda_1 = 0, \lambda_2 = 1/2(p+q), \lambda_3 = 1/2(p-q) \tag{4}$$

where

$$p = (k_{12} + k_{21} + k_{23} + k_{32}),$$
$$q = [p^2 - 4(k_{12}k_{23} + k_{12}k_{32} + k_{32}k_{21})]^{1/2}. \tag{5}$$

The general solutions for the X_i are determined using the conditions $x_0 = x_1 + x_2 + x_3$

for any time t and $x_0 = x_1$ $(t = 0)$ and thus we obtain

$$x_2 = x_0 k_{12}\left[\frac{k_{32}}{\lambda_2\lambda_3} + \frac{k_{32}-\lambda_2}{\lambda_2(\lambda_2-\lambda_3)}\exp(-\lambda_2 t) + \frac{\lambda_3 - k_{32}}{\lambda_3(\lambda_2-\lambda_3)}\exp(-\lambda_3 t)\right], \tag{6}$$

$$x_3 = x_0 k_{12} k_{23}\left[\frac{1}{\lambda_2\lambda_3} + \frac{\exp(-\lambda_2 t)}{\lambda_2(\lambda_2-\lambda_3)} - \frac{1}{\lambda_3(\lambda_2-\lambda_3)}\exp(-\lambda_3 t)\right]. \tag{7}$$

The total number of fluorescence photons emitted per molecule from states X_2 and X_3 is given by $Y = Y_2 + Y_3$ where

$$Y_2 = k'_{21}\left[\int_0^{\Delta t}(x_2/x_0)\mathrm{d}t\right] + k'_{21}[x_2(\Delta t) + x_3(\Delta t)]/k_{21}x_0 \tag{8}$$

and

$$Y_3 = k'_{32}\left[\int_0^{\Delta t}(x_3/x_0)\mathrm{d}t\right] + k'_{32}x_3(\Delta t)/k_{32}x_0 \tag{9}$$

with x_2 and x_3 are the molecular concentration in states X_2 and X_3 and x_0 is the total concentration.

Following the method developed [4] for excitation by a square shaped pulse of duration Δt, the integration can be performed yielding

$$Y_2 = \frac{k'_{21}\sigma_{12}I}{k_{21}}\left[\frac{k_{21}k_{32}\Delta t + k_{32} + k_{21} + \sigma_{23}I}{\lambda_2\lambda_3} - \frac{k_{21}k_{32}(\lambda_2+\lambda_3)}{\lambda_2^2\lambda_3^2} + \frac{(\lambda_2 - k_{32})(k_{21}-\lambda_2) + \lambda_2\sigma_{23}I\exp(-\lambda_2\Delta t)}{\lambda_2^2(\lambda_2-\lambda_3)} + \frac{(\lambda_3 - k_{32})(\lambda_3 - k_{21}) - \lambda_3\sigma_{23}I}{\lambda_3^2(\lambda_2-\lambda_3)}\exp(-\lambda_3\Delta t)\right] \tag{10}$$

and

$$Y_3 = \frac{k'_{32}\sigma_{12}\sigma_{23}I^2}{k_{32}}\left[\frac{\Delta t\, k_{32}}{\lambda_2\lambda_3} - \frac{k_{32}(\lambda_2+\lambda_3)}{\lambda_2^2\lambda_3^2} + \frac{(\lambda_2 - k_{32})\exp(-\lambda_2\Delta t)}{\lambda_2^2(\lambda_2-\lambda_3)} + \frac{(k_{32}-\lambda_3)\exp(-\lambda_3\Delta t)}{\lambda_3^2(\lambda_2-\lambda_3)}\right] \tag{11}$$

where

$$k_{12} = \sigma_{12}I \quad \text{and} \quad k_{23} = \sigma_{23}I. \tag{12}$$

For cases where the transmission of the system is intensity independent, the quantum yield is given by

$$\phi = Y/\sigma_{12}I\,\Delta t. \tag{13}$$

Thus ϕ is intensity dependent. It approaches the intensity independent form for low

intensities.

$$\text{Limit } I \to 0 \; \phi = \phi_0 = k'_{21}/k_{21} \tag{14}$$

A steady state is obtained for pulses of duration $\Delta t \gg 1/k_{ij}$.

Using (5), (6), (10) and (11) we find for the steady state limit of Y

$$Y = \frac{(k'_{21}k_{32} + k'_{32}\sigma_{23}I)\sigma_{12}I\,\Delta t}{\sigma_{12}\sigma_{23}I^2 + k_{32}\sigma_{12}I + k_{21}k_{32}}. \tag{15}$$

For cases where a steady state approximation is applicable, it is useful to derive an expression for Y and for an n-level system of the type

$$X_1 \underset{k_{21}}{\overset{\sigma_{12}I}{\rightleftharpoons}} X_2 \underset{k_{32}}{\overset{\sigma_{23}I}{\rightleftharpoons}} \ldots \underset{k_{n,n-1}}{\overset{\sigma_{n-1,n}I}{\rightleftharpoons}} X_n. \tag{16}$$

A straightforward calculation yields the following expression. The concentration x_i of the state X_i

$$x_i = \alpha_i x_0 \Big/ \sum_{i=1}^{n} \alpha_i \tag{17}$$

so that

$$\sum_{i=1}^{n} x_i = x_0$$

where

$$\alpha_i = I^{i-1} \prod_{j=1}^{n-1} k_{j+1,j} \prod_{j=1}^{i-1} \sigma_{j,j+1}/k_{j+1,j}$$

for

$$i = 2, 3, \ldots n \tag{18}$$

and

$$\alpha_i = \prod_{j=1}^{n-1} k_{j+1,j}. \tag{19}$$

The yield per molecule is

$$Y = \sum_{i=2}^{n} k'_{i,i-1}\,(x_i/x_0)\Delta t = \left(\sum_{i=2}^{n} k'_{i,i-1}\alpha_i \right) \Delta t \sum_{i=1}^{n} \alpha_i \tag{20}$$

The number of photons absorbed per unit volume in an optically thin sample is

$$N_{\text{abs}} = \sum_{i=1}^{n-1} \sigma_{i,i+1} I\, x_i \Delta t = x_0 I \Delta t \sum_{i=1}^{n-1} \sigma_{i,i+1} \sum_{i=1}^{n} \alpha_i. \tag{21}$$

Thus the quantum yield becomes

$$\phi = x_0\; Y/N_{\text{abs}} = \sum_{i=2}^{n} k'_{i,i-1}\,\alpha_i \Big/ \sum_{i=1}^{n-1} \sigma_{i,i+1}\,\alpha_i. \tag{22}$$

If the radiative lifetime of higher levels is larger than that of the lower ones, a maximum in the fluorescence as a function of laser intensity will be observed. For the three level case in steady state, this maximum in Y occurs when $\sigma_{12}\sigma_{23}I^2 = k_{21}k_{32}$ [8].

Equation (15) which was derived analytically for the time dependent case could also be obtained from equation for $n = 3$. Moreover, from (18) and (19) we obtain

$$\sigma_{i,i+1}\alpha_i/\sigma_{i+1,i+2}\alpha_{i+1} = k_{i+1,i}/\sigma_{i+1,i+2}I \tag{23}$$

If for all $i \geqslant 2$ the intensity is such that $k_{i+1,i} \gg \sigma_{i+1,i+2}I$ then the n-level case reduces to the three level case. For instance, then

$$\begin{aligned}\phi &= (k'_{21}\alpha_2 + k'_{32}\alpha_3)/(\sigma_{12}\alpha_1 + \sigma_{23}\alpha_2) \\ &= (k'_{21}k_{32} + k'_{32}\sigma_{23}I)/k_{32}(k_{21} + \sigma_{23}I)\end{aligned} \tag{24}$$

which is also obtained using (22), (15), (16) and (17) for $\Delta t \to \infty$.

For low intensities, $\sigma_{23}I \ll k_{32}$ and usually $k'_{21} \approx k'_{32}$ so that the following expression is obtained for the reciprocal relative quantum yield

$$\phi_0/\phi \approx 1 + \sigma_{23}I/k_{21}. \tag{25}$$

Plotting ϕ_0/ϕ versus I at low intensities should give a straight line with a slope equal to σ_{23}/k_{21}. If the fluorescence lifetime of the state X_2 is known its absorption cross-section can be determined or vice versa.

3. Calculations and quantum yield of 7-DAMC

Fluorescence yields were calculated using eqs (5) and (10)–(13) for various combinations of the molecular parameters k_{32}/k_{21} and for different excitation conditions. For a given laser pulse, the yield Y shows the expected dependence on the molecular parameters. For instance, for fixed $I\Delta t$ and $\sigma_{23} = \sigma_{12}$, Y decreased with increasing k_{32}/k_{21}. However, the general dependence of Y and ϕ on I and Δt does not change much with the molecular parameters. Hence the calculation performed for the case of $k_{32}/k_{21} = 10$ is taken as typical (figure 2).

The calculations show that the steady state is reached for practically all pulses of duration $\Delta t > 5/k_{21}$. Therefore, for most molecular systems steady state approximation

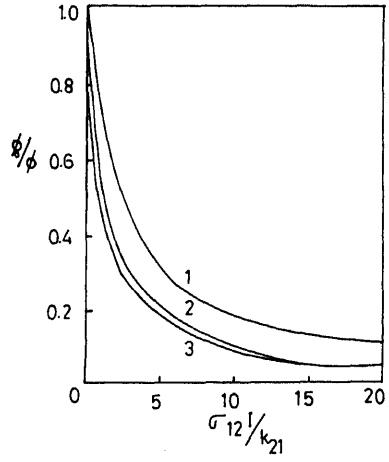

Figure 2. Dependence of quantum yield on laser intensity $k_{32}/k_{21} = 10$ and $\sigma_{12} = \sigma_{23}$. (Curve 1. $\Delta t k_{21} = 1{\cdot}0$; Curve 2. $\Delta t k_{21} = 5$; Curve 3. $\Delta t k_{21} = 10.0$.)

can be used to analyse laser-induced fluorescence process. The quantum yield calculated as a function of incident laser intensity is shown in figure 2. A strong quenching effect due to excited state absorption is observed for $\Delta t \cdot k_{21} > 5$ and more which indicates that more quenching is obtained for longer pulses. These effects appear to be a clear consequence of the low intensity values where steady state approximation holds good.

An experimental verification of the I dependence of ϕ is found in dye laser studies of Wieder [6]. Wieder's experiment was performed on 7-DAMC solution in ethanol using a nitrogen laser (337·1 nm) at a maximum intensity of 200 MW/cm^2. Since the laser pulse duration was 5 ns a steady state was reached in practice. From Wieder's data, a plot of the reciprocal relative quantum yield ϕ_0/ϕ versus I can be made. The result is shown in figure 3. It can be seen that a straight line is obtained for low I at the two concentrations. Further, the straight line type behaviour for 3×10^{-5} mol/l dye concentration exactly fits with (25). Even though one notices a similar behaviour for 5×10^{-5} mol/l concentration also, this does not follow strictly (25). This is due to the fact that the former concentration is optically thin while the latter is not. Therefore, we measured the slope of the 3×10^{-5} mol/l case, and find that $\sigma_{23}/k_{21} = 3 \times 10^{-26}$ cm^{2}s. In Wieder's experiment the transmission was intensity independent. $\sigma_{23} = \sigma_{12} = 1{\cdot}67 \times 10^{-17}$ cm^2, thus $k_{21} = 3{\cdot}01 \times 10^8$ s^{-1} a reasonable value. The reciprocal of k_{21}, gives the lifetime of 3·33 ns which agrees well with the

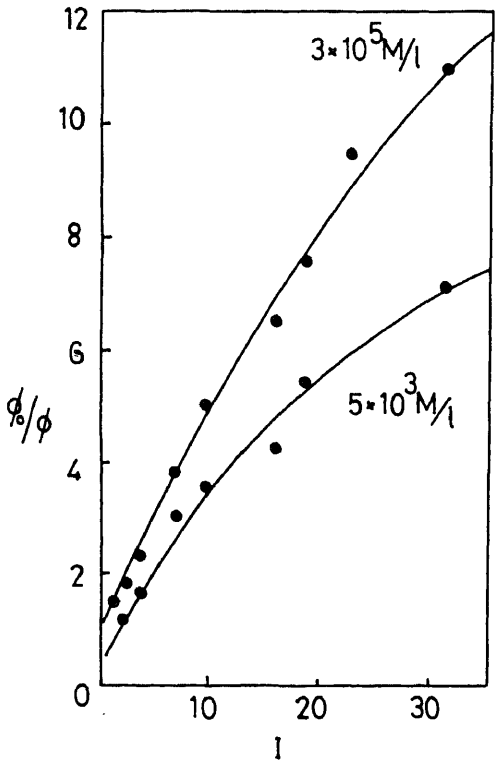

Figure 3. Reciprocal relative quantum yield of 7-DAMC as a function of N_2-laser intensity. Data are taken from ref. [6].

reported value of 3·5 ns [9]. The curvature of the plots at high intensities is due to the failure of the approximation $\sigma_{23} I \ll k_{32}$.

4. Fluorescence quenching in 7-DAMC and rhodamine 6G

Under the optically thin approximation, we have also analysed Wieder's data on fluorescence quenching. The analysis helps one to get a quantitative estimate of the competitive deexcitation process responsible for fluorescence quenching. For fluorescent molecules in an excited state, the fraction of molecules that radiate in the presence of competitive deexcitation process is given by

$$f = P_R \left(P_R + \sum_c P_c \right)^{-1}. \tag{26}$$

P_R is the spontaneous transition probability and $\Sigma_c P_c$ gives the sum total of the probabilities of competitive processes. In case absorption from the first excited singlet state is the dominant deexcitation process, then the effect on the fraction of the molecules should be a term $P_c = CI^x$ where I is the intensity of the pump radiation and C is a constant. We have then

$$I^x = \frac{P_R}{C}(1/f - 1). \tag{27}$$

Using the approximation [eqs (10) and (11)] we have examined the validity of this expression. Figure 4 shows the theoretical plot of $\log(1/f - 1)$ vs $\log I$ along with Wieder's plots for the two dyes. The theoretical and experimental curves show a slope of nearly unity as expected. However there is a large discrepancy between the

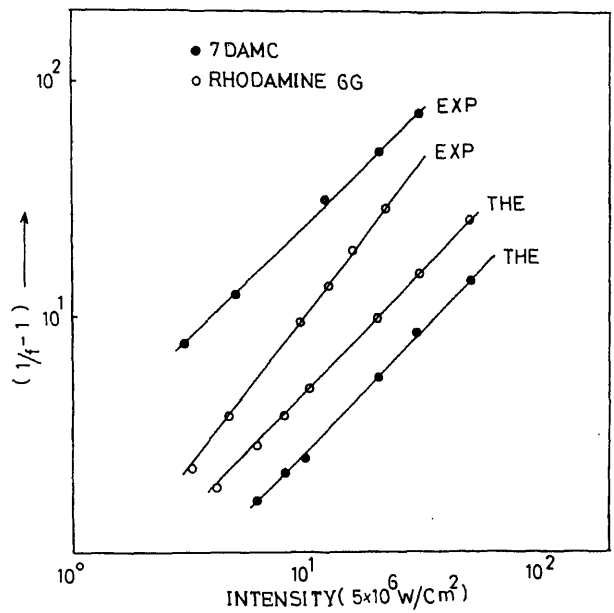

Figure 4. $\text{Log}(1/f - 1)$ vs $\log I$ plot.

theoretical and experimental curves. This could be explained by considering the following three important photophysical processes. Firstly, fluorescence quenching would result if the relaxation from the higher excited states to the X_2 state is less efficient than the X_3 to X_2 relaxation. Secondly, stimulated emission from X_2 to X_1 would also produce an additional intensity dependent fluorescence quenching. Thirdly, it is also likely that thermal heating may contribute to the quenching processes under high intensity excitation. It must be emphasized that too much reliance cannot be placed on fitting experimental results, where gaussian pulse has been used to the square pulse model theoretical curves. The general agreement on the nature of the experimental curves and theoretical curves of the square pulse approximation used indicates that this is a useful approximate theoretical model at least for understanding the general behaviour of the intensity dependence fluorescence quenching. Thus considering the general agreement on the nature of the experimental and theoretical curves the discrepancy between curves would be due to the above mentioned processes. Hence we cannot expect an exact fit between theoretical and experimental results. Moreover, a comparison of the two plots for the two dyes shows that rhodamine 6G has high quantum yield consistent with previous observations [2]. The probability of deexcitation process has been estimated to be of the order of 10^8/s and is found to increase with laser intensity except for a numerical factor.

5. Conclusions

1. It has been shown that the fluorescence quantum yield is a decreasing function of the pulse width for a given pump intensity. 2. The kinetic calculation is found to be applicable to optically thin systems and at lower laser intensities. 3. Fluorescence yields are of no value, unless they have been extrapolated to zero laser intensity. 4. Estimate of quantum yield and deexcitation probability shows that, in particular, excited state absorption should be a good competitor for the fluorescence emission.

Acknowledgements

Authors are thankful to DAE for financial assistance. One of the authors (CCG) is grateful to UGC for an FIP fellowship.

References

[1] J A Myer, C L Johnson, E Kierstead, R D Sharma and I Itzkan, *Appl. Phys. Lett.* **16**, 3 (1970)
[2] G Neumann and I Wieder, *Opt. Commun.* **5**, 197 (1972)
[3] M Hercher, *Appl. Opt.* **6**, 947 (1967)
[4] S Speiser, R V D Wert and J Kommandeur, *Chem. Phys.* **1**, 297 (1973)
[5] S L McCall and E L Hahn, *Phys. Rev.* **183**, 457 (1967)
[6] I Wieder, *Appl. Phys. Lett.* **21**, 318 (1972)
[7] A A Frost and R G Pearson, *Kinetics and mechanism* (New York: Wiley, 1961) p. 173
[8] Vander Deijl Makkes, J Dousma, S Spieser and J Kommandeur, *Chem. Phys. Lett.* **20**, 17 (1973)
[9] T Govindanunny and B M Sivaram, *J. Lumin.* **21**, 397 (1980)

PRAMANA
— journal of
physics

© Printed in India

Vol. 43, No. 3,
September 1994
pp. 245–253

Photoconductivity studies of ($PbCrO_4$-HgO-ZnO) composites

SADHANA DEVI and S G PRAKASH
Department of Electronics and Communication, University of Allahabad, Allahabad 211 002, India

MS received 5 February 1994; revised 22 June 1994

Abstract. This paper deals with the photoconductivity studies of ($PbCrO_4$-HgO-ZnO) composites comprising of base materials of three different energy gaps. The response of (10% $PbCrO_4$-80% HgO-10% ZnO) and (20% $PbCrO_4$-60% HgO-20% ZnO) composites is faster than that of other compositions and of base materials. The dark current for (20% $PbCrO_4$-60% HgO-20% ZnO) is trap limited-space charge limited at higher voltages while it shows non-ohmic behaviour at lower voltages. The photocurrent for (20% $PbCrO_4$-60% HgO-20% ZnO) composition shows non-ohmic behaviour at lower voltages and tends to saturation at higher voltages. The photocurrent for the above composition varies sublinearly with the intensity of illumination. The (10% $PbCrO_4$-80% HgO-10% ZnO) composition is the best suitable material for optical switching. The existence of discrete trap depths at 16°C appears plausible for different compositions.

Keywords. Dielectric; photosensitive; photoconductors.

PACS No. 72·40

1. Introduction

It is well known that the rise and decay curves of photocurrent are governed by the trapping states and recombination centres lying in the forbidden zone of a photoconductor. Therefore these curves can be used to understand the nature and distribution of traps and recombination centres. A good photosensitive material should not only show a large change in conductivity but also respond fast. If trapping centres are in abundance, the response time is slow. Trapping also increases the decay time, as the carriers are slowly released after removal of the excitation source. The increased carrier concentration in presence of light is a function of intensity of illumination, temperature, applied field and various other parameters [1]. The nature of current versus intensity curve gives an idea about the charge trapping and recombination processes taking place inside the material.

Photoconducting properties of a large number of single crystals have been studied. Thick and thin layers have also been investigated by several workers [2–6]. However relatively fewer attempts have been made for mixed binder layers. In the present investigations, the three base materials i.e. $PbCrO_4$, HgO, ZnO having different band gaps of values 2·3 eV, 0·3 eV and 3·2 eV respectively have been mixed in different proportion by weight in order to use the effect of composition and synthesizing conditions on photoconducting properties of mixed systems.

2. Experimental

The ($PbCrO_4$-HgO-ZnO) mixed lattices having different compositions were prepared by the usual technique. High purity base materials i.e. $PbCrO_4$, HgO, ZnO were mixed in different proportion by weight and ground for homogeneous mixing. The mixtures were fired at 400°C in a cylindrical furnace in air atmosphere for 40 min.

The finely powdered microcrystalline fired samples were added to polystyrene binder in benzene and sandwiched between two conducting surfaces of two glass plates. One of the surfaces of the glass plate was made conducting by spreading a layer of SnO_2 over it. The conducting layers of glass plates were kept in contact with the sandwiched binder layer. Thick binder layers were deposited on an area of about 3 cm^2 having thickness varying from 0·025 cm to 0·073 cm. Measurements were made with these parallel plate capacitors due to ease and economy of process.

The cell was connected to a nanoammeter (model NM-122, Scientific Equipment, Roorkee) and d.c. power supply in series and kept in a dark metallic box. The box consists of a hole on its upper surface and the cell was kept below the hole. Upper surface of the cell could be illuminated with radiations from a Hg-lamp. Intensity of illumination was varied by varying the slit width and the intensity over the cell surface was measured using a Luxmeter.

3. Results and discussion

Mixed systems having different proportions of base materials were prepared for comparative study. These are (20% $PbCrO_4$-60% HgO-20% ZnO), (60% $PbCrO_4$-20% HgO-20% ZnO), (20% $PbCrO_4$-20% HgO-60% ZnO) and (10% $PbCrO_4$-80% HgO -10% ZnO) apart from base materials. Photoconducting properties of these systems have been studied in order to obtain optimum conditions of photoresponse and to find possible use of the layers in many fields i.e. in light switching circuits, photoconductor photocells, electrophotography, pickup tube, light amplifiers etc. The results are as follows:

3.1 *Rise and decay of photocurrent*

The rise and decay of photocurrent for different compositions under white light is shown in figure 1. The photosensitivity of (10% $PbCrO_4$-80% HgO-10% ZnO) composition is more than the other mixed systems except pure HgO under experimental conditions. The response of (10% $PbCrO_4$-80% HgO-10% ZnO) and (20% $PbCrO_4$-60% HgO-20% ZnO) compositions is found to be fastest under experimental conditions. The response time for all compositions is listed in table 1, where response time is defined as the time required by the photocurrent to take 90 per cent of its maximum value. For 100% HgO, photocurrent continues to increase i.e. only positive photoconductivity results. Positive photoconductivity is defined as the increase in conductivity in presence of light. For (10% $PbCrO_4$-80% HgO-10% ZnO), 100% $PbCrO_4$, (20% $PbCrO_4$-60% HgO-20% ZnO), (20% $PbCrO_4$-20% HgO-60% ZnO) and (60% $PbCrO_4$-20% HgO-20% ZnO) compositions, the photocurrent rises as soon as the light is switched on but after acquiring a maximum value, it continues to decay for a very long time tending towards a saturation value i.e. both positive and negative photoconductivity results, where negative photoconductivity [7] is defined as the decrease in conductivity in presence of light. For (60% $PbCrO_4$-20% HgO-20% ZnO)

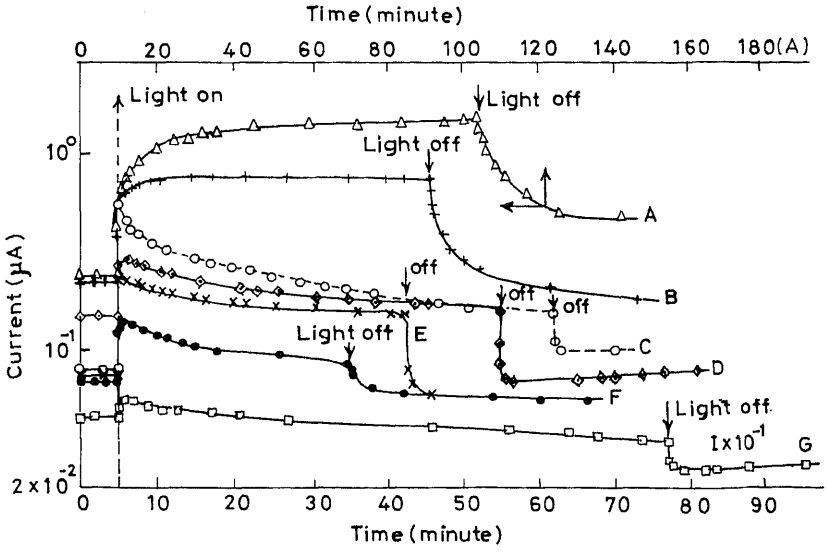

Figure 1. Rise and decay of photocurrent in layers having different compositions. A, B, C, D, E, F and G for 100% HgO, 100% ZnO, (10% $PbCrO_4$-80% HgO-10% ZnO), (60% $PbCrO_4$-20% HgO-20% ZnO), (20% $PbCrO_4$-60% HgO-20% ZnO), 100% $PbCrO_4$ and (20% $PbCrO_4$-20% HgO-60% ZnO) systems respectively; field = 81·6 V/cm, room temperature = 20·5°C and intensity of illumination = 2000 lux.

Table 1. Response time of photocurrent.

Composition	Response time (sec)
10% $PbCrO_4$-80% HgO-10% ZnO	2
20% $PbCrO_4$-60% HgO-20% ZnO	2
60% $PbCrO_4$-20% HgO-20% ZnO	9
20% $PbCrO_4$-20% HgO-60% ZnO	9
100% $PbCrO_4$	8
100% HgO	3360
100% ZnO	258

composition, positive photoconductivity is almost equal to the negative photoconductivity. For (20% $PbCrO_4$-20% HgO-60% ZnO) sample, negative photoconductivity becomes greater than the positive photoconductivity. However, for 100% $PbCrO_4$, (20% $PbCrO_4$-60% HgO-20% ZnO) and (10% $PbCrO_4$-80% HgO-10% ZnO) compositions, the positive photoconductivity is greater than the negative photoconductivity. For 100% ZnO sample, negative photoconductivity may be neglected in comparison to the positive photoconductivity.

When illumination of the photoconductor increases the density of electrons or holes or both, positive photoconductivity results. If with the elapse of time, the minority carriers are also excited from the imperfection centres, a negative photoconductivity results. This is due to the rapid recombination of minority carriers

with majority carriers. This explains why negative photoconductivity results with positive photoconductivity.

The response of (10% $PbCrO_4$-80% HgO-10% ZnO) and (20% $PbCrO_4$-60% HgO-20% ZnO) compositions is the fastest in comparison to the other compositions but the photocurrent for (10% $PbCrO_4$-80% HgO-10% ZnO) composition remains at its maximum value for a short while and then continues to decay rapidly under experimental conditions. However, the photo current for (20% $PbCrO_4$-60% HgO-20% ZnO) composition remains at its maximum value for a comparatively longer time before its decay. So, the general measurements i.e. effect of field, intensity of illumination etc. have been made for (20% $PbCrO_4$-60% HgO-20% ZnO) composition.

3.2 *Transient effect*

Photocurrent for mixed systems increases as soon as the light is switched on and after acquiring a maximum value, it begins to decay for a very long time even in the presence of light. When the light is switched off, the current takes a long time to reach its dark level or sometimes it goes below the dark level (figure 1). Now if the light is switched off before the decay of photocurrent starts, the current decays rapidly to reach its dark level (figure 2). Such type of studies have been carried out to explore the possible use of layers in switching circuits. The response of (10% $PbCrO_4$-80% HgO-10% ZnO) and (20% $PbCrO_4$-60% HgO-20% ZnO) compositions is very quick in comparison to other composites. As soon as the light is switched off, the (10% $PbCrO_4$-80% HgO-10% ZnO) composition acquires its dark level quickly in comparison to the other compositions. Thus the (10% $PbCrO_4$-80% HgO-10% ZnO) is best for optical switching.

The decay curves of photocurrent for the above compositions have been used to calculate the trap depths. The decay of photocurrents after the cessation of excitation is given in figure 3. Photocurrent (I_p) has been obtained by subtracting the dark

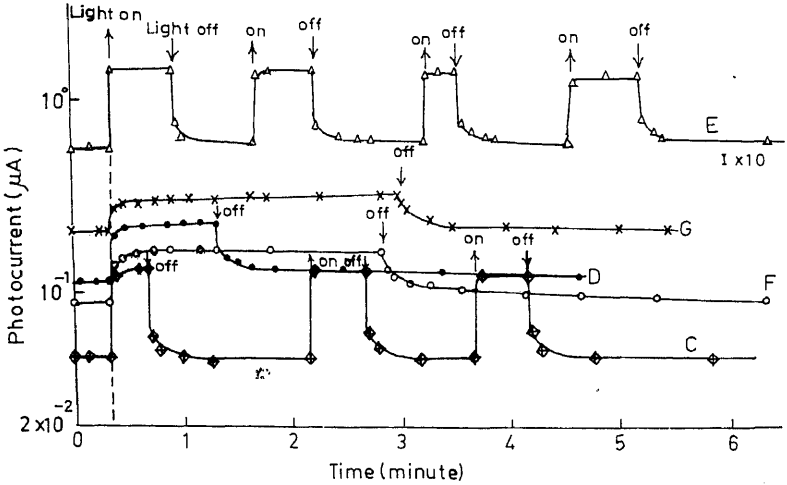

Figure 2. Rise and decay of photocurrent for different compositions. C, F, D, G and E for (10% $PbCrO_4$-80% HgO-10% ZnO), 100% $PbCrO_4$, (60% $PbCrO_4$-20% HgO-20% ZnO), (20% $PbCrO_4$-20% HgO-60% ZnO) and (20% $PbCrO_4$-60% HgO-20% ZnO) respectively; field = 81·6 V/cm; intensity = 1000 lux and room temperature = 16°C.

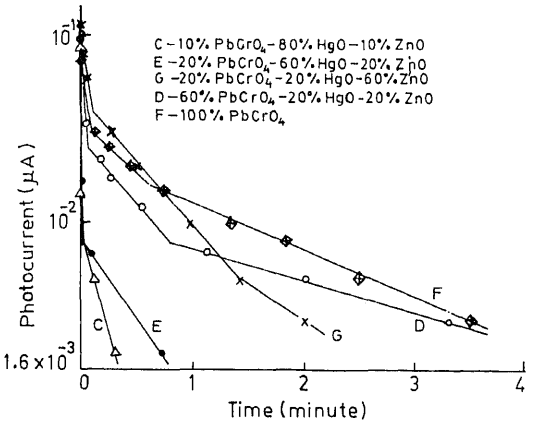

Figure 3. Decay of photocurrent for different compositions; field = 81·6 V/cm; intensity = 1000 lux and room temperature = 16°C.

Table 2. Calculated p-values for different compositions.

Composition	$p \times 10^3$		
	First exponential	Second exponential	Third exponential
10% $PbCrO_4$-80% HgO-10% ZnO	867	76·4	—
20% $PbCrO_4$-60% HgO-20% ZnO	822	33·0	—
60% $PbCrO_4$-20% HgO-20% ZnO	309	27·3	6·55
20% $PbCrO_4$-20% HgO-60% ZnO	162·6	26·8	11·9
100% $PbCrO_4$	201	22·1	9·71

current from the total current. The plots of log I_p versus time for decay mode show that decay cannot be governed by a single exponential law. This implies that the traps of different nature are situated at different energy depths below the lower edge of the conduction band.

Thus, the decay is given by the relation,

$$I = I_0 \exp(-pt), \tag{1}$$

where p is the probability of escape of an electron from the trap per second and its value is different for different straight line sections, I_0 is the current at the moment light is interrupted and I is the current at any instant of time. The calculated p-values (slopes of the straight lines) are listed in table 2.

The probability of an electron escaping from a trap is also given by the relation

$$p = S \exp(-E/kT), \tag{2}$$

where k is the Boltzmann constant, T is the absolute temperature and S is the frequency factor, the "attempt to escape frequency". It is defined as the number per second that the quanta from crystal vibrations (phonons) attempt to eject the electrons from

the traps multiplied by the probability of transition from trap to the conduction band, and is of the order of 10^9.

The trap depths (E) corresponding to different exponentials are calculated using (1) and (2) and is given by

$$E = kT\left[\log_e S - \log_e\left(\frac{\log_e I_0/I}{t}\right)\right]. \tag{3}$$

The calculated values of trap depths for different compositions are listed in table 3.

3.3 *Field dependence*

Dark current for (20% $PbCrO_4$-60% HgO-20% ZnO) composition begins to decay from its maximum value as soon as the voltage is switched on (figure 4). Dark current decays for a long time before acquiring a stable value. Measurements have been taken

Table 3. Trap ionization energies of different traps corresponding to different exponentials.

Composition	Trap depth (eV)		
	First exponential	Second exponential	Third exponential
10% $PbCrO_4$-80% HgO-10% ZnO	0·52	0·58	—
20% $PbCrO_4$-60% HgO-20% ZnO	0·52	0·6	—
60% $PbCrO_4$-20% HgO-20% ZnO	0·55	0·61	0·64
20% $PbCrO_4$-20% HgO-60% ZnO	0·56	0·61	0·63
100% $PbCrO_4$	0·56	0·61	0·63

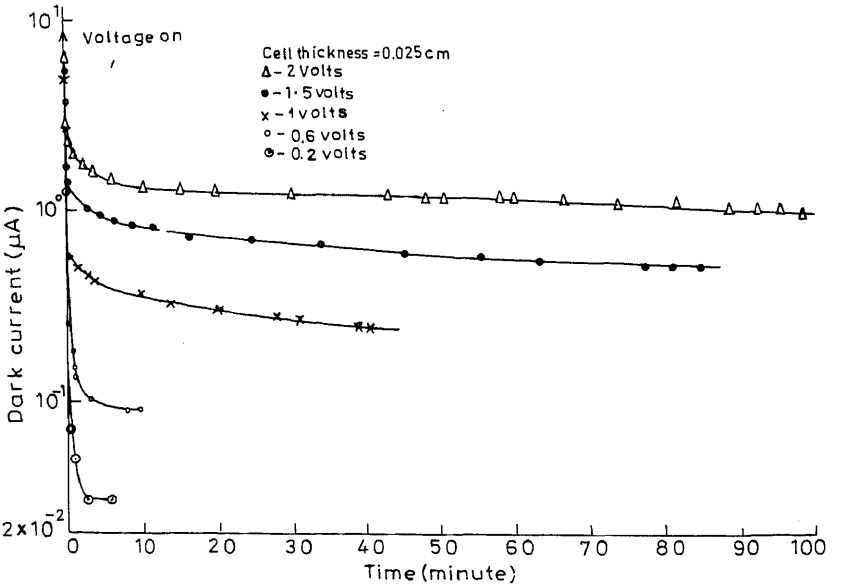

Figure 4. Decay of dark current at different fields for (20% $PbCrO_4$-60% HgO-20% ZnO) composition; room temperature = 32·5°C.

at different voltages. Decay of dark current with time indicates the presence of large density of trapping states inside the material. As soon as the voltage is switched on, dark current acquired its maximum value due to the motion of charge carriers but with the elapse of time, carriers begin to trap in trapping levels. As time passes, more and more charge carriers are trapped, thereby decreasing the dark current with time. At saturation (stable value of current), an equilibrium is established when the number of electrons making transition to the trapping levels from conduction band becomes equal to the number of electrons making transition to the conduction band from trapping levels per second.

Rise and decay of photocurrent for (20% $PbCrO_4$-60% HgO-20% ZnO) composition at different voltages is shown in figure 5. Figures 4 and 5 have been used to obtain figure 6 which shows the variation of dark current and photocurrent with voltage. Photocurrent was obtained by subtracting the dark current from the total current. The curves are drawn on a log-log scale. The curves are straight lines having different slopes at different regions of the curve. Only the photocurrent tends to saturation at higher voltage range. Thus, the straight line sections may be represented by $I \propto V^r$ where I is the current and r is the slope of the straight line section.

Above 0·6 V the dark current varies with voltage according to an index greater than 2. Smith and Rose [8] interpreted these currents as space charge limited currents and such type of variation was attributed to the effect of traps. Therefore, these currents may be interpreted as trap limited as well as space charge limited currents [9]. The non-ohmic behaviour ($r > 1$) of the photocurrent suggests that some carriers are being injected into the material. The photocurrent tends to saturation at high fields. This can be explained [4] on the basis of class-II states which are the imperfection centres lying in the forbidden gap just above the valence band. These class II centres have greater capture cross-section for holes than for electrons [10]. A dielectric material

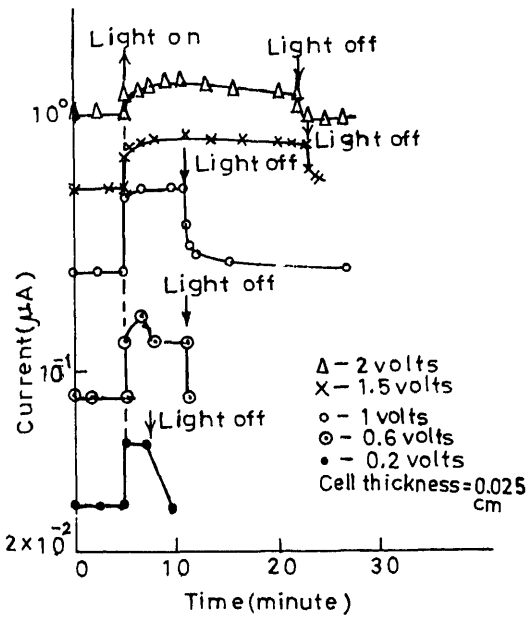

Figure 5. Rise and decay of photocurrent for (20% $PbCrO_4$-60% HgO-20% ZnO) composition at different fields; intensity = 5700 lux; room temperature = 32·5°C.

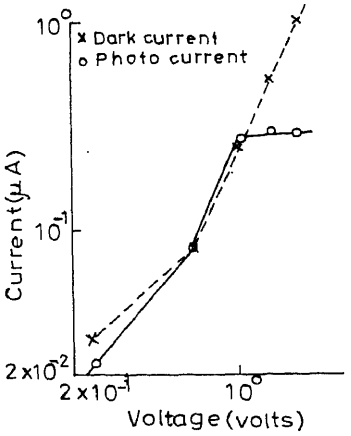

Figure 6. Variation of dark current and photocurrent with voltage for (20% $PbCrO_4$-60% HgO-20% ZnO) composition; intensity = 5700 lux; room temperature = 32·5°C.

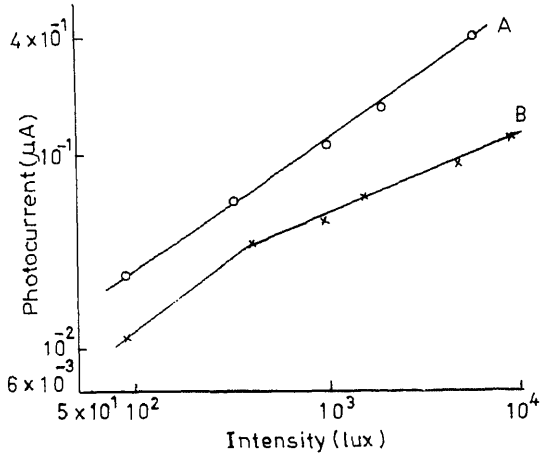

Figure 7. Variation of photocurrent with intensity of illumination for (20% $PbCrO_4$-60% HgO-20% ZnO) composition. A, at 30°C; B at 11°C and field = 40 V/cm.

has only one Fermi-level in the dark. But in the presence of light, there exists two Fermi-levels, one for electrons and another for holes. It may be assumed that at a particular light intensity and voltage the position of the Fermi-levels are such that they have just converted all the class-II states into recombination levels. An additional voltage causes the flow of more electrons into the material which raises the Fermi-level upwards towards the conduction band. Thus some of the class-II centres are converted into hole traps. This process desensitizes the sample and decreases electron life time with increasing voltage.

3.4 *Effect of intensity of illumination*

The variations of photocurrent with light intensity at two different temperatures are shown in figure 7 on a log-log scale. These are straight line curves. Thus the variation

can be represented by $I_p \propto L^r$. The value of r is < 1 for the whole region of intensity of illumination. This shows that photocurrent varies sublinearly with the intensity of illumination. This suggests a continuous trap distribution though exponential in nature below the lower edge of the conduction band. An increase in intensity would convert more of the trap levels to recombination levels thereby decreasing the electron lifetime and giving rise to observed sublinearity.

As the temperature is increased from 11°C to 30°C, photocurrent increases (figure 7) which suggests that the Fermi level is moving across an exponential trap distribution [7].

4. Conclusions

The response of (10% $PbCrO_4$-80% HgO-10% ZnO) and (20% $PbCrO_4$-60% HgO-20% ZnO) compositions is very quick. The existence of an exponential trap distribution below the lower edge of the conduction band and existence of sensitizing centres near the valence band are confirmed for (20% $PbCrO_4$-60% HgO-20% ZnO) composition. Dark current versus voltage curve for the (20% $PbCrO_4$-60% HgO-20% ZnO) composition, shows the flow of trap limited as well as space charge limited current inside the material at higher voltages. It is also concluded that the (10% $PbCrO_4$-80% HgO-10% ZnO) composite is best for optical switching. The existence of discrete trap depths appears plausible for different compositions.

Acknowledgement

One of the authors (SD) is grateful to CSIR, New Delhi for financial assistance.

References

[1] R E Aldrich, S L Hon and M L Horvill, *J. Appl. Phys.* **42**, 493 (1971)
[2] W H Leighton, *J. Appl. Phys.* **44**, 5011 (1973)
[3] R W Glew, *Thin solid films* **46**, 59 (1977)
[4] P K C Pillai, N Schroff, N Nand Kumar and A K Tripathi, *Phys. Rev.* **32**, 8228 (1985)
[5] Sadhana Devi and S G Prakash, *Pramana – J. Phys.* **39**, 145 (1992)
[6] Sadhana Devi and S G Prakash, *Indian J. Phys.* **A67**, 35 (1993)
[7] R H Bube, *Photoconductivity of solids* (John Wiley, New York, 1967) p. 404
R H Bube, *Photoconductivity of solids* (John Wiley, New York, 1967) p. 73
[8] R W Smith and A Rose, *Phys. Rev.* **97**, 1531 (1955)
[9] A Rose, *Phys. Rev.* **97**, 1538 (1955)
[10] A Rose, *Concepts of photoconductivity and allied problems* (Wiley, New York, 1963) p.43

PRAMANA
— journal of
physics

© Printed in India

Vol. 43, No. 4,
October 1994
pp. 255–272

A basis-free approach to time-reversal for symmetry groups

L C BIEDENHARN and E C G SUDARSHAN
Center for Particle Physics, Department of Physics, University of Texas at Austin, Austin, TX 78712, USA

MS received 26 April 1994; revised 5 September 1994

Abstract. We develop a basis-free approach to time-reversal for the quantal angular momentum group, $SU2$, and apply these methods to the physical symmetry $SU2_{\text{isospin}}$, $SU3_{\text{flavor}}$, $SU3_{\text{nuclear}}$ and the nuclear collective symmetry group $SL(3, R)$ of Gell-Mann and Tomonaga.

Keywords. Time reversal; quantum mechanics.

PACS No. 11·30

1. Introduction and summary

Of all the transformations on a quantum system those transformations relating to time reversal are the most natural; whenever there is time evolution one can ask: What is the time reversed description? However since the energy is always bounded from below a purely geometric unitary time reversal is not possible. Rather time reversal must be *Bewegungsumkehr* (reversal of all motions) and must therefore involve reversal of momenta but preserve the sign of position and energy. Time reversal in this sense can be required even of irreversible processes; and one can ask for tests of time reversal invariance in particle decay phenomena. The pioneering work of Wigner [1] for time-reversal in non-relativistic quantum mechanics, determined that alone among all symmetries the quantal time-reversal symmetry operator T is *non-linear* (or more precisely semi-linear). This result is certainly true in the context of the physically important Newtonian and Einsteinian relativities (the Galilei and Poincaré symmetry groups, respectively) but it does not follow that time-reversal must necessarily be implemented for *all* physical symmetry groups in the same semi-linear fashion.

We were led to these considerations by the problem of defining time-reversal for the internal symmetries of isospin and of flavor $SU3$, a problem which we have not, so far, found to have been discussed in the literature. In the course of our investigation we were plagued by the many distinct basis conventions (often contradictory) to be found in physical treatments of group symmetries, which for complex phases can be most confusing. Here the mathematicians have pointed the way: work if possible in a coordinate-free, basis-independent manner, for this way is logically, and usually actually, simpler.

To illustrate our procedure we will first re-examine time-reversal for the quantal angular momentum group, $SU2$ using basis-free methods (§ 2). Having established the methodology, we then turn (§ 3) to the original question of time-reversal for isospin and flavor $SU3$. We then turn to two other symmetry groups of interest in nuclear

physics: the nuclear $SU3$ group of Elliot [2] and the collective motion nuclear symmetry group, $SL(3, R)$ of Gell-Mann [3] and Tomonaga [4].

We have relegated to appendices several of the more detailed topics. For example, in Appendix A we detail difficulties of the basis-dependent approach to the results in § 2.

2. Time-reversal for angular momentum, $SU2$

Let us consider first the well-known case of time-reversal for $SU2$, the quantum angular momentum group. Time-reversal was defined by Wigner as reversal of motion (*Bewegungsumkehr*) based on the principle that for every physical motion there is an equally physical possible motion in reverse order. It follows that linear momentum, $\mathbf{P}$, reverses under motion-reversal, that is $T:\mathbf{P} \to -\mathbf{P}$. Since orbital angular momentum is defined by $\mathbf{L} = \mathbf{r} \times \mathbf{P}$, one sees that orbital angular momentum reverses: $T:\mathbf{L} \to -\mathbf{L}$. On grounds of uniformity, one assumes that *spin* angular momentum also reverses, [5] so that for the total angular momentum $J = \mathbf{L} + \mathbf{S}$, we have,

$$T:\mathbf{J} \to -\mathbf{J}. \tag{2.1}$$

For quantum mechanics to obey time-reversal, one postulates that the Schrödinger equation

$$H\psi = i\frac{\mathrm{d}}{\mathrm{d}t}\psi, \tag{2.2}$$

be invariant under $T:t \to -t$. This will be true if we require (as Wigner did) that the time-reversal operation T not only reverse time order ($t \to -t$), but also involves complex conjugation, denoted by K_0. Thus Wigner time-reversal is, at this stage of the discussion, the operation

$$T = \mathscr{T}K_0, \tag{2.3}$$

where $\mathscr{T}$ implies $t \to -t$.

The operation of time-reversal, (2.3), is consistent with the previous results, where T implied that $\mathbf{P} \to -\mathbf{P}$ and $\mathbf{L} \to -\mathbf{L}$, since the operators $\mathbf{P}$ and $\mathbf{L}$, as quantum observables, are Hermitian and hence formally real operators. The action of (2.3) is however problematic, since any given spin realization by matrix operators is basis dependent (so that the action by K_0 is not canonically-defined). The Hamiltonian is an observable and is required to be invariant under Wigner time-reversal. If the Hamiltonian involves electro-magnetism we see, from gauge invariance, that the combination (kinetic momentum), $\mathbf{p} - e\mathbf{A}/c$, enters so that we must have $T:\mathbf{A} \to -\mathbf{A}$. It follows that $T:\mathbf{E} \to \mathbf{E}$ and $\mathbf{B} \to -\mathbf{B}$.

We wish now to find *in a coordinate-free way* the consequences of Wigner time-reversal for a general angular momentum. Consider an arbitrary unitary irrep of $SU2$, say, $\mathbf{D}^{(J)}(g)$, where $\mathbf{D}$ is the (unitary) irrep labelled, as usual, by the total angular momentum j and g is a group element (a rotation).

The explicit matrix form of the irrep is given by

$$\mathbf{D}^{(J)}(g) \equiv e^{-i\boldsymbol{\omega}\cdot\mathbf{J}}, \tag{2.4}$$

where $\mathbf{J}$ is a $(2j+1) \times (2j+1)$ Hermitian matrix realization of the abstract operator

J, and $\boldsymbol{\omega} = \vartheta\hat{n}$ is explicitly real (ϑ = angle of rotation, $\hat{n}$ = unit vector denoting axis of rotation).

It might appear at this point that the action of time-reversal, eq. (2.3) on the irrep matrix $\mathbf{D}^{(j)}$, eq. (2.4), is now obvious: namely that under T both i and **J** reverse, so the irrep $\mathbf{D}^{(j)}$ is invariant. This conclusion is, however, not really warranted since the matrix $\mathbf{D}^{(j)}$ is *basis-dependent* and, to be precise, we must also examine the effect of time-reversal on the basis, *per se*. (The basis could be real, or, as is generally the case, complex, so that the basis itself could transform under T).

The difficulties caused by a choice of basis (see Appendix A) are made even worse by the fact that in writing eq. (2.4)—in the standard (physics) form—we are guilty of choosing a *complex* basis for the representations of a *real* Lie algebra [6] [7]. One can avoid this choice if one represents the $SU2$ Lie algebra (over the real field **R**) by generators which are *anti-Hermitian* operators. Such a choice, however, *conflicts* with a basic postulate of quantum mechanics: that generators are observables to be represented by *Hermitian* operators [8]. Nonetheless let us proceed in this explicitly real way and use anti-Hermitian generators, **K**, defined by

$$\mathbf{K} \equiv i\mathbf{J}, \tag{2.5}$$

so that in eq. (2.4),

$$\mathbf{D}(g) = e^{-\boldsymbol{\omega}\cdot\mathbf{K}}, \tag{2.6}$$

is a unitary representation with $\boldsymbol{\omega}$ real (numbers) and **K** anti-Hermitian generating a real Lie algebra ($su2$).

To answer the question as to how eq. (2.6) transforms under Wigner time-reversal, in a basis-independent way, one uses the Frobenius-Schur invariant (FSI)

$$\text{FSI} \equiv \int \mathrm{d}g \,\mathrm{tr}\,\mathbf{D}^{(\lambda)}(g^2) \tag{2.7}$$

and—for the general case—finds: [9] FSI = +1, −1 or 0 for irreps λ that are real, quaternionic ("pseudo real" [10]) or complex, respectively. All irreps of $SU2$ are found to be [9] either *real* (j = integer) or *quaternionic* ($j = \frac{1}{2}$–integer). (The Frobenius–Schur invariant is discussed further in Appendix B).

The Frobenius–Schur invariant answers the question for the angular momentum ($SU2$) irreps. Since there are no complex irreps, it follows that under time reversal, the unitary $SU2$ irreps, labelled by $j = 0, \frac{1}{2}, 1, \ldots$, are *invariant*.

This result does not, however, answer the question about the behaviour of the representative *matrices* under time-reversal. Put differently, the Frobenius–Schur invariant being non-zero guarantees only that the complex conjugated irrep matrix is *equivalent* to the original matrix (and not necessarily equal). In symbols

$$(\text{FSI} = \pm 1) \Rightarrow \mathbf{D}^{(\lambda)*} \simeq \mathbf{D}^{(\lambda)}, \tag{2.8}$$

that is,

$$\mathbf{D}^{(\lambda)*} = \mathbf{U}^{-1}\mathbf{D}^{(\lambda)}\mathbf{U}, \tag{2.9}$$

where **U** is a unitary matrix. (We cannot conclude that if FSI = ±1 then **U** = 1, since, even though the irrep is real, the matrix basis itself may be complex. See Appendix A).

The basis independent approach uses the fact that complex conjugation implies

the equivalence relation, eq. (2.9), which—using eq. (2.6)—may be written in terms of the (non-Hermitian) generators as the *linear* transformation

$$\mathbf{K} \to \mathbf{U}^{-1}\mathbf{K}\mathbf{U}. \tag{2.10}$$

Since this transformation (as an equivalence transformation) preserves all irreps (leaves j invariant) it must be an automorphism of the $su2$ Lie algebra. For $SU2$ there exist only two automorphisms (both inner):[11] the identity and the involutary Cartan automorphism, $\mathscr{C}$. To define the Cartan automorphism [12] in a basis-free way we use a Cartan splitting of the (complexified) Lie algebra, $\mathbf{g}$

$$\mathbf{g} = \mathbf{k} + \mathbf{p}, \tag{2.11}$$

where

$$[\mathbf{k}, \mathbf{k}] \subset \mathbf{k},\ [\mathbf{p}, \mathbf{k}] \subset \mathbf{p},\ [\mathbf{p}, \mathbf{p}] \subset \mathbf{k}. \tag{2.12}$$

A Cartan automorphism is the transformation

$$\mathscr{C}: \mathbf{k} \to \mathbf{k},\ \mathbf{p} \to -\mathbf{p}, \tag{2.13}$$

which clearly leaves the commutation relation, eq. (2.12), invariant [13].

The standard, basis-dependent, choice for the (anti-Hermitian) $su2$ Lie algebra generators in the (complex) Cartan basis yields for $\mathscr{C}$ the transformation

$$\mathscr{C}: K_z \to K_z,\ K_\pm \to -K_\pm, \tag{2.14}$$

or in the Cartesian basis

$$\mathscr{C}: K_z \to K_z,\ K_x \to -K_x,\ K_y \to -K_y. \tag{2.15}$$

Let us now apply these results to the physical angular momentum operator, $\mathbf{J}$. From (2.9) we have determined that complex conjugation (K_0) implies (2.10) the automorphism U, which is precisely the Cartan involution $\mathscr{C}$, eq. (2.13). We have thereby determined the action of complex conjugation on the anti-Hermitian generators $\mathbf{K}$, to be

$$K_0: \mathbf{K} \to \mathscr{C}(\mathbf{K}), \tag{2.16}$$

and hence, since $\mathbf{K} \equiv i\mathbf{J}$ (eq. (2.5)) we obtain

$$K_0: \mathbf{J} \to -\mathscr{C}(\mathbf{J}). \tag{2.17}$$

Since the action of time-reversal on $\mathbf{J}$ has been defined from physical principles (in eq. (2.1)) to be

$$T: \mathbf{J} \to -\mathbf{J}, \tag{2.18}$$

we can conclude (from eqs (2.3) and (2.18)) that the final basis-free form for the Wigner time reversal operator is

$$T = \mathscr{T}\mathscr{C}K_0. \tag{2.19}$$

(The three operators on the RHS of (2.19) can be shown to commute).

Equation (2.19) is the abstract form of Wigner's time-reversal operator, which has now been obtained in a basis-free (coordinate independent) way.

If we now combine the operations of complex conjugation, K_0, and the Cartan automorphism, $\mathscr{C}$, we find that the combined action $\mathscr{C}K_0$ on any unitary irreducible representation $\mathbf{D}(g)$ of $SU2$ is given by

$$\mathscr{C}K_0:\mathbf{D}(g)\to\mathscr{C}(\mathbf{D}^*(g))=\mathscr{C}(\mathbf{U}^{-1}\mathbf{D}(g)\mathbf{U}) \tag{2.20}$$

$$=\mathbf{U}^{-1}(\mathbf{U}^{-1}\mathbf{D}(g)\mathbf{U})\mathbf{U}=\mathbf{D}(g), \tag{2.21}$$

since $\mathscr{C}$ is involutary and $U^2=\pm\mathbf{1}$, see Appendix B. Thus the transformation $\mathscr{C}K_0$, and hence time-reversal, acts as the identity transformation on every unitary $SU2$ representation. (It does not follow that $\mathscr{C}K_0$ is the identity, because K_0 unlike $\mathscr{C}$, is not a linear transformation).

Remarks. (a) This basis-free derivation of the time-reversal operation is logically simpler, and more general, than the original (basis-dependent) derivation. For example, Wigner's derivation of time-reversal was explicitly non-relativistic and moreover restricted to spin $\frac{1}{2}$, taking the form

$$T_{\text{Wigner}}=\mathscr{T}K_0\cdot(\text{commutation with } i\sigma_y). \tag{2.22}$$

The basis-free derivation given above, however, is founded on Schrödinger's equation—and hence is valid for relativistic as well as non-relativistic quantum mechanics—and uses an automorphism for $SU2$ (which is clearly valid for all irreps). In consequence, the basis-free result, eq. (2.18), is valid for relativistic quantum mechanics and all spins. This result for relativistic time reversal was first given by Biedenharn [14] (for the Dirac equation) correcting previous incorrect results by Racah [15] and by Pauli [16]. For completeness, we should discuss time-reversal, in a basis-free way, for the Poincaré group (and Galilei group as well), but we forego this here.

(b) An advantage of the basis-free derivation is that eq. (2.18) implies the proper behaviour of the basis vectors of angular momentum irreps under time-reversal, [9] and correspondingly the correct time-reversal behaviour of the WCG coefficients.

(c) The basis-independent form of time-reversal shows that the Hamiltonian (for a time-reversal invariant theory) is *invariant* under T. This has the consequence that, in the Fermi theory of weak interactions, the five interaction constants S, V, T, A, P are *real* in a time-reversal adapted basis [17]. Expressed in terms of the standard model for weak interactions, the Kobayashi-Maskawa mass matrix [18] in the Cartan–Weyl basis diagonalizing the observable quantum numbers must be real if time-reversal is to be obeyed.

(d) As Wigner remarked [8], the fact that T is a non-linear operation prevents its (direct) use to define quantum numbers. However, T^2 is linear and, in fact, $T^2\to(-1)^{2j}$ is a quantum number, namely the FSI invariant.

(e) The fact that for fermionic systems (FSI $=-1=(-1)^{2j}$) the time reversal operator obeys $T^4=\mathbf{1}$ means that the Hilbert space of such systems is *quaternionic* and not just complex. One consequence is Kramer's theorem (namely, energy levels for FSI $=-1$ are at least doubly degenerate in electric fields) but there are other more subtle purely topological consequences [19].

3. Time-reversal for $SU(3)_{\text{flavor}}$

With these results for $SU2$ in hand, let us now examine the extension of time reversal to unitary symmetry, $SU(3)_{\text{flavor}}$, [20]. What does *Bewegungsumkehr* do to, say, a baryon in the octet representation? Clearly a baryon reversing its motion is still a baryon, in the same state of the same $SU3$ irrep, with the same charge, (where the charge operator $\mathbf{Q}_{\text{ch}}$ is defined by the $SU3$ generators $\mathbf{Q}_{\text{ch}} = \mathbf{I}_z + \frac{1}{2}\mathbf{Y}$).

Accordingly, we see that

$$T(\mathbf{D}^{(\lambda)}) = \mathbf{D}^{(\lambda)}, \tag{3.1}$$

where λ denotes an $SU3$ irrep, and moreover the charge operator $\mathbf{Q}$ must obey

$$T(\mathbf{Q}_{\text{ch}}) = \mathbf{Q}_{\text{ch}}, \tag{3.2}$$

which implies that both the isospin $\mathbf{I}$ and the hypercharge $\mathbf{Y}$ are invariant under T. The Frobenius–Schur invariant for $SU3$ has only two values: $+1$ and 0 corresponding to real and complex irreps [11]. Unlike $SU2$, complex conjugation is no longer an inner automorphism, but an outer automorphism for $SU3$ [11]. (This can be seen from the fact that $D^{(\lambda)*}$ is inequivalent to $\mathbf{D}^{(\lambda)}$ for irreps, such as the decimet **10**, with FSI = 0).

In particular, eq. (3.1) implies, for unitary irreps, defined by

$$\mathbf{D}^{(\lambda)}(g) \equiv \exp\left(- \sum_{\mu=1}^{8} \omega_\mu \mathbf{X}_\mu \right), \tag{3.3}$$

(where ω_μ are real parameters and $\mathbf{X}_\mu$ are anti-Hermitian generators for irrep λ), that the time-reversal operation for $SU3_{\text{flavor}}$ cannot involve complex conjugation. Equation (3.2) shows that at least four of the eight-anti-Hermitian generators are invariant under time-reversal. Thus the simplest realization of time reversal for flavor $SU3$ **is** the identity transformation, not only for the irreps (as was the case also for $SU2$) but also for the individual basis-vectors (since the generators would be unchanged, again unlike $SU2$).

Remark. This is simplest realization but are there other possibilities? To answer this consider again the $SU2$ case. There we learned that T was also the identity transformation on all irreps, but only because conjugation was an inner automorphism. It was this property that allowed the identity transformation for representations, and allowed compatibility with $\mathbf{J} \to -\mathbf{J}$ (achieved by combining conjugation with the Cartan automorphism). From this we conclude that the only other possibility available for time-reversal in (flavor) $SU3$ is a Cartan involutary inner automorphism. For $SU3$ there exist, besides the identity, only two distinct automorphisms

(*a*) $\mathbf{g} = \mathbf{k} + \mathbf{p}$, $\mathbf{k} = \{\lambda_2, \lambda_5, \lambda_7\}$,

$$\mathbf{p} = \{\lambda_1, \lambda_3, \lambda_4, \lambda_6, \lambda_8\}, \tag{3.4}$$

with

$$\mathscr{C}_a : \mathbf{k} \to \mathbf{k},\ \mathbf{p} \to -\mathbf{p}. \tag{3.5}$$

(Here the $\{\lambda_i\}$ are representations of the eight Gell-Mann matrices).

Clearly the automorphism $\mathscr{C}_a$ is not acceptable for time reversal since the charge

operator would not be invariant under $\mathscr{C}_a$. (The charge operator involves λ_3 and λ_8 which belong to the set **p**). Moreover $\mathscr{C}_a$ is outer.

(*b*) $$\mathbf{g} = \mathbf{k} + \mathbf{p},\ \mathbf{k} = \{\lambda_1, \lambda_2, \lambda_3, \lambda_8\} \tag{3.6}$$

and

$$\mathbf{p} = \{\lambda_4, \lambda_5, \lambda_6, \lambda_7\},$$

This automorphism, $\mathscr{C}_b$, is quite acceptable for time reversal since

$$\mathscr{C}_b(\mathbf{D}^{(\lambda)}) \cong \mathbf{D}^{(\lambda)}, \quad \text{and} \quad \mathscr{C}_b(\mathbf{Q}) = (\mathbf{Q}), \tag{3.7}$$

Moreover, all of the state vectors of every irrep are preserved under $\mathscr{C}_b$. ($\mathscr{C}_b$ is inner). [To see this last point, let us observe that the ket vector $|[M], (m)\rangle$ is defined (to within a complex constant) by the relations:

$$\mathbf{X}\cdot\mathbf{X}|[M], (m)\rangle = I_2([M]]\ |[M], (m)\rangle,$$

$$\mathbf{X}\cdot\mathbf{X}\circ\mathbf{X}|[M], (m)\rangle = I_3([M])\ |[M], (m)\rangle,$$

$$\sum_{\mu=1}^{3} \mathbf{I}_\mu^2 |[M], (m)\rangle = I_2(m_{12}m_{22})|[M], (m)\rangle,$$

$$\mathbf{I}_z|[M], (m)\rangle = \left(m_{11} - \frac{m_{12}+m_{22}}{2}\right)|[M], (m)\rangle,$$

and

$$\mathbf{Y}_8|[M], (m)\rangle = \left(\frac{m_{12}+m_{22}}{2} - \frac{M_{13}+M_{23}}{3}\right)|[M], (m)\rangle. \tag{3.8}$$

Here the states are defined by Gel'fand patterns: $|[M], (m)\rangle = \left|\left|\begin{pmatrix} M_{13} M_{23} 0 \\ m_{12} m_{22} \\ m_{11} \end{pmatrix}\right\rangle\right\rangle$, and $I_2([M])$ and $I_3([M])$ are eigenvalues of the two invariant operators of $SU3$, with $I_2(m_{12}, m_{22})$ being the eigenvalue of the Casimir invariant of $SU2$. The invariant operators of $SU3$ are denoted by $\mathbf{X}\cdot\mathbf{X}$ for the quadratic (Casimir) invariant and $\mathbf{X}\cdot\mathbf{X}\circ\mathbf{X}$ for the cubic invariant (with $\circ$ denoting the symmetric octet product). Clearly the automorphism $\mathscr{C}_b$ leaves every eigenvalue invariant, so that the irrep vectors are themselves invariant under $\mathscr{C}_b$].

The above remark shows that we have two distinct possibilities for time-reversal in $SU_{\text{flavor}}(3)$: either (a) the identity automorphism, or (b) the Cartan involuntary automorphism $\mathscr{C}_b$. It would be interesting to see whether or not there is a physical reason for choosing between these two options. (We hope to discuss this question in the near future).

The result that we have obtained for time-reversal in $SU3_{\text{flavor}}$ is that the $SU3$ irreps, as well as the carrier space vectors, are invariant under time-reversal. This is actually quite plausible *a priori* since flavor-symmetry is clearly not a space-time symmetry and should be therefore unaffected by space-time transformations. The only reason for supposing otherwise is that the lesson of Wigner time-reversal has been over-learned, and complex conjugation is not necessarily a general feature after all.

Such a result for non-spacetime (internal) symmetries such as $SU3_{\text{flavor}}$ is quite acceptable and plausible, but despite this there are grounds for worry. How is one

to distinguish, in the operation of complex conjugation, the imaginary unit used in describing quantal space-time states from the imaginary unit used in, say, flavor irrep vectors? Actually there is no real problem here since the flavor symmetry group must occur as an element in a direct product for the complete symmetry group, so that the space-time ket vectors ψ are distinct (and distinguishable) from flavor symmetry kets X in the tensor product states $\psi \otimes X$.

4. Time-reversal for nuclear $SU(3)$

The nuclear shell model of Mayer and Jensen has an approximate Hamiltonian symmetry, $SU3_{\text{nuclear}}$, the symmetry of the isotropic three-dimensional harmonic oscillator. This $SU3$ symmetry becomes more nearly exact in the limit that the spin-orbit splitting becomes zero. Since spin is neglected in this limit, one sees that the $SU2$ rotational symmetry consists of the orbital angular momentum $SO3$—a sub-group of $SU3$—and the separate spin symmetry, $SU2$. Thus one deals with the symmetry $(SU2_{\text{spin}}) \times (SU3_{\text{nucl}})$, which may be embedded in the larger symmetry $SU6$, somewhat reminiscent of, but actually quite distinct from, the Radicati-Gürsey baryonic $SU6$ symmetry.

Elliot [2] suggested that a feasible model for certain nuclear mass regions—the rotational nuclei—is the nuclear rotational symmetry $SU3$ generated by $\mathbf{L}$, the orbital angular momentum, and $\mathbf{Q}$, the mass quadrupole operator. Adding a quadrupole-quadrupole interaction to the $SU3$ invariant Hamiltonian, H_{symm}, leads to a total Hamiltonian with an $SU3$-splitting term, $\Delta H \propto \mathbf{L}^2$, as befits rotational nuclei.

To examine the time-reversal properties of this physical model, we begin by noting that the generators $\mathbf{L}$ and $\mathbf{Q}$ must have the physical time-reversal properties

$$T:\mathbf{L} \rightarrow -\mathbf{L} \text{ since } \mathbf{L} \text{ is an angular momentum,} \tag{4.1}$$

and

$$T:\mathbf{Q} \rightarrow +\mathbf{Q} \tag{4.2}$$

(since $\mathbf{Q}$ is interpreted in the Elliott model as a mass quadrupole operator).

The Frobenius–Schur invariant for $SU3$ has, as noted in § 3, only two values: $+1$ and 0, so the only real and complex (finite-dimensional) unitary irreps occur.

Explicitly real representations of the real Lie group $SU3$ may be generated from the adjoint realization using *real anti-symmetric* 8×8 generators and real parameters. Hence

$$K_0:\mathbf{D}(g) \rightarrow \mathbf{D}^*(g) = \mathbf{D}(g). \tag{4.3}$$

It follows from (4.3) that for the Hermitian generators, $\mathbf{L}$ and $\mathbf{Q}$, we have

$$K_0:\mathbf{L} \rightarrow -\mathbf{L},\ \mathbf{Q} \rightarrow -\mathbf{Q}. \tag{4.4}$$

In order to obtain the physical time-reversal properties, (4.1, 2), we must therefore use, in addition to K_0, the Cartan automorphism $\mathscr{C}_a$

$$\mathscr{C}_a:\mathbf{L} \rightarrow \mathbf{L},\ \mathbf{Q} \rightarrow -\mathbf{Q}, \tag{4.5}$$

which is associated to the Cartan splitting of $SU3$ with $\mathbf{k} = \{\mathbf{L}\}$ and $\mathbf{p} = \{\mathbf{Q}\}$ exactly as in (3.5) for the automorphism $\mathscr{C}_a$.

This automorphism $\mathscr{C}_a$ is an *outer* automorphism, a symmetry of the Coxeter–Dynkin diagram for $SU3$. (To see that $\mathscr{C}_a$ is outer, note that the unimodular condition for $SU3$ is $\det(D(g)) = 1$. The transformation (4.5) however has determinant -1, and thus cannot belong to the $SU3$ group).

Explicitly real representations, eq. (4.3), of $SU3$ (more properly representations of the adjoint group $SU3/Z3$) can be fully reduced (brought to block-diagonal form) only for the self-conjugate irreps (FSI = 1), (since we are using the real field **R**). Over the complex field any not-fully-reduced explicitly-real representation with FSI = 0 can be reduced to a direct sum of pairs of conjugate irreps (each with FSI = 0).

Since quantum mechanics requires the use of the complex field, irreducible complex representations necessarily will occur, so that this analysis of $SU3_{\text{nuclear}}$ using explicitly real structures must be extended to the complex case.

Let us consider then the defining 3×3 irrep of $SU3$ which has FSI = 0. The Hermitian generators of this irrep are the Gell–Mann matrices, $\{\lambda_i\}$, which divide into two distinct sets under complex conjugation:

(a) five real, symmetric, Hermitian generators

$$\{\lambda_1, \lambda_3, \lambda_4, \lambda_6, \lambda_8\} \equiv \{\mathbf{Q}\} \tag{4.6}$$

(b) three purely imaginary, anti-symmetric, Hermitian generators

$$\{\lambda_2, \lambda_5, \lambda_7\} \equiv \{\mathbf{L}\}. \tag{4.7}$$

This splitting is clearly basis-dependent for irreps of $SU3/Z3$ (since we gave *eight* purely imaginary, anti-symmetric, Hermitian generators in (4.3) and (4.4)), but for irreps of $SU3$ not belonging to $SU3/Z3$ this splitting is generic and basis-independent.

For this realization of the Hermitian $SU3$ generators, eqs (4.6 and 4.7), it follows that

$$K_0: \mathbf{L} \to -\mathbf{L} \text{ and } \mathbf{Q} \to +\mathbf{Q}. \tag{4.8}$$

This is exactly the desired time-reversal property of the physical $SU3_{\text{nuclear}}$ generators. It follows that time-reversal for $SU3_{\text{nuclear}}$ is given by

$$T = \mathscr{T} K_0. \tag{4.9}$$

To find out what happens to the representations, we use the technique of generating unitary representations of a real Lie algebra by anti-Hermitian generators: $\{\mathbf{L}, i\mathbf{Q}\}$. The representations thus have the form:

$$\mathbf{D}(g) = \exp(\boldsymbol{\alpha}\cdot\mathbf{L} + i\boldsymbol{\beta}\cdot\mathbf{Q}), \tag{4.10}$$

where $\boldsymbol{\alpha}, \boldsymbol{\beta}$ are explicitly real parameters

Clearly under time-reversal, eq. (4.9), we obtain

$$T: \mathbf{D}(g) = \mathbf{D}(\boldsymbol{\alpha}, \boldsymbol{\beta}) \to \mathbf{D}(\boldsymbol{\alpha}, -\boldsymbol{\beta}). \tag{4.11}$$

The representation $\mathbf{D}(\boldsymbol{\alpha}, -\boldsymbol{\beta})$ is, in general, *inequivalent* to the representation $\mathbf{D}(\boldsymbol{\alpha}, \boldsymbol{\beta})$. The effect of time-reversal on a (unitary) representation can be seen from (4.11), (4.12) and (4.5) to be the same as the action of the Cartan automorphism $\mathscr{C}_a$.

The automorphism, $\mathscr{C}_a$, can be shown from eq. (3.8) to effect on the $SU3_{\text{nuclear}}$

invariant operators the transformation

$$\mathscr{C}_a: I_2 \to I_2, I_3 \to -I_3. \tag{4.12}$$

(This result, (4.12), is not obvious since one needs to know that the symmetric product in I_3 leads to an invariant form containing cubic terms with an *odd* number of quadrupole generators). It follows that for unitary $SU3_{\text{nuclear}}$ irreps the operation: $\mathscr{C}_a T$ is equivalent to the identity transformation. (Just as in § 2, the two operations are not equal because T is non-linear).

Remarks. It would be of interest to see how time-reversal affects the basis vectors carrying an $SU3_{\text{nuclear}}$ irrep. The $SU3_{\text{nuclear}}$ ket vectors are uniquely labelled by five quantum numbers: $\mathbf{I}_2 \to \mathbf{I}_2$, $\mathbf{I}_3 \to \mathbf{I}_3$, $\mathbf{I}_2(SO3) \to L(L+1)$, $\mathbf{L}_z \to m$ and a multiplicity index ε (labelling the multiple occurrences of L). This last (fifth) index is canonically determined [21] (that is, without any arbitrary choice whatsoever.) Under time-reversal, the labels: I_2 and L are unchanged, whereas both I_3 and m reverse (change sign) [22]. That is

$$T: I_2 \to I_2,\ I_3 \to -I_3,\ L \to L,\ L_z \to -L_z. \tag{4.13}$$

From our experience with $SU2$ in § 2 we see that the transformation $L \to L, L_z \to -L_z$ induces the $SU2$ transformation given by

$$T: \left| \begin{matrix} I_2, I_3 \\ L, m \end{matrix} \right\rangle \to (-1)^{L-M} \left| \begin{matrix} I_2, -I_3 \\ L, -m \end{matrix} \right\rangle. \tag{4.14}$$

For ket vectors without multiplicity (vectors for which the label ε is unnecessary), eq. (4.14) gives a unique prescription. For ket vectors requiring ε-labels, the transformation induced by time-reversal must be diagonal, but the appropriate sign change, that may occur, is not fully known.

A physically important conclusion follows from the results given above. We see from eq. (4.12), and the discussion there, that under time-reversal, eq. (4.10), the irrep labels, (4.13) are not invariant. Expressed differently, but equivalently, the Elliott nuclear $SU3$ symmetry does not have a time-reversal invariant significance.

This basic inadequacy, along with the failure of the $SU3_{\text{nuclear}}$ symmetry to incorporate spin intrinsically, shows that the Elliott nuclear $SU3$ symmetry can be neither a fundamental symmetry nor an approximate (time-reversal invariant) symmetry in physics.

Remark. There is an interesting application of these results to the topological Skyrme-Witten model for hadrons [23]. There is an alternative procedure for injecting the static minimal energy soliton of this model into the $SU3_{\text{flavor}}$ group which involves using $\mathbf{L}$ (orbital angular momentum) and $\mathbf{Q}$ (the mass quadrupole) as $SU3_{\text{flavor}}$ generators [24]. This imbedding is far less satisfactory in its physical consequences than that used by Witten, but cannot (so far) be excluded. We see from the results above that this imbedding violates time-reversal invariance and is accordingly to be excluded. The imbedding discussed in § 5 below would appear to be satisfactory (since it is time-reversal invariant) but again it is excluded since the soliton is static (and accordingly the time-derivative $\dot{\mathbf{Q}}$ operator, eq. (5.1), vanishes).

5. Time-reversal for the Gell-Mann–Tomonaga nuclear collective symmetry group $SL(3,\mathscr{R})$

At about the same time that $SU3_{\text{nuclear}}$ was proposed for nuclear physics, non-compact internal symmetry groups were proposed as dynamical hadronic symmetries, generating Regge sequences for hadrons [25].

One such non-compact group, $SL(3,\mathscr{R})$, was also proposed as a nuclear symmetry [26]. This $SL(3,R)$ symmetry group is physically the group of rotations and volume-preserving deformations of three-space. Since nuclear matter has, as a rough approximation, an energy independent of shape, the suggestion that $SL(3,\mathscr{R})$ might be a useful symmetry for nuclear physics is certainly reasonable.

Gell–Mann had a very ingenious way to realize this symmetry. The group $SL(3,\mathscr{R})$ has two sets of Hermitian generators: the total angular momentum, **J**, and a quadrupolar deformation generator. For the quadrupolar generator, Gell-Mann proposed the time-derivative of the mass quadrupole operator **Q**. Since the Hamiltonian must contain $\mathbf{J}^2$, one can evaluate this time-derivative, at least approximately, as

$$\dot{\mathbf{Q}} \equiv \frac{\mathrm{d}}{\mathrm{d}t}\mathbf{Q} = i[H,\mathbf{Q}] \cong i[\mathbf{J}^2,\mathbf{Q}]. \tag{5.1}$$

The operators **J** and $\dot{\mathbf{Q}}$ have a commutator algebra that closes on $SL(3,\mathscr{R})$, that is, $\dot{\mathbf{Q}}$ transforms under **J** as a quadrupole and $[\dot{\mathbf{Q}},\dot{\mathbf{Q}}] = \lambda^2\mathbf{J}$ (with λ a length scale, $\hbar = c = 1$).

At roughly the same time, Tomonaga had been developing collective models for diverse physical problems including a two-dimensional nuclear collective model [3]. Applied to three-dimensions his techniques would have led him to precisely the Gell-Mann collective nuclear model [27].

This nuclear collective model has been developed further in the nuclear physics literature and subsumed in larger non-compact groups [28] [29]. Our purpose here is to examine the time-reversal properties of the model.

It is clear from the physical meaning of $\dot{\mathbf{Q}}$, as the time-derivative of a time-reversal invariant object **Q**, that we must have

$$T{:}\dot{\mathbf{Q}} \to -\dot{\mathbf{Q}}, \tag{5.2}$$

and moreover, from (2.1), we must have

$$T{:}\mathbf{J} \to -\mathbf{J}. \tag{5.3}$$

As observables, both **J** and $\dot{\mathbf{Q}}$ are Hermitian. To obtain a unitary representation we exponentiate the anti-Hermitian generators $i\mathbf{J}$ and $i\dot{\mathbf{Q}}$. For the anti-Hermitian generators we have

$$\begin{aligned} &T{:}i\mathbf{J} \to +i\mathbf{J} \\ &i\dot{\mathbf{Q}} \to +i\dot{\mathbf{Q}}. \end{aligned} \tag{5.4}$$

We see that, from (5.4) (since the group parameters are real), the unitary representation $\mathbf{D}(g)$ must obey.

$$T{:}\mathbf{D}(g) \to \mathbf{D}'(g) \cong \mathbf{D}(g). \tag{5.5}$$

that is to say, the irrep labels are invariant under time-reversal.

To be more specific (and thus specify whether or not an automorphism enters in the definition of the operator T) we must discuss the properties of $SL(3,\mathscr{R})$ representations in more detail [11]. The non-compact covering group; $\overline{SL(3,\mathscr{R})}$ has the topology $S^3 \times \mathscr{R}^5$, and, since the centre of this group is Z_2, there are spin representations with $g(Z_2) \neq \mathbf{1}$.

The defining irrep is given by the 3×3 matrix group over **R**. Clearly this representation is real. The generators are **L** given by the three 3×3 anti-symmetric matrices $(\mathbf{L})_{ik} = -ie_{ijk}$ and $\dot{\mathbf{Q}}$ by five 3×3 real, symmetric, and traceless matrices. Under complex conjugation we find

$$K_0: \mathbf{L} \to -\mathbf{L},\ \dot{\mathbf{Q}} \to +\dot{\mathbf{Q}}. \tag{5.6}$$

Thus to achieve the correct time-reversal properties we must augment K_0 by the Cartan outer automorphism

$$\mathscr{C}_a: \mathbf{L} \to +\mathbf{L}, \quad \dot{\mathbf{Q}} \to -\dot{\mathbf{Q}}. \tag{5.7}$$

It is the unitary irreps that are of physical interest, and all of these (except the trivial identity irrep) are of infinite dimensionality. It is a general result of abstract group theory [11] that all irreps of $SL(3,\mathscr{R})$ are real, as was the case for the defining non-unitary irrep given above.

Since the center of the group is Z_2, there are irreps having half-integer spin, as noted above. Such irreps were first constructed in [30], using a novel boson realization (the quadrupole generators are of *fourth* degree in the bosons).

The Hermitian generators of this boson realization are found to have the properties

compact: **J**, non-compact: $\dot{\mathbf{Q}}$

$$T = \mathscr{C}_a K_0: \mathbf{J} \to -\mathbf{J},\ \dot{\mathbf{Q}} \to -\dot{\mathbf{Q}}. \tag{5.8}$$

The representation generated by these boson operators, **L** and $\dot{\mathbf{Q}}$, acting on the space of boson polynomials (ket-vectors) is unitary and splits into three irreps

(i) $j = \frac{1}{2}, \frac{5}{2}, \frac{9}{2}, \ldots$ the so-called "quarkel",

(ii) $j = 0, 2, 4, \ldots,$

(iii) $j = 1, 3, 5, \ldots.$

There is only one irrep of type (i), which is, in fact, a discrete irrep. The irreps of type (ii) and (iii) are labelled by a continuous parameter. All three types of irrep are real and self-conjugate.

Remark. One might expect a fourth irrep:

(iv) $j = \frac{3}{2}, \frac{7}{2}, \frac{11}{2}, \ldots,$

but this set of states does not strictly define a unitary irrep. The operators do indeed obey the correct commutation relations on this set of states but the invariant operators I_2, I_3 have fixed eigenvalues on all but one of the states.

In our view, it appears remarkable that the collective nuclear symmetry model $\overline{(SL(3\mathscr{R}))}$ overcomes the two basic objections to Elliott's $SU3_{\text{nuclear}}$ symmetry, that is,

(a) The $\overline{SL(3,\mathscr{R})}$ model contains half-integer spin *intrinsically*, unlike the $SU(3)_{\text{nuclear}}$ model where half-integer spin is forbidden, and
(b) time-reversal preserves all the irrep labels of the $\overline{SL(3,\mathscr{R})}$ irreps again unlike $SU(3)_{\text{nuclear}}$.

The principal objection to $\overline{SL(3,R)}$ as a fundamental nuclear symmetry is that this symmetry predicts unlimitedly large rotational excitations whereas any real composite nucleus must surely break up eventually. For baryons the situations is quite different. Quark confinement (as schematized in the bag model) results in a deformable composite indecomposable system with finite volume at any energy. The symmetry $\overline{SL(3,R)}$ could very well be fundamental for such a structure.

6. Concluding remarks

We have shown in the foregoing discussion that there is no universal realization of time reversal for a generic symmetry group, but rather any time-reversal realization is conditioned essentially by the physical properties of the system. Thus we note that the spin and isospin symmetries behave differently under time reversal. This reflects the different nature of spin and isospin; the first one changes sign under time reversal and the second is invariant. In fact, all "internal" symmetries are unchanged while space-time symmetries exhibit the expected behavior under time reversal. We have also shown that the coordinate-free approach has the great advantages of both simplicity and clarity.

Acknowledgements

We would like to thank Prof. Luis Joaquin Boya for discussions on the topological properties of groups. This research was supported in part by the Department of Energy (contract no. DOE-ER40757-026).

Appendix A

The advantages of a basis-free approach can be most easily seen by comparing the procedure used in §2 to the complications, and vagaries, in the basis-dependent approach that is discussed below.

Consider $j=1$. We may choose to realize this irrep of the real Lie algebra of $su2$ by purely real, anti-Hermitian matrices, $\{\mathbf{K}_i\}$

$$(\mathbf{K}_i)_{jk} \equiv e_{ijk} \quad \text{with} \quad \mathbf{K}_1 = \begin{pmatrix} 0 & 0 & 0 \\ 0 & 0 & 1 \\ 0 & -1 & 0 \end{pmatrix},$$

$$\mathbf{K}_2 = \begin{pmatrix} 0 & 0 & -1 \\ 0 & 0 & 0 \\ 1 & 0 & 0 \end{pmatrix}, \quad \mathbf{K}_3 = \begin{pmatrix} 0 & 1 & 0 \\ -1 & 0 & 0 \\ 0 & 0 & 0 \end{pmatrix}, \tag{A1}$$

obeying the real Lie algebra,

$$[\mathbf{K}_i, \mathbf{K}_j] = -e_{ijk}\mathbf{K}_k. \tag{A2}$$

(Here $e_{ijk} = \pm 1$ for positive/negative permutations of 123 and 0 otherwise).

Time reversal for the physical angular momentum $\mathbf{J}^{(1)} = i\mathbf{K}$ is then simply complex conjugation, K_0

$$T = \mathscr{T}K_0 : \mathbf{J}^{(1)} \to -\mathbf{J}^{(1)}. \tag{A3}$$

Comparing this with the basis-free result

$$T = \mathscr{T}\mathscr{C}K_0, \tag{A4}$$

we see that the automorphism in (7.4) is now the identity automorphism.

Now let us consider this same $j = 1$ representation of $SU2$ using this time the standard (complex) basis of quantum physics

$$\mathbf{J}_1^{(1)} = 2^{-1/2}\begin{pmatrix} 0 & 1 & 0 \\ 1 & 0 & 1 \\ 0 & 1 & 0 \end{pmatrix},$$

$$\mathbf{J}_1^{(1)} = i2^{-1/2}\begin{pmatrix} 0 & -1 & 0 \\ 1 & 0 & -1 \\ 0 & 1 & 0 \end{pmatrix}, \quad \mathbf{J}_3^{(1)} = 2^{-1/2}\begin{pmatrix} 1 & 0 & 0 \\ 0 & 0 & 0 \\ 0 & 0 & -1 \end{pmatrix}, \tag{A5}$$

obeying,

$$[\mathbf{J}_i, \mathbf{J}_j] = ie_{ijk}\mathbf{J}_k. \tag{A6}$$

Time reversal for this $j = 1$ realization is now given by the product of two (commuting) operations

$$K_0: \begin{array}{l} J_1^{(1)} \to J_1^{(1)} \\ J_2^{(1)} \to -J_2^{(1)} \\ J_3^{(1)} \to J_3^{(1)}, \end{array} \tag{A7}$$

followed by:

$$\mathscr{C}: \begin{array}{l} J_1 \to -J_1 \\ J_2 \to J_2 \\ J_3 \to -J_3. \end{array} \tag{A8}$$

The resulting time reversal operator is

$$T = \mathscr{T}\mathscr{C}K_0, \tag{A9}$$

in agreement with the basis-free result, but now the automorphism is the Cartan automorphism with J_y as the $\mathbf{k}$ subset in the Cartan split.

These two realizations of the same abstract $j = 1$ representation show an important point: the particularities of the choice of basis can completely change the form of the time-reversal result, even to the point of concealing important general features (for example, the existence of the non-trivial automorphism necessary in the general case).

The basis-free approach has a further major advantage: it avoids all arbitrary phase conventions, and hence the frequent annoyance of inconsistent conventions in different places in the literature.

Let us illustrate this by using the (basis-dependent) WCG realization of the angular momentum operators

$$(J_M^{(j)})_{m',m} = (j(j+1)^{1/2} C^{j1j}_{mMm'}. \tag{A10}$$

The reader may, or may not, notice that the indices (m', m) on the LHS and on the RHS of (7.10) appear in reverse order. Let us show that this is correct using standard techniques

$$J_M|jm\rangle = \sum_{m'} |jm'\rangle\langle jm'|J_M|jm\rangle, \tag{A11}$$

where the matrix element in (7.11) is given in the standard way by the WCG coefficient

$$(J_M)_{m'm} = \langle jm'|J_M|jm\rangle = (j(j+1))^{1/2} C^{j1j}_{mMm'}, \tag{A12}$$

using the convention that the three pairs of indices (jm) in the WCG coefficient are read off from the matrix element in (7.11) from right to left.

This is only the beginning of the problems with angular momentum conventions! We face now the problem that the WCG coefficients use a "spherical tensor" notation, when we seek to obtain the usual (symmetric) cartesian realization. The problem here is a built-in clash of standard conventions:

(a) The Cartan complexification (which is standard in the literature) uses the operator choice:

$$J_\pm = J_x \pm iJ_y,\ J_0 = J_z, \tag{A13}$$

whereas,

(b) The WCG coefficients are based on the standard convention that angular momentum operators are phased (and normed) to accord with their rôle as a vector space carrying the adjoint $(j = 1)$ irrep:

$$\begin{aligned} J_+ &= -2^{-1/2}(J_x + iJ_y), \\ J_- &= 2^{-1/2}(J_x - iJ_y), \\ J_0 &= J_z. \end{aligned} \tag{A14}$$

(The conventions in (7.14) are the standard "time-reversal" phase conventions for the basis vectors, $|j, m\rangle$, namely:

$$T|j,m\rangle = (-1)^{j-m}|j,-m\rangle. \tag{A15}$$

With this convention the WCG are explicitly real. (To see that (7.14) and (7.15) are consistent recall that $T: \mathbf{J} \to -\mathbf{J}$).

If one recognizes [31] these conventional pitfalls, then it is an easy task to verify that the general angular momentum $(2j+1) \times (2j+1)$ matrix realization determined by (7.10) and (7.14) fits the time-reversal pattern of the $j = 1$ case, (7.7, 8, 9). (This includes the $j = \frac{1}{2}$ (Pauli matrix) realization as originally used by Wigner [1]).

Remark. Another clash of conventions is concealed in the above results: although the abstract automorphism depends on the Cartan split ($\mathbf{k} = J_z$) in ((7.13) above) the specific phase choices actually used for the WCG coefficients require that the automorphism in (7.8) single out the $\mathbf{k} = J_y$ Cartan split! The basis-free approach avoids such phase and label dependent "paradoxes".

Appendix B

Relation of the conjugation matrix U to the WCG coefficients

We may determine the relationship of the complex conjugation matrix transformation U to the Wigner–Clebsch–Gordan (WCG) coefficients by analyzing the identity

$$\mathbf{D}^{(\lambda)}(g)\mathbf{D}^{(\lambda)}(g^{-1}) = \mathbf{1}, \tag{B1}$$

for unitary irreps where

$$\mathbf{D}^{\dagger}(g) \equiv \tilde{\mathbf{D}}^{*}(g) = \mathbf{D}(g^{-1}). \tag{B2}$$

Inserting (A2) in (A1) and using the definition of the conjugation matrix U,

$$\mathbf{D}^{(\lambda)*}(g) \equiv \mathbf{U}^{-1}\mathbf{D}^{(\bar{\lambda})}(g)\mathbf{U}, \tag{B3}$$

where $\bar{\lambda}$ is the conjugate irrep to the irrep $\lambda(\bar{\lambda} = \lambda$ if, as for $SU(2)$, the irreps are self-conjugate). Thus we find

$$(\mathbf{D}^{(\lambda)}(g)\mathbf{D}^{(\lambda)}(g^{-1}))_{ij} = \sum_{k,l,m} D^{(\lambda)}_{ik}(g)\, U^{-1}_{jl}\, D^{(\bar{\lambda})}_{lm}(g)\, U_{mk} = (\mathbf{1})_{ij} \tag{B4}$$

Now we use the (generalized) Wigner product law for matrix irreps of compact groups

$$D^{(\lambda)}_{ij}(g) D^{(\mu)}_{i'j'}(g) = \sum_{\Gamma,\gamma,k,k'} \overset{\Gamma}{C}_{\lambda\mu\gamma ijk} \overset{\Gamma}{C}_{\lambda\mu\gamma i'j'k'} D^{(\gamma)}_{kk'}(g), \tag{B5}$$

where the $\overset{\Gamma}{C}_{\lambda\mu\gamma ijk}$ are (generalized) WCG coefficients, with Γ a multiplicity label.

Substitute (A5) in (A4), multiply both sides by the (normalized) group measure dg and integrate over the group G. One finds then

$$\begin{aligned}(\mathbf{1})_{ij} &= \sum_{k,l,m} \overset{\Gamma}{C}_{\lambda\bar{\lambda}0 il0} \overset{\Gamma}{C}_{\lambda\bar{\lambda}0 km0} U^{-1}_{jl} U_{mk} \\ &= \overset{\Gamma}{C}_{\lambda\bar{\lambda}0 i\bar{i}0} U^{-1}_{j\bar{i}} \underbrace{\left(\sum_{k} \overset{\Gamma}{C}_{\lambda\bar{\lambda}0 k\bar{k}0} U_{\bar{k}k} \right)}_{\text{numerical constant} \equiv A},\end{aligned} \tag{B6}$$

where the label $\bar{i}$ is conjugate to the label i, therefore

$$U_{j\bar{i}} = A C^{\lambda\bar{\lambda}0}_{ij0} \cdot \delta^{\bar{i}}_{j}. \tag{B7}$$

(Note that the multiplicity label Γ drops out for the coupling to the identity). Using (A7) and the unitary conditions for the conjugation matrix U we find

$$\delta_{ij} = \sum_k U_{ik} U_{jk}, = AA^* \cdot \delta_{ij} \cdot (C^{\lambda\bar{\lambda}0}_{ii0})^2 = AA^* \cdot \delta_{ij} \cdot (\dim \lambda)^{-1}. \tag{B8}$$

Thus the constant A has the value

$$A = e^{i\psi} \cdot (\dim \lambda)^{1/2}, \tag{B9}$$

showing that a phase of modulus one is arbitrary. The standard choice is $e^{i\psi} = 1$, with the result that

$$U_{ij} = (\dim \lambda)^{1/2} \cdot C^{\lambda\bar{\lambda}0}_{ij0}, = (\dim \lambda)^{1/2} \cdot C^{\lambda\bar{\lambda}0}_{ii0} \cdot \delta^{\bar{i}}_{j}. \tag{B10}$$

The WCG coefficient in (A10) is often called the metric for the irrep λ since it couples the ket-vectors of the irrep λ to the bra-vectors of the irrep $\bar{\lambda}$ to produce an invariant.

As an example of these relations let us consider the $SU2$ case. Here the representations are self-conjugate and the WCG coefficient has the value

$$C^{jj0}_{mm'0} = \delta^{-m}_{m'} \cdot (2j+1)^{1/2} \cdot (-1)^{j-m}. \tag{B11}$$

Thus the conjugation matrix is

$$U^{(j)}_{mm'} = \delta^{-m}_{m'} \cdot (-1)^{j-m}, \tag{B12}$$

so that

$$T|jm\rangle = (-1)^{j-m}|j, -m\rangle. \tag{B13}$$

From (A13) we see that

$$T^2|jm\rangle = (-1)^{2j}|j, m\rangle, \tag{B14}$$

so that for $SU2$ the Frobenius–Schur invariant is: FSI $= (-1)^{2j}$ as used in § 2 above.

References

[1] E P Wigner, Göttinger Nachrichten, *Math. Nachr.* **31**, 546 (1932)

[2] J P Elliott, *Proc. R. Soc.* **A245**, 128 (1958)

[3] (Private communication, 1968). cf. L C Biedenharn and P Truini, in *Elementary particles and the universe, essays in honor of Murray Gell-Mann*, edited by John H Schwarz, Cambridge Univ. Press, (Cambridge, 1991) p. 157 ff

[4] S Tomonaga, *Prog. Theor. Phys. (Jpn)* **13**, 467 (1955) (The promised paper applying this method to three dimensions was never published)

[5] Actually this is not an assumption. The distinction between spin and orbital angular momentum is that spin is defined to be translationally invariant: $[\mathbf{P}, \mathbf{S}] = 0$. By considering the relative orbital angular momenta of a composite system of two particles one sees that this (translationally invariant) angular momentum reverses under time reversal

[6] R Gilmore, *Lie groups, Lie algebras and some of their applications* (Wiley, New York, 1974)

[7] B G Wybourne, *Classical groups for physicists* (Wiley, New York, 1974)

[8] E P Wigner, *Group theory and its application to the quantum mechanics of atomic spectra* (Academic Press, New York, 1959)

[9] L C Biedenharn and J D Louck, *Angular momentum in quantum physics*, Vol 8 in the Ency. Math and Applications (edited by G -C Rota), (Cambridge Univ. Press, Cambridge, 1991)

[10] In the sense that a real quaternionic basis is used
[11] Jacques Tits, Tabellen zu den einfachen Lie Gruppen und ihren Darstellungen, *Lect. Notes in Math* **40** (Springer Verlag, Berlin, 1967)
[12] Robert Hermann, *Lie groups for physicists*, (W A Benjamin, Inc., New York, 1966)
[13] Every Cartan automorphism (except for $\mathbf{D}_4$) is involuntary, but not necessarily inner. The automorphisms corresponding to Dynkin diagram symmetries are outer [11]
[14] L C Biedenharn, *Phys. Rev.* **82**, 100 (1951)
[15] G Racah, *Nuovo. Cimento.* **14**, 322 (1937)
[16] W Pauli, *Rev. Mod. Phys.* **13**, 203 (1941)
[17] L C Biedenharn and M E Rose, *Phys. Rev.* **83**, 459 (1951)
[18] M Kobayashi and T Maskawa, *Prog. Theor. Phys.* **49**, 652 (1973)
[19] J E Avron, L Sadun, J Segert and B Simon, *Phys. Rev. Lett.* **61**, 1329 (1988)
[20] M Gell-Mann and Y Ne'eman, *The Eightfold way*, (W A Benjamin, Inc., New York, 1964)
[21] J D Louck and L C Biedenharn, *Adv. Quantum Chem.* **23**, 129 (1992)
[22] The behaviour of ε under conjugation is not fully known. It is known [21] that for the first occurrence of multiplicity (in the 27-plet) the two $L = 2$ states are split by a $\pm$ sign under C_a
[23] E Witten, *Nucl. Phys.* **B223**, 422, 433 (1983)
[24] A P Balachandran, V P Nair, S G Rajeev and A Stern, *Phys. Rev. Lett.* **49**, 1124 (1982)
A P Balachandran, V P Nair, S G Rajeev and A Stern, *Phys. Rev.* **D27**, 1153 (1983)
[25] Y Dothan, M Gell-Mann and Y Ne'eman, *Phys. Lett.* **17** 148 (1965)
[26] L Weaver and L C Biedenharn, *Phys. Lett.* **B32**, 326 (1970)
L Weaver and L C Biedenharn, *Nucl. Phys.* **A185**, 1 (1972)
[27] L Weaver, R Y Cusson and L C Biedenharn, *Ann. Phys.* **102**, 493 (1976)
[28] D J Rowe, M G Vassanji and J Carvalho, *Nucl. Phys.* **A504**, 76 (1989)
[29] G Rosensteel, in *Group theory and special symmetries in nuclear physics* (World Scientific, Singapore, 1992) pp. 332
[30] L C Biedenharn, R Y Cusson, M Y Han and O L Weaver, *Phys. Lett.* **B42**, 257 (1972)
[31] Even Wigner fell into these traps, using a phase convention for basis states in his nuclear reaction theory, which conflicted with his phase conventions [8] for the WCG coefficients.

PRAMANA
— journal of
physics

© Printed in India

Vol. 43, No. 4,
October 1994
pp. 273–278

The Lorentz–Dirac equation in curved spaces

JOSÉ L LÓPEZ-BONILLA, JESÚS MORALES and MARCO A ROSALES*
Areas de Física, División de C. B. I., Universidad Autónoma Metropolitana-Azcapotzalco, Apdo. Postal 16-306, 02200 México, D. F., Mexico
*Depto. de Física y Matemáticas, Escuela de Ciencias, Universidad de las Américas-Puebla, Apdo. Postal 100, Sta. Catarina Mártir, 72820 Puebla, Mexico

MS received 19 April 1994

Abstract. The Teitelboim–Plebañski method of average field is used to obtain the Lorentz–Dirac equation with gravitation.

Keywords. Liénard–Wiechert field; curved spaces; gravitational field; Lorentz–Dirac equation.

PACS Nos 03·50; 04·90

1. Introduction

The Lorentz–Dirac (LD) equation [1] describes the motion of a point charge in Minkowski space taking into account the radiation reaction [2]. Dirac's procedure to derive it consists in a) enclose a part of the world-line of the charge with a 3-cylinder of constant instantaneous distance [1, 3, 4], b) establish the energy and momentum balance through such a 3-space, c) take the limit as the cylinder contains only the path of the charge, and d) renormalize the mass of the particle. The result is known as the LD equation in absence of gravitational field. This procedure [1] was extended by DeWitt–Brehme [5] to curved space-times to obtain the corresponding LD equation in a given Riemannian geometry including, hence, the gravity. The calculations in [5] are long and tedious because Dirac's cylinder is used therein and this is not well adapted for retarded fields, and because of the authors need to make covariant Taylor expansions of the Maxwell tensor T_{ab} in a curved space the expression for Liénard–Wiechert's Faraday tensor F_{ij} is complicated. This, in turn, yields an equally complicated T_{ab} (constructed from F_{ij}). In view of these facts, the DeWitt–Brehme approach does not seem very appealing. Furthermore, it must be mentioned that these authors made a mistake in their calculations and therefore did not arrive at the right LD equation which was later pointed out and corrected by Hobbs [6] using Dirac's technique.

Teitelboim [7] and Plebañski [8] introduced the method of average field as an alternative to the process used in [1] and thus obtained, in a simple manner, the LD equation in absence of gravity. For calculations this method is better than that of Dirac because it can be applied with a Bhabha [9]–Synge [3] cylinder (very well adapted to retarded effects) and because it does not need T_{ab} but only F_{ij}, thus reducing the complexity of the calculations. In the next section we will show that the technique of the average field also works in curved spaces, and that it generates a very simple derivation (compared to those in [5, 6]) of the LD equation including a gravitational field; we have not found any applications of the average field method to Riemannian spaces in the literature.

2. The Lorentz–Dirac equation

We consider here the Riemannian geometry of the space-time (R_4) fixed and produced by physical sources according to some gravitational theory (general relativity, for example), and our aim is to derive the equation of motion of a point charge in such R_4 taking into account the Maxwell self-field of the particle. In other words, we accept that the mass and the gravitational and electromagnetic radiations of the charge do not alter the curvature of the space-time. The situation is far too complicated when these effects are included. Although this problem has been studied by Infeld–Wallace [10], Bazañski [11] and Carmeli [13, 14] among others, their technique is only approximate since they use the method employed by Einstein–Infeld–Hoffmann [15] to solve the problem on the motion in general relativity. Nevertheless, their results confirm the expressions of references [5, 6]. The process of [10–14] is applicable only to the slow motion [15] and nobody has ever investigated the corresponding problem for the fast motion [16, 17].

As it has been mentioned, we will consider that the mass, charge and the radiations of the particle do not produce gravitation: the equation of motion is a consequence of the curvature of R_4, the external electromagnetic field (Lorentz force) and its own Maxwell self-field (radiation reaction), but not its recoil by gravitational emission [18]. This avoids the approximation techniques and leads to an exact equation of motion, namely, the Lorentz–Dirac (LD) equation in curved spaces [5, 6]. Such an equation is simply obtained with the Teitelboim [7]–Plebañski [8] method which states that the motion of the particle obeys the Lorentz force:

$$m a_{b'}(s) = 4\pi q F_{b'c'}(s) v^{c'}(s) \tag{1}$$

where q, s, v_c, a_c, and m denote the electric charge, proper time, velocity, acceleration and (non-normalized) mass of the particle, respectively and the effective Faraday tensor F_{bc} consists of an external part $\underset{\text{ext}}{F_{bc}}$ and another part $\bar{F}_{bc}$ originated from the interaction of the particle with its own electromagnetic field

$$F_{bc}(s) = \underset{\text{ext}}{F_{bc}} + \bar{F}_{bc}(s). \tag{2}$$

The subtle point resides in the last term: It represents an average self-field at the position of the particle, and it is defined as

$$\bar{F}_{bc}(s) = \lim_{\tau \to s} \left\langle \underset{LW}{F_{bc}}(X^r) \right\rangle (\tau) \tag{3a}$$

$$= \lim_{\eta \to 0} \left\langle \underset{LW}{F_{bc}}(X^r) \right\rangle (s - \eta) \tag{3b}$$

where the following remarks must be kept in mind:

a) $\underset{LW}{F_{bc}}(X^r)$ is Liénard–Wiechert's Faraday tensor produced by the charge at the event X^r off the world-line

b) X^r denotes the events on a Bhabha [9]–Synge [3] tube keeping the proper time and the retarded distance constant [3, 4, 19]

c) $\langle\ \rangle$ represents an average to be defined below (see eq. (4))

d) $\left\langle F_{bc}(X^r) \right\rangle$ is a function of τ, the retarded proper time associated to the event X^r on the Bhabha–Synge cylinder

e) In the above function τ is replaced by $s-\eta$ with $\eta \ll 1$ and then $\left\langle F_{bc}(X^r) \right\rangle(s-\eta)$ is expanded in powers of η. Introducing the result into (1), (2), and (3b) we are lead (through mass renormalization) to the equation of motion.

This process was successfully employed by Teitelboim [7] and Plebañski [8] to derive the LD equation in the plane space-time (i.e., without gravitation). We show that it is also applicable to 4-spaces with a gravitational field, in which case the essential difficulty is to define the average $\langle\ \rangle$ in the presence of a curvature: we only know (from [7, 8]) that $\langle\ \rangle$ is an integral over a section of the Bhabha–Synge tube and that it takes an average over the corresponding solid angle subtended by the charge, but we ignore the integrand in $\langle\ \rangle$. In order to solve this difficulty we use:

i) the analysis of references [20, 21] over the volume element for a surface of constant retarded distance, ii) the parallel propagator [22] that allows the integral of a tensor to also have a tensor character, and iii) the average used by Isaacson [23] (see p. 970 of reference [24]) to obtain an effective energy tensor for gravitational waves:

Hence we have proposed the definition (not found in the literature on electrodynamics):

$$\left\langle F_{b'c'}(X^r) \right\rangle(\tau) = \frac{1}{4\pi} \int_{\omega,\tau=\text{constant}} g^i_{b'} g^j_{c'} F_{ij} \Delta^{1/2} \mathrm{d}\gamma \tag{4}$$

which, in absence of gravitation, reduces to the average employed in [7, 8]. In (4), the parallel propagator $g^q_{p'}$ "transports" the tensor F_{ij} from the point X^r (with retarded distance $\equiv \omega =$ constant and proper time $\equiv \tau =$ constant) to the corresponding retarded event [3, 4] $x^r(\tau)$; $\mathrm{d}\gamma = \sin\theta \mathrm{d}\theta \mathrm{d}\phi$ is the solid angle element in the rest frame of the particle, and Δ is a bi-scalar [5, 20, 21 25] (of great importance in the integration of tensor quantities) constructed in terms of the relevant concept of the "world function" Ω introduced by Ruse and Synge [5, 21, 22, 25–36]. The function Ω is a bi-scalar defined as the square of the geodesic distance between two points and contains all the geometric properties of the space-time; in general, it is very difficult to calculate Ω for a given metric: an approximation has been obtained only for the Schwartzschild [32] and Gödel [34] geometries. Fortunately, in diverse works on gravitation and electrodynamics there is no need to know it explicitly.

In Riemannian spaces it is not easy to perform exact calculations [40]. Therefore, it is necessary to use Taylor theorem as given by Ruse [26] in order to expand the tensor quantities that depend on two events very close to each other: this leads us to assume the uniqueness of the geodesic between any two points in R_4, and to construct with it the important concepts of world function Ω and parallel propagator $g_{p'q}$. Without Ω there is no way to perform covariant expansions, and without $g_{p'q}$ it is practically impossible that the integral of a tensor would possess tensor character. In other words, without these quantities it would be impossible to study electrodynamics in curved spaces.

From equation (3.52) of [5] we obtain the expression:

$$F_{\underset{LW}{bc}} = q \sum_{n=1}^{7} \left(A_{\underset{n}{bc}} - A_{\underset{n}{cb}} \right) \tag{5a}$$

with:

$$A_{\underset{1}{bc}} = -\omega^{-2}\Omega_{bi'}u_{cr'}v^{i'}v^{r'}, \qquad u_{cr'} = \Delta^{1/2}g_{cr'}$$

$$A_{\underset{2}{bc}} = \chi\omega^{-3}\Omega_b u_{cr'}v^{r'}, \qquad \chi = \Omega_{a'b'}v^{a'}v^{b'}$$

$$A_{\underset{3}{bc}} = -\omega^{-2}\Omega_b u_{cr'}(a^{r'} - \omega^{-1}Wv^{r'}), \qquad W = \Omega_j a^{j'} \tag{5b}$$

$$A_{\underset{4}{bc}} = -\omega^{-1}u_{br';c}v^{r'}, \qquad A_{\underset{5}{bc}} = -\omega^{-2}\Omega_b u_{cr';j'}v^{r'}v^{j'},$$

$$A_{\underset{6}{bc}} = \omega^{-1}\Omega_b v_{cr'}v^{r'}, \qquad A_{\underset{7}{bc}} = \int_{-8}^{s} v_{br';c}v^{r'}\,d\beta$$

where the notation of [22] for the covariant derivatives of Ω has been employed, and $v_{ac'}$ is a complicated function of the metric for which no exact expression exists [5] but, fortunately, the following approximations are known:

$$v_{br'} = -\frac{1}{2}g_b^{c'}\left(R_{r'c'} - \frac{R}{6}g_{r'c'} \right), \tag{5c}$$

$$\Delta^{1/2} = 1 - \frac{1}{12}R^{a'b'}\Omega_{a'}\Omega_{b'}$$

with R_{ij} being the Ricci tensor and $R = R_c^c$. Substitution of relations (5) into eq. (4) and integration over the solid angle of the resulting integrals, which can be found in references [3, 37] lead to

$$\left\langle F_{\underset{LW}{b'c'}} \right\rangle (s-\eta) \approx \frac{2}{3}q\eta^{-1}(a_{b'}v_{c'} - a_{c'}v_{b'})(s) - \frac{2}{3}q(A_{b'}v_{c'} - A_{c'}v_{b'})(s) -$$

$$\frac{q}{3}[(R_{b'j'}v_{c'} - R_{c'j'}v_{b'})v^{j'}](s) + q\int_{-\infty}^{s} f_{b'c'r'}v^{r'}\,d\beta + \theta(\eta) \tag{6a}$$

where $A_c = \delta a_c/\delta s$ is the superacceleration of the particle and

$$f_{b'c'r'} \equiv v_{b'r';c'} - v_{c'r';b'}. \tag{6b}$$

Thus, using eqs (1), (2), (3b) and (6) we are able to obtain the famous Lorentz–Dirac equation in curved spaces [5, 6] ($a^2 \equiv a^b a_b$):

$$m_{\text{obs}}a_r = 4\pi q\,\underset{\text{ext}}{F_{rc}}v^c + \frac{8\pi q^2}{3}(A_r - a^2 v_r) -$$

$$\frac{4\pi}{3}q^2(R_{cj}v^j v_r + R_{cr})v^c + 4\pi q v^j \int_{-\infty}^{s} f_{rjc}v^c\,d\beta \tag{7a}$$

with the normalization

$$m_{\text{obs}} = \lim_{\eta \to 0} \left(m + \frac{8\pi}{3} q^2 \eta^{-1} \right). \tag{7b}$$

The result (7a) coincides with (5.28) of the first article of [6] and with (2.23) of [38]. The expression (5.25) of [5] does not contain the Ricci tensor because, as Hobbs pointed out, their relation (5.11) was erroneously calculated. The integral in (7a) is a consequence of the non-local character of the electromagnetic field generated by the charge, i.e., the emitted radiation leaves a trace as it spreads through the curvature of the space-time. It is clear that this does not happen in special relativity, and in the second article of [6] it is proven that the mentioned integral vanishes in conformally plane spaces [39].

To obtain exact solutions for the LD equation in absence of gravitation is not a simple matter, hence, the difficulties are even bigger in curved spaces and we must invoke approximate situations: particle at low speed and/or weak gravitational field [41, 42]. Under such conditions Carmeli [13] studied the LD equation through the Frenet–Serret formulas [22] but, unfortunately, he used the wrong expression from [5] and so his work was incomplete; nobody has ever tried to correct Carmeli's results. In [41] the incorrect result from [5] was also used to analyze the path of a charged particle moving at a low speed in a weak gravitational field with spherical symmetry, and in [42] the corresponding quantum problem is studied. Sigal [43] made use of eq. (7a) to examine the electromagnetic radiation of a point charge in Robertson–Walker [22] cosmologies.

3. Conclusion

In this paper we have derived (7a) with the average field method, because in eq. (4) the Faraday tensor produced by the charge in motion is averaged thus eliminating some singularities at the position of the particle and allowing that the rest of the singularities cancel out when the mass renormalization is made. Unlike [5, 6] there was no need to know the Maxwell tensor T_{ab} or to calculate its energy flux through any 3-space, which shows the simplicity of the method with respect to the one used by Dirac.

Finally, using (4) it is useful to know that such an average is determined with the radiation coordinates $(\theta, \varphi, \omega, s)$ introduced by Florides–McCrea–Synge [21, 44, 45] which are well adapted to retarded effects. These coordinates are the generalization, for curved spaces, of those studied by Synge [3], Newman–Unti [46, 47] and Graef [48] in special relativity.

References

[1] P A M Dirac, *Proc. R. Soc. London* **A167**, 148 (1938)
[2] J L Jiménez, *Ciencia* (Mexico) **40**, 257 (1989)
[3] J L Synge, *Ann. Mat. Pura Appl.* (Italy) **84**, 33 (1970)
[4] J L López-Bonilla, *Rev. Colomb. Fis.* **17**, 1 (1985)
[5] B S DeWitt and R W Brehme, *Ann. Phys.* **47**, 220 (1960)
[6] J M Hobbs, *Ann. Phys.* **47**, 141 and 166 (1968)
[7] C Teitelboim, *Phys. Rev.* **D4**, 345 (1971)

[8] J Plebañski, *The structure of the field of point charges*, (internal report) CINVESTAV-IPN), Mexico (1972)
[9] H J Bhabha, *Proc. R. Soc. London* **A172**, 384 (1939)
[10] L Infeld and P R Wallace, *Phys. Rev.* **57** 797 (1940)
[11] S Bazański, *Acta Phys. Pol.* **15**, 363 (1956)
[12] P Havas, *Phys. Rev.* **108**, 1351 (1957)
[13] M Carmeli, *Phys. Rev.* **B138**, 1003 (1965)
[14] M Carmeli, *Ann. Phys.* **34**, 465 (1965)
[15] L Infeld and J Plebañski, *Motion and relativity* (Pergamon Press, 1960)
[16] B Bertotti and J Plebañski, *Ann. Phys.* **11**, 169 (1960)
[17] A Künel, *Ann. Phys.* **28**, 116 (1964)
[18] A Schild, Bull. Acad. Pol. Sci. **9**, 103 (1961)
[19] G Ares de Parga, J L López–Bonilla, G Ovando and T Matos, *Rev. Mex. Fis.* **36**, 194 (1990)
[20] D Villarroel, *Phys. Rev.* **D11**, 2733 (1975)
[21] J L López–Bonilla, *Acta Mex. Ciencia y Tecnol. (IPN)* **1**, 23 (1983)
[22] J L Synge, *Relativity: the general theory* (North-Holland, 1976) Chap. II
[23] R A Isaacson, *Phys. Rev.* **166**, 1272 (1968)
[24] C W Misner, K S Thorne and J A Wheeler, *Gravitation* (W H Freeman, San Francisco, 1970)
[25] B S DeWitt, *Phys. Rev.* **162**, 1239 (1967)
[26] H S Ruse, *Proc. London Math. Soc.* **32**, 87 (1931)
[27] J L Synge, *Proc. London Math. Soc.* **32**, 241 (1931)
[28] J L Synge, *Rend. Sem. Nat. Fis. Milano* 271 (1960)
[29] J L Synge, *Recent developments in general relativity* (Pergamon Press, 1962) p. 441
[30] J D Lathrop, *Ann. Phys.* **79**, 580 (1973)
[31] J D Lathrop, *Ann. Phys.* **95**, 508 (1975)
[32] H A Buchdahl and N P Warner, *Gen. Relativ. Gravit.* **10**, 911 (1979)
[33] H A Buchdahl, *Austr. J. Phys.* **32**, 405 (1979)
[34] N P Warner and H A Buchdahl, *J. Phys.* **A13**, 509 (1980)
[35] R W John, *Ann. Phys.* **41**, 1 (1984)
[36] R Schimming and D Matel–Kaminska, *Z. Anal. Anw.* **9**, 3 (1990)
[37] Ch G Van Weert, *Physica* **66**, 79 (1973)
[38] A O Barut and D Villarroel, *J. Phys.* **8**, 1537 (1975)
[39] G Ares de Parga, O Chavoya, J L López–Bonilla and G Ovando, *Rev. Mex. Fis.* **35**, 201 (1989)
[40] G N Plass, *Rev. Mod. Phys.* **33**, (1961)
[41] C M DeWitt and B S DeWitt, *Physics* **1**, 3 (1964)
[42] C M DeWitt and W G Wesley, *Gen. Relativ. Gravit.* **2**, 235 (1971)
[43] R Sigal, *J. Math. Phys.* **12**, 2490 (1971)
[44] P S Florides, J Mc Crea and J L Synge, *Proc. R. Soc. London* **A292**, 1 (1966)
[45] P S Florides and J L Synge, *Proc. R. Soc. London* **A323**, 1 (1971)
[46] E T Newman and T W J Unti, *J. Math. Phys.* **4**, 1467 (1963)
[47] G Ares de Parga, O Chavoya, J L López–Bonilla, E Luna and J Morales, *Rev. Mex. Fis.* **36**, 184 (1990)
[48] C Graef, *Rev. Mex. Fis.* **11**, 129 (1962)

PRAMANA
— journal of
physics

© Printed in India

Vol. 43, No. 4,
October 1994
pp. 279–287

Energy levels of the Schrödinger equation for some rational potentials in two-dimensional space using the inner product technique

M R M WITWIT and J P KILLINGBECK
Department of Applied Mathematics, University of Hull, HU6 7RX, England

MS received 14 February 1994; revised 5 July 1994

Abstract. The energy levels of a two-dimensional system are calculated for the rational potential, $V(x, y; \lambda, g) = x^2 + y^2 + \lambda\left[\frac{x^2}{(1+gx^2)} + \frac{y^2}{(1+gy^2)} + a_{xx}x^4 + a_{xy}x^2y^2 + a_{yy}y^4\right]$ using the inner product technique over a wide range of values of the perturbation parameters (g, λ) and for various eigenstates.

Keywords. Perturbation theory; rational potential; energy level calculation.

PACS No. 03·65

1. Introduction

There have been several investigations [1–18] of the energy levels and wave functions for the one-dimensional potential

$$V(x) = x^2 + \frac{\lambda x^2}{(1+gx^2)}. \tag{1}$$

As summarized by Mitra [1], this type of interaction occurs in several areas of physics. e.g. in laser theory [19], and in the study of zero-dimensional field theories with a nonlinear Lagrangian [20].

In the present paper, we calculate the eigenvalues of the Schrödinger equation

$$\left[-\frac{\partial^2}{\partial x^2} - \frac{\partial^2}{\partial y^2} + V(x, y) - E\right]\Psi_{nx,ny}(x, y) = 0 \tag{2}$$

in two-dimensional space, with the following potential:

$$V(x, y; \lambda, g) = x^2 + y^2 + \lambda\left[\frac{x^2}{(1+gx^2)} + \frac{y^2}{(1+gy^2)} + a_{xx}x^4 + a_{xy}x^2y^2 + a_{yy}y^4\right]. \tag{3}$$

We treat the problem in the context of the algebra of inner product perturbation theory. The perturbation series does not converge for arbitrary values of λ and g, but for sufficiently small values of g/λ the use of a renormalized series produces results of high accuracy, as the calculations show.

In earlier studies [21–23], the inner product technique has been used to handle finite polynomial potentials in two-dimensional space; the present work extends that perturbation technique to investigate some rational potentials in two dimensional space.

In § 2 we summarize the recurrence relations for calculating the energy eigenvalues. Calculations are carried out for several eigenstates. The results are discussed in § 3.

2. Recurrence relations for the potential (3) using the inner product technique

The inner product technique is usually used to treat polynomial potentials in one, two or three-dimensions. Earlier studies have dealt with finite polynomial potentials [21–25]. However, a rational potential leads to an infinite series expansion, for which extra questions of convergence arise, both for the potential expansion and for the calculated spectra. We have used an empirical numerical approach to handle these problems.

The perturbation calculations for the potentials $V(x, y)$ are made by expanding the functions $(1+gx^2)^{-1}$ and $(1+gy^2)^{-1}$ as power series in gx^2 and gy^2, respectively, which are valid for $gx^2, gy^2 \leqslant 1$. As x, y varies from $-\infty$ to $+\infty$, the functions run from 0 to 0, through 1 at $x, y = 0$, and are everywhere non-negative.

The potentials given by (3) can be written in the following form

$$V(x, y; \lambda, g) = x^2 + y^2 + \frac{2\lambda}{g} - \frac{\lambda}{g}\left[\frac{1}{(1+gx^2)} + \frac{1}{(1+gy^2)}\right] + \lambda\left[a_{xx}x^4 + a_{xy}x^2y^2 + a_{yy}y^4\right]. \tag{4}$$

We note that the potential of (4) exhibits two singularities at $x, y = \mp i/\sqrt{g}$, which determine the region of convergence of the power series for the potential. Intuitively, we expect that the limited radius of convergence $1/\sqrt{g}$ will not cause problems provided that the bound state wavefunctions considered are negligible at larger distances. This can be ascertained by studying the behaviour of the numerical results.

We investigate the inner product perturbation technique to compute the energy eigenvalues. This approach is suitable for computing the energy for a range of values of λ and g. The potential (4) can be expanded as

$$V(x, y; \lambda, g) = [1+\lambda][x^2+y^2] + \lambda \sum_{m=1}^{\infty} g^m V_m[x^{2(m+1)} + y^{2(m+1)}] + \lambda[a_{xx}x^4 + a_{xy}x^2y^2 + a_{yy}y^4]. \tag{5}$$

The potential coefficient V_m can be given as

$$V_m = (-1)^m. \tag{6}$$

For finite polynomial potentials, studies in the past [23, 24] have shown that the semi-convergent perturbation series for the energy which arise in both hypervirial and inner product perturbations methods will produce much improved estimates of eigenvalues if the Hamiltonian is partitioned suitably by introducing a renormalization parameter β, which redefines the perturbed and unperturbed parts of the potential.

Numerical tests showed that this procedure is also effective for the present calculations. Accordingly, we write the potential in the renormalized form

$$V_r(x, y; \lambda, g, \beta) = \mu^2[x^2 + y^2] + \lambda\Bigg[\sum_{m=1}^{\infty} (g^m V_m x^{2m+2} + y^{2m+2}) + a_{xx}x^4 + a_{xy}x^2y^2 + a_{yy}y^4 - \beta(x^2 + y^2)\Bigg] \tag{7}$$

where

$$\mu^2 = 1 + \lambda[1 + \beta]. \tag{8}$$

We have expanded the potentials as given by (7) to the limit at which any term beyond that limit makes no observable difference to the calculated eigenvalues. For our calculations this limit was reached at $m = 18$.

To find the recurrence relations which allow us to calculate the eigenvalues for the Schrödinger equation (2) we use the reference function:

$$\Phi(x, y) = (x^{nx}y^{ny})\exp\left[-\frac{\mu}{2}(x^2 + y^2)\right] \tag{9}$$

where n_x and n_y are state numbers, and start with the basic equation

$$EW(I, J) = \langle\psi|Hx^{2I}y^{2J}|\Phi\rangle \tag{10}$$

obtained by taking the inner product of the Schrödinger equation (2) with the reference function (9). The $W(I, J)$, sometimes called moments, are defined by

$$W(I, J) = \langle\Phi|x^{2I}y^{2J}|\psi\rangle. \tag{11}$$

We then substitute the perturbation expansions

$$W(I, J) = \sum_M W(I, J, M)\lambda^M \tag{12}$$

$$E = \sum_N E(N)\lambda^N \tag{13}$$

into the $W(I, J)$ recurrence relation given by (10). This gives a recurrence relations for the coefficients; for the renormalized potential $V_r(x, y; \lambda, g, \beta)$ given by (7) the relation can be written as

$$\begin{aligned}\sum_{N=0}^{M=80} E(N)\, W(I, J, M-N) &= a_{xx}\, W(I+2, J, M-1) \\ &+ a_{yy}\, W(I, J+2, M-1) + 2a_{xy}\, W(I+1, J+1, M-1) \\ &+ \sum_{m=0}^{m=18} V_\gamma[W(I+2+m, L, M-1) + W(I, L+2+m, M-1)] \\ &- \beta[W(I+1, J, M-1) + W(I, J+1, M-1)] \\ &+ \mu[4I + 4J + 2n_x + 2n_y + 2]\, W(I, J, M) - 2I[2I + 2n_x - 1] \\ &\times W(I-1, J, M) - 2J[2J + 2n_y - 1]\, W(I, J-1, M)\end{aligned} \tag{14}$$

where

$$V_y = V_m g^{m+1} \lambda. \tag{15}$$

The unperturbed energy can be formally expressed in the form adapted to (14);

$$E(0) = \mu[4S_x + 4S_y + 2n_x + 2n_y + 2] \tag{16}$$

The initial coefficient to start the calculation is chosen as

$$W(S_x, S_y, 0) = \mp\ W(S_y, S_x, 0) = 1, \qquad S_x = 0;\ S_y = 0, 1 \tag{17}$$

In the case of $a_{IJ} = a_{JI} I, J = x, y$ we can exploit the interchange symmetry between the coordinates $x - y$, when treating eigenstates which have even-symmetry i.e. $W(I, J, M) = W(J, I, M)$. In the general case $a_{IJ} \neq a_{JI} I, J = x, y$ we need to calculate all the elements of $W(I, J, M)$, so the calculations take more time. The indices are scanned in the order I, J, M as explained in [22] and the relations (14) is used to work out $W(I, J, M)$ in terms of lower order elements which are already known. $E(N)$ is found from the relation (14) for the special case $I = S_x$, $J = S_y$: the sum on the left-hand side becomes $E(N)$, because of the intermediate normalization convention $W(S_x, S_y, 0) = 1$ which we impose on the algorithm.

3. Results and discussion

We have used the technique described above to calculate the energy eigenvalues for the Schrödinger equation (2) with the potential (3) for several energy levels and for a wide range of values of g and λ.

In table 1 results are listed for several energy levels of the potential (3) with parameter values $0{\cdot}1 \leqslant g \leqslant 25$, $50 \leqslant \lambda \leqslant 10^6$ and different values of (a_{xx}, a_{xy}, a_{yy}). We list in table 1 energy levels for even states $\Psi^+_{0,0}, \Psi^+_{1,1}, \Psi^+_{0,2}, \Psi^+_{1,3}$, odd parity states $\Psi^-_{2,0}, \Psi^-_{3,1}$, and mixed parity states $\Psi^+_{0,1}, \Psi^-_{1,0}$.

A perusal of table 1 shows that for the case of a symmetric perturbation ($a_{IJ} = a_{JI}$ $I, J = x, y$), there is degeneracy between the energy levels $E^+_{0,1}$ and $E^-_{1,0}$, but that when $a_{IJ} \neq a_{JI}$ the degeneracy between the two levels is removed.

We note that the inner product technique can be used to give good accuracy even for higher values of g, with the condition that λ must take larger values also, so that $g/\lambda \ll 1$. Currently there are no other eigenvalue results available by any other method for the case of non zero a_{xx}, a_{xy}, a_{yy}; consequently it is not possible to infer the accuracy of the full set of our present results by a direct comparison. However, for some special cases, it is possible to check our calculations; for example, at $a_{xx} = a_{xy} = a_{yy} = 0$, the potential (3) reduces to the two independent rational potentials

$$V(x, y) = x^2 + y^2 + \lambda\left[\frac{x^2}{(1 + gx^2)} + \frac{y^2}{(1 + gy^2)}\right]. \tag{18}$$

The results were then checked to high accuracy against those obtained by other methods [1–18].

Table 2 presents our results for the case $a_{xx} = a_{xy} = a_{yy} = 0$ and for several sets of the perturbation parameters (λ, g) for four energy levels $E_{00}, E_{11}, E_{02}, E_1$, and compares them with the results of other authors [4, 12, 18]; the agreement is good.

It is important to note that the renormalization parameter β played a central role in the calculations. The best β values were obtained by numerical search, and the

Table 1. Eigenvalues of $(n_x, n_y; \pi)$ for potential $V(x, y; \lambda, g)$ for several sets of perturbation parameters, with parity label $\pi = +, -$ (even, odd) for the $x \leftrightarrow y$ interchange symmetry.

$a_{xx} = a_{yy} = a_{xy} = 0$					
λ	g	$(0,0;+)$	$(1,1;+)$	$(0,2;+) = (0,2;-)$	$(1,3;+) = (1,3;-)$
50	0·1	14·13739294460024	42·12147652941960	41·8325261660705	69·242236457451
100	0·1	19·95236017544604	59·56238222155314	59·2688705923498	98·294253345287
250	0·2	31·38997717776270	93·57807442488976	92·9891580016857	154·00533485355
10^3	0·3	62·83079458848092	187·5996835286759	186·710236911449	309·70676502022
10^6	15	1977·750732247667	5888·754774099638	5844·51520821301	9667·5588781476
10^5	5	625·0464453878115	1860·315995669344	1845·58334996124	3051·5701242599
10^4	2	197·0544988675318	585·2532593782995	579·389162668271	955·95272352918
750	0·3	54·36302223675705	162·1976611488305	161·310024781331	267·37696296559
10^5	7·5	621·4046973656084	1842·109963113371	1820·2118548527	2997·536638192
10^6	25	1963·188542923601	5815·954961157065	5743·069254515	9451·52771155
$a_{xx} = a_{yy} = 0,\ a_{xy} = 1$					
λ	g	$(0,0;+)$	$(1,1;+)$	$(0,2;+)$	$(0,2;-)$
100	0·1	20·428796830309	63·593898671174	62·30795391049	60·71212912769
10^3	0·2	63·47608880120434	192·7367089615628	191·123825848917	189·25730735814
10^4	0·5	199·9140161166052	601·5493280578457	599·338058826013	597·36849199487
10^5	1·5	630·7226117170389	1890·747795064366	1885·24800946273	1883·2320842835
10^6	10	1985·627293789743	5930·283887009240	5899·56809806731	5897·4987247331
10^6	5	1993·036163701651	5967·248805831557	5951·30702376958	5949·2756071125
10^5	2·5	629·2415222948872	1883·391010782965	1874·91687958059	1872·8775975446
10^4	1·2	198·7403439132433	595·7995887787918	591·188974247984	589·16432758322
750	0·2	55·00748918281799	167·3175624079931	165·703400234830	163·85610407164
10^3	0·3	63·33250012166826	192·0595505170565	190·136401555881	188·25240161525

(*Continued*)

Table 1. (*Continued*)

		$a_x = a_{yy} = 1;\ a_{xy} = 0{\cdot}5$			
λ	g	$(0, 1; \mp)$	$(1, 1; +)$	$(1, 3; +)$	$(1, 3; -)$
500	·02	94·16293177193399	142·7510837758178	247·537609820892	245·28411081796
500	0·1	93·87289520637112	142·2839759052216	246·308631788224	244·02683088828
10^3	·05	131·2046072057468	198·3818499649091	340·744749472108	338·32140536717
10^3	0·1	131·0132413280462	198·0713797855691	339·906679867980	337·46800836510
10^4	0·1	404·7016414826420	608·7613110901799	1025·74701490983	1022·9640807001
10^5	0·3	1268·795740923731	1904·821254273890	3184·52127207715	3181·5844764789
10^5	1·2	1264·833668248229	1898·241681785098	3165·10817598093	3162·1216463052
10^6	5	3982·952974282601	5972·623163375605	9918·50304330552	9915·4362467885
10^4	0·5	403·0074532295204	605·9674575180105	1017·73922846655	1014·8970661041
10^6	7·5	3971·875067350258	5954·182587507110	9863·66154284866	9860·5472969903
		$a_{xx} = 0{\cdot}5,\ a_{yy} = 1,\ a_{xy} = 0{\cdot}5$			
λ	g	$(0, 0; +)$	$(0, 1; +)$	$(1, 0; -)$	$(1, 1; +)$
500	·05	45·98409992482378	93·73106714926401	92·4616826324116	141·03139932664
500	0·1	45·91813691900291	93·54830791542479	92·2670099453513	140·72743781133
10^3	0·1	64·44912021522491	130·6760456172727	129·340600011615	196·64386388409
10^3	0·2	64·31312368363888	130·2925564929564	128·937717084886	195·80063339165
10^4	0·5	200·6379896370130	402·6411597727886	401·167871121420	604·14517717037
10^4	1·1	199·7760200658231	400·1164095932366	398·594216748625	599·94077824345
10^5	1·5	631·6065093220645	1263·314082923853	1261·62146500442	1894·1658895792
10^5	2·5	630·1354840697733	1258·762679611487	1257·21504905511	1886·8710786654
10^6	5	1993·925209178210	3982·572985130531	3981·03497751381	5970·7071703943
10^6	10	1986·532571998667	3960·452977358594	3958·86837658129	5933·8441937935

Table 2. Comparison of eigenvalues obtained by other authors with that of ours for the case $a_{xx} = a_{yy} = a_{xy} = 0$. First line represents the present calculation and the second line the other authors calculations.

λ	g	n_x	n_y	E_{n_x,n_y}	Ref. No.
				14·13739294460025	
		0	0	14·13739294460025	18
50	0·1			42·12147652941962	
		1	1	42·12147652941978	18
				41·83252416607061	
		0	2	41·83252416607262	18
				69·24223645745137	
		1	3	69·24223645748151	18
				19·95236017544605	
		0	0	19·95236017544604	12
100	0·1			59·56238222155314	
		1	1	59·56238222155314	12
				59·26887059234988	
		0	2	59·26887059234988	12
				98·29425334528761	
		1	3	98·29425334528771	12
				28·20643365600846	
		0	0	28·2064336	4
				84·32241196691308	
200	0·1	1	1	84·322412	4
				84·02634236270080	
		0	2	84·0263423	4
				139·5518252443544	
		1	3	139·5518253	4
				44·61685986890983	
		0	0	44·6168598	4
500	0·1			133·5521908019234	
		1	1	133·552190	4
				133·2543121800109	
		0	2	133·2543119	4
				221·5949081512796	
		1	3	221·5949084	4
				62·97888380258381	
		0	0	62·97888380258381	18
				188·3400998864952	
10^3	0·2	1	1	188·3400998864952	18
				187·7449887192327	
		0	2	187·7449887192327	18
				311·9188706892139	
		1	3	311·9188706892139	18
				62·68339936654150	
		0	0	62·68339936654150	18
				186·8627586495245	
10^3	0·4	1	1	186·8627586495246	18
				185·6811261797951	
		0	2	185·6811261797967	18
				307·5088936605492	
		1	3	307·5088936605725	18

Table 3. Convergence of some eigenvalues for the case $a_{xx} = a_{yy} = a_{xy} = 0$, for several values of λ and g with various values of the renormalization parameter β. The results underlined are from ref. [18].

λ	g	n_x	n_y	E_{n_x,n_y}	β
					0
				2·08	5
0·1	0·1	0	0	2·086	10
				2·08634	13
				2·086347426	
				6·501	0
				6·50052	1
				6·500522	2
10	0·1	0	0	6·50052243	5
				6·500522439	7
				6·500522440	10
				6·500522440828	
				4·779	4
5	0·1	0	0	4·77908301	6
				4·779083	14
				4·7790830902534	
					0
				81·43	7
				81.431	14
200	0·5	1	1	81·43136	100
				81·43136	120
				81·4313638	
				130·6178041	0
				130·6178041	8
500	0·5	1	1	130·6178041	10
				130·61780426	

results revealed the importance of finding a reasonably optimum β. We used the procedure of requiring stability of the result with respect to small variation of β at a given value of λ. The energy estimate is that given by the sum to the smallest term of the perturbation series; β controls the sharpness of this optimum result [23, 24], even for divergent series. Table 3 gives some examples for the present calculation.

It is obvious that this technique can be used to handle different types of potential. Work is currently in progress on the rational potentials in three dimensional system

$$V(x,y,z;\lambda,g) = x^2 + y^2 + z^2 + \lambda\left[\frac{x^2}{(1+gx^2)} + \frac{y^2}{(1+gy^2)} + \frac{z^2}{(1+gz^2)} + a_{xy}x^2y^2 + a_{xz}x^2z^2 + a_{yz}y^2z^2\right]. \tag{19}$$

Similar high accuracy results are obtainable for this problem as well.

Acknowledgement

The authors are grateful to the referees for valuable comments and suggestions in the light of which the paper has been revised.

References

[1] A K Mitra, *J. Math. Phys.*, **19**, 2018 (1979)
[2] S Galicia and J P Killingbeck, *Phys. Lett.* **A71**, 17 (1979)
[3] R S Kaushal, *J. Phys.* **A12**, L253 (1979)
[4] N Bessis and G Bessis, *J. Math. Phys.*, **21**, 2780 (1980)
[5] G P Flessas, *Phys. Lett.* **A83** 121 (1981)
[6] V S Varma, *J. Phys.* **A14**, L489 (1981)
[7] C S Lai and H E Lin, *J. Phys.* **A15**, 1495 (1982)
[8] M Znojil, *J. Phys.* **A16**, 293 (1983)
[9] V Fack and G V Berghe, *J. Phys.* **A18**, 3355 (1985)
[10] V Fack, De Meyer and G V Berghe, *J. Math. Phys.*, **27**, 1340 (1986)
[11] Y P Varshni, *Phys. Rev.* **A36**, 3009 (1987)
[12] R J W Hodgson, *J. Phys.* **A21**, 1563 (1983)
[13] Pinaki Roy, Rajkumar Roychoudhury and Y P Varshni, *J. Phys.* **A21**, 1589 (1988)
[14] J A C Gallas, *J. Phys.* **A21**, 3393 (1988)
[15] A Lakhtakia, *J. Phys.* **A22**, 1701 (1989)
[16] R Adhikari, R Dutt and Y P Varshni, *J. Math. Phys.*, **32**, 447 (1991)
[17] M R M Witwit, *J. Phys.* **A25**, 503 (1992)
[18] M R M Witwit and J P Killingbeck, *Can. J. Phys.*, **70** 1261 (1992)
[19] H Haken, Laser Theory, in Vol. XXV/9c of *Handbuch der Physik*, edited by S Flugge (Springer-Verlag, New York, 1970)
[20] H Risken and H D Vollmer, *Z. Phys.* **201** 323 (1967)
[21] R Blankenbecler, T De Grand and R L Sugar, *Phys. Rev.* **D21**, 1055 (1980)
[22] J P Killingbeck and M N Jones, *J. Phys.* **A19**, 705 (1986)
[23] M R M Witwit, *J. Phys.* **A24**, 4535 (1991)
[24] M R M Witwit and J P Killingbeck, *J. Phys.* **A26**, 3659 (1993)
[25] F M Fernandez and J F Ogilvie, *Phys. Lett.* **A178**, 11 (1993)

PRAMANA
— journal of
physics

© Printed in India

Vol. 43, No. 4,
October 1994
pp. 289–305

A new formalism for the statistical dynamics of vector spin systems

KAMLESH KUMARI and DEEPAK KUMAR*
Department of Physics, University of Roorkee, Roorkee 247 667, India
*School of Physical Sciences, Jawaharlal Nehru University, New Delhi 110 067, India

MS received 12 April 1994; revised 28 June 1994

Abstract. The relaxational dynamics of a classical vector Heisenberg spin system is studied using the Fokker–Planck equation. To calculate the eigenvalues of the Fokker–Planck operator, a new approach is introduced. In this connection, a number space repesentation is introduced, which enables us to visualize the eigenvalue structure of the Fokker–Planck operator. The mean field approximation is derived and a systematic method to improve the mean field approximation is presented.

Keywords. Relaxational dynamics; vector Heisenberg model; Fokker–Planck equation; mean field approximation.

PACS Nos 05·70; 75·10; 76·20

1. Introduction

In a previous paper [1] we introduced a new formalism to study the relaxational dynamics of a planar ferromagnet. This formalism was based on the Fokker–Planck equation for the time-dependent joint probability distribution of the spins in the system. Unlike most recent work [2, 3] on relaxational dynamics, particularly at the critical point, our work deals with fixed length spins. Our method mainly consists in finding out the eigenvalues of the Fokker–Planck operator, which are the relaxation rates in the system. To achieve this, we construct a convenient representation, which is somewhat analogous to the number space representation of second quantization. In this representation a new conservation principle becomes immediately obvious and certain, hitherto unnoticed, features of the relaxation eigenvalue spectrum of planar spin system are brought forth easily. Furthermore the formalism offers a systematic method of doing a perturbation expansion, renormalization group analysis and systematic improvement over the mean field approximation in problems involving dynamics of fixed length spins.

The purpose of the present paper is to extend this formalism to vector spin systems. The formalism for vector spin systems is considerably more complicated than that for planar spins due to additional degrees of freedom, namely azimuthal angles at each site. The paper is organized as follows. In § 2, we develop the Fokker–Planck equation for a system of classical spins interacting via Heisenberg Hamiltonian. This development is a generalization of the earlier work of Kubo and Hashitsume [4] on the relaxation of a single moment. In § 3 we construct a representation for the Fokker–Planck operator which is diagonal in the rotational diffusion operator. This

operator is independent for different spins and the interaction term acts to couple diffusion on different sites leading to a band structure for relaxation eigenvalues. It is shown in § 4 that the mean field approximation ignores all the bands except the lowest one. This observation then allows us to construct approximations which are systematic improvements over the mean field approximation. In § 5, the first such approximation is constructed. This section is of a demonstrational nature as the detailed analysis of the improved approximation and its physical consequences are not presented. We conclude with some remarks on the potentiality of the present work for further numerical studies.

2. Fokker–Planck equation for spin system

We consider a lattice of classical spins $\mathbf{S}_i$ of unit magnitude, interacting according to the Heisenberg model, with the Hamiltonian

$$H = -\frac{1}{2}\sum_{ij} J_{ij}\mathbf{S}_i\cdot\mathbf{S}_j - \mathbf{H}_0\cdot\sum_i \mathbf{S}_i, \tag{2.1}$$

where J_{ij}'s denote short-ranged exchange interactions and $\mathbf{H}_0$ is an external field, which we shall take to be along z-axis. The relaxational dynamics of the system is described through a set of Langevin equations for each spin, which are straightforward generalizations of the Landau–Lifshitz equation [5] for a single magnetic moment in interaction with heat bath. These are

$$\frac{d\mathbf{S}_i}{dt} = \gamma[\mathbf{h}_i + \mathbf{H}_i'(t)] \times \mathbf{S}_i - \gamma\eta(\mathbf{h}_i \times \mathbf{S}_i) \times \mathbf{S}_i \tag{2.2}$$

where

$$\mathbf{h}_i = \sum_j J_{ij}\mathbf{S}_j + \mathbf{H}_0 \tag{2.3}$$

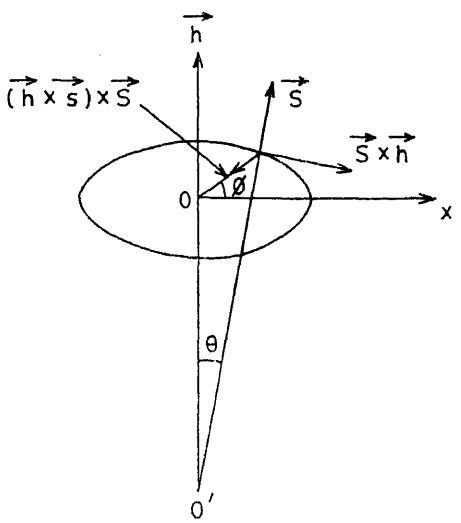

Figure 1. The figure denotes the direction of forces occurring in equation (2.2).

where γ is the gyromagnetic ratio, η the viscosity coefficient and $\mathbf{H}'_i(t)$ the random magnetic field at site i. The physical meaning of the various terms of (2.2) is as follows (see figure 1). The first term $\gamma \mathbf{h}_i \times \mathbf{S}_i$ describes the precession of the spin $\mathbf{S}_i$ about the local field $\mathbf{h}_i$ and this term conserves the energy $\mathbf{h}_i \cdot \mathbf{S}_i$. The remaining terms describe the effect of heat bath. As shown in figure 1 the frictional term $\gamma\eta(\mathbf{h}_i \times \mathbf{S}_i) \times \mathbf{S}_i$ acts to align the spin vector $\mathbf{S}_i$ along the direction of the local field $\mathbf{h}_i$, and is dissipative in nature. Finally the Brownian random force term is $\mathbf{S}_i \times \mathbf{H}'_i(t)$. Note both these terms are perpendicular to $\mathbf{S}_i$, so that the magnitude of the vector is preserved. $\mathbf{H}'_i(t)$ are taken to be Gaussian white noise, with the following usual properties for its components, $H'_{i\alpha}(t)$,

$$\langle H'_{i\alpha}(t) \rangle = 0, \tag{2.4a}$$

$$\gamma^2 \langle H'_{i\alpha}(t_1) H'_{j\beta}(t_2) \rangle = \delta_{ij}\delta_{\alpha\beta}\left[\frac{1}{\tau_\parallel}\delta_{\alpha z} + (1-\delta_{\alpha z})\frac{1}{\tau_\perp}\right]. \tag{2.4b}$$

Now we follow the treatment of Kubo and Hashitsume [4] for the single moment, in writing down the Liouville equation for time-dependent distribution function $\rho(\mathbf{S}_1, \ldots, \mathbf{S}_N, t)$. This is given by

$$\frac{\partial \rho}{\partial t}(\mathbf{S}_1, \mathbf{S}_2, \ldots, \mathbf{S}_N, t) = -\sum_{i\alpha} \frac{\partial}{\partial S_{i\alpha}} (\dot{S}_{i\alpha}\rho), \tag{2.5}$$

where $\dot{S}_{i\alpha}$ denotes the time derivative of $S_{i\alpha}$. Using (2.2), (2.5) can be written as

$$\frac{\partial \rho}{\partial t} = -i\gamma \sum_i [\mathbf{h}_i + \mathbf{H}'_i(t)] \cdot \mathbf{L}_i \rho - i\gamma\eta \sum_i \mathbf{h}_i \cdot (\mathbf{L}_i \times \mathbf{S}_i)\rho, \tag{2.6}$$

where $\mathbf{L}_i$'s denote angular-momentum-like operators given by

$$\mathbf{L}_j = -i\mathbf{S}_j \times \frac{\partial}{\partial \mathbf{S}_j}. \tag{2.7}$$

Our next task is to average over the random fields $\mathbf{H}'_i(t)$. This can be done using the interaction representation, for which purpose we write (2.6) as

$$\frac{\partial \rho}{\partial t} = -i[\mathscr{L}_0 + \mathscr{L}'(t)]\rho \tag{2.8}$$

$$\mathscr{L}_0 = \gamma \sum_i [\mathbf{h}_i \cdot \mathbf{L}_i + \eta \mathbf{h}_i \cdot (\mathbf{L}_i \times \mathbf{S}_i)] \tag{2.9}$$

and

$$\mathscr{L}'(t) = \gamma \sum_i \mathbf{H}'_i(t) \cdot \mathbf{L}_i. \tag{2.10}$$

Equation (2.8) is now solved in the interaction representation, the exact formal solution being

$$\rho(t) = \exp[-i\mathscr{L}_0 t] \exp_T \left[-i \int_0^t dt' \sum_j \mathbf{H}'_j(t') \cdot \mathbf{L}_{Ij}(t')\right] \rho(0), \tag{2.11}$$

where $\exp_T$ denotes the usual time-ordered exponential and

$$\mathbf{L}_{Ij} = \exp[i\mathscr{L}_0 t]\mathbf{L}_j \exp[-i\mathscr{L}_0 t] \tag{2.12}$$

Using the Gaussian properties given in (2.4) and denoting the average value of $\rho(t)$ by $P(t)$, one averages (2.11) to find

$$P(t) = \exp[-i\mathscr{L}_0 t]\exp_T\left[-\frac{1}{2}\int_0^t \mathrm{d}t' \sum_k \left\{\frac{1}{\tau_\parallel}(L_{Ik}^z(t'))^2 + \frac{1}{\tau_\perp}((L_{Ik}^x(t'))^2 + (L_{Ik}^y(t'))^2)\right\}\right]\rho(0) \tag{2.13}$$

$$= \exp\left[-i\mathscr{L}_0 t - \frac{t}{2}\sum_k \left\{\frac{1}{\tau_\parallel}(L_k^z)^2 + \frac{1}{\tau_\perp}(L_k^x)^2 + \frac{1}{\tau_\perp}(L_k^y)^2\right\}\right]\rho(0). \tag{2.14}$$

The last step is permissible as the two operators in the exponential are commuting and L^2 and L_z^2 are time independent.

From (2.14), the Fokker–Planck equation follows as

$$\frac{\partial P}{\partial t} = -WP \tag{2.15}$$

with

$$W = i\gamma\sum_j [\mathbf{h}_j\cdot\mathbf{L}_j + \eta\mathbf{h}_j\cdot(\mathbf{L}_j\times\mathbf{S}_j)] + \frac{1}{2}\sum_j\left[\frac{1}{\tau_\parallel}(L_j^z)^2 + \frac{1}{\tau_\perp}(L_j^x)^2 + \frac{1}{\tau_\perp}(L_j^y)^2\right] \tag{2.16}$$

The first term in the Fokker–Planck operator W is the Liouville term, while the second one corresponds to rotational diffusion of spins. It is straightforward to verify that the steady state solution of (2.15) is the equilibrium distribution function, $P_{\mathrm{eq}}(\mathbf{S}_i)$, given by

$$P_{\mathrm{eq}}(\mathbf{S}_i) = Z^{-1}\exp\left[\frac{\beta}{2}\sum_{ij} J_{ij}\mathbf{S}_i\cdot\mathbf{S}_j + \beta\mathbf{H}_0\cdot\sum_i \mathbf{S}_i\right] \tag{2.17}$$

provided the following Einstein relation holds

$$\frac{1}{\tau_\perp} = 2\gamma\eta k_B T. \tag{2.18}$$

Further Z is the equilibrium partition function for the system of (2.1). Note that only $\tau_\perp$ enters the Einstein relation. This is due to the fact that $\tau_\parallel$ controls the precessional motion (azimuthal angle) about the local field direction, while $\tau_\perp$ controls the relaxation towards the local axis (θ-angle). Clearly only the latter is of relevance for establishing thermal equilibrium. If we let $f(\{\mathbf{S}_i\}, t; \{\mathbf{S}_i'\}, 0)$ denote the conditional probability distribution, which is the solution of (2.15) with initial condition

$$f(\{\mathbf{S}_i\}, t; \{\mathbf{S}_i'\}, 0) = \prod_i \delta(\mathbf{S}_i - \mathbf{S}_i') \tag{2.19}$$

then we can write the correlation function between any two operators $A_1(\{\mathbf{S}_i\})$ and

$A_2(\{\mathbf{S}_i\})$ as

$$C_{A_1,A_2}(t) = \int \prod_i d\mathbf{S}_i d\mathbf{S}_i' A_1(\{\mathbf{S}_i\}) f(\{\mathbf{S}_i\}, t; \{\mathbf{S}_i'\}, 0) \times A_2(\{\mathbf{S}_i'\}) p_{eq}(\{\mathbf{S}_i'\}). \tag{2.20}$$

This correlation function can be recast in a Heisenberg-like representation by noting that formally the conditional probability distribution function can be written as

$$f(\{\mathbf{S}_i\}, t; \{\mathbf{S}_i'\}, 0) = \exp(-tW) \prod_i \delta(\mathbf{S}_i - \mathbf{S}_i').$$

Further we define inner products and adjoints by the following equations

$$(g_1, g_2) = \int d\Omega g_1^*(\Omega) g_2(\Omega)$$

$$(g_1, Ag_2) = \int d\Omega (A^+ g_1, g_2),$$

where g's represent functions of angular variables Ω corresponding to vector S and the integration is over the solid angle. Now

$$\begin{aligned} C_{A_1A_2}(t) &= \int\int \prod_i d\mathbf{S}_i d\mathbf{S}_i' A_1(\{\mathbf{S}_i\}) e^{-tW} \prod_i \delta(\mathbf{S}_i - \mathbf{S}_i') A_2(\{\mathbf{S}_i'\}) P_{eq}(\{\mathbf{S}_i'\}) \\ &= \int \prod_i d\mathbf{S}_i e^{-tW^+} A_1(\{\mathbf{S}_i\}) A_2(\{\mathbf{S}_i\}) P_{eq}(\{\mathbf{S}_i\}) \\ &= \langle A_1(t) A_2 \rangle, \end{aligned} \tag{2.21}$$

where $\langle\ \rangle$ denotes the average over the equilibrium distribution function and

$$A(t) = \exp(-tW^+) A. \tag{2.22}$$

Further note

$$\frac{dA}{dt} = -W^+ A. \tag{2.23}$$

At this point, it is useful to display the full form of W^+, which is

$$\begin{aligned} W^+ = &-i\gamma H_0 \sum_k L_k^z - i\gamma \sum_{j,k} J_{jk} \mathbf{S}_j \cdot \mathbf{L}_k + \frac{1}{2\tau_\perp} \sum_{j,k} \frac{i\beta}{2} J_{jk} (\mathbf{S}_k \times \mathbf{S}_j) \cdot (\mathbf{L}_k - \mathbf{L}_j) \\ &+ \frac{1}{2\tau_\parallel} \sum_k (L_k^z)^2 + \frac{1}{2\tau_\perp} \sum_k \{(L_k^x)^2 + (L_k^y)^2\} \end{aligned} \tag{2.24}$$

It is also of interest to write down the equations of motion for $\mathbf{S}_i$, using (2.24). These are

$$\frac{dS_i^z(t)}{dt} = \gamma \sum_j J_{ij} (\mathbf{S}_j \times \mathbf{S}_i)_z - \frac{1}{2\tau_\perp} \sum_j \beta J_{ij} [(\mathbf{S}_j \times \mathbf{S}_i) \times \mathbf{S}_i]_z - \frac{1}{\tau_\perp} S_i^z(t) \tag{2.25a}$$

$$\frac{dS_i^x(t)}{dt} = \gamma H_0 S_i^y(t) - \frac{1}{2\tau_\perp}\sum_j \beta J_{ij}[(\mathbf{S}_j \times \mathbf{S}_i) \times \mathbf{S}_i]_x + \gamma \sum_j J_{ij}(\mathbf{S}_j \times \mathbf{S}_i)_x - \frac{1}{2}\left(\frac{1}{\tau_\parallel} + \frac{1}{\tau_\perp}\right) S_i^x(t) \tag{2.25b}$$

$$\frac{dS_i^y(t)}{dt} = -\gamma H_0 S_i^x(t) - \frac{1}{2\tau_\perp}\sum_j \beta J_{ij}[(\mathbf{S}_j \times \mathbf{S}_i) \times \mathbf{S}_i]_y + \gamma \sum_j J_{ij}(\mathbf{S}_j \times \mathbf{S}_i)_y - \frac{1}{2}\left(\frac{1}{\tau_\parallel} + \frac{1}{\tau_\perp}\right) S_i^y(t) \tag{2.25c}$$

In deriving (2.25) we have made use of the following relations

$$L_k^\beta S_k^\alpha = (-i)\theta_{\alpha\beta\gamma} S_k^\gamma \tag{2.26a}$$

and

$$L_k^2 S_k^\alpha = 2S_k^\alpha \tag{2.26b}$$

Though (2.25a–c) are in Heisenberg representations, in the present context their physical meaning is obtained only when we take averages of over the equilibrium distribution function.

This dynamics in which the random noise has been averaged out differs from the Langevin equation essentially by the replacement of the random field term by the diffusion term.

3. Number space representation for Fokker–Planck operator

Since we are dealing with only periodic functions of angles at each site, we can introduce a basis of a complete set of spherical harmonics at each site. A typical member of the basis is denoted as

$$|l_1, m_1; l_2, m_2; \ldots\rangle = \prod_k Y_{l_k, m_k}(\theta_k, \phi_k) \tag{3.1}$$

where k runs over all the spins.

The utility of this basis lies in two points. First, the diffusion operator is diagonal in this basis. Second, the operator W^+ contains products of vector operators and angular momentum operators which can cause transitions in which l and m at a site change only by ± 1 or 0. Just to set the notation, we record here the operation of basic operators in this basis

$$L_k^2|\{l_k, m_k\}\rangle = l_k(l_k+1)|\{l_k, m_k\}\rangle \tag{3.2}$$

$$L_k^z|\{l_k, m_k\}\rangle = m_k|\{l_k, m_k\}\rangle \tag{3.3}$$

$$L_k^\pm|\{l_k, m_k\}\rangle = B_\pm(l_k, m_k)|\ldots l_k, m_k \pm 1, \ldots\rangle \tag{3.4}$$

$$S_k^z|\{l_k, m_k\}\rangle = A_{0+}(l_k, m_k)|\ldots l_k+1, m_k \ldots\rangle + A_{0-}(l_k, m_k)|\ldots l_k-1, m_k, \ldots\rangle \tag{3.5}$$

$$S_k^+|\{l_k, m_k\}\rangle = A_{++}(l_k, m_k)|\ldots l_k+1, m_k+1, \ldots\rangle + A_{+-}(l_k, m_k)|\ldots l_k-1, m_k+1, \ldots\rangle \tag{3.6a}$$

$$S_k^-|\{l_k,m_k\}\rangle = A_{-+}(l_k,m_k)|\ldots l_k+1,m_k-1,\ldots\rangle + A_{--}(l_k,m_k)|\ldots l_k-1,m_k-1,\ldots\rangle \tag{3.6b}$$

where $S^{\pm}=S^x\pm iS^y$ and $L^{\pm}$ are similarly defined. The coefficients $\{B_{\pm}\}$ and $\{A\}$ are collected together in Appendix-1 for ready reference. Using (3.2) to (3.6) it is straightforward to write the action of W^+ on a typical member of the basis. To see this we explicitly work out the action of the second term of W^+ ((2.24)), i.e.

$$\begin{aligned}\sum_{k,p} J_{k,p}\mathbf{S}_p\cdot\mathbf{L}_k|\{l_k,m_k\}\rangle &= \sum_{k,p} J_{k,p}[S_p^z L_k^z+\tfrac{1}{2}S_p^- L_k^+ +\tfrac{1}{2}S_p^+ L_k^-]|\{l_k,m_k\}\rangle \\ &= \sum_{k,p} J_{k,p}\Big[m_k \sum_{\sigma=\pm 1} A_{0\sigma}(l_p,m_p)|\ldots l_p\pm\sigma,m_p,\ldots\rangle \\ &\quad +\frac{1}{2}B_+(l_k,m_k)\sum_{\sigma=\pm 1} A_{-\sigma}(l_p,m_p)|\ldots l_k,m_k+1,\ldots,l_p\pm\sigma,m_p-1,\ldots \\ &\quad +\frac{1}{2}B_-(l_k,m_k)\sum_{\sigma=\pm 1} A_{+\sigma}(l_p,m_p)|\ldots l_k,m_k-1,\ldots,l_p\pm\sigma,m_p-1,\ldots\rangle\Big]\end{aligned} \tag{3.7}$$

First, note that in the transitions caused by this term the total azimuthal quantum number, i.e. $C=\sum_k m_k$, does not change. An examination of the other terms in W^+ shows that this is not just the property of the second term, but that the entire W^+ conserves C.

We shall now write the action of W^+ on a basis function in a compact form

$$\begin{aligned}W^+|\{l_k,m_k\}\rangle &= -i\gamma H_0\sum_k m_k|\{l_k,m_k\}\rangle \\ &\quad -i\gamma\sum_{k,p}\sum_{\substack{\sigma_p,\mu_p\\ \mu_k}} J_{k,p}g(l_k,m_k,\mu_k;l_p,m_p,\sigma_p,\mu_p)|\ldots l_k, m_k+\mu_k,\ldots,l_p+\sigma_p,m_p+\mu_p,\ldots\rangle \\ &\quad +\frac{1}{\tau_\perp}\sum_{k,p}\beta J_{k,p}\sum_{\substack{\sigma_k,\mu_k,\\ \mu_p,\sigma_p}} f(l_k,m_k,\sigma_k,\mu_k;l_p,m_p,\sigma_p,\mu_p)|\ldots l_k+\sigma_k, m_k+\mu_k,\ldots,l_p+\sigma_p,m_p+\mu_p,\ldots\rangle \\ &\quad +\frac{1}{2}\sum_k\left\{\frac{1}{\tau_\perp}l_k(l_k+1)+\left(\frac{1}{\tau_\parallel}-\frac{1}{\tau_\perp}\right)m_k^2\right\}|\{l_k,m_k\}\rangle\end{aligned} \tag{3.8}$$

where σ_k's take values ± 1 only, whereas μ_k's take values 1, 0, -1, with the constraint $\mu_k+\mu_p=0$. Note that the first two terms on the right hand side of (3.8) are imaginary. These correspond to the inertial precession of a spin in the external field and the internal field due to the other spins. In most of what follows we shall set $\mathbf{H}_0=0$ and drop the spin precession term which contributes an imaginary part to the eigenvalues of W^+. Clearly for the long time relaxation such a term is relatively less important. With $\mathbf{H}_0=0$, we can set $\tau_\parallel=\tau_\perp=\tau$. Now the off-diagonal terms come from the

friction part of the operator, i.e. the third term on the right hand side of (3.8). Here we have 8 off-diagonal terms corresponding to the possibilities $\mu_k = \mu_p = 0$; $\mu_k = 1$, $\mu_p = -1$; combining with $\sigma_k = \pm 1$, $\sigma_p = \pm 1$. The coefficients f and g are listed in Appendix-1.

4. The mean field approximation

We shall now use the above formalism to calculate the Green's function $G_{10,10}(\mathbf{R}_k, t|\mathbf{R}_j)$ defined as

$$G_{10,10}(\mathbf{R}_k, t|\mathbf{R}_j) = \theta(t)\langle Y_1^0(\theta_k(t), \phi_k(t))\ Y_1^0(\theta_j, \phi_j)\rangle. \tag{4.1}$$

where $\theta(t)$ is the step function.

The equation of motion for this function is

$$\frac{\partial}{\partial t} G_{10,10}(\mathbf{R}_k, t|\mathbf{R}_j) = C_{10,10}(\mathbf{R}_k|\mathbf{R}_j) - \theta(t)\langle [W^+\ Y_1^0(\theta_k, \phi_k)]\ Y_1^0(\theta_j, \phi_j)\rangle \tag{4.2}$$

where $C_{10,10}(\mathbf{R}_k|\mathbf{R}_j)$ is the equilibrium correlation function given by

$$C_{10,10}(\mathbf{R}_k|\mathbf{R}_j) = \langle Y_1^0(\theta_k, \phi_k)\ Y_1^0(\theta_j, \phi_j)\rangle. \tag{4.3}$$

Now, setting the external field to zero and ignoring the precessional term, the action of W^+ on $Y_1^0(\theta_k, \phi_k)$ is given by

$$\begin{aligned} W^+|\ldots l_k = 1, m_k = 0, \ldots\rangle &= \frac{1}{\tau}\Big|\ldots l_k = 1, m_k = 0, \ldots\Big\rangle \\ &- \frac{1}{4\tau}\sum_p \beta J_{kp}[\tfrac{4}{3}|\ldots l_p = 1, m_p = 0, \ldots\rangle \\ &+ \frac{2}{\sqrt{15}}\{|\ldots l_k = 2, m_k = -1, \ldots, l_p = 1, m_p = 1, \ldots\rangle \\ &+ |\ldots l_k = 2, m_k = 1, \ldots l_p = 1, m_p = -1, \ldots\rangle\} \\ &+ \frac{4}{3\sqrt{5}}\Big|\ldots l_k = 2, m_k = 0, \ldots l_p = 1, m_p = 0, \ldots\Big\rangle]. \end{aligned} \tag{4.4}$$

The explicit use of the forms of spherical harmonics in (4.4) shows that (4.4) is indeed equivalent to (2.25). Further (4.4) shows that the equation of motion for $G_{10,10}$ involves higher order Green's functions, as is expected in any many-body problem. To set up a systematic scheme of approximations, we note that in the above representation, at each site we have a discrete set of rotational diffusion states with eigenvalues $l(l+1)/\tau$ which are coupled by the interaction term. There are two physical effects of this coupling. First, the site levels broaden into bands which are well separated at high temperatures (because β is small). Second, it causes transitions between bands, by having a pair of coupled sites change their local states (see figure 2). For long times, clearly the lowest band is the most important one. So one can develop a set of approximations, by projecting out the higher bands from the calculations. The simplest

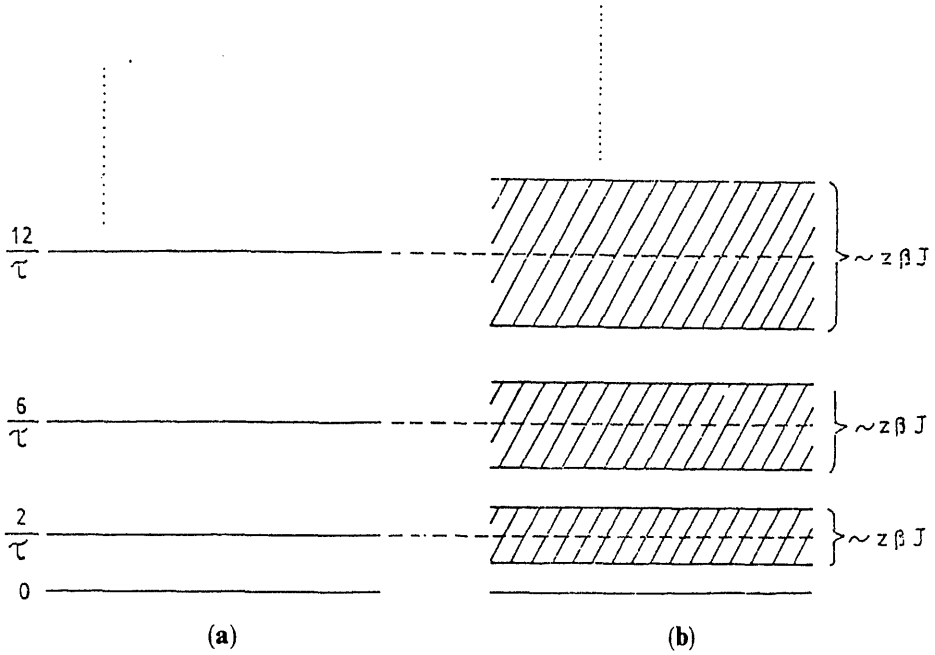

Figure 2. (**a**) The relaxational eigenvalues when $J = 0$. These correspond to relaxation of uncoupled spins due to thermal rotational diffusion. (**b**) Schematic structure of eigenvalues when $J \neq 0$. Now the rotational diffusion at different sites gets coupled leading to formation of bands much like tight-binding approximation.

of such approximations is clearly the one in which we just keep the lowest band. At the next level one can include a group of higher bands to which the lowest band couples directly and see their influence on the relaxation eigenvalues of the lowest band. Now we show that the simplest approximation discussed above leads to an analog of the mean field theory discussed by Edwards and Anderson [6] in the context of the planar spin glass. In this approximation, we drop the third, fourth and fifth terms on the right hand side of (4.4) as these correspond to a local excitation level of $\tau K = \Sigma_k l_k(l_k + 1) = 8$. Now the equation of motion for $G_{10,10}$ can be written as

$$\frac{\partial}{\partial t} G_{10,10}(\mathbf{R}_k, t|\mathbf{R}_j) = -\theta(t)\langle [W^+ Y_1^0(\theta_k, \phi_k)]\, Y_1^0(\theta_j, \phi_j)\rangle + C_{10,10}(\mathbf{R}_k|\mathbf{R}_j)$$

$$= -\frac{1}{\tau}\sum_p \left(\delta_{kj} - \frac{\beta J_{kj}}{3}\right) G_{10,10}(\mathbf{R}_p, t|\mathbf{R}_j) + C_{10,10}(\mathbf{R}_k|\mathbf{R}_j)$$

which for a translationally invariant system yields the following solution

$$G_{10,10}(R_k, t|R_j) = \frac{1}{N}\sum_q C_{10,10}(q) \exp -\frac{t}{\tau}\left(1 - \frac{\beta J(q)}{3}\right) \exp i\mathbf{q}\cdot(\mathbf{R}_k - \mathbf{R}_j) \tag{4.5}$$

where $C_{10,10}(q)$ and $J(q)$ denote the spatial Fourier transforms of $C_{10,10}(R_k|R_j)$ and

J_{kj} respectively. These are written as

$$C_{10,10}(q) = \sum_k \exp[iq\cdot(R_k - R_j)]\, C_{10,10}(R_k|R_j)$$

$$J(q) = \sum_j J_{kj} \exp[iq\cdot(R_k - R_j)]$$

eq. (4.5) is the analogue of Edwards–Anderson mean field result for vector spins. Note that this result has been derived here not by any ad hoc decoupling procedure, but by a systematic projection procedure. This procedure makes the nature of the result clear in the following way. It is seen that EA results amount to keeping the lowest band of relaxation eigenvalues, which clearly is good at long enough times. The correction to these results arise by considering the higher band of eigenvalues. These bands are certainly important at shorter times, and moreover since the couplings cause interband transitions, they also renormalize the lowest band and thus affecting the long time behaviour. The next section describes the procedure for improving the mean field result.

5. Beyond mean field theory

In this section we discuss a systematic procedure to incorporate the effects of the coupling of higher bands on the lowest lying band, which is the one responsible for long-time behaviour.

Now, we define a set of Green's functions,

$$\begin{aligned} G_{10,10}(R_k, t|R_j) &= \langle Y_1^0(\theta_k(t), \phi_k(t))\; Y_1^0(\theta_j, \phi_j)\rangle, \quad t>0 \\ &= 0, \qquad\qquad\qquad\qquad\quad t<0 \end{aligned} \tag{5.1}$$

$$\begin{aligned} G_{l_1m_1,l_2m_2,\ldots}(R_1, R_2, \ldots, t|R_j) &= \left\langle \prod_k Y_{l_k}^{m_k}(\theta_k(t), \phi_k(t))\; Y_1^0(\theta_j, \phi_j) \right\rangle, \quad t>0 \\ &= 0, \qquad\qquad\qquad\qquad\quad t<0 \end{aligned} \tag{5.2}$$

We also define their spatial Fourier transform and time-Laplace transform by the following relations

$$G_{10,10}(\mathbf{q}, t) = \sum_k \exp[i\mathbf{q}\cdot(\mathbf{R}_j - \mathbf{R}_k)]\, G_{10,10}(\mathbf{R}_k, t|\mathbf{R}_j) \tag{5.3}$$

$$\tilde{G}_{10,10}(\mathbf{q}, z) = \int_0^\infty \exp[izt]\, G_{10,10}(\mathbf{q}, t)\mathrm{d}t, \quad \mathrm{Im}\, z > 0 \tag{5.4}$$

$$\begin{aligned} \tilde{G}_{l_1m_1,l_2m_2,\ldots}(\mathbf{q}_1, \mathbf{q}_2, \ldots, z) = \sum_{\mathbf{R}_1,\mathbf{R}_2,\ldots} \int_0^\infty \exp[izt]\mathrm{d}t \exp\left[i\sum_k \mathbf{q}_k\cdot(\mathbf{R}_j - \mathbf{R}_k)\right] \\ \times G_{l_1m_1,l_2m_2,\ldots}(\mathbf{R}_1, \mathbf{R}_2, \ldots, t|\mathbf{R}_j) \end{aligned} \tag{5.5}$$

A point about notation: if any of the m's is negative, we denote it by a bar over it, i.e. $G_{1,-1}$ is written $G_{1\bar{1}}$. The equations of motion of the G's also involve the equilibrium

correlation functions, which we denote as

$$C_{l_1 m_1, l_2 m_2, \ldots}(\mathbf{R}_1, \mathbf{R}_2, \ldots) = \left\langle \prod_k Y_{l_k}^{m_k}(\theta_k, \phi_k) \right\rangle_0 . \tag{5.6}$$

The Fourier transform of the correlation functions are defined in the same way as the Green's functions.

We now write the equation of motion of $G_{10,10}(\mathbf{R}_k, t|\mathbf{R}_j)$ for $t > 0$,

$$\begin{aligned}\frac{\partial}{\partial t} G_{10,10}(\mathbf{R}_k, t|\mathbf{R}_j) &= -\langle [W^+ Y_1^0(\theta_k(t), \phi_k(t))]\, Y_1^0(\theta_j, \phi_j)\rangle \\ &= -\frac{1}{\tau} G_{10,10}(\mathbf{R}_k, t|\mathbf{R}_j) + \frac{\beta}{\tau} \sum_p J_{kp} \Bigg[\frac{1}{3} G_{10,10}(\mathbf{R}_p, t|\mathbf{R}_j) \\ &\quad + \frac{1}{2\sqrt{15}} \{ G_{2\bar{1},11}(\mathbf{R}_k, \mathbf{R}_p, t|\mathbf{R}_j) + G_{21,1\bar{1}}(\mathbf{R}_k, \mathbf{R}_p, t|\mathbf{R}_j) \} \\ &\quad - \frac{1}{3\sqrt{5}} G_{20,10}(\mathbf{R}_k, \mathbf{R}_p, t|\mathbf{R}_j) \Bigg]. \end{aligned} \tag{5.7}$$

Taking its Fourier and Laplace transform yields

$$\begin{aligned}\tilde{G}_{10,10}(\mathbf{q}, z) = \frac{1}{(r_q - iz)} \Bigg[C_{10,10}(\mathbf{q}) + \frac{\beta}{N\tau} \sum_{q_1} J(q_1) \Bigg[\frac{1}{2\sqrt{15}} \{ \tilde{G}_{2\bar{1},11}(\mathbf{q}-\mathbf{q}_1, \mathbf{q}_1; z) \\ + \tilde{G}_{21,1\bar{1}}(\mathbf{q}-\mathbf{q}_1, \mathbf{q}_1; z) \} - \frac{1}{3\sqrt{5}} \tilde{G}_{20,10}(\mathbf{q}-\mathbf{q}_1, \mathbf{q}_1; z) \Bigg] \Bigg] \end{aligned} \tag{5.8}$$

where

$$r_q = \frac{1}{\tau} \left(1 - \frac{\beta J(q)}{3} \right). \tag{5.9}$$

To go beyond mean-field theory, we now write the equations of motion for $G_{21,1\bar{1}}$, $G_{2\bar{1},11}$ and $G_{20,10}$ which follow by considering the action of W^+ on $|\ldots l_k = 2, m_k = 1, \ldots l_p = 1, m_p = -1, \ldots\rangle$, $|\ldots l_k = 2, m_k = -1, \ldots l_p = 1, m_p = 1, \ldots\rangle$ and $|\ldots l_k = 2, m_k = 0, \ldots l_p = 1, m_p = 0, \ldots\rangle$.

The action of W^+ on $|\ldots l_k = 2, m_k = 1, \ldots l_p = 1, m_p = -1, \ldots\rangle$ state is given by the following equation

$$\begin{aligned} W^+ \Big| \ldots l_k = 2, m_k = 1, \ldots l_p = 1, m_p = -1, \ldots \Big\rangle &= \frac{4}{\tau} \Big| \ldots l_k = 2, \\ &\qquad m_k = 1, \ldots l_p = 1, m_p = -1, \ldots \Big\rangle \\ + \frac{\beta}{4\tau} \Bigg[\sum_{j \neq k} J_{pj} \Bigg\{ \frac{2}{3\sqrt{5}} \Bigg| \ldots l_k = 2, m_k = 1, \ldots l_j = 1, m_j = -1, \ldots l_p = 2, \\ m_p = 0 \ldots \Big\rangle \end{aligned}$$

$$-\frac{2}{3}\Big|\ldots l_k=2,m_k=1,\ldots l_j=1,m_j=-1\ldots\rangle-\frac{2\sqrt{2}}{\sqrt{15}}\Big|\ldots l_k=2,$$

$$m_k=1,\ldots l_j=1,m_j=1,\ldots l_p=2,m_p=-2\ldots\rangle$$

$$+\frac{2}{\sqrt{15}}\Big|\ldots l_k=2,m_k=1,\ldots l_j=1,m_j=0,\ldots l_p=2,m_p=-1,\ldots\rangle$$

$$-\frac{4}{3\sqrt{5}}\Big|\ldots l_k=2,m_k=1,\ldots l_j=1,m=-1,\ldots l_p=2,m_p=0,\ldots\rangle$$

$$-\frac{2}{3\sqrt{5}}\Big|\ldots l_k=2,m_k=1,\ldots l_j=1,m_j=-1,\ldots\rangle\Big\}+J_{kp}\Big\{\frac{-4}{\sqrt{35}}\Big|\ldots l_k=3,$$

$$m_k=2,\ldots l_p=2,m_p=-2,\ldots\rangle$$

$$+\frac{2}{5\sqrt{7}}\Big|\ldots l_k=3,m_k=0,\ldots l_p=2,m_p=0,\ldots\rangle-\frac{2}{\sqrt{35}}\Big|\ldots l_k=3,m_k=0,\ldots\rangle$$

$$-\frac{2}{5\sqrt{3}}\Big|\ldots l_k=1,m_k=0,\ldots l_p=2,m_p=0,\ldots\rangle+\frac{2}{\sqrt{15}}\Big|\ldots l_k=1,m_k=0,\ldots\rangle$$

$$+\frac{6}{5\sqrt{7}}\Big|\ldots l_k=3,m_k=0,\ldots l_p=2,m_p=0,\ldots\rangle+\frac{6}{\sqrt{35}}\Big|\ldots l_k=3,m_k=0,\ldots\rangle$$

$$-\frac{4}{5\sqrt{7}}\Big|\ldots l_k=1,m_k=0,\ldots l_p=2,m_p=0,\ldots\rangle+\frac{4}{\sqrt{35}}\Big|\ldots l_k=1,m_k=0,\ldots\rangle$$

$$+\frac{6}{5}\sqrt{\frac{2}{7}}\Big|\ldots l_k=3,m_k=1,\ldots l_p=2,m_p=-1,\ldots\rangle-\frac{2}{5}\Big|\ldots l_k=1,m_k=1,\ldots$$

$$\ldots l_p=2,m_p=-1,\ldots\rangle$$

$$+\frac{2}{5}\sqrt{\frac{2}{7}}\Big|\ldots l_k=3,m_k=1,\ldots l_p=2,m_p=-1,\ldots\rangle-\frac{4}{5}\Big|\ldots l_k=1,m_k=1,\ldots$$

$$\ldots l_p=2,m_p=-1,\ldots\rangle$$

$$-\frac{4}{\sqrt{35}}\Big|\ldots l_k=3,m_k=2,\ldots l_p=2,m_p=-2,\ldots\rangle\Big\}\Big]. \tag{5.10}$$

From this equation, it is clear that the equation of motion for $G_{21,1\bar{1}}$ will introduce a number of higher order Green's functions, and to make things mathematically manageable, we must introduce a procedure to truncate these equations. The different terms occurring here correspond to different bands whose mean position is approximately given by the diagonal expectation value K of that term. The mean field approximation was obtained by retaining terms up to $K=2$. The next order approximation is obtained by keeping terms with $K\leqslant 8$. Retaining such terms reduces (5.10) to

$$W^+|\ldots l_k=2,m_k=1,\ldots,l_p=1,m_p=-1,\ldots\rangle=\frac{4}{\tau}\Big|\ldots l_k=2,m_k=1,\ldots,l_p=1,$$

$$m_p=-1,\ldots\rangle+\frac{\beta}{4\tau}\Bigg[-\frac{2}{3}\left(1+\frac{1}{\sqrt{5}}\right)\sum_{j\neq k}J_{pj}|\ldots l_k=2,m_k=1,\ldots$$

$$\ldots l_j=1,m_j=-1,\ldots\rangle+J_{kp}\Bigg\{-\frac{2}{5}\left(\frac{2}{\sqrt{7}}+\frac{1}{\sqrt{3}}\right)\Bigg|\ldots l_k=1,m_k=0,\ldots$$

$$\ldots l_p=2,m_p=0,\ldots\rangle+\frac{2}{\sqrt{5}}\left(\frac{1}{3}+\frac{2}{\sqrt{7}}\right)\Bigg|\ldots l_k=1,m_k=0,\ldots\rangle$$

$$-\frac{6}{5}\Big|\ldots l_k=1,m_k=1,\ldots l_p=2,m_p=-1,\ldots\rangle\Bigg\}\Bigg]. \tag{5.11}$$

Using this truncated equation, one obtains the following equation for $\tilde{G}_{21,1\bar{1}}(\mathbf{q}_1,\mathbf{q}_2;z)$,

$$\tilde{G}_{21,1\bar{1}}(\mathbf{q}_1,\mathbf{q}_2;z)=\frac{1}{-iz+r(q_1)+\frac{3}{\tau}+\frac{\beta}{6\tau}\left(1-\frac{1}{\sqrt{5}}\right)J(q_1)}\Bigg[C_{21,1\bar{1}}(\mathbf{q}_1,\mathbf{q}_2)$$

$$-\frac{\beta}{2}J(q_2)\Bigg\{\left(\frac{2}{\sqrt{7}}+\frac{1}{\sqrt{3}}\right)\left(-\frac{1}{5}\tilde{G}_{20,10}(\mathbf{q}_1,\mathbf{q}_2;z)+\frac{1}{\sqrt{5}}\tilde{G}_{10,10}(\mathbf{q}_1;z)\right)$$

$$-\frac{3}{5}\tilde{G}_{2\bar{1},11}(\mathbf{q}_1,\mathbf{q}_2;z)\Bigg\}\Bigg]. \tag{5.12}$$

Similarly, one can obtain the following equations for $\tilde{G}_{2\bar{1},11}(\mathbf{q}_1,\mathbf{q}_2;z)$ and $\tilde{G}_{20,10}(\mathbf{q}_1,\mathbf{q}_2;z)$

$$\tilde{G}_{2\bar{1},11}(\mathbf{q}_1,\mathbf{q}_2;z)=\frac{1}{-iz+r_{(q_1)}+\frac{3}{\tau}+\frac{\beta}{6\tau}\left(1-\frac{1}{\sqrt{5}}\right)J(q_1)}\Bigg[C_{2\bar{1},11}(\mathbf{q}_1,\mathbf{q}_2)$$

$$-\frac{\beta}{2\tau}J(q_2)\Bigg\{-\frac{1}{5}\left(\frac{1}{\sqrt{3}}+\frac{2}{\sqrt{7}}\right)\tilde{G}_{20,10}(\mathbf{q}_1,\mathbf{q}_2;z)-\frac{3}{5}G_{21,1\bar{1}}(\mathbf{q}_1;\mathbf{q}_2;z)$$

$$+\frac{1}{\sqrt{5}}\left(\frac{1}{\sqrt{3}}+\frac{2}{\sqrt{7}}\right)\tilde{G}_{10,10}(\mathbf{q}_1;z)\Bigg] \tag{5.13}$$

and

$$\tilde{G}_{20,10}(\mathbf{q}_1,\mathbf{q}_2;z)=\frac{1}{-iz+r_{(q_1)}+r_{(q_2)}+\frac{2}{\tau}-\frac{7}{15}\beta J(q_2)}\Bigg[C_{20,10}(\mathbf{q}_1,\mathbf{q}_2)$$

$$-\frac{\beta}{2\tau}J(q_2)\Bigg\{-\frac{2}{5}\tilde{G}_{10,10}(\mathbf{q}_1;z)-\frac{3}{5\sqrt{7}}\tilde{G}_{21,1\bar{1}}(\mathbf{q}_1,\mathbf{q}_2;z)+\tilde{G}_{2\bar{1},11}(\mathbf{q}_1,\mathbf{q}_2;z)\Bigg\}\Bigg] \tag{5.14}$$

Since this is a closed set of equations, one can obtain an expression for $G_{10,10}(\mathbf{q};z)$ to be

$$\tilde{G}_{10,10}(\mathbf{q};z) = \frac{A(\mathbf{q},z)}{\left[r_q - iz - \left\{\frac{\beta}{2N}\sum_{q_1} J_{(q_1)} \frac{1}{\sqrt{15}}\left(a_3 b_3 + \frac{\Gamma_2}{5} a_1 b_1 d_2 a_2 - \frac{\Gamma_2 a_1}{5} + \frac{3}{5}\Gamma_2 b_3 a_3\right) - \frac{2 d_2 a_2}{3\sqrt{5}}\right\}\right]} \tag{5.15}$$

with

$$A(\mathbf{q};z) = C_{10,10}(\mathbf{q}) + \frac{1}{\sqrt{15}}\left(b_3 d_3 + \frac{\Gamma_2}{5} a_1 b_1 d_2 + \frac{3}{5}\Gamma_2 b_3 d_3 - \frac{2 d_2}{\sqrt{3}}\right) \times C_{20,10}(\mathbf{q}_1, \mathbf{q}_2)$$

$$+ \frac{1}{\sqrt{15}}\left(b_3 + d_3 b_3 b_2 + \frac{\Gamma_2}{5} a_1 b_1 d_2 b_2 + \frac{3}{5}\Gamma_2 b_3 + \frac{3}{5}\Gamma_2 d_3 b_2 b_3 - \frac{2 d_2 b_2}{\sqrt{3}}\right) \times C_{21,1\bar{1}}(\mathbf{q}_1, \mathbf{q}_2)$$

$$+ \frac{1}{\sqrt{15}}\left(d_3 b_3 b_2 + b_1 + \frac{2}{5} a_1 b_1 d_2 b_2 + \frac{3}{5}\Gamma_2 d_3 b_2 b_3 - \frac{2 d_2 b_2}{\sqrt{3}}\right) \times C_{2\bar{1},11}(\mathbf{q}_1, \mathbf{q}_2)$$

$$a_1 = \frac{2}{\sqrt{7}} + \frac{1}{\sqrt{3}}, \quad \Gamma_2 = \frac{\beta J(q_2)}{\tau}$$

$$b_1(\mathbf{q};z) = \frac{1}{-iz + r_{(q_1)} + \frac{3}{\tau} + \frac{\beta}{6\tau}\left(1 - \frac{1}{\sqrt{5}}\right) J(\mathbf{q}_1)}$$

$$d(\mathbf{q};z) = \frac{1}{-iz + r_{(q_1)} + r_{(q_2)} + \frac{2}{\tau} - \frac{7}{15}\frac{\beta J(q_2)}{\tau}}$$

$$d_2(\mathbf{q};z) = \frac{d(\mathbf{q};z)}{1 - \frac{6 a_1 b_1 d \Gamma_2^2}{25\sqrt{7}\left(1 - \frac{3}{5} b_1 \Gamma_2\right)}}$$

$$b_2(\mathbf{q};z) = \frac{3\Gamma_2 b_1}{5\sqrt{7}\left(1 - \frac{3}{5} b_1 \Gamma_2\right)}$$

$$a_2(\mathbf{q};z) = \frac{2}{5}\Gamma_2\left\{1 - \frac{3 a_1 b_1 \Gamma_2}{\sqrt{35}\left(1 - \frac{3}{5} b_1 \Gamma_2\right)}\right\}$$

$$d_3(\mathbf{q};z)=\frac{\Gamma_2 a_1}{5}\left(1-\frac{3}{5}\Gamma_2 b_1\right)d_2$$

$$b_3(\mathbf{q};z)=\frac{b_1}{1+\left(\frac{3}{5}b_1\Gamma_2\right)^2}$$

$$a_3(\mathbf{q};z)=\frac{\Gamma_2 a_1}{\sqrt{5}}\left(1-\frac{3}{5}b_1\Gamma_2\right)\left(\frac{d_2 a_2}{\sqrt{5}}-1\right).$$

These equations have interesting implications which can be fully understood only by their numerical evaluation. They are in the spirit of usual field theory results as corrections occurs by addition of self energy terms to the denominator and to the spectral weight. However, we do not present such results here as in a later paper we shall study these equations numerically and extend the formalism to the critical dynamics.

6. Concluding remarks

To summarize, we have introduced in this paper a new method to deal with the statistical dynamics of vector spin systems. The method builds a series of approximations by systematically restricting the Hilbert space for the Fokker–Planck operator. Since the method is different from the usual field-theoretic methods, we expect that its numerical study will lead to elucidation of the notion of universality in dynamic critical behaviour. The method also reveals interesting qualitative features about the hierarchy in the relaxation spectrum of vector spin systems. This hierarchical feature which we believe has been pointed out for the first time, should provide new methods to implement renormalization group ideas in the studies of the dynamics of vector spin systems.

Appendix 1

$$B_{\pm}(l_k,m_k)=[(l_k\mp m_k)(l_k\pm m_k+1)]^{1/2}$$

$$A_{0+}(l,m)=\left[\frac{(l+m+1)(l-m+1)}{(2l+1)(2l+3)}\right]^{1/2}$$

$$A_{0-}(l,m)=\left[\frac{(l+m)(l-m)}{(2l+1)(2l+3)}\right]^{1/2}$$

$$A_{++}(l,m)=-\left[\frac{(l+m+1)(l+m+2)}{(2l+1)(2l+3)}\right]^{1/2}$$

$$A_{+-}(l,m)=\left[\frac{(l-m)(l-m-1)}{(2l+1)(2l-1)}\right]^{1/2}$$

$$A_{-+}(l,m)=\left[\frac{(l-m+1)(l-m+2)}{(2l+1)(2l+3)}\right]^{1/2}$$

$$A_{--}(l,m)=\left[\frac{(l+m)(l+m-1)}{(2l+1)(2l-1)}\right]^{1/2}$$

$$
\begin{aligned}
&g|\ldots l_k, m_k+\mu_k, \ldots, l_p+\sigma_p, m_p+\mu_p \ldots\rangle \\
&\quad = m_k\{A_{0+}(l_p, m_p)|\ldots l_k, m_k, \ldots, l_p+1, m_p \ldots\rangle \\
&\qquad + A_{0-}(l_p, m_p)|\ldots l_k, m_k, \ldots, l_p-1, m_p \ldots\rangle\} \\
&\quad + \frac{1}{2}B_+(l_k, m_k)\{A_{-+}(l_p, m_p)|\ldots l_k, m_k+1, \ldots, l_p+1, m_p-1, \ldots\rangle \\
&\qquad + A_{--}(l, m_p)|\ldots l_k, m_k+1, \ldots, l_p-1, m_p-1, \ldots\rangle\} \\
&\quad + \frac{1}{2}B_-(l_k, m_k)\{A_{++}(l_p, m_p)|\ldots l_k, m_k-1, \ldots, l_p+1, m_p+1, \ldots\rangle \\
&\qquad + A_{+-}(l_p, m_p)]\ldots l_k, m_k-1, \ldots, l_p-1, m_p+1, \ldots\rangle\} \\
&\sum_{\sigma_k, \sigma_p, \mu_k, \mu_p} f|\ldots l_k+\sigma_k, m_k+\mu_k, \ldots, l_p+\sigma_p, m_p+\mu_p \ldots\rangle \\
&\quad = m_k\Big\{A_{++}(l_k, m_k)\sum_{\sigma_p=\pm} A_{-\sigma_p}(l_p, m_p)|\ldots l_p+\sigma_p, m_p-1, \ldots, \\
&\qquad\qquad l_k+1, m_k+1, \ldots\rangle \\
&\qquad + A_{+-}(l_k, m_k)\sum_{\sigma_p=\pm} A_{-\sigma_p}(l_p, m_p)|\ldots l_p+\sigma_p, m_p-1, \ldots, l_k-1, m_k+1, \ldots\rangle \\
&\qquad - A_{-+}(l_k, m_k)\sum_{\sigma_p=\pm} A_{+\sigma_p}(l_p, m_p)|\ldots l_p+\sigma_p, m_p+1, \ldots, l_k+1, m_k-1, \ldots\rangle \\
&\qquad - A_{--}(l_k, m_k)\sum_{\sigma_p=\pm} A_{+\sigma_p}(l_p, m_p)|\ldots l_p+\sigma_p, m_p+1, \ldots, l_k-1, m_k-1, \ldots\rangle\Big\} \\
&\quad + B_-(l_k, m_k)\Big\{A_{0+}(l_k, m_k-1)\sum_{\sigma_p=\pm} A_{+\sigma_p}(l_p, m_p)|\ldots l_p+\sigma_p, m_p+1, \ldots \\
&\qquad\qquad \ldots, l_k+1, m_k-1, \ldots\rangle \\
&\qquad + A_{0-}(l_k, m_k-1)\sum_{\sigma_p=\pm} A_{+\sigma_p}(l_p, m_p)|\ldots l_p+\sigma_p, m_p+1, \ldots, m_k-1 \ldots\rangle \\
&\qquad - A_{++}(l_k, m_k-1)\sum_{\sigma_p=\pm} A_{0\sigma_p}(l_p, m_p)|\ldots l_p+\sigma_p, m_p, \ldots, l_k+1, m_k, \ldots\rangle \\
&\qquad - A_{+-}(l_k, m_k-1)\sum_{\sigma_p=\pm} A_{0\sigma_p}(l_p, m_p)|\ldots l_p+\sigma_p, m_p, \ldots, l_k-1, m_k, \ldots\rangle\Big\} \\
&\quad + B_+(l_k, m_k)\Big\{A_{-+}(l_k, m_k+1)\sum_{\sigma_p=\pm} A_{0\sigma_p}(l_p, m_p)|\ldots l_p+\sigma_p, m_p, \ldots \\
&\qquad\qquad \ldots l_k+1, m_k, \ldots\rangle \\
&\qquad + A_{--}(l_k, m_k+1)\sum_{\sigma_p=\pm} A_{0\sigma_p}(l_p, m_p)|\ldots l_p+\sigma_p, m_p, \ldots l_k-1, m_k, \ldots\rangle
\end{aligned}
$$

$$- A_{0+}(l_k, m_k + 1) \sum_{\sigma_p = \pm} A_{-\sigma_p}(l_p, m_p) | \ldots l_p + \sigma_p m_p, \ldots l_k + 1, m_k + 1, \ldots \rangle$$

$$\left. - A_{0-}(l_k, m_k + 1) \sum_{\sigma_p = \pm} A_{-\sigma_p}(l_p, m_p) | \ldots l_p + \sigma_p, m_p, \ldots, l_k - 1, m_k - 1, \ldots \rangle \right\}$$

References

[1] Kamlesh Kumari and Deepak Kumar, *Pramana – J. Phys.* **35**, 115 (1990)
[2] P C Hohenberg and B I Halperin, *Rev. Mod. Phys.* **49**, 435 (1977)
[3] C P Enz, *Dynamic critical phenomena and related topics* (Springer-Verlag, Heidelberg, 1979)
[4] R Kubo and Hashitsume, *Prog. Theor. Phys. Suppl.* **66**, 210 (1970)
[5] L D Landau and E M Lifshitz, *Phys. Z. Sowjetunion* **8**, 153 (1935)
[6] S F Edwards and P W Anderson, *J. Phys.* **F6**, 1927 (1976)

PRAMANA
— journal of
physics

© Printed in India

Vol. 43, No. 4,
October 1994
pp. 307–312

Collective mechanism for nuclear stopping and transverse flow in heavy-ion collisions

JITESH R BHATT, PREDHIMAN K KAW and JITENDRA C PARIKH†
Institute for Plasma Research, Bhat, Gandhinagar 382424, India
†Physical Research Laboratory, Navrangpura, Ahmedabad 380009, India

MS received 19 July 1994

Abstract. The role of filamentation instability of quark-gluon plasma, in explaining collective phenomena in relativistic heavy-ion collisions, has been analyzed. Using equations of SU(2) two fluid color hydrodynamics it is shown that this instability can significantly enhance nuclear stopping and might contribute to collective sideward flows.

Keywords. Heavy ion collisions; stopping power; collective mechanism.

PACS No. 12·38

Recently certain models [1] of nuclear collisions have shown that collective effects may become very significant in collisions of very heavy nuclei at relativistic energies. Numerical studies have shown that for Pb–Pb collisions, complete stopping may occur and collective sideward flow would be generated. The collision experiments of very heavy nuclei at this energy (~ 200 GeVA) have not yet been performed [2] but one tends to take the predictions of the models seriously because these models have been successful in explaining experimental data and observed partial transparency in collisions of light nuclei. A drawback of these models is that they require detailed and involved microscopic description of nuclear collisions [3] which fails to give one an insight into the observed collective phenomena. As a complementary intuitive picture, it is therefore important to look for a simple QCD based collective mechanism which can exhibit similar specific features. In this paper we consider one such mechanism viz. the filamentation instability.

If we assume in conformity with collisions of light nuclei, that transparency would set in collisions of heavy nuclei at energy ~ 200 GeVA, then the nuclear collision may be regarded as counter streaming color fluxes. Under these conditions instabilities related particularly with plasma streaming [4] are of interest. It is well-known that for relativistic plasma streams, the most important instability is the so-called filamentation instability [4], which leads to stratification of initially homogeneous and oppositely directed plasma fluxes interacting via mean vector fields [4] (gluon field for QGP). The mean fields are mixed waves (longitudinal + transverse) which for strongest instability have the propagation vector in a direction perpendicular to the stream velocity [4]. We have used SU(2) color hydrodynamic [5] (CHD) equations to describe the filamentation instability. Our work differs from earlier works [4] in that it describes both *linear* and *non-linear* aspects of filamentation instability and is therefore able to address questions related to collective stopping and sideward flow generation. We believe this is one of the first studies [6], which includes full non-

abelian physics for examining dynamic collective phenomena of QGP in classical limit. Basic CHD equations, which can be obtained from the QCD Lagrangian [7], contain three continuous physical quantities: density n, velocity field $\mathbf{V}$ and color charge vector $I_a (a = 1, 2, 3)$ which are functions of space-time and their dynamics is described by CHD equations [5]

$$\partial_t n_A + \nabla \cdot (n_A \mathbf{V}_A) = 0, \tag{1}$$

$$\partial_t \mathbf{V}_A + \mathbf{V}_A \cdot \nabla \mathbf{V}_A = (g/m_A)\sqrt{1 - V_A^2}\, I_{Aa}[\mathbf{E}_a + \mathbf{V}_A \times \mathbf{B}_a - \mathbf{V}_A(\mathbf{V}_A \cdot \mathbf{E}_a)], \tag{2}$$

$$\partial_t I_{Aa} + \mathbf{V}_A \cdot \nabla I_{Aa} = -g\varepsilon_{abc}[A_b^0 - \mathbf{V}_A \cdot \mathbf{A}_b] I_{Ac}, \tag{3}$$

In (1)–(3) the suffix A and m_A denote species label of color particles and mass of species A respectively. For light relativistic quarks mass m_A is replaced by (enthalpy density/number density) for the relevant quark fluid [5]; this then reproduces well-known perturbative QCD results. ε_{abc} is the Levi-Civita tensor and $A_a^\mu (\mu = 0, 1, 2, 3)$ are SU(2) gauge potentials which satisfy Yang-Mills equations $\partial_\mu F_a^{\mu\nu} + g\varepsilon_{abc} A_{\mu b} F_c^{\mu\nu} = j_a^\nu$. Here, j_a^ν represents matter current which can be expressed in terms of CHD variables as $j_a^0 = g\Sigma_A n_A I_{Aa}$ and $\mathbf{j}_a = g\Sigma_A n_A \mathbf{V}_A I_{Aa}$. Equations (1)–(3) together with Yang-Mills equations form a closed set of Lorentz and gauge covariant equations [8] which describe the evolution of the QGP self consistently. It should be noted that among the CHD variables n_A and $\mathbf{V}_A$ are gauge invariant quantities while the color vector I_{Aa} transforms gauge covariantly [8].

We consider the *simplest* SU(2) color hydrodynamic *model* for the nuclear collision: two species $A = 1, 2$ having the same mass are counter streaming with velocity $\pm V_0 (\sim 1)$ in the z-direction and their anti-particles are assumed to form an overall static colour neutralizing background. This is a simplified model for the true dynamics and its justification is given below. Both species are assumed to have homogeneous equilibrium densities and colour charge vectors which are assumed to be equal. We consider a filamentation mode propagating along x with electric field components along x and z and magnetic field components along y. After linearizing the equations and taking perturbations of the form $\exp[-i(kx - \omega t)]$ and making the gauge choice $A_a^0 = 0$, we obtain the dispersion relation $\omega_\pm^2 = k^2/2[1 \pm \sqrt{(1 + 8\omega_p^2 k^{-2})}]$ where, $\omega_p^2 = g^2 \rho_0 I_{0a}^2/m$ and ρ_0 is the equilibrium number density in the rest frame of color stream. Clearly the negative root of the dispersion relation gives rise to an instability. As ω_-^2 increases with k, the most unstable modes have $k^2 \gg \omega_p^2$ and in the lowest order in ω_p^2/k^2 one gets $\omega_-^2 \cong -2\omega_p^2$; this result is in agreement with linear kinetic theory result obtained by Mrowczynski [4]. If all four species had been taken as mobile, the space charge contributions simply add up and we get the same dispersion relation as above with ω_p^2 replaced by $2\omega_p^2$. Thus we see that our simpler model problem does not sacrifice significant physics. However, it gives us a considerable reduction in the number of nonlinear differential equations to be solved and it is our justification for using the simpler model. The linear analysis also shows that the color electric field is always opposite to the stream current direction. This provides a collective mechanism for deceleration of stream velocity as was also noted by Ivanov [9] in the context of hadron plasma. The minimum time in which the instability can grow is $t_{min} \sim |\omega_-|^{-1}$. If one uses finite temperature perturbative QCD value for ω_p for temperature range 160–200 MeV one finds $t_{min} \sim 0{\cdot}5$–$0{\cdot}7$ fm/c. This estimate is very conservative as smallness of g is assumed in the perturbative calculations. However, non-perturbative estimate of ω_p may be higher [8] and t_{min} can be further

reduced. We compare t_{min} with the total interaction time between the two nuclei [4], $t_{int} \sim 2r_0 A^{1/3} \sqrt{\frac{2M_N}{E_{Lab}}}$ where, A is the atomic number and $r_0 = 1{\cdot}2$ fm. For $U+U$ collisions at $E_{Lab} \simeq 200$ GeVA one gets $t_{int} \sim 1{\cdot}5$ fm/c. As $t_{min} < t_{int}$ the filamentation mode may indeed occur in RHIC (relativistic heavy ion collision) and drive up initial fluctuations. Since the number of e-foldings (t_{int}/t_{min}) is not very large, it is important to ascertain the initial fluctuation level. This can be done by comparing the ratio of field energy E_w to thermal energy E_{th} with the plasma parameter $\beta_p \sim 1/n\lambda_D^3$. Estimating these quantities we obtain

$$\frac{E_w}{E_{th}} \sim \frac{\omega_p^2 A^2}{T^4} \sim \frac{g^2 A^2}{T^2} \sim \beta_p$$

and using typical values of λ_D, n and T one gets $gA/\omega_p \sim 10^{-1}$. Thus within a time interval of a few t_{min} the perturbations will grow to a value where the analysis of the non-linear state generated by the instability can become important for RHIC.

For the study of the non-linear state the basic equations constitute a set of eighteen coupled non-linear partial differential equations which are very difficult to solve in their generality. Therefore we look for special solutions of these equations which are non-linear plane stationary waves [8]. Thus we assume that all the quantities depend just on a single variable $\zeta = x + \beta t$. Physically this means that we sacrifice our desire to reproduce the evolution of a linear instability into its saturated nonlinear state and instead focus on the question 'are there nonlinear superpositions of various wavelengths which give a state that is stationary in a moving frame?'. The implication is that if such nonlinear solutions exist, then the unstable waves are likely to saturate into these states. The parameter β expresses the ratio of the phase velocity of the nonlinear plane wave to the velocity of light and may take any value greater than 1. For a dilute plasma a value close to 1 may be assumed, although our calculations show that results are not very sensitive to its choice. With this assumption it is possible to integrate all the differential equations of hydrodynamics except those which correspond to color dynamic equations of one specie. If we introduce dimensionless variables $T = \Omega_p \zeta$, $A_{xa} = a_0^{-1} A_a^x$, $A_{za} = a_0^{-1} A_a^z$, $I_a = i_0^{-1} I_{1a}$, $V_{Ax} = \theta^{-1} V_A^x$ and $V_{Az} = \theta^{-1} V_A^z$ where i_0, a_0, θ and Ω_p are some normalizing factors, then the resulting equations can be written as

$$\dot{I}_a = \frac{\theta\alpha}{\beta} N_1 \varepsilon_{abc} [V_{1x} A_{xb} + V_{1z} A_{zb}] I_c, \tag{4}$$

$$\beta^2 \ddot{A}_{xa} - \alpha\varepsilon_{abc} A_{zb} \dot{A}_{zc} + \alpha^2 [(A_{zb})^2 A_{xa} - (A_{xb} A_{zb}) A_{za}] = j_{xa}, \tag{5}$$

$$(\beta^2 - 1)\ddot{A}_{za} + \alpha\varepsilon_{abc} [2A_{xb} \dot{A}_{zc} + \dot{A}_{xb} A_{zc}] + \alpha^2 [(A_{xb})^2 A_{za} - (A_{xb} A_{zb}) A_{xa}] = j_{za}, \tag{6}$$

where $N_1 = \beta/(\beta + \theta V_{1x})$ and dot denotes differentiation with respect to T. We have introduced three dimensionless parameters $\theta = gi_0 a_0/m$, $\Omega_p = \omega_p (1 - V_0^2)^{-1/4}$ and $\alpha = ga_0/\Omega_p$. The parameter θ essentially measures the ratio of canonical momentum to mass and hence is related to the velocity which could have value $\sim 10^{-1}$. The parameter α characterizes the strength of non-abelian terms in (6)–(8) and may be expressed in terms of other physical parameters $\alpha = gi_0 a_0/\omega_p = g\sqrt{mn_0}(\theta/\omega_p^2)$ which also have values in the same range as θ. Expressions for V_{Ax}, V_{Az} in terms of A_x, A_z

etc. have been obtained but are too lengthy to be reproduced here. Equations (4)–(6) are a set of nine coupled non-linear ordinary differential equations which have been solved numerically, using a fourth order variable step size Runge-Kutta method of sufficient accuracy. Energy and color charge conservation laws derived from the equations have been used as a check on the numerical scheme.

Typical results obtained from (4)–(6) are depicted in figures 1 to 3. Figure 1 depicts variation of V_{2z} with T. It clearly shows that for a choice of the non-abelian parameter $\alpha = 0{\cdot}5$, the mean flow in the nonlinear saturated state is $\simeq -0{\cdot}3$, well below the value $V_{2zO} = -9{\cdot}0$ that we start with at $T = 0$. One may see the stream deceleration as the nonlinear state sets up more clearly in figure 2, which depicts the auto-correlation of V_{2z}. Though the autocorrelation function oscillates a little, it shows an overall decay which shows that the flow velocity fields become chaotic in the nonlinear state. Figure 3 depicts the plot of V_{2x} with T. The figure shows that the transverse flow velocity is also chaotic in the nonlinear state but has acquired a mean value around 0·3. It is to be noted that the generation of mean transverse flow is a consequence of momentum conservation and growth of mixed wave propagating transversely. Looked at another way, the excited nonlinear waves generate a mean force in the transverse direction [$(\tilde{V}_z \times \tilde{B}_y)$ terms etc.] which produces a mean transverse flow. It must be emphasized that this feature of generation of transverse flows is completely independent of choice of initial conditions. Our non-linear theory assumes a given wave propagation direction and generates anisotropic flows. In an experiment, however, the transverse waves and flows will be isotropically distributed. The rearrangement from the initial conditions to set up the nonlinear state leads to

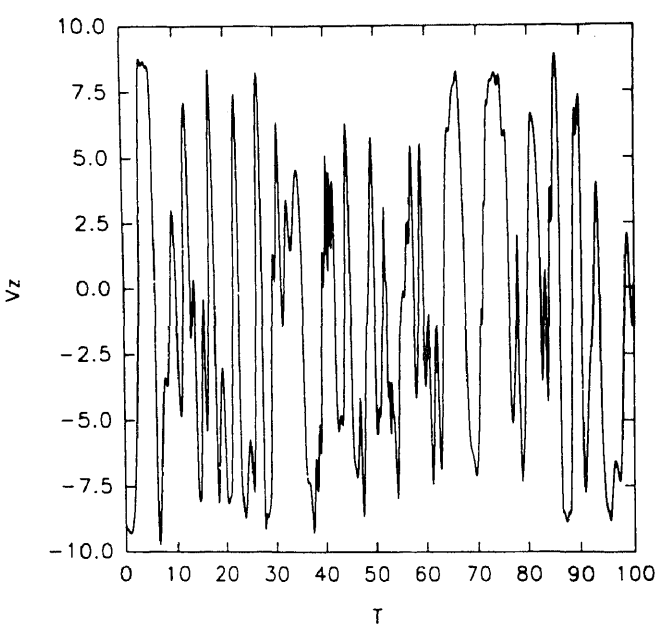

Figure 1. z-component of the flow velocity of specie 2 is plotted as function of T. The values of parameters are $\beta = 1{\cdot}1$, $\theta = 0{\cdot}1$ and $\alpha = 0{\cdot}5$. The intial velocity $V_0 = -9$ (in units of θ). The initial conditions are $I_{1a} = 1$; $(a = 1, 2, 3)$, $A_{xa} = A_{za} = 0$ and $\dot{A}_{x1} = 1{\cdot}4$, $\dot{A}_{x2} = 0{\cdot}2$, $\dot{A}_{x3} = 0{\cdot}3$, $\dot{A}_{z1} = 0{\cdot}2$, $\dot{A}_{z2} = -0{\cdot}3$, $\dot{A}_{z3} = 1{\cdot}1$. Mean velocity $= -3{\cdot}0$.

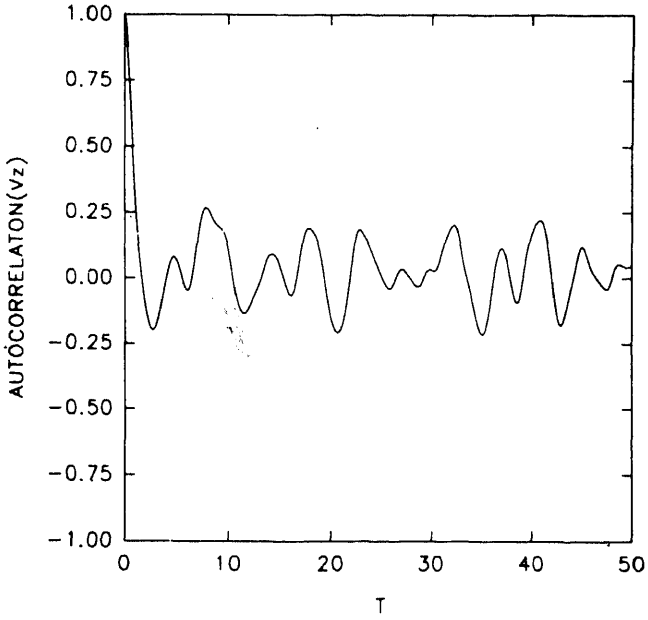

Figure 2. Auto-correlation of the velocity profile shown in figure 1.

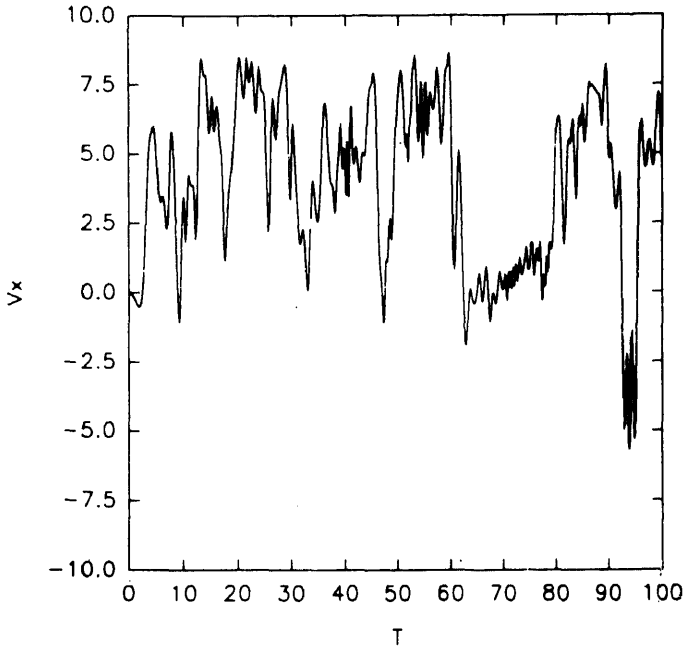

Figure 3. Transverse component of the flow velocity of specie 2 as a function of T. The mean velocity = 2·7 (in units of θ). Values of parameters and initial conditions are same as those in figure 1.

a conversion of about 90 per cent of the energy in coherent flows into chaotic oscillations and is characterized by a few plasma periods. Taking a typical plasma frequency ~ 200 MeV, this corresponds to a time-scale of order 1–2 fm/c which is smaller than a plasma life time of order several fm/c. This is consistent with thermalization time estimated by Shuryak [3]. Thus, (i) the linear growth times and nonlinear interaction times needed for setting up a chaotic nonlinear state are well within the plasma life-time, (ii) in the nonlinear plane wave states, the mean kinetic energy along z is considerably reduced and a net mean V_x is generated. Detailed investigations have shown that these numerical results are relatively independent of the choice of parameter β (i.e. phase velocity of nonlinear wave) and other initial conditions. They do, however, critically depend on the non-abelian parameter α. For $\alpha = 0$, we get prototype abelian plasma equations which when numerically integrated show negligible reduction of the initial V_z in the nonlinear state, and does not show generation of significant mean V_x. This seems to be related to the fact that in this case, solutions tend to be coherent and $\tilde{V} \times \tilde{B}$ forces phase average to a negligible value. Thus the collective stopping and transverse flow generation seems to be a specifically non-abelian effect. It may be stressed that had we used four mobile species instead of two, the coupled non-linear equations would still have exhibited similar chaotic behaviour.

In conclusion, we have shown that starting with an assumption of transparency one ends up in a non-linear state showing significant stopping due to non-abelian collective effects. This indicates that one fluid description might be justified for collisions of very heavy nuclei. Our results also indicate the presence of mean collective flow in the transverse direction. Our analysis also indicates that due to the mechanism we have considered baryon rich matter could be created in the central rapidity region.

References

[1] A B Kaidalov, *Nucl. Phys.* **A525**, 39c (1991);
Ch. Hartnack *et al Nucl. Phys.* **A538**, 53c (1992) and references cited therein
N S Amelin *et al*, *Phys. Lett.* **B261**, 352 (1991) and references cited therein
N S Amelin *et al*, *Phys. Rev. Lett.* **67**, 1523 (1991)
[2] H Gutbrod, *Nucl. Phys.* **A538**, 671c (1992)
[3] E Shuryak, *Phys. Rev. Lett.* **68**, 3270 (1992)
[4] S Mrowczynski, *Phys. Lett.* **B219**, 587 (1988)
Yu B Ivanov, *Nucl. Phys.* **A474**, 693 (1987)
Yu Prokovski and A Selikhov, *JETP. Lett.* **47**, 12 (1988)
[5] K Kajantie and C Montonen, *Phys. Scr.* **22**, 555 (1981)
[6] B Müller and A Trayanov, *Phys. Rev. Lett.* **68**, 3387 (1992) and see also Ref. (8)
[7] S K Wong, *Nuovo Cimento* **A65**, 689 (1970) and see also Ref. (5)
[8] J R Bhatt, P K Kaw and J C Parikh, *Phys. Rev.* **D39**, 646 (1989)
[9] Yu B Ivanov, in *Nuclear equation of state*, edited by W Greiner and H Stöcker, (Plenum, New-York, 1989) Part B
[10] H Sorge *et al*, *Phys. Rev. Lett.* **68**, 268 (1992)

PRAMANA
— journal of
physics

© Printed in India

Vol. 43, No. 4,
October 1994
pp. 313–317

Effect of two body core on the charge form factor of ^{3}He including three body force and meson exchange current

KALYANI PRASAD KANTA and TAPAN KUMAR DAS
Department of Physics, University of Burdwan, Burdwan 713 104, India
Department of Physics, University of Calcutta, 92, APC Road, Calcùtta 700 009, India

MS received 4 November 1993; revised 4 July 1994

Abstract. We compare the effect of two body core on the charge form factor of ^{3}He by the hyperspherical harmonics expansion method using various 2BF potentials with the inclusion of three body force. We also include the meson exchange current contribution to the CFF for the same potentials in addition to the 3BF. The results indicate that the combined effect of 3BF and MEC (i) moves q^2_{min} (the first diffraction minimum) appreciably to the left, amount of shift depends on the 2BF at $r_{12} \sim 0{\cdot}7$ fm and (ii) enhances F_{max} (the height of the secondary maximum of CFF) by an appreciable amount, the increment in general increases with the repulsive core of 2BF ($r \leqslant 0{\cdot}1$ fm).

Keywords. Charge form factor; three body force; hyperspherical harmonics expansion.

PACS No. 21·40

Experimentally observed charge form factor (CFF) of the trinucleon system has long eluded complete theoretical understanding. The observed first diffraction minimum (q^2_{min}) for ^{3}He occurs at $q^2_{min} = 11{\cdot}8\,\text{fm}^{-2}$ (q being the momentum transfer) and the magnitude of the secondary maximum (F_{max}) is about 6×10^{-3} at $q^2 = 15{\cdot}65\,\text{fm}^{-2}$ [1–3]. Calculations with standard two body force (2BF) produce q^2_{min} around $16\,\text{fm}^{-2}$ and $F_{max} \sim 10^{-3}$ [4–12]. A Fourier transform of experimental CFF with correction for finite size of the proton gives the point proton density, $\rho(r)$, which shows a pronounced central depression. Although it might be thought that a strongly repulsive 2BF core could produce a central hole in $\rho(r)$, it is immediately apparent that while such a core will produce a central hole for the equilateral triangle configuration (ETC), it will have no effect on the collinear configuration (CC), no matter how strong the repulsive core is. This is also borne out in theoretical calculations. A preference for ETC is provided by the nuclear three body force (3BF), which is attractive for ETC and repulsive for CC. However a 3BF without sufficiently strong repulsive 2BF core cannot produce a central hole and therefore fails to reproduce experimental CFF. Inclusion of standard 3BF [13–17] increases F_{max} slightly while q^2_{min} moves further out. Thus the effect of 3BF on CFF is marginal. However binding energy (BE) enhances by an appreciable amount, accounting for nearly the whole of the missing value in 2BF calculations.

In 1974 Kloet and Tjon [18] included meson exchange currents (MEC) contribution to the CFF of ^{3}He using standard 2BF and found that q^2_{min} moves closer to the experimental value and F_{max} increased to a value of about $2{\cdot}5 \times 10^{-3}$ at $q^2 = 16{\cdot}5\,\text{fm}^{-2}$. The contribution of the MEC at large momentum transfer is strongly

influenced by the nature of the wave function at very short separations, which in turn is determined by the softness of the 2BF core.

Thus the nature of the 2BF core is expected to play an important role in the behaviour of the CFF at large momentum transfers. This motivates us to study the behaviour of CFF for various 2BF with varying core softness when 3BF and MEC are included. We have adopted the hyperspherical harmonics expansion (HHE) method [10] to solve the trinucleon system. The ground state is represented by the space totally symmetric S-state for simplicity. Appropriate to this restriction, we choose only S-projected central (spin dependent or not) potentials. We concentrate our attention on two such potentials, viz Afnan–Tang S3 potential [19] and Malfleit–Tjon MTV potential [20]. In addition we have investigated softer potentials like (in increasing order of softness) Eikemeir–Hackenbroich S4 potential [21], Gogny-Pires–deTourreil (GPDT) potential [22], Volkov [23] and Baker potentials [24]. For the 3BF we choose the form given by Fujita–Miyazawa (FM-3BF) for the two pion exchange 3BF [25].

The exchange contribution to the CFF of ^{3}He is given by [18]

$$F_{ch}^{cz} = \frac{-g^2}{2(4\pi\sqrt{M})^3}[F_v(q^2) + G_v(q^2) + 3F_s(q^2) + 3G_s(q^2)]K(q^2) \tag{1}$$

where the function $K(q^2)$ is defined as,

$$K(q^2) = \int d\mathbf{p}_1 d\mathbf{p}'_1 d\mathbf{q}_1 \phi_0(p_1, q_1)\phi_0(p'_1, q'_1) \times \frac{q^2 - 2(\mathbf{p}_1 - \mathbf{p}'_1)\cdot\mathbf{q}\sqrt{M}}{\left[(\mathbf{p}_1 - \mathbf{p}'_1)\sqrt{M} - \frac{\mathbf{q}}{2}\right]^2 + \mu^2} \tag{2}$$

where $\phi_0(p, q)$ is the momentum space wave function for the S-state of trinucleon, $\mathbf{p}_1, \mathbf{q}_1$ are relative momenta and $q' = |\mathbf{q}_1 - (\mathbf{q}_1 - (\mathbf{q}/2\sqrt{3M})|$.

M and μ are the nucleon (939 MeV) and pion (139·6 MeV) masses respectively. F_v and F_s are respectively the isovector and isoscalar charge form factor of the nucleons, while G_v and G_s are its isovector and isoscalar magnetic form factors and are given in [26]. g is the πNN coupling constant.

Introducing Fourier transforms to express $K(q^2)$ in terms of the configuration space wave function $\psi(\mathbf{x}, \mathbf{y})$ obtained by the HHE method and doing the angular integrations analytically, we have

$$K(q^2) = \frac{4\pi^2 q}{M^{3/2}} \int \sum_{KK'} \mathcal{N}_K \mathcal{N}_{K'} u_K(r) u_{K'}(r) r^{-5/2\,(2)} P_{2K}^{00}(\phi)^{(2)} P_{2K'}^{00}(\phi)$$
$$\times j_0\left(\frac{qy}{2\sqrt{3}}\right) j_1\left(\frac{xq}{2}\right) \frac{\exp(-\mu x)}{x} x^2 y^2 \, dx\, dy \tag{3}$$

where $r = (x^2 + y^2)^{1/2}$ and $\tan\phi = x/y$ are the hyperspherical variables. The other quantities as well as the HHE method have been explained in other technical reports [10, 13]. The hyperradial wave function $u_K(r)$ is obtained by solving a set of coupled differential equations resulting from the HHE method. The contribution of MEC is then obtained by numerically evaluating the double integral (3).

The FM-3BF has a strong singularity (which goes as r^{-6} for $r \to 0$) and is attractive

for the equilateral triangle configuration. Unless regularized for very short separations, this will lead to unphysical results. Hence we introduce a phenomenological cut-off parameter (x_0), such that the 3BF is not allowed to diverge for $r < x_0$. For small values of x_0, the strongly attractive 3BF induces nodes near origin (NNO) in the ground state hyperradial wave function, which are manifestations of the unphysical nature of the 3BF interaction for such values of x_0. Hence we choose x_0 for each given 2BF by a criterion similar to that used by Das *et al* [13], namely x_0 should be such that no unphysical nodes appear in the hyperradial wave function, but F_{max} has the largest value. This highlights the effect of 3BF on F_{max} and may result in a somewhat larger value of F_{max}. However explicit calculations using the regularized FM-3BF ($C_p = 0{\cdot}9$, $x_0 = 0{\cdot}34$ fm) as well as Tucson–Melbourne (TM-3BF) [27] with $\Lambda^2 = 25$ and Brazil (BR-3BF) [28] with $\Lambda^2 = 25$ three body forces in addition to S3-2BF, produce respectively the values 1·580, 1·584 and 1·582 for F_{max} and 15·54 fm^{-2}, 15·85 fm^{-2} and 15·73 fm^{-2} for q^2_{min}. This demonstrates that the overall effect of the regularized FM-3BF is the same as other standard 3BF.

Inclusion of 3BF enhances calculated binding energy (BE) from 5·789 MeV to 6·485 MeV for the S3 potential and from 7·369 MeV to 8·361 MeV for the MTV potential. Calculated CFF's have been demonstrated in figures 1 and 2. In figure 1 we plot CFF of ^{3}He as a function of q^2 for 2BF (S3 and MTV) with and without MEC contribution. In figure 2, the same quantities are plotted when FM-3BF is added to the chosen 2BF. From these figures we see that with the inclusion of 3BF without MEC, q^2_{min} moves further out for both MTV and S3 potentials, while increment of F_{max} is marginal in both cases. However the effect of MEC is substantial for both. For

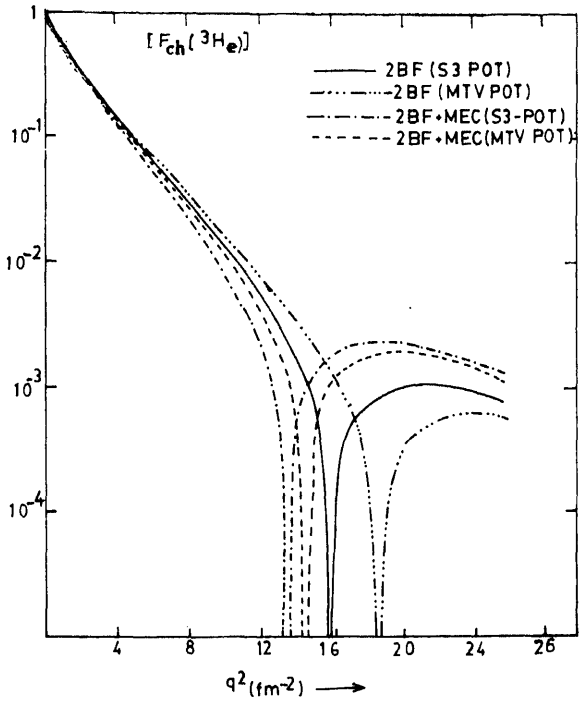

Figure 1. Absolute value of charge form factor of ^{3}He for 2BF with and without exchange correction.

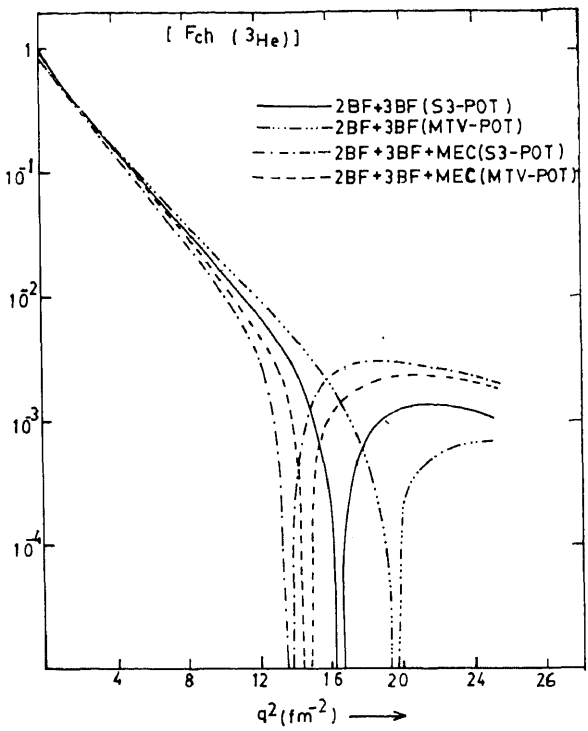

Figure 2. Absolute value of charge form factor of ^{3}He including 3BF with and without exchange correction.

S3 potential, values of q^2_{min} and F_{max} are 13·36 fm^{-2} and 2·24 × 10^{-3} respectively for MEC with 2BF alone. The corresponding values for MTV potential are 14·38 fm^{-2} and 1·85 × 10^{-3} respectively. For the MEC contribution in addition to 2BF plus 3BF, q^2_{min} and F_{max} take the values 13·61 fm^{-2} and 2·98 × 10^{-3} for S3 potential and 14·77 fm^{-2} and 2·37 × 10^{-3} for MTV potential. The MTV has a stronger repulsive core for $r_{ij} < 0{\cdot}1$ fm than S3 potential and we find the enhancement effects on q^2_{min} and F_{max} are larger in the direction of the experimental values for the MTV potential than the other. However the results including 3BF and MEC for MTV are worse than those for S3, since the CFF obtained with 2BF alone is far worse for MTV than S3 potential. From the calculations with other 2BF (Baker, Volkav, GPDT and S4) it was seen that enhancement effects on F_{max} due to the inclusion of 3BF and MEC generally increases with decreasing softness of the 2BF. Enhancement of BE due to the inclusion of 3BF over 2BF is fairly large and increases with decreasing softness of the 2BF core. The enhancement of q^2_{min} due to MEC contribution appears to be uncorrelated with 2BF core softness, if we consider the strengths of 2BF at ~ 0·1 fm, but it decreases as the value of 2BF at $r_{ij} \sim 0{\cdot}7$ fm increases. This may reflect the fact that $K(q^2)$ (eq. (3)) contains an oscillatory factor (through the spherical Bessel functions) and for a large value of $q(\sim 4\,\text{fm}^{-1})$ only small values of x and y should contribute. At very small values of x and y, the wave function itself decreases rapidly and the major contribution to $K(q^2)$ comes from intermediate values of x and y. As the attractive 2BF increases at such values of $x(=r_{12})$ and y which contribute dominantly to $K(q^2)$, the three body wave function $\psi(\mathbf{x}, \mathbf{y})$ increases and the contribution of MEC to CFF increases.

From the foregoing discussions we can draw the following conclusions.

(i) Inclusion of 3BF enhances BE, the enhancement being generally larger for stronger repulsive 2BF core ($r_{ij} \sim 0{\cdot}1$ fm).
(ii) Inclusion of 3BF increases F_{max} slightly but q^2_{min} moves in general outwards. Thus inclusion of 3BF makes the agreement of CFF worse.
(iii) Inclusion of MEC moves q^2_{min} inwards by appreciable amounts, the amount of shift appears to depend on the 2BF at $r_{12} \sim 0{\cdot}7$ fm.
(iv) Inclusion of MEC enhances F_{max} by an appreciable amount, the increment in general increases with the strength of repulsive core of 2BF ($r_{ij} \sim 0{\cdot}1$ fm).

In view of the above observations it may be concluded that the effects of the 3BF and MEC will be largest towards explaining the experimental data if the 2BF has (i) a very strong repulsive core at $r_{ij} \sim 0{\cdot}1$ fm and (ii) is strongly attractive at $r_{ij} \sim 0{\cdot}7$ fm.

This work has been financed by the DSA project of the Physics Department, Calcutta University, under a grant from the UGC, India.

References

[1] H Collard, R Hofstadter, E B Hughes, A Johansson and M R Yearian, *Phys. Rev.* **B57**, 138 (1965)
[2] J S McCarthy, I Sick, R R Whitney and M R Yearian, *Phys. Rev. Lett.* **25**, 894 (1970)
[3] J S McCarthy, I Sick and R R Whitney, *Phys. Rev.* **C15**, 1396 (1977)
[4] L D Faddeev, *Zh. Eksp. Teor. Fiz.* **39**, 1459 (1960)
[5] E P Harper, Y E Kim and A Tubis, *Phys. Rev. Lett.* **28**, 1533 (1972)
[6] T Sasakawa and T Sawada, *Phys. Rev.* **C19**, 2035 (1979)
[7] J A Tjon, B F Gibson and J S OConnell, *Phys. Rev. Lett.* **25**, 540 (1970)
[8] G L Payne, J L Friar, B F Gibson and I R Afnan, *Phys. Rev.* **C22**, 823 (1980)
[9] R A Malfliet and J A Tjon, *Ann. Phys.* **61**, 425 (1970)
[10] J L Ballot and M Fabre de la Ripelle, *Ann. Phys.* **127**, 62 (1980)
[11] G Ernes, J L Visschers and R Van Wageningen, *Ann. Phys.* **67**, 461 (1971)
[12] J R Bruinsma and R Van Wageningen, *Phys. Lett.* **B44**, 221 (1973)
[13] T K Das, H T Coelho and M Fabre de la Ripelle, *Phys. Rev.* **C26**, 2288 (1982)
[14] J L Friar, B F Gibson, G L Payne and C R Chen, *Phys. Rev.* **C34**, 1463 (1986)
[15] T Sasakawa, A Fukunaga and S Ishikawa, *Czech. J. Phys.* **B36**, 313 (1986)
[16] P U Sauer, *Nucl. Phys.* **A463**, 273c (1987)
[17] R Schiavilla, V R Pandharipande and D O Riska, *Phys. Rev.* **C41**, 309 (1990)
[18] W M Kloet and J A Tjon, *Phys. Lett.* **B49**, 419 (1974)
[19] I R Afnan and Y C Tang, *Phys. Rev.* **175**, 1337 (1968)
[20] R A Malfliet and J A Tjon, *Nucl. Phys.* **A127**, 161 (1969)
[21] H Eikemeier and H H Hackenbroich, *Z. Phys.* **195**, 412 (1966)
[22] D Gogny, P Pires and R de Tourreil, *Phys. Lett.* **B32**, 591 (1970)
[23] A B Volkov, *Nucl. Phys.* **74**, 33 (1965)
[24] G A Backer, J L Gammel, B J Hill and J G Wills, *Phys. Rev.* **125**, 1754 (1966)
[25] J Fujita and H Miyazawa, *Prog. Theor. Phys.* **17**, 360 (1957)
[26] T Janssens, R Hofstadter, E B Hugher and M R Yearian, *Phys. Rev.* **142**, 922 (1966)
[27] S A Coon, M D Scadron, P C McWarnee and B R Barrett, *Nucl. Phys.* **A317**, 242 (1979)
[28] H T Coelho, T K Das and M R Robilotta, *Phys. Rev.* **C28**, 1812 (1983)

PRAMANA
— journal of
physics

© Printed in India

Vol. 43, No. 4,
October 1994
pp. 319–337

Distribution of fusion barriers

A K MOHANTY and S K KATARIA
Nuclear Physics Division, Bhabha Atomic Research Centre, Bombay 400 085, India

MS received 14 February 1994; revised 16 June 1994

Abstract. Heavy ion fusion cross sections and compound nucleus average spin values obtained from distribution of fusion barriers are discussed. Various shapes of distribution functions are studied using a truncated Gaussian distribution function (TGD). It is shown that fusion cross section and average spin values are less sensitive to different parametrization of TGD function, whereas the second derivative of the product of energy and fusion cross sections (w.r.t. energy), obtained from the corresponding TGD functions are significantly different depending on the shape of the barrier distribution function. It is also shown by χ^2 analysis of fusion cross section data that some systems favour a narrow Gaussian distribution function whereas others, for which the vibrational and rotational collective states are less important, favour a flat barrier distribution. A physical interpretation of the dynamical process that gives rise to different barrier distribution is given in the framework of microscopic coupled channel calculations.

Keywords. Distribution of fusion barriers; fusion cross sections; spin distributions; simultaneous coupling; sequential coupling.

PACS Nos 25·70; 24·10

1. Introduction

Heavy ion fusion excitation functions and compound nucleus spin distributions are not yet understood fully in spite of extensive work in this field [1]. Various models have been used to understand the enhancement of fusion cross sections and broadening of spin distributions at energies near and below the Coulomb barrier. It is seen that, when energy approaches the Coulomb barrier, coupling to various low lying states [2], nucleon transfer [3, 4] and neck formation [5, 6] become quite important in giving rise to sub-barrier enhancement. While the above physical processes are different from each other, one common feature is that the fusing system finds a distribution of barriers. Thus one can write the fusion cross section as

$$\sigma_f(E) = \sum_l \int_0^\infty D(B)\sigma_l(E, B)\mathrm{d}B \tag{1}$$

where $\sigma_l(E, B)$ is the fusion probability for a given partial wave l and barrier height B. $D(B)$ is the probability distribution function of barrier height B where

$$\int_0^\infty D(B)\mathrm{d}B = 1. \tag{2}$$

Various shapes of barrier distribution function $D(B)$ required to fit the experimental $\sigma_f(E)$ have been explored. A well-known example is the Gaussian distribution of

barrier heights predicted for colliding nuclei undergoing slow deviations from sphericity [7]. In some cases, fits were generally obtained with flat distributions characterized by sharp cut-off values at the low energy [8,9]. This cut-off barrier height is correlated with the separation energies of the valence neutrons which has led to the conclusion that the neutron flow is the principal enhancement mechanism and that coupling to collective states plays a secondary role. This idea gets further support from the study of Rowley *et al* [10], where they derive the true barrier distribution from the second derivative of the product of energy and fusion cross section and it is shown that this quantity becomes quite broad when many neutron transfer channels are treated sequentially. Similarly, it was shown from precise experimental fusion cross section measurements [11] that the distribution function is asymmetric for deformed systems as expected on the basis of Wong's model where static deformation of both projectile and target are taken into account [12]. It is also known that in a normal coupled channel equations, where non-elastic channels are coupled directly to the elastic channel (this coupling scheme is called simultaneous coupling in ref. [10]), the resulting barrier distribution, having two significant peaks, is quite different. With increasing number of channels, these two peaks separate further. Therefore, one hopes to learn more about the mechanism of channel coupling from the underlying barrier distribution function which is different for different coupling mechanisms and this difference is not too obvious from the analysis of the fusion excitation function or from the average spin values.

In this work, we have studied in depth several barrier distribution functions which fit the experimental data. Different shapes of barrier distribution functions are generated by using a truncated Gaussian distribution function (TGD) where the width δ and the truncation limit t are taken as parameters. In § 1, experimental fusion cross sections are fitted for several systems using TGD function with different width parameter δ and t is adjusted for each δ in order to achieve the best fit. Various shapes of barrier distribution function starting from flat shape to narrow Gaussian shape can be used and all of them fit fusion cross sections and average spin values quite well. In other words, fusion cross sections and average spin values are less sensitive to different parametrizations of barrier distribution function. It is shown in § 2 that the effect of different parametrization can be seen prominently in the quantity $d^2(\sigma_f E)/dE^2$ which is quite different for different barrier distribution functions and therefore, carry more discriminating features. The available experimental fusion data for a large number of H. I. systems have been analysed using TGD parametrization and a careful χ^2 analysis of experimental fusion data shows that some systems favour a Gaussian barrier distribution while others favour a flat barrier distribution i.e. a TGD function with large width. In the last section, we give a qualitative interpretation to these observations in the framework of microscopic coupled channel calculations.

2. Fusion cross section and spin distribution

Heavy ion fusion cross section at a given energy E and partial wave l for a given barrier height B can be written as

$$\sigma_l(E, B) = (\pi/k^2)(2l + 1)\, T_l(E, B) \tag{3}$$

where $T_l(E, B)$ is the corresponding tunneling probability and can be calculated using

a simple barrier penetration model as given by

$$T_l(E,B) = \{1 + \exp[(2\pi/\hbar\omega)(B - E - l(l+1)\hbar^2/2\mu R_0^2)]\}^{-1} \quad (4)$$

where μ is the reduced mass in the entrance channel and R_0 is the fusion barrier radius. Therefore, $\sigma_l(E)$ summed over all barriers can be obtained from eq. (1), where $D(B)$ is chosen to have a Gaussian shape and is given by

$$D(B) = N\exp[-(B - V_0)^2/2\delta^2] \quad (5)$$

where N is the normalization constant and V_0 the average barrier height that explains the high energy fusion cross section. Similarly, average spin can be written as

$$\langle l \rangle = \frac{\Sigma l\sigma_l(E)}{\Sigma\sigma_l(E)}. \quad (6)$$

In the present analysis, it is difficult to fit fusion cross section for many systems using only a Gaussian distribution function. However, most of these experimental data can be fitted using TGD parametrization. This method has been used earlier by Reisdorf *et al* [13] to fit experimental cross sections for Ar^+ (Sm, Sn) systems. They find that the data are reproduced well when the Gaussian distribution is truncated at a limit δt, where δ is related to the deformation length β and t value lies between 2 and 3. Therefore, with TGD parametrization, eq. (1) is integrated from $V_0 - \delta t$ to $V_0 + \delta t$ instead of 0 to ∞. The normalization constant N is obtained from the relation

$$N\int_{V_0-\delta t}^{V_0+\delta t} D(B)\mathrm{d}B = 1. \quad (7)$$

In the least square analysis of fusion excitation functions, both parameters δ and t are varied so as to obtain minimum chi-square (χ^2) per degrees of freedom. Figure 1(a), shows the fitted fusion excitation function for three systems e.g. $^{40}Ar + {}^{122}Sn$, $^{58}Ni + {}^{64}Ni$ and $^{16}O + {}^{154}Sm$ with TGD parametrization for three different values of δ and figure 1(b), shows the corresponding derived average spin values. The truncation limit t for each system was obtained by minimizing χ^2 for a given value of width parameter δ. It can be seen from figure 1(a) that all the three fits are indistinguishable from each other and reproduce the experimental fusion cross sections rather well. The derived average spin values (see figure 1(b)) obtained from different width parameter δ are also indistinguishable from each other and this holds true for all other systems studied. The minimum values of χ^2/N as a function of δ are shown in figure 2 for various systems. These values along with various potential parameters used in the fits are listed in table for all the systems. As seen from figure 2, χ^2/N is very shallow as a function of δ for many systems, whereas for systems like Ar + Sm and Ge + Ge, where the t values are quite large, well defined minima are obtained. In these cases, χ^2/N changes significantly with any small change in δ parameter. For remaining systems, χ^2/N values for a sharp Gaussian distribution ($\delta = 4$ MeV) and for a flat distribution ($\delta = 20$ MeV) do not differ much and for these systems t values are rather small. In other words, a range of TGD functions for $D(B)$ can be used to fit the same experimental fusion data with similar quality of fits. On the other hand, if we look at the corresponding barrier dsitribution, (see figure 1(c)

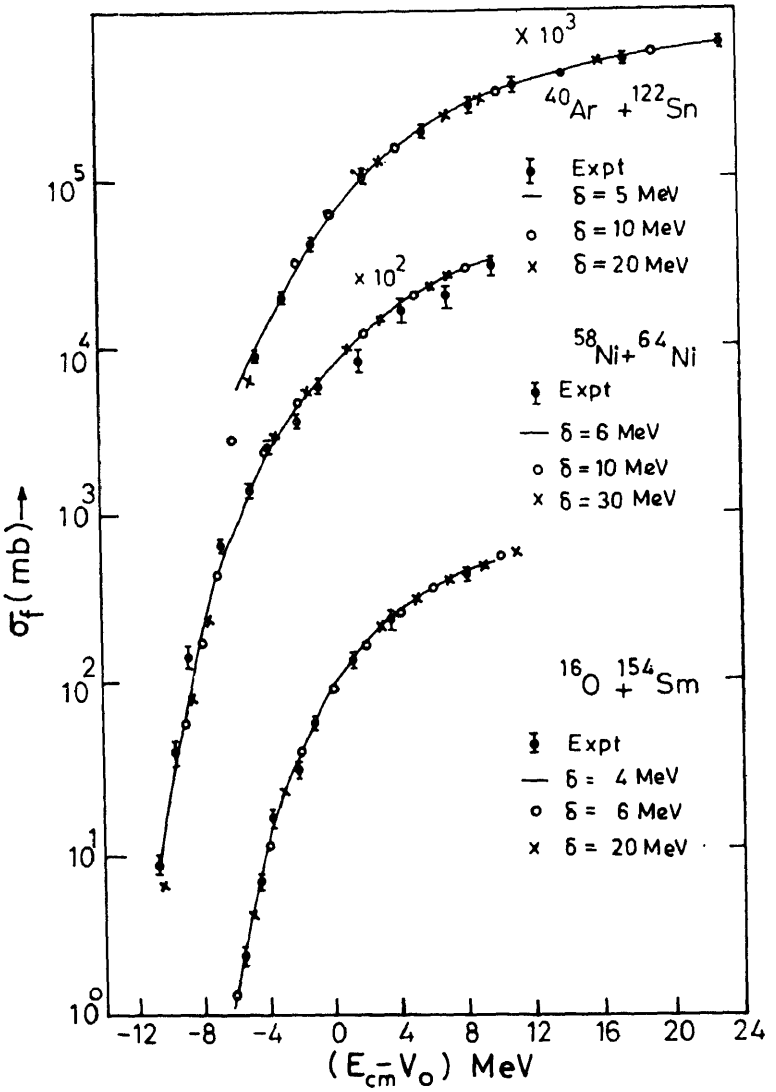

Figure 1(a). Fusion cross section versus $(E_{cm} - V_0)$ for $^{40}Ar + ^{122}Sn$, $^{58}Ni + ^{64}Ni$ and $^{16}O + ^{154}Sm$ systems for three different δ values shown in figure. The δ and t values are (5, 1·55), (10, 0·688), (20, 0·336) for $^{40}Ar + ^{122}Sn$ system, (6, 1·52), (10, 0·86) and (30, 0·275) for $^{58}Ni + ^{64}Ni$ system, (4, 1·47), (6, 0·92) and (20, 0·265) for $^{16}O + ^{154}Sm$ system. Experimental points are taken from refs. [13, 23, 21].

for $^{16}O + ^{154}Sm$ and $^{58}Ni + ^{64}Ni$ systems) they are completely different. There is a lower limit to δ, beyond which the distribution becomes narrow and it is not possible to reproduce fusion cross section.

Using one dimensional barrier penetration model for fusion to calculate fusion probability $\sigma_l(E, B)$ for a given barrier height B (Using (3) and (4)) and replacing the summation over l by an integral, eq. (1) can be written as

$$\sigma_f(E) = \int D(B)\sigma_w(E, B)\mathrm{d}B \tag{8}$$

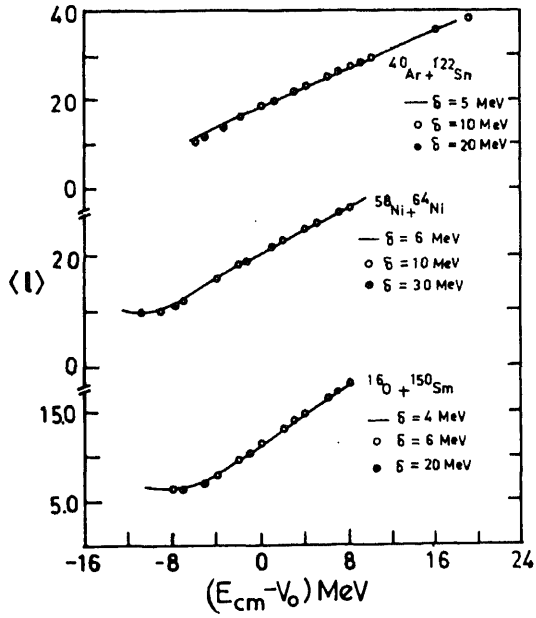

Figure 1(b). Average compound nucleus spin values versus $(E_{cm} - V_0)$ for $^{40}Ar + ^{122}Sn$, $^{58}Ni + ^{64}Ni$ and $^{16}O + ^{154}Sm$ for δ values used to fit fusion cross-section in figure 1(a).

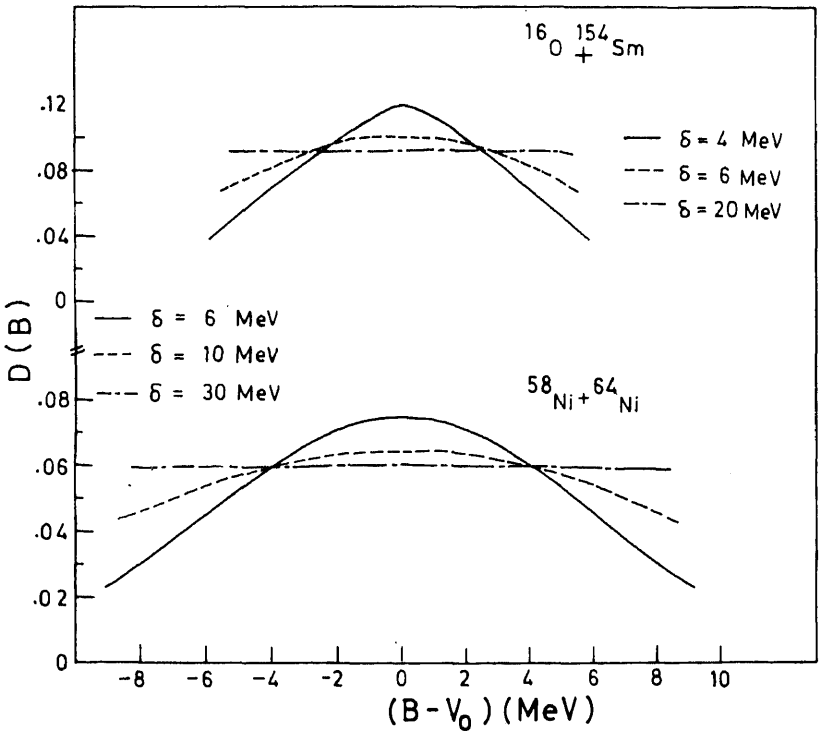

Figure 1(c). Barrier distribution function versus $(E_{cm} - V_0)$ for $^{16}O + ^{154}Sm$ and $^{58}Ni + ^{64}Ni$ systems for δ values used to fit fusion cross-section in figure 1(a).

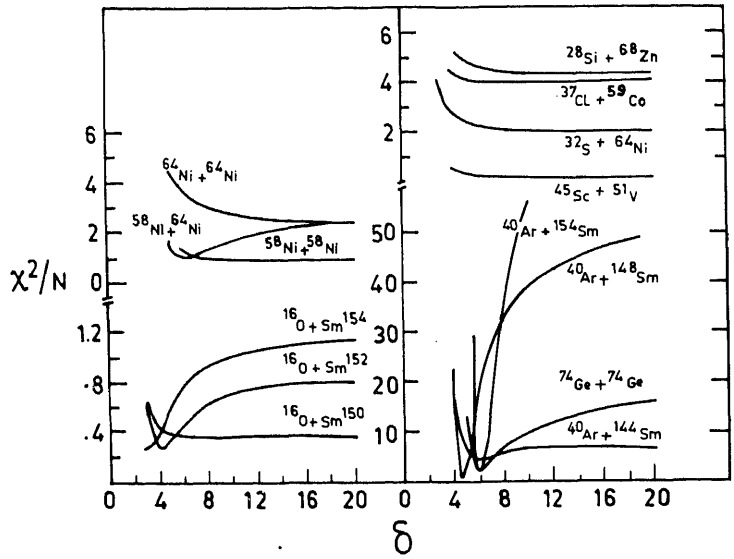

Figure 2. Minimum χ^2/N versus δ for different systems. For each δ, the value of t is adjusted to obtain minimum χ^2/N.

where $\sigma_w(E, B)$ is the l integrated fusion cross-section for a given barrier height B given by Wong's formula [12]

$$\sigma_w(E, B) = (\hbar\omega R_0^2/2E)\log\{1 + \exp[2\pi/\hbar\omega(E - B)]\} \tag{9}$$

In the above, the integration variable B varies from $V_0 - \delta t$ to $V_0 + \delta t$. For very large width, δt approaches a constant value and $D(B)$ can be approximately expressed as an uniform distribution given by $(2\delta t)^{-1}$. The fusion cross section for this uniform distribution can be written from eq. (8) as

$$\sigma_f = (2\delta t)^{-1} \int_{V_0 - \delta t}^{V_0 + \delta t} \sigma_w(E, B)\mathrm{d}B.$$

For $E \gg B$, the above integral reduces to

$$\sigma_f(E) = (2\delta t)^{-1} \int_{V_0 - \delta t}^{V_0 + \delta t} (\pi R_0^2/E)(E - B)\mathrm{d}B \tag{10}$$

which is very much similar to Stelson's barrier expression [8] except for the upper limit of integration. In Stelson's notation, $V_0 - \delta t$ represents the threshold barrier B_t for neutron flow and $D(B)$ is $[2(V_0 - B_t)]^{-1}$ in the range B_t and $(2V_0 - B_t)$ and zero outside this range. Stelson further sets $D(B)$ to zero for $E \leqslant 2V_0 - B_t$. Therefore, replacing the upper limit of integration in eq. (8) by E, one gets Stelson's expression

$$\sigma_f(E) = (\pi R_0^2/4)(V_0 - B_t)^{-1}(E - B_t)^2/E \tag{11}$$

for $E \leqslant 2V_0 - B_t$. This threshold barrier B_t is correlated by the above author with the separation energies of the valence neutrons and is related to the distance at which projectile and target potentials just allow neutrons to flow between the nuclei. As an

Table 1. The width δ of the distribution function and the corresponding truncation limit t are listed for many systems for which χ^2/N is minimum. The potential parameters $\hbar\omega$, R_0 and V_0 are taken from the systematics that explains the fusion cross-section at high energies. N is the number of data points.

System	δ	t	δt	χ^2/N	$\hbar\omega$	R_0	V_0	N	Ref.
$^{16}O + ^{154}Sm$	3·0	2·24	6·72	0·279	4·5	11·2	60	8	[21]
$^{16}O + ^{152}Sm$	4·0	1·32	5·28	0·26	4·5	11·2	60	7	[21, 22]
$^{16}O + ^{150}Sm$	8·0	0·537	4·29	0·363	4·5	11·2	60	8	[21]
$^{40}Ar + ^{154}Sm$	6·0	2·83	16·98	2·20	4·5	11·2	127·4	14	[13]
$^{40}Ar + ^{148}Sm$	4·5	2·89	13·01	1·07	4·5	11·2	128·4	12	[13]
$^{40}Ar + ^{144}Sm$	6·0	1·39	8·34	4·81	4·5	11·2	128·6	11	[13]
$^{40}Ar + ^{122}Sn$	20·0	0·336	6·72	1·93	4·5	11·2	106	12	[13]
$^{58}Ni + ^{64}Ni$	6·0	1·52	9·12	1·05	4·5	11·2	100	27	[23]
$^{64}Ni + ^{64}Ni$	20·0	0·372	7·44	2·40	4·5	11·2	97·8	13	[23]
$^{58}Ni + ^{58}Ni$	20·0	0·38	7·60	0·940	4·5	11·2	102	14	[23]
$^{32}S + ^{64}Ni$	20·0	0·255	5·10	2·112	4·0	10·2	59·1	14	[24]
$^{28}Si + ^{68}Zn$	20·0	0·254	5·08	8·61	4·0	9·5	56·2	14	[24]
$^{37}Cl + ^{59}Co$	10·0	0·38	3·80	8·22	4·0	9·5	56·2	14	[24]
$^{45}Sc + ^{51}V$	20·0	0·28	5·60	0·278	4·0	10·7	64	8	[24]
$^{74}Ge + ^{74}Ge$	6·0	2·9	17·4	3·14	4·2	10·5	125·4	25	[25]

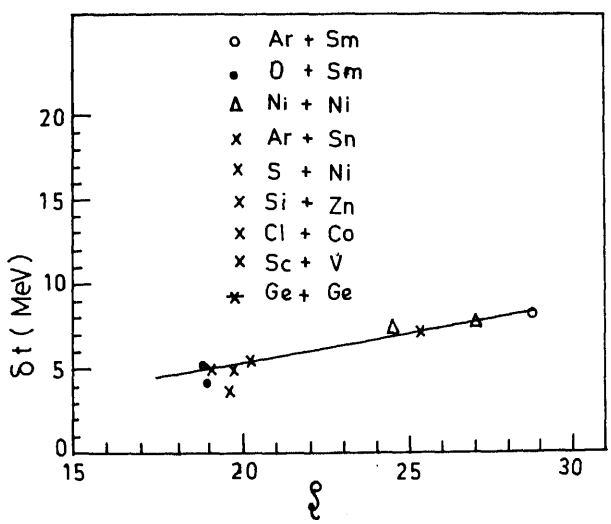

Figure 3. The optimal δt value versus effective fissility ξ for the systems which favour flat barrier distribution function.

example, based on some model calculation for $^{58}Ni + ^{58}Ni$ and $^{64}Ni + ^{64}Ni$ systems he finds B_t values around 94·2 and 89·2 MeV, the corresponding values of the lower limit of barrier distribution ($V_0 - \delta t$) as obtained in present analysis are 94·4 and 90·36 MeV (see table for above two systems at $\delta = 20$ MeV) which are in good agreement.

Similarly for $^{58}Ni + ^{64}Ni$ system, although a flat barrier distribution gives an accepetable fit, χ^2/N minimization occurs at $\delta = 6$ MeV which corresponds to a Gaussian barrier distribution. This suggests that the mechanism which gives results

in barrier distribution in $^{58}Ni + ^{64}Ni$ system is quite different from that of $^{58}Ni + ^{58}Ni$ and $^{64}Ni + ^{64}Ni$ systems. Except for $O + ^{152,154}Sm$, $Ar + Sm$, $Ge + Ge$ and $^{58}Ni + ^{64}Ni$ systems, the remaining system favours a flat distribution function. Figure 3 shows the plot of optimal δt (δt for which χ^2/N is minimum) versus ξ for all the systems which favour a flat barrier distribution listed in table where the effective fissility ξ is defined as

$$\frac{4Z_1Z_2}{A_1^{1/3}A_2^{1/3}(A_1^{1/3}+A_2^{1/3})}.$$

It is seen that the optimal δt values increase monotonically with ξ. As pointed out by Aguair *et al* [14] and Krappe *et al* [15], this dependence of the width δt on fissility parameter ξ can be correlated to the concept of neck formation or neutron flow which depends on the liquid drop model properties of the colliding partners.

3. Determination of distribution of barriers from fusion cross section

The differences in fusion cross sections can be seen prominently in the quantity $d^2(\sigma_f E)/dE^2$ as calculated for different barrier distribution functions [10, 16]. From (8) and (9), one can write

$$(\sigma_f E) = \pi R_0^2 \int D(B)\, L(x) dB, \tag{12}$$

$$\frac{d}{dE}(\sigma_f E) = \pi R_0^2 \int D(B)\, T(x) dB, \tag{13}$$

$$\frac{d^2}{dE^2}(\sigma_f E) = \pi R_0^2 \int D(B) G(x) dB. \tag{14}$$

The limits of integration on the right hand side are from $V_0 - \delta t$ to $V_0 + \delta t$

$$x = (2\pi/\hbar\omega)(E - B),$$

$$L(x) = (\hbar\omega/2\pi)\log[1 + \exp(x)],$$

$$T(x) = dL(x)/dx = [1 + \exp(-x)]^{-1},$$

$$G(x) = dT(x)/dx = (2\pi/\hbar\omega)\exp(x)/[1 + \exp(x)]^2.$$

As seen above, the integral in (12) is related to fusion cross section. The first derivative in (13) relates to the s-wave transmission T_0 at energy E. Similarly, the second derivative in (14) gives a direct measure of the barrier distribution function $D(B)$. The function $G(x)$ is a narrow width symmetric function and becomes a delta function in the limit $\hbar\omega \to 0$. Therefore, (14) can be written as

$$\frac{d^2}{dE^2}(\sigma_f E) = \pi R_0^2 \bar{D}(E) \tag{15}$$

where $\bar{D}(E)$ is the underlying barrier distribution smoothed by the function $G(x)$. Therefore, it is possible to extract a meaningful barrier distribution function from the above second derivative. It can also be seen that (13) gives the slope of the function

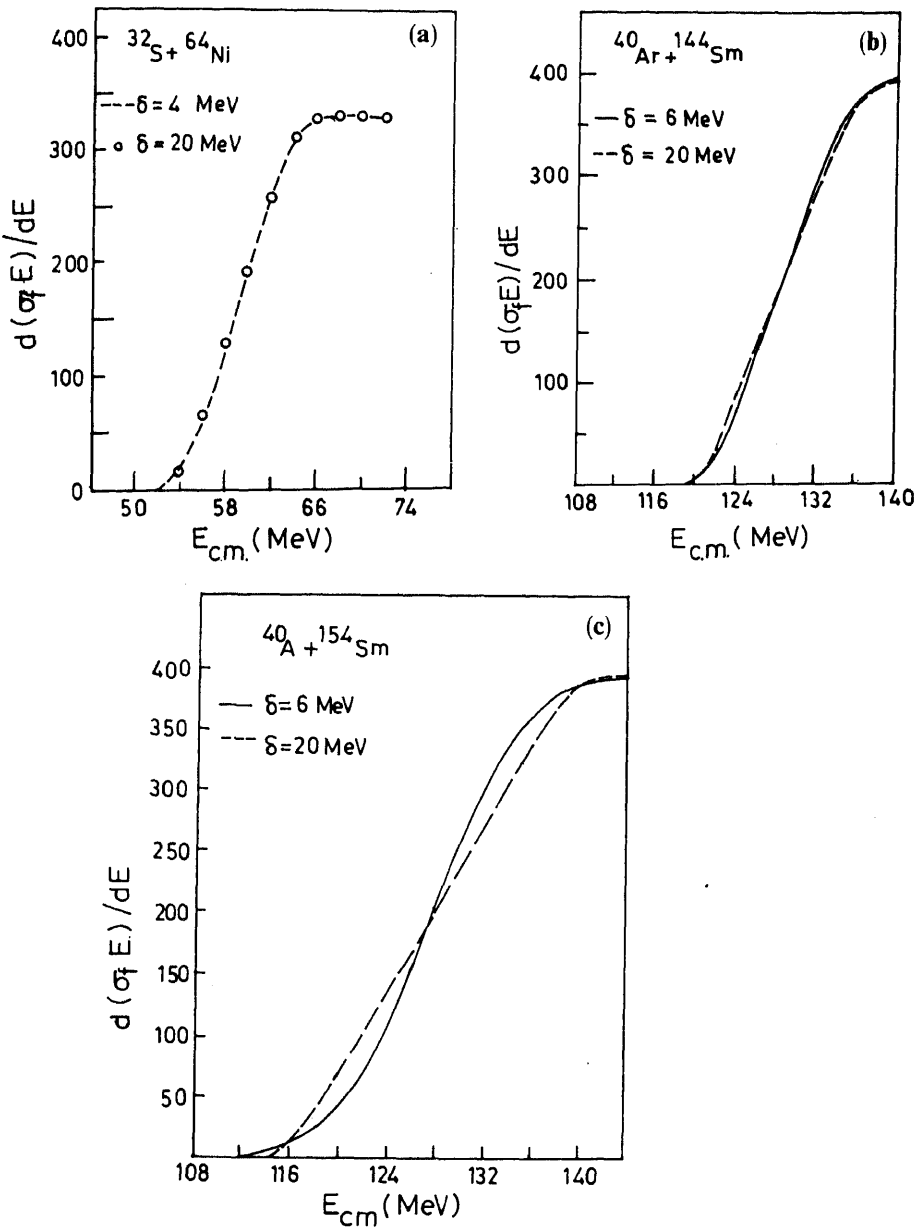

Figure 4(a, b, c). $d(\sigma_f E)/dE$ versus $E_{c.m.}$ for three typical systems with two different widths δ.

$(\sigma_f E)$. Therefore, any difference in the calculated fusion cross sections will get reflected through its first derivative which is the transmission coefficient T_0 at energy E. Similarly any differences in transmission coefficient can be seen prominently by its derivative as given by (14). Figures 4 and 5 show the plot of $d(\sigma_f E)/dE$ and $d^2(\sigma_f E)/dE^2$ as a function of energy E for three typical systems ($^{32}S + ^{64}Ni$ and $^{40}Ar + ^{144}Sm$ and $^{40}Ar + ^{154}Sm$) at two values of δ. The differences in first derivatives obtained from two extreme shapes of barrier distribution function are not significant for $^{32}S + ^{64}Ni$

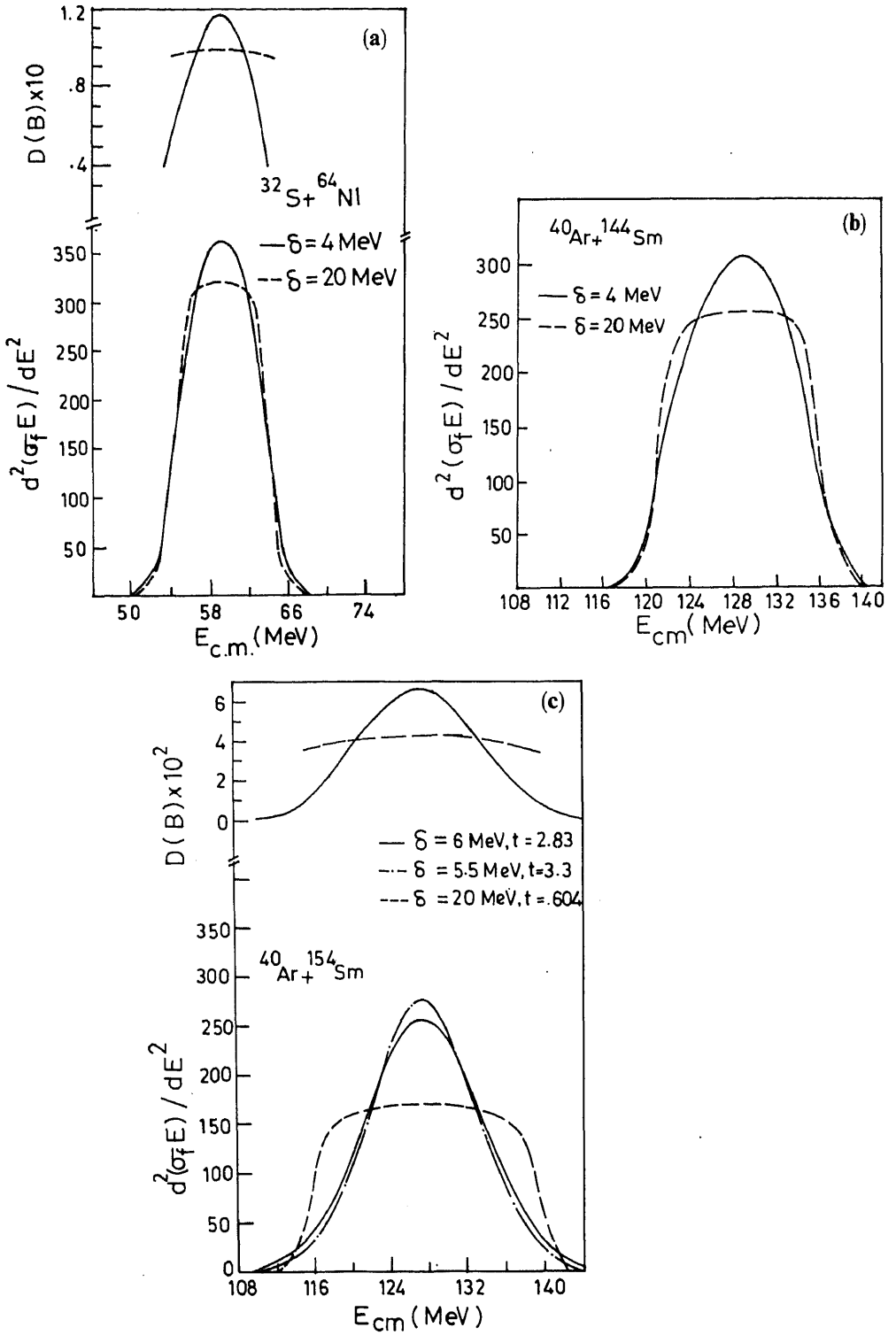

Figure 5(a, b, c). $d^2E(\sigma_f E)/dE^2$ versus $E_{c.m.}$ for the same system as that of figure 4. The upper part in figures 5(a) and 5(c) show the corresponding barrier distribution function.

and $^{40}Ar + ^{144}Sm$ systems (see figure 4). For $^{32}S + ^{64}Ni$ system, χ^2/N is minimum for $\delta = 20$ MeV ($t = 0{\cdot}255$) and for $^{40}Ar + ^{144}Sm$, χ^2/N is minimum for $\delta = 6$ MeV ($t = 1{\cdot}39$). For other values of δ, χ^2/N increases. However, this increase is not strong enough to bring out any significant differences in fusion cross section or in the average spin values. On the other hand, these small differences have become more distinct in figure 5 which relates to the true barrier function $D(B)$ smoothed by the function $G(x)$. Therefore, it is possible to extract the shape of the barrier distribution function from the experimental fusion cross-section as has been done for $^{16}O + ^{154}Sm$ system [11]. Even though, the second derivative is different for different $D(B)$ function, it is interesting to note that, in $^{32}S + ^{64}Ni$ (see figure 5(a)), this difference is seen only around the maximum whereas the width does not differ much. For such systems, which have small t values, the measurements of fusion cross-section need to be done very accurately in order to bring out this difference in distribution function. On the other hand, the system like $^{40}Ar + ^{154}Sm$, for which t is quite large, all shapes of barrier distribution function will not fit the fusion cross section as χ^2/N is minimum for a particular choice of δ and t parameters. The fits become quite poor for small changes in δ and t parameters (see figure 2). Therefore, for this type of system where the optimal δt is quite large, the barrier distribution function can be determined with greater accuracy by fitting the fusion cross-section itself. The second derivative and the distribution function $D(B)$ obtained for $\delta = 20$ MeV and $\delta = 5{\cdot}5$ MeV are also quite different as seen in figure 5(c) for the same system. In $^{16}O + ^{154}Sm$ system, as shown by Wei *et al* [11] and in the present case too, the data can be reproduced well if the distribution function is chosen to have a asymmetric Gaussian shape as shown in figure 6. In this case, the distribution function obtained from experimental

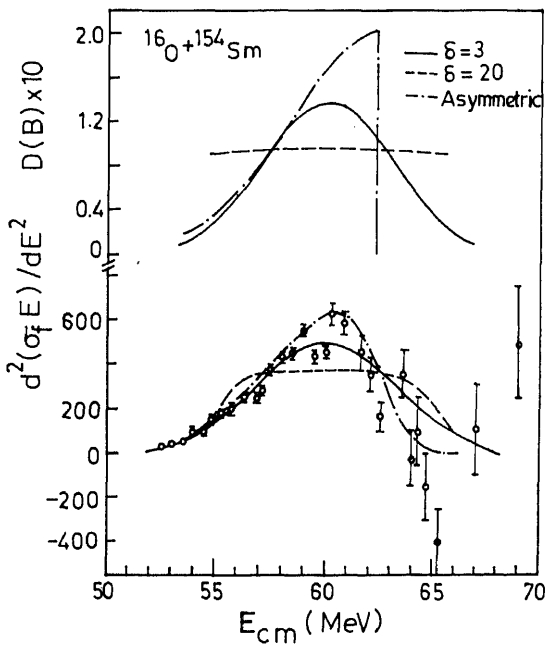

Figure 6. Same as figure 5, but for $^{16}O + ^{154}Sm$ system with $\delta = 3$ and 20 MeV and also with an asymmetric barrier shape as shown in upper part of the figure. The experimental points are taken from ref. [11].

data is asymmetric due to static deformation of ^{154}Sm and can be distinguished from a flat distribution. Even though the true barrier distribution for deformed target is asymmetric, we have considered only the symmetric distributions for simplicity.

4. Interpretation of distribution of barriers

It can be seen from figure 2 that most of the systems favour a large δ value. For these systems, the distribution function $D(B)$ is quite broad which is quite similar to that of a flat distribution. Stelson [8] often found necessary to describe heavy ion fusion cross-sections. Figure 2 shows that a few systems favour a Gaussian distribution function. In the following, we wish to understand these results in the microscopic framework of coupled channel calculations. In this approach, the set of coupled equations is solved approximately by diagonalizing the coupling matrix around the unperturbed barrier [17], which enables one to decouple the equations into a family of eigen channels where the total transmission is weighted sum of the transmission through each eigen channel given by

$$T(E) = \sum_{\alpha} |U_{\alpha 0}|^2 T_{\alpha 0}[E, V(r) + \lambda_{\alpha}(r)]. \tag{15}$$

$U_{\alpha 0}$ is the overlap probability which is evaluated at the unperturbed barrier position, $\lambda_{\alpha}(r)$ is the eigen value of the coupling matrix $M_{\alpha\beta}$. Following Rowley *et al* [10], the coupling scheme for the simultaneous and sequential inelastic and transfer as given by figures 7(a) and 7(b) is used in the following calculations. In figure 7(a), all the non-elastic channels (both inelastic and transfer) are coupled to the ground state

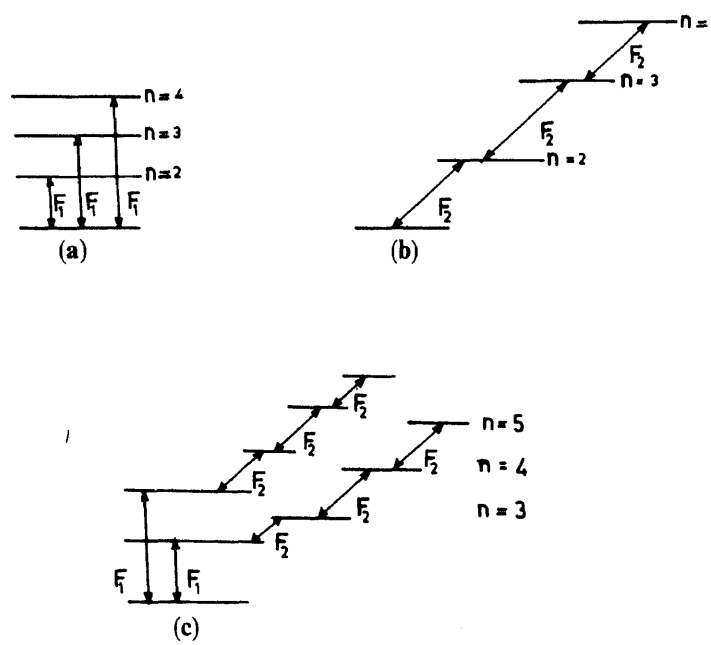

Figure 7(a). Schematic representation for simultaneous coupling; **7(b).** Schematic representation for sequential transfer; **7(c).** Schematic representation of sequential transfers that follows from the states inelastically excited.

directly and the coupling matrix is given by (as an example for $n = 5$)

$$M_{\alpha\beta} = \begin{vmatrix} 0 & F_1 & F_1 & F_1 & F_1 \\ F_1 & -Q & 0 & 0 & 0 \\ F_1 & 0 & -Q & 0 & 0 \\ F_1 & 0 & 0 & -Q & 0 \\ F_1 & 0 & 0 & 0 & -Q \end{vmatrix} \tag{16}$$

Figure 7(b) represents multinucleon transfer coupling scheme where a single nucleon (mostly neutron) transfer channel is coupled to the elastic ground state, the two neutron channel is coupled to the single neutron transfer channel, but not directly to the elastic channel. Similarly, a three neutron transfer channel is coupled to the two neutron transfer channel and so on. Accordingly, the coupling matrix is given by

$$M_{\alpha\beta} = \begin{vmatrix} 0 & F_2 & 0 & 0 & 0 \\ F_2 & -Q & F_2 & 0 & 0 \\ 0 & F_2 & -Q & F_2 & 0 \\ 0 & 0 & F_2 & -Q & F_2 \\ 0 & 0 & 0 & F_2 & -Q \end{vmatrix} \tag{17}$$

For simplicity, the coupling form factor is taken to be same at each step. In the case of neutron transfer, F_2 is taken as that of a one-particle transfer form factor given by [17]

$$F_2 = \frac{1}{(4\pi)^{1/2}}(3\text{ MeV})\exp[-(r - R_t)/a] \tag{18}$$

where $a = 1{\cdot}2$ and $R_t = r_t(A_1^{1/3} + A_2^{1/3})$. In (16), the coupling process is mostly due to inelastic excitations and the form factor F_1 is estimated from the collective model expression

$$F_1 = \frac{1}{(4\pi)^{1/2}}(-\beta R)\frac{\mathrm{d}V_n(r)}{\mathrm{d}r}. \tag{19}$$

In simultaneous coupling, if one of the channels is transfer channel, the same form factor F_2 can be used for single particle transfer. However, in the present case we estimate F_1 from (19), so that all the non-elastic channels are due to inelastic excitations only. These schematic coupling schemes given in figures 7(a) and 7(b), represent two extreme situations. If either the target or the projectile have a few low-lying collective states, the collision process might excite these states first, before many sequential transfers take place. This picture will give rise to different coupling schemes which are shown schematically in figure 7(c). Even though, the sequential transfers are initiated from many low-lying inelastic states, we consider only one such state and accordingly the coupling matrix is given by

$$M_{\alpha\beta} = \begin{vmatrix} 0 & F_1 & 0 & 0 & 0 \\ F_1 & -Q & F_2 & 0 & 0 \\ 0 & F_2 & -Q & F_2 & 0 \\ 0 & 0 & F_2 & -Q & F_2 \\ 0 & 0 & 0 & F_2 & -Q \end{vmatrix}. \tag{20}$$

An exact solution can be obtained by using a more realistic coupled channel code as one used in ref. [10], where transfer process is treated more acurately. However, we adopt a simple method to study some of the general properties more qualitatively that arises under different coupling schemes and to compare these results with the barrier distribution that are extracted fitting experimental fusion cross sections. Therefore, instead of diagonalizing these matrices at each r, we diagonalize them at a fixed $r = R_0$. In other words, a constant form factor is assumed which is the representative value of the coupling strength at the unperturbed barrier position R_0.

The barrier distribution that results from different coupling schemes are obtained by calculating fusion cross-section as a function of energy and then numerically evaluating the quantity $d^2(E\sigma)/dE^2$. This is shown in figure 8. With the normal value of r_t and a, which are of the order of 1·2 (see ref. 18), the coupling strength is not enough to give rise to a broad distribution. In Rowley *et al* [10], a large spectroscopic value for transfer is used which is roughly twice its normal value. One way to increase the strength is to use a larger radius parameter r_t in (18) which can be justified from

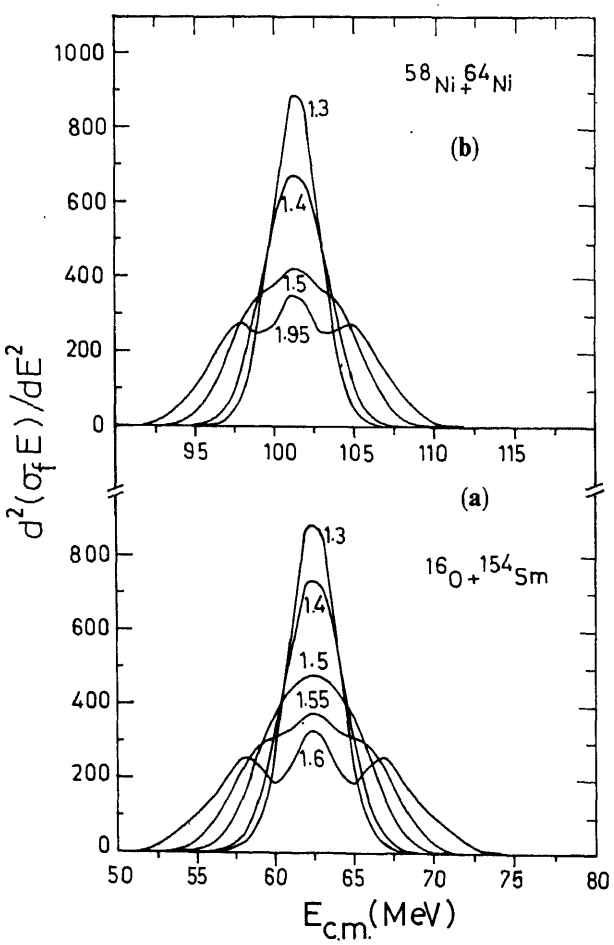

Figure 8(a, b). $d^2E(\sigma_f E)/dE^2$ versus $E_{c.m.}$ for $^{16}O + ^{154}Sm$ and $^{58}Ni + ^{64}Ni$ systems for sequential coupling scheme (figure 7(b)) with different values of r_t.

the fact that transfer can be initiated at a larger distance. Therefore, we treat r_t as a variable. Figure 8(a) shows the barrier distribution for $^{16}O + ^{154}Sm$ system and figure 8(b) for $^{58}Ni + ^{58}Ni$ system with different r_t values. It can be seen that the barrier distribution becomes broader with increasing value of r_t. There is a critical value of r_t at which the barrier distribution resembles with that of a flat barrier distribution. The similar trend is also seen for many other systems. It is interesting to note that r_t lies in the range of 1·4 to 1·6 fm for all the systems and is consistent with the r_0 values used in the analysis of the multinucleon transfer channels in the H.I. reactions. This suggests that the transfer process is initiated outside the Coulomb barrier and this value is practically same for all the systems. It can be mentioned here that these barrier distributions and the true barrier distributions that are discussed in § 2 are not same. For example, the barrier distribution for $^{16}O + ^{154}Sm$ is known to be asymmetric. The broad barrier distribution discussed here is only of academic interest as we want to study the effect of different coupling scheme on barrier distribution function irrespective of the system chosen.

In all these calculations, we had set Q value to zero. The results will be completely different with finite Q value. The barrier distribution for $Q = 0, -3$ and $+3$ MeV are shown in figure 9 for $^{16}O + ^{92}Zr$ system. Here again the choice of the system is arbitrary. The positive Q value makes barrier distribution more repulsive, while the negative value enhances the cross sections. This result is opposite to what happens in the case of simultaneous coupling. Moreover, the barrier distribution is no longer symmetric due to finite Q value effects. On the other hand, barrier distribution extracted from fitting the experimental fusion cross sections are rather flat for most of the systems, which suggests the sequential transfer with zero effective Q value as the most favoured one. As suggested in [19], this behaviour can be correlated to many repeated nucleon transfers between the orbitals of the two core nuclei such that the effective Q value is zero.

Next, we consider the effect of simultaneous coupling on barrier distribution $D(B)$ by diagonalizing the matrix given by (16). Figure 10(a) shows the plot of $d^2(\sigma_f E)/dE^2$ as a function of E_{cm} for $^{16}O + ^{92}Zr$ system for $n = 2, 3, 5$ with a typical β value of

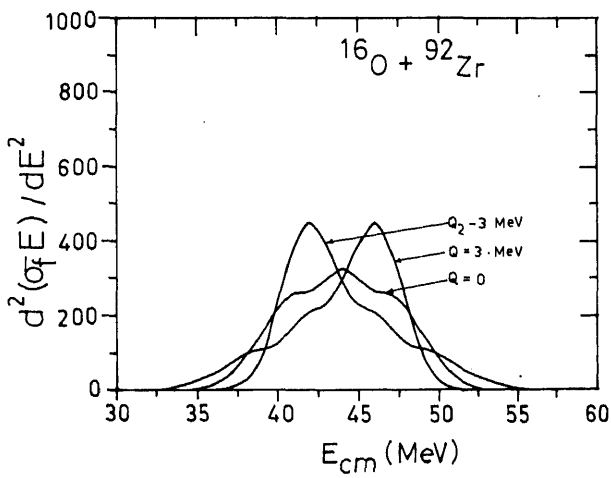

Figure 9. $d^2E(\sigma_f E)/dE^2$ versus $E_{c.m.}$ for $^{16}O + ^{92}Zr$ system for sequential coupling scheme (figure 7(b)) with $Q = -3$ MeV, O and $+3$ MeV.

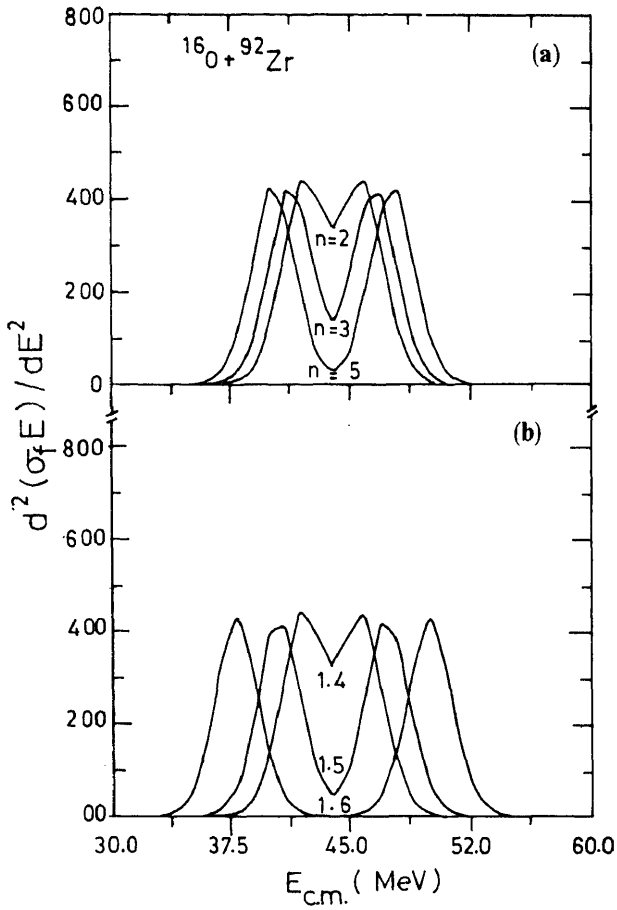

Figure 10(a). $d^2E(\sigma_f E)/dE^2$ versus $E_{c.m.}$ for $^{16}O + ^{92}Zr$ system for simultaneous coupling scheme (figure 7(a)) with $\beta_2 = 0{\cdot}25$ for different number of channels. **10(b).** Same as figure 10(a), but instead of F_1, the form factor F_2 is used with different r_t values for $n = 6$.

0·25. As expected [20], the barrier distribution shows double peaks and with more number of channels, the peaks are shifted further. Instead of number of channels, if the coupling strength is increased further, a similar behaviour in barrier distribution is seen. This is shown in figure 10(b) for $n = 5$ with form factor F_2 as a function of r_t. These calculations demonstrate that with the same coupling strength $r_t = 1{\cdot}6$ and $n = 6$, the sequential coupling gives a broad barrier distribution, while the simultaneous coupling results in a double hump distribution which can be understood either by increasing the number of channels or by increasing the coupling strength.

As seen from figure 2, although most of the system favours a flat barrier distribution, the barrier distribution for a few systems is of Gaussian type. This result cannot be understood on the basis of only simultaneous or sequential coupling studied so far. In order to obtain a Gaussian barrier distribution, we have to assume two different form factors F_1 and F_2 as given in (20). The basic assumption in this scheme is that before sequential transfer is initiated, the system gets coupled to low-lying inelastic states and thereafter sequential transfers follows. For simplicity, we have considered

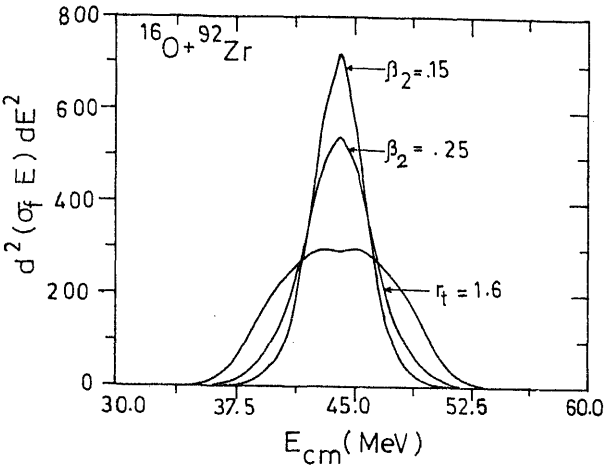

Figure 11. $d^2E(\sigma_f E)/dE^2$ versus $E_{c.m.}$ for $^{16}O + ^{92}Zr$ system. The sharp distribution corresponds to the coupling scheme given in figure 7(c) with $\beta_2 = 0{\cdot}25$ and 0·15. The broad distribution corresponds to the case of sequential coupling scheme with $r_t = 1{\cdot}6$.

only one inelastic state with form factor F_1. Figure 11 shows the plot of $d^2(\sigma_f E)/dE^2$ as a function of E_{cm} with two different β values of 0·25 and 0·15. The strength of F_2 is taken at $r_t = 1{\cdot}6$ fm. Replacement of F_1 with F_2 results in broad barrier distribution is also shown for comparison. Therefore, if we use F_1 different from F_2, the resultant distribution is of Gaussian type which is characteristic of many systems having low-lying collective states.

A study of low-lying levels of projectiles and targets for which the barrier distribution width is shown in figure 2, shows that Ge and Sm isotopes have more low-lying collective states in comparison to rest of the systems studied. Accordingly, the barrier distribution for the system where one of the partners is Ge or Sm, is of Gaussian type. It can also be seen, in comparison to $^{16}O + ^{150}Sm$, the barrier distribution is more sharp for $^{40}Ar + ^{144}Sm$, as Ar being a heavier projectile, the probability of inelastic excitation is higher in latter case than the former. It is also interesting to note that the barrier distribution of $^{58}Ni + ^{58}Ni$ and $^{64}Ni + ^{64}Ni$ are quite broad, whereas in $^{58}Ni + ^{64}Ni$, it is Gaussian. This can be understood on the basis of similar argument that this system is known to have a positive Q value $2n$ transfer channel. Therefore, this system couples simultaneously to the $2n$ channel with relatively small coupling strength F_2 (this form factor can be estimated from eq. (18) with $r_t = 1{\cdot}2$ fm.).

In summary, it is shown that, experimental fusion cross section for those systems which have less important collective degrees can be best explained by using a flat barrier distribution, while the systems having more collectiveness prefer a Gaussian barrier distribution. These various shapes of barrier distribution functions are generated by using a truncated Gaussian function where the width parameter δ and corresponding truncation limit t are fixed by χ^2 minimization. The optimal δt values for the systems which favour flat barrier distribution, increase monotonically with effective fissility ξ which can be correlated to the concept of neck formation or neutron flow which depends on the liquid drop properties of the colliding nucleus. Even though, a particular distribution function is favoured by a particular system, it is

seen that for those systems where the optimal t is small, many distribution functions can be used to get fusion cross section and average spin values which are indistinguishable from each other. However, these differences become prominent while comparing the second derivative $[d^2(\sigma_f E)/dE^2]$ obtained from different distribution functions. The observed different barrier distribution functions have been interpreted on the basis of a new model involving non-elastic processes in the framework of coupled channel formalism. It is known that the sequential coupling (due to multinucleon transfers) results in a broad barrier distributions which are quite similar to the flat barrier distributions often found necessary to fit the experimental fusion excitation functions. In the present work using a simple schematic model, it is also shown that the sequential coupling gives a very broad barrier distribution, while the simultaneous coupling results in a double hump distribution. As discussed before, although most of the system favours a flat barrier distribution, the barrier distribution for a few systems, having well developed collective states, are of Gaussian type. This result cannot be understood on the basis of either simultaneous or sequential coupling. Therefore, we have assumed a new coupling scheme wherein before sequential transfer is initiated, the system gets coupled to low-lying inelastic states and thereafter sequential transfers follows. This method results in Gaussian barrier distribution function.

Acknowledgements

We are very much thankful to Drs V S Ramamurthy, S S Kapoor, M A Nagarajan and S V S Sastry for illuminating discussions on several aspects of this study.

References

[1] M Beckerman, *Rep. Prog. Phys.* **51**, 1047 (1988)
[2] C H Dasso, S Landowne and A Winther, *Nucl. Phys.* **A405**, 381 (1983)
C H Dasso, S Landowne and A Winther, *Nucl. Phys.* **A407**, 221 (1983)
[3] I J Thompson, M A Nagarajan, J S Lilley and B R Fulton, *Phys. Lett.* **B157**, 250 (1985)
[4] S C Pieper, M J Rhoades-Brown and S Landowne, *Phys. Lett.* **B162**, 43 (1985)
[5] C E Aguiar, V C Barbosa, L F Canto and R Donangelo, *Nucl. Phys.* **A472**, 571 (1987)
A Iwamoto and K Haroda, *Z. Phys.* **A326**, 201 (1987)
[6] V S Ramamurthy, A K Mohanty, S K Kataria and G Rangarajan *Phys. Rev.* **C41**, 2702 (1990)
[7] H Esbensen, *Nucl. Phys.* **A352**, 147 (1981)
[8] P H Stelson, *Phys. Lett.* **B205**, 190 (1988)
[9] P H Stelson, H J Kim, M Beckerman, D Shapira and R L Robinson, *Phys. Rev.* **C41** 1584 (1990)
[10] N Rowley, *Nucl. Phys.* **A538**, 205c (1992)
N Rowley, I J Thompson and M A Nagarajan, *Phys. Lett.* **B282**, 27 (1992)
[11] J X Wei *et al*, *Phys. Rev. Lett.* **67**, 3368 (1991)
[12] C Y Wong, *Phys. Rev. Lett.* **31**, 766 (1973)
[13] W Reisdorf *et al*, *Nucl. Phys.* **A438**, 212 (1985)
[14] C E Aguair, A N Aleixo, V C Barbosa, L F Canto and R Donengelo, *Nucl. Phys.* **A500**, 195 (1989)
[15] H J Krappe, K Mohring, M C Nemes and H Rossner, *Z. Phys.* **A214**, 23 (1983)
[16] N Rowley *et al*, *Phys. Lett.* **B254**, 25 (1991)
[17] C H Dasso and S Landowne, *Phys. Lett.* **B183** 141 (1987)
[18] R A Broglia, G Pollarolo and A Winther, *Nucl. Phys.* **A406**, 369 (1983)

[19] B Imanishi and W Von-Oertzen, *Phys. Rep.* **155**, 29 (1987)
[20] A T Krupa, P Romain, M A Nagarajan and N Rowley, Preprint DL/NUC/P324T, Daresbury 1992
[21] R G Stokstad *et al*, *Phys. Rev.* **C21**, 2427 (1980)
[22] A H Wuosmaa *et al*, *Phys. Lett.* **B263**, 23 (1991)
[23] M Beckerman *et al*, *Phys. Rev.* **C23**, 1581 (1981)
M Beckerman *et al*, *Phys. Rev.* **C25**, 837 (1982)
[24] M DasGupta *et al*, *Nucl. Phys.* **A539**, 351 (1992)

PRAMANA
— journal of
physics

© Printed in India

Vol. 43, No. 4,
October 1994
pp. 339–352.

Level structures in the odd-odd nucleus ^{180}Re

ASHOK KUMAR JAIN, PRAKASH C SOOD* and RAYMOND K SHELINE†
Department of Physics, University of Roorkee, Roorkee 247 667, India
*Physics Department, Banaras Hindu University, Varanasi 221 005, India
†Florida State University, Tallahassee, FL 32306, USA

MS received 17 May 1994; revised 4 August 1994

Abstract. Experimental data on energy levels of the odd-odd deformed nucleus ^{180}Re obtained from radioactive-decay and heavy-ion reaction studies are analysed to deduce spin-parity and configuration assignments for the six observed rotational bands based on the selection rules for fast beta transitions, criteria for the relative-energy ordering of the triplet and singlet bandheads, two-particle-plus-rotor model calculations including Coriolis mixing, rotational energy systematics involving staggering features, and considerations of gyromagnetic ratios, signature splittings and rotational band alignments.

Keywords. Doubly odd deformed nucleus; Nilsson configuration assignments; Coriolis coupling calculations; systematics and g-factors.

PACS Nos 21·60; 27·70

1. Introduction

The presently available level scheme [1] of the odd-odd deformed nucleus $^{180}_{75}Re_{105}$ is confusing in that it consists of a number of subsets of disconnected rotational bands, mostly with tentative, and often conflicting, spin-parity and configuration assignments. A decade ago, the only information available on this level scheme came from the electron capture decay [2–5] of the 21·5 min O^+ ground state of ^{180}Os; this decay could populate only low-spin ($I < 2$) states. The proposed level scheme [1] suggests assignments for the four lowest levels [$E_x < 75$ keV] based on the systematics of single particle orbitals in the neighbouring nuclei. During the eighties, two independent heavy-ion fusion evaporation (HI, xn) reaction studies, one by the Brookhaven–Buenos Aires (BB) collaboration [6] and the other by the Jülich–Berlin–Copenhagen (JBC) collaboration [7–10], have yielded extensive transition data which could be grouped into several sets of rotational bands. However, in spite of persistent efforts, no connection with the earlier known low-spin states could be established, nor has it been possible to interconnect the various subsets of rotational bands revealed in the heavy-ion reaction studies. Further, the two recent studies by Kreiner *et al* [6] and Venkova *et al* [10], although identifying three similar band sequences, suggested totally different structures (band quantum numbers, spin-parities, configurations) for each of the identified bands. Even after continued efforts, spread over many years and trying out widely differing combinations of possible quasiparticle (qp) configurations, the JBC collaboration could advance only tentative assignments, often based on plausibility considerations. As explicitly pointed out by them [10], their suggested interpretations occassionally contain certain physically unacceptable

features, e.g. Gallagher-Moszkowski (GM) rule [11] violation and alignment inconsistencies, which cannot be explained within the so-far accepted characteristics of the residual neutron-proton interaction and the observed alignment features of Nilsson orbitals in neighbouring odd-A nuclei respectively.

Faced with this situation, we chose to re-examine the experimental data, guided by two-quasiparticle-plus-rotor model (TQPRM) calculations including Coriolis mixing, to decide between the conflicting assignments and to arrive at physically acceptable characterisations consistent with the deduced experimental features. In § 2, we scan the complete $2qp$ configuration space defined by the observed single-particle excitations in the (A-1) isotone and isotope for the neutrons and protons respectively; previously suggested characterisations of the observed bands within the scheme is also described. The outline of our formulation and the results for the various $2qp$ bandhead energies using the TQPRM are presented in § 3. In the final section, we critically examine the available experimental data and deduced properties for each of the identified bands with $K < 10$ (thus excluding $4qp$ structures from our discussion) to arrive at the $2qp$ configuration for each band, consistent with its known features. In common with the earlier investigations, we do not find it possible to interconnect the three pairs of bands under discussion based on the available experimental results.

2. Intrinsic excitations and observed bands

In the two-particle-rotor formulation for odd-odd deformed nuclei each neutron (in Nilsson orbital Ω_n) and proton (Ω_p) combination gives rise to a pair of bands with band quantum numbers $K_\pm = |\Omega_p \pm \Omega_n|$ with relative energy ordering given by the GM rule. According to this rule for Nilsson model asymptotic quantum numbers $[Nn_3\Lambda\Sigma]$, the spins-parallel triplet state K_T lies lower in energy than the spins-antiparallel singlet state K_S within each GM doublet. In table 1, we list $K^\pi(\Omega_p, \Omega_n)$ values for the $2qp$ intrinsic excitations in $^{180}_{75}Re_{105}$ arising from combining all observed Ω_p orbitals in $^{179}_{75}Re_{104}$ and Ω_n orbitals in $^{179}_{74}W_{105}$. The experimentally determined [12] excitation energies $E(\Omega_i)$ for each single particle orbital in the (A-1) isotope and isotone are also listed respectively in the top row and the first column in our table 1. A zeroth-order estimate of the $2qp$ excitation energy for a specified (Ω_p, Ω_n) configuration may be obtained by simply summing the corresponding $1qp$ energies listed here.

The lowest four levels, placed at 0·0, 20·1, 49·8, and 74·6 keV in ^{180}Re from ^{180}Os electron-capture decay (Refs 4 and 5), have been respectively assigned $I^\pi K$ values $1^-1, 1^+1, 2^-1$, and 2^+1, belonging to the $1^-[p_0n_0]$ and $1^+[p_1n_0]$ bands (henceforth referred to as band 1 and band 2) in the notation (p_i, n_j) of our table 1. These assignments are based on the log ft values for beta decay in the $^{180}Os \rightarrow {}^{180}Re \rightarrow {}^{180}W$ chain, multipolarities (E1, M1) of gamma transitions to the ground state in ^{180}Re, and Nilsson orbital systematics of the region.

Excluding the possible $4qp$ bands with $K \geqslant 10$, the two (HI, xn) reaction studies [6, 10] have three very similar bands for which dissimilar (conflicting) assignments have been suggested by the two groups. For the band with lowest $\Delta I = 1$ transition energies 208·8, 228·4, 246·0, 261·5, ..., keV, (hereafter referred to as band 3 which is band 1 of ref. [10] and band A of ref. [6]) Kreiner *et al* [6] suggested the character $8^+[p_1n_0]$ whereas Venkova *et al* [10] suggested its character as $6^-[p_0n_0]$. The two proposed assignments constitute singlet (K_S) counterparts of the $1^+[p_1n_0]$ and $1^-[p_0n_0]$ bands populated in electron-capture decay. However, no connection with the lower lying low-spin bands could be established, and consequently the bandhead

Table 1. The low-energy two-quasiparticle spectrum of ^{180}Re. The column headings denote the proton orbitals (p_i), their Nilsson quantum numbers $\Omega^{\pi}[Nn_3\Lambda\Sigma]$, and observed excitation energy (in keV) and the decoupling parameter a in the case of a $K = 1/2$ band in the neighbouring (A-1) isotope. Similarly, the rows contain the same information for the neutron orbitals from the (A-1) isotone. The band quantum numbers K are given in the order of $K_T(\Sigma = 1)$ followed by $K_S(\Sigma = 0)$; below each K value is listed its calculated position by using a zero-range residual n–p interaction [16–18]. A deformation $\delta = 0{\cdot}24$ and the interaction parameters $\alpha = 0{\cdot}21$ and $W = 4{\cdot}4$ MeV were used in the calculation.

p →	p_0		p_1		p_2	
^{179}Re	5/2$^+$[402↑]		9/2$^-$[514↑]		1/2$^-$[541↓]	
n ^{179}W	0·0 keV		80 keV		118·5; 5·9	
n_0	1^-	6^-	1^+	8^+	4^+	3^+
7/2$^-$[514↓]						
0·0	0	160	35	260	300	340
n_1	2^-	3^-	4^+	5^+	1^+	0^+
1/2$^-$[521↓]					GM inv?	
221·9; 0·82	335	435	490	550	470	400
n_2	7^+	2^+	9^-	0^-	4^-	5^-
9/2$^+$[624↑]						
308·9	450	510	290	350	600	660
n_3	5^-	0^-	7^+	2^+	2^+	3^+
5/2$^-$[512↑]						
430·2	380	425	480	565	750	760
n_4	6^+	1^+	8^-	1^-	1^-	4^-
7/2$^+$[633↑]	GM inv?					
477·3	680	665	585	600	815	855

energy for band 3 remains undefined. The next common band in both the heavy-ion reaction studies has the lowest $\Delta I = 1$ transition energies 134·4, 176·7, 210·0, 237·5,... keV (hereafter referred to as band 4 which is band 4 of ref. 10 and band B of ref. 6). Both investigators connect it to our band 3 with a 78·6-keV $E1$ transition, thus establishing opposite parities for these two bands and also defining the bandhead separation energy. However, Kreiner *et al* [6] suggest its configuration as strongly admixed $\{9^-[p_1n_2]; 8^-[p_1n_4]\}$ involving $i_{13/2}$ neutron orbitals, whereas Venkova *et al* [10] characterize it as $7^+[p_0n_2]$.

The third common band for the two groups has the lowest $\Delta I = 1$ transition energies 92·2, 149·3, 182·5, 220·7,... keV (hereafter referred to as band 5, same as in ref. 10 and band D of ref. 6). Kreiner *et al* [6] describe it as the strongly admixed $\{7^+[p_0n_2]; 6^+[p_0n_4]\}$ band involving $i_{13/2}$ neutron orbitals, whereas Venkova *et al* characterize it as $3^-[p_0n_1]$ singlet band. Another band, identified only by Venkova *et al* [10], but not seen by Kreiner *et al* has the lowest $\Delta I = 1$ transition energies 106·3, 133·2, 159·4, 173·4,... keV (hereafter referred to as band 6, in common with ref. 10). This band has the uncommon feature of turning decoupled at higher spins with no $\Delta I = 1$ observed transitions, and thus splitting into two separate $\Delta I = 2$ sequences. Further there are strong interband transitions linking bands 5 and 6, leading Venkova *et al*

to surmise that these two bands possibly constitute a $\Delta K = 1$ GM doublet (thus one of the odd particles occupies a $\Omega = 1/2$ orbital). Based on this reasoning, they characterize band 6 as the $2^-[p_0 n_1]$ triplet band while pointing out that this proposal violates the GM rule and cannot be explained within the present understanding of the residual neutron-proton interaction. In addition, both investigators list one more band each for which K is not a good quantum number: Kreiner *et al* [6] list it as a $\Delta I = 2$ sequence starting from $I^\pi = 5^+$ whereas Venkova *et al* [10] list it as a signature split band starting at $I^\pi = 7^-$. These stand-alone (not connected to any other identified level in ^{180}Re) bands in the two cases have differing transition energies, and may not even belong to this level scheme. Accordingly we restrict our analysis in the following to a discussion of the six bands with a view to arrive at their credible characterization, consistent with the known experimental features.

3. Formulation and 2QP bandhead energies

We use a two-quasiparticle-plus-rotor Hamiltonian written as [13–15],

$$H = H_{\text{intr}} + H_{\text{rot}} \tag{1}$$

where

$$H_{\text{intr}} = H_{\text{av}} + V_{\text{np}} \tag{2}$$

and

$$H_{\text{rot}} = \hbar^2/2\mathcal{I}(I^2 - I_3^2) + H_{\text{cor}} + H_{\text{ppc}} + H_{\text{irrot}}. \tag{3}$$

In writing (1) we have neglected the pairing and vibrational terms. The intrinsic Hamiltonian H_{intr} consists of an averaged single-particle potential (the Nilsson model in our case) and a residual neutron-proton interaction term. Other terms in the H_{rot} are defined as

$$H_{\text{cor}} = -\hbar^2/2\mathcal{I}(I^+ j^- + I^- j^+), \tag{4a}$$

$$H_{\text{ppc}} = \hbar^2/2\mathcal{I}(j_{\text{p}}^+ j_{\text{n}}^- + j_{\text{p}}^- j_{\text{n}}^+), \tag{4b}$$

$$H_{\text{irrot}} = \hbar^2/2\mathcal{I}[(j_{\text{p}}^2 - j_{\text{pz}}^2) + (j_{\text{n}}^2 - j_{\text{nz}}^2)], \tag{4c}$$

where the different quantities have their usual meaning. The basis eigenfunctions used are the symmetrized product of D^I_{MK} and the intrinsic wave functions $|K\alpha\rangle$,

$$|IMK\alpha\rangle = \sqrt{\frac{2I+1}{16\pi^2(1+\delta_{k0})}}\{D^I_{MK}|K\alpha\rangle + (-1)^{I+K} D^I_{M-K} R_i |K\alpha\rangle\} \tag{5}$$

where $\alpha = \rho_{\text{n}}\rho_{\text{p}}$ represents the odd-neutron and the odd-proton product state. First, we put all the coupling terms in (4) to be zero. Then by using the rest of the Hamiltonian, we calculate the unmixed $2qp$ bandhead energies as [16–18]

$$E_K(p_i n_j) = E(p_i) + E(n_j) + E_{\text{rot}}(K) + E_{\text{res}}(K) \tag{6}$$

where the first two terms represent the single quasi-proton and single quasi-neutron energies for the states in question, usually taken from the neighbouring (A – 1) isotone/isotope respectively. The last two terms represent respectively the zero-point rotational energy and the residual neutron-proton interaction energy. The residual n–p interaction energy is obtained from theory by using a zero range spin-dependent

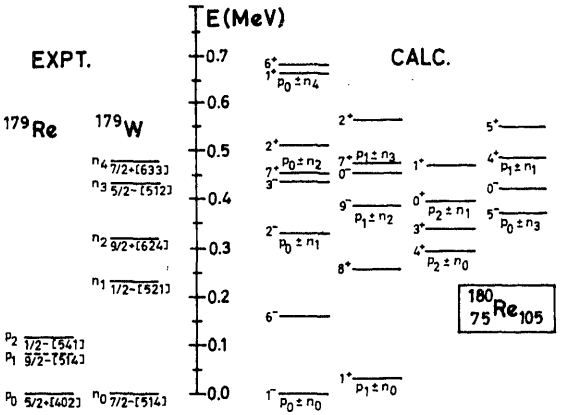

Figure 1. The calculated two-quasiparticle bandhead energies of ^{180}Re before Coriolis mixing are plotted on the right-hand side in the notation of table 1. On the left-hand side are shown the one-quasiparticle energies from the neighbouring odd-A nuclei [12]. Only the lowest three proton configurations and the lowest five neutron configurations are considered.

interaction and Nilsson wave functions. The resulting expression is [16]

$$E_{res}(K) = (1-\alpha)\, WA_0(K) \pm \alpha W A_\sigma(K) + (-1)^I B\delta_{K0} \tag{7}$$

where W is the strength parameter of the Wigner part, αW is the fractional strength of the spin-dependent part in the residual interaction, and A_0 and A_σ are the respective matrix elements. The last term represents the odd-even shift (or Newby shift) contribution in the case of $K=0$ bands [13, 19, 20]. We use an average value of $\alpha = 0{\cdot}21$, $W = 4{\cdot}4$ MeV, and the calculated excitation energies are listed in table 1 for all the $2qp$ configurations included in our calculation. The matrix elements for the case of the $\{9/2^-[514]_p, 7/2^-[514]_n\}$ configuration were attenuated by a factor of 0·5, as is the practice for the cases where all the Nilsson quantum numbers are the same giving an unusually large value of A_0 and A_σ. The resulting $2qp$ excitation spectrum along with the input $1qp$ energies are plotted in figure 1.

The coupling terms of (4) were then switched on and all bands were allowed to mix together. The moment-of-inertia parameters of the bands were taken either from neighbouring odd-odd nuclei where the band is known, or from the expression

$$\mathscr{T}_{o-o} = \mathscr{T}_p + \mathscr{T}_n - \mathscr{T}_{e-e} \tag{8}$$

which uses the moments of inertia of the odd neighbours and the even-even core.

4. Analysis and discussion

Now we discuss the configuration assignments for the three pairs of bands in the light of TQPRM predictions and various properties of respective energy levels observed or deduced directly from the experimental data.

4.1 *Bands populated in beta decay*

As mentioned in § 2, electron capture decay of the ^{180}Os 0^+ parent state populates 1^-(0·0 keV) and 2^-(49·8 keV) levels in ^{180}Re assigned as the lowest members of the

$1^-(p_0n_0)$ band, and also the 1^+(20·1 keV) and 2^+(74·6 keV) levels of the $1^+(p_1n_0)$ bands. The $^{180}_{76}Os_{104} \rightarrow {}^{180}_{75}Re_{105}$ decay involves breaking a proton pair in the ^{180}Os ground state and placing the transformed neutron in one of the unoccupied neutron orbitals above the N = 104 Fermi surface. The lowest neutron orbital above the N = 104 Fermi surface is $7/2^-[514]$. Thus the beta branches of ^{180}Os decay, feeding the ground and the first excited states of ^{180}Re, correspond to the transformations:

$$^{180}\text{Os}\{0^+\} \rightarrow {}^{180}\text{Re}\{1^-, 0{\cdot}0\,\text{keV}\}:$$

$$0^+\{5/2^+[402]^2_p\} \rightarrow 1^-\{5/2^+[402]_p, 7/2^-[514]_n\} \tag{9}$$

and

$$^{180}\text{Os}\{0^+\} \rightarrow {}^{180}\text{Re}\{1^+, 20{\cdot}1\,\text{keV}\}:$$

$$0^+\{9/2^-[514]^2_p\} \rightarrow 1^+\{9/2^-[514]_p, 7/2^-[514]_n\}. \tag{10}$$

A 'strong' selection rule for the allowed unhindered beta decay in the rare earth region has recently been established by Sood and Sheline [21]; according to this rule, any beta branch with $\log ft \leqslant 5{\cdot}2$ in the $A = 180$ region necessarily involves a $[514]_p \Leftrightarrow [514]_n$ spin-flip transition. The observed [1] $\log ft = 4{\cdot}5$ for the transition in (10) above, confirming the configuration $1^+(p_1n_0)$ for the 20·1-keV based band. Further the observed $\log ft = 4{\cdot}5$ for the ^{180}Re ground-state decay to the 1006·3-keV 2^- level in ^{180}W, which can only correspond to the transformation

$$^{180}\text{Re}, 1^-\{5/2^+[402]_p 7/2^-[514]_n\} \rightarrow {}^{180}\text{W}, 2^-\{5/2^+[402]_p 9/2^-[514]_p\}.$$

The $^{180}\text{Os} \rightarrow {}^{180}$Re decay level scheme also includes six other levels with $E_x = 218$–717 keV. However, no information is given about the intensities of individual beta branches, nor about which of these levels are directly fed. Accordingly it is presently not possible to propose any assignment for these levels. Based on our above discussion, we expect the following other transformations to directly populate ^{180}Re levels in this decay:

$$0^+\{9/2^-[514]^2_p\} \rightarrow 0^-\{9/2^-[514]_p 9/2^+[624]_n\},$$

$$0^+\{1/2^-[541]^2_p\} \rightarrow 1^+0 \text{ and } 1^+1\{1/2^-[541]_p 1/2^-[510]_n\},$$

$$0^+\{5/2^+[402]^2_p\} \rightarrow 2^-\{5/2^+[402]_p 1/2^-[510]_n\}.$$

The ^{180}Os decay needs further careful experiments including β–γ coincidence studies to elucidate this part of the ^{180}Re level scheme.

4.2 *Bands 3 and 4*

The (*HI*, *xn*) investigators [6, 10] agree that these two bands interconnect through a 78·6-keV *E*1 transition; this indicates opposite parities for the two bands with $\Delta K \leqslant 1$. Excepting this agreement, the groups give conflicting interpretation of data for the two bands. Whereas Kreiner *et al* characterized bands 3 and 4 (their bands A and B) as $8^+(p_1n_0)$ and mixed $\{9^-(p_1n_2); 8^-(p_1n_4)\}$ rotational bands, Venkova *et al* considered averaged mixing ratios and deduced gyromagnetic ratios g_K, along with Nilsson orbital systematics to suggest $6^-(p_0n_0)$ and $7^+(p_0n_2)$ characters for bands 3 (their band 1) and 4 respectively; they sought further confirmation of their assignment by considering rotational spacings and aligned angular momentum patterns. We

re-examine the data and various factors considered by Venkova *et al* in light of TQPRM predictions to arrive at an acceptable assignment for these bands.

First we consider the signature splitting expected for the above alternative assignments.

Signature splitting: The favoured signature is given by $\alpha_f = \{(-1)^{j_p - 1/2} + (-1)^{j_n - 1/2}\}$. The $5/2^+[402]_p$ orbital belongs to $d_{5/2}$ and $7/2^-[514]_n$ has a predominantly $h_{9/2}$ character in the Nilsson model. Therefore it gives the favoured signature $\alpha = 1$, favouring odd spins in the $K = 6^-$ band. Similarly, $9/2^+[624]_n$ belongs to $i_{13/2}$ and therefore $\alpha = 1$ signature would be favoured in $K = 7^+$ band also.

We however assign these bands as $K = 8^+$, $\{9/2^-[514]_p, 7/2^-[514]_n\}$ and $K = 9^-$, $\{9/2^-[514]_p, 9/2^+[624]_n\}$, respectively. According to our assignments $\alpha = 0$ signature would be favoured in both the bands and therefore even spins would lie lower in energy. Experimental data indeed show that even spins are actually favoured in both the bands. Note that changing $K = 6^-$ and 7^+ to $K = 8^+$ and 9^- will not change the favoured spin in the experimental data.

g_K- factors: The g_K factors deduced from the mixing ratios and angular distributions by Venkova *et al* and the Nilsson model estimates are summarized in table 2. The experimental values are $0{\cdot}92 \pm 0{\cdot}13$ for a $K = 6$ assignment and $0{\cdot}69 \pm 0{\cdot}09$ for a $K = 7$ assignment; these may be compared with the Nilsson-model estimates of 0·8 and 0·4 respectively. If we assign the K-values $K = 8$ and 9 to these two bands, the deduced g_K factors are $0{\cdot}75 \pm 0{\cdot}13$ and $0{\cdot}47 \pm 0{\cdot}09$ respectively which are in much better agreement with the Nilsson-model estimates of 0·8 and 0·5 for these two bands.

Systematics from neighbouring nuclei: A comparison of the behaviour of $K = 8$ and 9 bands observed with the same $2qp$ configuration in ^{178}Ta and ^{182}Re has been made with the proposed assignments in ^{180}Re in figure 2. The behaviour of the bands in all cases is very similar. This is a very strong indication in support of our assignments.

Table 2. Average gyromagnetic ratios g_k of bands in ^{180}Re as deduced by Venkova *et al* [10] from mixing ratios and angular distributions for different K values; the numbers in parentheses in columns 3 and 6 are extrapolated values. The entries in columns 4 and 7 are calculated g_k values [10] in the framework of the Nilsson model for the $2qp$ configuration specified in columns 2 and 5 in the notation of our table 1. The first row refers to band 1 of Venkova *et al* [10] which is the same as our band 3. Band 5 in our description has the admixed configuration as listed for the $K^\pi = 4^+$ entry in column 5.

Band No.	Venkova *et al* [10]			Ours		
	$K^\pi(p_i, n_j)$	g_k (expt)	g_k (calc)	$K^\pi(p_i, n_j)$	g_k (expt)	g_k (calc)
3	$6^-(p_0 n_0)$	$0{\cdot}92 \pm 0{\cdot}13$	0·8	$8^+(p_1 n_0)$	$0{\cdot}75 \pm 0{\cdot}13$	0·8
4	$7^+(p_1 n_3)$	$0{\cdot}69 \pm 0{\cdot}09$	0·4	$9^-(p_1 n_2)$	$(0{\cdot}47) \pm 0{\cdot}09$	0·5
5	$3^-(p_0 n_1)$	$1{\cdot}03 \pm 0{\cdot}10$	1·4	$4^+(p_2 n_0)$	$0{\cdot}86 \pm 0{\cdot}09$	0·3
				$(p_1 n_1)$		1·4
6	$2^-(p_0 n_1)$	$0{\cdot}08 \pm 0{\cdot}18$	1·3	$3^+(p_2 n_0)$	$(0{\cdot}25) \pm 0{\cdot}18$	0·2

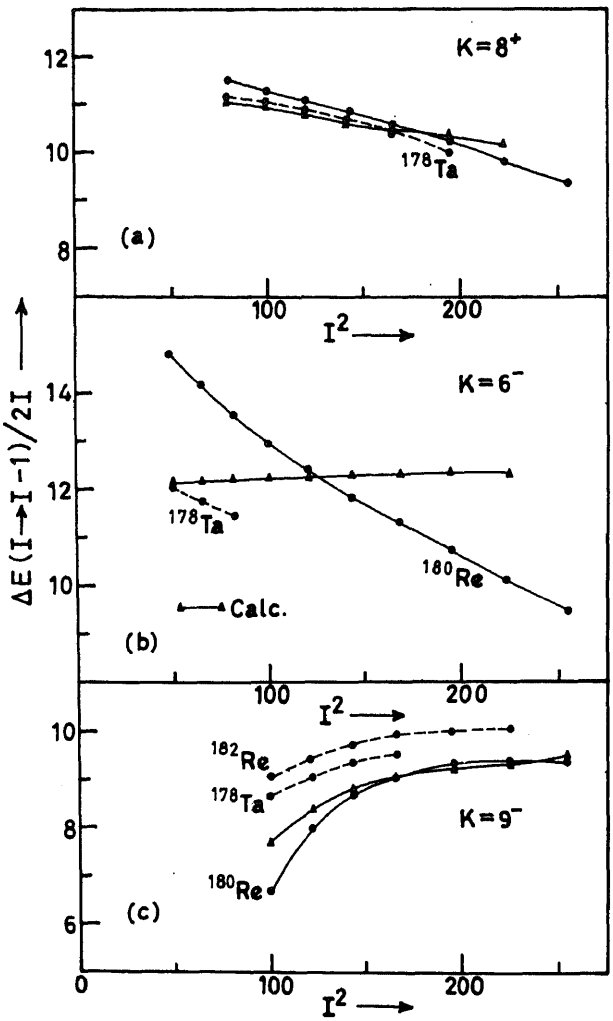

Figure 2. The behaviour of calculated rotational energy levels (shown by triangles joined by a solid line) for $K = 6$, 8 and 9 band assignments in ^{180}Re are compared with the actual data (dots joined by solid line) if the data were assigned these band quantum numbers. The energy difference $\Delta E(I \to I-1)/2I$ vs. the angular momentum square I^2 is plotted. Also shown by dashed lines are the experimental data for these bands in other odd-odd nuclei if available [24]. The experimental behaviour matches the calculated behaviour if the bands 3 and 4 are assigned the band quantum numbers $K = 8$ and 9 respectively.

Also, the compression of experimental energy levels of $K = 8$ and 9 bands is satisfactorily reproduced by the Coriolis mixing calculations as shown in figure 3.

Bandhead separation and GM splitting energy: The $K^\pi = 6^-$ bandhead assigned by Venkova *et al* is shown to feed a level with $I^\pi = 4^-$ or 5^- through a 134·5-keV γ-ray. The only origin of the 4^- or 5^- level is the $K^\pi = 1^-$ ground-state band. The observed separation for this GM pair in ^{176}Lu is 174 keV, whereas the $I^\pi = 4^-$ level of the

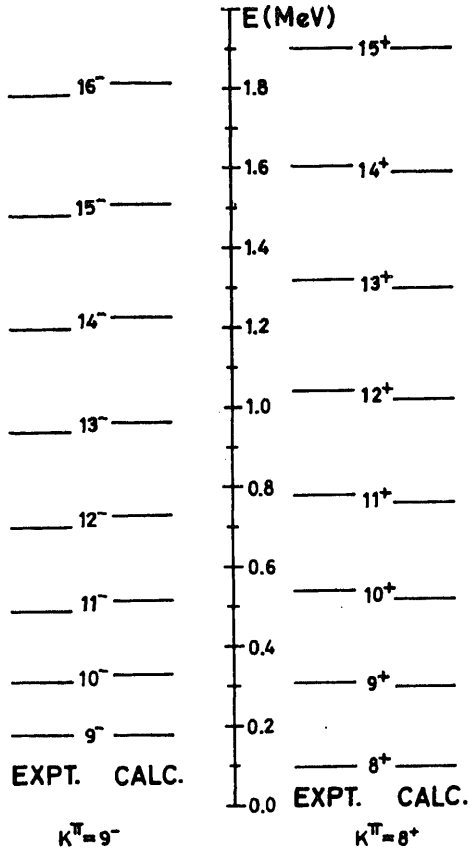

Figure 3. The rotational-energy levels of the $K = 8$ and 9 bands are compared with the calculated energy levels from the two-particle plus rotor model. The observed compression of the level energies is correctly reproduced.

$K^\pi = 1^-$ band is expected at $\geqslant 225$ keV. If we accept this assignment, it would imply an unacceptably large splitting ($\geqslant 360$ keV) of the $(6^- - 1^-)$ GM pair. It is therefore clear that the $K^\pi = 6^-$ assignment is not correct.

Similarly, band 4, assigned as the $K^\pi = 7^+$ band, lies barely 78·6 keV above the 6^- bandhead, whereas the expected separation is $\geqslant 250$ keV. Both the $K^\pi = 8^+$ and 9^- bands are expected to lie much lower and close together and satisfy all the criteria.

Alignment: The arguments in support of their assignments by Venkova *et al* based on alignments are not conclusive and do not exclude the configuration assignments made by us. The proton configuration used by Venkova *et al* is $5/2^+[402]_p$ whereas we replace this by $9/2^-[514]_p$, keeping the neutron configurations the same. We find that the alignment plots of $5/2^+[402]_p$ and $9/2^-[514]_p$ are very similar in their general behaviour as well as the total gain in alignment.

All the criteria/arguments therefore support the $K^\pi = 8^+(p_1 n_0)$ and $K^\pi = 9^-(p_1 n_2)$ assignments made by us.

4.3 *Bands 5 and 6*

Kreiner *et al* [6] identified only band 5 (labelled D by them) and assigned it an $i_{13/2}$ mixed $\{7^+(p_0n_2); 6^+(p_0n_4)\}$ configuration; however they deduced a value $K = 3{\cdot}59$ from the observed rotational spacings and also their calculations yielded $K_{calc} = 3{\cdot}89$ for this band.

On the other hand, Venkova *et al* [10] observed both of these bands and observed interband transitions for a few rotational levels connecting these two bands. The observed features indicated the same parity and $\Delta K = 1$ for these two bands with the higher-K band lying lower in energy, and also pointed to the possibility that the two bands may constitute a GM doublet with either the proton or the neutron occupying an $\Omega = 1/2$ orbital. Following these pointers and guided by the deduced mixing ratios δ and gyromagnetic ratios g_k, they proposed the lowest expected $\Omega = 1/2$ containing $2qp$ configuration (p_0n_1):$\{5/2^+[402]_p \pm 1/2^-[521]_n\}$ for these bands. However, as also discussed by them, this proposal has three serious shortcomings as discussed below.

First, by placing the $K^\pi = 3^-$ singlet band of the GM doublet lower in energy than its $K^\pi = 2^-$ triplet counterpart, the suggested assignment violates the GM rule. While critically examining the criteria for the applicability of the GM rule, Sood [22] had established the 'strong' rule that no violation of the GM rule is possible for cases wherein $K_T = K_< = |\Omega_p - \Omega_n|$, as is the case for this proposal. In view of this strong rule, the above suggested assignment is physically unacceptable. Secondly, their plots of alignment as a function of rotational frequency for the constituent orbitals for the neighbouring odd-A bands and for the bands 5 and 6 in ^{180}Re clearly reveal that the observed alignment variations of both these bands are inconsistent with their having a 5/2[402] proton orbital constituent. This is clearly reflected in the alignment plots (figure 4) of the orbitals under discussion from the neighbouring odd-A nuclei and also the bands 5 and 6 in ^{180}Re. We find that the 5/2[402] proton orbital exhibits a sharp rise at $\hbar\omega \approx 0{\cdot}27$ MeV, which is completely absent in bands 5 and 6. Thirdly the structure of the two bands is seen to differ markedly above the 5th rotational levels. Whereas the mixed dipole-quadrupole transitions are stronger than the stretched $E2$ transitions in band 5, band 6 separates into two stretched $E2$ sequences of different signatures with the $\Delta I = 1$ transitions having intensities too low to be observable. Also the alignment curves of bands 5 and 6 are seen to differ somewhat from each other. These features are inconsistent with their characterization as GM partners having the same configuration.

In view of these serious shortcomings of the proposed assignments for bands 5 and 6, we scanned the available configuration space, as shown in table 1, to look for bands of the same parity with $\Delta K = 1$ wherein the higher K is the triplet band. It is seen that the $K^\pi = 4^+$(triplet) and $K^\pi = 3^+$(singlet) bands of the (p_2n_0):$\{1/2[541]_p, 7/2[514]_n\}$ configuration meet these requirements. This choice does not violate the GM rule, nor does it contain the unacceptable (from alignment considerations) 5/2[402] proton orbital. The differing structure patterns for higher spins (above the levels connected by interband transitions) may result from mixing of another configuration in one of the bands. It is seen from table 1, and figure 1, that another $4^+(p_1n_1)$:$\{9/2[514]_p, 1/2[521]_n\}$ triplet band is expected not too far above the $4^+(p_2p_0)$; these two configurations may mix through $\Delta K = 0$ coupling [23], leading to structural differences for band 5 and band 6. Recalling that signature-dependent effects related to large decoupling parameters split the concerned bands into two

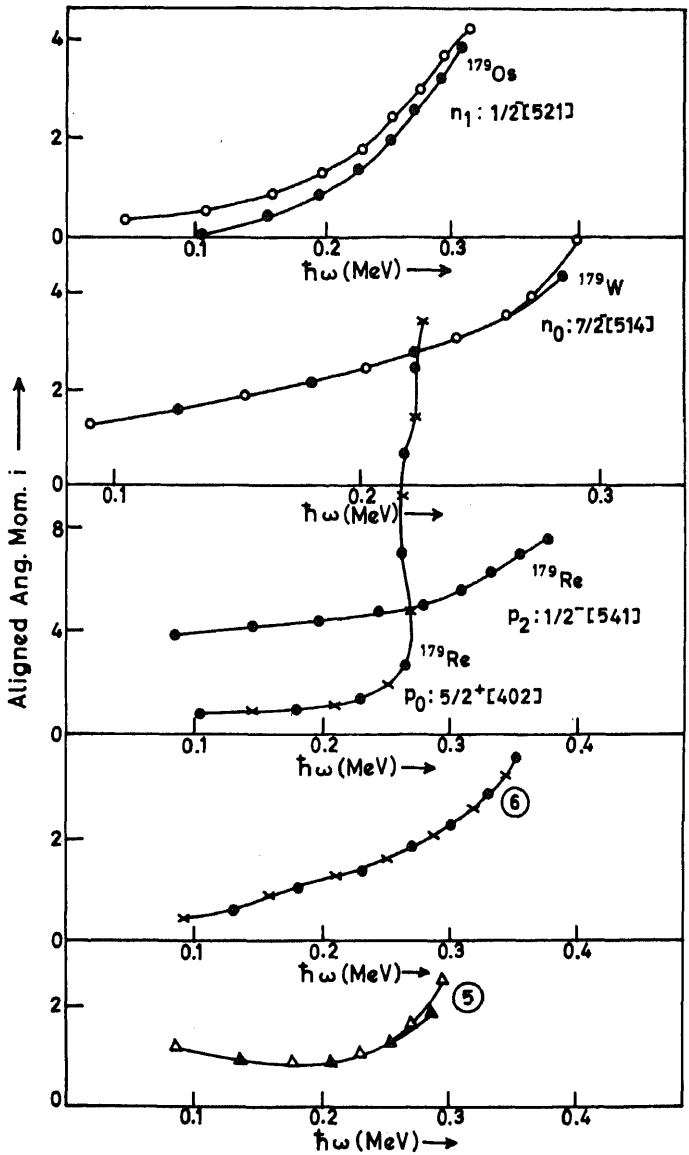

Figure 4. Plots of experimental aligned angular momenta i for the bands 5 and 6 in ^{180}Re and bands in neighbouring odd-A nuclei having configurations invoked to make configuration assignments for bands 5 and 6 as a function of the rotational frequency $\hbar\omega$ (adapted from ref. 10).

$\Delta I = 2$ sequences, we can relate the occurrence of such signature-split $\Delta I = 2$ sequences in band 6 to its $1/2[541]_p$ component which has decoupling parameter $a \approx 6{\cdot}0$. On the other hand, admixture of the $4^+(p_1 n_1)$ configuration with $1/2[521]_n$ component and decoupling parameter $a \approx 1{\cdot}0$ in band 5 results in the appearance of mixed dipole-quadrupole transitions in this band. Further support for these admixtures in band 5 comes from consideration of the gyromagnetic ratios g_k as listed in our table 2, we find that band 5 if assigned $K = 4$ has an experimental value in agreement with the

calculated Nilsson model value provided the $K^\pi = 4^+(p_2 n_0)$ band has a significant $4^+(p_1 n_1)$ component. It is also seen from table 2 that the assignment $2^-(p_0 n_1)$ of Venkova *et al* [10] for band 6 is clearly unacceptable on this point; our choice of a $3^+(p_2 n_0)$ configuration for this band yields satisfactory agreement. Further, as noted by Kreiner *et al* [6], the observed rotational level energies in band 5 yield $K \approx 4$ supporting our assignment.

Thus a consideration of all of these experimental and theoretical features, e.g. rotational level spacings, their alignments, signature splitting, g_k factors, singlet-triplet ordering etc., supports the admixed $4^+[(p_2 n_0); (p_1 n_1)]$ and $3^+(p_2 n_0)$ assignments for bands 5 and 6 respectively. This assignment has no physically unacceptable or experimentally inconsistent features as noticed for the earlier proposed $3^-(p_0 n_1)$ and $2^-(p_0 n_1)$ assignment for these bands.

5. Summary and conclusions

The experimental data on the energy levels of the odd-odd deformed nucleus ^{180}Re obtained from ^{180}Os ε-decay and from ^{170}Er$(14N, 4n\gamma)$, ^{176}Yb$(^{10}B, 6n\gamma)$ and ^{181}Ta$(\alpha, 5n\gamma)$ reaction studies have been examined to deduce the spin-parities (band quantum numbers K^π) and $2qp$ (Ω_p, Ω_n) configuration assignments for the three pairs of bands with $K < 10$. The earlier suggested, tentative and conflicting, assignments have been critically examined with a view to arrive at acceptable assignments free from the inconsistencies and physically undesirable characteristics of earlier proposals. $2qp$ bandhead-energy calculations for a zero range residual interaction including band mixing have been used for mapping the extended configuration space. Strong rules for the applicability of the GM rule for triplet-singlet ordering, and for configurational relationships in allowed unhindered beta decays, are used as guidelines.

Our analysis confirms the earlier suggested $I^\pi K$ and configuration assignments for the four lowest levels observed in ^{180}Os decay. For the pair of high-spin opposite-parity bands, where the higher lying 73 ± 3 ns bandhead is connected by a 78·6-keV $E1$ transition to the lower lying bandhead, we assign the configuration $9^-\{9/2[514]_p + 9/2[624]_n\}$ and $8^+\{9/2[514]_p + 7/2[514]_n\}$. These assignments are the same as given by Kreiner *et al* [6] who had also suggested additional $i_{13/2}$ mixing in the $K^\pi = 9^-$ band. For the pair of same-parity interconnected (through inter-band transitions) bands numbered 5 and 6 by us and also by Venkova *et al* [10], we assign the admixed configuration $4^+\{1/2[541]_p + 7/2[514]_n\}$ and $4^+\{9/2[514]_p - 1/2[521]_n\}$ for band 5 and $3^+\{1/2[541]_p - 7/2[514]_n\}$ for band 6. These assignments are shown to be consistent with all the features deduced for these bands in heavy-ion reaction studies and are free from the unphysical or undesirable characteristics noticed for the earlier tentative suggestions. In common with the earlier investigations of this level scheme, we also do not find it possible to interconnect these three pairs of bands or to connect the observed excitations with the ground state on the basis of available experimental data.

Acknowledgements

Valuable communications from E Browne, B Singh and R M Lieder are gratefully acknowledged. Useful comments from David Headly are highly appreciated. These investigations were supported by the Department of Atomic Energy, Govt. of India, at the University of Roorkee and Banaras Hindu University, and by the US National

Science Foundation under contract no. PHY-92-07336 with the Florida State University.

References

[1] E Browne 1987 *Nuclear Data Sheets* **52**, 127; private communication 1994
[2] K J Hofstetter and P J Daly, *Phys. Rev.* **152**, 1050 (1966), **159**, 1000 (1967)
[3] P F A Goudsmit, J Konijn and F W N de Boer, *Nucl. Phys.* **A104**, 497 (1967)
[4] B Harmatz and T H Handley, *Nucl. Phys.* **A121**, 481 (1968)
[5] J Konijn, P F A Goudsmit, F W N DeBoer and B J Meijer, *Nucl. Phys.* **A114**, 602 (1968)
[6] A J Kreiner, J Davidson, M Davidson, D Abriola, C Pomar and P Thieberger, *Phys. Rev.* **C36**, 2309 (1987)
[7] Ts Venkova, B Bochev, W Gast, T Kutsarova, R M Lieder, T Morek and G Sletten, *Annual Report* 1983, IKP, KFA Julich, Jul-Spez-255, 57 (1984)
[8] J Schaffler-Krah, Ts Venkova, B Bochev, W Gast, G Hebbinghaus, A Kramer-Flecken, T Kutsarova, R M Lieder, T Morek, G Sletten and W Urban, *Annual Report* 1984, IKP, KFA Julich, Jul-Spez-305, 126 (1985)
[9] Ts Venkova, R M Lieder, T Morek, W Gast, G Hebbinghaus, A Kramer-Flecken, J Schaffler-Krah, W Urban, H Kluge, K H Maier, A Maj and G Sletten, *Annual Report* 1985, IKP, KFA Julich, Jul-Spez-344, 49 (1986)
[10] Ts Venkova, R M Lieder, T Morek, W Gast, G Hebbinghaus, A Kramer-Flecken, J Schaffler-Krah, W Urban, G Sletten, H Kluge and K H Maier, *Nucl. Phys.* **A514**, 87 (1990)
[11] C J Gallagher and S A Moszkowski, *Phys. Rev.* **111**, 1282 (1958)
[12] A K Jain, R K Sheline, P C Sood and K Jain, *Rev. Mod. Phys.* **62**, 393 (1990)
[13] J P Boisson, R Piepenbring and W Ogle, *Phys. Rep.* **C26**, 99 (1976)
[14] A K Jain, J Kvasil, R K Sheline and R W Hoff, *Phys. Lett.* **B209**, 19 (1988)
[15] A K Jain, J Kvasil, R K Sheline and R W Hoff, *Phys. Rev.* **C40** 432 (1989)
[16] P C Sood and R N Singh, *Nucl. Phys.* **A373**, 519 (1982)
[17] P C Sood, R K Sheline and R S Ray, *Phys. Rev.* **C35**, 1922 (1987)
[18] P C Sood, R K Sheline and R W Hoff, *Pramana – J. Phys.* **30**, 93 (1988)
[19] P C Sood and R S Ray, *Pramana – J. Phys.* **27**, 537 (1986)
[20] A Goel, A K Jain, R W Hoff and R K Sheline, *Pramana – J. Phys.* **36**, 105 (1991)
[21] P C Sood and R K Sheline, *At. Data Nucl. Data Tables*, **43**, 259 (1989); P C Sood and R K Sheline *Phys. Scr.* **41**, 25 (1990)
[22] P C Sood, *Radiation effects* **95**, 115 (1986)
[23] H Massman, J O Rasmussen, T E Ward, P E Haustein and F M Bernthal, *Phys. Rev.* **C9**, 2312 (1974)
[24] R K Sheline, D M Headly, P C Sood, A K Jain, R W Hoff, D Nosek, J Kvasil and D G Burke, *At. Data Nucl. Data Tables* (to be submitted)

PRAMANA
— journal of
physics

© Printed in India

Vol. 43, No. 5,
November 1994
pp. 353–360

Sound velocity in binary liquid mixtures and the statistical mechanical theories

J D PANDEY, SHIKHA, A K SHUKLA and ANIL K SINGH*
Department of Chemistry, University of Allahabad, Allahabad 211 002, India
*Physics Department, Allahabad Degree College, Allahabad 211 004, India

MS received 10 January 1994; revised 23 August 1994

Abstract. Sound velocity in three binary liquid mixtures benzene + cyclohexane (I), cyclohexane + carbontetrachloride (II) and benzene + carbontetrachloride (III) has been measured. Significant structure and Flory – Patterson theories have been employed to evaluate ultrasonic velocity in the systems. The values are in good agreement with the experimental ones. A comparative study of significant structure theory and Flory–Patterson Theory has been made. Both the theories give satisfactory results for the three liquid mixtures.

Keywords. Significant structure theory; ultrasonic velocity; binary liquid mixture; Flory–Patterson theory

PACS Nos 43·00; 43·35

1. Introduction

The most widely used significant structure theory (SST) of liquids [1–4] has been employed by Choi and Jhon [5–6] for evaluating the sound velocity, internal pressure and van der Waals constant in pure liquids. Similar deductions were also carried out, recently, for molten salts [7–8] and liquid metals [9]. Although SST has been applied earlier to binary liquid mixtures [1, 10, 11] for calculating viscosity, surface tension and excess thermodynamic properties, its applicability for sound velocity in binary liquid mixtures has not, so far, been tested. Very recently [12] this theory has been applied quite successfully for transport properties in the case of ternary liquid systems. In the present paper SST has been applied for evaluating sound velocity in three different binary liquid mixtures. The results of theoretical calculations obtained from SST have been compared with those deducted from Flory–Patterson theory (FPT) [13–15], as well as the experimental values. The latter theory has recently been applied for estimating the sound velocity in varieties of liquid mixtures [16–21]. The three binary liquid mixtures considered for the present investigations are: benzene + cyclohexane (I), cyclohexane + carbontetrachloride (II), and benzene + carbon tetrachloride (III).

2. Experimental

Component liquids of BDH grade were distilled before use and their boiling points were recorded to ensure their purity [22]. Ultrasonic velocity was measured using an interferometer (supplied by M/S Mittal Enterprises, New Delhi, India) operating

at a frequency of 2·0 MHz. The density of liquids were measured by a precalibrated double stemmed pycnometer at a constant temperature of 298·15 K which was maintained by a thermostatically controlled bath to ±0·01°C. The uncertainties in velocity and density measurements were ±0·1 and ±0·0001 respectively.

3. Theoretical

The velocity of sound, u, obeys the relation

$$u=\left(\frac{C_p V}{C_V \beta_T M}\right)^{1/2}=\left(\frac{\gamma}{\beta_T \rho}\right)^{1/2}, \tag{1}$$

where γ, β_T and ρ are the ratio of C_p to C_V, isothermal compressibility and density respectively. All these quantities in SST are evaluated in terms of the partition function, f, using the relations,

$$C_p=C_V+\frac{\alpha^2 TV}{\beta_T}, \tag{2}$$

α being the thermal expansion coefficient.

$$C_V=\left[\frac{\partial}{\partial T}\left\{kT^2\left(\frac{\ln f}{T}\right)_V\right\}\right]. \tag{3}$$

$$\beta_T=\left[VkT\left(\frac{\partial^2 \ln f}{\partial V^2}\right)_T\right]^{-1} \tag{4}$$

$$\alpha=\frac{[\partial^2(-kT\ln f)/\partial V\cdot\partial T]_{T,V}}{VkT(\partial^2 \ln f/\partial V^2)_T} \tag{5}$$

However, it should be noted that the partition function, f, in the present case is the partition function of the mixture and can be expressed in terms of the partition functions, f_1 and f_2, of the pure components 1 and 2 respectively,

$$f=\left[\frac{(N_1+N_2)!}{N_1!N_2!}\right]f_1 f_2 \times [1+n(X-1)\exp-(\xi N(V_S/V))]$$
$$\exp[N(E_S/RT)(V_S/V)] \tag{6}$$

where

$$f_1=(f_{1S})^{N_1(V_S/V)}(f_{1g})^{N_1(V-V_S)/V},$$

and

$$f_2=(f_{2S})^{N_2(V_S/V)}(f_{2g})^{N_2(V-V_S)/V}.$$

Here, F_S, f_g, N_1, N_2, V_S, and V are respectively the solid like partition function, gas like partition function, number of molecules of types 1 and 2, the molar volume of the solid at the melting point and the molar volume of the liquid. X and ξ are given by V/V_S and $a\cdot E_S/[RT(X-1)]$, a being a proportionality factor, E_S is the energy of sublimation at the melting point and n is the coordination number of the lattice. The detailed expressions for f_{1S}, f_{2S}, f_{1g}, and f_{2g} for the various liquids under the present study viz. benzene, cyclohexane, and carbontetrachloride have been derived by Eyring and coworkers [10–11]. These expressions in conjunction with eqs (1) and (6) have

been used to deduce the value of the ultrasonic velocity in binary liquid mixtures from SST.

Sound velocity can also be deduced on the basis of FPT [13–16]. The method of deduction has also been extended to binary mixtures during recent years [16, 19–20]. The resulting expressions for the velocity of sound according to this theory has the following forms [23]:

$$u = 5{\cdot}663\left(\frac{k^2 P^{*4} T^{*2} L^2}{\rho^2 M}\right)^{1/6}\left[M\tilde{V}^{-5/3} - \left(\frac{V^{1/3}-1}{V^2}\right)\ln\left(\frac{\tilde{V}^{1/3}-0{\cdot}5}{\tilde{V}^{1/3}-1}\right)\right]^{2/3} \quad \text{(FPT-Altenberg Relation)} \tag{7}$$

and

$$u = \left(\frac{kP^{*2} T^*}{6{\cdot}3\times 10^{-4}\rho}\right)^{2/9}\left[M\tilde{V}^{-5/3} - \left(\frac{\tilde{V}^{1/3}-1}{\tilde{V}^2}\right)\ln\left(\frac{V^{1/3}-0{\cdot}5}{V^{1/3}-1{\cdot}0}\right)\right]^{2/3} \quad \text{(FPT-Auerbach Relation)} \tag{8}$$

where, P^*, T^*, and $\tilde{V}$ are respectively the characteristic pressure, characteristic temperature and reduced volume of the binary liquid mixtures, k is the Boltzmann constant, L, the Laschmidt number, and M is a constant having value less than 1. Its significance has been discussed earlier [15, 16]. Evaluation procedure for P^*, T^* and V are detailed out in previous papers [13–19]. The other symbols have their usual notations.

4. Results and discussion

The sound velocity, u, in three binary liquid mixtures, namely, benzene + cyclohexane (I), carbon tetrachloride + cyclohexane (II), and benzene + carbontetrachloride (III), at 298·15 K are computed theoretically from SST using eqs (1) to (6). Theoretical sound velocities for these three systems have also been evaluated on the basis of FPT, employed earlier [23] for such purpose, using two different approaches, vide eqs (7) and (8). The values of pure components parameters needed for these computations were taken from literature [10–11, 21–23]. Theoretically computed values of sound velocity in systems (I), (II), and (III) on the basis of SST and FPT are compared with those experimentally determined. The standard deviations (per cent) of theoretical values deduced from these theories with observed ones are:

	I	II	III
SST	0·76	3·53	2·97
FPT (Auerbach)	1·65	5·35	3·11
FPT (Altenberg)	5·66	3·96	6·98

Thus, both the statistical theories (SST and FPT) yield fairly reasonable agreement (within 7·0 per cent) for all the three systems under the present investigation.

The composition dependence of sound velocity in all the three binary liquid mixtures has been investigated both theoretically and experimentally. The results obtained from SST [vide eqs (1) to (6)] and FPT [vide eqs (7) and (8)] are shown graphically in figures 1–3 corresponding to systems (I), (II), and (III) respectively. In these figures the experimental sound velocity-composition curves have also been plotted. For the system benzene + cyclohexane (I), the theoretical and observed sound velocity values are plotted against the mole fraction of benzene. By increasing the benzene content in the mixture the velocity first decreases and then increases continuously. Such a trend is also observed in the case of theoretical sound velocity values deduced both from SST and FPT. The unusual trend in the velocity-composition curve observed here, both experimentally and theoretically at 298·15 K in the case of this system, has also been verified earlier by Reddy *et al* [24] at 27·5°C and by Moore *et al* [25] at 25°C.

Benzene is diatomic i.e. it can sustain induced ring current due to the presence of 6π electrons in the form of a closed loop, while cyclohexane is a flat ring without any such characteristics.

It is well known that benzene rings stack together side by side, with the π-electrons interacting to form weak bonds shown below by dotted lines while maintaining a minimum fixed distance. When cyclohexane is mixed the molecules of the two orient themselves in a way that there is disruption in the intermolecular π–π bonding of benzene ring currents, the two being identical in molecular shape and size. This explains the initial drop in ultrasonic velocity. On increasing the concentration of

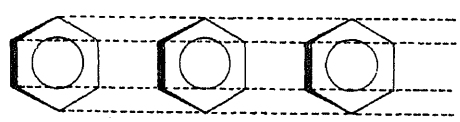

Stacking of benzene ring

either, there is no such disruption of orientation (stacking), resulting in continuous increase in the velocity.

By increasing the mole fraction of cyclohexane in system (II) and benzene in system (III), the sound velocity is found to increase continuously, as evident from figures 2 and 3. The same trend is also predicted by FPT and SST. Moreover, the experimental curve is very much closer to the theoretical curves obtained from both the theories. Such behaviour is in agreement with the earlier findings [24, 25]. Thus, it may be concluded that both the statistical mechanical theories (FPT and SST) predict the same trend of composition dependence of sound velocity as observed experimentally in case of all the three systems under the present investigation.

It appears from the magnitude of standard deviations that SST has an edge over the FPT in all the three systems. The validity of SST in case of binary liquid mixtures depends on two factors. Firstly, this theory does not contain any adjustable parameters, although a criticism is generally raised against this theory. This is regarding the number of adjustable parameters E_S, θ, V_S, a, and μ in the evaluation of partition functions. In these calculations the values of E_S, θ, and V_S are obtained from the solid state data, and μ and a obtained through the relations:

$$\mu = ZV_s/V$$

and

$$a = [(n-1)/2Z(V_m - V_S)^2]/V_m V_S.$$

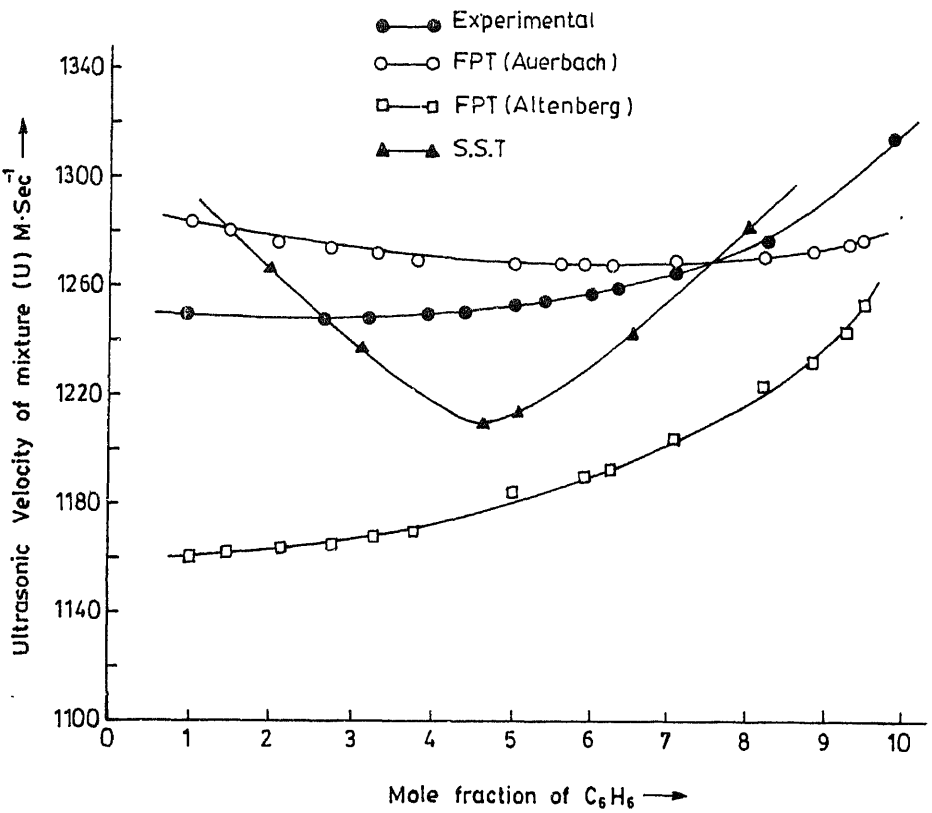

Figure 1. Variation of ultrasonic velocity of mixture $C_6H_6 + C_6H_{12}$ as function of mole fraction of benzene.

Thus, the introduction of adjustable parameters is avoided. Secondly, in formulating the partition functions, both solid like and gas like freedom have been considered, which gives an ideal representation of all the possible states. On the other hand, FPT contains one adjustable parameter i.e. the fraction of nearest neighbours which a molecule loses on moving from the bulk of the liquid to the surface, M. In the present case the value of M has been taken to be 0·28. However, it can vary from 0·26 to 0·31 [15, 17]. Another reason of discrepancy in FPT may be due to the use of empirical relations of Auerbach and Altenberg in transforming surface tension to sound velocity [23]. Although these relations have been well verified for liquid mixtures [16, 23]. Despite these facts FPT gives reasonable agreement with observed sound velocity values and its composition dependence for all the three systems (I), (II) and (III).

For most of the liquid mixtures the temperature dependence of ultrasonic velocity is given by,

$$u = \left(\frac{\Delta u}{\Delta t}\right) t + u_0. \tag{9}$$

Here, $\Delta u/\Delta t$ is the temperature coefficient of ultrasonic velocity and u_0 is the sound velocity at 0°C. It has been shown quite early by Rao [26] and verified by several workers that the following expression holds approximately true for many liquid

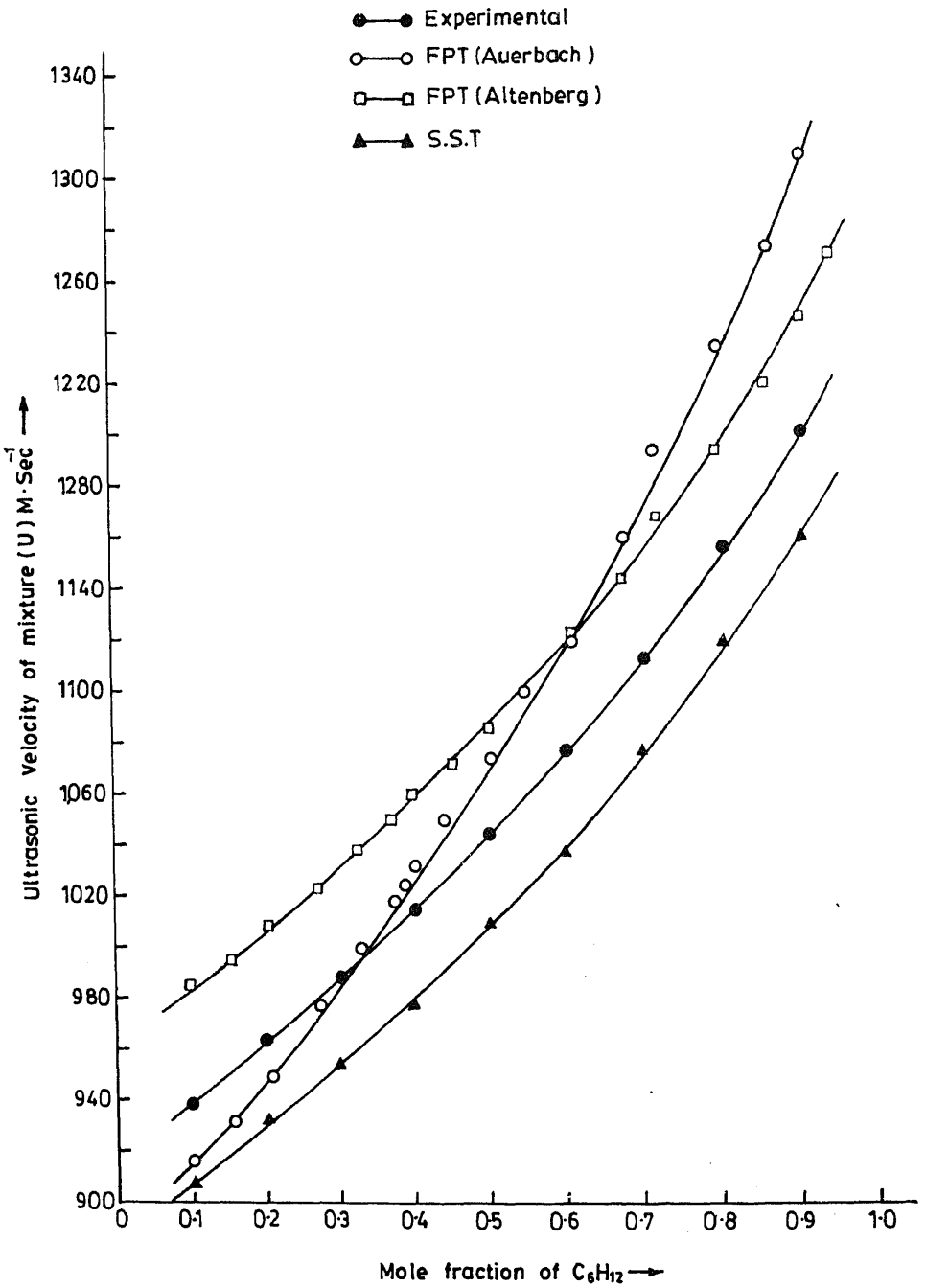

Figure 2. Variation of ultrasonic velocity of mixture $C_6H_{12} + CCl_4$ as a function of mole fraction of cyclohexane.

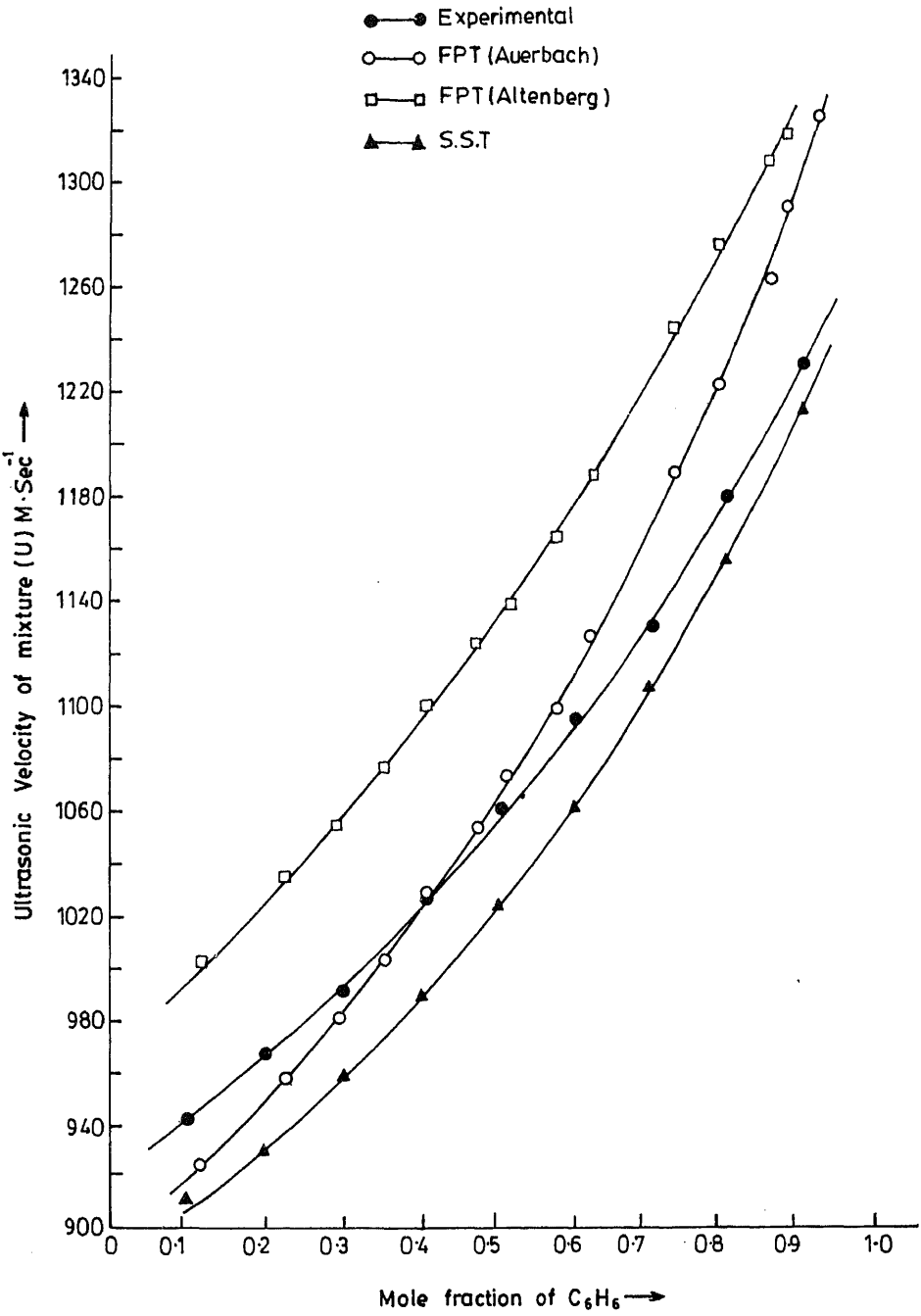

Figure 3. Variation of ultrasonic velocity of mixture $C_6H_6 + CCl_4$ as a function of mole fraction of benzene.

systems:

$$\frac{1}{u}\frac{\partial u}{\partial t} \approx 3\left(\frac{1}{\rho}\right)\left(\frac{\mathrm{d}\rho}{\mathrm{d}t}\right). \tag{10}$$

Since the density of liquid mixture decreases by increasing the temperature, the ultrasonic velocity will decrease by increasing the temperature. The temperature coefficient of ultrasonic velocity ($\Delta u/\Delta t$) in (9) is always negative for mixtures except aqueous mixtures where the situation is complicated. In the case of pure water the temperature corresponding to minimum in sound velocity shifts by the addition of other component. This is related with structural changes [27–28].

Acknowledgements

Authors are grateful to Dr (Mrs) Krishna Misra, Department of Chemistry, University of Allahabad for her valuable suggestions. The authors are also thankful to the CSIR, New Delhi for providing financial assistance.

References

[1] D Henderson, *Physical chemistry – An advanced treatise, liquid state* (Academic Press, New York, 1971) Vol. VIIIA, p. 335
[2] H Eyring, M S Jhon and S H Lee, *Proc. Natl. Acad. Sci.* (USA) **74**, 10 (1977)
[3] H Eyring, M S Jhon and R Ryoo, *Proc. Natl. Acad. Sci.* (USA) **77**, 4399 (1980)
[4] M S Jhon and J M Lee, *Bull. Korean Chem. Soc.* **1**, 26 (1980)
[5] D S Choi and M S Jhon, *Chem. Phys. Lett.* **5**, 57 (1970)
[6] M S Jhon, *Sound velocity and van der Waals forces in liquids according to significant structure theory, Chem. Dyn.* (Jhon-Wiley and Sons, Inc., London, 1971)
[7] J D Pandey, *Electrochimica Acta* **27**, 1092 (1982)
[8] J D Pandey and U Gupta, *Electrochimica Acta* **29**, 403 (1984)
[9] K N Swamy, *Acustica*, **29**, 183 (1973)
[10] H Eyring and S M Ma, *J. Chem. Phys.* **42**, 1920 (1965)
[11] K Liang, H Eyring and R P Marchi, *Proc. Natl. Acad. Sci.* (USA), **52**, 1107 (1964)
[12] J D Pandey, A K Shukla, Shikha and N Tripathi, *Indian J. Chem.* **A33**, in Press (1994)
[13] P J Flory, *J. Am. Chem. Soc.* **87**, 1833 (1965)
[14] P J Flory and A Abe, *J. Am. Chem. Soc.* **87**, 1838 (1965)
[15] D Patterson and A K Rastogi, *J. Phys. Chem.* **74**, 1067 (1970)
[16] J D Pandey, *J. Chem. Soc., Faraday Trans. II*, **76**, 1215 (1980)
[17] J D Pandey, V N P Srivastava, V Vyas and N Pant, *Indian J. Pure Appl. Phys.* **25**, 467 (1987)
[18] J D Pandey, R K Shukla, A K Shukla and R D Rai, *J. Chem. Thermodyn.*, **21**, 125 (1989)
[19] S L Oswal, *Acoust. Lett.* **14**, 17 (1990)
[20] D D Deshpande, J S Murty and M S Khanwalkar, *Acoust. Lett.* **13**, 121 (1990)
[21] J D Pandey, R D Rai, R K Shukla, A K Shukla and N Mishra, *Indian J. Pure Appl. Phys.* **31**, 84 (1993)
[22] CRC Handbook of Chemistry and Physics, (CRC Press, Boca, Raton, Florida) 60th Ed. (1979–80)
[23] J D Pandey, N Pant, N Agrawal and Shikha, *Acustica* **68**, 225 (1989)
[24] K C Reddy, S V Subrahmanyam and J Bhimasenachar, *J. Phys. Soc. Jpn.* **19**, 559 (1964)
[25] W R Moore and R J Fort, *Trans. Faraday Soc.* **61**, 2102 (1965)
[26] M R Rao, *J. Chem. Phys.* **14**, 109 (1940)
[27] S V Subrahmanyam and N M Moorthy, *J. Soln. Chem.* **4**, 347 (1975)
[28] K C Reddy and N P Rao, *Z. Physik. Chemie.* (Neue Folge), **100**, 133 (1976)

PRAMANA
— journal of
physics

© Printed in India

Vol. 43, No. 5,
November 1994
pp. 361–372

Isothermal compressibility and sound velocity of binary liquid systems: Application of hard sphere models

J D PANDEY, P JAIN and V VYAS
Department of Chemistry, University of Allahabad, Allahabad 211 002, India

MS received 5 February 1994; revised 29 August 1994

Abstract. Sound velocity and density were measured in six binary liquid mixtures namely, *n*-heptane + toluene (I); *n*-heptane + *n*-hexane (II); toluene + *n*-hexane (III); cyclohexane + *n*-heptane (IV); cyclohexane + *n*-hexane (V), and *n*-decane + *n*-hexane (VI) at 298·15 K. The experimental isothermal compressibility has been evaluated from measured values of density and sound velocity. The isothermal compressibility of these mixtures has been calculated theoretically using different models for the hard sphere equation of state and also using Flory's statistical theory. The computed values of isothermal compressibility were also compared with the experimentally evaluated values. A satisfactory agreement has been observed.

Keywords. Isothermal compressibility; sound velocity; density; binary liquid systems; hard sphere equation of state.

PACS Nos 43·00; 51·40; 62·60; 62·65

1. Introduction

The prime object of sound velocity and density measurements in liquid systems is to estimate the value of isentropic compressibility (β_s) which cannot be done by any other method. Isentropic compressibility has been widely used to study the molecular interactions through its excess value. On the other hand, it can also be used to deduce other useful thermodynamic properties e.g. isothermal compressibility, (β_T), heat capacity ratio (γ), internal pressure (P_i), cohesive energy density, (CED) etc. Latter parameters are only accessible from β_s provided the values of thermal expansion coefficient, (α) and heat capacity at constant pressure (C_p) are known. Isothermal compressibility and heat capacities ratio are the two key parameters in molecular thermodynamics of fluid phase equilibria. Various hard sphere equations of state have been applied to evaluate the values of β_T, γ, and sound velocity (c) of pure liquids under varying physical conditions [1–5]. Such models were also applied to a few binary liquid mixtures [6–7] for estimating β_T. The theoretical values of β_T compared with the experimental values which were obtained from β_s, α, and C_p data. Experimental measurement of β_T for some binary mixtures have been reported earlier [8–9]. In the present work, the results of experimental measurements of sound velocity (c) in and density (ρ) of six binary liquid mixtures, namely—*n*-heptane + toluene (I); *n*-heptane + *n*-hexane (II); toluene + *n*-hexane (III); cyclohexane + *n*-heptane (IV); cyclohexane + *n*-hexane (V) and *n*-decane + *n*-hexane (VI) are reported at 298·15 K. Further, density and sound velocity data were employed to evaluate β_T with the help of empirical equation derived. β_T values were also estimated with the help of various

important hard sphere models. Another approach i.e. Flory's statistical theory [10–11] is also used to compute β_T values of binary liquid systems under the present investigation. This method has also been used earlier by a few workers [12–15]. The set of β_T values obtained are compared with the experimental β_T value deduced from the derived equation. With the help of sound velocity and density data, the values of γ and β_s for all the systems are also computed. This is entirely a new approach for estimating isothermal compressibility of liquid mixtures.

2. Experimental

All the organic liquids used were of analytic reagent grade and were obtained from BDH Chemicals Ltd., England. These chemicals were further purified by double distillation. Densities and speeds of sound were measured at 298·15 K. Densities were determined with a precalibrated bicapillary pyknometer with an accuracy of $\pm 0{\cdot}3\,\mathrm{kg/m^3}$ (approx. 0·05%). Speed of sound measurements were made with a single crystal variable path ultrasonic interferometer at 2 MHz frequency and the data were accurate to $\pm 0{\cdot}01$ per cent.

The purity of the samples were checked by comparing the measured density of the compounds with those reported in literature [16]. The measured densities and speeds of sound along with the literature values are presented in table 1.

3. Theoretical

The isothermal compressibilities of six binary liquid mixtures were evaluated using the following rigid sphere equations of state:

$$\frac{PV}{NkT} = \frac{1+y+y^2}{(1-y)^3} \quad [17] \tag{1}$$

$$\frac{PV}{NkT} = \frac{1+2y+3y^2}{(1-y)^2} \quad [18\text{–}19] \tag{2}$$

$$\frac{PV}{NkT} = \frac{1+y+y^2-y^3}{(1-y)^3} \quad [20] \tag{3}$$

Table 1. Density (ρ) and sound velocity (c) of pure component liquids at 298·15 K.

Component	$\rho \times 10^{-3}(\mathrm{kg\,m^{-3}})$		$c(\mathrm{ms^{-1}})$	
	Present study	Lit.	Present study	Lit.
Toluene	0·8626	0·8625	1304·3	1304·0
Cyclohexane	0·7736	0·7738	1252·0	1253·3
n-Hexane	0·6548	0·6550	1075·8	1076·0
n-Heptane	0·6790	0·6795	1131·0	1131·0
n-Decane	0·7260	0·7263	1125·0	1225·2

$$\frac{PV}{NkT} = \frac{1}{(1-y)^4} \qquad [21] \tag{4}$$

$$\frac{PV}{NkT} = \frac{1}{(1-y)^2} \qquad [22] \tag{5}$$

$$\frac{PV}{NkT} = \frac{1+y^2/8}{(1-y)^2} \qquad [23] \tag{6}$$

$$\frac{PV}{NkT} = 1 + 4y + 10y^2 + 18{\cdot}36y^3 + 28{\cdot}2y^4 + 39{\cdot}5y^4 + \ldots \quad [24] \tag{7}$$

where, P V, T, N and k are respectively the pressure, volume, absolute temperature, Avogadro's number and Boltzmann constant. y is the packing fraction equal to $\pi a^3 N/6V$ in all cases, a being the hard sphere diameter of the molecule. The expressions for the isothermal compressibility, β_T, corresponding to eqs (1) to (7) are obtained as:

$$\beta_T = \frac{V}{RT}\frac{(1-y)^4}{(1+2y)^2} \tag{8}$$

$$\beta_T = \frac{V}{RT}\frac{(1-y)^3}{1+5y+9y^2-3y^3} \tag{9}$$

$$\beta_T = \frac{V}{RT}\frac{(1-y)^4}{1+4y+4y^2-4y^3+y^4} \tag{10}$$

$$\beta_T = \frac{V}{RT}\frac{(1-y)^5}{1+3y} \tag{11}$$

$$\beta_T = \frac{V}{RT}\frac{(1-y)^3}{1+y} \tag{12}$$

$$\beta_T = \frac{V}{RT}\frac{8(1-y)^3}{8+8y+3y^2-y^3} \tag{13}$$

$$\beta_T = \frac{V}{RT}(1+8y+30y^2+73{\cdot}44y^3+141{\cdot}0y^4+273{\cdot}0y^5)^{-1} \tag{14}$$

Flory's theory yields the following expression [10–11] for the isothermal compressibility:

$$\beta_T = \frac{\alpha_T \tilde{V}^2}{P^*} \tag{15}$$

where, $\tilde{V}$ and P^* are respectively the reduced volume and characteristic pressure of the liquid mixture. Values of $\tilde{V}$ and P^* were evaluated by the procedure detailed out by Flory and used by other workers [12–15].

In 1966, Mc-Gowan [25] suggested the following relationship between isothermal compressibility and surface tension (σ):

$$\beta_T \sigma^{3/2} = 1{\cdot}33 \times 10^{-8} \quad \text{(cgs units)} \tag{16}$$

The Auerbach relationship [26] between speed of sound (c) and surface tension (σ),

$$c = \left(\frac{\sigma}{6{\cdot}4 \times 10^{-4}\rho}\right)^{2/3} \tag{17}$$

has been employed by a number of workers during recent years [12–15, 27] in the case of pure liquids, solutions and non-electrolytes, molten salts and liquid metals. From (14) and (15), one gets,

$$\beta_T = \frac{1{\cdot}33 \times 10^{-8}}{(6{\cdot}3 \times 10^{-4} c^{3/2} \cdot \rho)^{3/2}} \tag{18}$$

This expression gives a direct relationship between isothermal compressibility, speed of sound and density. This relation has been tested for a variety of liquids under varying physical conditions.

4. Results and discussion

The experimental values of sound velocity (c) and density (ρ) of all the pure component liquids of various binary systems at 298·15 K have been determined and recorded in table 1 along with the literature values. The agreement between the two set of values is good. Density and sound velocity of six binary liquid mixtures (I–VI) at 298·15 K have been measured as a function of composition, and the values are recorded in columns two and three of tables 2–7. Sound velocity and density data, obtained for all the six binaries, have been utilized to estimate the experimental values of isothermal compressibilities (β_T) from (18). These values are reported in column four of each table (tables 2–7) for the respective systems mentioned. Two sets of data are generated for computing the theoretical values of β_T for all the binary mixtures. In one set various hard sphere models, vide eqs (1)–(7), have been used. The corresponding values of compressibility have been computed from eqs (8)–(14). As (12) and (13) corresponding to models (5) due to Frisch [22] and (6) due to Henderson [23] did not yield satisfactory values, we have not reported β_T values obtained from these equations. Theoretical values of β_T computed from (8)–(11) and (14) for various binary liquid mixtures under the present investigation are presented in columns five, six, seven, eight and nine respectively of each table (tables 2–7). A second set of theoretical β_T values are computed from Flory's statistical theory using (15). These values are recorded in the last column of each table (tables 2–7). The experimental values of isothermal compressibility of all the six binary liquid mixtures were estimated from sound velocity and density data in conjunction with (18). The values of β_T, thus obtained are plotted against mole fraction of one component in the mixture. These plots are shown in figure 1. In the case of system (I), the experimental values of β_T increased continuously (table 2) on increasing the mole fraction of the first component n-heptane. A similar trend is also obtained theoretically, as is evident from the results of columns five to nine of table 2. The values of β_T computed from Flory theory for this system also show a similar trend (last column of the table 2). It has been observed that in the case of system I i.e. n-heptane and toluene the value of β_T increases continuously with the increasing molar fraction of component 1 while in the other systems it decreases. The probable reason for this is that in this system the two components have equal number of carbon atoms i.e. one is the cyclic analogue of

Table 2. Density, sound velocity and isothermal compressibility of binary system – *n*-heptane (x_1) + toluene (x_2) (I) at 298·15 K.

x_1	$\rho \times 10^{-3}$ (kg m^{-3})	c (ms^{-1})	$\beta_T \times 10^{12}$ (m^2 N^{-1}) (Exptl.)	$\beta_T \times 10^{12}$ (Theoretical) (m^2 N^{-1})					
				Eq. (8)	Eq. (9)	Eq. (10)	Eq. (11)	Eq. (14)	Eq. (15)
0·2979	0·8693	1247·3	112·30	102·17	142·05	112·77	85·42	147·23	167·04
0·3162	0·8667	1243·0	113·62	103·06	143·19	113·68	86·21	148·33	170·04
0·3325	0·8637	1240·5	114·73	103·80	144·17	114·49	86·85	149·29	172·04
0·3519	0·8601	1237·2	116·15	104·53	145·15	115·28	87·47	150·26	173·74
0·3707	0·8564	1233·7	117·65	105·78	146·80	116·63	88·58	151·81	175·50
0·3902	0·8532	1230·0	119·19	106·76	147·99	117·69	89·43	153·03	177·40
0·4029	0·8500	1228·0	120·23	107·53	149·01	118·53	90·10	154·03	179·45
0·4282	0·8468	1224·0	121·80	108·51	148·98	119·60	90·96	155·29	181·26
0·4484	0·8433	1220·0	123·47	109·62	151·72	120·79	91·93	156·67	183·92
0·4684	0·8394	1216·0	125·25	110·82	153·25	122·09	92·98	158·16	185·32
0·4874	0·8363	1213·8	126·46	111·58	154·26	122·92	93·62	159·17	187·47
0·5023	0·8225	1211·0	130·33	114·60	158·19	126·19	96·25	163·04	182·06
0·5227	0·8188	1206·5	130·32	115·93	162·74	127·63	97·43	164·67	183·73
0·5442	0·8153	1203·7	133·87	116·90	161·17	128·68	98·27	165·94	189·81
0·5646	0·8122	1199·0	135·83	118·17	162·78	130·05	99·37	167·48	187·61

Table 3. Density, sound velocity and isothermal compressibility of binary system – n-heptane (x_1) + n-hexane (x_2) (II) at 298·15 K.

x_1	$\rho \times 10^{-3}$ (kg m^{-3})	c (ms^{-2})	$\beta_T \times 10^{12}$ (m^2 N^{-1}) (Exptl.)	$\beta_T \times 10^{12}$ (Theor.) (m^2 N^{-1})					
				Eq. (8)	Eq. (9)	Eq. (10)	Eq. (11)	Eq. (14)	Eq. (15)
0·3388	0·6614	1091·1	228·53	168·31	223·88	183·50	144·64	224·74	198·04
0·3598	0·6628	1092·2	227·29	167·83	223·42	183·01	144·18	212·40	198·23
0·3782	0·6606	1093·9	227·63	168·47	224·31	183·73	144·72	225·37	196·65
0·4001	0·6639	1094·4	223·54	167·56	223·28	182·76	143·08	224·37	196·30
0·4193	0·6636	1095·1	225·53	167·81	223·69	183·05	144·07	224·83	196·51
0·4394	0·6646	1096·5	224·37	157·44	223·33	182·63	143·70	224·55	196·24
0·4604	0·6656	1097·0	223·64	167·31	223·25	182·56	143·55	225·54	193·15
0·4782	0·6663	1098·5	222·60	166·67	222·92	182·22	143·21	224·30	190·26
0·4986	0·6672	1099·6	221·65	166·72	222·70	181·96	142·94	224·15	195·35
0·5191	0·6681	1101·8	220·21	165·53	221·40	180·74	141·79	223·10	195·29
0·5395	0·6693	1102·8	219·17	164·43	220·25	180·13	140·74	222·10	195·11
0·5594	0·6729	1104·0	216·89	164·60	220·36	179·76	140·93	222·12	195·85
0·5795	0·6716	1104·9	217·12	165·15	221·15	180·37	141·38	222·96	195·59
0·6025	0·6730	1105·6	216·13	164·87	220·89	180·10	141·10	222·77	194·42
0·6185	0·6736	1106·0	215·67	164·74	220·77	180·00	140·97	222·69	194·51

Table 4. Density, sound velocity and isothermal compressibility of binary system – toluene (x_1) + *n*-hexane (x_2) (III) at 298·15 K.

x_1	$\rho \times 10^{-3}$ (kg m^{-3})	c (ms^{-1})	$\beta_T \times 10^{12}$ (m^2 N^{-1}) (Exptl.)	$\beta_T \times 10^{12}$ (Theoretical) (m^2 N^{-1})					
				Eq. (8)	Eq. (9)	Eq. (10)	Eq. (11)	Eq. (14)	Eq. (15)
0·4074	0·7936	1149·7	154·57	124·30	167·96	136·09	105·82	170·39	198·55
0·4299	0·7984	1153·3	152·10	123·09	166·48	134·81	104·73	168·99	196·33
0·4486	0·8018	1159·5	149·32	121·61	164·72	133·23	103·37	167·38	192·03
0·4704	0·8058	1163·3	147·13	120·56	163·43	132·11	102·42	166·18	191·78
0·4919	0·8111	1167·0	144·65	119·26	161·83	130·72	101·26	164·66	188·65
0·5114	0·8157	1172·0	142·05	117·83	160·09	129·20	99·96	163·04	188·32
0·5290	0·8188	1176·0	140·17	116·87	158·93	128·18	99·07	161·97	186·21
0·5491	0·8286	1181·0	137·63	115·47	157·21	126·66	97·81	160·36	180·27
0·5584	0·8278	1183·0	136·06	114·47	155·98	125·61	96·94	157·19	183·52
0·5880	0·8323	1188·0	133·68	113·37	154·64	124·44	95·94	157·94	176·05
0·6088	0·8368	1194·0	131·11	111·90	152·88	122·88	94·61	156·31	173·94
0·6275	0·8400	1199·1	129·12	110·81	151·57	121·72	93·62	155·41	175·31
0·6453	0·8512	1203·6	125·51	108·36	148·47	119·08	91·45	152·14	176·87
0·6637	0·8527	1208·2	124·12	107·70	147·70	118·39	90·84	151·46	174·23
0·6829	0·8537	1213·1	122·78	107·11	147·02	117·76	90·24	150·88	170·64

Table 5. Density, sound velocity and isothermal compressibility of binary system – cyclohexane (x_1) + *n*-heptane (x_2) (IV) at 298·15 K.

x_1	$\rho \times 10^{-3}$ (kg m^{-3})	c (ms^{-1})	$\beta_T \times 10^{12}$ (m^2 N^{-1}) (Exptl.)	$\beta_T \times 10^{12}$ (Theor.) (m^2 N^{-1})					
				Eq. (8)	Eq. (9)	Eq. (10)	Eq. (11)	Eq. (14)	Eq. (15)
0·2227	0·7184	1156·0	177·27	144·22	196·11	158·17	122·30	199·83	193·14
0·2689	0·7214	1162·1	174·09	141·20	193·19	155·74	120·35	196·94	185·80
0·3158	0·7236	1167·8	171·40	140·10	190·70	153·69	118·72	194·47	182·34
0·3588	0·7191	1171·8	171·68	140·45	191·06	154·06	119·07	194·76	177·73
0·4016	0·7243	1177·2	168·09	139·44	189·46	152·90	118·30	192·95	176·65
0·4433	0·7307	1182·0	164·38	135·11	184·05	148·27	114·14	187·80	175·68
0·4861	0·7334	1187·9	161·71	133·20	181·55	146·18	112·79	185·31	172·90
0·5270	0·7361	1191·9	159·55	131·69	179·50	144·52	111·49	183·24	171·26
0·5642	0·7384	1196·0	157·58	130·22	177·55	142·92	110·24	181·28	169·50
0·6019	0·7412	1201·2	155·17	128·48	175·26	141·02	108·73	179·01	167·36
0·6414	9·7438	1205·8	153·03	126·93	173·20	139·68	107·40	176·94	164·55
0·6795	0·7463	1210·6	150·91	125·39	171·15	137·66	106·07	174·89	162·27
0·7164	0·7482	1215·9	148·86	123·92	169·22	136·06	104·80	172·97	160·89
0·7521	0·7518	1220·0	146·68	122·30	167·06	134·29	103·41	170·81	159·01
0·7877	0·7547	1224·0	144·77	120·89	165·17	132·75	102·20	168·90	158·48

Table 6. Density, sound velocity and isothermal compressibility of binary system – cyclohexane (x_1) + *n*-hexane (x_2) (V) at 298·15 K.

x_1	$\rho \times 10^{-3}$ (kg m^{-3})	c (ms^{-1})	$\beta_T \times 10^{12}$ (m^2 N^{-1}) (Exptl.)	$\beta_T \times 10^{12}$ (Theor.) (m^2 N^{-1})					
				Eq. (8)	Eq. (9)	Eq. (10)	Eq. (11)	Eq. (14)	Eq. (15)
0·2189	0·6821	1110·0	209·98	154·04	204·90	168·11	132·42	205·65	195·63
0·2541	0·6860	1118·8	204·48	151·21	201·53	164·94	129·83	202·53	193·67
0·2981	0·6914	1134·9	195·70	146·41	195·87	159·87	125·41	197·35	191·33
0·3150	0·6932	1135·0	194·90	146·11	195·44	156·97	125·17	196·89	190·33
0·3647	0·6990	1142·3	189·72	143·46	192·18	156·71	123·86	193·79	186·84
0·3897	0·7022	1149·8	185·67	141·23	189·50	154·33	120·74	191·32	186·13
0·4258	0·7065	1155·4	181·98	139·31	187·15	152·29	119·03	189·08	184·02
0·4777	0·7129	1163·2	176·84	136·57	183·36	149·36	116·57	185·86	180·98
0·5029	0·7157	1170·2	173·51	134·72	181·54	147·39	114·88	183·80	178·93
0·5675	0·7232	1180·3	167·48	131·50	177·55	143·94	112·80	180·03	175·28
0·5799	0·7250	1182·7	166·09	130·71	176·58	143·10	111·28	179·11	173·33
0·6012	0·7275	1188·9	163·31	129·10	174·66	141·40	109·82	177·33	173·20
0·6695	0·7356	1200·0	157·29	125·88	170·65	137·94	106·94	173·52	168·71
0·7187	0·7415	1210·6	152·38	122·97	167·10	134·84	104·32	170·20	165·45
0·7888	0·7499	1221·8	146·75	119·80	163·16	131·44	101·49	166·20	160·74

Table 7. Density, sound velocity and isothermal compressibility of binary system – *n*-decane (x_1) + *n*-hexane (x_2) (VI) at 298·15 K.

x_1	$\rho \times 10^{-3}$ (kg m^{-3})	c (ms^{-1})	$\beta_T \times 10^{12}$ (m^2 N^{-1}) (Exptl.)	$\beta_T \times 10^{12}$ (Theoretical) (m^2 N^{-1})					
				Eq. (8)	Eq. (9)	Eq. (10)	Eq. (11)	Eq. (14)	Eq. (15)
0·0187	0·6663	1075·5	233·46	165·85	219·42	180·54	143·05	219·48	208·11
0·0588	0·6697	1080·1	229·47	166·02	220·33	180·88	142·91	220·83	205·15
0·1008	0·6730	1087·9	224·13	165·40	220·40	180·41	142·03	221·03	202·13
0·1436	0·6774	1094·6	218·90	164·72	220·33	179·86	141·12	221·97	199·63
0·1896	0·6777	1100·0	216·35	165·94	222·66	181·34	141·88	224·79	196·40
0·2348	0·6850	1108·4	209·28	163·84	220·86	179·36	139·68	223·67	194·15
0·2886	0·6883	1118·8	203·46	163·00	220·84	178·59	138·54	224·44	190·78
0·3350	0·6917	1127·5	198·47	162·12	220·58	177·83	137·42	224·87	188·26
0·3872	0·6943	1135·4	194·28	161·99	221·30	177·88	136·96	226·29	185·30
0·4449	0·6987	1142·8	189·65	161·63	221·76	177·69	136·29	227·48	182·48
0·5009	0·7012	1152·3	185·16	161·18	222·15	177·41	135·51	228·68	178·16
0·5627	0·7071	1161·9	179·46	159·83	221·17	176·16	133·94	228·82	177·39
0·6248	0·7099	1173·9	174·33	158·80	222·50	175·37	132·62	229·56	174·41
0·6944	0·7114	1184·1	170·42	158·29	222·75	175·69	132·25	231·85	170·71
0·7655	0·7144	1195·6	165·71	157·70	220·08	175·19	131·24	233·16	167·93

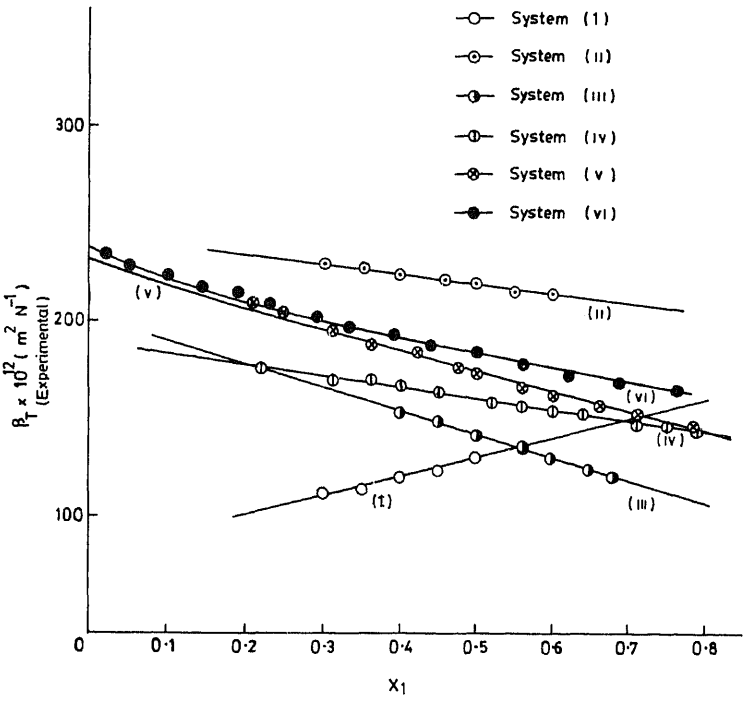

Figure 1. Isothermal compressibility β_T vs mole fraction (X_1) of component 1 for the systems (I) to (VI).

the other with aromatic characters, where π electrons play an important role in the molar interaction as is evident from their structures:

When the experimental and theoretically computed values of β_T for all other systems (II–IV) are examined (tables 3–7), it is observed that in each case β_T decreases on increasing the mole fraction of the first component. A similar trend in the variation of β_T has also been shown from Flory's theory (last column of each table).

Table 7 lists the average percentage deviations obtained in compressibility values for all the systems under the present study. From this table it is observed that (10) due to Carnahan and Starling [20] provides good agreement with the experimental values for all the systems, the observed deviations being not more than 18·12 per cent. Equations (9) due to Werthein and Thiel [18] and (14) due to Hoover and Ree [24] give better agreement with the experimental values specially for the system, *n*-heptane + *n*-hexane, the observed deviations being not more than 0·17 per cent for (9) and 0·48 per cent for Eq. (14). Carnahan and Starling equation (10) gives good agreement in the case of the system *n*-heptane + toluene, deviations being not more than 1·85 per cent. In the case of system IV (cyclohexane + *n*-heptane) a similar agreement from all the equations has been obtained. But in the case of system V (cyclohexane + *n*-hexane) eqs (9), (14) and (15) yield better agreement.

The present study demonstrates that Flory's statistical theory, vide (15), yields good agreement for almost all the systems except for I and III. In the hard sphere models attractive and repulsive forces are taken into account that give better agreement with

Table 8. Average percentage deviation of isothermal compressibility β_T, at 298·15 K with experimental values.

System	Eq. (8)	Eq. (9)	Eq. (10)	Eq. (11)	Eq. (14)	Eq. (15)
n-Heptane + toluene	10·9	− 23·36	1·85	25·32	− 27·33	− 46·44
n-Heptane + *n*-hexane	24·99	− 0·17	18·12	35·70	− 0·48	− 11·96
Toluene + *n*-hexane	16·29	− 13·95	8·17	29·07	− 16·15	− 32·98
Cyclohexane + *n*-heptane	17·52	− 12·43	9·45	30·16	− 14·76	− 7·17
Cyclohexane + *n*-hexane	22·97	− 3·56	15·88	34·19	− 4·75	− 1·44
n-Decane + *n*-hexane	18·58	− 10·85	10·63	30·97	− 13·19	5·69

the observed β_T values. The superiority of Carnathan and Starling's hard sphere model has also been demonstrated earlier by other workers [28–29].

References

[1] J D Pandey, B R Chaturvedi and N Pant, *Acoust. Lett.* **4**, 92 (1980)
[2] D K Majumdar and A R Purkait, *Indian J. Pure Appl. Phys.* **19**, 973 (1981)
[3] N Pant, C V Chaturvedi and G D Chaturvedi, *Z. Physik. Chem.* (Leipzig) **264**, 513 (1983)
[4] J D Pandey and U Gupta, *Z. Physik. Chem.* (Leipzig), **268**, 477 (1987)
[5] J D Pandey and K Misra, *Acoustic Lett.* **6**, 148 (1983)
[6] B P Shukla and S N Dubey, *Acoustic Lett.* **9**, 71 (1985)
[7] J D Pandey, G P Dubey, B P Shukla and S N Dubey, *Acustica*, **80**, 92 (1994)
[8] M Diaz Pena, G Tardagos, C Menduinar and R L Arenosa, *J. Chem. Thermodyn.* **11**, 67 (1979)
[9] M B Ewing and K N Marsh, *J. Chem. Thermodyn.* **9**, 371 (1977)
[10] P J Flory, *J. Am. Chem. Soc.* **87**, 1833 (1965)
[11] P J Flory and A Abe, *J. Am. Chem. Soc.* **87**, 1838 (1965)
[12] J D Pandey and R L Mishra, *Acustica*, **32**, 200 (1978)
[13] J D Pandey and R L Mishra, *Chem. Scr.* **13**, 63 (1978)
[14] J D Pandey, N Pant, N Agrawal and Shikha, *Acustica* **68**, 225 (1989)
[15] J D Pandey, R K Shukla, A K Shukla and R D Rai, *J. Chem. Thermodyn.* **21**, 125 (1989)
[16] CRC Handbook of Chem & Phys ed 60 (CRC Press, Boca Raton, Florida, 1979–80)
[17] J L Lebowitz, H L Frisch and E Helford, *J. Chem. Phys.* **34**, 1037 (1961)
[18] E Thiel, *J. Chem. Phys.* **39**, 474 (1963)
[19] M S Wertheim, *Phys. Rev. Lett.* **10**, 321 (1963)
[20] N F Carnahan and K E Starling, *J. Chem. Phys.* **51**, 635 (1969)
[21] E A Guggenheim, *Mol. Phys.* **9**, 43 (1965)
[22] H L Frisch, *Adv. Chem. Phys.* **6**, 229 (1964)
[23] D Henderson, *Mol. Phys.* **30**, 971 (1975)
[24] W G Hoover and F H Ree, *J. Chem. Phys.* **48**, 3609 (1968)
[25] J G Mc-Gowan, *Nature (London)*, **210**, 1255 (1966)
[26] N Auerbach, *Experimentia* **4**, 473 (1948)
[27] M R Islam and S K Quadri, *Acoust. Lett.* **11**, 237 (1988)
[28] G A Mansoori, N F Carnathan, K E Starling and T W Leland, *J. Chem. Phys.* **54**, 1523 (1971)
[29] F Kohler, R Kohler and P Svedja, *Fluid Phase Equilibria*, **27**, 189 (1986)

PRAMANA
— journal of
physics

© Printed in India

Vol. 43, No. 5,
November 1994
pp. 373–377

Transport coefficients of quasicrystals

K RAMA MOHANA RAO and P HEMAGIRI RAO*
Department of Applied Mathematics, Andhra University, Visakapatnam 530003, India
*Department of Mathematics, Bapatla Engineering College, Bapatla 522101, India

MS received 2 May 1994; revised 29 October 1994

Abstract. The transport coefficients for the nine point groups $5(C_5)$, $\bar{5}(S_{10})$, $\overline{10}(C_{5h})$, $\overline{10}\ m2(D_{5h})$, $52(D_5)$, $5m(C_{5v})$, $\bar{5}\ 2m(D_{5d})$, $235(I)$, $2/m\ \bar{3}\ \bar{5}(I_h)$—which represent the symmetry groups of the quasicrystals in two and three dimensions—have been evaluated and tabulated in this work, employing group-theoretical methods.

Keywords. Galvanomagnetic and thermomagnetic effects; quasicrystals; transport phenomena; non-vanishing and independent tensor coefficients.

PACS No. 78·20

1. Introduction

The discovery of stable icosahedral phases like the Al–Li–Cu, Al–Cu–Ru by Tsai *et al* [1] and the later determination of their structural long-range order by Guryan *et al* [2], have provided one of the best systems for investigation of unusual electronic properties in icosahedral quasicrystals. With the recent discovery of some thermodynamically stable quasicrystals [3], experimental studies on the physical properties such as resistivity, magnetoresistance, Hall effect, specific heat, etc., of quasicrystalline materials have begun [4]. The work reported by Sokoloff [5] and Kitaev and Pisma [6] revealed that the electronic properties of perfect icosahedral quasicrystals are different from those of the perfect crystals. A more recent study on the Al–Cu–Mg and Ga–Mg–Zn icosahedral alloys by Wagner *et al* [7] showed distinct features in their electronic properties. However, a comprehensive account of the tensor coefficients pertaining to the transport properties of the symmetry groups of the quasicrystals has not been reported, to the best of the knowledge of the authors. Hence an attempt is made in this note to obtain the non-vanishing and independent scheme of tensor coefficients pertaining to some identified transport properties in respect of the seven pentagonal and two icosahedral point groups: $5(C_5)$, $\bar{5}(S_{10})$, $\overline{10}(C_{5h})$, $\overline{10}\ m2(D_{5h})$, $52(D_5)$, $5\ m(C_{5v})$, $\bar{5}\ 2m(D_{5d})$; $235(I)$, $2/m\ \bar{3}\ \bar{5}(I_h)$—which are quasicrystals' symmetry groups in two and three dimensions—employing the group-theoretical methods.

Since a good amount of experimental work is being carried out on the structure determination and physical properties of a new class of quasicrystalline materials, the authors believe that the tensor coefficients obtained here may serve as valuable check on the experimental determination of transport coefficients, measured in respect of various new materials that exhibit the symmetry of one of the aforesaid point groups. In table 1, a brief classification of the transport properties is made and the

Table 1. Classification of transport properties and character of the reducible representation corresponding to the physical property.

Physical property representing the relation between	Compound character χ_ρ^Γ for the physical property	Maximum number of independent coefficients needed	Transport phenomenon exhibited
Vector and a vector ($\rho_{ik}^0 = \rho_{ki}^0$)	$4C^2 \pm 2C$	6	Electrical resistivity; Thermal conductivity
Second rank anti-symmetric tensor and axial vector (same as axial vector and axial vector) ($\rho_{ikl} = -\rho_{kil}$)	$4C^2 \pm 4C + 1$	9	First order Hall effect, first order Leduc–Righi effect
Second rank symmetric tensor and second rank symmetric tensor (ρ_{iklm}) Notation: In contracted notation this tensor is represented by a fourth rank tensor ρ_{mn}	$(4C^2 \pm 2C)^2$	36	First order magneto-resistance, First order magneto-thermal conductivity piezo-resistance
Axial vector and totally symmetric third rank tensor ($\rho_{iklmn} = -\rho_{kilmn}$ for all permutations of the indices l, m, n). Notation: In contracted notation this tensor is represented with three components p_{qrs} following the notation developed in [11]	$((1 \pm 2C)$ $(\pm 8C^3 + 4C^2 \mp 2C)$	30	Second order Hall effect, Second order Leduc–Righi effect

In table 1, C stands for the cosine of the angle of rotation ϕ in the symmetry operation. The + or − sign in the compound character χ_ρ^Γ, have to be taken according to whether the symmetry operation under consideration is a proper rotation or an improper rotation.

notation adopted for denoting the property tensors of various ranks corresponding to the considered transport property is explained. In table 2, the non-vanishing tensor components evaluated for the nine point groups are tabulated in a compact form as was done by Kumaraswamy and Krishnamurthy [8].

2. Transport phenomena, evaluation of tensor coefficients and results

It is well-known that the effect of magnetic field on the electrical and thermoelectrical properties in the absence of a temperature gradient is called galvanomagnetic effect. Physical properties such as electrical resistivity, first order Hall effect, first order magneto-resistance, and second order Hall effect are known as the galvanomagnetic effects. The components of the tensors ρ_{ik}^0, ρ_{ikl}, ρ_{iklm} and ρ_{iklmn} representing respectively the aforesaid four galvanomagnetic effects are called galvanomagnetic coefficients. Similarly the effect of magnetic field on the thermoelectric and thermal properties in

Table 2. Non-vanishing tensor coefficients ρ^0_{ik}, ρ_{ikl}, ρ_{mn}, p_{qrs}.

Pentagonal/ icosahedral point group	Number of independent coefficients needed				Non-vanishing coefficients			
	ρ^0_{ik}	ρ_{ikl}	ρ_{mn}	p_{qrs}	ρ^0_{ik}	ρ_{ikl}	ρ_{mn}	p_{qrs}
5, $\bar{5}$, $\overline{10}$	2	3	8	6	$\rho^0_{11}=\rho^0_{22}$, ρ^0_{33}	ρ_{123}, $\rho_{131}=\rho_{232}$, $\rho_{132}=-\rho_{231}$	$\rho_{11}=\rho_{22}, \rho_{12}=\rho_{21}$, $\rho_{13}=\rho_{23}, \rho_{16}=-\rho_{26}=-\rho_{61}=\rho_{62}, \rho_{31}=\rho_{32}$, $\rho_{33}, \rho_{44}=\rho_{55}, \rho_{45}=-\rho_{54}, 2\rho_{66}=\rho_{11}-\rho_{12}$	$p_{111}=3p_{112}=3p_{216}=p_{222}$, $p_{113}=p_{223}$, $3p_{116}=p_{122}=-p_{211}=-3p_{212}$, $p_{123}=-p_{213}$, $p_{315}=p_{324}$, p_{333}
52, 5m, $\overline{10}$ $m2$, $\bar{5}$ $2m$	2	2	6	4	$\rho^0_{11}=\rho^0_{22}$, ρ^0_{33}	ρ_{123}, $\rho_{132}=-\rho_{231}$	$\rho_{11}=\rho_{22}, \rho_{12}=\rho_{21}$, $\rho_{13}=\rho_{23}, \rho_{31}=\rho_{32}$, $\rho_{33}, \rho_{44}=\rho_{55}$, $2\rho_{66}=\rho_{11}-\rho_{12}$	$p_{111}=3p_{112}=3p_{216}=p_{222}$, $p_{113}=p_{223}$, $p_{315}=p_{324}$, p_{333}
235, $2/m$ $\bar{3}$ $\bar{5}$	1	1	2	1	$\rho^0_{11}=\rho^0_{22}=\rho^0_{33}$	$\rho_{123}=-\rho_{132}=\rho_{231}$	$\rho_{11}=\rho_{22}=\rho_{33}$, $\rho_{12}=\rho_{13}=\rho_{21}=\rho_{23}=\rho_{31}=\rho_{32}, 2\rho_{44}=2\rho_{55}=2\rho_{66}=\rho_{11}-\rho_{12}$	$p_{111}=3p_{112}=3p_{113}=3p_{216}=p_{222}=3p_{223}=3p_{315}=3p_{324}=p_{333}$

the absence of an electric current is called thermomagnetic effect. Thermal conductivity, first order Leduc–Righi effect, first order magnetothermal conductivity, second order Leduc–Righi effect are some known thermomagnetic effects. These effects are represented respectively by the tensors K_{ik}, K_{ikl}, K_{iklm}, K_{iklmn} and the components of these tensors are known as thermomagnetic coefficients. Since the ρ and K coefficients of corresponding order are tensors of the same rank and kind, they have identical schemes of non-vanishing and independent coefficients. The galvanomagnetic effects and the thermomagnetic effects are together known as the transport phenomena [9, 11].

The permutation (of indices) symmetries and other characteristics (like peseudo, or polar, time-reversal symmetric or otherwise) of the tensors ρ^0_{ik}, ρ_{ikl}, ρ_{iklm} and ρ_{iklmn} together with the character χ^{Γ}_{ρ} of the corresponding reducible representation are briefly summarized in table 1. The maximum number n_i of non-vanishing and independent coefficients required by each one of the nine point groups, corresponding to the property tensor under consideration are determined employing the well-known formula

$$n_i = \frac{1}{g}\sum_{\rho} h_{\rho}\chi^{\Gamma}_{\rho}(R)\chi^{\Gamma_i}_{\rho}(R) \tag{1}$$

with the usual notation. The n_is obtained using this formula are given in table 2.

In order to determine the non-vanishing, independent coefficients the following transformation equations are used.

$$\begin{aligned}
&\rho^0_{ik} = a_{im}a_{kn}\rho^0_{mn} \quad \text{with} \quad \rho^0_{ik} = \rho^0_{ki}\\
&\rho_{ikl} = a_{im}a_{kn}a_{lp}\rho_{mnp} \quad \text{with} \quad \rho_{ikl} = -\rho_{kil}\\
&\rho_{iklm} = a_{ip}a_{kq}a_{lr}a_{ms}\rho_{pqrs} \quad \text{with} \quad \rho_{ikim} = \rho_{ikml} = \rho_{kilm} = \rho_{kiml}\\
&\rho'_{iklmn} = a_{ip}a_{kq}a_{lr}a_{ms}a_{nt}\rho_{pqrst}\\
&\rho_{iklmn} = -\rho_{kilmn} \quad \text{for all permutations of } l, m, n.
\end{aligned} \tag{2}$$

where a_{im} are the elements of the transformation matrix.

By demanding the invariance of the components under symmetry transformations (2), the desired results are obtained. The coefficients thus obtained in respect of all the nine point groups are listed in table 2 in a compact form as was done [8].

From table 2, it can be seen that the number of non-vanishing and independent tensor coefficients for the ρ^0_{ik}, ρ_{ikl}, ρ_{iklm}, ρ_{iklmn} obtained in respect of the icosahedral point groups are 1, 1, 2 and 1 respectively, fewer than those needed for any one of the 32 crystallographic point groups. It may be noted that the above tensor coefficients (ρ's) are just the same as those needed for an isotropic medium.

In view of the interest now being shown by several experimentalists on the electronic and other physical properties of the quasicrystalline materials (alloys) [4, 10], it is hoped that the results reported here may be useful to material scientists in systematizing transport data on quasicrystals.

Acknowledgement

The authors are thankful to the referee for constructive suggestions for modification.

References

[1] A Tsai, A Inoue and T Masumoto, *Jpn. J. Appl. Phys.* **26**, L1505 (1987)
[2] C A Guryan, A I Goldman, P W Stephens, K Hiraga, A Tsai, A Inoue and T Masumoto, *Phys. Rev. Lett.* **62**, 2409 (1989)
[3] Y Calvayarac, A Quivy, M Bessiee, S Lefebve, M Cornier Quiquandon and D Gratias, *J. Phys. (Paris)* **51**, 417 (1990)
[4] T Klein, C Berger, D Mayou and F Cyrot–Lackman, *Phys. Rev. Lett.* **66**, 2907 (1991)
[5] J B Sokoloff, *Phys. Rev. Lett.* **57**, 2223 (1986)
[6] A Yu Kitaev, *Zh Pisma Eksp. Teor. Fiz.* **48**, 270 (1988)
A Yu Kitaev, *JETP Lett.* **298**, 48 (1988)
[7] J L Wagner, B D Biggs and S J Poon, *Phys. Rev. Lett.* **65**, 203 (1990)
[8] K Kumaraswamy and N Krishnamurthy, *Acta Cryst.* **A36**, 760 (1980)
[9] J F Nye, *Physical properties of crystals* (Oxford: Clarendon, 1985)
[10] C Berger and J J Prejcan, *Phys. Rev. Lett.* **64**, 1769 (1990)
[11] S Bhagavantham, *Crystal symmetry and physical properties* (Academic, London, 1966)

PRAMANA
— journal of
physics

© Printed in India

Vol. 43, No. 5,
November 1994
pp. 379–389

Phonons and periodons in IV–VI semiconductor superlattices

NABONITA D CHOWDHURY and SANKAR P SANYAL
Department of Physics, Barkatullah University, Bhopal 462026, India

MS received 1 June 1994; revised 19 September 1994

Abstract. We have calculated the phonon and periodon dispersion relations in IV–VI semiconducting bulk PbTe and SnTe and their superlattice structure. The model used here is a one-dimensional lattice which includes harmonic interactions up to second neighbours as well as on-site nonlinear electron-ion interactions at the anion site. We calculate the phonon and periodon dispersion relations in bulk and PbTe–SnTe superlattice for the transverse optic and acoustic modes using the transfer matrix method. Our analysis has predicted correct nature of the folding of acoustic and confinement of optical phonons at various frequency intervals corresponding to pass and stop bands of the superlattices.

Keywords. Phonons; non-linear excitation; superlattice.

PACS No. 63·20

1. Introduction

During the last few decades, the ferroelectric IV–VI compounds (PbTe, SnTe) have generated a considerable interest in structural phase transition and mode softening [1–5]. These compounds exhibit soft mode behaviour at the zone centre and zero gap transition, depending on temperature and composition of the alloy systems. The ferroelectric [4, 5] and phonon [6] properties of IV–VI compounds have been investigated extensively in the recent past. It is known from literature that the transverse optical branches of these compounds show some anomalous behaviour in the middle of the $[0, 0, \xi]$ direction. This occurs because of the presence of free carriers due to intrinsic defects in the crystals. Bilz *et al* [7] have calculated the transverse phonon modes by using a simple diatomic linear chain model with first and second nearest neighbour core-core interactions and nonlinear polarizability at the chalcogen ion site. They have also extended their treatment to obtain an exact solution which can describe the phonon anomalies, electro-optic phenomena and the nonlinear excitations such as periodons [7]. In order to understand the interactions between the phonons and periodons, Bussmann-Holder have used an isotropic monoatomic polarizable linear chain model and calculated the periodon amplitude and dispersion curves [7].

It is revealed from literature that apart from the investigation of the electronic and dynamical properties of the bulk materials, modulated structures (i.e., superlattices) of these compounds are also investigated [8–10]. In the present paper we report the calculated vibrational properties of the less investigated IV–VI semiconducting superlattices (PbTe–SnTe). For this system, only a comparative study of the structural and superconducting properties of epitaxial grown superlattices (PbTe–SnTe, PbTe–SnS)

has been reported [9] and also galvanomagnetic properties are studied [10]. In the superlattice structure, it is expected that the IV–VI compounds will manifest a variety of nonlinear phenomena because of the non-linear polarizability of chalcogen ion.

In the present paper we have calculated the phonon and periodon dispersion relation in bulk PbTe and SnTe and their superlattice structure. We have developed a nonlinear lattice dynamical theory which includes the effect of first neighbour on-site and inter-site and second neighbour inter-site interactions in the one-dimensional diatomic chain model with nonlinear fourth order polarization potential at the anion site. Using this model, the phonon and periodon dispersion curves for transverse acoustic and optic modes are calculated without using self consistent phonon approximation. We have used the transfer matrix approach for calculating the dispersion curves in PbTe–SnTe superlattices, both for phonons and periodons.

2. Theory

2.1 *Bulk semiconductors*

In bulk structure, our model consists of a one-dimensional diatomic chain in which the cations (Pb, Sn) are assumed to be linearly polarizable and the anions (Te) are

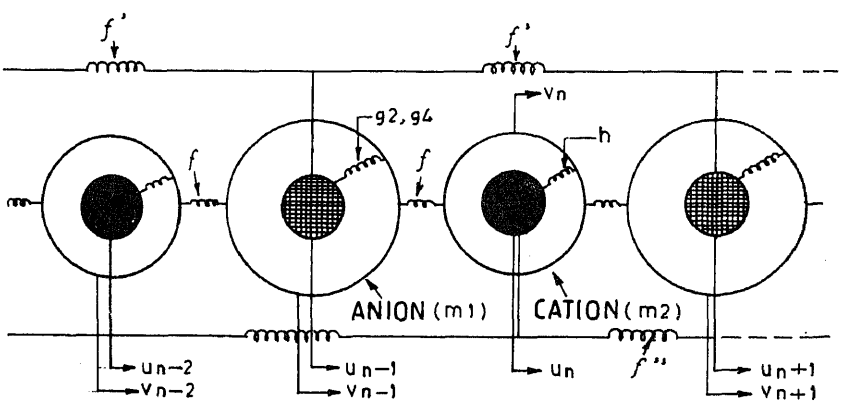

Figure 1(a). One-dimensional ϕ^4 linear chain model with nearest and next nearest neighbour interactions.

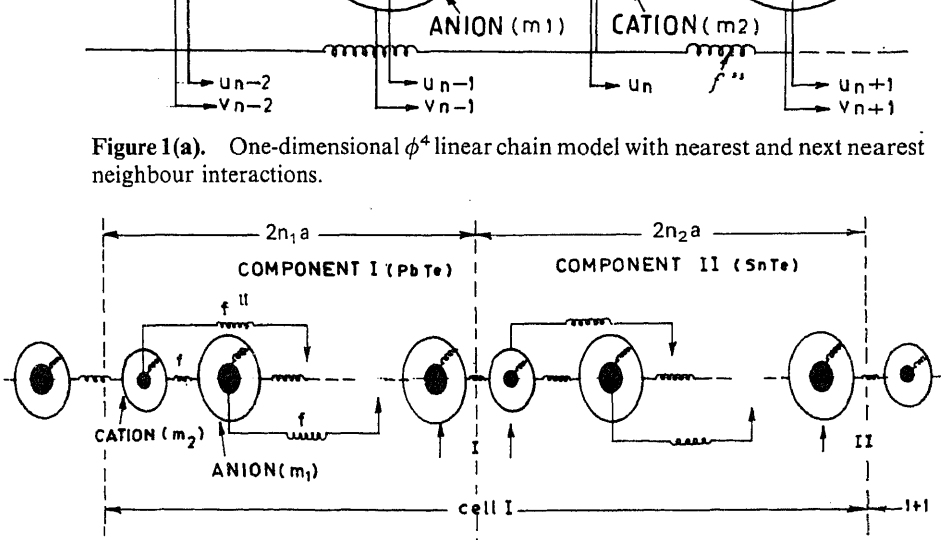

Figure 1(b). Linear chain model of a one-dimensional superlattice with nearest and next nearest neighbour interactions.

assumed to be nonlinearly polarizable, which are configurationally unstable in nature. Anionic shell-core coupling consists of an attractive harmonic (g_2) and a fourth order repulsive force constants (g_4). The one-dimensional diatomic lattice with different types of interactions is shown in figure 1(a). f is the first neighbour interaction between the shells of anion and cation and f' and f'' are the force constants due to second neighbour interactions between the cores of cation and anion. h is the attractive cationic force constant.

In view of this, the equation of motion can be written as

$$m_1 \ddot{u}_{n-1} = g_2 w_{n-1} + g_4 w_{n-1}^3 + f'(u_{n+1} + u_{n-3} - 2u_{n-1}) \tag{1}$$

$$m_2 \ddot{u}_n = f''(u_{n+2} + u_{n-2} - 2u_n) + hw_n \tag{2}$$

$$m_{e_1} \ddot{v}_{n-1} = -g_2 w_n - g_4 w_{n-1}^3 + f(w_n + w_{n-2} - 2w_{n-1}) + f(u_n + u_{n-2} - 2u_{n-1}) \tag{3}$$

$$m_{e_2} \ddot{v}_n = -hw_n + f(w_{n+1} + w_{n-1} - 2w_n) + f(u_{n+1} + u_{n-1} - 2u_n) \tag{4}$$

where m_1, m_2 and $m_{e(i)}$ $(i = 1, 2)$ are the masses of anion, cation and the valence electrons of anion and cation respectively. $u_{n\pm1, n\pm3, n\pm5,\ldots}$ are the displacements of the cores of anion and $u_{n,n\pm2,n\pm4,\ldots}$ are the displacements of the cores of cation in the linear infinite chain. By considering adiabatic condition (i.e., $m_e \approx 0$), the LHS of (3) and (4) vanishes. Also we define a relative core-shell coordinate as $w_{n-1(n)} = v_{n-1(n)} - u_{n-1(n)}$.

For calculating the phonon dispersion, both the anions and cations are considered to be linearly polarizable (i.e., $g_4 = 0$). We assume the following solutions for solving the equations of motion. For the anions, the solutions are

$$w_{n-1} = A \sin(\omega t - (n-1)qa), \tag{5}$$

$$u_{n-1} = B \sin(\omega t - (n-1)qa). \tag{6}$$

For cation we write the displacements as

$$u_n = \alpha u_{n-1} \tag{7}$$

where α is an arbitrary constant. Equations (3) and (4), together with above considerations results to

$$w_{n-1} = \frac{f}{(g_2 + 2f)}[(u_n + u_{n-2} - 2u_{n-1}) + (w_n + w_{n-2})], \tag{8}$$

$$w_n = \frac{f}{(h + 2f)}[(u_{n+1} + u_{n-1} - 2u_n) + (w_{n+1} + w_{n-1})]. \tag{9}$$

Substituting (5), (6), (7) in (8) one gets the ratio of the amplitudes as

$$\frac{A}{B} = \frac{2f}{(g_2 + 4f \sin^2(qa/2))}(\alpha \cos qa - 1). \tag{10}$$

Equation (9) also results in the following amplitude ratio

$$\frac{A}{B} = \frac{2f}{(h + 4f \sin^2(qa/2))}(\cos qa - \alpha). \tag{11}$$

The constant α which relates the displacements of the atoms of the neighbouring unit cells can be obtained by substituting (5), (6), (7) and (10) in (7) as

$$\alpha = \frac{\left[-m_1\omega^2 + 4f' \sin^2(qa/2) + \dfrac{2g_2 f}{(g_2 + 4f\sin^2(qa/2))} \right]}{\dfrac{2g_2 f \cos qa}{(g_2 + 4f\sin^2(qa/2))}}. \tag{12}$$

Similarly from (2) α can be obtained by substituting (5), (6), (7) and (11) in (7) as

$$\alpha = \frac{\dfrac{2hf\cos qa}{(h + 4f\sin^2(qa/2))}}{\left[-m_2\omega^2 + 4f''\sin^2(qa/2) + \dfrac{2hf}{(h + 4f\sin^2(qa/2))} \right]}. \tag{13}$$

Equating (12) and (13) we obtain the phonon dispersion relation for bulk as

$$\omega^4 + Z\omega^2 + Y = 0 \tag{14}$$

with

$$Z = -\left[\frac{1}{m_1}\left(4f' \sin^2(qa/2) + \frac{2g_2 f}{(g_2 + 4f\sin^2(qa/2))} \right) + \frac{1}{m_2}\left(4f'' \sin^2(qa/2) + \frac{2hf}{(h + 4f\sin^2(qa/2))} \right) \right] \tag{15}$$

$$Y = \frac{1}{m_1 m_2}\left[\left\{ \left(4f' \sin^2(qa/2) + \frac{2g_2 f}{(g_2 + 4f\sin^2(qa/2))} \right) \cdot \left(4f'' \sin^2(qa/2) + \frac{2hf}{(h + 4f\sin^2(qa/2))} \right) \right\} - \frac{4g_2 hf^2 \cos^2 qa}{(g_2 + 4f\sin^2(qa/2))(h + 4f\sin^2(qa/2))} \right]. \tag{16}$$

To obtain the periodon dispersion relation, we have considered the anions to be nonlinearly polarizable and cations to be linearly polarizable and used adiabatic approximation. Bilz [7] has already shown that the periodon frequencies are subharmonics of the corresponding phonon eigen frequencies with equal scaling by a factor of three which reduces the Brillouin zone into one third of its value. Exact nonlinear periodic solutions can be expressed as

$$w_{n-1} = A \sin(\omega t - (n-1)qa) \tag{17}$$

$$u_{n-1} = B \sin(\omega t - (n-1)qa) + C \sin 3(\omega t - (n-1)qa). \tag{18}$$

The ratio of the amplitudes can be derived from (1) and by equating the coefficients of $\sin(\omega t - (n-1)qa)$ as

$$\frac{A}{B} = \frac{-m_1\omega^2 + 4f'\sin^2(qa/2) - 2f(\alpha\cos qa - 1)}{-4f\sin^2(qa/2)}. \tag{19}$$

Equating the coefficients of $\sin 3(\omega t-(n-1)qa)$ in (1), the constant α is defined as

$$\alpha=\frac{-9m_1\omega_P^2+4f'\sin^2(3qa/2)+2f}{2f\cos 3qa} \tag{20}$$

where ω_P is the periodon frequency.

Similar sets of equation can also be obtained for the amplitude ratio A/B by using (2) for mass m_2. This can be done by equating the coefficients of $\sin(\omega t-(n-1)qa)$ and is given by

$$\frac{A}{B}=\frac{-m_2\alpha\omega^2+4f''\sin^2(qa/2)+\dfrac{2hf}{h+2f}(\cos qa-\alpha)}{\dfrac{2hf}{(h+2f)}\cos qa}. \tag{21}$$

For the periodon dispersion, the value of α obtained from (2) as

$$\alpha=\frac{-4f''\sin^2(3qa/2)+\dfrac{2hf}{(h+2f)}\cos 3qa}{-9m_2\omega_P^2+\dfrac{2hf}{(h+2f)}}. \tag{22}$$

The dispersion relation for the periodon in the diatomic chain can be obtained by equating the values of α (from (20) and (22)) obtained for two different masses as

$$\omega_P^4+Z'\omega_P^2+Y'=0 \tag{23}$$

with

$$Z'=-\frac{2}{9}\left[\frac{1}{m_1}(2f'\sin^2(3qa/2)+f)+\frac{1}{m_2}\left(\frac{hf}{(h+2f)}\right)\right] \tag{24}$$

$$Y'=\frac{4}{81m_1m_2}\left[(2f'\sin^2(3qa/2)+f)\left(\frac{hf}{(h+2f)}\right)-f\cos 3qa\left(-2f''\sin^2(3qa/2)+\frac{hf}{(h+2f)}\cos 3qa\right)\right] \tag{25}$$

and the squared amplitude is obtained from (3), (17), (18) and (19) as

$$A^2=\frac{4g_2}{3g_4}\left[1+\frac{4f}{g_2}\left(\frac{m_1\omega_P^2-4f'\sin^2(qa/2)+f(\alpha\cos qa-1)}{m_1\omega_P^2-4f'\sin^2(qa/2)+2f(\alpha\cos qa-1)}\right)\sin^2(qa/2)\right]. \tag{26}$$

2.2 *Superlattice structure*

The layered structure or superlattice consists of alternating layers of thickness d_1 of the constituent I and of thickness d_2 of constituent II. Different specimens can be prepared so that d_1 and d_2 have any value from two or three atomic spacing up to the order of 100 nm. For simplicity, we have assumed that the interatomic lattice spacing (a) and the elastic constants (c_{ij}) have the same values in both the components of the periodically layered structures. The physical properties of the layered structures

are greatly modified as compared to the bulk materials, due to the increase in the spatial period ($D = 2(n_1 + n_2)a$). As a consequence a new Brillouin zone at the wavevector π/D is developed perpendicular to the interfaces. A schematic diagram for a one-dimensional diatomic bilayer superlattice with different force constants is shown in figure 1(b). The derivation of phonon dispersion relation in superlattices has been given in detail in [11] by using the transfer matrix method. The dispersion relation for bilayer compound semiconductor superlattice is given by [12]

$$\cos QD = \cos q_1 d_1 \cos q_2 d_2 + \left[1 - \frac{1}{2}\left(\frac{\alpha_1}{\alpha_2} + \frac{\alpha_2}{\alpha_1}\right)\frac{1}{\cos q_1 a \cos q_2 a}\right]\frac{\sin q_1 d_1 \sin q_2 d_2}{\tan q_1 a \tan q_2 a}. \quad (27)$$

For the calculation of phonon dispersion curves in semiconductor superlattice, $\alpha_i (i = 1, 2$, for two different layers) are obtained from (12) and (13) and the phonon wave vectors q_1 and q_2 as a function of frequency are obtained from (14).

Similarly the periodon dispersion relation in superlattice structure, is obtained for the different periodon wave vectors q_1 and q_2 as a function of frequency from (23) and the values of α_i from (20) and (22). In the case of phonon dispersion, a new Brillouin zone appears with wavevector $QD = 2\pi$, which becomes twice the Brillouin zone in bulk (i.e., $qa = \pi$). As mentioned before, the frequency of the periodon becomes maximum at one third of the phonon wave vector. Therefore for the periodon dispersion, the boundary of the Brillouin zone lies at $2\pi/3$ value of the phonon wave vector.

3. Results and discussion

The polarizability model developed in the theory calculates the dispersion curves for the transverse acoustic and ferroelectric transverse optic mode. In the IV–VI semiconductor, we have calculated the phonon and periodon's transverse branches by fitting the model parameters f, f', f'', g_2, h and g_4 to the experimental zone centre frequencies. These branches are of quite interest as it undergoes mode softening at the ferroelectric phase transition of these compounds. In the present case, SnTe undergoes a transition to a ferroelectric state with a finite transition temperature of 98 K, whereas PbTe does not undergo phase transition and remain paraelectric for all temperatures. Also the soft mode concept is extended to the periodon case to understand the coupling between nonlinear modes and normal phonon modes.

In figures 2(a) and (b), we have plotted the transverse optic and acoustic branches of the phonon dispersion relations for bulk (PbTe and SnTe) (shown in figure 2(a)) and their superlattice structure (PbTe–SnTe), consisting each of six layers (shown in figure 2(b)). We have also shown in figure 2(a), the experimental points for bulk PbTe at 293 K taken from ref. [13] and SnTe at 100 K from ref. [4, p-90]. The corresponding parameters for the calculation of the phonon dispersion curves are defined in table 1. In the phonon dispersion curves of bulk PbTe and SnTe, we have observed some discrepancies in the calculated and experimental values of the transverse optic mode around the wavevector (0, 0, 0·3) to (0, 0, 0·8). This is mainly because our present analysis does not consider the effect of screening due to the free carriers in the systems. This fact however, is not a serious limitation of our predicted results, for such a simple model which can qualitatively explain the nature of the branches in the dispersion curves. In adjoining figure 2(b) we have shown the phonon dispersion curves (TO and TA) for $(PbTe)_6$–$(SnTe)_6$ superlattices.

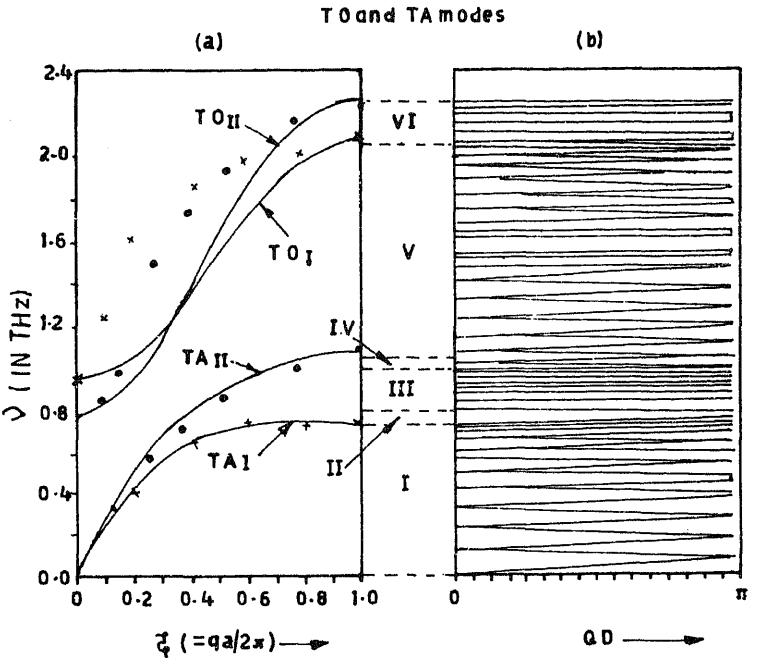

Figure 2(a). Bulk phonon dispersion curves of transverse acoustic and optic branches of PbTe (I) and SnTe (II). ν $(=\omega/2\pi)$ is the reduced frequency and $\xi(=qa/2\pi)$ is the reduced wavevector. Experimental points for PbTe [×] and SnTe [●] are taken from ref. [13] and [4, p. 90] respectively.
Figure 2(b). Phonon dispersion curves of transverse acoustic and optic branches of PbTe–SnTe superlattice with $n_2 = n_1 = 6$.

Table 1. Parameters for phonon dispersion in bulk (PbTe and SnTe).

Parameters	Value	
	SnTe	PbTe
$f(10^4 g/s^2)$	0·1237	0·2385
$f'(10^4 g/s^2)$	0·997	0·745
$f''(10^4 g/s^2)$	0·1655	0·085
$g_2(10^4 g/s^2)$	− 59.9	− 55·9
$h(10^4 g/s^2)$	− 111·246	− 103·0
m_1(a.m.u.)	127·5	127·5
m_2(a.m.u.)	118·7	207·2

To interpret the results of bulk and superlattice dispersion curves, we have divided the frequency axis into six regions on the basis of the values of the real and complex wavevectors of the components I (PbTe) and II (SnTe), which is indicated in table 2. This type of frequency division was given in ref. [12, p-260] for simple superlattice structure. In region I, both the wavevectors q_{TA_I} and $q_{TA_{II}}$ are real, which implies that in very low frequency dispersion region, we obtain broad pass and narrow stop bands.

Table 2. Frequency intervals of figure 2(a).

Frequency interval	q_{TA_I}	$q_{TA_{II}}$	q_{TO_I}	$q_{TO_{II}}$	Nature of superlattice phonon dispersion curves.
I	R	R	I	I	Broad pass and narrow stop acoustic bands.
II	C	R	I	I	Broad stop and narrow pass acoustic bands.
III	I	R	I	R	Broad stop acoustic and optic modes.
IV	I	R	R	R	Broad pass bands for optic modes and broad stop bands for acoustic modes.
V	I	I	R	R	Narrow stop and broad pass bands for optic modes.
VI	I	I	I	R	Broad stop optic bands.

R = real, C = complex, I = pure imaginary

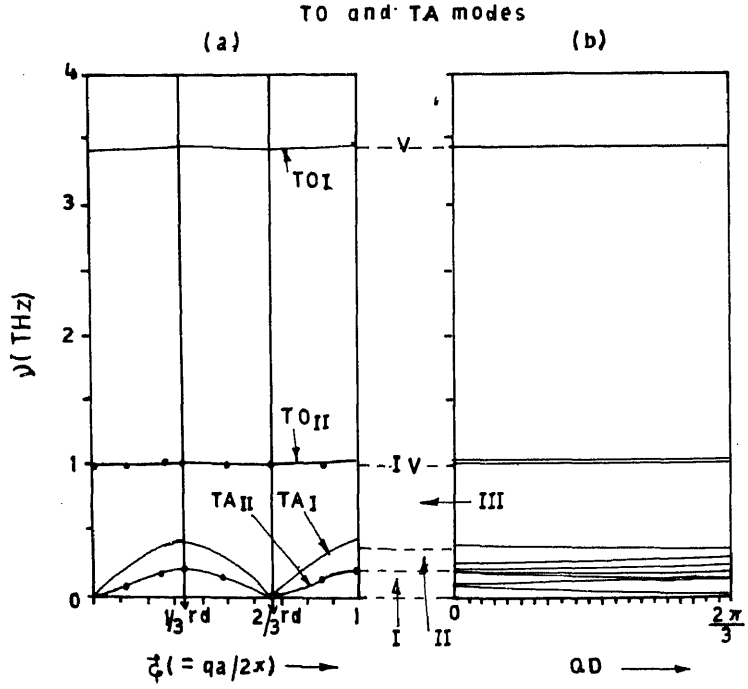

Figure 3(a). Bulk periodon dispersion curves of transverse acoustic and optic branches of PbTe (I) and SnTe (II). Model calculation results of SnTe [●] are taken from ref. [4] p. 90.

Figure 3(b). Periodon dispersion curves of transverse acoustic and optic branches of PbTe–SnTe superlattice with $n_2 = n_1 = 6$.

Hence the modes are propagating in nature in the frequency interval $0 < \nu < 0{\cdot}6$ THz. From $\nu = 0{\cdot}6$ to $0{\cdot}75$ THz., the wavevectors q_{TA_I} remains constant from 0·4 to 1·0 whereas the wavevector $q_{TA_{II}}$ increases from 0·25 to 0·475. In this frequency interval, the modes are propagating as well as confined in some of the regions. In region II (i.e., $0{\cdot}75 < \nu < 0{\cdot}78$), only $q_{TA_{II}}$ is real which results into broad stop and narrow pass bands. The transverse acoustic modes of SnTe become confined in this frequency interval. In region III (i.e., $0{\cdot}78 < \nu < 0{\cdot}96$) the wavevectors $q_{TO_{II}}$ and $q_{TA_{II}}$ are only real, which shows that we obtain broad stop bands in this region. In region IV (i.e., $0{\cdot}96 < \nu < 1{\cdot}05$) three wavevectors i.e., $q_{TA_{II}}$, q_{TO_I} and $q_{TO_{II}}$ are real, which signifies that the optical modes are propagating in nature and the acoustic modes of SnTe remain confined. In region V, the optical modes in both the materials are real. The frequency varies from 1·05 to 2·075 and the dispersion obtained there consists of narrow stop and broad pass bands. In the region VI, only the wavevector $q_{TO_{II}}$ is real in magnitude. As expected we obtained there broad stop bands.

In figures 3(a) and (b), we have obtained the periodon dispersion relation in bulk and superlattice structure of PbTe and SnTe layers. From the figure 3(a), it is noted that the transverse optic modes of periodon remain constant for all the wavevectors and the transverse acoustic modes become maximum at one third of the reduced wavevector [4]. Hence in the periodon treatment, the Brillouin zone reduces to one third of the phonon case. For the material SnTe, Bilz *et al* [7] have calculated the periodon dispersion relation in which it is found that the LO phonon become degenerate with the TO phonon at the zone centre. The periodon frequency obtained from their calculation are also shown in figure 3(a) for SnTe material. For PbTe, no such measurements are available. Corresponding to the wavevector obtained in bulk,

Table 3. Parameters for periodon dispersion in bulk.

Parameters (10^4 g/s^2)	Value	
	SnTe	PbTe
f	3·8145	44·302
f'	0·012	0·05
f''	0·073	0·53
h	−0·0777	−0·9

Table 4. Frequency intervals of figure 3(a).

Frequency interval	q_{TA_I}	$q_{TA_{II}}$	q_{TO_I}	$q_{TO_{II}}$	Properties of superlattice periodon dispersion curves.
I	R	R	I	I	Broad pass and narrow stop acoustic bands.
II	C	R	I	I	Broad stop bands for acoustic modes.
III	I	I	I	I	No solutions.
IV	I	I	C	R	Broad stop optic bands.
V	I	I	R	C	Broad stop optic bands.

R = real, C = complex, I = Imaginary

we have obtained the periodon dispersion relation which is shown in figure 3(b). The corresponding model parameters and the frequency interval are given in tables 3 and 4 respectively. In region I (i.e., from $0 < \nu < 0{\cdot}1875$), the wavevectors q_{TA_I} and $q_{TA_{II}}$ are real which give rise to propagating nature of the acoustic modes. In region II (i.e., from $0{\cdot}1875 < \nu < 0{\cdot}375$) only the wavevectors $q_{TA_{II}}$ is real. The acoustic modes become confined. At $\nu = 1$ and 3·42 THz., the transverse optical modes of SnTe and PbTe are real respectively. Hence we observe a single line at those frequencies. We have thus understood the nature of the different physical solutions obtained in the different regions of the phonon and periodon dispersion in bulk and superlattice structure of IV–VI semiconductors. This type of study in superlattices will help in the understanding of various electronic and vibrational properties.

Acknowledgement

One of us (NDC) is grateful to Council of Scientific and Industrial Research, India for the award of Research Associateship.

References

[1] Yu I Ravich, B A Efimova and I A Smirnow, *Semiconducting Lead Chalcogenides*, edited by L S Stil'bans (Plenum, New York, 1970)
H Heinrich, A Lopez-Otero, L Palmetshofer and L D Haas, In *Lattice defects in semiconductors*, edited by F A Huntley, Inst. Phys. Conf. Ser. 23, (Institute of Physics, Bristol, 1974)
K Lischka, *Appl. Phys.* **A29**, 177 (1982).

[2] M E Lines and A M Glass, *Principles and applications of ferroelectrics and related materials*, The Int. Series of Monographson Physics (Clarendon, Oxford, 1977).

[3] H Preier, *Appl. Phys.* **20**, 189 (1979)
H Holloway, *Thin Solid Films* **11**, 105 (1980)

[4] A Bussmann-Holder, H Bilz and P Vogl, in *Dynamical properties IV–VI compound*, (Springer–Verlag, Berlin, 1987)

[5] W Cochran, *Adv. Phys.* **9**, 387 (1960)
K Schubert and H Fricke, *Z. Naturforchung* **6a**, 781 (1953)
L Muldawer, *J. Nonmetals* **1**, 177 (1973)
R T Bate, D L Carter and J S Wrobel, *Phys. Rev. Lett.* **25**, 159 (1970)

[6] M M Elcombe, *Proc. R. Soc.* (London) **A300**, 210 (1967)
W Cochran, R A Cowley, G Dolling and M M Elcombe, *Proc. R. Soc.* (*London*) **A293**, 433 (1966)
P R Vijayaraghawan, S K Sinha and P K Iyengar, *Proc. nuclear and solid state physics symposium, Bangalore* (1973)
E R Cowley, J K Darby and G S Pawley, *J. Phys.* **C2**, 1916 (1969)
G S Pawley, W Cochran, R A Cowley and G Dolling, *Phys. Rev. Lett.* **17**, 753 (1966)

[7] H Bilz, A Bussmann-Holder, G Benedek, H Buttner and D Strausch, *Ferroelectrics* **25**, 339 (1980)
H Bilz, H Buttner, A Bussmann-Holder, W Kress and U Schroder, *Phys. Rev. Lett.* **48**, 264 (1982)

[8] H Kinoshita and H Fujiyasu, *J. Appl. Phys.* **51**, 5845 (1980)
E F Fantner and G Bauer, *Two dimensional series in solid state sciences* (Springer–Verlag, 1984) **53**, 207

[9] O A Mironov, S V Christyakov, I Yu Skrylev, A I Federenko, A Yu Sepatov, B A Savitskii, O N Nashchekines and M Oszwaldowski, *Acta Phys. Pol.* **A80**, 329 (1991)

[10] O A Mironov, S V Christyakov, I Yu Skrylev, A I Federenko, A Yu Sepatov, B A Savitskii, L P Shpakovskaya, O N Nashekina and M Oszwaldowski, *Superlattice microstructure* **8**, 361 (1990)
[11] S Rath and S P Sanyal, *Phys. Status Solidi.* **B176**, 63 (1993)
S Rath and S P Sanyal, *Pramana – J. Phys.* **41**, 21 (1993)
[12] M G Cottam and D R Tilley, eds. *Introduction to surface and superlattice excitations* (Cambridge University Press, 1989) p. 259
[13] W Cochran, R A Cowley, G Dolling and M M Elcombe, *Proc. R. Soc.* (*London*) **A293**, 433 (1966).

PRAMANA
— journal of
physics

© Printed in India

Vol. 43, No. 5,
November 1994
pp. 391–400

Electronic contribution to electric field gradient in β-gallium

B K ACHARYA and N C MOHAPATRA*
Department of Physics, Govt. Science College, Chatrapur 761 020, India
*Department of Physics, Berhampur University, Berhampur 760 007, India

MS received 27 June 1994; revised 30 September 1994

Abstract. Electronic contribution to electric field gradient (EFG) in β-Ga has been calculated for the first time using the band wave functions. The results show that the magnitudes of the quadrupole resonance frequency and the net EFG agree with experiment to within 7% and 2% respectively.

Keywords. Electric field gradient; β-gallium; model potential.

PACS No. 76·60

1. Introduction

There has been extensive experimental investigation of quadrupole interaction in the solid phase of β-Ga. Pure quadrupole resonance frequency and its temperature variation are available [1–2] from nuclear quadrupole resonance experiments. The sign of EFG has also been predicted indirectly from the experimental and theoretical values of quadrupole anomaly [3–4]. In contrast to this, very little work has been done in theory to understand the quadrupole interaction in β-Ga. The only theoretical work available in literature [5–6] pertains to the evaluation of the ionic contribution to EFG in this solid. The latter is negative in sign [6] and is only a small per cent of the experimental EFG. This suggests that the electronic contribution must be quite significant.

While energy band calculations in β-Ga using pseudopotential [7] and augmented plane waves [8] are available, evaluation of the EFG using the band wave functions from these calculations has not been carried out. Nor are there calculations of EFG in β-Ga using the more recent methods, like the molecular clusters [9] and the full potential-linearized-augmented-plane waves procedures [10]. It is this deficiency which has motivated us to carry out an energy band calculation for the evaluation of the electronic contribution to EFG in β-Ga.

A non-local model potential has been used to obtain the band energy and eigen functions in the Brillouin Zone (BZ). The cartesian components of the EFG tensor are then evaluated using these wave functions. The net EFG tensor obtained as a sum of contributions from lattice ions and conduction electrons is diagonalized to give the principal z-component and the asymmetry parameter. A comparison with experiment shows that the magnitudes of the calculated resonance frequency and the net EFG agree with experiment to within 7% and 2% respectively. There is however discrepancy with respect to the sign of the net EFG and the magnitude of the asymmetry parameter. Plausible explanations are offered for the existing discrepancy.

The paper is organized as follows. In §2, the theory of electric quadrupole interaction in β-Ga is briefly described. Results and discussions are presented in §3. Section 4 summarizes the conclusions.

2. Theory

The study of crystal structure of β-Ga [11] reveals that its unit cell is monoclinic and contains four atoms. The primitive cell, on the other hand, contains two atoms per cell. The lattice parameters [6] at 248 K are, $a = 2{\cdot}766$ Å, $b = 8{\cdot}053$ Å, $c = 3.332$ Å and $\beta = 92°03'$. For evaluating the components of EFG tensor, cartesian axes are set up such that the y and z axes are respectively in the directions of **b** and **c** crystal axes. The x-axis is then fixed from the requirement that x, y, z form a right-handed system. The symmetry of the crystal lattice combined with the above mentioned choice of cartesian axes predicts zero value for the cartesian components, q_{xy} and q_{yz} of the EFG tensor. This leaves only q_{xx}, q_{zz} and q_{xz} components of the traceless symmetric tensor to be determined. The lattice-ion contribution to these components, evaluated in the point-ion approximation, are taken from the work of Lodge [6] after making certain modifications which are described later. Atomic units (au), where $e^2 = 2$, $\hbar = 1$ and $m = 1/2$ have been used throughout in the calculation unless stated otherwise.

For the electronic contribution to EFG an energy band calculation has been carried out using a non-local model potential [12]. The band energies $E_n(\mathbf{k})$ and the eigen functions are obtained as solution of the secular equation,

$$|H_{\mathbf{k}+\mathbf{K},\mathbf{k}+\mathbf{K}'} - E_n(\mathbf{k})\delta_{\mathbf{K}\mathbf{K}'}| = 0, \tag{1}$$

where the matrix element of the model Hamiltonian H in a plane wave basis is given by

$$H_{\mathbf{k}+\mathbf{K},\mathbf{k}+\mathbf{K}'} = |\mathbf{k}+\mathbf{K}|^2 \delta_{\mathbf{K}\mathbf{K}} + V(\mathbf{k}+\mathbf{K}, \mathbf{k}+\mathbf{K}'). \tag{2}$$

The second term in (2) is the Fourier transform of the non-local model potential, **k** and **K** are the wave vector in the *BZ* and the reciprocal lattice vector respectively. The model wave function χ, expanded in a plane wave basis with coefficients $C_n(\mathbf{k}, \mathbf{K})$ determined variationally is written as

$$\chi_n(\mathbf{k}, \mathbf{r}) = \sum_{\mathbf{K}} C_n(\mathbf{k}, \mathbf{K}) \mathrm{PW}(\mathbf{k}+\mathbf{K}, \mathbf{r}) \tag{3}$$

where PW is the normalized plane wave,

$$\mathrm{PW}(\mathbf{k}+\mathbf{K}, \mathbf{r}) = \frac{1}{\sqrt{N\Omega}} \exp(i(\mathbf{k}+\mathbf{K})\cdot\mathbf{r}) \tag{4}$$

with N and Ω being the number of atoms in the solid and the volume per atom respectively.

By orthogonalizing χ_n to the crystal core states, each of which is represented by a single tight-binding function ϕ_j, the band wave function Ψ_n is obtained as

$$\Psi_n(\mathbf{k}, \mathbf{r}) = \sum_{\mathbf{K}} C_n(\mathbf{k}, \mathbf{K}) \left[\mathrm{PW}(\mathbf{k}+\mathbf{K}, \mathbf{r}) - \sum_j \langle \phi_j(\mathbf{k}) | \mathrm{PW}(\mathbf{k}+\mathbf{K}) \rangle \phi_j(\mathbf{k}, \mathbf{r}) \right] \tag{5}$$

The tight binding function for the jth core state is defined by

$$\phi_j(\mathbf{k},\mathbf{r}) = \frac{1}{\sqrt{N}} \sum_{\mu} \exp(i\mathbf{k}\cdot\mathbf{R}_\mu) u_j(\mathbf{r}-\mathbf{R}_\mu), \tag{6}$$

where $\mathbf{R}_\mu$ is the direct lattice vector and u_j is the jth atomic core function.

The cartesian components of EFG tensor due to the band electrons may be evaluated using the standard [13] relation,

$$q_{ij} = -\sum_{n,\mathbf{k}} \int \Psi_n^*(\mathbf{k},\mathbf{r}) \frac{\hat{q}_{ij}}{r^3} \Psi_n(\mathbf{k},\mathbf{r})[1-\gamma(r)]\,\mathrm{d}^3 r, \tag{7}$$

where $\gamma(r)$ is the radially dependent antishielding factor [14], $\hat{q}_{ij}$ is the angular operator of the ij-component of the EFG tensor. The sum in (7) is taken over all the occupied bands n at the $\mathbf{k}$ points in the BZ and the negative sign is due to the negative charge on electron. The angular operators $\hat{q}_{xx}$, $\hat{q}_{zz}$ and $\hat{q}_{xz}$, for example, are given [6] by

$$\begin{aligned} \hat{q}_{xx} &= 3\sin^2\theta\cos^2\phi - 1 \\ \hat{q}_{zz} &= 3\cos^2\theta - 1 \\ \hat{q}_{xz} &= 3\sin\theta\cos\theta\cos\phi, \end{aligned} \tag{8}$$

where θ, ϕ are the polar angles of the radius vector $\mathbf{r}$ measured from the nucleus in question.

Using (5), (6) and (8) in (7) and carrying out a considerable amount of simplification, we finally obtain

$$\begin{aligned} q_{xx} = {} & \frac{32\pi}{\Omega} \sum_{\mathbf{k}} \omega_{\mathbf{k}} \sum_t \sum_{\mathbf{K}>\mathbf{K}'} C_t(\mathbf{k},\mathbf{K}) C_t(\mathbf{k},\mathbf{K}') S(\mathbf{K}-\mathbf{K}') D(|\mathbf{K}'-\mathbf{K}|) \\ & \times \left\{ \left(\frac{6\pi}{5}\right)^{1/2} (Y_{22}(\mathbf{K}'-\mathbf{K}) + Y_{22}^*(\mathbf{K}'-\mathbf{K})) - \left(\frac{4\pi}{5}\right)^{1/2} Y_{20}(\mathbf{K}'-\mathbf{K}) \right\} \\ & - \frac{64\pi^2}{\Omega} \sum_{\mathbf{k}} \omega_{\mathbf{k}} \sum_t \sum_{\mathbf{K},\mathbf{K}'} \sum_{n_1 l_1 m_1} \sum_{n_2 l_2 m_2} C_t(\mathbf{k},\mathbf{K}) C_t(\mathbf{k},\mathbf{K}') (i)^{l_2 - l_1} \\ & \times Y_{l_1 m_1}(\mathbf{k}+\mathbf{K})\, Y_{l_2 m_2}^*(\mathbf{k}+\mathbf{K}') I(|\mathbf{k}+\mathbf{K}|, n_1 l_1) I(|\mathbf{k}+\mathbf{K}'|, n_2 l_2) \\ & \times S(\mathbf{K}) S(\mathbf{K}') F(n_1 l_1, n_2 l_2) \left\{ \left(\frac{6\pi}{5}\right)^{1/2} (\langle l_1 m_1 | 22 | l_2 m_2 \rangle \right. \\ & \left. + \langle l_1 m_1 | 2-2 | l_2 m_2 \rangle) - \left(\frac{4\pi}{5}\right)^{1/2} \langle l_1 m_1 | 20 | l_2 m_2 \rangle \right\} \\ & + \frac{128\pi^2}{\Omega} \mathrm{Re} \left(\sum_{\mathbf{k}} \omega_{\mathbf{k}} \sum_t \sum_{\mathbf{K},\mathbf{K}'} C_t(\mathbf{k},\mathbf{K}) C_t(\mathbf{k},\mathbf{K}') \sum_{n_1 l_1 m_1} (i)^{l_1} \right. \\ & \times Y_{l_1 m_1}^*(\mathbf{k}+\mathbf{K}') I(|\mathbf{k}+\mathbf{K}'|, n_1 l_1) S(\mathbf{K}) S(\mathbf{K}') \sum_{l' m'} (-i)^{l'} \\ & \times Y_{l' m'}(\mathbf{k}+\mathbf{K}) H(n_1 l_1, l', |\mathbf{k}+\mathbf{K}|) \left\{ \left(\frac{6\pi}{5}\right)^{1/2} (\langle l' m' | 22 | l_1 m_1 \rangle \right. \\ & \left. \left. + \langle l' m' | 2-2 | l_1 m_1 \rangle) - \left(\frac{4\pi}{5}\right)^{1/2} \langle l' m' | 20 | l_1 m_1 \rangle \right\} \right). \end{aligned} \tag{9}$$

$$q_{zz} = \frac{32\pi}{\Omega}\sum_{\mathbf{k}}\omega_{\mathbf{k}}\sum_{t}\sum_{\mathbf{K}>\mathbf{K}'} C_t(\mathbf{k},\mathbf{K})C_t(\mathbf{k},\mathbf{K}')S(\mathbf{K}-\mathbf{K}')D(|\mathbf{K}'-\mathbf{K}|)\left(\frac{16\pi}{5}\right)^{1/2}$$
$$\times Y_{20}(\mathbf{K}'-\mathbf{K}) - \frac{64\pi^2}{\Omega}\sum_{\mathbf{k}}\omega_{\mathbf{k}}\sum_{t}\sum_{\mathbf{K},\mathbf{K}'}\sum_{n_1 l_1 m_1}\sum_{n_2 l_2 m_2} C_t(\mathbf{k},\mathbf{K})C_t(\mathbf{k},\mathbf{K}')(i)^{l_2-l_1}$$
$$\times Y_{l_1 m_1}(\mathbf{k}+\mathbf{K})\, Y^*_{l_2 m_2}(\mathbf{k}+\mathbf{K}')I(|\mathbf{k}+\mathbf{K}|,n_1 l_1)I(|\mathbf{k}+\mathbf{K}'|,n_2 l_2)$$
$$\times S(\mathbf{K})S(\mathbf{K}')F(n_1 l_1, n_2 l_2)\left(\frac{16\pi}{5}\right)^{1/2}\langle l_1 m_1|20|l_2 m_2\rangle$$
$$+\frac{128\pi^2}{\Omega}\mathrm{Re}\left(\sum_{\mathbf{k}}\omega_{\mathbf{k}}\sum_{t}\sum_{\mathbf{K},\mathbf{K}'} C_t(\mathbf{k},\mathbf{K})C_t(\mathbf{k},\mathbf{K}')S(\mathbf{K})S(\mathbf{K}')\right.$$
$$\sum_{n_1 l_1 m_1}(i)^{l_1} Y^*_{l_1 m_1}(\mathbf{k}+\mathbf{K})I(|\mathbf{k}+\mathbf{K}'|,n_1 l_1)\sum_{l'm'}(-i)^{l'} Y_{l'm'}(\mathbf{k}+\mathbf{K})$$
$$\left.\times H(n_1 l_1, l', |\mathbf{k}+\mathbf{K}|)\left(\frac{16\pi}{5}\right)^{1/2}\langle l'm'|20|l_1 m_1\rangle\right), \tag{10}$$

and

$$q_{xz} = -\frac{32\pi}{\Omega}\sum_{\mathbf{k}}\omega_{\mathbf{k}}\sum_{t}\sum_{\mathbf{K}>\mathbf{K}'} C_t(\mathbf{k},\mathbf{K})C_t(\mathbf{k},\mathbf{K}')S(\mathbf{K}-\mathbf{K}')D(|\mathbf{K}'-\mathbf{K}|)$$
$$\times\left(\frac{6\pi}{5}\right)^{1/2}\{Y_{21}(\mathbf{K}'-\mathbf{K}) + Y^*_{21}(\mathbf{K}'-\mathbf{K})\}$$
$$-\frac{64\pi^2}{\Omega}\sum_{\mathbf{k}}\omega_{\mathbf{k}}\sum_{t}\sum_{\mathbf{K},\mathbf{K}'} C_t(\mathbf{k},\mathbf{K})C_t(\mathbf{k},\mathbf{K}')S(\mathbf{K})S(\mathbf{K}')\sum_{n_1 l_1 m_1}\sum_{n_2 l_2 m_2}(i)^{l_2-l_1}$$
$$\times Y_{l_1 m_1}(\mathbf{k}+\mathbf{K})\, Y^*_{l_2 m_2}(\mathbf{k}+\mathbf{K}')F(n_1 l_1, n_2 l_2)I(|\mathbf{k}+\mathbf{K}|,n_1 l_1)$$
$$I(|\mathbf{k}+\mathbf{K}'|,n_2 l_2)$$
$$\times\left\{-\left(\frac{6\pi}{5}\right)^{1/2}(\langle l_1 m_1|21|l_2 m_2\rangle - \langle l_1 m_1|2-1|l_2 m_2\rangle)\right\}$$
$$-\frac{128\pi^2}{\Omega}\mathrm{Re}\left(\sum_{\mathbf{k}}\omega_{\mathbf{k}}\sum_{t}\sum_{\mathbf{K},\mathbf{K}'} C_t(\mathbf{k},\mathbf{K})C_t(\mathbf{k},\mathbf{K}')S(\mathbf{K})S(\mathbf{K}')\right.$$
$$\times\sum_{n_1 l_1 m_1}(i)^{l_1} Y^*_{l_1 m_1}(\mathbf{k}+\mathbf{K}')I(|\mathbf{k}+\mathbf{K}'|,n_1 l_1)\sum_{l'm'}(-i)^{l'} Y_{l'm'}(\mathbf{k}+\mathbf{K})$$
$$\left.\times H(n_1 l_1, l', |\mathbf{k}+\mathbf{K}|)\left(\frac{6\pi}{5}\right)^{1/2}\{\langle l'm'|21|l_1 m_1\rangle + \langle l_1 m_1|21|l'm'\rangle\}\right). \tag{11}$$

where

$$D(|\mathbf{K}'-\mathbf{K}|) = \int_0^\infty j_2(|\mathbf{K}'-\mathbf{K}|r)\frac{\{1-\gamma(r)\}}{r}\,\mathrm{d}r, \tag{12}$$

$$I(|\mathbf{k}+\mathbf{K}|,nl) = \int_0^\infty P_{nl}(r)j_l(|\mathbf{k}+\mathbf{K}|r)r\,\mathrm{d}r, \tag{13}$$

$$F(n_1 l_1, n_2 l_2) = \int_0^\infty P_{n_1 l_1}(r)P_{n_2 l_2}(r)\frac{\{1-\gamma(r)\}}{r^3}\,\mathrm{d}r, \tag{14}$$

$$H\{n_1 l_1, l', |\mathbf{k}+\mathbf{K}|\} = \int_0^\infty P_{n_1 l_1}(r) j_{l'}(|\mathbf{k}+\mathbf{K}|r) \frac{\{1-\gamma(r)\}}{r^2} \mathrm{d}r, \tag{15}$$

and

$$\langle l_1 m_1 | l_2 m_2 | l_3 m_3 \rangle = \int Y^*_{l_1 m_1}(\hat{r})\, Y_{l_2 m_2}(\hat{r})\, Y_{l_3 m_3}(\hat{r}) \sin\theta \mathrm{d}\theta \mathrm{d}\phi \tag{16}$$

The **k**-sums in (9)–(11) are taken over the irreducible part of the *BZ*. The first, the second and the third **k**-sums in each of the equations (9)–(11) give respectively the contributions from the plane wave, tight binding and the hybrid (i.e. plane wave-tight binding and tight binding-plane wave) part of the integral in (7). The symbols $\omega_{\mathbf{k}}, t, S$ and i used in (9), (10) and (11) are respectively the weighting factor assigned to **k** point, the occupied band index, the structure factor and the imaginary number $\sqrt{-1}$. The functions Y_{lm}, j_l and P_{nl} are the standard spherical harmonics, the spherical Bessel function of order l and the radial part of the atomic core function respectively. The latter is normalized according to the relation,

$$\int_0^\infty P^2_{nl}(r)\mathrm{d}r = 1. \tag{17}$$

The quantum numbers specifying the atomic core states are denoted by n, l, and m. The integrals in (12)–(15) and (17) were evaluated using the standard 5-point numerical integration procedure after generating the corresponding integrands at 201 mesh points each, chosen in a logarithmic r scale,

$$r_n = r_1 \exp(-(n-1)h) \quad \text{with} \quad r_1 \simeq 0{\cdot}00097 \text{ au and } h = 0{\cdot}05 \text{ au}.$$

The farthest distance up to which the integrations were carried out has the value $r_{201} \simeq 21{\cdot}45618$ au.

The angular integrals in (16), whose values for allowed angular momentum quantum numbers are tabulated by Tinkham [15] were used directly.

3. Results and discussion

In constructing the band wave functions Ψ_n, the atomic core functions used in the present work are those of Clementi [16]. In order to carry out the **k**-sum in (9)–(11), 176 sample **k** points are suitably chosen in $\frac{1}{4}$th irreducible part of the *BZ*. For this purpose the wedge denoting the irreducible part of the *BZ* is divided into 176 volume elements, out of which 150 elements are parallelopipeds and the remaining 26 elements are triangular prisms. The **k**-vectors denoting the centroids of these elements are used as the representative points. To each **k** point so chosen, a weighting factor in proportion to the volume it represents is assigned. Thus, the effective number of **k** points chosen in the full *BZ* comes to 704. Energy and eigen functions are calculated at each of these 176 **k**-points. For this purpose the model wave function at each **k** point is expanded in 23 plane waves corresponding to the shortest 23 wave vectors, $|\mathbf{k}+\mathbf{K}|$ for that **k**-point. Thus, the size of the matrix diagonalized at each **k**-point is 23×23. With this choice, convergence of energy and eigen functions is good. The energies of the occupied bands have converged to within 0·001 Ryd. We wish to remark here that a choice of more representative **k** points than 176 in irreducible part of *BZ* would, in principle, give more accurate result. But the computation time as

well as the memory for storage of data increase many fold. From past experience as well as the the present calculation we have found that the accuracy of EFG with respect to variation in the number of **k** points is good to within 1% for the number of **k**-points choosen in the present work.

We have compared the results of the present band calculation with those of APW calculation [8]. Not only the shape of the bands but also the Fermi energy and the density of states $\mathcal{N}(E_F)$ agree quite well. While the Fermi energy E_F in the present calculation, measured from the bottom of the band as zero of energy scale, turns out to be 0·784 Ryd, it is 0·807 Ryd in APW calculation [8]. The density of states $\mathcal{N}(E_F)$ in the present calculation is found approximately $(0{\cdot}97 \pm 0{\cdot}01)\,\mathcal{N}_0(E_F)$, where $\mathcal{N}_0(E_F)$ is the free-electron value. This compares well with the value of $(0{\cdot}96 \pm 0{\cdot}04)\,\mathcal{N}_0(E_F)$ obtained in APW calculation [8]. It also agrees reasonably well with density of states, $\mathcal{N}(E_F) = (0{\cdot}92 \pm 0{\cdot}09)\,\mathcal{N}_0(E_F)$ deduced indirectly [8] from the measured values of the electron specific heat. In arriving at the measured value for the density of states, the effect of electron-phonon interaction has been duly taken into consideration [8]. The value of electron-phonon enchancement factor used [8] for this purpose is $\lambda = 0{\cdot}63$.

There is however a minor discrepancy between the two calculations with regard to the filling of the fifth band. While in the APW calculation [8], the fifth band is vacant, in the present work, there is a small electron pocket in this band. The other band calculation in β-Ga is by Hunderi [7]. However, he had used the same form factor [12] as used in the present work but with a less number of basis functions and an approximate β equal to 90°. The details of E_F and $\mathcal{N}(E_F)$ are however not available in ref. [7] for comparison with the present work.

Next we discuss the results of field gradients. Since the values of $\gamma(r)$ for β-Ga in solid state are not available, the integral in (12), (14) and (15) have been evaluated by assuming $\gamma(r) = 0$. This assumption would lead to a negligible error in the contribution to EFG arising from the tight binding part of the band wave functions. This is so because in the region (see integrals (14) and (15)) where the amplitude of the tight-binding function is large, $\gamma(r)$ is small and where $\gamma(r)$ is large the amplitude of atomic wave function is negligible. The plane wave (PW) contribution, on the other hand, is likely to be significantly affected on account of the relatively long range nature of plane wave states (see integral (12)) and the saturation value of $\gamma(r)$ at large r. In the absence of solid state $\gamma(r)$, we have estimated the shielding for the PW contribution as follows. The shielded PW contribution to q_{xx}, q_{zz} and q_{xz} are calculated using the available [17] free-ion $\gamma(r)$. From these the ratios of the shielded to the corresponding unshielded ($r(r) = 0$) PW contributions are obtained. These are found to be approximately 1·76, 1·96 and 0·55 for q_{xx}, q_{zz} and q_{xz} respectively. To get the corresponding numbers in the solid state, that is, the ratios of the shielded plane wave contributions using solid-state $(1 - \gamma(r))$ to the corresponding unshielded PW contributions, we have used the approximation,

$$\{1 - \gamma(r)\}_{\text{solid}} \approx \{1 - \gamma(r)\}_{\text{free-ion}} \frac{(1 - \gamma_\infty)_{\text{solid}}}{(1 - \gamma_\infty)_{\text{free-ion}}} \tag{18}$$

and used this in the integral (12) to obtain the shielded PW contribution in solid state. This approximation is very good at large distance where $\gamma(r)$ is nearly a constant equal to the value of γ_∞ for the respective system. From this approximation, it is easy to see that the shielding factors, that is, the ratios of the shielded PW contribution

using solid state $(1-\gamma(r))$ to the unshielded PW contribution are approximately equal to the product of $(1-\gamma_\infty)_{\text{solid}}/(1-\gamma_\infty)_{\text{free-ion}}$ and the corresponding shielding factors obtained using free-ion $(1-\gamma(r))$.

The ionic contributions to EFG, as previously stated, are taken from the work of Lodge [6] with the following modifications. The cartesian axes chosen in the present work are different from those of Lodge [6] who had taken x and z axes parallel to **c** and **b** axes respectively. Therefore his results needed to be transformed to our coordinate system. Secondly, the free-ion value of the antishielding factor γ_∞ used by Lodge [6] was replaced by the value of γ_∞ appropriate to the solid state. The latter taken from the work of Schmidt *et al* [18] is equal to $-16{\cdot}986$.

We wish to remark here that in evaluating the ionic contribution the point-ion approximation has been used for all the distant ions than the one at whose site EFG is required. This is a reasonably good approximation considering the fact that the overlap of the spherical cores of the distant ions with that of the ion in question is negligible. The effect arising from the deformation of the core of the ion in question by the distant ions and the nuclear quadrupole moment has however been included through the Sternheimer antishielding factor. But the contribution to EFG due to the induced multipoles of the deformed cores of the distant ions, which is expected to be small has been neglected.

The components of EFG tensor in the chosen axes system arising from the lattice ions as well as the band electrons are listed in table 1. The net EFG tensor is diagonalized and the principal components q_{XX}, q_{YY} and q_{ZZ} are identified according to the criterion,

$$|q_{XX}| \leqslant |q_{YY}| \leqslant |q_{ZZ}|. \tag{19}$$

The asymmetry parameter is calculated using the relation,

$$\eta = \frac{q_{XX} - q_{YY}}{q_{ZZ}} \tag{20}$$

The pure quadrupole resonance frequency is related [2] to q_{ZZ} and η by

$$\nu = \frac{e^2 q_{ZZ} Q}{2h}\left(1+\frac{\eta^2}{3}\right)^{1/2} \tag{21}$$

where e, h and Q are respectively the charge on electron, Planck's constant and the quadrupole moment of the nucleus in question. For the isotope ^{69}Ga, $Q = 0{\cdot}168$ barns [6].

Each component of electronic EFG tensor in table 1 consists of a sum of contributions from a pure plane wave part and a non-plane wave part of the band wave function Ψ_n. As discussed in ref. [13], the non-plane wave part has been further split into a sum of $s-d$, $p-p$, $d-d$ type terms depending on the angular momentum of tight-binding states involved in these contributions and a 'distant' term arising from the $l=0$ component of the charge distribution on all the other lattice sites than the one in question. The PW and the none plane wave type contributions are summarized in table 2. It may be noted from this table that for each component of EFG, the $p-p$ term has the largest magnitude. This is understandable because, the p-orbitals give rise to the most asymmetric charge distribution. Now coming back to table 1, one notices that between the two diagonal components q_{xx} and q_{zz} of the

Table 1. Components of EFG tensor in crystal axes system. All the EFG's are expressed in atomic units.

Contribution	q_{xx}	q_{zz}	q_{xz}
Electronic	−0·29488	0·16284	0·00289
Ionic	0·04478	−0·12373	0·00786
Total	−0·25010	0·03911	0·01075

Table 2. Electronic contibution to various components of EFG tensor in β-Ga. All the EFG's are expressed in atomic units.

	PW	$s-d$	$p-p$	$d-d$	dist.	total
q_{xx}	−0·01789	−0·00540	−0·26444	−0·00792	0·00082	−0·29488
q_{zz}	0·05615	−0·00002	0·10261	0·00635	−0·00225	0·16284
q_{xz}	−0·00097	0·00045	0·00292	0·00035	0·00014	0·00289

Table 3. Net EFG, asymmetry parameter and pure quadrupole resonance frequency in β-Ga at 248 K. The EFGs are expressed in atomic units and the resonance frequency in MHz.

Theory			Expt.[a]		
q	η	ν	$\lvert q\rvert$	η	$\lvert\nu\rvert$
−0·250	0·684	−5·318	0·247	0·305	4·952

[a]These data are taken from [2] after interpolation.

electronic contribution, the former is larger in magnitude than the latter. This suggests that the electron distribution around x-axis is more compact and localized than in the yz plane. The ionic contributions, on the other hand, show an opposite trend.

Table 3 summarizes the experimental [2] and the theoretical results for the field gradient, asymmetry parameter and the resonance frequency at 248 K. The experimental data listed are the results of interpolation made from the temperature dependent data given in ref. [2]. The experimental EFG has been deduced by using the prue quadrupole resonance frequency and the asymmetry parameter in (21).

A comparison of data in table 3 shows that the magnitudes of the calculated quadrupole resonance frequency and the net EFG agree with experiment to within 7% and 2% respectively. There is however discrepancy with respect to the sign of the EFG and the magnitude of η. While theory gives negative sign, experiment [3] predicts a positive sign for the net EFG. The latter prediction is based on the quadrupole anomaly data [3] and the sign of the anisotropic Knight shift in β-Ga [2]. We offer the following plausible explanations for the said discrepancy.

In order to see whether the approximate shielding factor used in the present work for the PW contribution could be responsible for the discrepancy, we have calculated the net EFG q and η for three sets of progressively increasing shielding factors. The results are summarized in table 4. In this table the first row refers to free-ion shielding

Table 4. Variation in the EFG and asymmetry parameter with the change in the shielding factors of the *xx*, *zz* and *xz* components of the plane wave contribution. The EFGs are expressed in atomic units.

Components			q	η
xx	*zz*	*xz*		
1·76	1·96	0·55	−0·244	0·842
2·75	3·07	0·85	−0·250	0·684
5·28	5·88	1·62	−0·267	0·319

factor, the second row gives the shielding factors used in the present work and are obtained by multiplying the corresponding free-ion shielding factors by the ratio $(1-\gamma_\infty)_{\text{solid}}/(1-\gamma_\infty)_{\text{free-ion}}$. The third row lists a set of shielding factors which give η and the magnitude of q very close to the corresponding experimental values. It may be noted that in all these cases, in spite of variation in shielding factors, the sign of the net EFG is negative with negligible variation in magnitudes. The asymmetry parameter, on the other hand, varies appreciably. So we conclude that any uncertainty in the PW shielding factor may not account for the sign reversal of the net EFG. On the other hand, there are reasons to believe that this discrepancy may owe its origin to the theoretical value of quadrupole anomaly [4] and the experimental value of anisotropic Knight shift [2], both of which were used in predicting the sign of the experimental EFG as positive.

As to the quadrupole anomaly, eq. (12) of Pyykkö [4] which has been used in obtaining the expression for the pseudo quadrupole contribution does not hold for β-Ga since the latter does not have a three fold or higher rotational symmetry axis, a condition for the validity of the said equation. Secondly and more importantly, the experimental [2] deduction of anisotropic Knight shift K' from the relation, $K(\theta)=K_{\text{iso}}+\frac{1}{2}K'\,(3\cos^2\theta-1)$ may be erroneous in β-Ga as the latter is neither axially symmetric nor the principal axis of its Knight shift tensor is coincident with q_{zz}, the two requirements for the validity of the above relation. Hence the sign of K' determined in experiment [2] may not be reliable and therefore all subsequent analysis using K' for the prediction of the sign of EFG may fall apart. In order to settle the discrepancy in the sign of the EFG, it is therefore suggested that more direct measurement of the sign than deducing it from the quadrupole anomaly data be performed. The procedure of time-differential-perturbed-angular-correlation (TDPAC) involving β-γ correlation [19] and the one that uses Mössbauer spectroscopy (MS) [20] may be used for the direct measurement of the sign of the EFG.

It is hoped that the shielding factors in the third row of table 4, which give better values of q and η may result if the values of $\gamma(r)$ appropriate to the solid state are used in the calculation of EFG.

4. Conclusion

In conclusion, we state that the model potential calculation gives the magnitude of EFG and the quadrupole resonance frequency in β-Ga in good agreement with experiment. The results, particularly the asymmetry parameter are expected to

improve, if the values of $\gamma(r)$ appropriate to solid state are used. For settling the existing discrepancy in the sign of the EFG, it is suggested that more direct measurement of the sign as accomplished in TDPAC or MS be performed rather than deducing it from the quadrupole anomaly data.

References

[1] S L Segel, R D Heyding and E F W Seymore, *Phys. Rev. Lett.* **28**, 970 (1972)
[2] J D Stroud and S L Segel, *J. Phys.* **F5**, 1981 (1975)
[3] S L Segel and J D Stroud, *J. Phys.* **F5**, 1986 (1975)
[4] P Pyykkö, *J. Phys.* **F1**, 102 (1971)
[5] M Valic and D L Williams, *J. Phys. Chem. Solids* **30**, 2337 (1969)
[6] K W Lodge, *J. Phys.* **F8**, 443 (1978)
[7] O Hunderi, *J. Phys.* **F5**, 883 (1975)
[8] J D Stroud and M J Strott, *J. Phys.* **F5**, 166 (1975)
[9] R Coehoorn and K H J Buschow, *Phys. Rev.* **B42**, 4665 (1990)
[10] P Blaha, K Schwartz and P H Deleriche, *Phys. Rev.* **B37**, 2792 (1988)
[11] L Bosio, R Cortes and A Defrain, *J. Chem. Phys.* **70**, 357 (1973)
[12] M Appapillai and A R Williams, *J. Phys.* **F3**, 359 (1973)
[13] N C Mohapatra, P C Pattanaik, M D Thompson and T P Das, *Phys. Rev.* **B16**, 3001 (1977)
[14] R M Sternheimer, *Phys. Rev.* **130** 1423 (1963)
[15] M Tinkham, *Group theory and quantum mechanics* (McGraw-Hill Book Company, New York 1964)
[16] E Clementi, *Tables of atomic functions* (New York: IBM 1965)
[17] S K Padhi and N C Mohapatra, *Phys. Rev.* **B29**, 5199 (1984)
[18] P C Schmidt, K D Sen, T P Das and A Weiss, *Phys. Rev.* **B22**, 4167 (1980)
[19] R S Raghavan, P Raghavan and E N Kaufmann, *Phys. Rev. Lett.* **C12**, 2022 (1974)
[20] G K Werthiem, *Mössobauer effect* (Academic Press, New York, 1964)

PRAMANA
— journal of
physics

© Printed in India

Vol. 43, No. 5,
November 1994
pp. 401–406

Application of laser beam deflection technique to study the diffusion process in electrolyte solutions

ACHAMMA KURIAN[1], C V BINDHU, S S HARILAL, RIJU C ISSAC, V P N NAMPOORI and C P G VALLABHAN
Laser Division, Department of Physics, Cochin University of Science and Technology, Cochin 682 022, India
[1] Also at Department of Physics, Catholicate College, Pathanamthitta 689 645, India

MS received 27 June 1994

Abstract. A simple method based on laser beam deflection to study the variation of diffusion coefficient with concentration in a solution is presented. When a properly fanned out laser beam is passed through a rectangular cell filled with solution having concentration gradient, the emergent beam traces out a curved pattern on a screen. By taking measurements on the pattern at different concentrations, the variation of diffusion coefficient with concentration can be determined.

Keywords. Laser beam deflection; diffusion coefficient.

PACS Nos 05·60; 42·20; 42·60

1. Introduction

Laser beam deflection (LBD) technique is an effective and sensitive method for studying the refractive index gradient (RIG) created in a medium by various causes like temperature and concentration variations [1]. In this method, a laser beam with a gaussian profile is allowed to pass through a well defined region in which the refractive index gradient has been created by some physical effect. The amount of deflection suffered by the laser beam is a direct measure of RIG that has been caused in the defined region and hence yields the value of the parameters of the physical processes that create the RIG. Various features of the LBD method has been extensively discussed in the literature [2, 3]. In this work we have used the LBD method to study the different processes in electrolytic solutions. The variation of the diffusion coefficient with concentration has been worked out using the above method.

The concentration dependence of diffusion coefficient has been studied by various workers using different techniques. Some of such techniques are conductometric method [4], isotopic tracer method [5] and interferometric method [6]. All these techniques involve the study of the concentration of diffusing species at a particular point as a function of time. This is repeated at various spatial points. In the present method it is possible to determine the diffusing properties in the diffusing medium simultaneously at various spatial points. This will help us to identify the presence of any spatial anisotropy in the medium.

2. Principle

The schematic of the experimental set up is shown in figure 1. Laser beam is passed through a cylindrical lens mounted with its axis at 45° to the vertical. The emerging fan of rays then passes through a rectangular glass cell containing the liquid. The fanned out laser beam is deflected at the interface and the curved image of the deflected beam can be obtained on the screen kept at a distance from the cell. The magnitude of beam deflection [7] is

$$z = ad\frac{\partial n}{\partial y} \tag{1}$$

where a is the distance between the cell and the screen, d the thickness of the cell and $\partial n/\partial y$ is the refractive index gradient. Since $\partial n/\partial y$ is proportional to concentration gradient $\partial C/\partial y$, one can write

$$z = Kad\frac{\partial C}{\partial y}$$

where K is a constant.

Introducing a horizontal coordinate x on the screen for the rays passing through the depth y in the cell, and with an appropriate choice of origin, x is related to y through the expression

$$x = (a+b)\frac{y}{b} \tag{2}$$

where b is the distance from the cell to the origin of the fan of rays. The magnitude of deflection is different for different concentrations. In the case of electrolytic solutions, diffusion coefficient (D) depends on concentration. Then the diffusion equation can be written as [8]

$$\frac{\partial C}{\partial t} = D(C)\frac{\partial^2 C}{\partial y^2} + \frac{\mathrm{d}D(C)}{\mathrm{d}C}\left(\frac{\partial C}{\partial y}\right)^2. \tag{3}$$

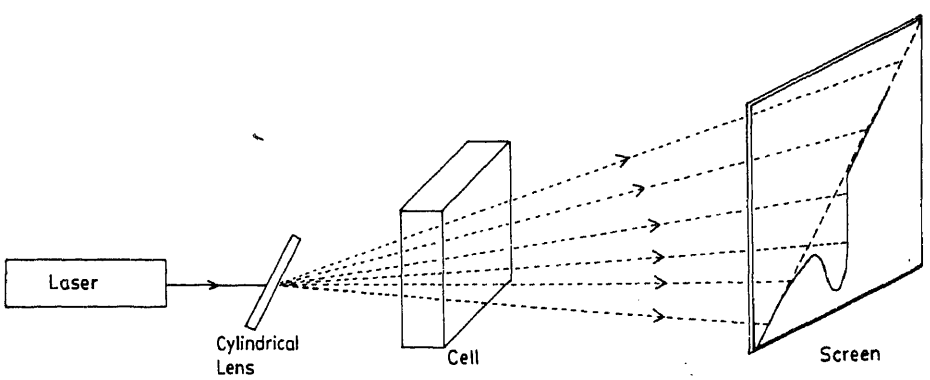

Figure 1. Schematic diagram of the experimental set-up.

Substituting $x = y/t^{1/2}$, (3) becomes

$$\frac{d^2C}{dx^2} + \frac{x}{2D}\frac{dC}{dx} + \frac{D'}{D}\left(\frac{dC}{dy}\right)^2 = 0 \tag{4}$$

where

$$D' = \frac{dD}{dC}.$$

These nonlinear equations defining D as an arbitrary function of C cannot be integrated. Usually the method is to find $D(C)$ experimentally and (4) can be written as

$$\frac{d}{dx}\left(D\frac{dC}{dx}\right) = -\frac{X}{2}\frac{dC}{dx} \tag{5}$$

and

$$D(C) = -\frac{1}{2}\frac{dx}{dC}\int x\,dC \tag{6}$$

Right hand side of (6) can be evaluated experimentally. One of the simplest forms of $D(C)$ is to write

$$D(C) = D_0 + D_1 C^{1/2} + D_2 C + D_3 C^{3/2} + \ldots \tag{7}$$

such that

$$|D_{i+1}| \ll |D_i|.$$

For low concentration, $D(C) = D_0$ which corresponds to concentration independent case. Taking a step-like variation of concentration in a plane within the medium we can write

$$\left(\frac{\partial C}{\partial y}\right)_i = -\frac{C_0}{2\sqrt{\pi Dt}}\exp(-y^2/4Dt) \tag{8}$$

which is a gaussian function, and will be of the same shape traced out by the deflected beam at the boundary as seen from figure 1. Thus we write the shape of the beam trajectory inside the liquid as

$$Z(y) = K\exp(-y^2/4Dt) \tag{9}$$

As time evolves, the boundary smears out until the concentration gradient disappears. This will result into the broadening of the gaussian function. From (7) one can evaluate D from the half width ($y_{1/2}$) of the gaussian function as

$$D = \frac{y_{1/2}^2}{4t\ln 2} \tag{10}$$

3. Results and discussion

Figure 1 shows the experimental configuration used for the determination of D. Laser beam from a frequency stabilized 10 mW He–Ne laser (Spectra Physics) of wavelength 632·8 nm is passed through a cylindrical lens. A glass rod of diameter half centimeter

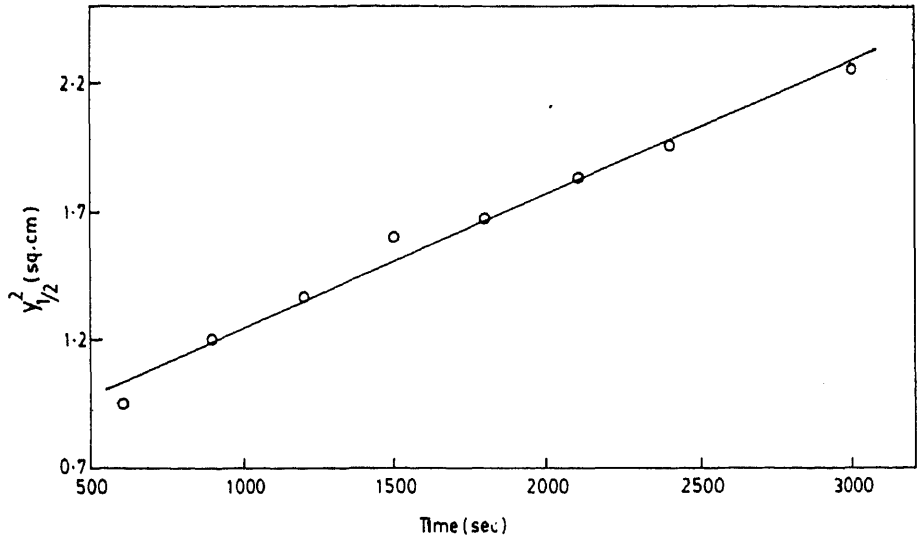

Figure 2. Variation of $y_{1/2}^2$ with time.

mounted 45° to the vertical can be used in the place of cylindrical lens. The solvent (water) is poured into the cell and an equal amount of aqueous solution of $BaCl_2$ with appropriate concentration is carefully micropippetted to the bottom of the cell in order to minimize the initial mixing of the liquids. One can thus create a clear boundary between the solvent and solution so as to create a step-like variation of concentration. The emerging rays from the cylindrical lens while passing through the solution gets deflected at the interface. The image due to the emergent beam is traced out on a graph paper at different intervals of time after the interface is formed. The depth of the different layers of the liquid is calculated using equation (2) and the value of dC/dy is calculated using (1). A graph is plotted connecting dC/dy and y. The half width of the curve at half maximum ($y_{1/2}$) of dC/dy is measured for a particular time. This is repeated for different values of time. A graph is plotted between $y_{1/2}^2$ and t (figure 2) and its slope can be used to evaluate D. The above experiment is repeated for different concentrations of the solution.

The variation of D with the concentration of electrolytic solutions is due to the presence of attractive and repulsive forces between the ions [8]. Variation of D as a function of $\sqrt{C}$ are given in figure 3 showing well defined minima for $BaCl_2$ at $\sqrt{C} = 0.4523$ molar. In the low concentration region, the distance between the different cations (or anions) decreases as concentration is increased so that increased attractive force between them causes decrease in the mobility of the ions, thereby decreasing the diffusion rate. Above an optimum concentration the mean free path between the cations (or anions) becomes small so that repulsive force predominates thereby enhancing the mobility of the ions and increase in D. Figure 3 compares the results obtained from the present method with those of conductometric method [3] in the case of $BaCl_2$ solution. Results are in close agreement. In the low concentration region the experimental results coincide with those predicted by Onsager–Fuoss theory [9].

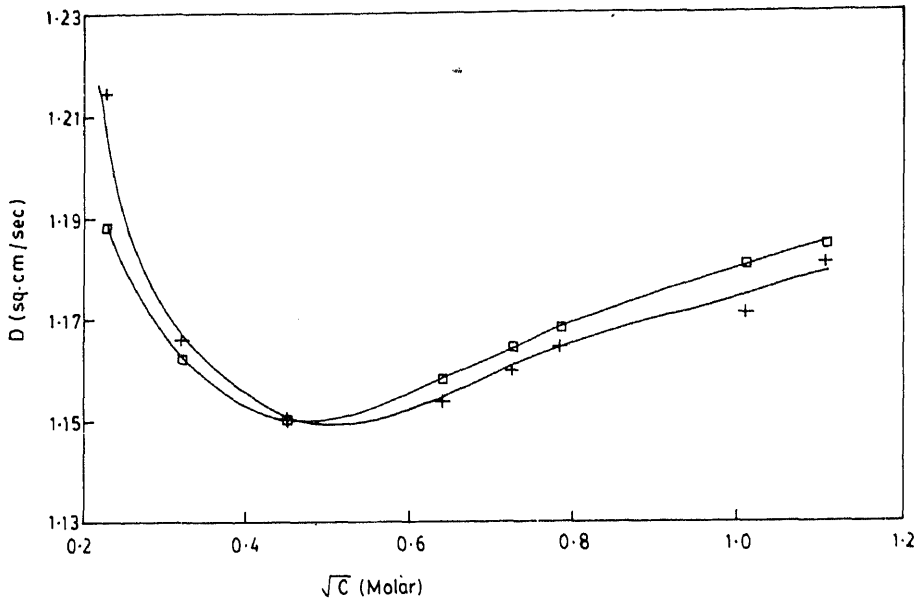

Figure 3. Variation of diffusion coefficient with concentration for $BaCl_2$ (+ – using the present LBD method, □ – using conductometric method).

4. Conclusions

Concentration dependence of diffusion coefficient of ions can be explained on the basis of various ion-solvent and ion-ion interactions. At infinite dilutions, number densities of the ions are small so that, ion-ion and ion-solvent molecular interactions are less. However as concentration increases such interactions get enhanced so that transport properties will become concentration dependent. One can therefore write D as a polynomial in C so that

$$D(C) = D_0 + D_1 C^{1/2} + D_2 C + D_3 C^{2/3} + \ldots$$

The technique described in the present work can also be used to evaluate temperature dependence of refractive index of liquids. Such temperature coefficient of refractive index is an important quantity to study various thermo optical phenomena like photothermal deflections and thermal lens effect. Another possible extension of the work is to study the phase transition in binary liquids in which disappearance of the distortions in the image will indicate transition from multicomponent to homogeneous conditions of the liquid mixture.

Acknowledgements

Financial assistance from DST (India) is greatly acknowledged. AK and CVB are thankful to University Grants Commission (India) for financial assistance and SSH is grateful to CSIR (India) for research fellowship.

References

[1] Shojiro Nemoto, *Appl. Opt.* **31**, 6690 (1992)
[2] A J Barnard and B Ahlborn, *Am. J. Phys.* **43**, 573 (1975)
[3] A C Boccara, D Fournier and J Badoz, *J. Appl. Phys.* **36**, 130 (1980)
[4] H S Harned, *Chem. Rev.* **40**, 461 (1947)
[5] J H Wang and J W Kennedy, *J. Am. Chem. Soc.*, **72**, 2080 (1949)
[6] V Vitagliano and D A Lyons, *J. Am. Chem. Soc.*, **78**, 1549 (1956)
[7] Reeta Vyas and R Gupta, *Appl. Opt.*, **27**, 4701 (1988)
[8] W Jost, *Diffusion of Solids, Liquids, Gases*, III edn. (New York, Academic Press, 1952) Ch. I and XI
[9] L Onsager and R M Fuoss, *J. Phys. Chem.*, **36**, 2689 (1932)

PRAMANA
— journal of
physics

© Printed in India

Vol. 43, No. 5,
November 1994
pp. 407–408

Electric field gradient in transition metal: Scandium

B B PANIGRAHI and N C MOHAPATRA*
Department of Physics, Khallikote College, Berhampur 760001, India
*Department of Physics, Berhampur University, Berhampur 760007, India

MS received 30 September 1994

Abstract. Corrections to results of electric field gradient (EFG) already published [*Pramana – J. Phys.* **41**, 443 (1993)] are reported. The corrected net EFG is: $q = -8{\cdot}01 \times 10^{13}$ esu/cm^3 against the published value $q = 16{\cdot}06 \times 10^{13}$ esu/cm^3. The present result agrees reasonably well with the experimental result, $|q_{expt}| = 13 \times 10^{13}$ esu/cm^3.

Recently, a computational error is detected, which modifies the results of EFG, we have already published [1]. The error was committed mainly in the part that evaluated the p–p contribution [1] to EFG by the conduction electrons. The corrected results are summarized in table 1 which must replace the table 1 of the published work [1].

In addition, the lattice parameters as well as the temperature were also misquoted in the previous work [1]. The right parameters are: $a = 6{\cdot}25311$ au and $c = 9{\cdot}96509$ au. The temperature at which EFG's are calculated is 293 K instead of 11 K as reported before [1].

The discussions and conclusions made in the published work [1] remain almost unchanged except that they now refer to the corrected numbers. Although the corrected net EFG suffers a sign reversal from the one already published [1], the agreement with experiment is still considered reasonably good because the sign of experimental EFG is not determined. The computational error however does not affect the introduction and theory section of the published work [1].

References

[1] B B Panigrahi and N C Mohapatra, *Pramana – J. Phys.* **41**, 443 (1993)
[2] P Blaha, K Schwartz and P H Dederichs, *Phys. Rev.* **B37**, 2792 (1988)

Table 1. Various components of EFG in hcp scandium metal. All the EFG's are expressed in units of 10^{13} esu/cm^3.

	Present work											
	q_{el}											
q_{latt}	PW–PW unshielded	PW–PW shielded	s–d	p–p	p–f	dist.	Total (unshielded)	Total (shielded)	Net q Colm. 1 + Colm. 8	Net q Colm. 1 + Colm. 9	Other work [2] q	Expt. $\lvert q \rvert$
122·17	−0·45	−5·72	−4·81	−118·23	−1·32	−0·10	−124·91	−130·18	−2·74	−8·01	32·0	13·0

PRAMANA
— journal of
physics

© Printed in India

Vol. 43, No. 5,
November 1994
pp. 409

Corrigendum

Computation of collective modes and acoustic investigations at different temperatures of vitrous silica

R V GOPALA RAO and R VENKATESH

(*Pramana – J. Phys.*, 43, pp. 201–209, September 1994)

The following acknowledgement was inadvertently omitted from the paper:

"One of us (RVGR) acknowledges the support of INSA, New Delhi, through a Senior Scientist position."

PRAMANA
— journal of
physics

© Printed in India

Vol. 43, No. 6,
December 1994
pp. 411–420

A new perturbative approach to the classical anharmonic oscillator

S S VASAN and M SEETHARAMAN
Department of Theoretical Physics, University of Madras, Guindy Campus, Madras 600025, India

MS received 8 July 1994

Abstract. The periodic motion of the classical anharmonic oscillator characterized by the potential $V(x) = 1/2\, x^2 + \lambda/2k\, x^{2k}$ is considered. The period is first determined to all orders in λ in a perturbative series. Making use of this, the solution of the nonlinear equation of motion is then expressed in the form of a Fourier series. The Fourier coefficients are obtained by solving simple algebraic relations. Secular terms are inherently absent in this perturbative scheme. Explicit solution is presented for general k up to the second order, from which the Duffing and the sextic oscillator results follow as special cases.

Keywords. Classical AHO; secular term-free perturbative solution.

PACS No. 03·20

1. Introduction

The time evolution of many classical systems is governed by nonlinear equations of motion that do not admit exact solutions. Anharmonic oscillators of various types comprise one class of such systems. In general, the motion of a nonlinear system can be determined only through some approximation method or other. A standard procedure is to treat the system as a linear system perturbed by the nonlinearity, and attempt to find a perturbative solution of the equation of motion. When this is done in a straightforward manner, what results is often a solution marred by secular terms, which render it unacceptable. In the case of the anharmonic oscillators, the secular terms make the solution nonperiodic and unbounded, whereas one knows on physical grounds that the motion is both bounded and periodic. Several techniques have been developed for eliminating secular terms from perturbative solutions [1]. In the Lindstedt–Poincare method, for instance, one introduces a scaled time variable, and expands both the solution and the scaling factor in separate perturbation series. Using the equation of motion, the unknowns are determined, order by order, in such a way that the secular term is cancelled out in every order. The other approximation methods proceed in a similar way, the secular terms being eliminated order by order.

A different approach is possible for a nonlinear system whose motion is known to be periodic. For such a system the solution can be expanded in a Fourier series with a fundamental period equal to the period T of oscillatory motion. The Fourier coefficients will then be functions of the perturbation parameter λ present in the problem. Expanding T in a power series in λ, one can determine perturbatively all the unknowns, order by order, as functions of λ. Secular terms are inherently absent

in this scheme. A systematic perturbative formalism along these lines has been developed by Helleman and Montroll [2]. For the anharmonic oscillator (AHO) system, the H–M scheme amounts to determining simultaneously the frequency of the periodic motion and the displacement by writing separate perturbation series for each one. The coefficients in the two series are obtained from a nonlinear recurrence relation.

In the case of the AHO system a variation of the Fourier series method is possible, which differs significantly from the H–M method and offers considerable advantage. It is based on the fact that the period of classical motion of the AHO can be determined, quite independently of the detailed behaviour of the displacement as a function of time. This point does not seem to have been noticed in the literature. Once the period is determined, the original nonlinear differential equation reduces to a set of simple uncoupled linear algebraic equations for the Fourier coefficients. The rather involved analysis of Helleman and Montroll can be completely bypassed. The present paper demonstrates this in detail.

We consider the periodic motion of the anharmonic oscillator characterized by the potential energy

$$V(x)=\frac{1}{2}x^2+\frac{1}{2k}\lambda x^{2k}, \qquad \lambda>0$$

where k is a positive integer. The period is first computed to all orders in the parameter λ. We then obtain the solution $x(t)$ for general k explicitly up to the second order. Our perturbative solution reproduces (up to order λ^2) the known closed form results for the Duffing and the sextic anharmonic oscillators.

2. Perturbative expansion for period

The Hamiltonian for the general AHO is taken to be

$$H=\frac{1}{2}p^2+\frac{1}{2}x^2+\frac{1}{2k}\lambda x^{2k}. \tag{1}$$

This leads to the nonlinear equation of motion

$$\ddot{x}+x+\lambda x^{2k-1}=0. \tag{2}$$

We are interested in solving (2) subject to the initial conditions

$$x(0)=A, \quad \dot{x}(0)=0. \tag{3}$$

Since H is conserved, there exists the first integral

$$\frac{1}{2}\dot{x}^2+\frac{1}{2}x^2+\frac{1}{2k}\lambda x^{2k}=E, \tag{4}$$

E being the total energy. From (4) it follows that the period T of oscillation is given by

$$T=\sqrt{2}\int_{-A}^{A}\frac{\mathrm{d}x}{[E-(1/2)x^2-(\lambda/2k)x^{2k}]^{1/2}} \tag{5}$$

where $x=\pm A$ are the turning points defined by $E=V(x)$ [cf. (3)].

Classical AHO

We convert the real integral above into a contour integral in the z plane of the form

$$T = \frac{1}{\sqrt{2}} \oint \frac{dz}{[E - (1/2)z^2 - (\lambda/2k)z^{2k}]^{1/2}} \tag{6}$$

where the contour encloses only a branch cut joining $+A$ and $-A$, and no other singularity of the integrand. The branch of the square root chosen is that which is positive real on the upper lip of the cut; this necessitates that the contour be traversed clockwise. The above contour integral representation for the period proves to be particularly advantageous, as will be evident from what follows.

Making a perturbation expansion of the integrand in (6) in powers of λ, we obtain

$$\sqrt{2}\, T = \sum_{n=0}^{\infty} \binom{-\frac{1}{2}}{n} \left(-\frac{\lambda}{2k}\right)^n I_n \tag{7}$$

where I_n is the integral

$$I_n = \oint \frac{dz\, z^{2nk}}{(E - (1/2)z^2)^{n+1/2}} \tag{8}$$

In a different context we have considered similar contour integrals [3, 4]. To evaluate I_n, we rewrite it in the following form, with a simpler denominator for the integrand:

$$I_n = \frac{(-2)^n}{(2n-1)!!} \frac{\partial^n}{\partial E^n} \oint \frac{dz\, z^{2nk}}{(E - (1/2)z^2)^{1/2}} \tag{9}$$

Now, the change of variable $z = \sqrt{2E}\, t$ enables the integrand's dependence on E to be factored out. We get

$$\oint \frac{dz\, z^{2nk}}{(E - (1/2)z^2)^{1/2}} = \sqrt{2}(2E)^{nk} \oint \frac{dt\, t^{2nk}}{(1-t^2)^{1/2}}. \tag{10}$$

We observe that the integrand in (10) has only integrable singularities at $t = \pm 1$. Therefore we can evaluate it by compressing the contour on to the real axis. Thus

$$\oint \frac{dt\, t^{2nk}}{(1-t^2)^{1/2}} = 2 \int_{-1}^{1} \frac{dt\, t^{2nk}}{(1-t^2)^{1/2}} = 2B\left(nk + \frac{1}{2}, \frac{1}{2}\right), \tag{11}$$

where B is the Euler beta function defined by $B(x, y) = \Gamma(x)\Gamma(y)/\Gamma(x+y)$. Substituting (10) and (11) in (9), and the resulting expression in (7), we get after some simplification

$$T = 2\pi \sum_{n=0}^{\infty} \binom{2nk}{nk} \binom{nk}{n} \left(-\frac{\lambda E^{k-1}}{2^k \cdot 2k}\right)^n. \tag{12}$$

We note at this point that the various manipulations performed on (8) are feasible because of its form as a closed contour integral in the complex plane. To derive the above expansion for T directly from the real integral (5) would entail far more labour.

The result (12) for the period is a perturbative series in λ whose coefficients are functions of the energy E, except for the case $k = 1$. For $k = 1$ the series can be

summed, and yields, as it should, the value $T = 2\pi(1+\lambda)^{-1/2}$. The value of E is fixed by the initial conditions. For the conditions that we have chosen (see (3) above), the energy is the following function of the initial displacement A:

$$E = \frac{1}{2}A^2 + \frac{\lambda}{2k}A^{2k}. \tag{13}$$

Substituting for E in (12), we may obtain T in terms of λ and A. It is also possible to derive the following series for T in powers of A, by inserting (13) in (5) directly:

$$T = 2\pi \sum_{n=0}^{\infty} C_n \left(\frac{\lambda A^{2k-2}}{k}\right)^n \tag{14a}$$

where

$$C_n = \frac{1}{\pi}\binom{-\frac{1}{2}}{n}\int_{-1}^{+1}\frac{du(1-u^{2k})^n}{(1-u^2)^{n+1/2}} = \sum_{m=0}^{n}\frac{(-1)^m}{2^{2km}}\binom{n}{m}\binom{km}{n}\binom{2km}{km}. \tag{14b}$$

Introducing the frequency Ω, and expanding it in a perturbative series

$$\Omega = \frac{2\pi}{T} = 1 + \lambda\Omega_1 + \lambda^2\Omega_2 + \ldots \tag{15a}$$

we note that the coefficients Ω_i will be functions of the parameter A. These can be determined using (12) or (14). The explicit expressions for Ω_1 and Ω_2 are

$$\Omega_1 = \frac{1}{2^{2k}}\binom{2k}{k}A^{2k-2} \tag{15b}$$

$$\Omega_2 = \frac{1}{2^{4k}}\left\{\binom{2k}{k}^2 + 2^{2k}\frac{(k-1)}{k}\binom{2k}{k} - \frac{2k-1}{k}\binom{4k}{2k}\right\}A^{4k-4}. \tag{15c}$$

The higher order coefficients Ω_i when needed can be calculated either from (12) and (13) or form (14).

We conclude this section with the following point. Had we chosen, instead of (1), the Hamiltonian

$$\tilde{H} = \frac{1}{2m}p^2 + \frac{1}{2}m\omega^2x^2 + \frac{1}{2k}\alpha x^{2k},$$

the corresponding period $T(m, \omega, \alpha, E)$ would be related to the period defined by (5) through the equation

$$T(m, \omega, \alpha, E) = \frac{1}{\omega}T(1, 1, \lambda, E) \tag{16a}$$

where

$$\lambda = \alpha/(m\omega^2)^k. \tag{16b}$$

This scaling law for the period is derived from (5) by a simple scaling of the integration variable. There is no loss of generality therefore in choosing for the Hamiltonian the form given in (1). It may be noted that the scaling law for T regarded as a function of A is $T(m, \omega, \alpha, A) = \omega^{-1}\,T(1, 1, \alpha/m\omega^2, A)$.

3. First order solution

The solution to the equation of motion must be a periodic function with period T. Since in the absence of the anharmonic term the solution satisfying the initial conditions (3) is $A\cos t$, we write for the first order solution $x(t) = A\cos\Omega t + \lambda f(t)$. The function f itself must also have the same period, and can therefore be expressed as a Fourier series. The initial velocity having been taken as zero, the series for f will not contain any sine terms. Writing $f(t) = \Sigma C_n \cos n\Omega t$, we can deduce from the structure of the equation of motion that the series for $f(t)$ contains only a finite number of odd cosine terms, and no even cosine terms. We are thus led to write

$$x(t) = A\cos\Omega t + \lambda \sum_{n=0}^{k-1} a_n \cos(2n+1)\Omega t + O(\lambda^2). \tag{17}$$

It is necessary that the coefficients a_n obey the relation

$$\sum_{n=0}^{k-1} a_n = 0 \tag{18}$$

in order that the initial condition $x(0) = A$ be satisfied. We shall see that it is always possible to ensure condition (18).

Substituting (17) into (2), using the expansion $\Omega^2 = 1 + 2\lambda\Omega_1 + O(\lambda^2)$, and retaining only terms of order λ, we arrive at the equation

$$\sum_{n=0}^{k-1} a_n[1-(2n+1)^2]\cos(2n+1)\Omega t$$

$$= 2\Omega_1 A\cos\Omega t - \frac{A^{2k-1}}{2^{2k-2}} \sum_{n=0}^{k-1} \binom{2k-1}{k-1-n} \cos(2n+1)\Omega t. \tag{19}$$

In obtaining (19) we have made use of the standard formula

$$\cos^{2k-1}\theta = \frac{1}{2^{2k-2}} \sum_{n=0}^{k-1} \binom{2k-1}{k-1-n} \cos(2n+1)\theta.$$

The coefficients a_n can be determined from (19). We observe that on the lhs of (19), the coefficient of $\cos\Omega t$ vanishes. Therefore, for consistency, the rhs also must be free of $\cos\Omega t$ term. Indeed it is so, as can be easily checked. The coefficient of $\cos\Omega t$ term on the rhs is

$$2A\left\{\Omega_1 - \frac{A^{2k-2}}{2^{2k-1}}\binom{2k-1}{k-1}\right\},$$

and this vanishes because of (15b). Therefore, a_0 in (17) is arbitrary. All the other a_n's are determined uniquely by (19), with the result

$$a_n = \frac{1}{(2n+1)^2 - 1} \frac{A^{2k-1}}{2^{2k-2}} \binom{2k-1}{k-1-n}, \quad n > 0. \tag{20}$$

It is now evident that in order to satisfy (18) we should set

$$a_0 = \sum_{n=1}^{k-1} \frac{1}{1-(2n+1)^2} \frac{A^{2k-1}}{2^{2k-2}} \binom{2k-1}{k-1-n}.$$

The summation on the rhs can be carried out using the identity

$$\sum_{m=0}^{k-2}\binom{2k-1}{m}\frac{1}{(k-m)(k-m-1)}=\frac{1}{2k}\left[(k+1)\binom{2k}{k}-2^{2k}\right]$$

and we get

$$a_0=\frac{A^{2k-1}}{2k\,2^{2k}}\left[2^{2k}-(k+1)\binom{2k}{k}\right]. \tag{21}$$

We thus have the solution to first order

$$x(t)=A\cos\Omega t+\lambda\sum_{n=0}^{k-1}a_n\cos(2n+1)\Omega t, \tag{22}$$

with a_0 given by (21) and $a_n, n>0$, by (20).

4. Solution to second order

To determine the solution to the second order in λ, we make the following ansatz

$$x(t)=A\cos\Omega t+\lambda\sum_{n=0}^{k-1}a_n\cos(2n+1)\Omega t + \lambda^2\sum_{n=0}^{2(k-1)}b_n\cos(2n+1)\Omega t+O(\lambda^3) \tag{23}$$

where the first order coefficients a_n have already been obtained. We observe first that

$$\begin{aligned}\ddot{x}+x=&[-2\lambda\Omega_1-\lambda^2(\Omega_1^2+2\Omega_2)]A\cos\Omega t\\&+\lambda\sum a_n[1-(2n+1)^2-2\lambda\Omega_1(2n+1)^2]\cos(2n+1)\Omega t\\&+\lambda^2\sum b_n[1-(2n+1)^2]\cos(2n+1)\Omega t\end{aligned}$$

where we have used the expansion $\Omega^2=1+2\lambda\Omega_1+\lambda^2(\Omega_1^2+2\Omega_2)$ and retained terms up to order λ^2. The nonlinear term yields, to this order,

$$\lambda x^{2k-1}=\lambda A^{2k-1}\cos^{2k-1}\Omega t+\lambda^2(2k-1)A^{2k-2}\cos^{2k-2}\Omega t.\sum a_n\cos(2n+1)\Omega t.$$

Picking out the λ^2 terms from the above we get

$$\begin{aligned}&\sum_{n=0}^{2k-2}b_n[1-(2n+1)^2]\cos(2n+1)\Omega t\\&=(\Omega_1^2+2\Omega_2)A\cos\Omega t+2\Omega_1\sum_{n=0}^{k-1}a_n(2n+1)^2\cos(2n+1)\Omega t\\&\quad-(2k-1)A^{2k-2}\sum_{n=0}^{k-1}a_n\cos(2n+1)\Omega t\cos^{2k-2}\Omega t.\end{aligned} \tag{24}$$

Using the formula

$$\cos^{2n}\theta = \frac{1}{2^{2n}}\left[\binom{2n}{n} + \sum_{m=0}^{n-1} 2\binom{2n}{m}\cos 2(n-m)\theta\right]$$

the last term on the rhs of (24) can be expressed as sum of cosines. After some algebra we get

$$\sum_{n=0}^{2k-2} b_n[1-(2n+1)^2]\cos(2n+1)\Omega t$$

$$= C\cos\Omega t + 2\Omega_1 \sum_{n=1}^{k-1} a_n[(2n+1)^2 - k]\cos(2n+1)\Omega t$$

$$-\frac{(2k-1)A^{2k-2}}{2^{2k-2}}\left\{\sum_{n=1}^{2k-2} f_n\cos(2n+1)\Omega t + \sum_{n=1}^{k-2} g_n\cos(2n+1)\Omega t\right\} \tag{25a}$$

where

$$f_n = \sum_{m=0}^{n-1} a_m\binom{2k-2}{k-1-n+m}, \tag{25b}$$

$$g_n = \sum_{m=n+1}^{n+k-1} a_m\binom{2k-2}{k-1+n-m} + \sum_{m=0}^{k-2-n} a_m\binom{2k-2}{k-2-n-m}, \tag{25c}$$

$$C = A\left(\Omega_1^2 + 2\Omega_2 + \frac{(k^2-1)}{k}\Omega_1^2\right) + 2\Omega_1\frac{(1-k)}{k}A^{2k-1}$$

$$-\frac{(2k-1)A^{2k-2}}{2^{2k-2}}\sum_{m=0}^{k-2} a_{m+1}\binom{2k-1}{k-2-m}. \tag{26}$$

The second order coefficients b_n are to be determined from (25), the rhs of which involves only known quantities. As in the first order, the coefficient b_0 on the lhs is zero. On the rhs, C is found to vanish on substituting the known values of a_n, Ω_1 and Ω_2 in (26). This makes b_0 arbitrary. The other b_n's are determined uniquely by (25). Taking $a_n = 0$ for $n \geqslant k$ (a_n given by (20) vanishes in fact for $n \geqslant k$), the sum over n on the rhs of (25a) can be extended from $k-1$ to $2k-2$. Putting in the value of Ω_1 and rearranging terms, we get finally the expression

$$b_n = \frac{A^{2k-2}}{2^{2k}n(n+1)}\left\{-\frac{(2n+1)^2}{2}\binom{2k}{k}a_n + (2k-1)\sum_{m=0}^{n+k-1}\binom{2k-2}{k-1-n+m}a_m\right.$$

$$\left. + (2k-1)\sum_{m=0}^{k-2-n}\binom{2k-2}{k-2-n-m}a_m\right\}, \qquad n>0. \tag{27}$$

As in the case of a_0 in first order, the arbitrary coefficient b_0 is fixed by the requirement that $\Sigma_{n=0}^{2k-2} b_n = 0$ thus ensuring that the initial condition $x(0) = A$ is satisfied in the second order also.

5. General solution

The solution derived above corresponds to a particular set of initial conditions, namely arbitrary displacement and zero velocity. The analysis of the AHO is simplest

with these conditions. It is possible to obtain from this particular solution the general solution corresponding to arbitrary initial position and velocity. To this end, we note that the equation of motion (2) is invariant under time translations. Therefore, if we replace Ωt in (23) by $\Omega t + \phi$, we still have a solution, but with the change that A is no longer identifiable as the initial displacement $x(0)$. Explicitly, the new solution

$$\tilde{x}(t) = A\cos(\Omega t + \phi) + \lambda \sum a_n \cos(2n+1)(\Omega t + \phi) + \lambda^2 \sum b_n \cos(2n+1)(\Omega t + \phi) + O(\lambda^3) \tag{28}$$

is seen to contain two arbitrary parameters A and ϕ, which serve to accommodate arbitrary initial conditions. It should be noted that the frequency Ω occurring in (28) does not change: it is still the same function of the parameter A. This is due to the fact that the frequency of the AHO is determined by the value of E, which is a constant of the motion, and for a given E, there is always an instant at which the velocity vanishes. For arbitrary initial values x_0 and v_0, one may use the form (28) and determine A and ϕ in terms of x_0 and v_0, which is not a simple task. Alternatively, one can use the solution (23) but with the time being reckoned from the instant at which the velocity vanishes.

6. Special cases

It is instructive to consider two special cases in which the equation of motion can be solved in closed form. These are the Duffing oscillator ($k = 2$) and the sextic AHO ($k = 3$).

In the Duffing case, our perturbative solution is

$$x(t) = A\cos\Omega t + \frac{\lambda A^3}{32}(\cos 3\Omega t - \cos\Omega t) + \frac{\lambda^2 A^5}{1024}(\cos 5\Omega t - 24\cos 3\Omega t + 23\cos\Omega t) + O(\lambda^3) \tag{29}$$

with the frequency given by

$$\Omega = 1 + \frac{3}{8}\lambda A^2 - \frac{21}{256}\lambda^2 A^4 + O(\lambda^3). \tag{30}$$

The exact solution satisfying the same initial conditions as (29) can be expressed as

$$x(t) = A\, cn(\sqrt{1+\lambda A^2}\, t, k) \tag{31}$$

where cn is the Jacobian elliptic function whose modulus k is given by

$$k^2 = \frac{\lambda A^2}{2}(1+\lambda A^2)^{-1}. \tag{32}$$

The exact period of oscillation is

$$T = 4K(k)(1+\lambda A^2)^{-1/2} \tag{33}$$

where $K(k)$ is the complete elliptic integral of the first kind. The expression (30)

coincides up to order λ^2 with the expansion for Ω in powers of λ obtained from (33). By making use of the standard Fourier series expansion of the *cn* function [5] we can show that (29) is the same as (31) up to order λ^2.

Similar results hold also in the case of the sextic AHO. The exact solution for this case can be written in the form

$$x(t)=\frac{A\,cn\,u}{dn\,u}\left[\frac{1+dn\,2u}{1+\gamma+(1-\gamma)cn\,2u}\right]^{1/2} \tag{34}$$

where

$$u=\sqrt{\alpha\beta}\,t,\quad \alpha=(1+\lambda A^4)^{1/2},\quad \beta=\left(1+\frac{\lambda A^4}{3}\right)^{1/2},\quad \gamma=\frac{\alpha}{\beta} \tag{35}$$

and the modulus of the elliptic functions *cn* and *dn* is

$$k^2=\frac{1}{2}\left[1-\frac{1}{\alpha\beta}\left(1+\frac{1}{2}\lambda A^4\right)\right] \tag{36}$$

The frequency of this periodic solution is

$$\Omega=\pi\sqrt{\alpha\beta}/2K(k) \tag{37}$$

Expanding the solution (34) in powers of λ, we get

$$\begin{aligned}x(t)=A\cos\Omega t&+\frac{\lambda A^5}{384}(\cos 5\Omega t+15\cos 3\Omega t-16\cos\Omega t)\\&+\frac{\lambda^2 A^9}{294912}(3\cos 9\Omega t+95\cos 7\Omega t-7680\cos 3\Omega t+7582\cos\Omega t)\\&+O(\lambda^3)\end{aligned} \tag{38}$$

which is precisely the solution generated by our second order formula (23). Similarly, we get from (37) the expansion

$$\Omega=1+\frac{5}{16}\lambda A^4-\frac{215}{3072}\lambda^2 A^8+O(\lambda^3). \tag{39}$$

which coincides with the result derived from (15).

7. Discussion

We have presented above explicit classical solution to the general anharmonic oscillator up to the second order in the anharmonicity. Novel features of our perturbative approach are the prior determination of the period T of classical motion (to all orders in the nonlinearity parameter λ) and its subsequent use to develop a small-coupling expansion for the solution which is free of secular terms. In usual perturbative treatments, the frequency Ω and the displacement $x(t)$ are found simultaneously in every order of the approximation, which makes the analysis of the general AHO rather involved. In our method we exploit the fact that the AHO has a well defined period which can be determined independently, without any references to the dis-

placement $x(t)$ (except for the initial conditions). With the frequency of classical motion Ω in hand, physical reasoning suggests a perturbative ansatz for $x(t)$ as a Fourier series with Ω as the fundamental frequency. As we have seen, the Fourier coefficients can be systematically determined order by order, the unknown coefficients in any given order satisfying uncoupled, linear algebraic equations involving coefficients of the preceding orders. In every order one coefficient is left undetermined and arbitrary by the equations. This gives us the freedom to ensure that the initial condition $x(0) = A$ is satisfied in every order of the approximation.

The Fourier series ansatz for the displacement $x(t)$ guarantees the absence of secular terms in the perturbation expansion, as noted also by Helleman and Montroll [2] earlier. For the ansatz to work, it is essential that there should be no $\cos \Omega t$ terms on the rhs of the first order equation (19) and the second order equation (25). The use of the correct Ω ensures the absence of these unwanted terms. We note that if $\cos \Omega t$ term were present on the rhs of (19) or (25), the ansatz would fail, implying that the solution is then not periodic, which is tantamount to the presence of secular terms in the solution.

Our analysis of the general AHO system is far simpler than that presented by Helleman and Montroll. As noted earlier, they expand both $x(t)$ and Ω in series in powers of λ, and obtain a nonlinear recurrence relation for the coefficients. It would be a cumbersome task to extract the coefficients from their recurrence relation. These authors have not given any explicit expressions either for the frequency or for the displacement.

In this work our analysis does not go beyond order λ^2, as it is rarely that one would need to go further. There is however no difficulty in principle in including higher orders. Nor is there any difficulty in adapting the method to AHO's with anharmonic terms which are even polynomials of degree $2k$.

References

[1] A H Nayfeh, *Perturbation methods* (Wiley, New York, 1973)
[2] R H G Helleman and E W Montroll, *Physica* **74**, 22 (1974)
[3] M Seetharaman and S S Vasan, *J. Math. Phys.* **27**, 1031 (1986)
[4] S S Vasan, M Seetharaman and L Sushama, *Pramana – J. Phys.* **40**, 177 (1993)
[5] P F Byrd and M D Friedman, *Handbook of elliptic integrals for engineers and scientists*, 2nd edn. (Springer–Verlag, New York, 1971)

PRAMANA
— journal of
physics

© Printed in India

Vol. 43, No. 6,
December 1994
pp. 421–429

Scaling relations in the Lyapunov exponents of one dimensional maps

P R KRISHNAN NAIR*, V M NANDAKUMARAN and G AMBIKA*
Department of Physics, Cochin University of Science and Technology, Cochin 682 022, India
*Permanent Address: Department of Physics, Maharajas College, Cochin 682 011, India

MS received 6 January 1994; revised 31 May 1994

Abstract. We establish numerically the validity of Huberman–Rudnick scaling relation for Lyapunov exponents during the period doubling route to chaos in one dimensional maps. We extend our studies to the context of a combination map, where the scaling index is found to be different.

Keywords. One dimensional maps; Chaos; period doubling; scaling behaviour; Lyapunov characteristic exponents.

PACS Nos 05·45; 05·40; 47·52

1. Introduction

The behaviour of nonlinear dynamical systems can be analysed most extensively using one-dimensional iterative maps. These maps undergo a transition from regular to chaotic behaviour at certain values of the system parameter; the most prominent route for this transition being the period doubling scenario [1]. Studies related to the universal nature of indices associated with this scenario have resulted in the classification of one-dimensional maps into different universality classes, based on z, the order of the maximum of the map [2]. The chaotic state is detected most often, using an index called the Lyapunov characteristic exponent (λ). It gives a quantitative measure of the average separation of two initially close orbits as the system evolves in time. A positive value for λ is an unambiguous signature of chaos while a negative value implies periodic or quasiperiodic behaviour in the system. As such, λ can be referred to as an order parameter in the transition from periodic to chaotic state. In this context, the scaling behaviour of λ during the transition from order to chaos is important and interesting in understanding the onset of chaos in the system. The nature of this scaling near the period doubling accumulation point has been theoretically worked out for one dimensional maps by Huberman and Rudnick [3]. They have shown that the Lyapunov characteristic exponent follows the relation,

$$\lambda \propto |a - a_\infty|^\nu \tag{1}$$

where a_∞ is the value of the control parameter a at the period doubling accumulation point and

δ being the Feigenbaum universality constant. This scaling law in the context of quadratic maps has been verified experimentally using a sinusoidally driven diode circuit [4]. A scaling theory for noisy period doubling transition to chaos has been developed by Shraiman *et al* [5] in which it is shown that in the limit of the noise amplitude tending to zero, the Huberman–Rudnick [H–R] relation is recovered.

The H–R relation indicates that the exponent ν depends on z through δ which is different for different universality classes. However, it is not clear whether ν may depend on z in some other way. To the best of our knowledge, no numerical investigations have been reported for z other than 2. In this paper, we report the results of a detailed numerical study of the scaling law near a_∞ in one dimensional maps for different z values. We prove the universal validity of the H–R relation and at the same time extend the studies to combination maps. Such maps, when combined using maps belonging to the same universality class and therefore with the same δ value are found to have different scaling indices.

This paper is organized as follows. In § 2 we give the details of our numerical analysis for maps of different universality classes. The period doubling accumulation point a_∞ for different z-values are determined and the nature of the scaling of λ obtained by plotting $\log\lambda$ against $\log|a-a_\infty|$. In § 3 we extend the analysis to a combination map defined there. The salient features of this map during the onset of chaos and the scaling of its λ are included. Our concluding remarks and comments are given in § 4.

2. Scaling law for general one-dimensional maps

We start by considering maps of the form,

$$X_{n+1} = 1 - a_1|X_n|^z \tag{3}$$

defined on the interval $(-1, 1)$, with the control parameter a_1 lying between 0 and 2. This is a unimodal map with the critical point $X_c = 0$; z denotes the order of the maximum at X_c. This map can be transformed into one on the unit interval (0, 1) by a nonlinear transformation [1].

The transformed map then becomes

$$X_{n+1} = f(X_n) = \left(\frac{a}{4}\right) - 2^{(z-2)}a\left|X_n - \frac{1}{2}\right|^z \tag{4}$$

with $0 < a < 4$ and $X_c = \frac{1}{2}$.

The Lyapunov characteristic exponent in the context of such maps is defined as

$$\lambda = \lim_{N\to\infty} \frac{1}{N} \sum_{i=0}^{N-1} \ln|f'(X_i)| \tag{5}$$

This can be used as such in the computation of λ for different z-values [6]. However, a numerical analysis poses the following difficulties. Since round off errors may possibly build up in a computer, λ can be computed only by setting an upper bound for N which may lead to some truncation error. In our computations N is fixed as 10,000. Again the proximity of a large number of periodic windows within the chaotic regime near the accumulation point reduces the number of useful values of λ, especially for large values of z. But this can be overcome to some extent by adding a very weak

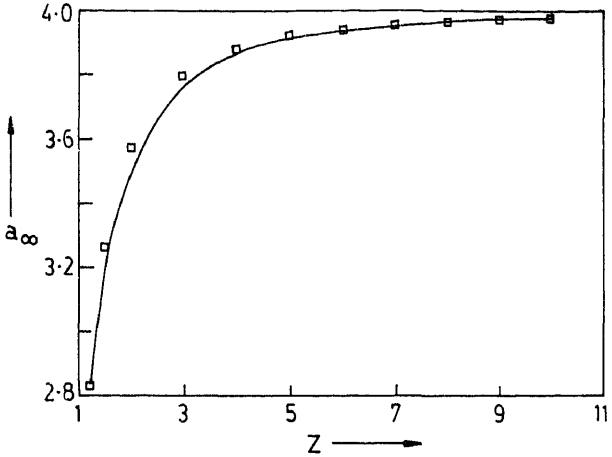

Figure 1. Variation of a_∞ with z, the order of the maximum of the map. Note that as z increases, the chaotic regime $a_\infty < a < 4$ shrinks and becomes very narrow for $z > 10$.

noise to the system. Such a noise term smoothens the curve for λ against a [7]. Thus for high values of z, we added a small amplitude noise term $\approx 10^{-15}$, for computational purposes.

Starting with $z = 1{\cdot}2$, the λ values for the map (4) are computed with values of a increased in small steps. The value of a_∞ at which transition to chaos is roughly estimated as that value of a at which λ changes from negative to positive value for the first time. Then the value of a is varied in further small steps around this rough estimate and a better value for a_∞ is obtained. Continuing this process, the value of a_∞ is determined up to an accuracy of 10^{-6}–10^{-8}. The Lyapunov characteristic exponent (λ) is then computed for a number of values of $a > a_\infty$ and very near to a_∞. This was repeated for different z-values.

For higher values of z, λ in the chaotic side near a_∞ changes to negative values quite often. This is due to the presence of a large number of periodic windows in the chaotic regime. The variation of a_∞ with z is sketched in figure 1. For large z, the value of a_∞ approaches the fully chaotic limit $a = 4$ and the entire chaotic regime shrinks to a narrow region in the parameter space. Since the chaotic regime has to accommodate all the periodic windows, it is clear that a large number of periodic windows will be found near a_∞, especially for high values of z. The addition of a small noise can wash out the fine structure of the periodic windows in the chaotic region. For $z \geqslant 2$, we added a Gaussian noise of zero mean and variance 0·2. The typical strength for the noise amplitude was 10^{-15}. Such a low noise cannot seriously affect the scaling behaviour of the system. It is to be emphasized that even with noise, the problem of periodic windows cannot be completely overcome. Thus for very high z-values ($z \geqslant 4$), we report the envelope scaling for λ, with the periodic windows avoided.

For each value of z, we obtain a plot of $\log \lambda$ against $\log|a - a_\infty|$ and the line of best fit is drawn. Its slope gives an estimate of ν. A typical log–log plot is presented in figure 2. From the available values of δ for different z-values [8], the theoretical value for ν using (2) is calculated. These results are compared in table 1. Giving

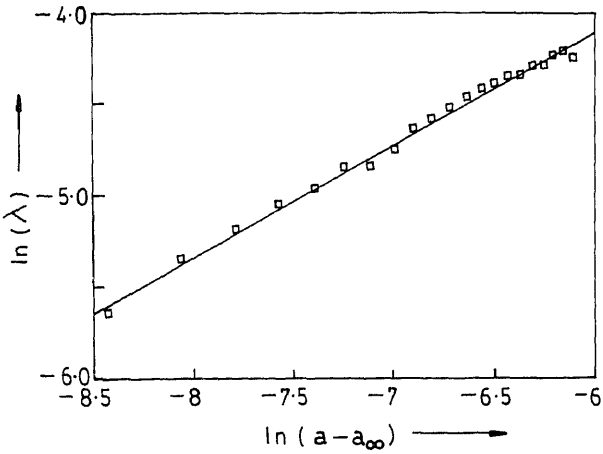

Figure 2. A typical log–log plot of λ vs $(a - a_\infty)$ for $z = 1{\cdot}2$. The slope of the line gives the scaling exponent ν.

Table 1. The scaling index ν for different values of z, calculated numerically and using H–R relation.

Order of maximum (z)	ν (numerical)	ν (using H–R) $= (\ln 2/\ln \delta)$
1·2	0·60171	0·6057799
1·5	0·52281	0·5192090
2·0	0·42117	0·4498200
3·0	0·40711	0·3834490
4·0	0·30117	0·3489280
5·0	0·29953	0·3266080

allowance for possible computational errors, we can say that there is excellent agreement with the H–R scaling relation.

3. Combination of two maps of the quadratic family

We consider the dynamics of a combination map obtained by combining a sinusoidal map with the well known logistic map. This map is thus an example of a two parameter one dimensional map and is given by,

$$X_{n+1} = f(X_n, \mu, A) = \mu X_n(1 - X_n) - A \sin(\pi X_n). \tag{6}$$

Here both the maps $f_1(X_n, \mu) = \mu X_n(1 - X_n)$ and $f_2(X_n, A) = A \sin(\pi X_n)$ belong to the same universality class viz, the quadratic family.

The map defined in (6) has an extremum at $X = \frac{1}{2}$ which is a second order maximum for A ranging from $(\mu/4 - 1)$ to $(2\mu/\pi^2)$ while it is a minimum for $2\mu/\pi^2 < A < \mu/4$. Thus there is a point of inflexion at $X = 1/2$ when $A = 2\mu/\pi^2$. Consequently $f(X_n, \mu, A)$ is one humped for $(\mu/4 - 1) < A < 2\mu/\pi^2$ and two humped for $2\mu/\pi^2 < A < \mu/4$. For

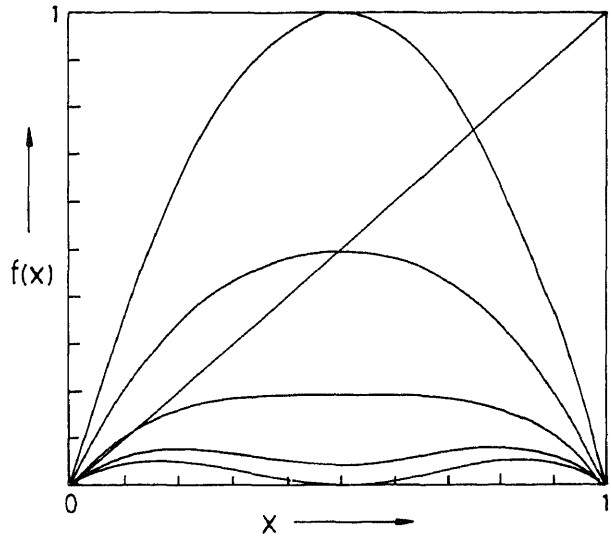

Figure 3. The combination map $f(X)$ given in (6) for $\mu = 4$. The curves correspond to $A = 0$, 0·5, $8/\pi^2$, $3/\pi$ and 1 in that order from top to bottom.

any value of μ, the corresponding minimum value for A is $(\mu/4 - 1)$ and this occurs as $f(X_n, \mu, A)$ becomes equal to 1. Likewise the maximum value of A for a given value of μ is $\mu/4$ which occurs as $f(X_n, \mu, A)$ becomes equal to zero. These features are made evident in figure 3 where $f(X_n, \mu, A)$ is plotted as a function of X_n for different values of A, keeping $\mu = 4$. We thus observe that the parameter A must lie between $(\mu/4 - 1)$ and $(\mu/4)$ so as to keep the iterates of the combined map within the unit interval (0, 1).

With μ fixed at 4, we do a detailed numerical analysis of the system in (6). The parameter A is increased slowly in steps of 0·001 and a bifurcation diagram is drawn (figure 4). It is interesting to note that the system retraces the entire period doubling route to chaos in the reverse order as A is slowly tuned and finally settles down to a one cycle for $A \geqslant 0{\cdot}2435$. Here, the effect of the combination of the sinusoidal term to the logistic one is to reduce the height of the maximum at $X = 1/2$ as the parameter A is increased, as is clear from figure 3. Further, if we start from a value of μ corresponding to one of the periodic cycles of the logistic map, by applying a negative value for A, the system can be brought to chaotic state.

It can be shown that in the one humped region of the map viz, $(\mu/4 - 1) < A < 2\mu/\pi^2$, the Schwarzian derivative of the function $f(X_n, \mu A)$ is negative over the entire range (0, 1) for X. This means that period doubling is generic in the system [9].

By changing the value of μ, a parameter space plot for the system is drawn (figure 5). This gives details regarding the transition from chaos to order and vice versa. For each chosen value of μ, the Lyapunov characteristic exponent is calculated by varying A in steps of 0·001 and A_∞ is determined as before. The thick line that represents the values of A_∞ for each value of μ is thus the transition line between order and chaos. The lines parallel to it (only two are shown in figure 5) represent the bifurcation curves along which each period doubling occurs. The shaded region corresponds to the chaotic regime of the system, where the L.C.E is generally positive, except for windows of periodicity within the chaotic regime. The lowermost line corresponds

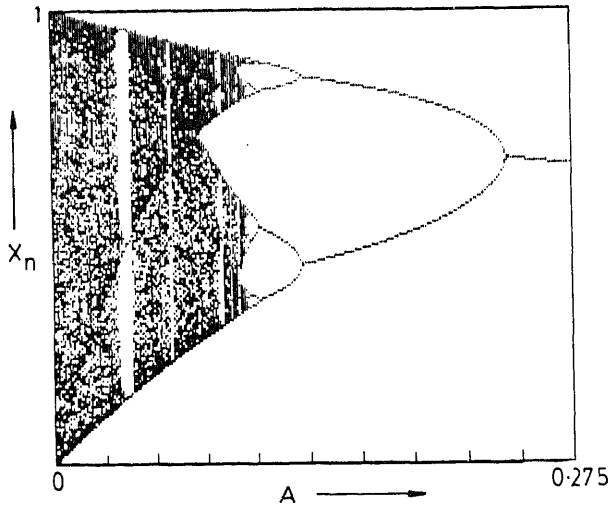

Figure 4. Bifurcation structure of the map in (6). With $\mu = 4$ and $A = 0$, the system is fully chaotic. As A is slowly tuned, periodic cycles are traced in the reverse direction.

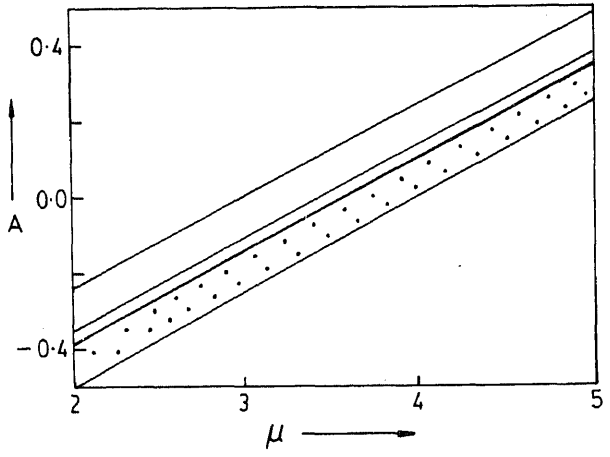

Figure 5. The parameter space (μ, A) of the combination map. The thick line represents the transition from order to chaos while the lines parallel to it, are the bifurcation curves.

to $A = (\mu/4 - 1)$. By extending this line upwards, we observe that we can increase the value of μ beyond $\mu = 4$ also, by taking suitable high values for A.

Since the bifurcation curves in the parameter space (μ, A) are parallel lines, it is clear that the Feigenbaum index δ defined in terms of the bifurcation values A_n for fixed μ, must be the same as the δ for the logistic map alone.

Scaling of the Lyapunov exponent

In order to investigate the scaling behaviour of λ for the combination map, we use the same numerical procedure discussed in § 2. Keeping the value of $\mu = 4$, λ for the

Table 2. The scaling index ν and accumulation point A_∞ for the combination map considered in § 3, for various values of μ.

μ	A_∞	ν
3·0	−0·1382968450	0·9989838
3·5	−0·0170178750	0·9677731
4·0	0·1046909450	0·9936844
32	7·2212675805	0·9996790

system is computed by slowly varying the parameter A. This enables us to obtain the value of A_∞, the parameter value at which transition from chaos to order occurs, up to an accuracy of 10^{-8}. Then the value of A is varied in steps of 10^{-8} around A_∞ and the corresponding values of λ are determined. The slope of the line of best fit obtained by plotting $\log|\lambda|$ against $\log|A - A_\infty|$ is determined as the scaling index ν. This is repeated for $\mu = 3{\cdot}5$ and 3 also. We then extend the investigations for a very high value of μ namely $\mu = 32$. Here, the parameter A can vary from 7 to 8. In the latter case, the combination map is two humped from the very beginning. The results are presented in table 2.

From table 2, it is clear that in all the cases studied for the combination map, the scaling index is entirely different from that for the logistic map. The scaling index for the combination map is almost unity for all the cases considered. It is to be noted that this map has the same δ as the quadratic map. This would mean that the scaling relation in this case does not follow the H–R law. From the log–log plot for the combination map given in figure 6, it is evident that the points lie exactly along a straight line. The proximity of the periodic windows does not seem to hinder the numerical computations in this case. This could mean that periodic windows are less in number or they have been smeared out by the additional term in the map.

In an attempt to see why the combination map does not follow the H–R scaling relation, we carried out a detailed numerical analysis of the chaotic regime of the map. The control parameter A is slowly and carefully varied and a series of bifurcation

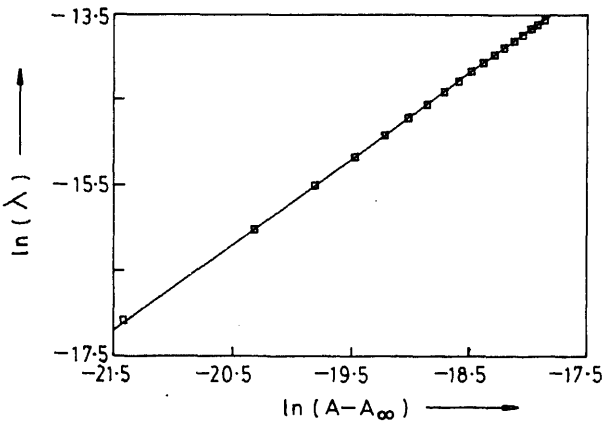

Figure 6. The LCE scaling for the combination map, $\ln|A - A_\infty|$ is plotted against $\ln|\lambda|$. Here, the value of $\mu = 32$. ν in this case is found to be ≈ 1.

Table 3. Parameter values for successive bifurcations of the chaotic band of the combination map and its convergence rate δ_n.

Parameter value (A_n)	Convergence rate δ_n
0·07909091	—
0·09954546	—
0·10360000	5·0449130
0·10444000	4·8267857
0·10463500	4·3076923
0·10467600	4·7560975
0·10468445	4·8235300
0·10468625	4·7222222

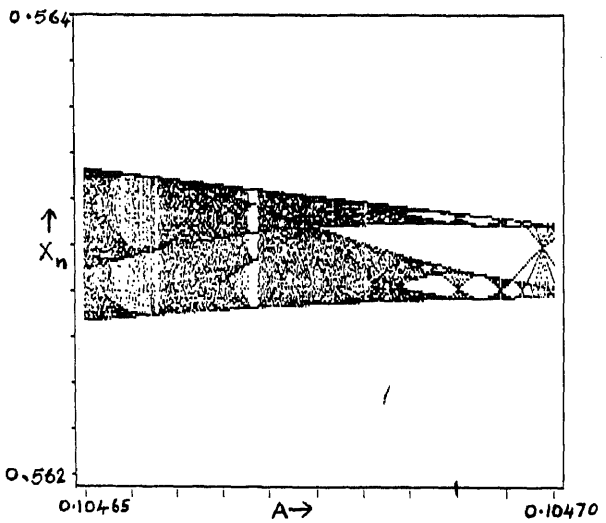

Figure 7. The band structure of the combination map on an enlarged scale. As A increases towards A_∞, merging of bands take place.

diagrams are drawn on an enlarged scale. This enabled us to observe the fine structure of the chaotic bands. With $\mu = 4$ and $A = 0$, the system is in the fully chaotic state. As A is increased towards A_∞, the chaotic band undergoes a series of bifurcations. After each bifurcation, one of the branches is taken and the bifurcation diagram is drawn on an enlarged scale. The control parameter is increased in very small steps and the next bifurcation point is obtained. Continuing this process, we could trace out the values of A up to the 8th stage of band bifurcation. The values of A at which successive band bifurcations occur and the convergence rate δ_n calculated in terms of these A-values are presented in table 3. With further increase of the control parameter A towards A_∞, recombination of bands is seen. Figure 7 shows the corresponding bifurcation diagram, in which merging of bands can be seen. Thus it is clear that in the case of the combination map, band bifurcation does not take place

ad infinitum. This incomplete nature of the cascade of bifurcations in the case of the combination map could be the possible reason for the scaling behaviour of its Lyapunov characteristic exponent (λ) to be different from the H–R law.

4. Concluding remarks

The work presented above establishes the validity of Huberman–Rudnick scaling law for different universality classes of one dimensional maps. However, we also find that it is possible to consider certain combinations of maps for which the Huberman–Rudnick law is not obeyed, as far as the scaling of the Lyapunov characteristic exponent is concerned. These combination maps have almost the same bifurcation structure as single maps. But our investigations indicate that the behaviour of the combination map in the immediate neighbourhood of A_∞ is entirely different. What we observe is a series of band splittings and mergings before the system enters the periodic region. The exact reason as to why the cascade of band bifurcations is not complete is not yet clear. This is currently being investigated.

Acknowledgements

We thank the referee for useful comments and suggestions. One of us (GA) gratefully acknowledges the financial support from CSIR, New Delhi, through a research associateship.

References

[1] G Ambika and K Babu Joseph, *Pramana – J. Phys.* **39**, 193 (1992)
[2] M J Feigenbaum, *J. Stat. Phys.* **21**, 665 (1979)
[3] B A Huberman and J Rudnick, *Phys. Rev. Lett.* **45**, 154 (1980)
[4] S C Johnstone and R C Hilborne, *Phys. Rev.* **A37**, 2680 (1988)
[5] B Shraiman, E Wayne and P C Martin, *Phys. Rev. Lett.* **46**, 935 (1981)
[6] J C Earnshaw and D Haughey, *Am. J. Phys.* **61**, 5 (1993)
[7] J P Crutchfield, J D Farmer and B A Huberman, *Phys. Rep.* **92**, 45 (1982)
[8] B Hu and I I Satija, *Phys. Lett.* **A98**, 143 (1983)
[9] H G Schuster, *Deterministic chaos*, (Physik Verlag, Weinheim, 1984)

PRAMANA
— journal of
physics

© Printed in India

Vol. 43, No. 6,
December 1994
pp. 431–442

Controlling chaos: Stabilization of fixed points and creation of new stable attractors in 1-D maps

SANGEETA D GADRE and V S VARMA
Department of Physics and Astrophysics, University of Delhi, Delhi 110 007, India

MS received 16 March 1994; revised 2 September 1994

Abstract. In this paper we have tried to stabilize the unstable fixed points for a class of 1-D maps by using a multiplicative nonlinear feedback control mechanism. We have also used such control to create new attractors (which did not exist in the original system), to suit our requirement. The control is also found to work in the presence of noise.

Keywords. Controlling chaos; unstable fixed points; Lyapunov exponents; transient time; noise.

PACS No. 05·45

1. Introduction

Chaos in physical systems was believed to be unreliable, uncontrollable and therefore undesirable until Pecora and Carroll [1, 3] and Ott, Grebogi and Yorke [4, 5] demonstrated that chaos is manageable, exploitable and even invaluable. A chaotic system in general, cannot be made to converge to a freely evolving desired trajectory, whether periodic or chaotic, due to the inherent unpredictability of the system. The control of chaos in this context consists of forcing the system to evolve along a desired trajectory. Pecora and Carroll succeeded in achieving this by using a suitable drive variable. They demonstrated that two identical chaotic systems driven by a common signal display asymptotic convergence of their trajectories even though they may have started from very different initial conditions. They could do this provided the Lyapunov exponents of the driven system were all negative. Such behaviour was not only demonstrated numerically but also confirmed experimentally.

Ott, Grebogi and Yorke (OGY) succeeded in forcing a chaotic system on to one of its own unstable periodic orbits by making a set of small time-dependent perturbations on the system parameters in such a way that the desired periodic orbit was stabilized. They demonstrated their method numerically by controlling the Hénon map. They also pointed out that as an infinite number of unstable periodic orbits are embedded in a chaotic attractor, the stabilization of these unstable periodic orbits leads to an enhancement of the system's performance as well as to the adaptability of the system to varying performance requirements. The effectiveness of the OGY method of control has also been confirmed experimentally in several systems [6–8].

Güémez and Matías [9] suggested a new method for controlling chaos in the case of iterated maps. They stabilized a given unstable periodic orbit by applying series of regular proportional feedbacks in the form of pulses to the variable of the

map. This method does not change system parameters. They illustrated it with an application to the logistic and exponential maps.

In this paper we have tried to stabilize the unstable fixed points of a map by modifying the equation which controls the dynamics of the system. Using such control we have also tried to create new attractors which did not already exist in the system. This leads to the stabilization of the system to arbitrary trajectories and not just to already existing unstable trajectories. We have also tested our control in the presence of noise and found it to be working effectively. We have restricted ourselves to those 1-D maps which are of the form $F(\lambda, x) = \lambda G(x)$ or can be put in this form by a suitable transformation [10–12]. We have chosen the logistic map as an example and studied the behaviour of this map modified by the chosen control mechanism.

2. Exponential control

Consider a discrete deterministic nonlinear dynamical system governed by

$$x_{n+1} = F(\lambda, x_n) = \lambda G(x_n). \tag{1}$$

Here x_n is the response of the system at the time n and λ is the parameter which remains constant and determines the asymptotic behaviour of a typical trajectory of the attractor. The dynamics is assumed to be known and expressed exactly through the nonlinear function F. Such systems may display periodic, quasiperiodic or chaotic behaviour depending on the value of the control parameter λ. As mentioned in the introduction, one of the aims of this paper is to stabilize the existing unstable fixed points of periodicity say k i.e. $(x_1^*, x_2^*, \ldots, x_k^*)$ of the map F. The stabilization is done by replacing the parameter λ in (1) by the multiplicative nonlinear feedback control

$$\lambda^* \exp\left(\varepsilon \prod_{i=1}^{k} (x_n - x_i^*)\right) \tag{2}$$

which becomes equal to λ^* as soon as x_n becomes equal to any of the x_i^*s. Here ε measures the stiffness of the control mechanism and λ^* is the value of the parameter corresponding to the unstable fixed points $(x_1^*, x_2^*, \ldots, x_k^*)$ of the unmodulated map F to which the system is to be made to converge. In the presence of such control, the dynamics of the modulated system is governed by

$$x_{n+1} = F\left(\lambda^* \exp\left(\varepsilon \prod_{i=1}^{k} (x_n - x_i^*)\right), x_n\right) \equiv f(\lambda^*, \varepsilon, x_n). \tag{3}$$

The form of the modulated system f is such that it is almost a trivial exercise to show that the fixed points of period k of $F(\lambda^*, x)$, are also the fixed points of the same periodicity k of the corresponding $f(\lambda^*, \varepsilon, x)$ (although f may possess other fixed points in addition). The slope α of the map $f^k(\lambda^*, \varepsilon, x_n)$ at any one of the fixed points $x_r^*, r = 1, 2, \ldots, k$, of the system is given by

$$\alpha(\varepsilon) = \left.\frac{\mathrm{d}f^k}{\mathrm{d}x}\right|_{x_r^*}$$

$$= \left.\frac{\mathrm{d}f}{\mathrm{d}x}\right|_{x_k^*} \left.\frac{\mathrm{d}f}{\mathrm{d}x}\right|_{x_{k-1}^*} \cdots \left.\frac{\mathrm{d}f}{\mathrm{d}x}\right|_{x_1^*}$$

$$= \prod_{j=1}^{k} \left(\lambda^* \frac{dG}{dx}\bigg|_{x_j^*} + \lambda^* \varepsilon G(x_j^*) \prod_{\substack{i=1 \\ i \neq j}}^{k} (x_j^* - x_i^*) \right)$$

$$= \prod_{j=1}^{k} \frac{dF}{dx}\bigg|_{x_j^*} + \varepsilon g(\varepsilon, \lambda^*)$$

$$= \alpha(0) + \varepsilon g(\varepsilon, \lambda^*),$$

where

$$\alpha(0) = \prod_{j=1}^{k} \frac{dF}{dx}\bigg|_{x_j^*} = \frac{dF^k}{dx}\bigg|_{x_r^*}$$

is the slope of the unmodulated map F at $x = x_r^*$ and $\varepsilon g(\varepsilon, \lambda^*)$ is a polynomial in ε of degree k. When a fixed point x_r^* of the map F with periodicity k becomes unstable through a period doubling route to chaos then $dF^k/dx|_{x_r^*} < -1$. For x_r^* to be a stable fixed point of f^k we must have $-1 < \alpha(\varepsilon) < +1$. When k is odd then $\alpha(\varepsilon) \to \infty$ as ε tends to either $+\infty$ or $-\infty$. Also $\alpha(0) < -1$. Hence there exists a range of ε for which $-1 < \alpha(\varepsilon) < +1$ and x_r^* becomes a stable fixed point of f^k for ε in this range. Similarly, when k is a multiple of 4, it can be shown that $\alpha(\varepsilon) \to +\infty$ as $\varepsilon \to \infty$. However, for other values of k, $\alpha(\varepsilon)$ may not lie in the open interval $(-1, 1)$ for any value of ε, depending on the form of the function F and values of the x_r^*s. In such cases the control will not be able to force the system to converge to the unstable fixed points $\{x_r^*\}$. Whereas for unstable fixed points x_r^* of the map F with periodicity k, created by tangent bifurcation $dF^k/dx|_{x_r^*} > 1$. When k is odd then $\alpha(\varepsilon) \to -\infty$ as ε tends to either $-\infty$ or $+\infty$. Also $\alpha(0) > 1$. Hence there exists a range of ε for which $\alpha(\varepsilon)$ lies in the range $(-1, 1)$ and x_r^* becomes a stable fixed point of f^k for ε in this range. Similarly, when k is even but not a multiple of 4, it can be shown that $\alpha(\varepsilon) \to -\infty$ as $\varepsilon \to \infty$.

Some other features of our choice of control are:

(i) the control becomes passive once the desired goal $(x_1^*, x_2^*, \ldots, x_k^*)$ is achieved. If fluctuations drive the system off the desired orbit, the control reactivates itself;
(ii) as the control is a positive unbounded function, it can take any value lying between 0 and ∞. Consequently the modulated system $f(\lambda^*, \varepsilon, x)$ may or may not remain bounded for $0 \leqslant x \leqslant 1$, and this depends on the form of the unmodulated function $F(\lambda^*, x)$. For example, for $F(\lambda^*, x) = 4\lambda^* x(1-x)$, the modulated system remains bounded for $k = 1$ and $0 \leqslant x \leqslant 1$ in the desired range of ε, whereas for $F(\lambda^*, x) = 1 - \lambda^* (2x-1)^2$ this is not so;
(iii) the control also destabilizes stable fixed points F for some values of ε;
(iv) the form of the control is such that the unstable fixed point $x^* = 0$ cannot be stabilized by putting $x^* = 0$ in (2). The reason is obvious. df/dx evaluated at such a point is the same as $dF/dx|_{x=0}$. So the Lyapunov exponent of the modulated map f given by eq. (3) remains the same as that of the unmodulated map F given by eq. (1). However, $x^* = 0$ may get stabilized in the process of stabilizing a non-zero unstable fixed point of the map as can be seen in the logistic map (§ 3·1).

A quantity of obvious interest in the context of controlling chaos is the time required for the system to settle on to the desired orbit. This of course depends on the stiffness of the control ε. For a given ε we study the length of the transient τ required for the system to approach within a distance ω of the desired orbit starting from some initial point. If ω_0 is the initial distance from the desired orbit, then it is

clear that τ and ω are related by $\omega = \omega_0 \exp(\Lambda\tau)$, where Λ is the real part of the largest Lyapunov exponent. The slope of the plot τ against $\ln(\omega/\omega_0)$ is nothing but $1/\Lambda$. The values of the Lyapunov exponents determined in this manner are found to be in good agreement with those obtained analytically. We also study the transient time τ required for settling on to the desired orbit within a given accuracy ω as a function of ε and find that it exhibits the same behaviour as the Lyapunov exponent as a function of ε for that orbit.

3. Behaviour of the logistic map while stabilizing an unstable fixed point of period 1

The logistic map with control (2) is given by

$$x_{n+1} = 4\lambda^* \exp(\varepsilon(x_n - x_u^*))x_n(1 - x_n) \equiv f(\lambda^*, \varepsilon, x_n) \tag{4}$$

where $0 < x_n < 1$, $0 < \lambda^* < 1$ and $x_u^* = 1 - 1/(4\lambda^*)$ is an unstable fixed point of period one for $0{\cdot}75 < \lambda^* \leqslant 1$. The variation of $\mathrm{d}f/\mathrm{d}x|_{x_u^*}$ with λ^*, for different values of ε, is shown by circled lines in figure 1. The figure shows that small values of ε can only stabilize small values of x_u^* while larger x_u^*s can be stabilized by increasing ε. Although a large stiffness constant stabilizes large x_u^*s it also destabilizes small x_u^*s. Furthermore, any x_u^* can only be stabilized provided ε lies within a range $\varepsilon_{\min} < \varepsilon < \varepsilon_{\max}$. The end points of this range, i.e. $\varepsilon_{\min}$ and $\varepsilon_{\max}$, can be obtained by using the conditions $\mathrm{d}f/\mathrm{d}x|_{x_u^*} > -1$ and $\mathrm{d}f/\mathrm{d}x_{x_u^*} < 1$. For the logistic map the range of values of ε, for which x_u^* becomes a stable fixed point as a result of the modulation by the control

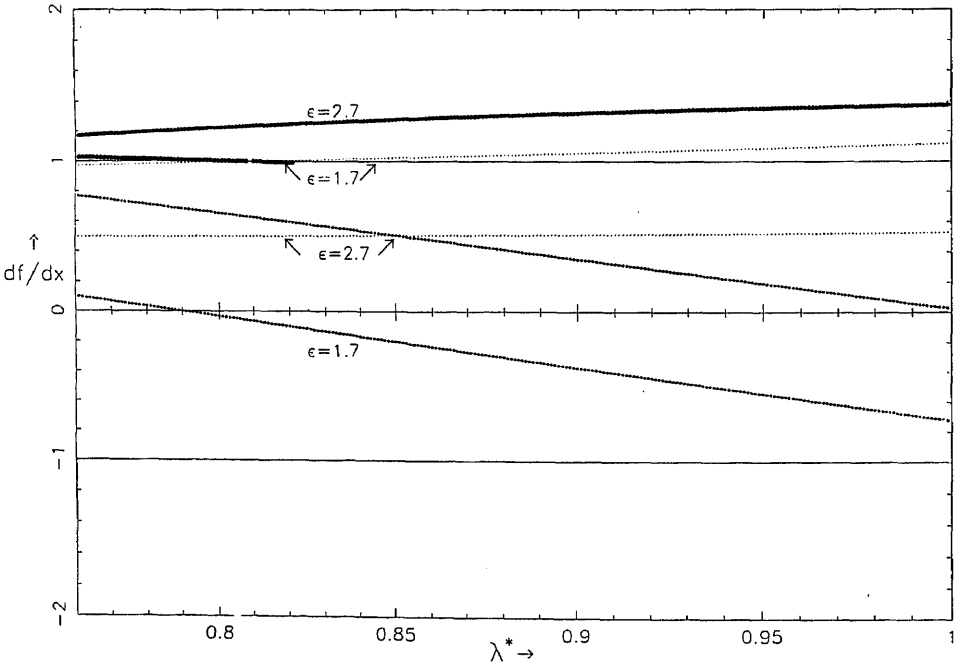

Figure 1. The variation of $\mathrm{d}f/\mathrm{d}x$ for the logistic map evaluated at $x = 0$, $\tilde{x}$ and x_u^* and λ^* is represented by dotted, bold and circled lines respectively for $\varepsilon = 1{\cdot}7$ and $2{\cdot}7$.

(2) is $(-3+4\lambda^*)/(-1+4\lambda^*) < \varepsilon < 4\lambda^*$. This range of ε for which x_u^* becomes a stable fixed point of the modulated map using the control (2) is plotted against λ^* in figure 2.

The form of $f(\lambda^*, \varepsilon, x)$ for the logistic map is such that the two fixed points of F i.e. $x=0$ and x_u^* are also the fixed points of f for $0 \leqslant x \leqslant 1$. For a given ε, there exists a critical value λ_c of λ^* for which $\mathrm{d}f/\mathrm{d}x|_{x=0}$ is exactly equal to 1. For $\lambda^* < \lambda_c$, $\mathrm{d}f/\mathrm{d}x|_{x=0} < 1$, hence the function $f(\lambda^*, \varepsilon, x)$ lies below the line $y=x$ for small x in the x, f plot. Therefore $f(\lambda^*, \varepsilon, x)$ must intersect the line $y=x$ at least at one point $\tilde{x}$ between $x=0$ and $x=x_u^*$ (which is not true of the unmodulated map). Thus for a given ε, for $\lambda^* > \lambda_c$ the map f has only two fixed points $x=0$ and x_u^*, whereas for $\lambda^* < \lambda_c$, f possesses a third fixed point $\tilde{x}$. The plots of $\mathrm{d}f/\mathrm{d}x$, evaluated at $x=0, \tilde{x}$ and x_u^*, against λ^* for different ε have been shown by dotted, bold and circled lines respectively in figure 1. Note that for $\varepsilon = 1{\cdot}7$, $\lambda_c \simeq 0{\cdot}82$ and $\mathrm{d}f/\mathrm{d}x|_{\tilde{x}}$ (bold line) stops there because $\tilde{x}$, as explained above, ceases to exist for values of $\lambda^* > 0{\cdot}82$.

An important feature of our control is that although, in general, such modulation can make the system unbounded (even though the unmodulated system is bounded), this is not the case for the logistic map for $\varepsilon_{\min} < \varepsilon < \varepsilon_{\max}$. This can be shown by calculating $f(\lambda^*, \varepsilon, x_{\max})$ at different values of λ^* and ε, where $x_{\max} = 1/2 - 1/\varepsilon + \sqrt{(1/4 + 1/(\varepsilon^2))}$ is the value of x at which f has an extremum. Thus, within the specified range of ε, all itineraries of the logistic map in the presence of our control mechanism always remain bounded in $[0, 1]$. Consequently the basin of attraction of x_u^*, which is the only stable fixed point of f for $\lambda^* > \lambda_c$, is the entire domain of x for such values of λ^*. For $\lambda^* < \lambda_c$, there are two stable fixed points $x=0$ and $x=x_u^*$. The domains

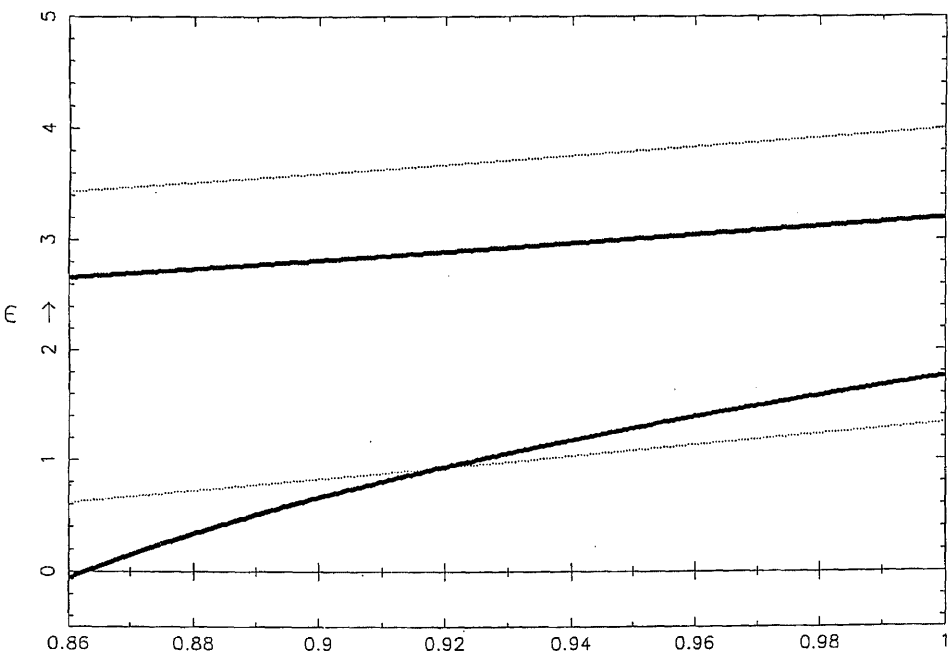

Figure 2. The range of ε for which unstable fixed points of the logistic map with periodicities 1 and 2 can be stabilized for different λ^*, using the exponential control, is represented by dotted and bold lines respectively.

of attraction of the two stable fixed points are disjoint and between them exhaust the entire domain of x. It is found numerically that the basin of attraction of $x = 0$ is $0 < x < \tilde{x}$ and $x_t < x < 1$, where x_t is the value of x such that $f(x_t) = f(\tilde{x}) = \tilde{x}$ and the basin of attraction of x_u^* is $\tilde{x} < x < x_t$. These are shown in figure 3.

Another feature worth noticing is that f remains bounded in $[0, 1]$ even for some values of $\lambda > 1$ for which F, i.e. the logistic map, is unbounded. Therefore the unstable period-one fixed point x_u^* of the logistic map can also be stabilized for $\lambda^* > 1$. The analysis is the same as for $\lambda^* < 1$. Thus, with the present control, it is possible to make the system bounded even for those values of λ for which the unmodulated system is unbounded, and the system can be made to converge to the corresponding fixed points if it is so desired.

For a given λ^* and ε, we study the transient time τ required by the system for settling on to the fixed point x_u^* of the map. We plot τ as a function of $\ln(\omega/\omega_0)$ in figure 4 for $\lambda = 0{\cdot}9$ and $\varepsilon = 2{\cdot}2$. From the slope of the graph, the Lyapunov exponent $= -0{\cdot}133$ which is in good agreement with the value $-0{\cdot}13036$ obtained analytically. We also plot τ against ε for fixed λ and ω in figure 5 and find that τ is a decreasing function of ε. However, there is an optimum stiffness of control, beyond which increasing ε increases τ. This behaviour of τ is the same as that of the Lyapunov exponent for the map as a function of ε. The optimum value of ε corresponds to that value of ε for which the Lyapunov exponent is minimum. This is found to be a general feature of the control.

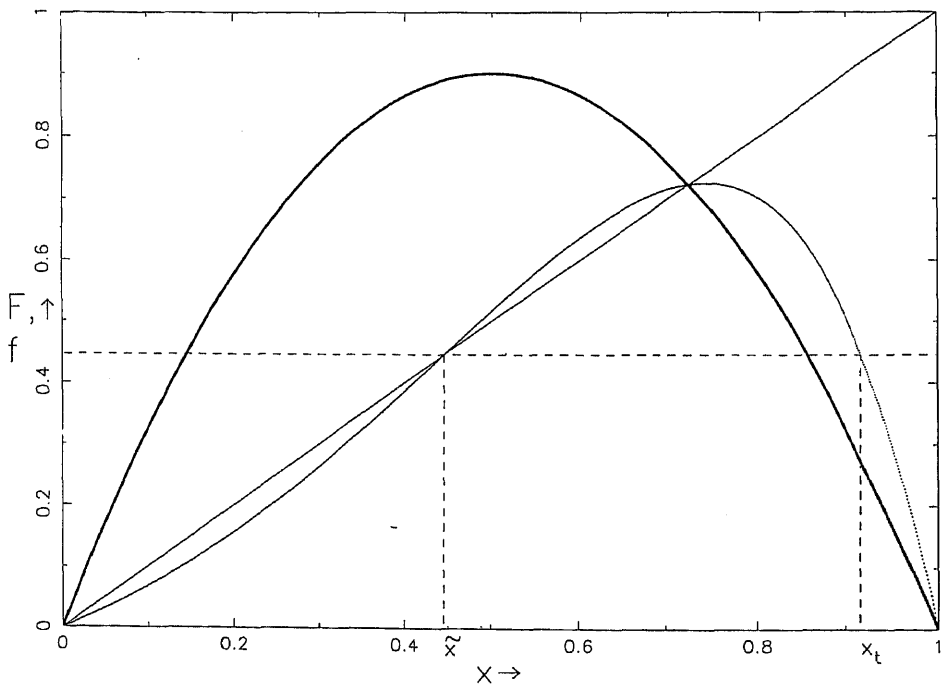

Figure 3. The basins of attraction of $x = 0$ and x_u^* for $\lambda^* = 0{\cdot}9$ and $\varepsilon = 2{\cdot}5$ for the logistic map, where the bold and dotted curves represent the functions F and f as functions of x respectively.

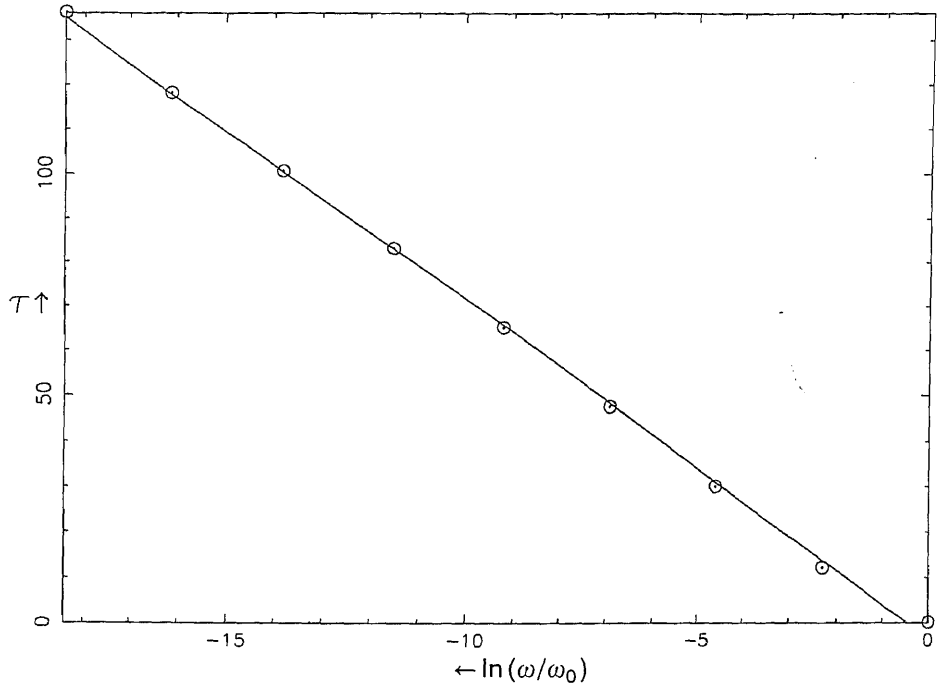

Figure 4. Plot of the transient time τ vs $\ln(\omega/\omega_0)$ for the logistic map with $\lambda^* = 0{\cdot}9$ and $\varepsilon = 2{\cdot}2$.

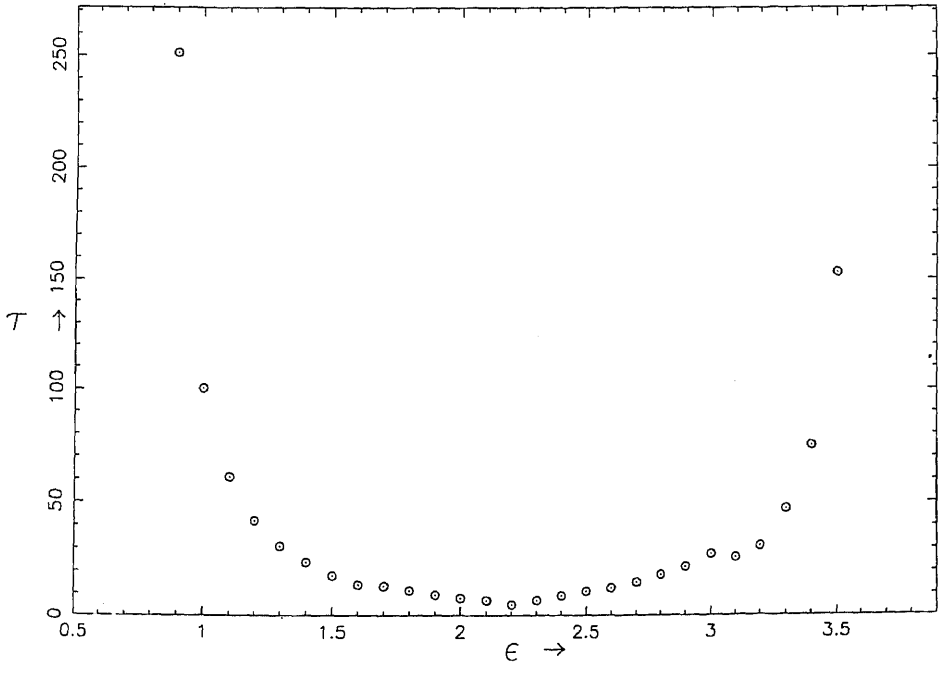

Figure 5. Plot of the transient time τ vs ε for the logistic map with $\lambda^* = 0{\cdot}9$ and $\omega = 10^{-7}$

3.1 *Behaviour of the logistic map while stabilizing period-2 fixed points*

The form of the control for stabilizing the logistic map to the period-2 unstable fixed points (x_1^*, x_2^*) for $\lambda^* > 0{\cdot}86238$, is given by

$$x_{n+1} = 4\lambda^* \exp(\varepsilon(x_n - x_1^*)(x_n - x_2^*))x_n(1 - x_n),$$
$$\equiv \mathscr{F}(\lambda^*, \varepsilon, x_n) \tag{5}$$

where $x_1^* = (1 + 4\lambda^* + \sqrt{(1-4\lambda^*)^2 - 4})/(8\lambda^*)$ and $x_2^* = (1 + 4\lambda^* - \sqrt{(1-4\lambda^*)^2 - 4})/(8\lambda^*)$. The variation of $d\mathscr{F}^2/dx|_{x_1^*, x_2^*}$ with λ^* for different values of ε is shown by circled lines in figure 6. The plot shows that the fixed points (x_1^*, x_2^*) corresponding to small λ^* can be stabilized using small values of ε while those corresponding to larger λ^* are stabilized by taking large values of ε. But large ε also tends to destabilize fixed points corresponding to small λ^* (the same situation as was observed with period-1 control). It also shows that there exists a range of values of $\varepsilon, \varepsilon'_{\min} < \varepsilon < \varepsilon'_{\max}$, for a given λ^*, for which (x_1^*, x_2^*) become the stable fixed points of the $\mathscr{F}^2$ map. Expressions for $\varepsilon'_{\min}(\lambda^*)$ and $\varepsilon'_{\max}(\lambda^*)$ can be obtained from the constraints $d\mathscr{F}^2/dx|_{x_1^*, x_2^*} > -1$ and $d\mathscr{F}^2/dx|_{x_1^*, x_2^*} < 1$ respectively. The range of values of ε for which (x_1^*, x_2^*) become stable fixed points of the $\mathscr{F}^2$ map is plotted against λ^* in figure 2.

It is also found numerically that for a given ε, there exists a critical value λ_{c1} of λ^* such that for $\lambda^* > \lambda_{c1}$, $\mathscr{F}^2(\lambda^*, \varepsilon, x)$ has four fixed points. These are $x = 0, x_1^*, \bar{x}, x_2^*$,

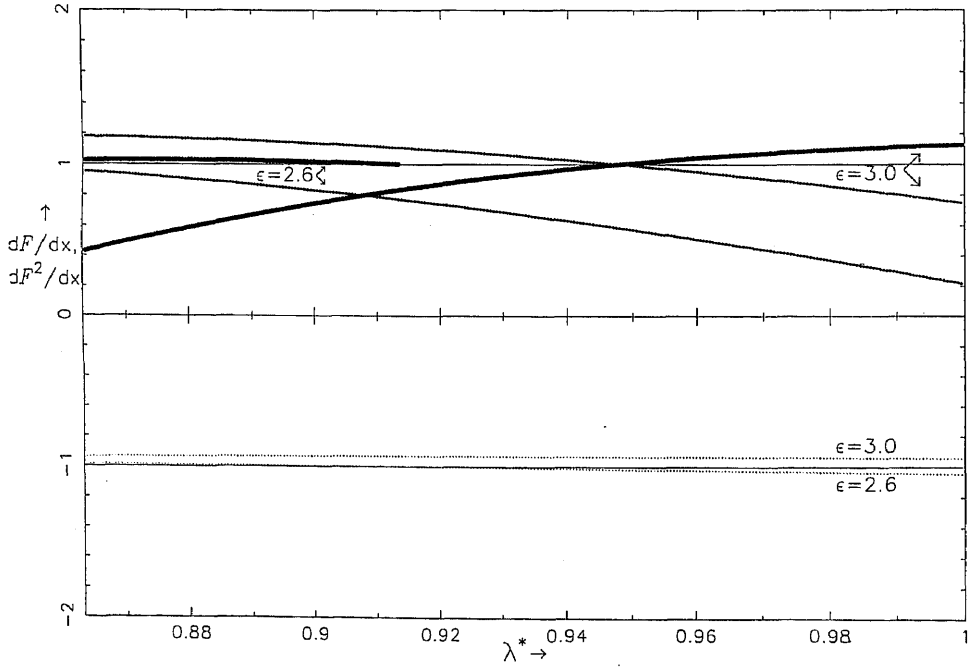

Figure 6. The variation of $d\mathscr{F}^2/dx$ for the logistic map evaluated at x'_1 (or x'_2) and x_1^* (or x_2^*) with λ^* is represented by bold and circled lines respectively for $\varepsilon = 2{\cdot}6$ and $3{\cdot}0$. The dotted line represents the variation of $d\mathscr{F}/dx$ evaluated at $x = \bar{x}$ for the same λ^* and ε's.

where x_1^*, x_2^* belong to the desired period-2 attractor, while the fixed points $x = 0$ and $\bar{x}$ are each of period 1. For $\lambda^* < \lambda_{c1}$, $\mathscr{F}^2(\lambda^*, \varepsilon, x)$ has two more fixed points x_1', x_2' in addition to the four fixed points mentioned above. Together x_1', x_2' form a new period-2 attractor. Variations of $d\mathscr{F}^2/dx|_{x_1^*, x_2^*}$, $d\mathscr{F}^2/dx|_{x_1', x_2'}$, $d\mathscr{F}/dx|_{\bar{x}}$ with λ^* for different values of ε are shown by circled, bold and dotted lines respectively in figure 6. Note that we are not studying the behaviour of $d\mathscr{F}/dx|_{x=0} = 4\lambda^* \exp(\varepsilon x_1^* x_2^*)$ which is always greater than one for $\lambda^* > 0{\cdot}86238$ and $\varepsilon > 0$, (which is required for stabilizing x_1^* and x_2^*) and hence $x = 0$ remains an unstable fixed point for $\varepsilon > 0$. For a given ε, the critical value λ_{c1} of λ^* can be obtained from the equation $d\mathscr{F}/dx|_{\bar{x}} = -1$. Figure 6 also shows that for a given ε and $\lambda^* < \lambda_{c1}$, either the desired period-2 attractor (x_1^*, x_2^*) or the new period-2 attractor (x_1', x_2') is stable. Another feature of period-2 control for the logistic map is that the function $\mathscr{F}^2(\lambda^*, \varepsilon, x)$ is not always bounded in the range $[0, 1]$ for $0 \leqslant x \leqslant 1$.

The transient τ shows a similar behaviour as in the previous section.

The control is found to work effectively for higher periods as well as for period cycles, which are created by tangent bifurcation, in the chaotic regime. We tested the control for stabilizing unstable fixed points of periods 3, 4 and 5 cycles and found it to be effective. The general features of the control remain the same.

4. Stabilization of arbitrary fixed points and the effect of noise

With exponential control it is possible to create new stable attractors which do not exist in the unmodulated system. This allows the stabilization of the system to arbitrary selected points. As an example we again take the logistic map. Suppose the aim is to stabilize the system to say a period-2 attractor (x_1, x_2) which does not exist in the unmodulated map, implying that x_1 and x_2 are not the fixed points of $F^2(\lambda, x)$. In order to achieve this the equations governing the dynamics in the presence of control are

$$\begin{aligned} x_{n+1} &= 4\lambda_1 \exp(\varepsilon(x_n - x_1)(x_n - x_2)) x_n(1 - x_n) \\ &\equiv g(x_n) \end{aligned}$$

and

$$\begin{aligned} x_{n+2} &= 4\lambda_2 \exp(\varepsilon(x_{n+1} - x_1)(x_{n+1} - x_2)) x_{n+1}(1 - x_{n+1}) \\ &\equiv g^2(x_n) \end{aligned} \tag{6}$$

where λ_1 and λ_2 are given by

$$\lambda_1 = \frac{x_2}{4x_1(1 - x_1)}$$

and

$$\lambda_2 = \frac{x_1}{4x_2(1 - x_2)}.$$

The coordinates of the points lying in the region enclosed by the curves and the axes in figure 7 represent combinations of x_1 and x_2 for which $dg^2/dx|_{x_1, x_2}$ lies in $(-1, 1)$, implying that such combinations can be stabilized using the logistic map with exponential control.

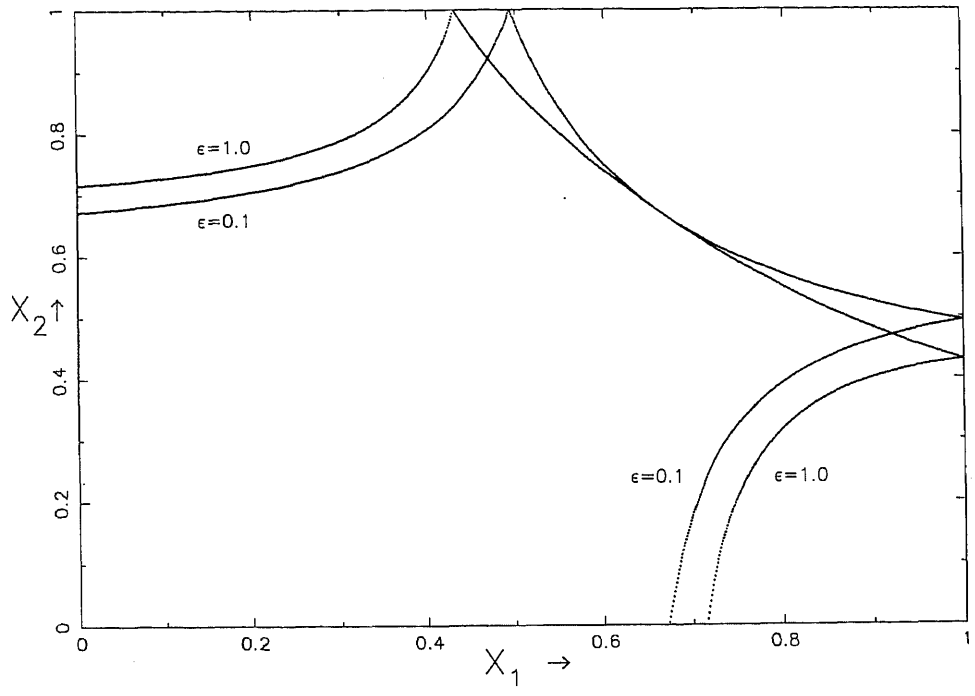

Figure 7. The coordinates of the points lying in the region enclosed by the curves and the axes represent the combinations of x_1 and x_2 which can be stabilized using the logistic map and the exponential control for $\varepsilon = 0{\cdot}1$ and $1{\cdot}0$.

This procedure can easily be extended to stabilize the system to trajectories of higher periods even when points on the trajectory do not correspond to either stable or unstable fixed points of the unmodulated map.

Next, we consider the issue of noise. We add term $\beta\delta_n$ to the right hand side of (4) of the modulated logistic map, where δ_n is a random quantity which has a Gaussian probability density with zero mean and unit standard deviation while β measures the noise level. We find that the exponential control given by (2) is capable of forcing the noisy modulated map to the desired fixed point x_u^* for the stiffness constant ε lying in the range $(\varepsilon_{\min}, \varepsilon_{\max})$, within an accuracy of the order of β. However, the basin of attraction of x_u^* gets affected by the value of β. Figure 8 shows the orbit plot, x_n vs n for 1000 iterates of the noisy modulated logistic map for $\mu = 0{\cdot}9$, $\varepsilon = 0{\cdot}9$ and $\beta = 0{\cdot}001$ starting from an initial state $x_0 = 0{\cdot}1$ and demonstrates the effectiveness of the control. We have also tested our control in the presence of noise which has a uniform distribution over [0, 1] and found the control to work effectively. The control is also found to stabilize desired higher period orbits as well as allowed combinations of arbitrary points in the noisy logistic map for the given range of values of ε.

We have also tested our control on the following 1-D maps and found it to work effectively with features similar to those described above:

(i) $F(\lambda, x) = \lambda \sin(\pi x)$

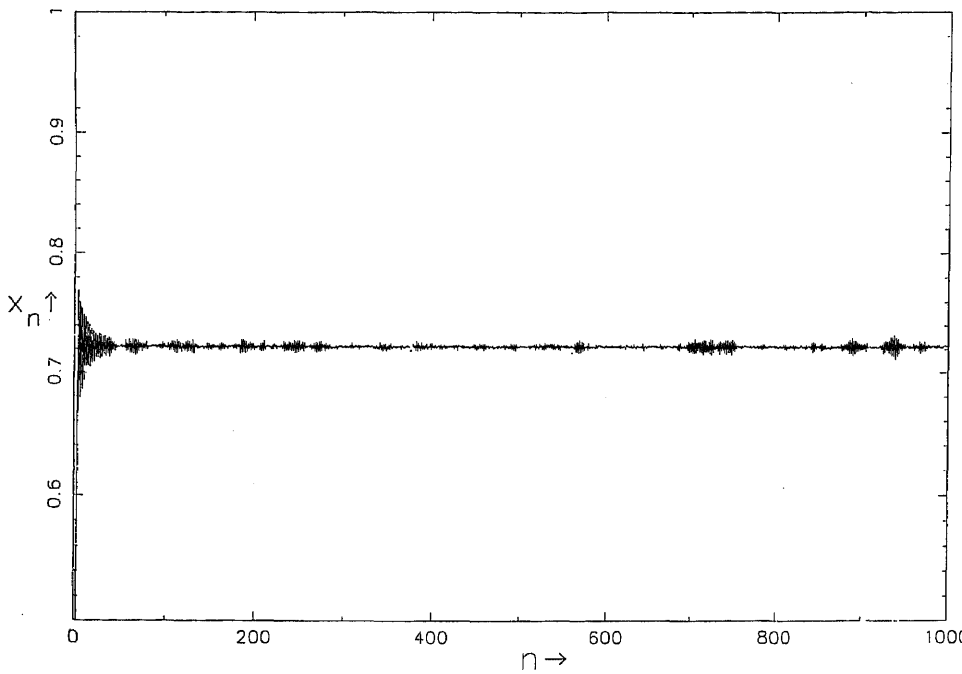

Figure 8. The orbit plot, x_n vs n for 1000 iterates of the modulated logistic map in the presence of noise having a Gaussian probability with zero mean and unit standard deviation, for $\mu = 0{\cdot}9$, $\varepsilon = 0{\cdot}9$ and $\beta = 0{\cdot}001$ starting from an initial state $x_0 = 0{\cdot}1$.

(ii) $F(\lambda, x) = \dfrac{4^{4/3}}{3} \lambda x(1 - x^3)$.

(iii) $F(\lambda, x) = 1 - \lambda |x|^2$.

5. Conclusion

The control suggested in this paper is a multiplicative nonlinear feedback control with which it is possible to stabilize unstable fixed points with periodicities that are (i) odd or (ii) multiples of 4 when created through period doubling route to chaos or (iii) with periodicities that are even but not multiples of 4 when created by tangent bifurcation for suitable ranges of the stiffness constant ε for 1 D maps which are of the form $F(\lambda, x) = \lambda G(x)$ or can be put in this form by a suitable transformation. Unstable fixed points of other periods may or may not be stabilized depending on the form of the function F and the values of the desired fixed points. The variation of the length of the transient τ as a function of ε for a given accuracy ω shows that τ is a decreasing function of ε. However there exists an optimum stiffness of control beyond which increasing ε can increase τ. The behaviour of the Lyapunov exponent as a function of ε is the same as that of τ. The optimum value of ε for which τ is minimum also corresponds to the most negative value, i.e. minimum, of Λ. In addition, it is also possible to stabilize arbitrary points, according to the required response of

the system, which do not correspond to either stable or unstable fixed points of the unmodulated map. The control is found to work effectively even in the presence of noise.

Acknowledgements

We thank Inter University Centre for Astronomy and Astrophysics (IUCAA) for allowing the use of their computing facility. One of the authors (SDG) is grateful to Kirori Mal College, University of Delhi, for granting study leave.

References

[1] L M Pecora and T L Carroll, *Phys. Rev. Lett.* **64**, 821 (1990)
[2] L M Pecora and T L Carroll, *Phys. Rev. Lett.* **67**, 645 (1991)
[3] L M Pecora and T L Carroll, *Phys. Rev.* **A44**, 2374 (1991)
[4] E Ott, C Grebogi and J A Yorke, *Phys. Rev. Lett.* **64**, 1196 (1990)
[5] T Shinbrot, E Ott, C Grebogi and J A Yorke, *Phys. Rev. Lett.* **65**, 3215 (1990)
[6] W L Ditto, S N Rauseo and M L Spano, *Phys. Rev. Lett.* **65**, 3211 (1990)
[7] E R Hunt, *Phys. Rev. Lett.* **67**, 1953 (1991)
[8] C Reyl, L Flepp, R Badii and E Brun, *Phys. Rev.* **E47**, 267 (1993)
[9] J Güémez and M A Matias, *Phys. Lett.* **A181**, 29 (1993)
[10] P Cvitanović, *Universality in chaos* (Hilger, Bristol, 1984)
[11] K H Becker and M Dörfler, *Dynamical systems and fractals* (Cambridge, Cambridge, 1989)
[12] M C de Sousa Vieira, *J. Stat. Phys.* **53**, 1315 (1988)

PRAMANA
— journal of
physics

© Printed in India

Vol. 43, No. 6,
December 1994
pp. 443–451

Mass spectrum of elementary particles in a temperature-dependent model

G P MALIK, SANTOKH SINGH[a] and VIJAYA S VARMA[b]
School of Environmental Sciences, Jawaharlal Nehru University, New Delhi 110 067, India
[a] Physics Department, Deshbandhu College, Delhi University, New Delhi 110 019, India
[b] Department of Physics and Astrophysics, Delhi University, Delhi 110 007, India

MS received 8 September 1993; revised 25 April 1994

Abstract. We show that the temperature-generalization of a popular model of quark-confinement seems to provide a rather interesting insight into the origin of mass of elementary particles: as the universe cooled, there was an era when particles did not have an identity since their masses were variable; the temperature at which the conversion of these 'nomadic' particles into 'elementary' particles took place seems to have been governed by the value of a dimensionless coupling constant C_c. For $C_c = 0{\cdot}001 (0{\cdot}1)$ this temperature is of the order of 10^9 K (10^{11} K), below which the particle masses do not change.

Keywords. Origin of mass of elementary particles; quark-confinement; temperature-generalized Bethe-Salpeter equation; harmonic oscillator kernel.

PACS No. 11·10

1. Introduction

Mass of an elementary particle is generally taken to be one of its intrinsic attributes, to be experimentally determined. This implies that a physical theory must at the outset have as an input, besides other inputs, as many empirical parameters (masses) as there are elementary particles. Since it is an aim of physics to try and explain natural phenomena on the basis of as few inputs as possible, it is no surprise that physicists have wondered, from time to time, if the large set of observed masses could be obtained from a much smaller set of empirical parameters and a physical principle. Stated differently, these considerations imply the questions: What is the origin of mass of elementary particles? Is there a theory which explains why these particles have the masses that they possess?

Possibly, Einstein's [1] perception of elementary particles as "condensations of the electromagnetic field" marks the conceptual beginning in the above direction. It is interesting to note that Hoyle's [2] concern with the large numbers problem (why does the ratio of the electrical force and the gravitational force between protons equal the ratio of the cosmological distance and the atomic distance?) – spanning a period of 50 years – led him to conclude that the problem is related to the nature of mass. Specifically, demanding the invariance of the line element under a conformal transformation, he asserted that the phenomenon of mass arises from a field interaction; It cannot be an intrinsic property of the particle alone. Essentially similar conclusion was reached by Castell [3] from a different route. In his study of the Bose-Einstein condensation of photons, Castell showed the existence of a second phase for photons

which he identified with the matter in the universe. He was thus able to compute a critical temperature (T_c) of $4{\cdot}5 \times 10^{11}$ K, corresponding to a critical mass (m_c) of 39 MeV. Since m_c is about 1/3 of the mass of π meson, Castell interpreted this as providing a connection between the structure of the universe and the properties of elementary particles. One is thus led back to Einstein's perception of massive elementary particles as droplets of photon vapour – with cosmology playing an essential role in the scheme. Indeed, these attempts bring an impressive sweep of ideas to bear on the problem. Nonetheless, it seems to us, we must follow another approach for the most tangible realization of the aim stated above, viz., obtaining the mass spectrum of elementary particles with minimal empirical inputs. The inputs in this approach are the postulate of existence of a few quarks and a mechanism for their confinement. If the quark masses are taken as given, one may vary the parameters of the confining mechanism and attempt to identify the observed particles with the various bound states of these quarks.

Three distinct stages have marked the development of the quark-confinement picture so far. In the first stage, a variety of potentials were investigated with a view to compatibility with the phenomenological features (non-observability of free quarks, rising Regge trajectories, power-law fall off of form factors, etc.) expected of a dynamical model of hadrons [4, 5]. In the next stage, the need to incorporate these features into the framework of relativistic quantum field theory naturally led to the study of the Bethe-Salpeter (BS) equation with a variety of confining kernels [5, 6, 7]. Finally, efforts have recently been directed at investigating the deconfining effects of increasing baryon density [8, 9] and temperature [10, 11, 12].

It is the purpose of this note to present an approach which, in a sense, integrates the three stages of development discussed above. The essence of the approach is to incorporate temperature and density in the BS equation itself, and to study the resulting temperature-generalized equation. We note that the desired generalization can be achieved irrespective of the choice of the confining kernel so long as its use is restricted to the instantaneous (or static) approximation, which indeed is the case in respect of almost all such kernels studied so far [5, 6, 7, 13]. In the next section, therefore, we deal with the temperature-generalization of the BS equation for the bound states of two quarks (treated as spinless) without specifying the kernel used. Our choice of the kernel is dealt with in § 3. The solutions of the resulting equation and their general features are presented in § 4. The final section is devoted to a discussion of our results.

2. Temperature-generalization of the BS equation

The BS equation of interest is:

$$[(P/2+p)^2+m^2-i\varepsilon][(P/2-p)^2+m^2-i\varepsilon]\phi(p) = (-ig^2/\pi^2)\int \mathrm{d}^4q\, V(p-q)\phi(q), \qquad (1)$$

which describes the bound states of two equal mass (m) particles. P and p are, respectively, the centre-of-mass and the relative 4-momenta of these particles; g is the strength of interaction between the exchanged particle and each of the constituents of the bound state; the metric used is space-preferred. Equation (1) has been written down in the ladder approximation.

In the instantaneous approximation (which neglects the time of propagation of the exchanged particle) one may set

$$V(p-q) = (2\pi)^{-1}\, V(\mathbf{p}-\mathbf{q}) \tag{2}$$

whence, in the frame $(P=0, E)$, (1) may be written as

$$D(p)\phi(p) = (-ig)^2/(2\pi^3) \int d^4q\; V(\mathbf{p}-\mathbf{q})\phi(q), \tag{3}$$

where

$$D(p) = [(p_0 + E/2)^2 - (\mathbf{p}^2 + m^2) + i\varepsilon] \times [(p_0 - E/2)^2 - (\mathbf{p}^2 + m^2) + i\varepsilon]. \tag{4}$$

The choice of $V(\mathbf{p}-\mathbf{q})$ will be spelled out shortly; it does not affect the temperature-generalization of the model, which is carried out as described below.

Since the RHS of (3) is a function of $\mathbf{p}$ alone and not of p_0, we may define

$$D(p)\phi(p) = S(\mathbf{p}), \tag{5}$$

which satisfies the equation

$$S(\mathbf{p}) = (-ig^2)/(2\pi^3) \int \mathrm{d}^3q V(\mathbf{p}-\mathbf{q}) S(\mathbf{q}) I(\mathbf{q}^2), \tag{6}$$

where

$$I(\mathbf{q}^2) = \int \mathrm{d}q_0 / D(q). \tag{7}$$

The desired generalization is achieved by affecting the following substitutions [14, 15, 16] in (7)

$$\int \mathrm{d}q_0 \to (2\pi i/\beta) \sum_n,\; q_0 \to 2\pi n i/\beta \tag{8}$$

where $\beta = (k_\beta\, T)^{-1}$, k_β being the Boltzmann constant and T the temperature. Note that it is the adoption of the instantaneous approximation which enables us here to temperature-generalize the integral equation under consideration. The use of the recipe (8) in (7) requires some care. It will be seen that the recipe comprises two distinct operations, namely Wick rotation and discretization of the internal energy variable. In affecting the former, one must ensure that the poles and the cuts of the BS equation are not crossed. Thus, for $E > 2m$, (7), (4) and (8) yield

$$[I(\mathbf{q}^2) \to \sum = \frac{i\pi A(\mathbf{q}^2)}{\beta E(\mathbf{q}^2 + m^2)^{1/2}(\mathbf{q}^2 + m^2 - E^2/4)}, \tag{9}$$

where

$$A(\mathbf{q}^2) = A_1 \coth(A_2) + A_2 \coth(|A_1|),$$
$$A_1 = (\beta/2)(E/2 - \sqrt{\mathbf{q}^2 + m^2}), \tag{10}$$

and

$$A_2 = (\beta/2)(E/2 + \sqrt{\mathbf{q}^2 + m^2}).$$

In the limit $T = 0$, (9) and (10) yield the standard result of integration over q_0 in

(7), viz.,

$$\int dp_0/D(q) = i\pi/[2(\mathbf{q}^2 + m^2)^{1/2}(\mathbf{q}^2 + m^2 - E^2/4)]. \tag{11}$$

We note that the case $E < 2m$ has been dealt with in [17].

3. The choice of the kernel

We now deal with the choice of $V(\mathbf{p} - \mathbf{q})$. Among the kernels that have been used in the BS equation to study the problem of confinement of quarks, the one that is interpretable as a harmonic oscillator in the nonrelativistic limit has been by far the most popular [5, 6, 7, 13]. This is easy to understand. Such a kernel not only confines the quarks in a steeply rising potential, yields rising Regge trajectories etc., but also possesses the virtue of being mathematically tractable. Additionally, of course, it enables one to study the oscillator on a quantum scale, an interesting problem in itself. In the following we employ a kernel originally given in [7], but in the form studied in [13]. As has been discussed [7, 13], the static limit of the usual kernel representing the exchange of a massive scalar particle of mass μ yields merely the screened Coulomb or Yukuwa interaction of the form $\exp(-\mu r)/r$. However, higher derivatives with respect to μ of such a kernel soften the singularity at the origin and produce interactions rising asymptotically in configuration space and hence confining in character. Thus, following these authors, we have

$$\begin{aligned} V(\mathbf{p} - \mathbf{q}) &= \lim_{\mu \to 0} d^3/d\mu^3 [1/\{(p-q)^2 + \mu^2 - i\varepsilon\}] \\ &= \lim_{\mu \to 0} 24\mu[\mathbf{p} - \mathbf{q})^2 - \mu^2]/[(\mathbf{p} - \mathbf{q})^2 + \mu^2]^4 \\ &= 2\pi^2 \Delta_p \delta^3(\mathbf{p} - \mathbf{q}). \end{aligned} \tag{12}$$

From (6), (9) and (12) we obtain

$$\Delta_p \chi(\mathbf{p}) = \frac{(\beta E/g^2)(\mathbf{p}^2 + m^2)^{1/2}(\mathbf{p}^2 + m^2 - E^2/4)\chi(\mathbf{p})}{A(\mathbf{p}^2)}, \tag{13}$$

where

$$\chi(\mathbf{p}) = \frac{A(p^2)S(\mathbf{p})}{(p^2 + m^2)^{1/2}(p^2 + m^2 - E^2/4)}. \tag{14}$$

In interpreting (13), the many body origin of the BS equation from which it is derived must be borne in mind. The building blocks of the latter equation are the finite-temperature Green's functions. Recall that the one-particle temperature Green's function describes the motion of one particle added to the many-body system. Since such a function is a propagator, it contains detailed dynamic information; besides, it contains all statistical mechanical information because it is an expectation value in the grand canonical ensemble [18]. Thus, the $T \neq 0$ BS equation may be said to provide a description of the many-body system whose constituents are in a paired

state [19]. It will be seen that the chemical potential of the species being considered has not been incorporated into our equation; this is easily achieved by replacing $p^2/(2m)$ by $p^2/(2m)+\tilde{\mu}$ in (9) and (10), where $\tilde{\mu}$ is the chemical potential. In the $\tilde{\mu}=0$ limit being considered by us, one may regard the $T=0$ BS equation as describing the bound-state of a 2-particle system in a heated vacuum [20]. Correspondingly, (13) may be said to describe the bound-state system interacting via a temperature-modified potential [21].

4. The solutions

We now proceed to solve (13). Setting

$$\chi(\mathbf{p})=\chi_l(p)\ Y_{l,m}(\Theta,\Phi)/p, \quad (p=|\mathbf{p}|) \tag{15}$$

the radial part of (13) may be separated as

$$\chi_l''(k)-[l(l+1)/k^2]\chi_l(k) = \frac{(\beta Em^5/g^2)(1+k^2)^{1/2}[k^2+1-E^2/(4m^2)]\chi_l(k)}{A(k^2)}, \tag{16}$$

where k is the dimensionless variable

$$k=p/m. \tag{17}$$

The definitions

$$\begin{aligned}
&\alpha=\beta Em^5/g^2\\
&s_1=(m\beta/2)[E/(2m)-1],\ T_1=\tanh(s_1)\\
&s_2=(m\beta/2)[E/(2m)+1],\ T_2=\tanh(s_2)\\
&\tilde{k}^2=\beta p^2/(4m)=m\beta k^2/4,\ T_3=\tanh(\tilde{k}^2)\\
&\gamma^2=E^2/(4m^2)-1>0
\end{aligned} \tag{18}$$

enable us to write the multiplier of $\chi_l(k)$ on the RHS of (16) as

$$\frac{\alpha(1+k^2)^{1/2}(k^2-\gamma^2)(T_2+T_3)(T_1-T_3)}{s_1T_1+s_2T_2-T_3^2(s_1T_2+s_2T_1)+Z_1T_3+Z_2\tilde{k}^2} \tag{19}$$

where

$$\begin{aligned}
Z_1&=T_1T_2(s_1-s_2)+s_2-s_1\\
Z_2&=T_1-T_2-2T_1T_2T_3+2T_3+T_3^2(T_2-T_1).
\end{aligned}$$

From (19) it is transparent that we shall get temperature-independent results so long as s_1 and s_2 are large enough to yield $T_1=T_2=1$. For $m=1{\cdot}5$ GeV and $C_c=g^2/m^{2{\cdot}5}=0{\cdot}1$, this is found to be so for T up to about 10^{11} K. For temperatures exceeding this, we resort to the high-temperature approximation, viz.,

$$T_3=\tanh(\tilde{k}^2)=\tilde{k}^2. \tag{20}$$

On retaining terms to order $\tilde{k}^2$, (19) is given by

$$\frac{\alpha(1+k^2)^{1/2}(k^2-\gamma^2)[T_1\,T_2+\tilde{k}^2(T_1-T_2)]}{[s_1\,T_1+s_2\,T_2+\tilde{k}^2\{(s_2-s_1)(1-T_1\,T_2)+T_2-T_1\}]}$$
$$=\frac{\alpha[-T_1\,T_2\gamma^2+k^2\{-(1/4)m\beta\gamma^2(T_1-T_2)+(1-\gamma^2/2)\,T_1\,T_2\}]}{u_1[1+(1/4)u_2 m\beta k^2/u_1]} \tag{21}$$

where we have assumed the kinematics to be nonrelativistic ($k \ll 1$), and have set

$$u_1 = s_1\,T_1 + s_2\,T_2$$
$$u_2 = (s_2-s_1)(1-T_1\,T_2)+T_2-T_1. \tag{22}$$

Substitution of (21) into (16) yields a Schrödinger equation with a rational potential. Note that if it should turn out that

$$u = (u_2/u_1)(m\beta k^2/4) \ll 1 \tag{23}$$

for the values of m, g and T of interest, then (21) can be cast into a particularly simple form:

$$\text{RHS of (16)} = -Q^2 + \Lambda^2 k^2, \tag{24}$$

where

$$Q^2 = \alpha T_1\,T_2\gamma^2/u_1 \tag{25}$$

and

$$\Lambda^2 = (\alpha/u_1)[(1/4)m\beta\gamma^2(u_2\,T_1\,T_2/u_1+T_2-T_1)+T_1\,T_2(1-\gamma^2/2)]. \tag{26}$$

From (16) and (24) we therefore obtain

$$\chi_l''(k)+[Q^2-\Lambda^2k^2-l(l+1)/k^2]\chi_l(k)=0, \tag{27}$$

which is readily recognized as the Schrödinger equation for the (energy-dependent) spherical oscillator potential. The energy eigenvalues of (27) may be numerically obtained from

$$Q^2/(2\Lambda) = (n+3/2); \tag{28}$$

the eigenfunctions of the equation being given by

$$\chi_{n,l} \sim {}_1F_1(-n_r, l+3/2; \Lambda k^2), \tag{29}$$

where $n_r = (n-1)/2$.

Equation (16)—together with (19) and (27)—enables us to study the model under consideration over a wide range of temperatures. We have done so for several choices of m (e.g., $m = 5, 10$ MeV and 1·5 GeV) and the dimensionless coupling constant $C_c = g/m^{2\cdot5}$ (e.g., $C_0 = 0{\cdot}001$ to 1·0). The consistency of our approximations has been checked by calculating the expectation value of

$$\langle k^2\rangle_n = \langle \beta p^2/(4m)\rangle_n = (2n+3)(\beta m/8\Lambda). \tag{30}$$

From (30) the validity of (20) can be directly checked; also we can now calculate u and hence check the accuracy of the approximation made in (23). Indeed, for a fixed m, one may not expect our approximations to be valid for all values of C_c. The general features of the temperature-generalized model considered by us are:

(a) For any chosen value of m, there exists an upper limit for C_c up to which our approximations, viz., (20) and (23) are valid.
(b) For any admissible values of m and C_c there exists a certain temperature T up to which the model admits solutions which differ little from the corresponding solutions for the $T = 0$ model. For $m = 1{\cdot}5$ GeV and $C_c = 0{\cdot}001$, for which we present our results in table 1 as an illustration, T_c is of the order of 10^9 K.
(c) For $T > T_c$, the energy eigenvalues of the system increase with temperature. This result is consistent with the accepted view that the force between the quarks, or the "spring constant", increases with their separation since—after a threshold temperature (T_c)—one would expect the separation between the constituents of our system to increase.
(d) We have restricted our study of the model up to a temperature T for which $k_B T < m$, since it would be clearly inadmissible to trust the results of a nonrelativistic approach beyond this temperature.
(e) For values of C_c for which the approximation made in (23) does not hold, one must indeed resort to a study of the Schrödinger equation with the rational potential, viz., (21).

4. Concluding remarks

a) That the use of the recipe given in (8) enables one to obtain the analytic expression for any $T \neq 0$ Feynman diagram from its $T = 0$ counterpart is familiar to most workers

Table 1. The first ten energy eigenvalues of the temperature-generalized model for $m = 1500$ MeV and $C_c = 0{\cdot}001$ at different temperatures. The final entries in each column correspond, for the $n = 0$ state, to the values of $\langle \tilde{k}^2 \rangle$ and u [see eqs (20) and (23)], respectively.

Temp(K)	$0 - 1 \times 10^9$	1×10^{10}	1×10^{11}	1×10^{12}	1×10^{13}
n			E_n(MeV)		
0	3003·179	3004·164	3008·858	3019·051	3040·895
1	3005·294	3006·012	3012·445	3026·746	3057·331
2	3007·406	3007·837	3015·569	3033·434	3071·579
3	3009·516	3009·737	3018·404	3039·492	3084·455
4	3011·622	3011·723	3021·036	3045·103	3096·356
5	3013·726	3013·767	3023·516	3050·373	3107·510
6	3015·826	3015·842	3025·874	3055·369	3118·062
7	3017·924	3017·930	3028·136	3060·139	3128·131
8	3020·018	3020·020	3030·316	3064·719	3137·775
9	3022·110	3022·111	3032·429	3069·133	3147·058
$\langle \tilde{k}^2 \rangle$, u		0·42, 0·07	0·07, 0·05	0·01, 0·01	0·003, 0·005,

in condensed matter physics/finite temperature field theory (for a brief description of the origin of the recipe, we refer the reader to [22]). What we have been concerned with in this paper is the temperature-generalization of an *integral equation*, which incorporates not only the sum of a class of Feynman diagrams, but also the (to be determined) Bethe-Salpeter wavefunction. That the recipe should suffice for this purpose is, perhaps, not clear. One might therefore desire that an *ab initio* derivation of the $T \neq 0$ Bethe-Salpeter equation be attempted to check if, in fact, the use of the recipe yields the same equation. Such an exercise has already been done for the Bethe-Salpeter equation for the bound states of a many electron-proton system [19]: it relies on the familiar property of periodicity of the Green's functions in the variable $\tau(= i\beta)$, and the homogeneity of the medium; it does not require any additional assumptions. The result is, of course, that the $T \neq 0$ equation derived from first principles agrees with the $T \neq 0$ equation obtained via the well-known recipe used by us [22]. We note that a careful interpretation of the thermal Bethe-Salpeter equation has been given in the text.

b) It seems worthwhile to draw attention to somewhat different frameworks within which the effect of temperature on hadron properties has been recently investigated. Bernard and Meissner [12], for example, use the topological chiral soliton model based on a nonlinear meson theory of interacting pions (ρ-and w- mesons) for the description of the nucleon. The nucleon properties are determined by the mesonic parameters. For the temperature-dependence of these meson parameters, they use rigorous results from chiral perturbanon theory as well as predictions from the Nambu-Jona-Lasinio model. Another approach to the problem employs the Monte Carlo methods to study SU(2) Yang-Mills theory on a lattice at finite temperature [25, 26, 27]. In each of these investigations a physical property of primary interest is the temperature which marks the transition between the unconfined and the confined phases. Indeed, the signal of this transition is different in the two approaches. Thus, Bernard and Meissner [12] find that close to a certain temperature, the effective nucleon mass decreases sharply and the baryon charge is spread out. Eventually, nucleons lose their individual character, which is taken to be the signal of deconfinement. Kuti *et al* [26], on the other hand, distinguish the two phases by the different behaviours of a correlation function defined in terms of thermal Wilson loops. Interestingly enough, the transition temperatures in the two approaches are, respectively, 180 MeV and 160 ± 30 MeV. These translate to about 10^{12} K. If we interpret the temperature regime in which our bound state system has non-constant energy eigenvalues as the unconfined phase, the corresponding temperature in our approach is of the order of 10^{11} K for $C_c = 0{\cdot}1$.

c) The incorporation of chemical potential into the model has been discussed in the text; it is easy to see that while it will shift the spectrum of bound state eigenvalues, it will not alter the general features of the solutions obtained by us. Work is currently in progress to study the effect of temperature and chemical potential in bringing about the deconfining phase.

d) That the elementary particles had a 'nomadic' phase before they found their niche seems to be a rather interesting result; see also [12] in this connection. We note that we have been led to it by following an approach which incorporates temperature in the dynamics itself. It seems pertinent to conclude by drawing attention to what seem to be significant results obtained by following the same approach in another field, viz., astrophysical plasmas [21–24].

Acknowledgements

The authors would like to thank Professors L K Pande, S R Chaudhuri, Deepak Kumar, Ashok Goyal and J Subba Rao for useful discussions.

References

[1] A Einstein, *Sidelights on Relativity* (Dover, New York, 1983)
[2] F Hoyle, *Astrophys. Space Sci.* **168**, 59 (1990)
[3] L Castell, In *Quantum theory and gravitation* edited by A R Marlow (Academic, New York, 1980) p. 147
[4] C Quigg and J L Rossner, *Phys. Rep.* **56**, 167 (1976)
[5] H J W Muller-Kirsten, SLAC-PUB 1525(T) (1975)
[6] C Alabiso and G Schierholz, *Nucl. Phys.* **B126**, 461 (1977)
[7] J R Henley, *Phys. Rev.* **D20**, 2532 (1979)
[8] V Bernard and U-G Meissner, *Nucl. Phys.* **A489**, 647 (1988) and references therein
[9] A Kovick, *Phys. Rev.* **D33**, 1785 (1986)
[10] V Bernard, U-G Meissner and I Zahed, *Phys. Rev.* **D36**, 819 (1987)
[11] T Hatsuda and T Kunihiro, *Phys. Lett.* **B198**, 819 (1987)
[12] V Bernard and Ù-G Meissner, *Ann. Phys.* **206**, 50 (1991)
[13] S N Biswas, K Datta and Ashok Goyal, *Phys. Rev.* **D25** (1982) 2199
[14] D A Kirzhnits, *Field theoretical methods in many-body systems* (Pergamon, New York, 1967)
[15] A D Linde, *Rep. Prog. Phys.* **42**, 389 (1979)
[16] L Dolan and R Jackiw, *Phys. Rev.* **D9**, 3320 (1974)
[17] G P Malik and L K Pande, *Phys. Rev.* **D37**, 3742 (1988)
[18] L P Kadanoff and G Bayme, *Quantum statistical mechanics – Green's function methods* (Benjamin, New York, 1962)
[19] L K Pande, *Pramana – J. Phys.* **37**, 39 (1991)
[20] J F Donoghue, B R Holstein and R W Robinett, *Ann. Phys. (N.Y.)* **164**, 233 (1985)
[21] G P Malik, L K Pande and V S Varma, *Pramana – J. Phys.* **32**, L89 (1989)
[22] G P Malik, L K Pande and V S Varma, *Astrophys. J.* **379**, 788 (1991)
[23] G P Malik, U Malik and V S Varma, *Astrophys. Space Sci.* **199**, 299 (1993)
[24] G P Malik, U Malik, L K Pande and V S Varma, *Astrophys. J.* (to appear)
[25] L D Mclerran and B Svetitsky, *Phys. Lett.* **B98**, 195 (1981)
[26] J Kuti, J Polonyl and K Szlachanyl, *Phys. Lett.* **B98**, 199 (1981)
[27] J Engels, F Karsch, H Satz and I Montvay, *Phys. Lett.* **B101**, 89 (1981)

PRAMANA
— journal of
physics

© Printed in India

Vol. 43, No. 6,
December 1994
pp. 453–465

New answer to the solar neutrino problem

MARC DIXMIER
15 rue Le Brun, 75013 Paris, France

MS received 23 June 1993; revised 4 July 1994.

Abstract. We suggest a new answer to the problem of the solar neutrinos: a neutrino-photon interaction that would cause the neutrinos to disappear before they leave the sun or make them lose energy towards detection thresholds. We calculate the available energy in the system of the centre of mass, and show that the photons may be endowed with a pseudo-cross-section in the system of the sun. Under the assumption of an absorption, made to simplify the neutrino transport calculation, the chlorine experiment yields: $\sigma_a = 1{\cdot}8(^{+0{\cdot}7}_{-1{\cdot}0}) * 10^{-9}$ barn, which is close to $g_\beta/(\hbar c) = 4{\cdot}49 * 10^{-9}$ barn. The escape probability is substantially larger for the gallium neutrinos than for the chlorine neutrinos. Thermal radiation in the core of a supernova is suppressed by electrical conductivity, therefore the neutrinos from SN1987A could escape; they interacted with the photon piston in the outer layers of the supernova and the interaction has to be a scattering. The cosmological implications of a neutrino-photon interaction are discussed; Hubble's constant may have to be modified. The case of an elastic scattering between neutrino and photon is discussed in more detail.

Keywords. Solar neutrino; neutrino-photon interactions; supernova; cosmology.

PACS Nos 96·60; 13·15; 97·60; 98·80

1. Introduction

The solar neutrino problem consists of the fact that the counting rate of the neutrinos detected on earth via the reaction $^{37}Cl(\nu_e, e^-)^{37}$ Ar is only about 28% of the rate predicted from the standard solar model [1]. More recently, experiments using the reaction $^{71}Ga(\nu_e, e^-)^{71}Ge$, which has a lower detection threshold, also indicate an important deficit in the counting rate of the solar neutrinos [2]. Various solutions have been proposed to this puzzle (see for instance [3]). This article intends to suggest a new solution: a *neutrino-photon interaction* that would cause the absorption of part of the neutrinos during their passage through the sun or, which amounts to the same from the viewpoint of measurements of earth, the simple or multiple scattering of those neutrinos, thereby transporting them to energies for which the detection cross-section is smaller or null; since the photon densities which exist outside the sun itself are very small the property according to which neutrinos propagate freely, as observed on earth, would not be modified.

The standard model of the electroweak interaction conserves the photon couplings of classical electromagnetism and therefore within this model the photon field is not coupled with the neutrino field ([4], chap. 5). This would not preclude a neutrino-photon interaction via a neutrino magnetic moment; however, a calculation by Aydin *et al* [5] indicates that the resulting scattering cross-section would be extremely small,

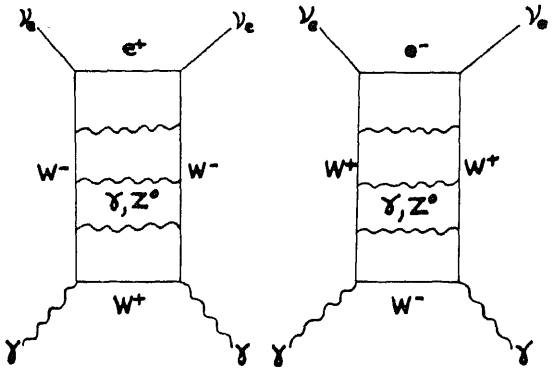

Figure 1. Possible Feynman diagrams of the neutrino-photon interaction.

considering the upper limits on the magnetic moment of the neutrino from astrophysics and from neutrino-electron scattering [6].

Cohen-Tannoudji suggested to us [7] that if the two W bosons exchanged between ν_e and γ in the diagrams of figure 1 were strongly coupled the $\nu_e - \gamma$ interaction would become a first-order process and could therefore give rise to a substantial cross-section (the existence of such strongly coupled pairs of W bosons has already been suggested by Chanowitz in his strong-coupling hypothesis to account for electroweak symmetry breaking, see [8], figure 2b). Das [9] has also shown that a spontaneous breaking of supersymmetry would lead to a neutrino-photon coupling.

The neutrino-photon weak coupling theory of Bandyopadhyay, Chaudhuri *et al* (see for instance Bandyopadhyay [10, 11a]) could also lead logically to a neutrino-photon interaction; it is to be noted, though, that according to Stothers [12] this theory is excluded by the astrophysical evidence regarding the cooling rates of white dwarfs and red supergiants, but a neutrino-photon interaction such as we assume in this article might reduce the impact of Stothers' argument.

Finally it should be observed that, within (stellar) plasmas, photons become plasmons endowed with rest mass, thereby allowing processes such as $\gamma \to \nu + \bar{\nu}$ to take place [13].

In this article, we shall speculate no further on the possible causes of our postulated interaction but shall estimate the order of magnitude of the pseudo-cross-section that this interaction should have in order to account for the solar neutrino counting deficit, and shall speculate briefly on some other astrophysical implications of such an interaction.

2. Basics

2.1 *Black body radiation in vacuo*

Within an empty parallelepipedic box of volume V, the number of states for photons of energy comprised within the interval $(E_\gamma, E_\gamma + \mathrm{d}E_\gamma)$ amounts to

$$\mathrm{d}N_\gamma = \frac{8\pi}{(hc)^3} V E_\gamma^2 \mathrm{d}E_\gamma. \tag{1}$$

Let us write

$$x = \frac{E_\gamma}{kT} \tag{2}$$

where k is the Boltzmann constant and T is the absolute temperature. The spectrum of the number of photons in vacuo assumes the form

$$p(x) = \frac{1}{2\zeta(3)} \frac{x^2}{e^x - 1} \tag{3}$$

and the corresponding number density of photons is [14]

$$n_\gamma = \rho T^3 \tag{4}$$

$$\rho = 16\pi\zeta(3)\left(\frac{k}{hc}\right)^3 = 2{\cdot}0286(2)^*10^7\, \gamma m^{-3}\, \mathrm{K}^{-3}. \tag{5}$$

The model of black body radiation in vacuo is currently in use, for instance in [16], to compute pressures and radiative heat transfer within stars. We shall use this model to evaluate the photon population within the sun; we shall see however in § 4 that this model is no longer valid in the central regions of a supernova.

2.2 *Kinematics of the neutrino-photon interaction*

Since we are considering the interaction between two particles that propagate at limit velocity (we may neglect a possible rest mass of the neutrino within the energy domain considered [17]) we cannot as usual take for granted a reaction rate relative to the target density in the co-ordinate system of the centre of mass of the two particles.

Let $\mathbf{p}$ be the linear momentum of a particle and let E be its total energy, which boils down to its kinetic energy in the problem under discussion. Let us consider a neutrino and a photon with their directions of motion making an angle ψ in the non-primed co-ordinate system (co-ordinate system of the sun): see figure 2. The velocity of the centre of mass of the two particles is

$$\mathbf{v} = c\frac{\mathbf{p}_{\nu_e} + \mathbf{p}_\gamma}{\mathrm{p}_{\nu_e} + \mathrm{p}_\gamma}. \tag{6}$$

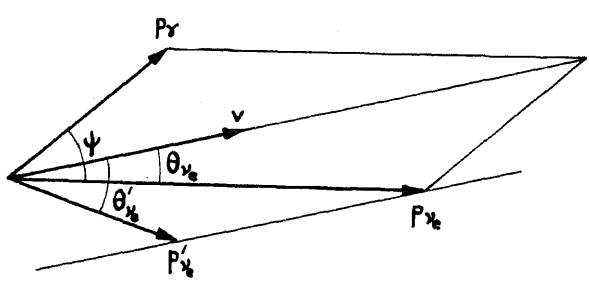

Figure 2. Kinematics of the neutrino-photon interaction: $\mathbf{p}_{\nu_e}$ = linear momentum of the neutrino in the co-ordinate system of the Sun; $\mathbf{p}_\gamma$ = linear momentum of the photon in the same system; $\mathbf{v}$ = velocity of the centre of mass (system); $\mathbf{p}'_{\nu_e}$ = linear momentum of the neutrino in that system.

Excluding the physically impossible case in which the neutrino and the photon move exactly in the same direction,

$$\beta = \frac{|\mathbf{v}|}{c} < 1 \tag{7}$$

and the passage to the new co-ordinate system is allowed.
Calculating $|\mathbf{v}|^2$, we find:

$$\beta = \left[1 - \frac{2p_{\nu_e}p_\gamma}{(p_{\nu_e}+p_\gamma)^2}(1-\cos\psi)\right]^{1/2}, \tag{8}$$

$$(1-\beta^2)^{1/2} = \frac{[2p_{\nu_e}p_\gamma(1-\cos\psi)]^{1/2}}{p_{\nu_e}+p_\gamma}. \tag{9}$$

Let θ_{ν_e} be the angle between $\mathbf{v}$ and the direction of motion of the neutrino, angle which is contained in the direction of planes defined by $\mathbf{p}_{\nu_e}$ and $\mathbf{p}_\gamma$; we have

$$\theta_{\nu_e} = \cos^{-1}\frac{p_{\nu_e}+p_\gamma\cos\psi}{[(p_{\nu_e})^2+(p_\gamma)^2+2p_{\nu_e}p_\gamma\cos\psi]^{1/2}} \tag{10}$$

The direction of $\mathbf{v}$ is completely defined by this formula and by the fact that $\mathbf{v}$ must be contained within the angle formed by $\mathbf{p}_{\nu_e}$ and $\mathbf{p}_\gamma$. Let us then define the **Ox** axis of the non-primed co-ordinate system as parallel to $\mathbf{v}$ and in the same sense, so that $v = |\mathbf{v}|$ in the adjunct Lorentz transform; then, E'_{ν_e} being the total energy of the neutrino in the co-ordinate system of the centre of mass (primed co-ordinate system), we find

$$E'_{\nu_e} = c\left[\frac{p_{\nu_e}p_\gamma(1-\cos\psi)}{2}\right]^{1/2} \tag{11}$$

and

$$E'_\gamma = E'_{\nu_e} \tag{12}$$

as expected for particles with an equal rest mass, and the available energy is

$$E'_G = [2(1-\cos\psi)E_{\nu_e}E_\gamma]^{1/2}. \tag{13}$$

For the component of $\mathbf{p}'_{\nu_e}$ along the axis **Ox'**, the adjunct Lorentz transform provides

$$p'_{\nu_e,x} = \frac{(1-\beta^2)^{1/2}}{\beta}\frac{p_{\nu_e}-p_\gamma}{2} \tag{14}$$

and

$$p'_{\gamma,x} = -p'_{\nu_e,x}. \tag{15}$$

Let now θ'_{ν_e} be the angle between the axis **Ox'** and the direction of motion of the neutrino in the co-ordinate system of the centre of mass; we have

$$\theta'_{\nu_e} = \cos^{-1}\frac{p_{\nu_e}-p_\gamma}{[(p_{\nu_e})^2+(p_\gamma)^2+2p_{\nu_e}p_\gamma\cos\psi]^{1/2}}. \tag{16}$$

The direction of $\mathbf{p}'_{\nu_e}$ is completely defined by this formula and by the fact that $\mathbf{p}'_{\nu_e}$

Table 1. Estimate $(2kTE_{\nu_e})^{1/2}$ of the available energy in the system of the centre of mass of ν_e and γ, in KeV, as a function of the energy of the neutrino in MeV and of the temperature of the medium in million degree Kelvin.

T \ E_{ν_e}	0·2	0·5	2	10
1	6	9	19	42
5	13	21	42	93
15	23	36	72	161

must be on the same side of $\mathbf{v}$ as $\mathbf{p}_{\nu_e}$; $\mathbf{p}'_{\nu_e}$ is located in the forward or backward hemisphere when $E_{\nu_e} > E_\gamma$ or $E_{\nu_e} < E_\gamma$.

For a crude estimate of the available energy let us take $\cos\psi = 0$ and $E_\gamma = kT$ in (13); we are thus led to table 1, which shows that E'_G usually is in the order of the tens of keV.

In the absence of data about the nature of a neutrino-photon interaction, we cannot undertake a computation of the angular distribution of the reaction products; however, the case of an elastic scattering has been investigated in the Appendix.

As for each of the reaction rates that the total reaction rate must comprise, we may write it down, in the center-of-mass co-ordinate system, under the form

$$\tau'_{\nu_e} = \sigma(E'_G)cn'_\gamma \tag{17}$$

where τ'_{ν_e} is the reaction rate, σ has the dimension of a cross-section, c is the velocity of light and n'_γ is the density, in the centre-of-mass co-ordinate system, of the photons having a typical energy E_γ and making a typical angle ψ with the neutrino motion in the co-ordinate system of the sun; σ must of course be averaged on the possible states of polarization of the photon and over the possible states of relative angular momentum.

When transposing the reaction rate from the centre-of-mass co-ordinate system to the co-ordinate system of the sun one has to apply a factor $(1-\beta^2)^{1/2}$ because of time dilation, but the target density has to be reduced by the same factor (it is higher in the c.m. co-ordinate system because of proper length contraction) so that the reaction rate relative to the target density, σc, is conserved. Since the neutrino always propagates at velocity c, we may compute its interaction probability in the co-ordinate system of the sun as if the photons encountered by the neutrino were endowed with the "cross-section" $\sigma(E'_G)$ in that co-ordinate system.

3. Application to solar neutrino attenuation

As for the standard solar model, we shall rely on the tables of values given in ([16], chap. 3, § 8) after a book by M. Schwarzschild. We need to know temperature as a function of radius, from which the number density of photons can be obtained through (4), and the relevant neutrino source as a function of radius. As for the total neutrino source, in a star such as the sun it is proportional to the fusion power density. The data of [16] only give the local power deposit, not taking into account the neutrinos, but the difference is negligible for the simplified calculation that we intend to achieve (let us however observe that following our hypothesis the neutrino interactions must

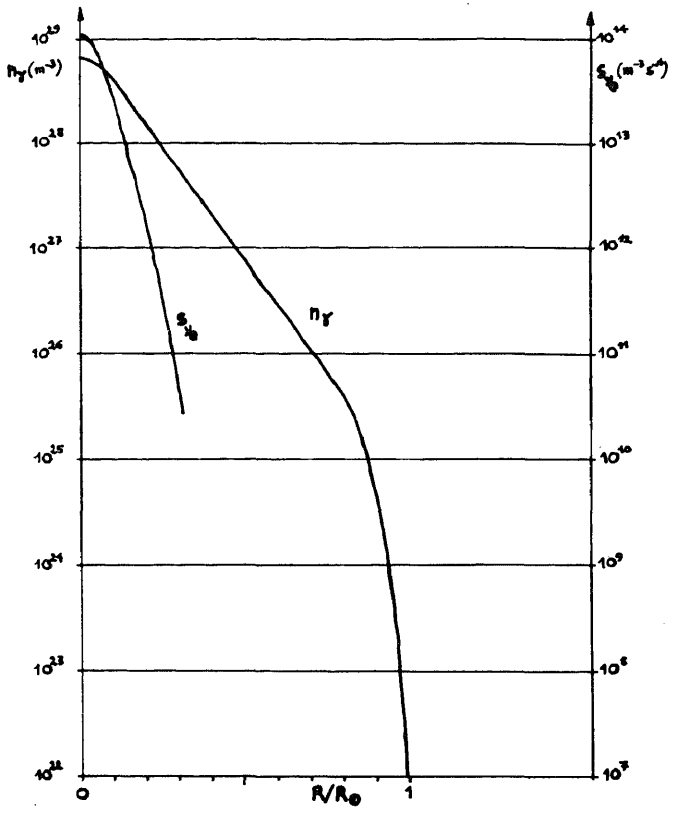

Figure 3. Photon number density and neutrino source density as functions of the distance from the centre of the Sun (standard model).

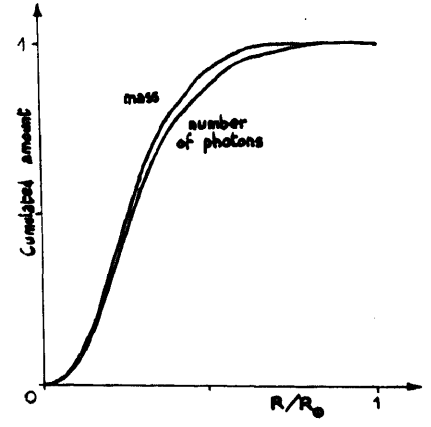

Figure 4. Integrated distributions of the mass and of the number of photons as functions of the distance from the centre of the sun (standard model; curve for mass is from [16], figure 3–3).

produce an additional energy deposit, noticeably in the peripheral layers of the star, that could somewhat modify the solar model; we shall return to this issue in § 4).

Figure 3 represents the total neutrino source density and the photon number density as functions of the radius. In figure 4, one can see that the radial distribution of photons within the sun is roughly proportional to the radial distribution of mass and that nearly all the photons, as well as nearly all the mass, are contained within a sphere of radius $0{\cdot}7 * R_{\odot}$; we find that the total number of photons within the sun is $1{\cdot}10 * 10^{54}$ whereas the total number of matter particles (electrons and nuclei) is $1{\cdot}94 * 10^{57}$, or 1 photon per 1760 matter particles.

Figure 3 shows than the total neutrino source is much more concentrated near the centre of the sun than the photon distribution is, and J N Bahcall *et al* ([1], table 7) have shown that this is even truer of the high-energy neutrino sources. Since the escape probability P_0 of a neutrino must have a minimum at the centre of the sun, it is therefore stationary around this point and a good approximation for computing the average value of P_0 will be to assume that all high-energy neutrinos are being emitted at the very centre of the sun. In the absence of data about the neutrino-photon interaction we shall assume it to be an absorption in order to simplify the neutrino transport calculation, which then boils down to an integration (although we shall see in § 4 that the real interaction has to be a scattering), and, since (13) shows that the available energy E'_G is not extremely variable, we shall attribute to the photons an average pseudo-cross-section independent of the temperature of the medium as well as of the energy of the neutrinos; this will at least provide us with an order of magnitude of the total pseudo-cross-section to account for solar neutrino attenuation. The escape probability of the high-energy neutrinos is therefore

$$\bar{P}_0 \cong \exp\left(-\sigma_a \int_0^{R_\odot} n_\gamma(R)\mathrm{d}R\right) \tag{18}$$

According to Bahcall *et al* [1], the neutrino source of the sun without attenuation, as detected by ^{37}Cl nuclei, is worth $(7{\cdot}6 \pm 3{\cdot}3)$ SNU [20], whereas the experiment on earth detects $(2{\cdot}1 \pm 0{\cdot}3)$ SNU [21]; therefore

$$\bar{P}_0 = 0{\cdot}28^{+0{\cdot}28}_{-0{\cdot}11} \tag{19}$$

Since

$$\int_0^{R_\odot} n_\gamma(R)\mathrm{d}R = 7{\cdot}18 * 10^{36}\,\gamma m^{-2} \tag{20}$$

there comes {20}:

$$\sigma_a \cong 1{\cdot}8\left(^{+0{\cdot}7}_{-1{\cdot}0}\right) * 10^{-9}\,\text{barn}. \tag{21}$$

As for the attenuation of the total neutrino source, a finite-difference computer calculation enabled us to find the corresponding $\bar{P}_0$ as a function of σ_a. This curve is shown in figure 5; with the above range of values for σ_a, there comes

$$\bar{P}_0 = 0{\cdot}41^{+0{\cdot}25}_{-0{\cdot}21} \tag{22}$$

This could account for the apparently higher rate of capture of neutrinos by ^{71}Ga in the preliminary results of the gallium experiments [2].

If we consider the physical coefficient g_β in the Hamiltonian of β disintegration

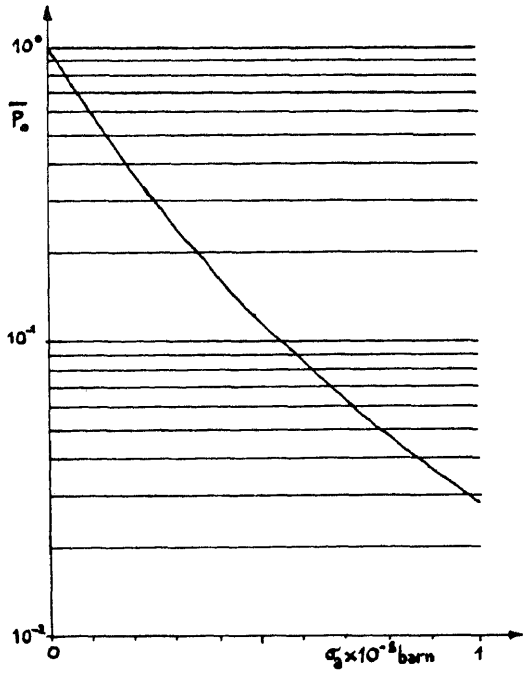

Figure 5. Average probability for a neutrino to leave the sun as function of the pseudo-cross-section of the photon, in the case of an absorption.

([22], chap. 15, § 6) we may deduce a quantity σ' having the dimension of a cross-section

$$\sigma' = \frac{g_\beta}{\hbar c} = 4{\cdot}485(13) * 10^{-9}\,\text{barn} \tag{23}$$

which is very close to σ_a; we believe that this unlikely coincidence is a strong argument in favour of our hypothesis.

The idea of a neutrino-photon interaction is reminiscent of the Compton effect and suggests the idea of a neutrino that would only be a neutral electron [23]; the Thomson cross-section is of course much larger than σ'.

4. Application to supernova SN1987A

In a star such as the sun, the inferior cut-off energy of the plasma for electromagnetic waves

$$E_p = \hbar e \left(\frac{n_e}{\varepsilon_0 m_e} \right)^{1/2} \tag{24}$$

(ε_o being the vacuum permittivity, n_e the electron density and m_e the electron mass) is always small when compared to kT: using the data of Kourganoff [16] we find that, at the centre of the sun, $E_p = 0{\cdot}29\,\text{keV}$ and $kT = 1{\cdot}26\,\text{keV}$; at $R/R_\odot = 0{\cdot}3$, $E_p = 0{\cdot}097\,\text{keV}$ and $kT = 0{\cdot}59\,\text{keV}$; at $R/R_\odot = 0{\cdot}7$, $E_p = 0{\cdot}0093\,\text{keV}$ and $kT = 0{\cdot}16$

keV. But such is not the case inside a supernova, where the cut-off energy becomes much larger than kT. Consider first the centre of a pre-supernova of 15 solar masses ([24], figure 1): for temperature $T = 7{\cdot}62*10^9$ K and density $d = 9{\cdot}95*10^{12}$ kg m^{-3}, assuming for the sake of simplicity totally ionized ^{56}Fe, there comes :$E_p = 1{\cdot}96$ MeV and $kT = 0{\cdot}66$ MeV. Away from the centre E_p decreases with respect to kT. Both become equal to 0·56 MeV at a radius of 560 km enclosing 0·85 solar mass; after that E_p fast becomes much smaller than kT. Consider next, after the implosion has occurred, a neutron star at the density of nuclear matter, or $3*10^{17}$ kg m^{-3}, but with still 25% of protons ([25]; the assumption on the relative concentration of protons, which falls to 5% in a star that has cooled off, is not essential), there comes: $E_p =$ 250 MeV, whereas kT may be of the order of 10 MeV.

These are about the conditions that exist in the core of a supernova after collapse [24]; therefore the density of photons even at thermal equilibrium must be very small. However the conditions at the so-called neutrinosphere, about 40 km from the centre, are relatively softer: $kT \sim 5$ MeV and $d \sim 10^{14}$ kg m^{-3} [24] which with the very crude approximation of totally ionized ^{56}Fe gives $E_p = 6{\cdot}2$ MeV; therefore the photon density, although smaller than that of black body radiation in vacuo, can be up to the same order of magnitude.

Let us assume that the absorption pseudo-cross-section that we have already found to account for the solar neutrino deficit still holds although we are now dealing with hard photons and hard neutrinos and anti-neutrinos (what follows would not necessarily apply to other neutrino flavours than that of the electron). From (4) and (21), assuming black-body radiation in vacuo and neglecting the flow velocity of stellar matter, the locally defined mean-free-path of the neutrinos, considering only their interaction with the photons, is

$$\Lambda = (\sigma_a \rho T^3)^{-1} \sim (6{\cdot}5 \times 10^9/T)^3. \tag{25}$$

At the centre of the sun we would have $\Lambda = 88{,}000$ km. For $kT = 5$ MeV we have $\Lambda = 1{\cdot}4$ mm; for $kT = 1$ MeV, $\Lambda = 176$ mm; for $kT = 100$ keV, $\Lambda = 176$ m; for $kT = 10$ keV, $\Lambda = 176$ km and for $kT = 1$ keV, $\Lambda = 176{,}000$ km.

The neutrinos can actually leave the star since they have been observed in the case of SN1987A [26, 27] therefore their interaction with the photons must be a scattering. This would not preclude $\bar{\nu}_e$ detection on earth since we are dealing with hard neutrinos, of the order of tens of MeV on arrival.

What will therefore happen is that the ν_e emitted through electronic capture on nuclei in the core matter and the $\nu, \bar{\nu}$ (or at least the $\nu_e, \bar{\nu}_e$) emitted during the cooling-off of the core will push on the stellar matter, via the photon distribution within that matter, at a radius of the order of but smaller than that of the so-called neutrinosphere, and expel the outer layers of the star with tremendous energy. These neutrinos as well as those trapped inside the ejecta will finally be released when the ejecta cool off or are dispersed, and will rejoin in outer space those which have already been able to diffuse through the outer layers of the star (thus contributing in their own way to the ejection process). All these must have contributed to the time spread of about 10 s of the neutrino burst detected on earth. Here is a new answer to the puzzle of how the explosion of type II supernovae is at all possible [28].

One should observe that the introduction of a cut-off energy for the photons tends to reduce radiation pressure and, which is more important, radiative heat transfer; a complete study of this problem would also take into account the presence of a general magnetic field and the role of the polarons.

5. Other implications of a neutrino-photon interaction

It suffices to look at the value of the optical thickness in (20) to understand that a neutrino-photon interaction cannot be directly observed on earth, even using a powerful focussed laser beam. One should rather count on the discovery of a sub-nuclear reaction in which that interaction would be an intermediate step or hope for a theoretical prediction that would also account for the agreement between σ_a and σ'. One should also look at the consequences of such an interaction for stellar balance and stellar evolution in general.

On the other hand, a neutrino-photon interaction may have important consequences in cosmology. For instance, let us consider a photon from the big bang which has been travelling through space since the origin of our universe; let us assume that this photon encounters along its way the current density of primordial ν_e and $\bar{\nu}_e$, estimated at $1{\cdot}1*10^8\ \nu\,\mathrm{m}^{-3}$ [29]. The optical thickness of the neutrinos encountered by this photon will then be about

$$\frac{2}{3}\frac{cn_\nu}{H_0} = 9*10^{33}\ \nu\,\mathrm{m}^{-2} \tag{26}$$

where H_0 is Hubble's constant, taken by us to be $\cong 75$ km/(s Mpc). Since the kinematics before the interaction are symmetrical between photon and neutrino—still assuming the rest masses to be negligible—if we apply bluntly the cross-section found in § 3 to $\bar{\nu}_e$ as well as ν_e, we find that the photon has 0·16% chances to interact with a neutrino before reaching us. The probability of interaction is, in fact, much higher and even infinite, since the density of primordial neutrinos in the aged universe decreases as $[\mathscr{R}(t)]^{-3}$, $\mathscr{R}(t)$ being the radius of the universe at age t. Of course, one should also take into account the other neutrino flavours.

It is to be noted that if the photon-neutrino interaction is an elastic scattering the neutrino population of the universe will stay in thermal equilibrium with its photon population well after it has ceased to be coupled with nuclei.

It general, there would be an attenuation of the photons coming from far-remote sources which should lead to a reassessment of Hubble's constant, leading to an increase in its value since the distance of the sources would currently be overestimated.

On the other hand, it has been observed that, if the rest mass of the neutrinos is larger than $1\ \mathrm{eV}/c^2$, they may be captured by the gravitational field of galaxies [29]. Karoji *et al* have discovered an excess redshift for the light sources that are visible through galactic clusters [30]. To explain this effect, these authors rule out summarily the idea of a neutrino-photon interaction; however, as they themselves notice, the type of interaction required to explain this excess redshift without suppressing the punctual appearance of the sources is a scattering with a very large cross-section and a very small exchange of transverse momentum. If this was by any chance the case, Hubble's constant would have to be strongly reduced with respect to the currently accepted values.

6. Conclusion

In this article, we propose a new answer to the problem of the sub-detection of the solar neutrinos: a neutrino-photon interaction which would cause the neutrinos to

disappear before they leave the sun or which would make them lose energy. The assumption of an absorption, made to simplify the transport calculation, leads to: $\sigma_a \cong 1{\cdot}8{*}10^{-9}$ barn, in striking agreement with the quantity of the same dimension deduced from the Hamiltonian of β disintegration. The detection probability is substantially larger for the gallium than for the chlorine neutrinos. The observation of the neutrinos from SN1987A does not contradict our hypothesis since thermal radiation is strongly suppressed in the core of a supernova by the electrical conductivity of the medium; the neutrinos interact with the photon piston present in the outer layers of the supernova, thus contributing to their ejection, and the interaction must definitely be a scattering. Our interaction is difficult to observe on earth but it has important implications in astrophysics and cosmology. Word is now to the theoreticians.

Acknowledgements

The author thanks Dr C Thomas de Montpreville for his help with the computer calculations and the bibliographic search for this article. He also thanks the referee for bringing his attention on to new aspects of the supernova problem.

Appendix

Elastic scattering between a neutrino and a photon

As announced in § 2·2 we are going to investigate the case of an elastic scattering, analogous with the Compton effect. Let $\mathbf{q}'_{\nu_e}$ be the kinetic momentum of the neutrino in the c.m. system after the interaction has taken place ($\mathbf{q}'_{\nu_e}$ need not be contained within the plane of figure 2) and let F'_{ν_e} be the corresponding energy, which must be equal to E'_{ν_e} in this case; finally, let ι'_{ν_e} be the angle between $\mathbf{q}'_{\nu_e}$ and $\mathbf{v}$. Let $\mathbf{q}_{\nu_e}$, F_{ν_e} and ι'_{ν_e} be the corresponding elements in the system of the sun. The adjunct Lorentz transform yields

$$\cos \iota_{\nu_e} = \frac{\cos \iota'_{\nu_e} + \beta}{1 + \beta \cos \iota'_{\nu_e}} \tag{A1}$$

If all the domain of values of ι'_{ν_e} is covered the same is true for ι_{ν_e}; of course, for ι_{ν_e}, the forward domain of directions with respect to $\mathbf{v}$ is favoured.

Table 2. Energy of the neutrino after an elastic scattering with a photon.

$\cos \iota'_{\nu_e}$	$\cos \iota_{\nu_e}$	F_{ν_e}
-1	-1	$E'_{\nu_e}[(1-\beta)/(1+\beta)]^{1/2}$
$-\beta$	0	$E'_{\nu_e}(1-\beta^2)^{1/2} = E_{\nu_e} E_\gamma (1-\cos\psi)/(E_{\nu_e} + E_\gamma)$
0	β	$E'_{\nu_e}/(1-\beta^2)^{1/2} = (E_{\nu_e} + E_\gamma)/2$
1	1	$E'_{\nu_e}[(1+\beta)/(1-\beta)]^{1/2}$
$-\cos \theta'_{\nu_e}$	$\cos(\psi - \theta_{\nu_e})$	E_γ
$\cos \theta'_{\nu_e}$	$\cos \theta_{\nu_e}$	E'_{ν_e}

The adjunct Lorentz transform also yields

$$F_{\nu_e} = E'_{\nu_e} \frac{(1-\beta^2)^{1/2}}{1-\beta\cos\iota_{\nu_e}} \tag{A2}$$

and we may draw up table 2. If the domain of values of ι'_{ν_e} is homogeneously covered the interaction is a powerful slowing-down in the co-ordinate system of the sun, since the neutrino and the photon may even exchange their energies. On the other hand, it may also happen that the neutrino gain energy through its interaction with the photon: such is the case when $\iota'_{\nu_e} < \theta'_{\nu_e}$; that is logical since the interaction might be part of a thermalization process. Of course, in any eventuality we have

$$0 \leqslant F_{\nu_e} \leqslant E_{\nu_e} + E_\gamma \tag{A3}$$

References

[1] J N Bahcall *et al, Rev. Mod. Phys.* **54**, 767 (1982)
[2] M Cribier and D Vignaud, *La Recherche,* 246, p. 1052 (1992)
[3] J N Bahcall, *Neutrino astrophysics,* C.U.P (1989)
[4] K Grotz and H V Klapdor, *The weak interaction in nuclear, particle and astrophysics* (Adam Hilger) (1990)
[5] Z Z Aydin, A O Barut and I H Duru, *Phys. Rev.* **D28**, 2872 (1983)
[6] J Bernstein, Ruderman M and G Feinberg, *Phys. Rev.* **132**, 1227 (1963)
[7] G Cohen-Tannoudji, private communication (1987)
[8] M S Chanowitz, in '*Results and perspectives in particle physics*', rencontres de physique de la vallee d'Aoste; Gif-sur-Yvette, editions Frontieres; edited by M Greco (1987)
[9] A Das, *Int. J. Theor. Phys.* **23**, 295 (1984)
[10] P Bandyopadhyay, *Nuovo Cimento* **38**, 1912 (1965)
[11] P Bandyopadhyay, *Nuovo Cimento* **A55**, 367 (1968)
[11a] P Bandyopadhyay, *Phys. Rev.* **173**, 1481 (1968)
[12] R B Stothers, *Phys. Rev.* **D2**, 1417 (1970)
[13] J B Adams, M A Ruderman and C -H Woo, *Phys. Rev.* **129**, 1383 (1963)
[14] Throughout this article we refer to the values of the fundamental constants given in the evaluation by Barry N Taylor and Stanley J Brodsky which is reproduced in [15]
[15] Particle Data Group, *Particle Properties Data Booklet,* April 1982, Lawrence Berkeley Laboratory, 1982
[16] V Kourganoff, *Introduction to advanced astrophysics,* (Dordrecht, D. Reidel Publishing Co, 1980)
[17] The most recent upper limits on the rest mass of the electron anti-neutrino from the β disintegration of tritium are 17·6 eV/c^2 [18] and 13·4 eV/c^2 [19]
[18] M Fritschi *et al, Phys. Lett.* **B173**, 485 (1986)
[19] J F Wilkerson *et al,* in *New and exotic phenomena* '90', rencontres de Moriond, edited by O Fackler and J Tran Thanh Van, January 1990; Gif-sur-Yvette, editions Frontieres (1990)
[20] 1 Solar neutrino unit = 10^{-36} absorption per target particle and per second on earth; 1 barn = 10^{-28} m^2
[21] B T Cleveland, R Davis Jr and J K Rowley, in *Weak interactions as probes of unification,* A.I.P. Conference Proceedings edited by G B Collins *et al* #72, p. 322 (1981)
[22] R Omnes, *Introduction a l'Etude des Particules Elementaires,* (Paris, Ediscience, 1970)
[23] Is (e, ν_e) an isospin doublet like (n, p)? The law of conservation of the leptonic number would then be of the same nature as that of the baryonic number
[24] S E Woosley and T A Weaver, *Ann. Rev. Astron. Astrophys.* **24**, 205 (1986)
[25] R I Epstein and C J Pethick, *Europhys. News,* **11**, 7 (1980)
[26] K Hirata *et al, Phys. Rev. Lett.* **58**, 1490 (1987)
[27] R M Bionta, G Blewitt, C B Bretton and D Casper, *Phys. Rev. Lett.*, **58**, 1494 (1987)

[28] If we use the value of σ_a in (21) as an estimate we find that the attenuation of the SN1987A neutrinos, during their journey to the earth, by the photons of the cosmological background radiation is about 1 part in 10^7.
[29] M J Rees, in *Proceedings of the Sixth General Conference of the E.P.S.*, Prague, 27–31 August 1984, **1**, 223 (1984)
[30] H Karoji, L Nottale and J -P Vigier, *C. R. Acad. Sci. Paris* **B281**, 409 (1975)

PRAMANA
— journal of
physics

© Printed in India

Vol. 43, No. 6,
December 1994
pp. 467–476

Dynamic color screening in a classical quark plasma

JITESH R BHATT,[†] PREDHIMAN K KAW[†] and JITENDRA C PARIKH[‡]
[†]Institute for Plasma Research, Bhat, Gandhinagar 382424, India
[‡]Physical Research Laboratory, Navrangpura, Ahmedabad 380009, India

MS received 19 July 1994

Abstract. Screening of a moving infinite color sheet source is examined in a quark plasma at finite temperature. The classical chromohydrodynamic equations for quarks are integrated, to obtain profiles for quark current density, which in turn are used to solve the SU(2) Yang-Mills equations numerically. This provides a classical but non-perturbative treatment for the screening of a moving source in quark plasma.

The results show two interesting features. We observe that if the test source is at rest the screening does not depend on the color dynamics and the behavior is very similar to that in Coulomb plasma. When the test source is moving with non-relativistic velocity the non-abelian features manifest themselves by weakening the screening and also by exhibiting an oscillatory profile with distance.

Keywords. Quark plasma; color screening.

PACS No. 12·38

1. Introduction

The screening of a color electric field in quark gluon plasma (QGP) is of considerable interest since it is a reflection of collective behaviour of the system and also because it leads to signatures for detecting the formation of QGP in the laboratory. For example, it was proposed that if the plasma is produced in heavy ion collisions, then due to screening effects charge anti-correlations [1] between pions of similar rapidity and production [2] of $J/\Psi(c\bar{c})$ mesons would be suppressed.

Early estimates of the static screening length have been based on perturbative QCD [3] and classical kinetic theory of abelian plasmas [4]. One obtains standard results at bare 1-loop level in QCD and the linearized calculational level in classical theories. Static screening phenomenon has been studied non-perturbatively using lattice methods [5] and one finds the usual form of the screened potential. Screening of *moving* charges in a quark-gluon plasma is a problem of great interest because of its direct relevance to signatures (J/Ψ suppression) from heavy-ion collisions. However, such calculations have so far been done only in the abelian limit [6] by using the methods of classical Coulomb plasma physics [7]. It is therefore of considerable interest to extend these classical calculations into the non-abelian non-perturbative regime. This is especially important because presently there are no known quantum field theoretic techniques which can be used to study this problem.

In this paper we analyze the *non-abelian* screening of a moving test source in a *classical* quark plasma. We restrict our attention to test particles travelling with non-relativistic velocities $V_0^2/c^2 \ll 1$. This is justified for considering J/ψ screening in

current experiments (such as NA38 experiment) where the transverse momenta of the particles is peaked around $p_T^2 \simeq 0{\cdot}6(\mathrm{GeV})^2/c^2 \ll m_{J/\psi}$ [8]. We have also not included effects due to the energy loss $\mathrm{d}E/\mathrm{d}x$ of the test particles. As shown by Gyulassy and Thoma [9] recently, this effect is also negligible for a slowly moving heavy particle. We may now emphasize at the outset that for studying the screening problem it is not essential to use kinetic equations. In fact in Coulomb plasmas it is standard practice to use fluid equations [7]. Moreover to simplify the calculations further one often uses slab geometry [7]. We basically follow this approach in order to carry out a non-perturbative study of screening in quark matter. For this purpose we have extended the color hydrodynamic (CHD) equations for quarks derived by Kajantie and Montonen [10] by adding a pressure gradient term in the momentum balance equation and coupling it to an equation of state for the massless quark gas. The self-consistent Yang-Mills equations in the presence of the test source are then solved in the slab geometry. We find that non-perturbative color precession effects produce a significant weakening of the screening of a moving color sheet source.

It ought to be mentioned that in a classical non-abelian theory there is an inherent difficulty in studying the screening of a test charge, because the charge of the test source can flow into gauge fields and vice-versa. This question has not been adequately addressed in earlier classical studies of screening in QGP. Consequently, in this paper, we use the expression for an effective Debye length to define a gauge invariant charge to study the non-abelian screening.

Section 2 contains a description of the basic equations used for studying the screening. In § 3 we discuss the screening for a static and a moving source, and present numerical results for a few sample cases, from amongst a large number of investigations that we have carried out. It must be pointed out that the broad qualitative features of oscillations and of weakened screening of a moving source, are present in all our numerical studies having different boundary conditions and values of parameters. Finally, § 4 contains a brief summary and conclusions.

2. Basic equations for screening

The CHD equations [10] describe the quark matter fluid in terms of three dynamical quantities, the gauge invariant number density $n(\mathbf{x}, t)$, the gauge invariant velocity field $\mathbf{V}(\mathbf{x}, t)$ and gauge covariant color charge $I_a(\mathbf{x}, t)$. Gauge transformation properties of these hydrodynamic variables and the CHD equation have been discussed in [11]. As mentioned earlier we have extended these equations by including a pressure gradient term in the force equation, and an equation of state relating pressure with temperature. The equation of state is chosen in such a manner that it account for the ultrarelativistic internal motions of the plasma particles. The basic equations are,

$$\frac{\partial n_A}{\partial t} + \nabla\cdot(n_A \mathbf{V}_A) = 0 \tag{1}$$

$$m_A\left[\frac{\partial \mathbf{V}_A}{\partial t} + \mathbf{V}_A\cdot\nabla\mathbf{V}_A\right] = gI_{Aa}[\mathbf{E}_a + \mathbf{V}_A \times \mathbf{B}_a] - \frac{1}{n_A}\nabla P_A \tag{2}$$

$$\left[\frac{\partial I_{Aa}}{\partial t} + \mathbf{V}_A\cdot\nabla I_{Aa}\right] = -g\varepsilon_{abc}[A_b^0 - \mathbf{V}_A\cdot\mathbf{A}_b]I_{Ac} \tag{3}$$

where m_A and P_A denote the mass and the pressure of particles of specie A and the

components of color electric and magnetic fields E_a and B_a are respectively defined by $E_a^i = F_a^{i0}$ and $B_a^i = -\frac{1}{2}\varepsilon^{ijk}F_a^{jk}$. Here $F_a^{\mu\nu}$ is the color field tensor

$$F_a^{\mu\nu} = \partial^\mu A_a^\nu - \partial^\nu A_a^\mu + g\varepsilon_{abc}A_b^\mu A_c^\nu \tag{4}$$

with Lorentz indices $\mu, \nu = 0, 1, 2, 3$ and (SU(2)) color indices $a = 1, 2, 3$. In (2), there would be a term involving collisions between particles belonging to different species. This is neglected in the present work and the justification for it is given in Appendix A.

The color fields are governed by the Yang-Mills equation

$$\partial_\mu F_a^{\mu\nu} + g\varepsilon_{abc}A_{\mu b}F_c^{\mu\nu} = j_a^\nu \tag{5}$$

where the quark (four) current j_a^ν is expressed in terms of the quark fluid variables according to

$$j_a^0 = g\sum_A n_A I_{Aa}, \tag{6}$$

$$\mathbf{j}_a = g\sum_A n_A \mathbf{V}_A I_{Aa}. \tag{7}$$

Using (1), (3), (6) and (7) one can readily show that the covariant current continuity equation is identically satisfied [8]. In the absence of any perturbations, the plasma is assumed to satisfy a color neutrality condition $\Sigma_A n_{A0} I_{Aa_0} = 0$. This strictly follows work of Kajantie and Montonen [10] and physically assumes that each color is separately giving color neutrality because of several compensating species in equilibrium. This color neutrality permits a wide class of non-abelian phenomena [10, 11]. It is true that a more general form of color neutrality may be essential in a baryon rich QGP. We have not investigated this more general class of non-abelian problem due to their complexity.

For the equation of state (eos) and number density we choose the ideal relativistic gas equations,

$$P_A = h_s N_d T_A^4 \tag{8}$$

$$n_A = d_s N_d T_A^3 \tag{9}$$

where N_d is the number of degrees of freedom and h_s and d_s are factors which depend upon the statistics. For an SU(2) massless quark gas of a single flavor $N_d = 4$,

$$h_s = \frac{7}{8}\left[\frac{\pi^2}{90}\right] \text{ and } d_s = \frac{3}{4}\left[\frac{\zeta(3)}{\pi^2}\right].$$

The above equations have been written for the quark component of QGP. It has recently been pointed out by Elze and Heinz [12] that gluons can also have classical dynamic equations similar to those of quarks (i.e. Eqs (1)–(3)). If such equations are included in the treatment, the contribution of gluons will simply add to that from quarks and define a new plasma frequency and a new screening length. We thus expect that for the non-abelian problem also the addition of new species (viz. gluons) is not going to change the qualitative conclusions significantly.

The basic problem we wish to consider is the screening of a moving test charge that is introduced in the QGP. For simplicity, we consider a moving infinite sheet

charge as the test source; this reduces the problem to 1-d (z) variations (for similar simplifications in Coulomb plasmas see ref. (7)). The test charge polarizes the plasma and we solve the self consistent Yang-Mills field equations coupled with the plasma response to analyze the screening effects. We consider a plasma consisting of two species (particles and antiparticles) and go to a frame in which the test source is at *rest* but the plasma is moving. In this frame when no perturbation is introduced, the two species move with equal velocity V_0 in the z-direction and have equilibrium density n_0. The color neutrality condition in equilibrium is $I_{1a0} = -I_{2a0}$ and hence the equilibrium current is zero. We consider a steady-state $\left(\frac{\partial}{\partial t} = 0\right)$ and drop the coupling to magnetic sector ($A_a^1 = A_a^2 = 0$) since the velocity of the test source is assumed to be non-relativistic ($V_0 \ll 1$). Finally, we make the gauge choice $A_a^3 = 0$ and write the equations for screening as

$$\frac{d^2 A_a^0}{dz^2} = -g \sum_A n_A I_{Aa} - 4\pi g K_a \delta(z), \tag{10}$$

$$g\varepsilon_{abc} A_b^0 \frac{dA_c^0}{dz} = g \sum_A n_A V_A I_{Aa}, \tag{11}$$

$$\frac{d}{dz}(n_A V_A) = 0, \tag{12}$$

$$g I_{Aa} \frac{dA_a^0}{dz} = -\frac{1}{n_A} \frac{dP_A}{dz}, \tag{13}$$

$$V_A \frac{dI_{Aa}}{dz} = -g\varepsilon_{abc} A_b^0 I_{Ac}. \tag{14}$$

In (10) K_a is the color charge component of the test sheet source. An interesting non-abelian feature is seen in (11) (Ampere's law) where, unlike the Coulomb (abelian) plasma, the steady state currents, affect the static potential in the non-abelian plasmas. In writing (13), we have ignored the mean energy of each specie compared to the thermal energy of that specie i.e. $m_A V_A^2 \ll T_A$. This is justified as the thermal velocity of the plasma particle is comparable to the velocity of light (due to the choice of eos).

The covariant current conservation equation for the present case takes the form

$$\frac{d}{dz} j_a + g\varepsilon_{abc} A_b^0 j_c^0 = 0$$

Note from (10) and (11) that $j_a^0 = -d^2 A_a^0/dz^2$ and $j_a = g\varepsilon_{abc} A_b^0 dA_c^0/dz$ (remembering that the test charge K_a, being at rest in the frame of calculation, contributes to j_a^0 but not to j_a). Substitution in the above equation shows that it is identically satisfied.

Equation (12) may be readily solved to yield

$$n_1 V_1 = n_0 V_0 = n_2 V_2 \tag{15}$$

Combining (15) and (11) one can find

$$I_{1a} + I_{2a} = \frac{1}{n_0 V_0} \varepsilon_{abc} A_b^0 \frac{dA_c^0}{dz}. \tag{16}$$

We can now express I_{2a}, T_A and n_A in terms of I_{1A} and A_a^0 and obtain the final equations for screening in the dimensionless form

$$\frac{d^2 A_a}{dZ^2} = I_a(I_b A_b) + \frac{1}{3}\frac{\beta d_s}{4h_s} I_a (I_b A_b)^3 - \alpha \varepsilon_{abc} A_b \frac{dA_c}{dZ}\left[1 + \frac{\beta d_s}{4h_s} I_s A_b\right]^3 - S_a \tag{17}$$

$$\frac{dI_a}{dZ} = -\alpha\left[1 - \frac{\beta d_s}{4h_s} I_b A_b\right]^3 \varepsilon_{abc} A_b I_c. \tag{18}$$

We define

$$\Lambda_D^{-2} = \left[\frac{3N_d d_s^2}{2h_s}\right] g^2 i_0^2 T_0^2 \tag{19}$$

which can be identified as the linear ('perturbative') Debye length and the scaled variables are $Z = z/\Lambda_D$, $A_a = a_0^{-1} A_a^0$, $I_a = i_0^{-1} I_{1a}$ where a_0, i_0, T_0 are normalizing factors and S_a is the source term. We also introduce the dimensionless parameters $\alpha = \dfrac{g a_0 \Lambda_D}{V_0}$ and $\beta = \dfrac{g i_0 a_0}{T_0}$. The dimensionless parameter β essentially measures the ratio of 'average' potential energy per particle to average kinetic energy and as in Coulomb plasmas is given by $\beta = \dfrac{g i_0 a_0}{T_0} \simeq (n\Lambda_D^3)^{-1}$. The parameter α characterizes the strength of the non-abelian terms in Eqs (17 and 18) and may also be written as $\alpha = \dfrac{g a_0 \Lambda_D}{V_0} = g\beta\left[\dfrac{\sigma \Lambda_D^4 \varepsilon_{th}}{\varepsilon_{kin}}\right]^{1/2}$ where σ is the mass density, $\varepsilon_{kin} = m n_0 \dfrac{V_0^2}{2}$ and ε_{th} the thermal energy of plasma particles. For a typical QGP that might be produced in heavy ion collisions $\Lambda_D \sim 1/4 - 1/3$ fm, $\varepsilon_{th} \sim 2 - 5\,\text{GeV/fm}^3$ and with $V_0 \leqslant 0{\cdot}4$, we find $\beta \sim 10^{-1} - 10^{-2}$ and $\alpha \geqslant g\,10^{-2}$.

3. Screening effects for static and moving sources

First we consider the screening of a moving test charge. Equations (17) and (18) may be combined to generate an equation for $I_a A_a$, viz.

$$\frac{d^2(I_a A_a)}{dZ^2} = \left[I_a^2 - 6\alpha\theta I_a \varepsilon_{abc} A_b \frac{dA_c}{dZ}\right]\left[1 + \frac{\theta^2}{3}(I_b A_b)^2\right](I_a A_a) - S \tag{20}$$

where $\theta = \dfrac{\beta d_s}{4h_s}$. The 'potential' energy $I_a A_a$ is a gauge invariant quantity in the static $\left(\dfrac{\partial}{\partial t} = 0\right)$ case and the equation above shows that it is screened by a non-abelian Debye length Λ_{DNA}, which is a dynamical quantity given by the gauge invariant expression

$$\Lambda_{DNA}^{-2} = \left[I_a^2 - 6\alpha\theta I_a \varepsilon_{abc} A_b \frac{dA_c}{dZ}\right]\left[1 + \frac{\theta^2}{3}(I_b A_b)^2\right]. \tag{21}$$

From (23) we may also define a gauge invariant charge $Q_{inv}^2 = I_a^2 - 6\alpha\theta I_a \varepsilon_{abc} A_b (dA_c/dZ)$

which takes into account exchange of color charge with the gauge fields. This expression is similar to that obtained in earlier studies [13] of color screening in classical Yang-Mills theories with an external source.

Next we demonstrate that for static charges ($V_1, V_2 \to 0$) we recover the usual abelian screening results. From (15) we note that since n_1 and n_2 are finite even when $V_0 \to 0$, V_0/V_A must also stay finite in this limit. If we now mutiply (16) by V_1 or V_2 and then take limit $V_1, V_2 \to 0$, we get the constraint conditions,

$$\varepsilon_{abc} A_b \frac{dA_c}{dZ} = 0. \tag{22}$$

In this limit A_a and (dA_a/dZ) are vectors parallel in color space. Consequently, the non-abelian term disappears from (20) and the right hand side will become function of $I_a A_a$ only. Thus, in solving (20) the dynamics of I_a (Eq. (18)) is redundant and the screening behavior is similar to that of a Coulomb plasma. It should be noted that the covariant continuity equation for quark current would give, in the limit $V_0 \to 0$, $\varepsilon_{abc} A_b I_c = 0$. However, as we have used both Gauss and Ampere's equations, the constraints arising from the continuity equation are not neccessary. Finally on integration, (20) gives (for $V_0 \to 0$) the well-known Debye screening result with the Debye length Λ_D given by the 'perturbative' expression, Eq. (19).

In order to study (17 and 18) further, we first look for conservation laws. We find

$$\sum_a I_a^2 = \text{constant}, \tag{23}$$

$$\sum_a \left[\frac{dA_a}{dZ}\right]^2 - (I_b A_b)^2 - \frac{\theta^2}{6}(I_b A_b)^4 = E, \tag{24}$$

$$\sum_a \alpha^2 M_a^2 - \frac{\alpha}{3\theta} I_b M_b = M, \tag{25}$$

where $M_a = \varepsilon_{abc} A_b (dA_a/dZ)$ and M is a constant. Equation (23) is an obvious reflection of SU(2) color algebra and allows precession of color charge **I** keeping its magnitude constant. Equation (24) may be interpreted in terms of field energy and thermal energy of the particles. Unlike an oscillatory solution where there is a conservation law for the sum of field and particle energies we get for a screened system, an invariance of the difference in energies. It implies that the particle and the field energies are simultaneously large or small so as to preserve the difference. As regard (25) we note that M_1, M_2 and M_3 are related to color charge fluctuations of the Yang-Mills fields. The second term of right hand side of (25) is a consequence of the exchange of color charge between the fields and particles.

We would like to emphasize that all the important quantities described above and subsequently used below in numerical calculations viz. $I_a E_a$, $I_a A_a$, Q^2_{inv} and the conserved quantities are gauge invariant under the class of static gauge transformation $U = U(x)$ as A^0 transforms covariantly. The gauge invariance of Q^2_{inv} has been explicitly demonstrated for general case in [13].

To fully investigate the novel qualitative and quantitative features of non-abelian screening we must solve eqs (17) and (18) numerically. Before proceeding with the numerical solutions we must specify the boundary conditions on the variables A_a, I_a, (dA_a/dZ) etc. However, all these variables are gauge dependent. To study the

screening in a gauge invariant manner, we construct useful gauge invariant quantities such as potential energy, the force $I_a E_a$, the gauge invariant charge Q^2_{inv} and use these and the three invariant given by eqs (23–25) to specify the boundary conditions. As the fields are screened at large distances, we expect the non-abelian field strength to vanish at distances large compared to Debye length and to have $I_a E_a \to 0$, $I_a A_a \to 0$ and $Q^2_{\text{inv}} \to I_a^2$ as $Z \to \infty$.

In figures 1 and 2 we have plotted the gauge invariant force $\left(-I_a \dfrac{dA_a}{dZ} \equiv IE\right)$ on a color charged quark fluid element as a function of distance from the test source. This way of studying the screening has advantage over the usual potential vs. distance plots. This is because two different sets of boundary conditions related say by a global gauge transformation can give very different behaviour in the potential vs. distance plots [14] while IE vs. distance plots remain invariant. For this reason the non-abelian screening can be studied uniquely in terms of physically meaningful gauge invariant quantities.

In order to study the effect of the velocity of test source on the screening, we vary the parameter α. Clearly a change in the value of α will alter the values of the gauge invariant charge (eq. (21)) and the conserved quantity M (eq. (25)) at the boundary. To ensure that the six gauge invariant physical quantities mentioned above remain fixed at the boundary we vary the boundary values of gauge dependent quantities A_a, and (dA_a/dZ). Indeed, it is found that under the transformations $\alpha \to \alpha' = \alpha + d$ and $A_a \to A_a$ where,

$$\tilde{A}_a = -\frac{d}{\alpha + d} \frac{I_b A_b}{IE} \frac{dA_a}{dZ} + \frac{\alpha}{\alpha + d} A_a \tag{26}$$

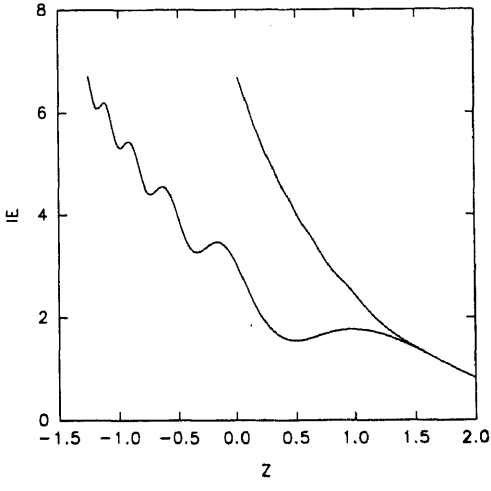

Figure 1. The screening of the force $IE(\equiv I_a E_a)$ acting on a fluid element at a distance z from the infinite sheet test charge. z is in units of "perturbative" Debye length. The value of the parameter β is 0·1.
The upper curve repesents $\alpha = 15$ case and the lower curve corresponds to $\alpha = 2$ case with the boundary values of the gauge invariant quantities $I_a A_a = 0{\cdot}8569683$, $I_a(dA_a/dZ) = -0{\cdot}85696827$ and $Q^2_{\text{inv}} = 0{\cdot}9961094$. The values of the conserved quantities are $E = 0{\cdot}002824$, $M = 11{\cdot}49416$ and $\sum_a I_a^2 = 0{\cdot}9961$.

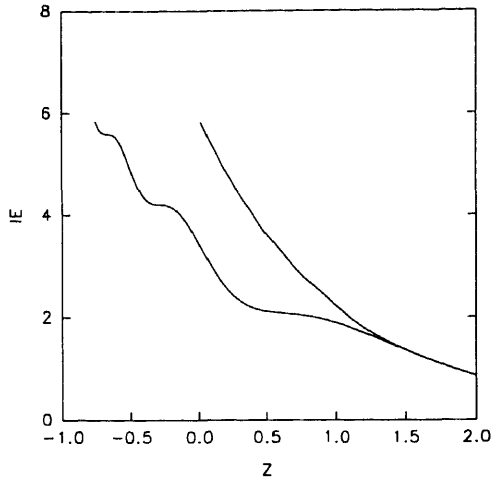

Figure 2. Caption same as figure 1. The upper curve represents the case $\alpha = 15$ and the lower curve corresponds to $\alpha = 2$ case with the boundary values of the gauge invariant quantities $I_a A_a = 0{\cdot}9901809$, $I_a(\mathrm{d}A_a/\mathrm{d}Z) = -0{\cdot}8162973$ and $Q^2_{\mathrm{inv}} = 1{\cdot}101744$. The values of the conserved quantities are $E = -0{\cdot}37477$, $M = 15{\cdot}46753$ and $\sum_a I_a^2 = 1{\cdot}1$.

all the physical quantities at the boundary remain fixed. Further it clearly shows that when $d \to \infty$ (i.e. $V_0 \to 0$), A_a become parallel to $(\mathrm{d}A_a/\mathrm{d}Z)$ as should be the case.

The numerical approach we adopt is the fourth order Runge-Kutta method, with variable step size. The conserved quantities defined in (23)–(25) are used as checks for accuracy of the numerical integration scheme. In the numerical integration, it is necessary to specify the boundary conditions with high accuracy (i) to make certain that the equations give a screening (not an exponentially increasing) solution and (ii) to ensure that the constancy of conserved quantities is good to several significant places.

Figure 1 shows the force for two values of α viz. $\alpha = 2$ and $\alpha = 15$; higher α corresponds to slower moving particles. In order to compare the abelian screening with the non-abelian one, we integrate the equations backward from a point far away from the charge. The value of $I_a E_a$ at this location ($Z = 2$ in the figure which is two abelian Debye lengths from origin) be the same. As we integrate the equations towards the source we go up to value of Z where $I_a E_a$ again takes the same values. This is because we expect the $I_a E_a$ near a source to have the same magnitude. Thus we notice from the figures that the source for the non-abelian case (lower curve) is located at a *farther* distance from $Z = 2$. First we note that the force shows typical screening behavior. Treating fall-off distance of IE as measure of screening length we find that screening is weaker for higher velocity (lower α) by 38%. Figure 2 shows similar results for a different set of boundary conditions and again shows a significant weakening of screening (62%) as a function of particle velocity V_0. It is also noted that non-abelian effects lead to a novel oscillatory behavior of IE over and above the mean screening effects (clearly seen in figures 1 and 2). These new features may be understood in terms of non-abelian effects that lead to a precession (see (14)) of the color charge vector of the fluid element. As a result its orientation is not always

opposite to the color vector of the moving charge, and therefore a larger distance is needed to screen the field of a moving test source. These are qualitatively new effects and have not been described before. It is clear that as α increases (and velocity diminishes), the oscillatory behavior should diminish and screening becomes more and more abelian. This is demonstrated by our numerical results.

It should be emphasized that over many different sets of boundary conditions, the numerical solutions have been studied and it was found that the qualitative features of the solutions are similar. Hence, the general features of our results are independent of any specific choice of parameters and the boundary conditions. The numerical results presented are merely representative of a large set of parameter choices and boundary conditions.

4. Summary and conclusions

To summarize, we have investigated the dynamic screening of an infinite color sheet source, moving in quark matter. We find that non-abelian effects lead to a significant modification of the screening of a moving test source. Firstly, there are oscillations in the screening behavior and secondly and more importantly there is significant weakening of the mean screening. The former effect is similar in nature to non-abelian longitudinal plasma oscillations discovered recently by the authors [11]. The latter is a consequence of the precession of the color charge vector of the screening plasma fluid, which weakens its screening effects.

It ought to be made clear that the well-known non-perturbative, non-abelian problem of magnetic mass [15], that would remove the infrared divergences [15], in perturbative QCD at finite temperature has not been examined by us. As pointed out by Nadkarni [16], due to the infrared problem, a non-perturbative study is required even for the static screening of a color source. Thus, our omission of the magnetic effects has prevented us from studying this question. All the same, we have shown that, for moving sources, there are new non-abelian effects in the purely electric sector due to precession of color charges. A full treatment of the screening problem would include these new effects together with other non-abelian features arising from the magnetic sector.

Finally, it is interesting to speculate that, the weakening of screening due to non-abelian effects found by us, may also contribute to the increase of survival probability of J/Ψ with p_T that is experimentally observed [8].

Appendix A

If two species interpenetrate, there would be some transfer of momentum from one specie to another. In this situation, the equation of motion for the two species can be (phenomenologically) written as

$$m\left[\frac{\partial \mathbf{V}_1}{\partial t}+\mathbf{V}_1\cdot\nabla\mathbf{V}_1\right]=gI_{1a}[\mathbf{E}_a+\mathbf{V}_1\times\mathbf{B}_a]-\frac{\nabla P_1}{n_1}-\nu_m(\mathbf{V}_1-\mathbf{V}_2), \tag{27}$$

$$m\left[\frac{\partial \mathbf{V}_2}{\partial t}+\mathbf{V}_2\cdot\nabla\mathbf{V}_2\right]=gI_{2a}[\mathbf{E}_a+\mathbf{V}_2\times\mathbf{B}_a]-\frac{\nabla P_2}{n_2}+\nu_m(\mathbf{V}_1-\mathbf{V}_2). \tag{28}$$

Here ν is the collision frequency, which is related to the mean free path and the

thermal velocity $\langle V_0 \rangle$ by the formula $v = \langle V_0 \rangle / l$. In the equations above, one can take the length scale for the pressure gradient term to be of the order of screening length Λ_D. Thus, we may neglect the collision term if $\frac{P}{n\Lambda_D} \gg \frac{m\langle V_0 \rangle}{l} V_h$ where, V_h is the hydrodynamic velocity.

We take the Debye length $\Lambda_D \simeq 1/4 - 1/3$ fm, and the mean free path [17] $l = 0{\cdot}5$ fm for a QGP with energy density $\varepsilon = 2$ GeV/fm^3, so that $\Lambda_D/l \sim 1$. Now for a high temperature plasma, in which the test particle has a large rest mass ($m_q \gg T$) we have $\langle V_0 \rangle / V_h \gg 1$. Thus, for the model studies discussed in this work the neglect of the collision term is justified.

References

[1] J A Lopez, J C Parikh and P J Siemens, *Phys. Rev. Lett.* **53**, 1216 (1984)
[2] T Matsui and H Satz, *Phys. Lett.* **B178**, 416 (1986)
[3] D J Gross, R D Pisarski and L G Yaffe, *Rev. Mod. Phys.* **53**, 43 (1981)
[4] H -Th Elze and U Heinz, *Phys. Rep.* **183**, 81 (1986)
U Heinz, *Ann. Phys. (N. Y.)* **168**, 148 (1986)
[5] F Karsch, in *Quark–gluon plasma*, edited by R Hwa (World Scientific, Singapore, 1990)
[6] M C Chu and T Matsui, *Phys. Rev.* **D39**, 1892 (1989)
[7] D R Nicholson, *Introduction to plasma theory* (John Wiley, New York, 1983)
N A Krall and A W Trivelpiece, *Principles of plasma physics* (McGraw Hill, New York, 1973)
[8] R A Salmeron, in *Quark-gluon plasma*, Research Report in Physics edited by B Sinha, S Pal and S Raha (Springer-Verlag, Berlin, 1990)
[9] M H Thoma and M Gyulassy, *Nucl. Phys.* **B351**, 491 (1991)
[10] K Kajantie and C Montonen, *Phys. Scr.* **22**, 555 (1980)
[11] J R Bhatt, P K Kaw and J C Parikh, *Phys. Rev.* **D39**, 646 (1989)
[12] Th Elze and U Heinz, in *Quark-gluon plasma*, edited by R Hwa (World-Scientific, Singapore, 1990)
[13] C H Lai and C H Oh, *Phys. Rev.* **D29**, 1805 (1984)
M P Isidro Filho, A K Kerman and Howard Trottier D, *Phys. Rev.* **D40**, 4142 (1990)
[14] W B Campbell, D W Joseph and T A Morgan, *Phys. Lett.* **B96**, 352 (1980)
[15] A D Linde, *Rep. Prog. Phys.* **42**, 389 (1979); *Phys. Lett.* **B96**, 289 (1980)
[16] S Nadkarni, *Phys. Rev.* **D33**, 3738 (1986); **D34**, 3904 (1986)
[17] G Baym *et al Nucl. Phys.* **A407**, 541 (1983)

PRAMANA
— journal of
physics

© Printed in India

Vol. 43, No. 6,
December 1994
pp. 477–485

Systematic trends in the line strengths of E1 transitions in the oxygen isoelectronic sequence

ANJU AGRAWAL and K L BALUJA
Department of Physics and Astrophysics, University of Delhi, Delhi 110007, India

MS received 11 July 1994

Abstract. Line strengths S for the dipole allowed transitions within the $n = 2$ complex of the oxygen isoelectronic sequence have been fitted in the form $Z^2S = A + B/(Z - C)$, where Z is the nuclear charge of a particular ion. The constants A, B and C are determined by using a non-linear least square method. The data for S are taken from the configuration interaction calculations which included internal, semi-internal and all external type correlations for ions in the range $Z = 8 - 25$. It is shown that the values of A obtained from the fit for all the transitions are in excellent accord with the ab-initio values obtained in the hydrogenic limit $Z \rightarrow \infty$ provided near degeneracy effects are included in the ground state multiplet $1s^2 2s^2 2p^4\,{}^1S$.

Keywords. Line strength; oscillator strength; hydrogenic limit; near-degeneracy.

PACS No. 32·70

1. Introduction

Accurate values of optical oscillator strengths of various transitions of ions are of interest in astrophysics [1] and fusion research [2]. They provide information on the abundance of elements in the spectrum of the solar corona and chromosphere. These important data are useful in establishing models for stellar atmospheres. The optical strengths are related to refractive index, the dipole polarizability and diamagnetic susceptibility of the system through sum rules [3–5]. It is well-known [6] that the generalized oscillator strength for a particular transition at zero momentum transfer is equal to the optical oscillator strength for that transition. An accurate knowledge of the optical oscillator strength can then be used as a correction factor for the entire range of momentum transfer to derive accurate electron collision cross-sections.

Beam-foil spectroscopy [7] is often employed to measure the lifetime of an excited state. A beam of fast ions from an accelerator is allowed to pass through a thin foil causing excitations in the ions due to collisions. However, other excited states often blend the decay curve of the state of interest. There may also be undetected systematic errors which may further compound the problem. There are various methods available [8] for the calculation of atomic transition probabilities. The calculations involve the modulus of the electric dipole transition matrix element which requires accurate knowledge of the wavefunctions of the states involved. The matrix element is extremely sensitive to the quality of the wavefunctions so it is important to obtain accurate wavefunctions. Fischer [9] has developed the numerical multi-configurational Hartree Fock (HF) method in which the orbitals of the configuration are all of HF type. The method of superposition of configurations was developed by Hibbert [10] in which

the reference function is an analytic HF function with each HF orbital expressed as a linear combination of Slater orbitals. When interacting configurations are included, the variational parameters of the reference function are not reoptimized. These configuration interaction methods include correlation which depends upon the span of the basis functions included in the calculation.

Particular applications may require oscillator strength data along an isoelectronic sequence or along a homologous series or along a Rydberg series [11]. Since each individual case requires a protracted calculation, it is natural that isoelectronic studies be made by methods with which we can extrapolate or interpolate. Smith *et al* [12] have given a general review of systematic trends in oscillator strengths. An interpolation curve based on the perturbation theory [13] may be employed to give information about the missing data. An interpolation curve for the line strength S is more convenient. In particular the form $Z^2S = A + B/(Z - C)$, where Z is the nuclear charge and A, B and C are the parameters to be determined via a non-linear least square fit has been used by Trabert [14] to study the isoelectronic trends in the experimentally determined S values for the dipole allowed transitions in the Be sequence. This functional form was used by Baluja and Agrawal [15] for the isoelectronic study of S for the dipole allowed transitions in the carbon sequence. It was shown that the values of A obtained from the fit for all the transitions were in excellent accord with the ab-initio values obtained in the hydrogenic limit $Z \to \infty$ provided near degeneracy effects [16] were included. The present work is an extension of our previous work [15]. In the present work we have fitted the S values for the dipole allowed transitions in the $n = 2$ complex for O-sequence in the range $Z = 8 - 25$. In the O-sequence, the near degeneracy effects arise in the ground state multiplet $1s^2 2s^2 2p^4\,{}^1S$. The two '2s' electrons are promoted to two '2p' electrons giving rise to the near degenerate configuration state $1s^2 2p^6\,{}^1S$. The near degeneracy effect in the other ground state multiplets $1s^2 2s^2 2p^4\,{}^3P, {}^1D$ is absent due to angular momentum coupling rules. The present work investigates the effect of near degeneracy on the value of A for the ${}^1S$ state. For the ${}^3P$ and ${}^1D$ states, the A values correspond to the single configurational value.

2. Theory

The multiplet line strength S between an initial bound state ϕ and a final bound state ϕ' is given by [9]

$$S = \left| \left\langle \phi \left| \sum_{i=1}^{N} \mathbf{r}_i \right| \phi' \right\rangle \right|^2 \tag{1}$$

where the summation is taken over all the electrons of the atom, $\mathbf{r}_i$ is the dipole operator for the ith electron. The corresponding oscillator strength is given by [9]

$$f = 2\Delta E\, S/(3g) \tag{2}$$

where ΔE is the excitation energy (in a.u.) and $g = (2L + 1)(2S + 1)$ is the statistical weight of the initial state.

According to the perturbation theory [13], the f value for a particular transition within an isoelectronic sequence may be expanded in inverse powers of Z

$$f = \sum_{i=0}^{\infty} f_i / Z^i. \tag{3}$$

The corresponding expansion for S is

$$Z^2 S = \sum_{i=0}^{\infty} S_i / Z^i. \tag{4}$$

Equation (4) can be rewritten in a more compact fashion as

$$Z^2 S = A + \frac{B}{(Z - C)} \tag{5}$$

where C is sometimes erroneously interpretted as a screening constant which takes into account the effect of higher terms. The nuclear charge Z now simply becomes a tuning parameter of the isoelectronic sequence. Equation (5) has been originally suggested by Edlen [17]. This form due to enhanced linearity permits extrapolative and interpolative predictions for missing data with high accuracy. It also reveals questionable data.

For the determination of the parameters A, B and C we minimized the sum of squares of residues given by

$$\sum_i \delta_i^2 = \sum_i (A + B/(Z_i - C) - Z_i^2 S_i)^2 \tag{6}$$

The data for S_i were taken from the CI calculations [18] for ions with Z in the range $Z = 8 - 25$. The minimization of $\sum_i \delta_i^2$ yielded the following equations for the coefficients A, B and C

$$\frac{\left(-\frac{1}{N}\sum_i Z_i^2 S_i\right)\left(\sum_i \frac{1}{Z_i - C}\right) + \sum_i \frac{Z_i^2 S_i}{(Z_i - C)}}{\left[-\frac{1}{N}\left(\sum_i \frac{1}{Z_i - C}\right)^2\right] + \sum_i \frac{1}{(Z_i - C)^2}} = \frac{\left(-\frac{1}{N}\sum_i Z_i^2 S_i\right)\left(\sum_i \frac{1}{(Z_i - C)^2}\right) + \sum_i \frac{Z_i^2 S_i}{(Z_i - C)^2}}{\left[-\frac{1}{N}\sum_i \frac{1}{(Z_i - C)^2}\right]\left(\sum_i \frac{1}{Z_i - C}\right) + \sum_i \frac{1}{(Z_i - C)^3}}. \tag{7}$$

$$B = \frac{\sum_i \frac{Z_i^2 S_i}{(Z_i - C)^2} - \left(\frac{1}{N}\right)\left(\sum_i \frac{1}{(Z_i - C)^2}\right)\left(\sum_i Z_i^2 S_i\right)}{\sum_i \frac{1}{(Z_i - C)^3}\left[\frac{1}{N}\sum_i \frac{1}{(Z_i - C)^2}\right]\left(\sum_i \frac{1}{Z_i - C}\right)} \tag{8}$$

$$A = -\frac{B}{N}\sum_i \frac{1}{Z_i - C} + \frac{1}{N}\sum_i Z_i^2 S_i \tag{9}$$

where N is the number of data points in the iso-electronic sequence. The parameter C was obtained by iteration using the bisection method [19]. The coefficients B and A were then determined from (8) and (9) respectively. We obtained excellent fits for

all the transitions. The resulting χ^2 is of the order of 10^{-4} or smaller for all the transitions studied here.

It is clear from (5) that the parameter A is the value of Z^2S when $Z \to \infty$. In this limit, all the Hartree Fock orbitals assume their hydrogenic character as the quantum defect vanishes. It is of interest to calculate the value of A ab-initio and compare with the corresponding fitted values. The ground state configuration of O-like ions is $1s^2 2s^2 2p^4$ which gives rise to three even parity multiplet states ^{3}P, ^{1}D and ^1S, the other states are forbidden due to Pauli exclusion principle. When two '2s' electrons are promoted to two '2p' electronic state we get the configuration $1s^2 2p^6$ which necessarily gives a ^1S state. This near degenerate, configuration mixes strongly with the HF state $1s^2 2s^2 2p^4\, ^1S$ indicating a strong correlation. This effect increases with nuclear charge and is dependent upon the state. It influences the electronic charge distribution which affects the atomic properties. For ^1S state, we express the wavefunction $\phi(LS\pi)$ in the LS coupled representation as a linear combination of the HF wavefunction ϕ_1 and the near degenerate wavefunction ϕ_2

$$\phi(LS\pi) = c_1 \phi_1(1s^2 2s^2 2p^4\, ^1S) + c_2 \phi_2(1s^2 2p^6\, ^1S) \tag{10}$$

where L, S and π are the total orbital, total spin angular momentum and the parity of the state. For the states ^3P and ^1D there are no near degenerate states, so ϕ is a HF state for these cases. The configurational wavefunctions ϕ_i are constructed from the one-electron function

$$u_{nlm_l}(\mathbf{r}, m_s) = \frac{1}{r} P_{nl}(r)\, Y_{lm_l}(\theta, \phi)\chi(m_s) \tag{11}$$

where $\chi(m_s)$ is the spin wavefunction and $Y_{lm_l}(\theta, \phi)$ is a spherical harmonic. The ϕ_i satisfy the orthonormality condition

$$\langle \phi_i | \phi_j \rangle = \delta_{ij} \tag{12}$$

The expansion coefficients c_i can be calculated by solving a pair of simultaneous equations given by

$$\sum_{i=1}^{2} c_i (H_{ji} - E\delta_{ji}) = 0, \quad j = 1, 2 \tag{13}$$

where

$$H_{ij} = \langle \phi_i | H | \phi_j \rangle \tag{14}$$

where H is the Hamiltonian of the ion. The eigenvalues E_λ are calculated by diagonalizing the Hamiltonian matrix and we finally obtain

$$\frac{c_1}{c_2} = \frac{-2H_{12}}{[(H_{11} - H_{22}) \pm \sqrt{(H_{11} - H_{22})^2 + 4H_{12}H_{21}}]}. \tag{15}$$

It is now trivial to calculate c_1 and c_2 by employing the normalization condition $c_1^2 + c_2^2 = 1$. All we need is the values of the Hamiltonian matrix elements.

Using Slater's approach [20], we obtain the following expressions for the Hamiltonian matrix elements of the two ^1S states of the oxygen sequence. The matrix element H_{11} corresponds to the HF state $1s^2 2s^2 2p^4\, ^1S$ whereas H_{22} corresponds

to the near-degenerate $1s^2 2p^6\,{}^1S$ state

$$H_{11} = 2I(1s,1s) + 2I(2s,2s) + 4I(2p,2p) + F^0(1s,1s) + 4F^0(1s,2s) - 2G^0(1s,2s) + F^0(2s,2s) + 8F^0(1s,2p) - 4G^1(1s,2p)/3 + 8F^0(2s,2p) - 4G^1(2s,2p)/3 + 6F^0(2p,2p), \tag{16}$$

$$H_{22} = 2I(1s,1s) + 6I(2p,2p) + F^0(1s,1s) + 12F^0(1s,2p) - 2G^1(1s,2p) + 15F^0(2p,2p) - 6F^2(2p,2p)/5, \tag{17}$$

$$H_{21} = H_{12} = G^1(2s,2p)/\sqrt{3}. \tag{18}$$

The integrals $I(nl, nl)$ are the one-electron integrals, $F^k(nl, n'l')$ and $G^k(nl, n'l')$ are the two-electron Slater's integrals [20]. For hydrogenic orbitals, these integrals can be easily evaluated. These energy integrals (for $Z = 1$) in atomic units are $I(1s,1s) = -1/2, I(2s,2s) = I(2p,2p) = -1/8$; $F^0(1s,1s) = 5/8$, $F^0(1s,2s) = 17/81$, $F^0(2s,2s) = 77/512$, $F^0(1s,2p) = 59/243$, $F^0(2s,2p) = 83/512$, $F^0(2p,2p) = 93/512$, $F^2(2p,2p) = 45/512$, $G^0(1s,2s) = 16/729$, $G^1(1s,2p) = 112/2187$, $G^1(2s,2p) = 45/512$. It is now trivial to calculate c_1 and c_2 from (15). We obtain $c_1 = 0{\cdot}979327757$, $c_2 = -0{\cdot}202279866$. The zeroth order multiplet strength can now be written as

$$S(LS\pi \to L'S'\pi') = |\langle \phi(LS\pi)|\mathbf{r}|\phi_3(L'S'\pi')\rangle|^2 \tag{19}$$

where $\phi(LS\pi)$ is the ground state wavefunction, $\phi_3(L'S'\pi')$ is the excited state wavefunction belonging to the configuration $1s^2 2s 2p^5$. For ${}^3P$ and ${}^1D$ multiplets of the ground state ϕ is simply a single configuration wavefunction whereas for ${}^1S$ state it is an admixture of HF $1s^2 2p^4\,{}^1S$ state and the near degenerate state $1s^2 2p^6\,{}^1S$. The **r** summed over all electrons is the position vector operator of tensorial rank one. We can now write

$$S_0(LS \to L'S') = c_1^2 S_1 + c_2^2 S_2 + 2c_1 c_2 \sqrt{S_1 S_2} \tag{20}$$

where

$$S_1 = |\langle \phi_1(1s^2 2s^2 2p^4; LS\pi)|\mathbf{r}|\phi_3(1s^2 2s 2p^5, L'S'\pi')|^2 \tag{21}$$

$$S_2 = |\langle \phi_2(1s^2 2p^6; {}^1S)|\mathbf{r}|\phi_3(1s^2 2s 2p^5; L'S'\pi')\rangle|^2. \tag{22}$$

If we represent each ϕ_i as simply an antisymmetrized product of hydrogenic orbitals then we can express the LS line strength matrix in terms of Racah's reduced matrix elements [21]. Racah's algebra [21] can be used to decouple the wavefunctions until only the dipole integral between single electron orbitals remain. This decoupling allows us to write

$$S_i = \Lambda \sigma^2, \quad i = 1, 2 \tag{23}$$

where Λ is the angular factor which depends upon the coupling of angular momenta of the electrons and σ is the hydrogenic transition integral

$$\sigma(2s \to 2p) = \int_0^\infty P_{2s}(r) P_{2p}(r) r\,dr = \sqrt{27}/Z. \tag{24}$$

The angular factors Λ for each transition can be worked out by using the standard

Racah algebra. This requires evaluation of Racah's coefficients and the fractional parentage coefficients. These angular factors are

$$\wedge(2s^2 2p^4\,{}^3P \rightarrow 2s2p^5\,{}^3P^0) = 6,$$

$$\wedge(2s^2 2p^4\,{}^1D \rightarrow 2s2p^5\,{}^1P^0) = 10/3,$$

$$\wedge(2s^2 2p^4\,{}^1S \rightarrow 2s2p^5\,{}^1P^0) = 2/3,$$

and

$$\wedge(2p^6\,{}^1S \rightarrow 2s2p^5\,{}^1P^0) = 2.$$

We now finally obtain the zeroth order multiplet strengths for various transitions in the hydrogenic limit

$$Z^2 S_0(2s^2 2p^4\,{}^3P \rightarrow 2s2p^5\,{}^3P^0) = 162,$$

$$Z^2 S_0(2s^2 2p^4\,{}^1D \rightarrow 2s2p^5\,{}^1P^0) = 90,$$

$$Z^2 S_0(2s^2 2p^4\,{}^1S \rightarrow 2s2p^5\,{}^1P^0) = 18,$$

$$Z^2 S_0(2p^6\,{}^1S \rightarrow 2s2p^5\,{}^1P^0) = 54,$$

$$Z^2 S_0(2s^2 2p^4 + 2p^6;\,{}^1S \rightarrow 2s2p^5\,{}^1P^0) = 7.12.$$

It is worth noting that for the transition ${}^1S \rightarrow {}^1P^0$, the effect of near-degeneracy is to reduce the hydrogenic value of $Z^2 S_0 = A$ from 18 to 7·12.

Results and discussion

We now compare the ab-initio values of A calculated above with the fitted values of A from the minimization procedure. The data used for S_i were taken from the configurational interaction calculation [18]. These elaborate calculations included internal, semi-internal and all external type correlation effects [22]. In the internal type corelation two 2s orbitals are promoted to two 2p orbitals within the Hartree–Fock sea which consists of 1s, 2s and 2p orbitals. In the semi-internal type correlation, one electron jumps outside the HF sea with $n \geqslant 3$ whereas the other electron shifts within the sea. In the all-external type correlation two electrons from the sea are shifted outside the sea with $n \geqslant 3$. Parity is conserved in all the shifts. All those correlating configurations were included which could be built from the orbitals $3l$. The internal type correlation is present only in the ${}^1S$ state of the ground state configuration, in the other transitions this is absent due to the property of parity conservation. These elaborate CI calculations for 17 ions in the O-sequence produced excellent values of the energies of all the atomic states involved for all the ions. It also yielded accurate values of the transition probabilities of various dipole allowed transitions within $n = 2$ complex. The agreement with the experimental values was excellent.

The values of the parameters A, B and C obtained for various transitions through the minimization procedure are listed in table 1 for full CI and HF calculations. The HF data were taken from the work of Gupta and Baluja [23]. We obtained excellent fits for all the transitions. This is reflected in the very small value of χ^2. We notice from table 1 that there is an excellent agreement with fitted values of A with the single configuration ab-initio values of $Z^2 S_0$ for the transitions ${}^3P \rightarrow {}^3P^0$ and ${}^1D \rightarrow {}^1P^0$. However for the transition ${}^1S \rightarrow {}^1P^0$, the fitted value of $A = 8{\cdot}2856$ is less than half

of its single configuration value of $A_{HF} = 18$. This poor agreement is due to the absence of near degenerate effect in the single configuration scheme for ^1S state. But when this effect is included the ab-initio value $A = 7{\cdot}12$ is in fair agreement with the fitted value. We also note that the single configuration fitted value of 17·46 agrees closely with ab-initio value 18·0. It is very important that where near degeneracy effects are present, they must be included in the zeroth-order calculation of line strengths for the correct interpretation of the hydrogenic limit. This limit checks the accuracy of the fitted values of A.

Table 1. Values of A, B, C, χ^2 and Z^2S_0 for various transitions in the O-sequence.

Transition	A	B	C	χ^2	Z^2S_0
$2s^2 2p^4\,{}^3P \rightarrow$	161·6813	764·3139	3.1936	8·09(−6)*	162·0
$\rightarrow 2s2p^5\,{}^3P^0$	(157·06)	(1292·98)	(4·3953)	(8·09(−6))	(162·0)
$2s^2 2p^4\,{}^1D \rightarrow$	87·3021	532·5121	3·4479	4·40(−4)	90·0
$\rightarrow 2s2p^5\,{}^1P^0$	(87·27)	(718·16)	(4·3953)	(4·79(−5))	(90·0)
$2s^2 2p^4\,{}^1S \rightarrow$	8·2856	114·1842	−6·2861	1·28(−4)	7·12
$\rightarrow 2s2p^5\,{}^1P^0$	(17·46)	(143·638)	(4·3953)	(9·19(−6))	(18)

The values within the braces are those of single configuration (HF) case.
*$a(-b)$ implies $a\,10^{-b}$

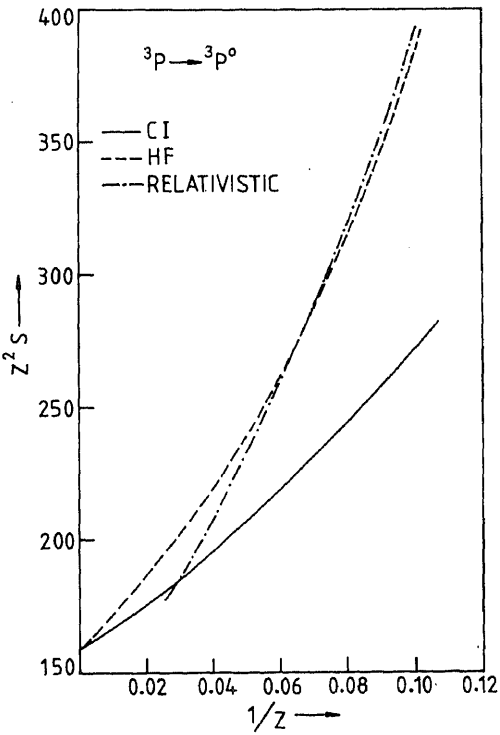

Figure 1. Variation of Z^2S with $1/Z$ for the transition $2s^2 2p^4\,{}^3P \rightarrow 2s2p^5\,{}^3P^0$ for ions in the oxygen isoelectronic sequence. —— Full CI (present results); --- HF (present results); —·— Cheng *et al* (24). Relativistic.

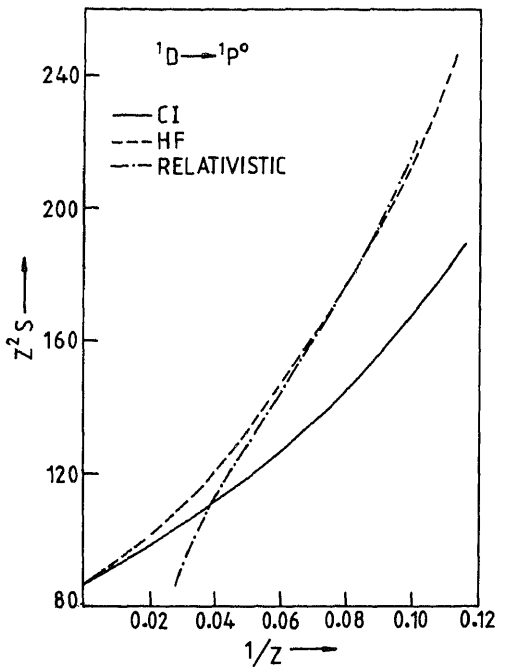

Figure 2. Same as in figure 1 but for the transition $2s^2 2p^4\, {}^1D \rightarrow 2s2p^5\, {}^1P^0$.

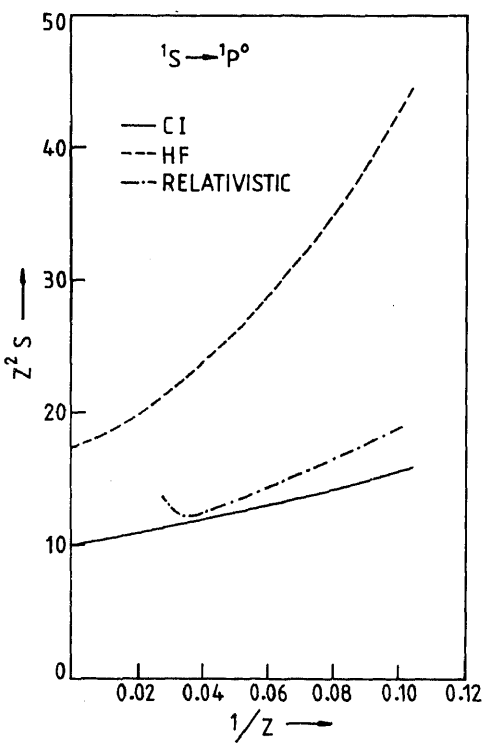

Figure 3. Same as in figure 1 but for the transition $2s^2 2p^4\, {}^1S \rightarrow 2s2p^5\, {}^1P^0$.

In figure 1, we have displayed Z^2S values against $1/Z$ for the transition $^3P \rightarrow {}^3P^0$. The values of S correspond to the full CI and HF calculations. We have also shown the results obtained by Cheng *et al* [24] using the Dirac formalism which employed a restricted $j-j$ basis set including only the configurations within the $n=2$ complex. It is well known that $j-j$ coupling scheme is inadequate near the neutral end where the *LS* coupling scheme prevails. Since our CI calculations included more correlation, our values lie lower than theirs for $Z \leqslant 25$ and our HF values. As Z increases the effect of correlation is diluted and both the curves tend to come nearer. However, since Cheng *et al* calculations included relativistic effects, it does not converge to the HF value of 162. Our non-relativistic curves for CI and HF cases converge extremely close to this value in the limit $Z \rightarrow \infty$. The relativistic effects increase with increasing Z. If we discard the higher $Z(>20)$ values of Cheng *et al*, we notice that their curve apparently converges to the non-relativistic limit. This is a good check on their calculation and our CI calculation.

A similar trend is noticed in figure 2 for the transition $^1D \rightarrow {}^1P^0$. Figure 3 displays the results for the $^1S \rightarrow {}^1P^0$ transition. Since our HF results do not include near degenerate correlation, it lies above the other two curves. The results of Cheng *et al* [24] included near degeneracy effect within the relativistic formalism, it lies between HF and our full CI curve which included all types of correlation. The HF curve converges to the limiting value 17·46 which is extremely close to the ab-initio value of 18. However, this is not the correct limit when correlations are included. Once again, if we extend the results of Cheng *et al* for values $Z \leqslant 20$, their curve and our full CI curves converge nearly to the correct limiting value.

References

[1] D E Osterbrock, *Astrophysics of gaseous nebulae* (Freeman, San Francisco, 1974)
[2] E Hinnov and S Suckewer, *Phys. Lett.* **A79**, 298 (1980)
[3] A L Stewart, in *Advances in atomic and molecular physics* edited by D R Bates and I Estermann (Academic Press: New York, 1967) vol. 3
[4] A Dalgarno and N Lynn, *Proc. Phys. Soc. (London)* **A70**, 802 (1957)
[5] J W Cooper, *Phys. Rev.* **128**, 681 (1962)
[6] M Inokuti, *Rev. Mod. Phys.* **43**, 297 (1971)
[7] S Bashkin, *Nucl. Instrum. Methods* **20**, 88 (1964)
[8] R Crossley, *Phys. Scr.* **T8**, 117 (1984)
[9] C F Fischer, *The Hartree–Fock method for atoms* (Wiley, New York, 1977)
[10] A Hibbert, *Comput. Phys. Commun.* **9**, 141 (1975)
[11] W L Wiese, *Beam foil spectroscopy* edited by S Bashkin (Springer, Heidelberg, 1976)
[12] M W Smith, G A Martin and W L Wiese, *Nucl. Instrum. Methods* **110**, 219 (1973)
[13] A Dalgarno, *Nucl. Instrum Methods* **110**, 183 (1973)
[14] E Träbert, *Z. Phys.* **D9**, 143 (1988)
[15] K L Baluja and A Agrawal, *Z. Phys.* **D**, (in press) (1994)
[16] D Layzer, *Ann. Phys.* **8**, 271 (1959)
[17] B Edlen, *Phys. Scr.* **17**, 565 (1978)
[18] K L Baluja and C J Zeippen, *J. Phys.* **B21**, 15 (1988)
[19] J B Scarborough, in *Numerical mathematical analysis* (Oxford & IBH, New Delhi, 1966)
[20] J C Slater, *Quantum theory of atomic structure* (McGraw Hill, New York, 1960) vol. 1
[21] I I Sobelman, *Atomic spectra and radiative transitions* (Springer, Berlin, Heidelberg, New York, 1979)
[22] I Oksüz and O Sinanoglu, *Phys. Rev.* **181**, 42 (1969)
[23] A Gupta and K L Baluja, *Indian J. Pure Appl. Phys.* **31**, 297 (1993)
[24] K T Cheng, Y K Kim and J P Desclaux, *At. Data Nucl. Data Tables* **24**, 111 (1979)

PRAMANA
— journal of
physics

© Printed in India

Vol. 43, No. 6,
December 1994
pp. 487–493

Einstein A-coefficients for rotational transitions in the HN_2O^+

S CHANDRA[1,2] and A K SHARMA[1]
[1]Department of Physics, University of Gorakhpur, Gorakhpur 273 009, India
[2]Inter-University Centre for Astronomy and Astrophysics, Post Bag 4, Ganeshkhind, Pune 411 007, India

MS received 12 April 1994; revised 18 July 1994

Abstract. Einstein A-values for the electric dipole transitions between the rotational levels up to 540 cm^{-1} and $J = 11$ in the ground vibrational state of the protonated N_2O (i.e., HN_2O^+) are calculated. The coefficients are used to compute the mean radiative lifetimes of the levels. These A-values can be used for analysing the spectra from astronomical objects, if observed.

Keywords. Einstein A-coefficients; rotational transitions; asymmetric top molecule; HN_2O^+-molecule.

PACS Nos 32·30; 32·70

1. Introduction

A number of molecules have been observed in the astronomical objects. Some of them have been even found in the vibrationally excited states. For analysing the spectra from astronomical objects, the Einstein A-values are one of the important parameters [1, 2 and references cited therein]. Bogey *et al* [3] made predictions of some rotational transitions of HN_2O^+ (protonated nitrous oxide) that may be of astrophysical interest. They used magnetically confined negative glow discharge to investigate the millimeter wave spectrum of HN_2O^+ in the 132–290 GHz. They also derived the rotational and distortional molecular constants. Since the molecule may be of astrophysical interest, the analysis of the observations would require the knowledge of transition probabilities (i.e., the Einstein A-values). Therefore, in the present communication we have calculated the Einstein A-coefficients for the electric dipole transitions between the rotational levels up to 540 cm^{-1} and $J = 11$.

2. Einstein A-coefficients for HN_2O^+

The HN_2O^+ is a a-type asymmetric top molecule with dipole moment $\mu = 2{\cdot}4$ D. Details of the calculations of Einstein A-values for a-type asymmetric top molecules are the same as published in Chandra *et al* [1] and Jaruschewski *et al* [4]. The rotational wave functions for the asymmetric top molecule can be described by linear combinations of symmetric top wave functions:

$$\psi_{J\tau M}(\alpha, \beta, \gamma) = \left(\frac{2J+1}{8\pi^2}\right)^{1/2} \sum_{K=-J}^{J} g^J_{\tau K} D^J_{MK}(\alpha, \beta, \gamma) \tag{1}$$

where α, β, γ are the Eulerian angles specifying the orientation of the molecule, J the rotational quantum number, $g^J_{\tau K}$ the expansion coefficients, D^J_{MK} the Wigner D-functions, and the pseudo quantum number τ is defined by

$$\tau = K_{-1} - K_{+1}. \tag{2}$$

The rotational transitions are governed by the selection rules

$$J: \Delta J = 0, \quad \pm 1$$

$$K_{-1}, \quad K_{+1}: \quad \text{odd, even} \leftrightarrow \text{odd, odd}$$

$$\text{even, odd} \leftrightarrow \text{even, even.}$$

In the representation in which the axis of quantization is along the a-axis of inertia, the expression for the line strength is given by

$$S(J'_{\tau'} \to J_{\tau}) = \mu^2 (2J+1) \left[\sum_{K=-J}^{J} g^J_{\tau K} g^{J'}_{\tau' K} C^{J'K}_{JK10} \right]^2 \tag{3}$$

where the C's are Clebsch–Gordan coefficients. The transition probabilities follow directly from the line strength

$$A(J'_{\tau'} \to J_{\tau}) = \frac{64\pi^4 \nu^3 S(J'_{\tau'} \to J_{\tau})}{3hc^3 (2J'+1)} \tag{4}$$

where the frequency ν corresponds to the energy difference of the two levels.

3. Molecular constants

The molecular constants for the ground vibrational state of the protonated N_2O are reported by Bogey *et al* [3], and are given in table 1.

4. Results and discussion

The calculated values of the Einstein A-coefficients for the trnasitions $J'\tau' \to J\tau$ are given in tables 2 and 3. Here the primed parameters correspond to the upper level

Table 1. Molecular constants for protonated N_2O.

A	623923·(1420)[a]	MHz
B	11301·5587(19)	MHz
C	11084·2784(19)	MHz
D_J	5·3371(30)	kHz
D_{JK}	726·54(83)	kHz
D_K	242·8	kHz
d_1	−0·0910(34)	kHz
d_2	−0·0240(33)	kHz
H_{KJ}	0·35(11)	kHz
L_{KJ}	0·0891(46)	kHz

[a]Numbers in parentheses represent one standard deviation in unit of the last quoted digit.

Table 2. Einstein A-coefficients for ortho-HN_2O^+.

J'	τ'	J	τ	$A(s^{-1})$	J'	τ'	J	τ	$A(s^{-1})$	J'	τ'	J	τ	$A(s^{-1})$
1	1	1	0	3·4387D − 13	2	−1	1	0	1·7785D − 06	2	0	1	1	1·8311D − 06
2	0	2	−1	3·0949D − 12	3	−2	2	−1	7·6221D − 06	3	−1	2	0	7·8473D − 06
3	−1	3	−2	1·2380D − 11	4	−3	3	−2	1·9760D − 05	4	−2	3	−1	2·0344D − 05
4	−2	4	−3	3·4390D − 11	5	−4	4	−3	4·0418D − 05	5	−3	4	−2	4·1612D − 05
5	−3	5	−4	7·7381D − 11	6	−5	5	−4	7·1817D − 05	6	−4	5	−3	7·3940D − 05
6	−4	6	−5	1·5168D − 10	7	−6	6	−5	1·1618D − 04	7	−5	6	−4	1·1961D − 04
7	−5	7	−6	2·6966D − 10	8	−7	7	−6	1·7572D − 04	8	−6	7	−5	1·8092D − 04
8	−6	8	−7	4·4581D − 10	9	−8	8	−7	2·4031D − 04	9	−7	8	−6	3·6756D − 05
9	−7	9	−8	3·2655D − 13	10	−9	9	−8	2·8143D − 04	10	−8	9	−7	1·1192D − 04
10	−8	10	−9	8·4718D − 10	11	−10	10	−9	3·9649D − 11	11	−9	11	−10	1·8139D − 07
3	2	2	−1	2·3085D − 08	3	2	3	−1	1·9395D − 08	3	2	4	−3	4·7174D − 09
3	3	2	0	2·3088D − 08	3	3	3	−2	1·9390D − 08	3	3	4	−2	4·7194D − 09
4	1	3	−2	4·7767D − 08	4	1	4	−2	4·8879D − 08	4	1	5	−4	1·3506D − 08
4	1	3	2	9·3429D − 06	4	2	3	−1	4·7780D − 08	4	2	4	−3	4·8858D − 08
4	2	5	−3	1·3514D − 08	4	2	3	3	9·3429D − 06	5	0	4	−3	7·6042D − 08
5	0	5	−3	8·6903D − 08	5	0	6	−5	2·5939D − 08	5	0	4	1	2·7300D − 05
5	1	4	−2	7·6078D − 08	5	1	5	−4	8·6845D − 08	5	1	6	−4	2·5961D − 08
5	1	4	2	2·7300D − 05	6	−1	5	−4	1·0866D − 07	6	−1	6	−4	1·3303D − 07
6	−1	7	−6	4·1729D − 08	6	−1	5	0	5·6131D − 05	6	0	5	−3	1·0874D − 07
6	0	6	−5	1·3290D − 07	6	0	7	−5	4·1776D − 08	6	0	5	1	5·6131D − 05
7	−2	6	−5	1·4605D − 07	7	−2	7	−5	1·8709D − 07	7	−2	8	−7	6·0652D − 08
7	−2	6	−1	9·8092D − 05	7	−1	6	−4	1·4620D − 07	7	−1	7	−6	1·8686D − 07
7	−1	8	−6	6·0738D − 08	7	−1	6	0	9·8092D − 05	8	−3	7	−6	1·8849D − 07
8	−3	8	−6	2·4902D − 07	8	−3	9	−8	7·9078D − 08	8	−3	7	−2	1·5543D − 04
8	−2	7	−5	1·8874D − 07	8	−2	8	−7	2·4862D − 07	8	−2	9	−7	1·3600D − 08
8	−2	7	−1	1·5543D − 04	9	−3	8	−6	2·3664D − 07	9	−3	9	−8	1·9183D − 06
9	−3	10	−8	4·2039D − 08	9	−3	8	−2	2·3041D − 04	9	−4	8	−7	2·3622D − 07
9	−4	9	−7	4·6135D − 07	9	−4	10	−9	4·9071D − 08	9	−4	8	−3	2·3041D − 04
10	−5	9	−8	4·3963D − 07	10	−5	10	−8	1·6578D − 06	10	−5	9	−4	3·2526D − 04

10	−4	9	−7	3·2434D−07	10	−4	10	−9	1·0573D−06	10	−4	9	−3	3·2526D−04
11	−5	10	−8	2·9546D−11	11	−5	11	−10	7·2724	11	−5	10	−4	2·0638D−07
11	−6	10	−9	1·5443D−08	11	−6	11	−9	6·6712	11	−6	10	−5	2·9232D−05
11	−6	11	−5	3·7478D−11	5	5	4	2	1·0506D−07	5	5	5	0	4·6539D−08
5	5	6	0	6·7657D−09	5	4	4	1	1·0506D−07	5	4	5	1	4·6539D−08
5	4	6	−1	6·7657D−09	6	3	5	0	2·0509D−07	6	3	6	0	1·2188D−07
6	3	7	−2	2·1440D−08	6	3	5	4	2·2806D−05	6	4	5	1	2·0509D−07
6	4	6	−1	1·2188D−07	6	4	7	−1	2·1440D−08	6	4	5	5	2·2806D−05
7	3	7	−6	1·4935D−13	7	3	6	0	3·0675D−07	7	3	7	−2	2·1938D−07
7	3	8	−2	4·4033D−08	7	3	6	4	5·8695D−05	7	2	6	−1	3·0675D−07
7	2	7	−1	2·1938D−07	7	2	8	−3	4·4033D−08	7	2	6	3	5·8695D−05
8	2	8	−7	1·0005D−13	8	2	7	−1	4·1326D−07	8	2	8	−3	3·3607D−07
8	2	9	−3	7·4303D−08	8	2	7	3	1·0992D−04	8	1	8	−6	3·3696D−13
8	1	7	−2	4·1326D−07	8	1	8	−2	3·3607D−07	8	1	9	−4	7·4303D−08
8	1	7	2	1·0992D−04										

Table 3. Einstein A-coefficients for para-HN_2O^+.

J'	τ'	J	τ	$A(s^{-1})$	J'	τ'	J	τ	$A(s^{-1})$	J'	τ'	J	τ	$A(s^{-1})$
1	−1	0	0	2·5070D−07	2	−2	1	−1	2·4067D−06	3	−3	2	−2	8·7025D−06
4	−4	3	−3	2·1392D−05	5	−5	4	−4	4·2728D−05	6	−6	5	−5	7·4967D−05
7	−7	6	−6	1·2036D−04	8	−8	7	−7	1·4894D−04	9	−9	8	−8	1·8619D−05
10	−10	9	−9	2·2759D−12	11	−11	10	−10	8·1222D−05	2	1	2	−2	1·5515D−08
2	2	1	−1	9·8283D−09	2	2	3	−3	5·7096D−09	3	0	3	−3	3·8786D−08
3	0	2	1	4·8310D−06	3	1	2	−2	2·4036D−08	3	1	4	−4	1·4866D−08
3	1	2	2	4·8311D−06	4	−1	4	−4	6·9813D−08	4	−1	3	0	1·6032D−05
4	0	3	−3	4·3193D−08	4	0	5	−5	2·6968D−08	4	0	3	1	1·6032D−05
5	−2	5	−5	1·0859D−07	5	−2	4	−1	3·5865D−05	5	−1	4	−4	6·7724D−08

5	−1	6	−6	4·1682D−08	5	−1	4	0	3·5866D−05	6	−3	6	−6	1·5513D−07
6	−3	5	−2	6·6588D−05	6	−2	5	−5	9·8029D−08	6	−2	7	−7	5·8723D−08
6	−2	5	−1	6·6591D−05	7	−4	7	−7	2·0941D−07	7	−4	6	−3	1·1046D−04
7	−3	6	−6	1·3451D−07	7	−3	8	−8	6·5558D−08	7	−3	6	−2	1·1046D−04
8	−5	8	−8	2·0430D−07	8	−5	7	−4	1·6972D−04	8	−4	7	−7	1·7756D−07
8	−4	9	−9	7·3886D−08	8	−4	7	−3	1·6973D−04	9	−6	9	−9	8·6872D−08
9	−6	8	−5	2·4663D−04	9	−5	8	−8	1·0657D−08	9	−5	8	−4	2·4665D−04
10	−6	9	−9	7·7178D−10	10	−6	11	−11	6·5412D−02	10	−6	9	−5	5·3744D−07
10	−7	10	−10	7·9899D−01	10	−7	9	−6	3·2623D−05	10	−7	10	−6	1·6218D−10
11	−7	10	−10	1·0893D−01	11	−7	10	−6	8·0527D−05	11	−8	11	−11	3·1520D−01
11	−8	10	−7	1·3026D−04	11	−8	11	−7	1·3706D−08	4	3	3	0	5·6305D−08
4	3	4	0	3·2579D−08	4	3	5	−2	5·9264D−09	4	4	3	1	5·6305D−08
4	4	4	−1	3·2579D−08	4	4	5	−1	5·9264D−09	5	2	4	−1	1·1156D−07
5	2	5	−1	8·3771D−08	5	2	6	−3	1·8015D−08	5	2	4	3	1·5337D−05
5	3	4	0	1·1156D−07	5	3	5	−2	8·3771D−08	5	3	6	−2	1·8015D−08
5	3	4	4	1·5337D−05	6	1	6	−6	1·4099D−13	6	1	5	−2	1·7008D−07
6	1	6	−2	1·4958D−07	6	1	7	−4	3·5955D−08	6	1	5	2	4·1526D−05
6	2	5	−1	1·7008D−07	6	2	6	−3	1·4958D−07	6	2	7	−3	3·5955D−08
6	2	5	3	4·1526D−05	7	0	7	−7	4·0091D−13	7	0	6	−3	2·3370D−07
7	0	7	−3	2·2852D−07	7	0	8	−5	5·9425D−08	7	0	6	1	8·0823D−05
7	1	6	−6	2·3051D−13	7	1	8	−8	1·2139D−13	7	1	6	−2	2·3370D−07
7	1	7	−4	2·2852D−07	7	1	8	−4	5·9425D−08	7	1	6	2	8·0823D−05
8	−1	8	−8	7·1563D−13	8	−1	7	−4	3·0340D−07	8	−1	8	−4	3·1991D−07
8	−1	9	−6	8·8143D−08	8	−1	7	0	1·3548D−04	8	0	7	−7	5·2628D−13
8	0	9	−9	3·6451D−13	8	0	7	−3	3·0340D−07	8	0	8	−5	3·1991D−07
8	0	9	−5	8·8141D−08	8	0	7	1	1·3548D−04	9	−2	9	−9	1·1368D−12
9	−2	8	−5	3·7978D−07	9	−2	9	−5	4·2341D−07	9	−2	10	−7	1·3698D−08
9	−2	8	−1	2·0774D−04	9	−1	8	−8	1·4518D−12	9	−1	8	−4	3·7977D−07
9	−1	9	−6	4·2342D−07	9	−1	10	−6	2·3054D−10	9	−1	8	0	2·0774D−04
10	−2	11	−11	1·2646D−05	10	−2	9	−5	4·6324D−07	10	−2	10	−7	4·7673D−05
10	−2	11	−7	5·2613D−06	10	−2	9	−1	2·9986D−04	10	−3	10	−10	2·1023D−05
10	−3	9	−6	4·6325D−07	10	−3	10	−6	8·6727D−06	10	−3	11	−8	7·3368D−08
10	−3	9	−2	2·9986D−04	11	−3	10	−10	7·3914D−05	11	−3	10	−6	3·1559D−05
11	−3	11	−8	1·2337D−04	11	−3	10	−2	4·1406D−04	11	−4	11	−11	3·2729D−06
11	−4	10	−7	4·0272D−07	11	−4	11	−7	1·4460D−06	11	−4	10	−3	4·1407D−04

Table 4. Energies and radiative lifetimes for ortho- and para-levels of HN_2O^+.

J'	τ'	$E(cm^{-1})$	$T(s)$	J'	τ'	$E(cm^{-1})$	$T(s)$
1	0	21·1815	—	0	0	0·0	—
1	1	21·1888	2·908D + 12	1	− 1	0·7467	3·989D + 06
2	− 1	22·6676	5·623D + 05	2	− 2	2·2401	4·155D + 05
2	0	22·6893	5·461D + 05	3	− 3	4·4802	1·149D + 05
3	− 2	24·8967	1·312D + 05	4	− 4	7·4670	4·675D + 04
3	− 1	24·9402	1·274D + 05	5	− 5	11·2004	2·340D + 04
4	− 3	27·8688	5·061D + 04	6	− 6	15·6805	1·334D + 04
4	− 2	27·9413	4·915D + 04	7	− 7	20·9071	8·308D + 03
5	− 4	31·5839	2·474D + 04	8	− 8	26·8357	6·714D + 03
5	− 3	31·6926	2·403D + 04	9	− 9	33·3443	5·371D + 04
6	− 5	36·0419	1·392D + 04	10	− 10	40·5912	4·394D + 11
6	− 4	36·1942	1·352D + 04	11	− 11	48·7430	1·231D + 04
7	− 6	41·2429	8·607D + 03	2	1	83·9933	6·446D + 07
7	− 5	41·4459	8·360D + 03	2	2	83·9933	6·436D + 07
8	− 7	47·1868	5·691D + 03	3	0	86·2329	2·053D + 05
8	− 6	47·4478	5·527D + 03	3	1	86·2329	2·053D + 05
9	− 8	53·8575	4·161D + 03	4	− 1	89·2189	6·211D + 04
9	− 7	53·8789	2·721D + 04	4	0	89·2189	6·210D + 04
10	− 9	61·2105	3·553D + 03	5	− 2	92·9514	2·780D + 04
10	− 8	61·6303	8·935D + 03	5	− 1	92·9515	2·780D + 04
11	− 10	69·0172	2·522D + 10	6	− 3	97·4303	1·498D + 04
11	− 9	69·4957	5·513D + 06	6	− 2	97·4305	1·498D + 04
3	2	188·4233	2·119D + 07	7	− 4	102·6557	9·036D + 03
3	3	188·4233	2·119D + 07	7	− 3	102·6560	9·036D + 03
4	1	191·4084	1·058D + 05	8	− 5	108·6275	5·885D + 03
4	2	191·4084	1·058D + 05	8	− 4	108·6279	5·883D + 03
5	0	195·1397	3·638D + 04	9	− 6	115·3456	4·053D + 03
5	1	195·1397	3·638D + 04	9	− 5	115·3462	4·054D + 03
6	− 1	199·6173	1·773D + 04	10	− 6	122·3664	1·529D + 01
6	0	199·6173	1·773D + 04	10	− 7	122·4144	1·252
7	− 2	204·8410	1·015D + 04	11	− 7	130·5217	9·173
7	− 1	204·8410	1·015D + 04	11	− 8	130·8120	3·171
8	− 3	210·8109	6·412D + 03	4	3	334·4732	1·055D + 07
8	− 2	210·8109	6·415D + 03	4	4	334·4732	1·055D + 07
9	− 3	217·5270	4·299D + 03	5	2	338·2029	6·431D + 04
9	− 4	217·5270	4·326D + 03	5	3	338·2029	6·431D + 04
10	− 5	224·9891	3·055D + 03	6	1	342·6786	2·388D + 04
10	− 4	224·9891	3·061D + 03	6	2	342·6786	2·388D + 04
11	− 5	232·8100	1·375D − 01	7	0	347·9001	1·229D + 04
11	− 6	232·8390	1·499D − 01	7	1	347·9001	1·229D + 04
5	5	522·1409	6·315D + 06	8	− 1	353·8675	7·343D + 03
5	4	522·1409	6·315D + 06	8	0	353·8675	7·343D + 03
6	3	526·6144	4·319D + 04	9	− 2	360·5807	4·795D + 03
6	4	526·6144	4·319D + 04	9	− 1	360·5807	4·795D + 03
7	3	531·8334	1·687D + 04	10	− 2	368·0397	2·733D + 03
7	2	531·8334	1·687D + 04	10	− 3	368·0397	3·029D + 03
8	2	537·7979	9·030D + 03	11	− 3	376·2444	1·555D + 03
8	1	537·7979	9·030D + 03	11	− 4	376·2444	2·386D + 03

of transition whereas the unprimed parameters correspond to the lower level. The Einstein A-coefficients are used to calculate the mean radiative lifetimes defined by

$$T_{j'\tau'} = 1 \Big/ \sum_{j\tau} A(J'\tau' \to J\tau).$$

The values of the mean radiative lifetimes of the levels are given in table 4.

The Einstein A-coefficients may be used for analysing the spectra of HN_2O^+ from astronomical objects, if observed. Although N_2O has not been detected in the interstellar medium, the calculations by Mitchell [5] have shown that N_2O could be relatively abundant in a shocked intersteller cloud with the speed of the shocks less than 15 km/s. The detection of N_2O however could be difficult because of its very low dipole moment $\mu = 0{\cdot}16$ debye. But the search for the protonated N_2O seems more promising because of its large dipole moment $\mu = 2{\cdot}4$ debye.

Acknowledgements

This work was partly done during one of the authors (SC) visit to Inter-University Centre for Astronomy and Astrophysics, Pune. Financial supports from the Council of Scientific and Industrial Research, New Delhi and the Indian Space Research Organisation, Bangalore are thankfully acknowledged.

References

[1] S Chandra, W H Kegel and D A Varshalovich, *Astron. Astrophys. Suppl.* **58**, 687 (1984)
[2] S Chandra, D A Varshalovich and W H Kegel, *Pramana – J. Phys.* **25**, 557 (1985)
[3] M Bogey, C Demuynck, J L Destombes and A R W Mckellar, *Astron. Astrophys.* **167**, L13 (1986)
[4] S Jaruschewski, S Chandra, D A Varshalovich and W H Kegel, *Astron. Astrophys. Suppl.* **63**, 307 (1986)
[5] G F Mitchell, *Astrophys. J. Suppl. Ser.* **54**, 81 (1984)

PRAMANA
— journal of
physics

© Printed in India

Vol. 43, No. 6,
December 1994
pp. 495–502

Vibrationally elastic $e^- - H_2O$ scattering at intermediate energies

K N JOSHIPURA, MINAXI VINODKUMAR* and P M PATEL*
Department of Physics, Sardar Patel University, Vallabh Vidyanagar 388 120, India
*V.P. & R.P.T.P. Science College, Vallabh Vidyanagar 388 120, India

MS received 14 December 1993; revised 13 April 1994

Abstract. Vibrationally elastic total cross-sections of e^-–H_2O scattering are calculated at intermediate energies $E_i = 10$–300 eV. The interaction potentials are treated in spherical models. The dipole rotational excitation, which is significant but not dominant above 10 eV, is treated incoherently. Effects of electronic excitation-ionization, significant above 30 eV or so, are considered through a complex optical potential. A dynamically distorted charge-density is employed to calculate the imaginary part of the complex potential. Comparisons are made with recent theoretical and experimental data. The mutual agreement is better in total cross-sections than in differential cross-sections.

Keywords. Elastic and inelastic electron-scattering; optical potential, total cross-sections.

PACS No. 34·80

1. Introduction

This paper deals with some of the theoretical aspects of the scattering of electrons by water molecules. This has been recently investigated by Itikawa and co-workers and by others [1–3]. We confine ourselves mainly to total cross-sections of e^-–H_2O scattering, for which experimental data have been given by Johnstone and Newell [4], Sueoka *et al* [5] and others. All these workers have also emphasized the importance of the study of e^-–H_2O scattering.

The interaction of an electron with a molecule like H_2O is in general nonspherical. Rotational excitation of the molecule due to the long range dipole potential dominates the e^-–H_2O total cross-sections at low energies. At intermediate and high energies, short range interactions become more significant. At such energies the total e^-–H_2O cross-section can be calculated by assuming the molecule to be spherical and the only important nonspherical effect, that of the dipole rotation, may be incorporated incoherently [3]. We have presently adopted this approach to calculate the total e^-–H_2O cross-sections at intermediate energies. $E_i = 10$–300 eV. Jain [3] calculated these cross-sections by starting with a polarized target charge-density to generate the spherical complex optical potential. Now, the target charge-polarization is a dynamic (energy-dependent) phenomenon, hence we have presently obtained the polarized part of the charge-density through a dynamic polarization potential as well as through its asymptotic form. On the other hand Okamoto *et al* [1] have considered the static (unperturbed) charge-density in their calculations at $E_i = 6 - 50$ eV. They made no allowance for the electronic excitation–ionization channels in their calculations. They

have given a theoretical forward-scattering correction to the experimental total e^-–H_2O cross-sections.

We have employed complex optical potential to calculate the total (elastic + inelastic) cross-sections Q_T^S, within a spherical charge-density, distorted by a dynamic as well as static polarization potential. The nonspherical contribution Q_T^{NS} to the total cross-section, corresponding to rotational excitation is treated separately in the point dipole first Born approximation (PDFBA), following Itikawa [6]. We also examine the overall effect of electronic excitation and ionization channels on elastic e^-–H_2O scattering. Our total as well as differential cross-sections are compared with the recent theoretical and experimental data. The differences in the present results, arising out of (a) unperturbed and perturbed target charge density, and, (b) real and complex potential, are discussed.

2. Theory

Considering the incident electron energies to be intermediate and high, we write the total e^-–H_2O scattering cross-section Q_{tot} as an incoherent sum of the spherical and nonspherical contributions in the following manner

$$Q_{tot} = Q_T^S + Q_T^{NS} \tag{1}$$

Okamato *et al* [1] calculated the total cross-sections in two ways viz. (i) by starting with the complete nonspherical real potential and (ii) by starting with real spherical potential and adding the dipole correction, as in (1). The difference between their two calculations is significant at low energies, roughly below 30 eV. Thus in the present energy range the incoherent approach of (1) is quite suitable.

Now the spherical contribution Q_T^S to the total cross-section (1) is obtained here by starting with an accurate charge-density $\rho_0(r)$ of H_2O, given by Katase *et al* [7]. We represent the e^-–H_2O system by a complex, spherical, energy-dependent optical potential,

$$V_{opt}(r, E_i) = V_{st}(r) + V_{ex}(r, E_i) + V_{pol} + iV_{abs}(r, E_i) \tag{2}$$

where V_{st} is the static potential obtained directly from the static charge-density $\rho_0(r)$. The exchange potential V_{ex} is obtained following the free-electron-gas-exchange model of Hara [8]. For the absorption potential V_{abs} we have adopted the quasi-free Pauli-blocking model given by Truhlar and coworkers [9]. The polarization effects (represented by V_{pol} in (2)) are adequately described, at intermediate energies, by the correlation-polarization potential (see [10, 11]). Towards high energies ($E_i \geq 80$ eV here) we have adopted for V_{pol}, a dynamic polarization potential,

$$V_{dp}(r, E_i) = -\frac{1}{2}\frac{\alpha_0 \cdot r^2}{(r^2 + r_c^2)^3} \tag{3}$$

with

$$r_c = 0{\cdot}375k/\Delta$$

here α_0 and Δ are respectively, the average spherical polarizability and the average excitation energy of the target molecule. Further, k is the incident momentum (in a.u.). In (3) a shorter-range term varying asymptotically as r^{-6} may be added, but

that requires a reliable value of the quadrupole polarizability of the molecule. Moreover, the extra term would be ineffective in view of (7) to follow. Now, the incident electron perturbs the target charge distribution, hence the exchange and the absorption potentials (effective near the target) must be derived from a polarized (rather static) charge-density. We have presently calculated the polarized part of the charge-density, denoted by $\rho_{pol}(r, E_i)$, from the dynamic polarization potential $V_{dp}(r, E_i)$, through the Poisson equation,

$$\nabla^2 V_{pol}(r, E_i) = -4\pi\rho_{pol}(r, E_i). \tag{4}$$

Using (3) and (4), the dynamic correction to the charge-density is,

$$\rho_{pol}(r, E_i) = \frac{1}{4\pi}\left[\frac{3\alpha_0}{(r^2+r_c^2)^3} - \frac{21\alpha_0 r^2}{(r^2+r_c^2)^4} + \frac{24\alpha_0 r^4}{(r^2+r_c^2)^5}\right]. \tag{5}$$

If we start with the static asymptotic form $-\alpha_0/2r^4$ of the polarization potential and use the Poisson equation, we obtain the static-correction to the charge-density as $\Delta\rho = 3\alpha_0/2\pi r^6$.

Thus, we introduce the dynamically distorted charge-density,

$$\rho'(r, E_i) = \rho_0(r) + \rho_{pol}(r, E_i). \tag{6a}$$

The statically distorted charge-density would be,

$$\rho(r) = \rho_0(r) + \Delta\rho \tag{6b}$$

Note that unlike $\Delta\rho$, the correction $\rho_{pol} \to 0$ at high energies, making it theoretically more satisfying.

The polarization potential of (3) fails to account for the polarization effect at low energies [11]. Actually at small r, the picture of dipole charge-polarization of the target by an external electron breaks down. For e^-–H_2O scattering this may be the case, typically at $r \leqslant r_{O-H}$, where $r_{O-H} = 1{\cdot}81\ a_0$ is the O–H bond length in H_2O. At such separations the static-exchange potentials dominate, hence we take

$$\rho_{pol}(r, E_i) = 0, \quad \text{if} \quad r \leqslant r_{O-H} \tag{7}$$

Thus, we have considered (6a, 6b) along with (7) to derive the short range potentials.

It is the absorption potential that is modified appreciably by the use of corrections over $\rho_0(r)$. Towards scattering calculations we solved the Schrödinger equation numerically for the real and the imaginary parts of V_{opt} (for details see [12]). The partial wave phase-shifts thus obtained were employed to calculate the total (elastic + inelastic) cross-sections Q_T^S, viz,

$$Q_T^S = Q_{el} + Q_{inel} \tag{8}$$

where, Q_{el} is the total elastic cross-section and Q_{inel} is the total inelastic cross-section, in the complex potential. We have also calculated the purely elastic cross-sections, σ_{el} obtained by setting $V_{abs} = 0$ in (2).

The dipole contribution Q_T^{NS} in (1) was obtained in the PDFBA [6]. This differs somewhat from the expression of Collins and Norcross [13] in that the former treats H_2O as an asymmetric top.

3. Results and discussion

3.1 *Total cross-sections*

We calculated vibrationally elastic $e^- - H_2O$ total cross-sections Q_{tot} at energies $E_i = 10-300$ eV. The polarized charge density, (6) and (7), affects the absorption potential and hence Q_T^S. The total inelastic cross-section Q_{inel} is enhanced by the corrections via (6a) and (6b) in the charge-density, as observed by Jain [3]. However, our correction ρ_{pol} is energy-dependent. This is not so with the calculations of Jain [3], which therefore, overestimate the cross-sections at higher energies. Towards lower energies ($\leqslant 10$ eV) the polarized part of the charge-density has no significant effect on the cross-sections. Table 1 shows our calculated cross-sections Q_{inel} at $E_i = 30-300$ eV. These are compared here mutually in three models for V_{abs}, with (i) no correction over ρ_0, (ii) dynamic correction via (6a), and (iii) static correction via (6b). The quantity of column 3 (table 1) calculated via (6a) is closer to the theoretical ionization cross-sections Q_{ion} (column 5) given by Khare and Meath [14], especially towards high energies. The Q_{inel} including the static correction (column 4, table 1) are higher at high energies, similar to the results of Jain [3]. We have not included the experimental Q_{ion} data of Orient and Srivastava [15] which are still higher at the peak. Recent measurements of Rao [16], not shown, lie somewhat above the

Table 1. Inelastic cross-sections Q_{inel} (in 10^{-16} cm^2) for $e^- - H_2O$ scattering.

	Q_{inel} (present)			
Energy (eV)	No correction (ρ_0 only)	Dynamical correction eq. (6a)	Static correction eq. (6b)	Q_{ion}^* (theoretical)
30	0·33	0·71	0·76	1·1
50	1·07	1·61	1·92	1·9
80	1·62	1·88	2·93	2·1
100	1·76	1·91	3·00	2·1
300	1·31	1·30	1·89	1·4

*Values obtained from the graphical ionization cross-sections of Khare and Meath [14]

Table 2. The present total cross-sections σ_{el}, Q_T^S and Q_{el} (all in 10^{-16} cm^2) for $e^- - H_2O$ scattering, in spherical interactions.

E_i (eV)	Real potential σ_{el}	Complex potential	
		Q_T^S	$Q_{el} = Q_T^S - Q_{inel}$
10	10·2	10·2	10·2
30	7·7	8·3	7·6
50	4·2	5·0	3·9
80	3·6	4·9	3·1
100	2·9	4·3	2·4

values of columns 3 and 5 of table 1 and exhibit a similar energy-dependence. At high energies the entries of columns 2 and 3 tend to agree. This justifies the use of the dynamically perturbed charge-density in our results shown next.

Also investigated presently is the effect of inelastic scattering on elastic scattering at intermediate energies. We calculated the purely elastic cross-sections σ_{el} in a real spherical e^-–H_2O potential. Table 2 exhibits the total cross-sections σ_{el} and the total (elastic + inelastic) cross-sections Q_T^S, together with the total elastic cross-sections, Q_{el} (see (8)). The quantity Q_{inel} represents the overall effect of the electronic (excitation and ionization) channels, at a given energy. It becomes significant above 30 eV and shows a broad peak near 100 eV. Therefore, our values of σ_{el} and Q_T^S (table 2) are close to each other up to about 30 eV only. As E_i increases they differ significantly, with $Q_T^S > \sigma_{el}$, and $\sigma_{el} > Q_{el}$. Thus for $E_i > 30$ eV or so, the effects of electronic channels must be taken into account. This has not been done by Okamoto *et al* [1] in their calculations at $E_i = 6$–50 eV.

Now a quantity that offers a meaningful comparison with experimental data is Q_{tot} of (1). To compare the theoretical results with the experimental ones, we have considered the forward-scattering correction to the measured total cross-sections Q_{tot}, as given theoretically by Okamoto *et al* [1]. The correction ΔQ_{tot}, corresponds to the strong forward scattering by polar molecules like H_2O and is found to fit well with the formula,

$$\Delta Q_{tot}(E_i) = a \cdot (E_i)^{-b} \tag{9}$$

where $a = 30$, and $b = 0{\cdot}75$.

This formula holds good in the present energy range. The (undetected) correction ΔQ_{tot} must be added to the measured total cross-section Q_{tot} for a comparison with the theoretical value at a given energy. Table 3 shows the present values of Q_{tot} along with that of Jain [3]. Also shown are the total cross-sections averaged over the rotational-state distribution at the gas (H_2O) temperature 300 K, i.e. Q (300 K) given by Okamoto *et al* [1]. The last column of table 3 shows the measured cross-sections, with the correction of (9) given in the brackets.

Towards low energies the theoretical values in table 3 are quite similar, indicating (i) a subdued role of the polarized charge-density, and (ii) the dominance of Q_T^{NS} over

Table 3. Total (elastic plus inelastic) cross-sections* Q_{tot} (in 10^{-16} cm^2) for e^-–H_2O scattering.

	Theory			Experimental results
E_i (eV)	Present Q_{tot}	Jain [3]	Okamoto *et al* [1]	(Correction ΔQ_{tot}**)
10	23·1	23·18	23·10	13·89[@] (5·55)
30	13·8	13·08	12·27	11·29[@] (2·46)
50	8·6	10·13	8·35	7·76[@] (1·65)
80	7·4	8·14	—	6·3[£] (1·1)
100	6·2	7·71	—	5·6[£] (0·95)
300	2·8	4·0	—	3·2[£] (0·4)

*See eqn. (1); **See eqn. (9); [@] Johnstone and Newell [4]; [£] Sueoka *et al* [5, 17]

Q_T^S. As E_i increases, we find $Q_T^{NS} < Q_T^S$. Above 30 eV (nearly) Q_{tot} of Jain [3] are higher than ours because of his energy independent ρ_{pol}. At such energies, the cross-sections of Okamoto *et al* [1] are somewhat lower, mainly because of their neglect of the inelastic electronic channels.

Various experiments done so far on total $e^- - H_2O$ cross-sections differ from each other as well as from the corresponding theories also. Johnstone and Newell [4] integrated their measured elastic differential cross-sections at $E_i = 6$–50 eV. The measurements were done for scattering angles 10–120 degrees and were extrapolated to derive the integrated cross-sections. A comparison in table 3 reveals that the integrated cross-sections of Johnstone and Newell [4] are lower than the present and the other theories, but if the correction ΔQ_{tot} is added (along with inelastic contribution) to the reported measurements, then the theory and the experiment tend to agree. The directly measured Q_{tot} above 50 eV in table 3 are those of Sueoka *et al* [5, 17]. The present results are closer to these measurements also. At 300 eV the agreement is not so good.

3.2 *Differential cross-sections (DCS)*

Vibrationally elastic $e^- - H_2O$ DCS including the dipole-rotation, obtained from our theory are shown in figures 1, 2 and 3 at sample energies 50, 100 and 300 eV respectively. Shown at 50 eV (figure 1) are our theoretical DCS under (i) the complex potential alongwith the dynamically polarized charge-density and (ii) the real potential, with $V_{abs} = 0$. These two calculations differ marginally and agree qualitatively with

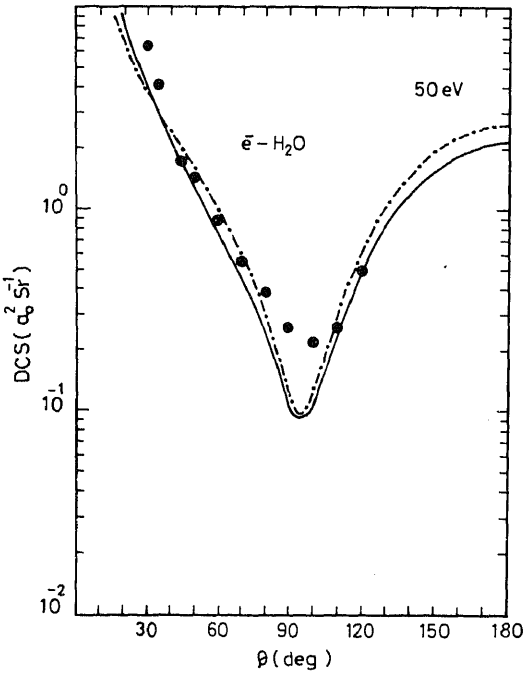

Figure 1. DCS in a_0^2/Sr for $e^- - H_2O$ scattering at 50 eV. ——— present results with dynamically polarized charge-density (complex potential); —·—·—·— Present results with real potential; ● Experimental DCS of Johnstone and Newell (1991).

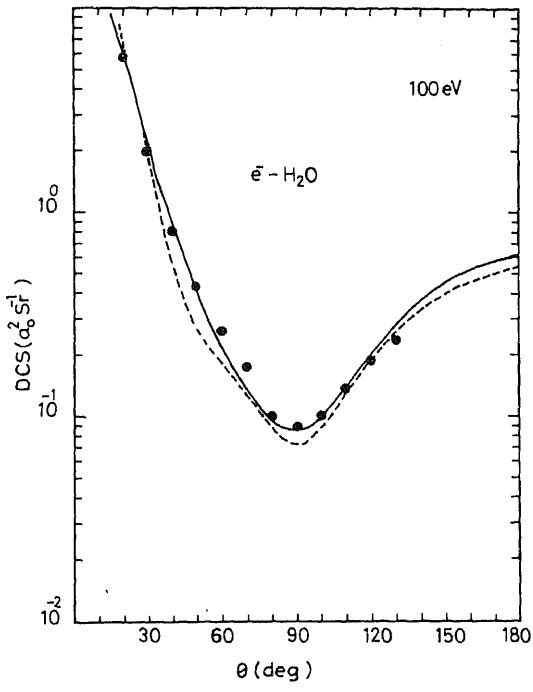

Figure 2. —— Same as in figure 1 but at 100 eV. ---- Present results with statically polarized charge-density (complex potential); ● Experimental DCS of Katase *et al* (1986).

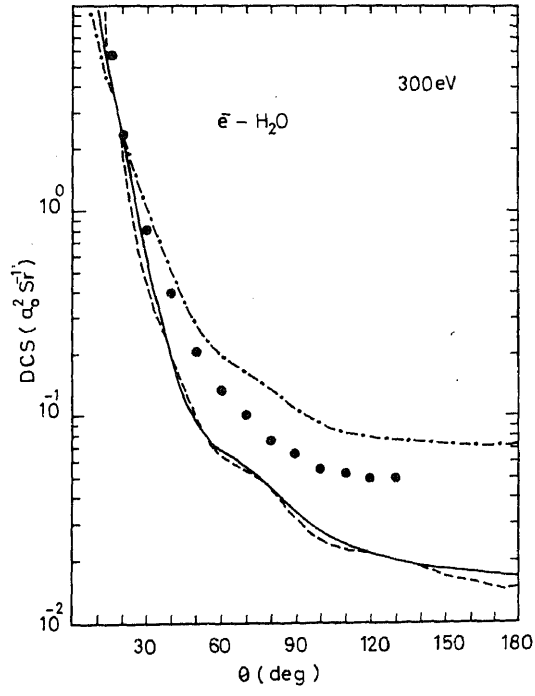

Figure 3. ———— Same as in figure 1 but at 300 eV; ---- Same as in figure 2, but at 300 eV; —·—·— Present results with real potential ● Experimental DCS of Katase *et al* (1986).

the experimental DCS of Johnstone and Newell [4]. Our models of (6a) and (6b) do not differ much here. The minimum in the DCS around 100° is deeper in our theory. At 100 eV (figure 2) the present theory, including the dynamical correction (6a) favours the measurements of Katase *et al* [7], better than that with the static correction (6b). Towards high energies the DCS in complex potential, tend to be rather lower at intermediate and large angles. As has been noted earlier [12, 18] this is due to an excessive loss of flux to the inelastic channels, at small r, predicted by the present V_{abs}. We can see from figure 3 (at 300 eV) that the present DCS in the complex potential are lower than the measured DCS of Katase *et al* [7] at intermediate and large angles, while those in the real potential are correspondingly higher. The dynamically polarized charge-density, on which we have focussed attention in this paper, does not appreciably correct this behaviour of the theoretical DCS.

Thus from the present study on $e^- - H_2O$ scattering we conclude the following. The rotational excitation cross-sections, represented through PDFBA are dominant up to about 10 eV and significant even at 100 eV or so, but the present method of calculation, via (1) is satisfactory at intermediate and high energies. The electronically inelastic channels are significant from about 30 eV onwards. The distortion of the target charge-density also assumes significance at these energies, but it should be treated dynamically. An energy-independent polarized charge-density results into overestimation in total cross-sections at high energies. The present Q_{inel} with dynamical distortion, are consistent with the ionization cross-sections. Beyond 300 eV the static charge-density would be sufficient to obtain reliable total cross-sections. Our theoretical DCS are not as good as our total cross-sections. The present absorption potential appears to be rather strong at large E_i and small r.

Acknowledgement

This research was supported in part by the University Grants Commission, New Delhi through a major research project to KNJ.

References

[1] Y Okamoto, K Onda and Y Itikawa, *J. Phys.* **B26**, 745 (1993)
[2] J Yuan and Z Zhang, *Phys. Rev.* **A45**, 4565 (1992)
[3] A Jain, *J. Phys.* **B21**, 905 (1988)
[4] W M Johnstone and W R Newell, *J. Phys.* **B24**, 3633 (1991)
[5] O Sueoka, S Mori and Y Katayama, *J. Phys.* **B19**, L373 (1986)
[6] Y Itikawa, *J. Phys. Soc. Jpn.* **32**, 217 (1972)
[7] A Katase, K Ishibashi, Y Matsuomoto, T Sakae, S Maezono, E Murakami, K Watanabe and H Maki *J. Phys.* **B19**, 2715 (1986)
[8] S Hara, *J. Phys. Soc. Jpn.* **22**, 710 (1967)
[9] G Staszewska, D Schwenke, D Thirumalai and D G Truhlar, *Phys. Rev.* **A28**, 2740 (1983)
[10] N T Padial and D W Norcross *Phys. Rev.* **A29**, 174 (1984)
[11] K N Joshipura and P M Patel, *Pramana – J. Phys.* **38**, 329 (1992)
[12] K N Joshipura and P M Patel, *Phys. Rev.* **A48**, 2464 (1993)
[13] L A Collins and D W Norcross, *Phys. Rev.* **A18**, 467 (1978)
[14] S P Khare and W J Meath, *J. Phys.* **B20**, 2101 (1987)
[15] J Orient and S K Srivastava, *J. Phys.* **B20**, 3923 (1987)
[16] M V V S Rao, (Private Communication) (1994)
[17] O Sueoka, S Mori and Y Katayama, *J. Phys.* **B20**, 3237 (1987)
[18] A Jain, *Phys. Rev.* **A34**, 3707 (1986)

PRAMANA
— journal of
physics

© Printed in India

Vol. 43, No. 6,
December 1994
pp. 503–508

String theory in five dimensional cosmological models

SUBENOY CHAKRABORTY and GOPAL CHANDRA NANDY*
Department of Mathematics, Jadavpur University, Calcutta 700032, India
*Department of Physics, Modern School, Calcutta 700017, India

MS received 30 July 1993; revised 2 August 1994

Abstract. A study on string theory has been done in five dimensional flat space-time. Barotropic equation of state and p-string model are discussed. Also a polynomial relation between the two scale factors is assumed. In some special cases the solution reduces to generalized Kasner metric. Further diminision of extra dimension with the evolution of universe is exhibited. A detailed study of phase-space analysis is done for geometric string model.

Keywords. String theory; higher dimension; contraction; phase space.

PACS Nos 98·90; 04·20

1. Introduction

The unification of gravitational forces with other forces in nature is not possible in the usual 4-dimensional space-time. So higher dimensional theory may be useful to meet this challenge in quantum field theory. Recently, the development of super string theory [1] and 10 dimensional $N = 1$ Yang-Mills supergravity in its field theory limit suggest the importance of theories in more than 4-dimensional space-time. Also the experimental detection of time variation of fundamental constants provide strong evidence for the existence of extra-dimensions [2]. Moreover, in recent years the variable gravity 5D theory of Wesson [3] deserves serious attention. Here the 4D space-time is extended to 5D space-time-mass in which the fifth co-ordinate is the rest mass. If the rest mass is treated as constant then the theory reduces to general relativity and is thus an extension of Einstein's theory of gravitation.

In cosmology, this higher dimensional theory might be useful at the early stages of the evolution of the universe. It is generally assumed that the extra dimensions contract to the Planckian length scale or remain constant with the evolution of the universe. Higher dimensional solutions both for cosmological and non-cosmological cases have been performed recently by several workers [4–8]. String theory does not seem to have been considered in higher dimension earlier. As string concept is useful before the particle creation and can explain galaxy formation, it is interesting to study string cosmology in higher dimensional theory.

In this addendum we have studied string theory for flat Kaluza–Klein metric. A polynomial relation is assumed between the metric coefficients to solve the field equations. The barotropic equation of state and p-string model are considered for separate solutions. Some solutions correspond to generalized Kasner metric. Further the field equations reduce to an autonomous system for geometric string model and phase-space solutions are studied in detail.

2. Einstein field equations and their solutions

The five dimensional line element due to Gron [8] is

$$dS^2 = -dt^2 + R^2(dx^2 + dy^2 + dz^2) + A^2 dm^2, \tag{1}$$

Unlike Wesson [3], the fifth co-ordinate is taken to be space-like and the metric co-efficients are assumed to be functions of time only.

The energy momentum tensor for the string-dust system is [9],

$$T_{\mu\gamma} = \rho V_\mu V_\gamma - \lambda x_\mu x_\gamma, \tag{2}$$

where ρ is the rest energy density of the cloud of strings with particles attached to them and λ is the tension density of the string cloud. The five-velocity vector V^μ has the components $V^\mu = (1,0,0,0,0)$ and x^μ represents string's direction which is taken along the extra dimension i.e. $x^\mu = (0,0,0,0,A^{-1})$. Also V^μ and x_μ will satisfy

$$V^\mu V_\mu = -x^\mu x_\mu = -1 \text{ and } V^\mu x_\mu = 0.$$

So the non-vanishing components of the Einstein's equation

$$R_{\mu\gamma} - \tfrac{1}{2}Rg_{\mu\gamma} = -T_{\mu\gamma},$$

are

$$3\frac{\dot{R}^2}{R^2} + 3\frac{\dot{R}}{R}\frac{\dot{A}}{A} = \rho, \tag{3}$$

$$2\frac{\ddot{R}}{R} + \frac{\dot{R}^2}{R^2} + 2\frac{\dot{R}}{R}\frac{\dot{A}}{A} + \frac{\ddot{A}}{A} = 0, \tag{4}$$

and

$$\frac{\ddot{R}}{R} + \frac{\dot{R}^2}{R^2} = \lambda. \tag{5}$$

The Bianchi identity is

$$\dot{\rho} + 3\frac{\dot{R}}{R}\rho + (\rho - \lambda)\frac{\dot{A}}{A} = 0. \tag{6}$$

We shall now discuss solutions of these field equations for two different equation of state for string model.

Case I: Barotropic equation of state

Here ρ and λ are connected by an arbitrary relation

$$\rho = \rho(\lambda).$$

Let us assume

$$A = \mu R^n, \quad \mu, n \text{ are constants}, \tag{7}$$

between the scale factors for unique solution of the field equations and we obtain

solutions as follows

$$R = R_0(t - t_0)^{\alpha},$$
$$A = A_0(t - t_0)^{n\alpha},$$
$$\rho = 3(n+1)\alpha^2(t - t_0)^{-2}, \tag{8}$$
$$\lambda = \frac{(1 - n^2)\alpha}{(3 + 2n + n^2)}(t - t_0)^{-2}.$$

Here t_0 and R_0 are arbitrary constants and

$$A_0 = \mu R_0^n,$$
$$\alpha = (2 + n)/(3 + 2n + n^2).$$

We note that if $n > 0$ then R and A behave identically. $t = t_0$ is the initial epoch and it is a point singularity. With the evolution of the universe the two scale factors increase with time while string and particle energy density gradually decrease (for $n > 1$ string density is unphysical).

For $n = 0$ the scale factor corresponding to extra-dimension is constant in time, otherwise it is identical to $n > 0$.

If $n < 0$, the initial epoch $t = t_0$ is a line singularity and with the evolution of the universe R increases while A decreases. Thus extra-dimension becomes insignificant as the time proceeds after the creation and we are left with real four dimensional world. For $n = -1$, $\rho = \lambda = 0$ and the solution then corresponds to generalized Kasner metric [10]. Further, for $n < -2$ the solution corresponds to contracting model of the universe, which is not of much interest here.

Case 2. Takabayashi string

Here the equation of state is [11]

$$\rho = (1 + W)\lambda, \tag{9}$$

with $W > 0$, a constant.

Now eliminating ρ and λ from (3) and (5) using (9) we obtain

$$A = CR^{(W-2)/3}\dot{R}^{(1+W)/3}. \tag{10}$$

If we substitute A from (10) in the field equations (4), we obtain a differential equation in R which is complicated in nature and difficult to solve. So for simplicity we take $W = 2$. Then from (10)

$$A = C\dot{R}, \tag{11}$$

and the corresponding differential equation in R is

$$\frac{\dddot{R}}{\dot{R}} + 4\frac{\ddot{R}}{R} + \frac{\dot{R}^2}{R^2} = 0. \tag{12}$$

For particular choice of the integration constant we have the following two sets of

solutions

$$R \propto (t-t_0)^{1/2}, \quad \rho \propto (t-t_0)^{-2}$$
$$A \propto (t-t_0)^{-1/2}, \quad \lambda \propto (t-t_0)^{-2}, \tag{13}$$

and

$$R \propto (t-t_0)^{2/3}, \quad \rho \propto (t-t_0)^{-2},$$
$$A \propto (t-t_0)^{-1/3}, \quad \lambda \propto (t-t_0)^{-2}. \tag{14}$$

The first set of solutions is the well-known generalized Kasner metric [8]. As before $t=t_0$ is the initial instant of the universe in both the cases and with the expansion of the universe the extradimension and the string concept gradually dies out. So we are left with the real four dimensional universe.

3. Autonomous system

We shall now consider the autonomous system for the flat case $k=0$. In geometric string model the field equations (3) – (5) become

$$3\frac{\dot{R}^2}{R^2} + 3\frac{\dot{R}}{R}\frac{\dot{A}}{A} = \rho,$$
$$2\frac{\ddot{R}}{R} + \frac{\dot{R}^2}{R^2} + 2\frac{\dot{R}}{R}\frac{\dot{A}}{A} + \frac{\ddot{A}}{A} = 0,$$
$$\frac{\ddot{R}}{R} + \frac{\dot{R}^2}{R^2} = \rho.$$

These equations can be interpreted as the field equations for five dimensional space-time with string membrane along the extra dimension [12]. The change of variables

$$x = \dot{R}/R, \quad y = \dot{A}/A,$$

reduce the about field equations (after eliminating ρ) in the canonical form

$$\dot{x} = -x^2 + xy,$$
$$\dot{y} = -x^2 - y^2 - 4xy. \tag{15}$$

It has only one critical point $(0,0)$ which is degenerate in nature. To analyse this dynamical system we introduce

$$u = x, \quad v = y/x, \quad \frac{d\tau}{dt} = |x| = \varepsilon x \quad (\varepsilon = \pm 1). \tag{16}$$

Then from (15) and (16)

$$\frac{du}{d\tau} = \varepsilon u(-1+v),$$
$$\frac{dv}{d\tau} = -\varepsilon(2v+1)(v+1). \tag{17}$$

The particular solutions of this system are

$$u = u_0 \exp[(v_i - 1)], \quad v_i = -1 \text{ or } -\tfrac{1}{2}. \tag{18}$$

These solutions correspond to the special solutions of the system (15) and can be interpreted as straight lines in the xy-plane. Also these solutions approach the degenerate critical point $(0,0)$ along the tangent vectors $(1, v_i)$.

We shall now discuss in detail the rectilinear solutions (18) which satisfy

$$\frac{du}{d\tau} = \varepsilon u(v - 1).$$

In the old variables we have

$$\frac{\dot{x}}{x^2} = (v_i - 1), \quad y = v_i x,$$

whose solutions are

$$x = \frac{-1}{(v_i - 1)t - 1/x_0}, \quad y = \frac{-1}{(1 - 1/v_i)t - (1/v_i x_0)}. \tag{19}$$

Here $(x_0, y_0 = v_i \cdot x_0)$ are the initial conditions in phase space. Therefore the scale factors have the expressions

$$R = K[(v_i - 1)t - 1/x_0]^{1/(1 - v_i)},$$
$$A = K[(1 - 1/v_i)t - 1/v_i \cdot x_0]^{(v_i/1 - v_i)}. \tag{20}$$

For expanding universe, the scale factor R should be an increasing function of time while the scale factor A corresponding to extra dimension should decrease or be a constant to have compactification of extra dimensions. This is possible for both $v_i : v_i = -\frac{1}{2}$ or -1. Thus the phase space analysis exhibits solutions which represent expanding universe with contraction of extradimensions.

Acknowledgement

The authors wish to thank the relativity and cosmology research group at the Jadavpur University, for helpful discussion.

References

[1] E Witten, *Phys. Lett.* **B144**, 351 (1984)
[2] W J Marciano, *Phys. Rev. Lett.* **52**, 489 (1984)
[3] P S Wesson, *Astron. Astrophys.* **119**, 145 (1983)
P S Wesson, *Astron. Astrophys.* **143**, 233 (1985)
[4] S Chakraborty and A Chakraborty, *Pramana – J. Phys.* **40**, 207 (1993)
[5] S Chatterjee, *Gen. Relativ. Gravit.* **18**, 1073 (1986)
S Chatterjee, *Astron. Astrophys.* **179**, 1 (1987)
[6] S Chatterjee, A Banerjee and B Bhui, *Phys. Lett.* **A140**, 91 (1990) and references therein
[7] T Fukui, *Gen. Relativ. Gravit.* **19**, 43 (1987)
[8] O Gron, *Astron. Astrophys.* **193**, 1 (1988)

[9] P S Letelier, *Phys. Rev.* **D28**, 2414 (1983)
[10] A Chodes and S Detweiler, *Phys. Rev.* **D21**, 2167 (1980)
[11] T Takabayashi, *Determinism, causality and particles* edited by M Flat (Reidel Derbreacht: Holland, 1978) p. 179
[12] B Boisseau and P S Letelier, *Class Quantum Gravit.* **8**, 1141 (1991)

SUBJECT INDEX

General and Mathematical Physics

Stationary anharmonic oscillators in the particle-in-a-box basis: Near-exact results *A K Chandra and K Bhattacharyya* 117–128

A basis-free approach to time-reversal for symmetry groups *L C Biedenharn and E C G Sudarshan* 255–272

Energy levels of the Schrödinger equation for some rational potentials in two-dimensional space using the inner product technique *M R M Witwit and J P Killingbeck* 279–288

A new perturbative approach to the classical anharmonic oscillator *S S Vasan and M Seetharaman* 411–420

Scaling relations in the Lyapunov exponents of one dimensional maps *P R Krishnan Nair, V M Nandakumaran and G Ambika* 421–429

Controlling chaos: Stabilization of fixed points and creation of new stable attractors in 1-D maps *Sangeeta D Gadre and V S Varma* 431–442

Relativity and Gravitation

The Lorentz–Dirac equation in curved spaces *Jose L Lopez-Bonilla, Jesus Morales and Marco A Rosales* 273–278

Statistical Physics

First-order transition in a 2D classical XY-model using microcanonical Monte Carlo simulations *Smita Ota and S B Ota* 129–137

A new formalism for the statistical dynamics of vector spin systems *Kamlesh Kumari and Deepak Kumar* 289–306

Particle Physics

Perturbative and nonperturbative quark masses in structure functions *D K Choudhury and Ranjita Deka* 139–153

Electromagnetic mass differences of t-flavored hadrons in modified bag model *Bishwaranjan Dash, Sripati Kumar Nayak and Lambodar P Singh* 155–163

Mass spectrum of elementary particles in a temperature-dependent model *G P Malik, Santokh Singh and V S Varma* 443–451

New answer to the solar neutrino problem *Marc Dixmier* 453–465

Dynamic color screening in a classical quark plasma *Jitesh R Bhatt, Predhiman K Kaw and Jitendra C Parikh* 467–476

Nuclear Physics

Single nucleon distribution based on shell-model and matrix ensemble theory *Nazakat Ullah* 165–168

Collective mechanism for nuclear stopping and transverse flow in heavy-ion collisions *Jitesh R Bhatt, Predhiman K Kaw and Jitendra C Parikh* 307–312

Effect of two body core on the charge form factor of ^{3}He including three body force and meson exchange current *Kalyani Prasad Kanta and Tapan Kumar Das* 313–318

Distribution of fusion barriers *A K Mohanty and S K Kataria* 319–338

Level structure in the odd–odd nucleus ^{180}Re *Ashok Kumar Jain, Prakash C Sood and Raymond K Sheline* 339–352

Atomic and Molecular Physics

Electron impact double ionization of Ba and Ba^+ *L K Jha, S N Chatterjee and B N Roy* 169–174

Use of a diabatic molecular expansion in studies on electron capture by He^{2+} ions in helium at keV energies *C Chaudhuri, S Sanyal (nee Ganguly) and T K Rai Dastidar* 175–179

Systematic trends in the line strengths of E1 transitions in the oxygen isoelectronic sequence *Anju Agrawal and K L Baluja* 477–485

Einstein A-coefficients for rotational transitions in the HN_2O^+ *S Chandra and A K Sharma* 487–493

Vibrationally elastic e^-–H_2O scattering at intermediate energies *K N Joshipura, Minaxi Vinodkumar and P M Patel* 495–502

Lasers, Optics and Spectroscopy

Enhanced bistability with the line-narrowed modes in a non-linear modulated index Fabry-Perot cavity *S Dutta Gupta* 67–72

New band system of MnSe molecule *K N Uttam, R Gopal and M M Joshi* 73–80

Overtone spectroscopy of benzaldehyde *P K Srivastava, G Ullas and S B Rai* 231–236

Fluorescence quenching in dyes under an optically thin approximation *George C Chennattucherry, G Ajithkumar and N V Unnikrishnan* 237–244

Condensed Matter Physics

Search for a precursor crystal-to-crystal phase transition to amorphization in α-GeO_2 and α-$AlPO_4$ under pressure *M S Somayazulu, Nandini Garg, Surinder M Sharma and S K Sikka* 1–9

Effect of Fe substitution on the thermal expansion of the high T_c superconductor $Y_1Ba_2Cu_3O_y$ *Ashok Rao, Om Prakash, S N Das and P N Dheer* 11–19

Magnetism, exchange and crystal field parameters in the orbitally unquenched Ising antiferromagnet $FePS_3$ *Nirmala Chandrasekharan and Sukumaran Vasudevan* 21–31

X-ray diffraction studies of RbBr-RbI mixed crystals *T Kumara Swamy, K G Subhadra and D B Sirdeshmukh* 33–39

Interplay of superconductivity and antiferromagnetism in $SmRh_4B_4$ *T C Loya and S L Kakani* 41–54

Photoconductivity and dark conductivity studies of solution-gas interface grown Ag_2S films *P S Nikam and C B Shinde* 55–65

Second order elastic anomalies in barium titanate from orthorhombic to rhombohedral phase transition *B Subramanyam* 181–187

High pressure studies on $AgI–Ag_2O–MoO_3$ glasses *B Vaidhyanathan, S Asokan and K J Rao* 189–192

Investigation of phonon anomalies in intermediate valence compounds SmS and $Sm_{0.75}Y_{0.25}S$ *Prafulla Kumar Jha and Sankar P Sanyal* 193–199

Computation of collective modes and acoustic investigations at different temperatures of vitrous silica *R V Gopala Rao and R Venkatesh* 201–209

Even harmonics of AC susceptibility in some sintered pellets of high temperature superconductors *A Das, A Bajpai, A Banerjee and R Srinivasan* 211–217

Electric and dielectric properties of solution-gas interface grown amorphous AgCl films *P S Nikam and K A Pathan* 219–229

Photoconductivity studies of ($PbCrO_4$–HgO–ZnO) composites
Sadhana Devi and S G Prakash 245–253

Sound velocity in binary liquid mixtures and the statistical mechanical theories *J D Pandey, Shikha, A K Shukla and Anil K Singh* 353–360

Isothermal compressibility and sound velocity of binary liquid systems: Application of hard sphere models *J D Pandey, P Jain and V Vyas* 361–372

Transport coefficients of quasicrystals *K Rama Mohan Rao and P Hemagiri Rao* 373–378

Phonons and periodons in IV–VI semiconductor superlattices
Nabonita D Chowdhury and Sankar P Sanyal 379–390

Electronic contribution to electric field gradient in β-gallium
B K Acharya and N C Mohapatra 391–400

Experimental Techniques and Instrumentation

Thermal diffusion factors of hydrogenic trace mixtures with helium by column calibration factor *G Dasgupta, A K Datta and S Acharyya* 81–89

Construction of broadband homonuclear TOCSY sequences via numerical optimization *N Sambasiva Rao and Narsimha Reddy* 91–99

Design and fabrication of a high temperature X-ray powder diffraction camera *Mohd. Ateequddin, K A Hussain, K G Subhadra and D B Sirdeshmukh* 101–115

Application of laser beam deflection technique to study the diffusion process in electrolyte solutions *Achamma Kurian, C V Bindhu, S S Harilal, Riju C Issac, V P N Nampoori and C P G Vallabhan* 401–406

Addendum

Electric field gradient in transition metal: Scandium
B B Panigrahi and N C Mohapatra 407–408

String theory in five dimensional cosmological models
Subenoy Chakraborty and Gopal Chandra Nandy 503–508

Corrigendum

Computation of collective modes and acoustic investigations at different temperatures of vitrous silica *R V Gopala Rao and R Venkatesh* 409–410

AUTHOR INDEX

Acharya B K
Electronic contribution to electric field gradient in β-gallium 391
Acharyya S
see Dasgupta G 81
Agrawal Anju
Systematic trends in the line strengths of E1 transitions in the oxygen isoelectronic sequence 477
Ajithkumar G
see Chennattucherry George C 237
Ambika G
see Krishnan Nair P R 421
Asokan S
see Vaidhyanathan B 189
Ateequddin Mohd.
Design and fabrication of a high temperature X-ray powder diffraction camera 101

Bajpai A
see Das A 211
Baluja K L
see Agrawal Anju 477
Banerjee A
see Das A 211
Bhatt Jitesh R
Collective mechanism for nuclear stopping and transverse flow in heavy-ion collisions 307
Dynamic color screening in a classical quark plasma 467
Bhattacharyya K
see Chandra A K 117
Biedenharn L C
A basis-free approach to time-reversal for symmetry groups 255
Bindhu C V
see Kurian Achamma 401
Chakraborty Subenoy
String theory in five dimensional cosmological models 503
Chandra A K
Stationary anharmonic oscillators in the particle-in-a-box basis: Near-exact results 117
Chandra S
Einstein A-coefficients for rotational transitions in the HN_2O^+ 487
Chandrasekharan Nirmala
Magnetism, exchange and crystal field parameters in the orbitally unquenched Ising antiferromagnet $FePS_3$ 21
Chatterjee S N
see Jha L K 169
Chaudhuri C
Use of a diabatic molecular expansion in studies on electron capture by He^{2+} ions in helium at keV energies 175
Choudhury D K
Perturbative and nonperturbative quark masses in structure functions 139
Chowdhury Nabonita D
Phonons and periodons in IV–VI semiconductor superlattices 379

Das A
Even harmonics of AC susceptibility in some sintered pellets of high temperature superconductors 211
Das S N
see Rao Ashok 11
Das Tapan Kumar
see Kanta Kalyani Prasad 313
Dasgupta G
Thermal diffusion factors of hydrogenic trace mixtures with helium by column calibration factor 81
Dash Bishwaranjan
Electromagnetic mass differences of *t*-flavored hadrons in modified bag model 155
Datta A K
see Dasgupta G 81
Deepak Kumar
see Kumari Kamlesh 289
Deka Ranjita
see Choudhury D K 139
Devi Sadhana
Photoconductivity studies of ($PbCrO_4$–HgO–ZnO) composites 245

Dheer P N
see Rao Ashok 11
Dixmier Marc
New answer to the solar neutrino problem 453
Dutta Gupta S
Enhanced bistability with the line-narrowed modes in a non-linear modulated index Fabry-Perot cavity 67

Gadre Sangeeta D
Controlling chaos: Stabilization of fixed points and creation of new stable attractors in 1-D maps 431
Garg Nandini
see Somayazulu M S 1
George C Chennattucherry
Fluorescence quenching in dyes under an optically thin approximation 237
Gopal R
see Uttam K N 73
Gopala Rao R V
Corrigendum 409

Harilal S S
see Kurian Achamma 401
Hemagiri Rao P
see Mohan Rao K Rama 373
Hussain K A
see Ateequddin Mohd. 101

Issac Riju C
see Kurian Achamma 401

Jain Ashok Kumar
Level structure in the odd–odd nucleus ^{180}Re 339
Jain P
see Pandey J D 363
Jha L K
Electron impact double ionization of Ba and Ba^+ 169
Jha Prafulla Kumar
Investigation of phonon anomalies in intermediate valence compounds SmS and $Sm_{0.75}Y_{0.25}S$ 193
Joshi M M
see Uttam K N 73
Joshipura K N
Vibrationally elastic e^-–H_2O scattering at intermediate energies 495

Kakani S L
see Loya T C 41
Kanta Kalyani Prasad
Effect of two body core on the charge form factor of ^{3}He including three body force and meson exchange current 313
Kataria S K
see Mohanty A K 319
Kaw Predhiman K
see Bhatt Jitesh R 307, 467
Killingbeck J P
see Witwit M R M 279
Krishnan Nair P R
Scaling relations in the Lyapunov exponents of one dimensional maps 421
Kumara Swamy T
X-ray diffraction studies of RbBr–RbI mixed crystals 33
Kumari Kamlesh
A new formalism for the statistical dynamics of vector spin systems 289
Kurian Achamma
Application of laser beam deflection technique to study the diffusion process in electrolyte solutions 401

Lopez-Bonilla Jose L
The Lorentz-Dirac equation in curved spaces 273
Loya T C
Interplay of superconductivity and antiferromagnetism in $SmRh_4B_4$ 41

Malik G P
Mass spectrum of elementary particles in a temperature-dependent model 443
Mohanty A K
Distribution of fusion barriers 319
Mohapatra N C
see Acharya B K 391
see Panigrahi B B 401
Morales Jesus
see Lopez-Bonilla Jose L 273

Nampoori V P N
see Kurian Achamma 401
Nandakumaran V M
see Krishnan Nair P R 421
Nandy Gopal Chandra
see Chakraborty Subenoy 503
Nayak Sripati Kumar
see Dash Bishwaranjan 155
Nikam P S
Photoconductivity and dark conductivity studies of solution-gas interface grown Ag_2S films 55
Electric and dielectric properties of solution-gas interface grown amorphous AgCl films 219

Ota S B
see Ota Smita 129
Ota Smita
First-order transition in a 2D classical XY-model using microcanonical Monte Carlo simulations 129

Pandey J D
Sound velocity in binary liquid mixtures and the statistical mechanical theories 353
Isothermal compressibility and sound velocity of binary liquid systems: Application of hard sphere models 363
Panigrahi B B
Electric field gradient in transition metal: Scandium 401
Parikh Jitendra C
see Bhatt Jitesh R 307, 467
Patel P M
see Joshipura K N 495
Pathan K A
see Nikam P S 219
Prakash Om
see Rao Ashok 11
Prakash S G
see Devi Sadhana 245

Rai Dastidar T K
see Chaudhuri C 175
Rai S B
see Srivastava P K 231
Rao Ashok
Effect of Fe substitution on the thermal expansion of the high T_c superconductor $Y_1Ba_2Cu_3O_y$ 11
Rao K Rama Mohana
Transport coefficients of quasicrystals 373
Rao K J
see Vaidhyanathan B 189
Rao N Sambasiva
Construction of broadband homonuclear TOCSY sequences via numerical optimization 91
Rao R V Gopala
Computation of collective modes and acoustic investigations at different temperatures of vitrous silica 201
Reddy Narsimha
see Rao N Sambasiva 91
Rosales Marco A
see Lopez-Bonilla Jose L 273
Roy B N
see Jha L K 169

Sanyal S (nee Ganguly)
see Chaudhuri C 175
Sanyal Sankar P
see Jha Prafulla Kumar 193
see Chowdhury Nabonita D 379
Seetharaman M
see Vasan S S 411
Sharma A K
see Chandra S 487
Sharma Surinder M
see Somayazulu M S 1
Sheline Raymond K
see Jain Ashok Kumar 339
Shikha
see Pandey J D 353
Shinde C B
see Nikam P S 55
Shukla A K
see Pandey J D 353
Sikka S K
see Somayazulu M S 1
Singh Anil K
see Pandey J D 353
Singh Lambodar P
see Dash Bishwaranjan 155
Singh Santokh
see Malik G P 443
Sirdeshmukh D B
see Kumara Swamy T 33
see Ateequddin Mohd. 101
Somayazulu M S
Search for a precursor crystal-to-crystal phase transition to amorphization in α-GeO_2 and α-$AlPO_4$ under pressure 1
Sood Prakash C
see Jain Ashok Kumar 339
Srinivasan R
see Das A 211
Srivastava P K
Overtone spectroscopy of benzaldehyde 231
Subhadra K G
see Kumara Swamy T 33
see Ateequddin Mohd. 101
Subramanyam B
Second order elastic anomalies in barium titanate from orthorhombic to rhombohedral phase transition 181
Sudarshan E C G
see Biedenharn L C 255

Ullah Nazakat
Single nucleon distribution based on shell-model and matrix ensemble theory 165
Ullas G
see Srivastava P K 231

Unnikrishnan N V
see Chennattucherry George C 237
Uttam K N
New band system of MnSe molecule 73

Vaidhyanathan B
High pressure studies on $AgI-Ag_2O-MoO_3$ glasses 189
Vallabhan C P G
see Kurian Achamma 401
Varma V S
see Gadre Sangeeta D 431
see Malik G P 443
Vasan S S
A new perturbative approach to the classical anharmonic oscillator 411
Vasudevan Sukumaran
see Chandrasekharan Nirmala 21
Venkatesh R
see Rao Gopala R V 201, 411
Vinodkumar Minaxi
see Joshipura K N 495
Vyas V
see Pandey J D 363

Witwit M R M
Energy levels of the Schrödinger equation for some rational potentials in two-dimensional space using the inner product 279